Low-Mass Dark Matter Search Results and Radiogenic Backgrounds for the Cryogenic Dark Matter Search

A DISSERTATION
SUBMITTED TO THE FACULTY OF THE GRADUATE SCHOOL
OF THE UNIVERSITY OF MINNESOTA
BY

Mark David Pepin

IN PARTIAL FULFILLMENT OF THE REQUIREMENTS
FOR THE DEGREE OF
Doctor of Philosophy

Dr. Priscilla Cushman, Advisor

December, 2016

Acknowledgements

Dissertations are often considered the "culminating work" of the individual author, but the author never truly acts alone in creating the research. A network of people has stood behind and supported me during my graduate years, and I can say with certainty that this accomplishment is only possible because of them.

The University of Minnesota CDMS group has most directly supported and pushed the scientific research contained herein. As the Ph.D. system essentially still follows a medieval guild/apprenticeship model, deep appreciation is due first and foremost to my advisor, Prisca Cushman. Your guidance and keen insight improved my work immensely and pushed me to consider all things possible. Thank you for mentoring me in the ways of being a research physicist. Much advice was also given by Vuk Mandic during group meetings, and he often gave a perspective previously overlooked.

When I joined the UMN group, three members in particular were there to bring me into the fold. They were crucial in helping me navigate both the CDMS Collaboration and the ways of lunching. I am grateful to Scott Fallows, Tommy Hofer, and Anthony Villano for helping me develop as a scientist and for collectively enduring the many near-futile attempts to obtain chips at Leo's Burritos. I owe thanks also to D'Ann Barker, who later came along and was always encouraging and supportive in our search for the liquid dark matter which keeps the universe going: R.I.P. Espresso Expose and the wonderful caffeine supplied there. To the members of "the lab", Hassan Chagani, Matt Fritts, Jianjie Zhang, Roxanne Radpour, Allison Kennedy, Hannah Rogers, Nick Mast, and David Standberg, thanks for the general support and to Roxanne and Allison in particular for mad softball managing skills.

To my classmates in graduate school: we survived the rigors of classes, the GWE, and adjusting to life in graduate school together. That support structure was crucial to

I owe everything to my family. To Mom and Dad, I can only guess your thoughts when your third son ALSO declared as a physics major. Thank you for putting up with the many nerdy conversions around holiday dinner tables, for showing patience on my long road here, and for always encouraging me to give my all in everything I do. To John and Eric, thank you for being role models in your academic pursuits and pushing me to do better at every turn. To my boys Gabriel and David, your smiles and giggles are infectious and always helped lift me up when I was over-stressed and over-worried.

Lastly, words cannot express my indebtedness and gratitude to my wife, Kay. I know there were times when you weren't *quite* convinced that I was actually going to finish. I love you for sticking with me until the end, wrestling with our young ones by yourself so I could work, and humoring me as I fretted over this detail or that. Although I'm sure being formally known as Dr. and Mr. Pepin was good fun for you, I am finally here and look forward to tackling what's next as the Drs. Pepin.

For my wife, Kay,
who has encouraged and suported me since I first learned to love physics.

Abstract

An ever-increasing amount of evidence suggests that approximately one quarter of the energy in the universe is composed of some non-luminous, and hitherto unknown, "dark matter". Physicists from numerous sub-fields have been working on and trying to solve the dark matter problem for decades. The common solution is the existence of some new type of elementary particle with particular focus on weakly interacting massive particles (WIMPs). One avenue of dark matter research is to create an extremely sensitive particle detector with the goal of directly observing the interaction of WIMPs with standard matter. The Cryogenic Dark Matter Search (CDMS) project operated at the Soudan Underground Laboratory from 2003–2015, under the CDMS II and SuperCDMS Soudan experiments, with this goal of directly detecting dark matter. The next installation, SuperCDMS SNOLAB, is planned for near-future operation.

The reason the dark-matter particle has not yet been observed in traditional particle physics experiments is that it must have very small cross sections, thus making such interactions extremely rare. In order to identify these rare events in the presence of a background of known particles and interactions, direct detection experiments employ various types and amounts of shielding to prevent known backgrounds from reaching the instrumented detector(s). CDMS utilized various γ and neutron shielding to such an effect that the shielding, and other experimental components, themselves were sources of background. These radiogenic backgrounds must be understood to have confidence in any WIMP-search result. For this dissertation, radiogenic background studies and estimates were performed for various analyses covering CDMS II, SuperCDMS Soudan, and SuperCDMS SNOLAB.

Lower-mass dark matter $\left(\mathcal{O}\left(10 \text{ GeV}/c^2\right)\right)$ has become more prominent in the past few years. The CDMS detectors can be operated in an alternative, higher-biased, mode

to decrease their energy thresholds and correspondingly increase their sensitivity to low-mass WIMPs. This is the CDMS low ionization threshold experiment (CDMSlite), which has pushed the frontier at lower WIMP masses. This dissertation describes the second run of CDMSlite at Soudan: its hardware, operations, analysis, and results. The results include new WIMP mass-cross section upper limits on the spin-independent and spin-dependent WIMP-nucleon interactions. Thanks to the lower background and threshold in this run compared to the first CDMSlite run, these limits are the most sensitive in the world below WIMP masses of ~ 4 GeV/c^2. This demonstrates also the great promise and utility of the high-voltage operating mode in the SuperCDMS SNOLAB experiment.

Table of Contents

List of Tables

List of Figures

xxiii

Part I

Introduction

Chapter 1

The Missing Matter Problem

1.1 The History of Cosmology

Human beings have theorized on the origin of the universe since the dawn of civilization. The earliest cosmological descriptions were in the form of mythical creation accounts, such as the *Enuma Elish* of Mesopotamia [1], the stories of Atum or Ptah of Egypt [2], or the Genesis account of Israel [3]. Hellenistic natural philosophers first proposed theories which purported general principles later adopted, and definitively proven, by modern science. Democritus (c.460–c.370 BCE) hypothesized that matter is composed of discrete building blocks: atoms. The theoretical basis for the modern atomic theory of matter would be derived by Einstein over 2000 years later [4]. Aristarchus of Samos (c.310–c.230 BCE) was the first known Western philosopher of heliocentricism, the theory that the Earth revolves around the sun as opposed to the commonly held opposite view [5]. By the premises that the Sun and stars remain fixed, with the planets moving around the Sun, Aristarchus also correctly deduced that in order to explain the non-observation of parallax, the stars must be at a much greater distance than was commonly thought. The ancient natural philosophers were faced with two choices: (1) a geocentric universe or (2) this vast distance to the stars. Choice (1) was accepted almost exclusively, including by Ptolemy (c.100–c.170 CE) [6], whose mathematical model of the universe, coupled with the physical model of Aristotle (384-322 BCE) [7], would dominate the Western view of the cosmos for hundreds of years to come.

The heliocentric idea did not re-enter Western thought on a grand scale until the 16$^{\text{th}}$

century with the publication of *De revolutionibus orbium coelestium* by Copernicus [8].[1]
His heliocentric hypothesis began what is commonly called "The Copernican Revolu-
tion" and contributed to the budding, early-modern, science of the day. The Copernican
system was advocated for by Kepler [10] and Galileo [11], however a common objection
during their time was that there was no believable physical model upon which to base
the heliocentric construct. Such a physical model was provided by Newton in 1687 [12]
in the form of his law of universal gravitation

$$\boldsymbol{F} = \frac{G_{\mathrm{N}}m}{r^2}M(r)\,\hat{\boldsymbol{r}} \tag{1.1}$$

$$= \frac{G_{\mathrm{N}}m}{r^2}\int_{V(r'<r)}\rho(r')\,\mathrm{d}V'\,\hat{\boldsymbol{r}}, \tag{1.2}$$

where $\boldsymbol{F}$ is the magnitude of the force exerted on a mass m, a distance r from the mass
distribution $M(r)$, which has density $\rho(r)$ within the volume V. The direction of the
force $\hat{\boldsymbol{r}}$ points from m to the center of mass of $M(r)$. The proportionality constant,
called Newton's Gravitational Constant, is measured as $G_{\mathrm{N}} = 6.671 \times 10^{-11}\ \mathrm{N\,m^2\,kg^{-2}}$.
The "universal" aspect of Newton's theory was that he applied the same law at all
length scales: on the Earth, Earth and Moon, Earth and Sun, Sun and other planets,
Sun and other stars. This last idea led to the realization that the Sun and other stars
are of the same type of object in an infinite space [13].[2]

The "Copernican Principle," which initially only applied to the universe revolving
around the Sun instead of the Earth, was now broadened to include the concept that the
Sun has no privileged location in the universe. Armed with the now fully accepted theory
of Newton, the attention of astronomers for the 18th and 19th centuries focused on the
previously conceived "fixed" stars. The stars were found to have proper motion (thus,
not at all fixed) [14], distances were computed by finally observing stellar parallax [15],
the theory of Milky Way as a entity composed of many stars was proposed [16] and
solidified by observations [17], and nebulae were discovered, some of which were later
resolved to be composed of stars, leading to the "island universe" theory expounding
non-Milky Way galaxies [18]. Other areas of science, such as spectroscopy, chemistry,

---

[1] Although Copernicus certainly knew of Aristarchus as one of many ancient philosophers, the
assertion that his heliocentric ideas were directly influenced by Aristarchus is weak [9].

[2] Albeit, Newton recognized that it was an infinite space which would collapse under gravity without
intervention from another agent.

and thermodynamics, were also applied to the heavens (the birth of astrophysics), which in turn lead to a return of true cosmological questions: where did the universe come from, will the universe end, and is it truly infinite? These were the primary questions asked and tools available leading into the 20th century, when a new model to describe the universe was discovered and modern cosmology born.

1.2 Evolution and Contents of the Universe

Einstein's general theory of relativity [19] is the tool used by modern cosmologists to model the universe. His theory relates the geometry of space-time to its contents through the field equations

$$G_{\mu\nu} = \frac{8\pi G_{\text{N}}}{c^4} T_{\mu\nu} - \Lambda g_{\mu\nu}, \tag{1.3}$$

where the Einstein tensor $G_{\mu\nu}$[3] contains all geometrical information, the energy-momentum tensor $T_{\mu\nu}$ describes the contents of space-time, and Λ is an allowed cosmological constant. Einstein's tensor depends upon the metric $g_{\mu\nu}$ for the given space-time. To describe the universe as a whole, modern physicists again expand the Copernican Principle to the "Cosmological Principal," which states that the mass distribution of the universe is isotropic and homogeneous. Such a universe is uniquely described by the Robertson-Walker (RW) metric[4]

$$(c\,\mathrm{d}\tau)^2 = -(c\,\mathrm{d}t)^2 + a(t)\left(\frac{1}{1-\kappa r^2}\,\mathrm{d}r^2 + r^2\left(\mathrm{d}\theta^2 + \sin^2\theta\,\mathrm{d}\phi^2\right)\right), \tag{1.4}$$

where $\mathrm{d}\tau$ is the differential interval, κ is a constant describing the curvature of the universe, $a(t)$ is a dimensionless scale factor allowing for the expansion of the universe, and elements of $g_{\mu\nu}$ are given by pre-factors of the corresponding spherical-coordinate differentials. If $\kappa = 0$, the universe is flat while for $\kappa \gtrless 0$ the universe is closed/open respectively. The scale factor is defined such that, for the present time t_0, $a(t_0) \equiv a_0 = 1$.

---

[3] Greek letters index over $\alpha \in \{0, 1, 2, 3\}$.

[4] The metric was originally discovered separately by Friedmann [20] and Lemaître [21] and then generally studied by Robertson [22] and Walker [23]. The full title is often given as the FLRW metric, or any variant of these letters.

The solutions to the field equations using the RW metric are the Friedmann equations

$$\left(\frac{\dot{a}}{a}\right)^2 = \frac{8\pi G_{\mathrm{N}}}{3}\rho - \frac{\kappa c^2}{a^2} + \frac{\Lambda c^2}{3} \tag{1.5}$$

$$\frac{\ddot{a}}{a} = -\frac{4\pi G_{\mathrm{N}}}{3}\left(\rho + \frac{3p}{c^2}\right) + \frac{\Lambda c^2}{3}, \tag{1.6}$$

where ρc^2 and p are the energy density and pressure of the given contents of space-time.[5] The left-hand-side of Eq. 1.5 defines the Hubble parameter $H \equiv \dot{a}/a$. The current value of the Hubble parameter is termed the Hubble Constant and is often parameterized as $H_0 = 100 \cdot h \ \mathrm{km\,s^{-1}\,Mpc^{-1}}$. The Friedmann equations demonstrate how the evolution of the universe depends completely on its contents.

The primary components of the universe are radiation (electromagnetic radiation or relativistic particles), matter (dust, non-relativistic particles), and cosmological constant (which is identified with the modern observations of dark energy). The matter and radiation energy densities ρ_{M} and ρ_{R} enter the Friedmann equations through the energy density as $\rho = \rho_{\mathrm{M}} + \rho_{\mathrm{R}}$. The energy density of the cosmological constant ρ_{Λ} is defined to mimic ρ_{M} and ρ_{R} as

$$\rho_{\Lambda} = \frac{\Lambda c^2}{8\pi G_{\mathrm{N}}}. \tag{1.7}$$

This allows Eq. 1.5 to be rewritten, summing over $i = \mathrm{M, R, \Lambda}$, as

$$1 = \sum_i \frac{8\pi G_{\mathrm{N}}}{3H^2}\rho_i - \frac{\kappa c^2}{H^2 a^2} \tag{1.8}$$

$$1 = \sum_i \frac{\rho_i}{\rho_c} + \frac{\rho_{\kappa}}{\rho_c} \tag{1.9}$$

$$1 = \sum_i \Omega_i + \Omega_{\kappa} \tag{1.10}$$

$$1 = \Omega + \Omega_{\kappa} \tag{1.11}$$

where several new notations have been introduced. For each component of the universe, the density parameter Ω_i of that component is defined as the ratio between ρ_i and the

---

[5] As defined here ρ is a mass density, but it is still called the energy density, with any factors of c implied.

Component	w_i	$\rho_i(a)$	$a(t)$
Matter	0	$\propto a^{-3}$	$\propto t^{2/3}$
Radiation	1/3	$\propto a^{-4}$	$\propto t^{1/2}$
Cosmological Constant	−1	Constant	$\propto e^{H_\Lambda t}$
Curvature	−1/3	$\propto a^{-2}$	$\propto t$

Table 1.1: Components of the universe, their equation of state parameters, how their energies densities evolve as functions of the scale factor, and how a universe composed of just that component would evolve as a function of time.

critical density

$$\rho_c \equiv \frac{3H^2}{8\pi G_{\mathrm{N}}}. \tag{1.12}$$

The sum of the physical energy densities is called the total density parameter Ω.[6] The curvature term in the Friedmann equation, although a global characteristic of space-time and not a physical component, is also written in terms of an effective density $\rho_\kappa/\rho_c \equiv \Omega_\kappa$, where $\rho_\kappa \equiv -3\kappa c^2/8\pi G_{\mathrm{N}} a^2$.

How exactly these components, and therefore the universe, evolve with time is determined from energy-momentum conservation:

$$\rho_i = \rho_{i,0} a^{-3(1+w_i)} \tag{1.13}$$

$$\Omega_i = \left(\frac{H_0}{H}\right)^2 \Omega_{i,0} a^{-3(1+w_i)}, \tag{1.14}$$

where the subscript 0 indicates the current value of a quantity and w_i defines the equation of state for each component as $p = w\rho c^2$. The Friedmann equation can be solved for an individual component by using Eq. 1.13. The equation of state parameters and how the density and scale factor evolve for each component are summarized in Table 1.1. For all cases, $a \to 0$ as $t \to 0$, i.e. a single component universe expands with time.

The evolution of the Hubble parameter, either into the past or future, is found from

---

[6] The use of subscripts on density parameters can be inconsistent and confusing in the literature and context is often necessary to determine which quantity is being discussed.

inserting Eq. 1.14 into Eq. 1.10 as

$$H^2 = H_0^2 \left(\Omega_{M,0} a^{-3} + \Omega_{R,0} a^{-4} + \Omega_{\Lambda,0} + (1 - \Omega_0)\, a^{-2} \right), \tag{1.15}$$

where the contribution from curvature is measured from the sum of the other components via Eq. 1.11. Yet another common notation for discussing the evolution of the universe is cosmological redshift, which measures the shift in the wavelength of light between when it was emitted and absorbed due to the expansion of space between the source and receiver

$$z \equiv \frac{\lambda_{\text{obs}}}{\lambda_{\text{emit}}} - 1 = \frac{a_0}{a} - 1. \tag{1.16}$$

In the past, $z \to \infty$ while at the present $z_0 = 0$.

Equation 1.15 implies that the early universe ($a \to 0$) was dominated by radiation, with density $\rho_{\text{R}} \propto a^{-4}$ tending towards large values. From the Stephan-Boltzmann law [24, 25], the density is related to the temperature as $\rho_{\text{R}} \propto T^4$. Thus, in earlier times, the universe was smaller, denser, and hotter and it has been expanding and cooling ever since. This is the idea popularly called the "Big Bang." The predictions of the Big Bang, and their subsequent measurements, are immensely important for modern cosmology.

Combining various forms of measurements yields the observed parameters of the universe given in Table 1.2. The curvature of the universe is consistent with a flat geometry. Assuming flatness, the current dominant component is the cosmological constant, which is identified with the accelerated expansion of the universe and attributed to dark energy [26, 27].[7] The contribution from radiation is negligible in the present epoch. Matter composes $\sim 31\,\%$ of the energy density, but only $\sim 16\,\%$ is accounted for by baryons with the remainder attributed to non-baryonic, non-relativistic (cold), and non-luminous dark matter. This model for the universe, which contains no curvature, dark energy (Λ), and cold dark matter (CDM) is termed the standard ΛCDM model.

---

[7] Whether the equation of state of dark energy is identically $w = -1$, i.e. whether it is a true constant, is still an active area of study yielding $w = -1.019^{+0.075}_{-0.08}$ [28]. For the purposes here, $w = -1$ is assumed.

Parameter	Symbol	Value
Hubble Constant	$H_0 = 100h$	67.74 ± 0.46 km s^{-1} Mpc^{-1}
Curvature	$\Omega_{\kappa,0}$	$0.0008^{+0.0040}_{-0.0039}$
Matter Density	$\Omega_{\mathrm{M},0}$	0.3089 ± 0.0062
Baryon Density	$\Omega_{\mathrm{B},0}$	0.0499 ± 0.0022
Cosmological Constant Density	$\Omega_{\Lambda,0}$	0.6911 ± 0.0062
Radiation Density	$\Omega_{\mathrm{R},0}$	$(9.161 \pm 0.057) \times 10^{-5}$

Table 1.2: Cosmological Parameters of the observed universe [28, 29]. The radiation density is found through the measured redshift of the matter-radiation equality epoch.

1.3 Evidence for Dark Matter

The evidence that a majority of the matter in the universe is non-baryonic, non-relativistic, and non-luminous comes from numerous astrophysical and cosmological sources from both cosmic (large) and galactic (small) length scales. Historically, this problem has been termed the "missing matter problem," and this section presents a selection of these indicators to argue the case that dark matter is essential to the modern understanding of the universe.

1.3.1 Galactic Dynamics

One of the most striking pieces of evidence for dark matter comes from the observation of galactic rotation curves. In understanding the rotational dynamics of spiral galaxies, simple Newtonian dynamics are still valid. The expected rotational velocity of an object at some radius r from a mass distribution $M(r)$ is found by equating Eq. 1.1 to the centripetal force which gives

$$v_{\mathrm{rot}} = \sqrt{\frac{G_{\mathrm{N}} M(r)}{r}}. \tag{1.17}$$

At distances greater than the size of the distribution, $v_{\mathrm{rot}} \propto r^{-1/2}$. For a spiral galaxy, the distribution $M(r)$ corresponds to the luminous bulge and disk and the fall-off is expected for objects orbiting outside of the disk.

In the 1970's, it was discovered that the measured rotation curves of spiral galaxies generally did not match this expected relationship. The earliest measurements were
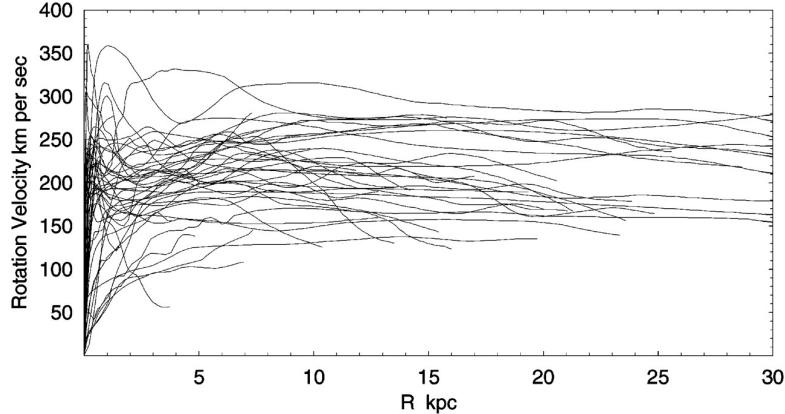
Figure 1.1: Rotation curves of several spiral galaxies showing the rotational velocity of astrophysical bodies as a function of their distance from the center of the galaxy. The flat behavior at high radii indicates a source of matter with density $\rho \propto r^{-2}$ in addition to the luminous disk. Figure from [32].

done by Rubin [30, 31] and a selection of measured curves can be seen in Fig. 1.1. The velocities are found by measuring the Doppler shift of spectral features such as the carbon monoxide line in the inner portion of the galaxy, optical lines in the disk and the HI line outside of the luminous disk [32]. As is evident in the figure, these curves do not fall as $r^{-1/2}$ at high radii. This implies a mass distribution of $\rho(r) \propto r^{-2}$. Additional measurements of the scale height of HI gas in the Milky Way indicate that the density extends above the disk plane [33], suggesting a roughly spherical halo of dark matter surrounding the galaxy [34].

Dark matter is also needed at a smaller scale to explain discrepancies in the number of dwarf galaxies which accompany the Milky Way. Structure formation predictions typically estimate a larger number of dwarf galaxies than are observable with luminous matter [35, 36]. The commonly proposed solution is that there are dark-matter dominated dwarf galaxies which make up the difference [37, 38]. Numerous such dark-matter dominated dwarf galaxies have recently been discovered using the Sloan Digital Sky Survey [39–41], Keck II telescope [42], and the Dark Energy Survey [43–46]. The observation of these primarily dark matter dwarf galaxies bring observations and predictions closer to agreement and also demonstrate that dwarf galaxies are some of the most dark-matter dominated objects in the universe.

1.3.2 Galaxy Clusters

The earliest evidence acknowledging that there may be non-luminous matter in the universe came from the study of galaxy clusters in the 1930's by Zwicky and Smith. The basis for these studies was to use the observed velocities of the galaxies in the cluster to determine the total mass of the cluster. This was done through the virial theorem, assuming the clusters are gravitationally bound and in equilibrium,

$$2 \langle T \rangle = \langle V \rangle, \tag{1.18}$$

where $\langle T \rangle$ and $\langle V \rangle$ are the average kinetic and potential energies of the system. This then implies

$$\langle v^2 \rangle \sim G_{\mathrm{N}} M \left\langle \frac{1}{r} \right\rangle. \tag{1.19}$$

Using the best estimates for the individual galaxies' velocity and estimates of the size of the cluster, Zwicky estimated that the mass of the Coma cluster was several hundred times larger then that estimated from the luminous matter [47, 48]. His 1933 paper stated, "If this would be confirmed we would get the surprising result that dark matter is present in much greater amount than luminous matter." [47], which is the first use of the phrase "dark matter". Smith performed a similar computation on the Virgo cluster [49] and reached similar conclusions. Although the numerical accuracy of these early results are no longer correct, their general conclusions still hold.

Only ~10 % of the universe's baryons are in stars/galaxies, leaving the rest dispersed as dust between these bodies (Sec. 1.3.3). In a galaxy cluster, this intracluster medium (ICM) falls into the cluster's deep potential well, compresses, heats up, and emits x rays [50]. Observing these x rays gives an indication of the mass and distribution of the ICM. Using Chandra data of 13 nearby galaxy clusters, Vikhlinin *et al.* found that the ICM composed only ~5–10 % of the total cluster mass [51], implying the majority of the mass is non-baryonic. Cluster dynamics can also be used to measure cosmological parameters, giving values of Ω_{M} and the equation of state of dark energy [52].

Gravitational lensing is also used to determine the mass of galaxy clusters. Lensing is a prediction of general relativity whereby massive bodies bend rays of light. How the light is bent depends upon the profile of the lensing mass, and thus a measured

deflection pattern from background sources can be used to infer a foreground mass distribution [53].

A spectacular example of the convergence of the x-ray and lensing techniques is that of cluster 1E 0657-558, commonly called the "Bullet Cluster" [54]. This cluster is in fact a merger of two subclusters, where the centers of the clusters passed through each other ~100 Myr ago. During such a merger, the galaxies themselves are expected to act as point particles and pass each other by, while the ICMs should collide and become stalled between the centers of the two clusters. Observations of x rays from the Chandra telescope show exactly this [55]. This is compared with the gravity map derived from gravitational lensing, which finds the centers of gravity coinciding with the luminous matter. The conclusion is that the center of baryonic matter (the ICM) and the centers of gravity (dark matter) do not coincide. This can be interpreted by the presence of collisionless[8] dark matter, centered on the luminous clusters, which also passed through itself while the baryonic matter was stripped in the collision. These measurements are artistically represented in Fig. 1.2, where an optical image from the Hubble Space Telescope and Magellan telescopes is overlaid with color maps representing the Chandra x-ray measurement and lensing map. A similar configuration is seen in cluster MACS J0025.41222 [57] while cluster Abel 520 appears to show the x-ray and lensing maps overlapping in the center of the collision, neither of which correspond to the optical structure [58]. Resolving the observations in Abel 520 is an open area of investigation.

1.3.3 Big-Bang Nucleosynthesis

In the hot and dense early universe, all particles were in thermal equilibrium with the radiation background, i.e. the creation and annihilation rates of processes were equal. At $t \sim 1$–3 min after the Big Bang, the universe cooled enough such that free protons and neutrons could enter bound states and form light nuclei. This processes, known as Big-Bang Nucleosynthesis (BBN), created the majority of the light elements in the universe.

The full process was governed by a set of differential equations [60], which depend upon several parameters: the number of relativistic degrees of freedom at the current

---

[8] Limits can be set on the self-interacting properties of dark matter from such a situation [56].
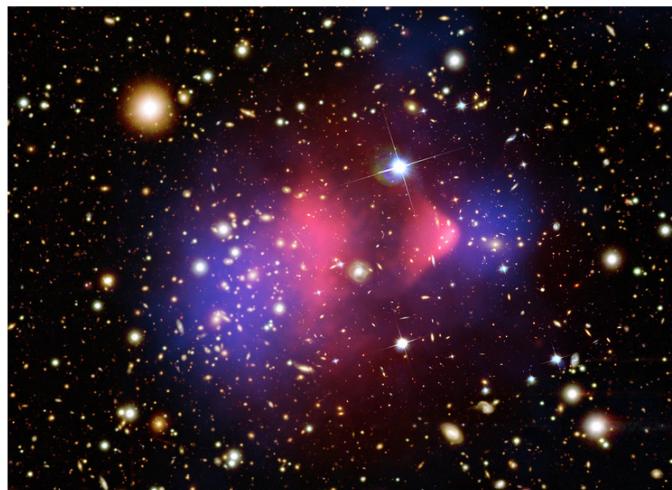
Figure 1.2: Composite image of the Bullet Cluster (1E 0657-558). The red and blue shading represent the center of mass according to x ray and weak lensing respectively. The shading do not overlap, implying that the hot ICM, which emits x rays, does not correspond to the bulk of the matter in the cluster. Photo credit: X-ray: NASA/CXC/CfA/M.Markevitch *et al.*; Optical: NASA/STScI; Magellan/U.Arizona/D.Clowe *et al.*; Lensing Map: NASA/STScI; ESO WFI; Magellan/U.Arizona/D.Clowe *et al.* [59].

temperature, nuclear physics to dictate how the elements formed, and the baryon-to-photon ratio $\eta = n_B/n_\gamma$, where n_B and n_γ are the baryon and photon number densities. In brief, how much and at what temperature an element formed was governed by how the binding energy of the nuclei related to the energy distribution of the background radiation. If η was higher, the high-energy tail of the distribution would have delayed the formation of elements. BBN calculations predict the primordial abundance of ^{2}D, ^{3}H, ^{3}He. ^{4}He, ^{7}Li, and ^{7}Be.[9] The last two were the heaviest nuclei formed in BBN due to the instability of the next accessible nuclei. Heavier elements were later created astrophysically in the burning of stars, where systems with higher metalicity (more higher-Z nuclei, "metals") are younger as they were created from the matter of previous stars.

The predictions of BBN depend upon all physics at higher energies, including potentially new dark matter physics [29, 61]. These predictions are compared with astrophysical measurements (see, e.g. [61, 62] for reviews of these measurements) of primordial elemental abundances in Fig. 1.3 as a function of η. The predictions and measurements of ^{4}He and deuterium are in good agreement, while that of ^{7}Li, which is most sensitive to nuclear physics and/or new physics, is not. Solving the "lithium problem" is an outstanding area of research.

The precise measurement of deuterium, using low-metalicity quasars, gives a measurement of $(5.8 \leq \eta \leq 6.6) \times 10^{-10}$ at the 90 % confidence level [29]. Since the n_B and n_γ dilute equally with the expansion of the universe, a measurement of η also gives a measurement of $\Omega_{B,0}$ as

$$\eta = \frac{n_B}{n_\gamma} = \frac{\Omega_{B,0}\rho_{c,0}}{\langle m_B \rangle \, n_{\gamma,0}}, \tag{1.20}$$

where $\langle m_B \rangle$ is the average baryon mass (close to that of a proton) and $n_{\gamma,0}$ is independently measured through the cosmic microwave background radiation (Sec. 1.3.4). The bounds on the baryonic-matter density parameter are then

$$0.021 \leq \Omega_{B,0}h^2 \leq 0.024 \tag{1.21}$$

at 95 % confidence [29]. Using the value of h in Table 1.2 gives $0.027 \leq \Omega_{B,0} \leq 0.053$, significantly less than the total matter content of the universe $\Omega_{M,0} \sim 0.3$: a majority

---

[9] ^{7}Be decays by electron capture to ^{7}Li.
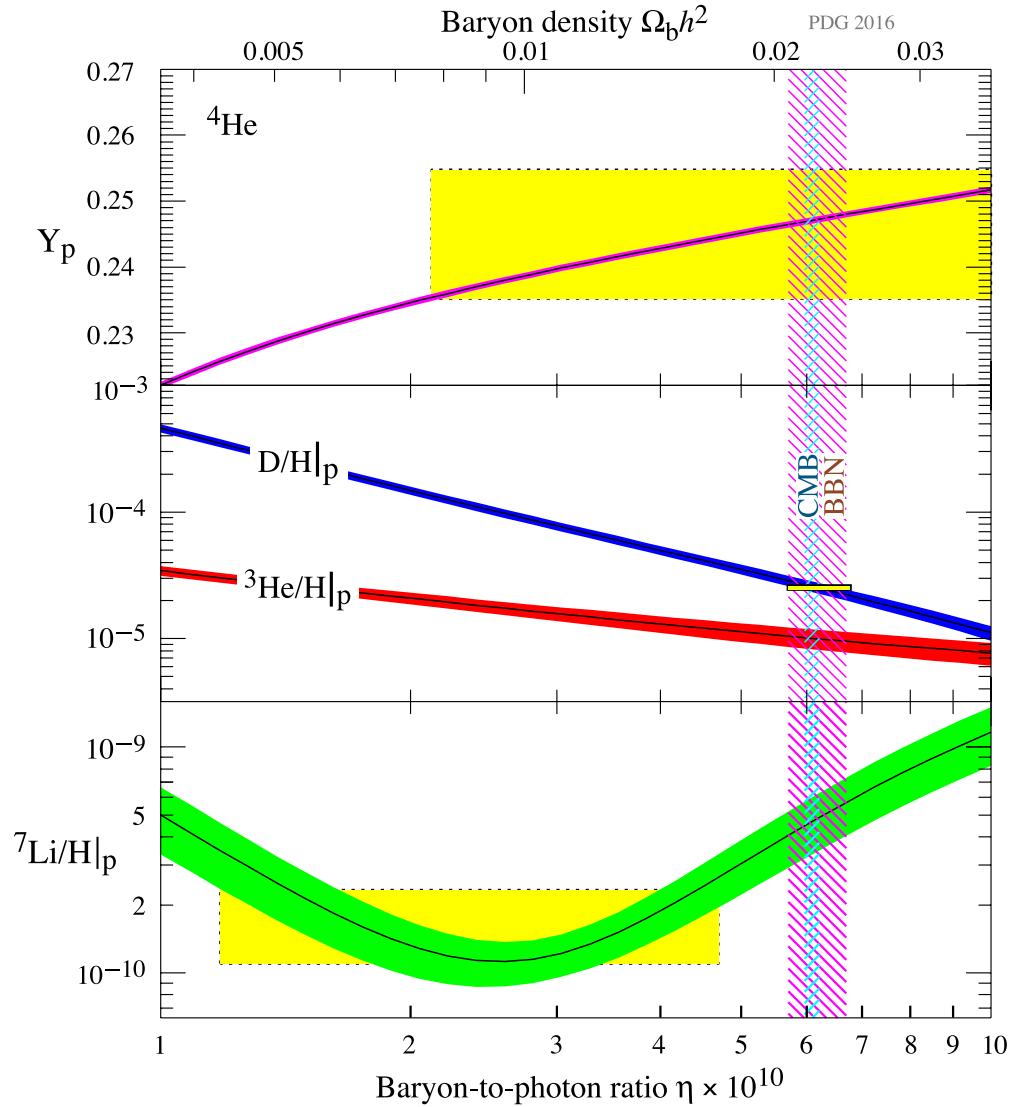
Figure 1.3: Comparison of the predictions of BBN and astrophysical observations (yellow boxes) for primordial abundances of ^{4}He (magenta band, Y_p is the mass abundance of ^{4}He), ^{2}D (blue band), ^{3}He (red band), and ^{7}Li (green band). The vertical bands indicate the baryon-to-photon ratio η inferred from the deuterium abundance (magenta hatch) and CMB (cyan hatch). Figure from [29].

of the matter in the universe, according to BBN, must be non-baryonic.[10]

1.3.4   Cosmic Microwave Background Radiation

At $z = 1089.90 \pm 0.23$ ($t = 372,000$ yr) [28] recombination and decoupling occurred. Recombination was the process by which free protons and electrons became bound into neutral hydrogen. In doing so, the free electron density n_e greatly decreased, as did the interaction rate for Thomson scattering of radiation with those electrons $\Gamma_\gamma = n_e \sigma_T$. As this rate fell below the expansion rate of the universe, matter and radiation lost thermal contact. The mean-free-path of the radiation increased to the s of the universe, and the decoupled photons have been mostly free-streaming ever since. They have been red-shifted to the microwave and are known as the Cosmic Microwave Background (CMB) radiation.

If the universe were completely homogeneous and isotropic, as the cosmological principle assumes, then the prediction from the hot Big-Bang model is a perfect blackbody power spectrum for the CMB. To within very small precision, the CMB is observed to be this blackbody with a temperature of 2.72548 ± 0.00057 K [64]. However, the cosmological principle breaks down on small scales as anisotropies are observed in the temperature map at the level of 10^{-5}. Much information about the content of the universe can be obtained for studying these anisotropies, a recent map of which is shown in Fig. 1.4 from the Planck satellite.

The anisotropies are typically decomposed into a spherical harmonic expansion as

$$T(\theta, \phi) = \sum_{\ell m} a_{\ell m} Y_{\ell m}(\theta, \phi). \tag{1.22}$$

The angular power spectrum from the decomposition is

$$C_\ell = \frac{1}{2\ell + 1} \sum_{m=-\ell}^{\ell} |a_{\ell m}|^2, \tag{1.23}$$

---

[10] Additionally, the luminous-matter density parameter of the universe is $\Omega_{\mathrm{Lum}} \simeq 0.0016$ [63], indicating that most baryonic matter is itself dark; likely diffuse intergalactic medium such as the ICM in clusters.
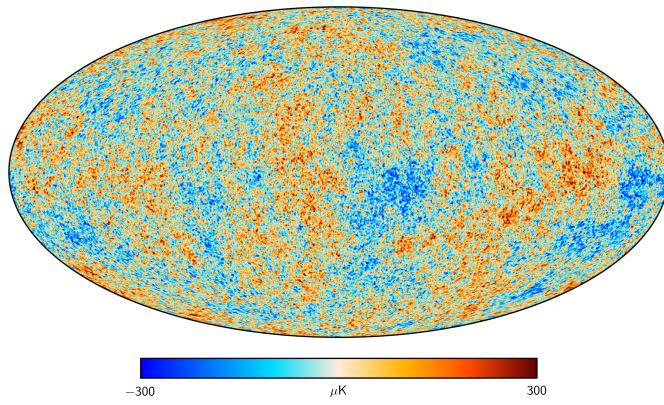
Figure 1.4: Temperature anisotropy map of the CMB from a joint analysis of the Planck satellite, WMAP satellite, and 408 MHz emission as performed by the Planck collaboration. These anisotropies are on the order of 10^{-5} compared to the monopole blackbody spectrum with temperature 2.72548 ± 0.00057 K. Cosmological parameters can be derived from the power spectrum corresponding to the anisotropies. Image credit: ESA [65]

and the "band power," the quantity usually plotted, is $\mathcal{D}_\ell^{TT} = \ell\,(\ell+1)\,C_\ell/2\pi$.[11] The monopole ($\ell = 0$) portion of this expansion corresponds to the perfect blackbody component while the dipole ($\ell = 1$) corresponds to Doppler shifting of the monopole component due to the galaxy moving relative to the CMB. The higher moments, $\ell \geq 2$, give insight into the physics and status of the universe during decoupling. The power spectrum measured by the Planck satellite, along with their best-fit curve, is given in Fig. 1.5.

The first three peaks ($30 < \ell < 1000$) are strongly related to the global geometry and contents of the universe at the time of decoupling. To understand why, consider the matter-radiation fluid leading up to decoupling. After the universe became matter dominated ($z = 3371 \pm 32$, $t = 51,810$ yr [28]), primordial over densities in the matter-radiation fluid became gravitational wells which matter fell into. Non-coupling matter, that which does not interact with the radiation, fell into the wells and remained there. Baryons also fell in, but, since they were coupled to radiation, also experienced a pressure which pushed them out of the wells. The interplay between the gravitational well and the radiation pressure created acoustic oscillations in the baryon-radiation fluid. These compressions of the matter density led to variations in the temperature of the eventually

---

[11] The TT superscript denotes this as the temperature-temperature power map, as opposed to polarization modes also derived from the map.
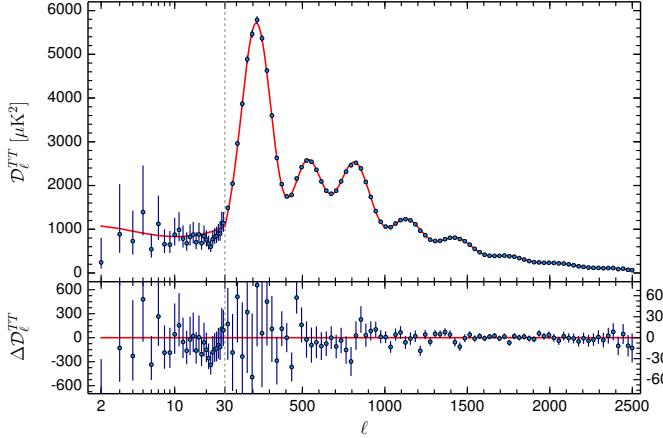
Figure 1.5: Band power spectrum of the CMB as measured by the Planck satellite (with 1σ uncertainty) along with a best fit curve (top) and the residuals of that curve (bottom). Cosmological parameters can be derived by the location and strengths of the various peaks in the spectrum. Image from [65].

emitted photons [66].

The band power peaks seen in the CMB correspond to the oscillatory modes in the fluid which were at the minimum/maximum portions of their oscillation when decoupling occurred. The wavenumber which reached its first compression by decoupling, related to the sound horizon in the fluid, indicates the expansion rate of the universe before decoupling occurred. This in turn relates to the radiation and matter densities. Additionally, the angular size of the horizon, as observed today, depends on the curvature of the universe. Thus, the location of, and the inter-peak distance between (in ℓ), the peaks can be used to measure Ω_κ, Ω_M and Ω_Λ. The photon density of the CMB itself gives a measure of Ω_R and η (see Fig. 1.3). Additionally, the presence of baryons at decoupling decreased the heights of even numbered peaks compared to the odd numbered peaks: the difference between the height of the second peak compared to the first and third gives an indicator of Ω_B.

A great deal more physics can be extracted from the CMB spectrum and must be included for a robust fit of the measurement [67–69]. The best fit to the 2015 Planck spectrum shown in Fig. 1.5 yields [28, 70]

$$\Omega_{B,0} h^2 = 0.02222 \pm 0.00023$$

$$\Omega_{M,0} h^2 = 0.14262 \pm 0.0020$$

$$h = 0.6731 \pm 0.0096$$

The baryon content does not account for the full matter content, arguing for the presence

of non-coupling matter which did not interact with the radiation prior to decoupling.

1.3.5 Large Scale Structure

The large scale structure (LSS) of matter observed today (i.e. the largest galaxy clusters) is a direct consequence of primordial density perturbations (the same which also gave rise to the anisotropies in the CMB) and their growth through the evolution of the universe. A full study of the growth of energy-density perturbations requires a Jeans analysis of perturbations in a fluid [66, 68]. In such an analysis, the density is written as $\rho = \rho_0 (1 + \delta)$ and the behavior of δ considered by transforming to k space and studying the perturbation δ_k of individual k modes. How any given δ_k grows depends upon when the mode becomes sub-horizon,[12] whether the perturbation is in baryons or non-coupled matter (radiation and cosmological constant do not cluster), and which component of the universe is dominant. The growth of any given mode can be summarized as:

- For modes which were super-horizon at the end of inflation,[13] δ_k grew as a^2 during the radiation dominated epoch. If they were still super-horizon after matter-radiation equality, they grew as a.

- If a mode was sub-horizon during the radiation dominated epoch, the perturbation's growth depended on if the fluctuation is in baryons or non-coupled matter. If non-coupled matter, δ_k grew logarithmically, while for baryonic matter, it oscillated in the baryon-radiation fluid and remained (on average) a constant size.

- After matter-radiation equality, non-coupled matter fluctuations grew as a while baryons continued to oscillate.

- Post decoupling, baryonic perturbations also grew as a.

- Once the cosmological constant become the dominant component of the universe, the matter perturbations ceased to grow.

---

[12] Sub-horizon is defined as when the length scale of the mode is less than the distance light could have traveled since the Big Bang, i.e. a casually connected region

[13] Inflation is a proposed period of rapid growth shortly after the Big Bang which solves numerous cosmological problems [71–73].
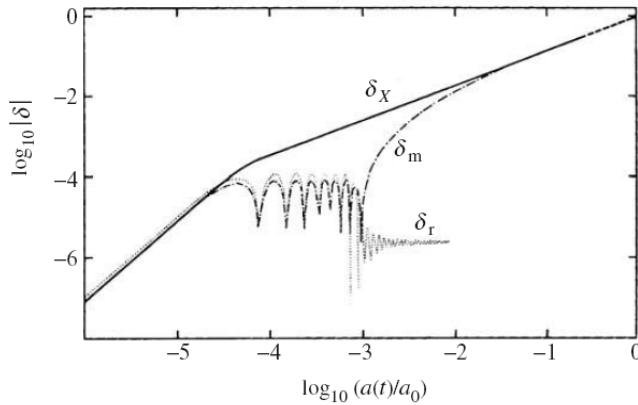
Figure 1.6: Evolution of a density perturbation δ for a mode which enters the horizon after matter-radiation equality at $h = a/a_0 \sim 10^{-4.5}$. After entering the horizon, the non-coupled matter (dark matter) perturbation δ_X grows with a, while that of baryons δ_m and radiation δ_r oscillate until decoupling at $H \sim 10^{-3}$. After decoupling the baryonic matter quickly falls into the preexisting wells of δ_X and radiation dampens out. Figure from [74].

This can be seen visually in Fig. 1.6 which shows the growth of δ_k for a mode which enters the horizon after matter-radiation equality. The non-coupled matter's growth begins immediately, while baryons and radiation oscillate until decoupling.

In a baryon-only universe, the density perturbations could only begin growing after decoupling when $a = 9.16 \times 10^{-4}$ and their size was, as seen in the CMB, $\mathcal{O}(10^{-5})$. Evolving these perturbations to $z \sim 0.5$ (matter-cosmological constant equality) gives $\delta \sim 0.055$, far less than observations of LSS today of $\delta \sim 100$ [75]. A baryon only universe could not create the evolved structures observed today. However, if there was a form of non-coupled matter, such as neutral dark matter, the wells could begin growing immediately after matter-radiation equality and be significantly larger at decoupling. The newly decoupled baryons would then quickly fall into the dark-matter wells and begin to evolve into the structure observed today as seen in Fig. 1.6.

The growth of structure described above is linear, but the collapse of these perturbations into the structure seen today is nonlinear and requires simulations to fully understand. These so-called "N-body" simulations take non-coupled dark matter particles with some initial perturbations and evolve the system from early times to the present. One such simulation, the Millennium simulation, evolved $N = 2160^3$ particles starting at $z = 127$ in a cube $500 \, \mathrm{Mpc} \, h^{-1}$ on a side [76]. The initial conditions assumed $\Omega_\mathrm{B} = 0.045$ and $\Omega_\mathrm{M} = 0.25$. The results from that simulation are compared to various
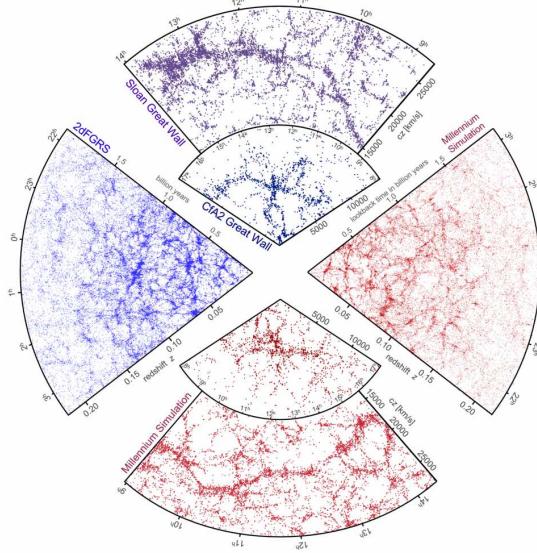
Figure 1.7: Comparison of N-body simulation results and galaxy survey measurements. The red wedges (right and bottom) are chosen from the Millennium simulation [76] while the blue wedges (left and top) are from various galaxy surveys: Sloan Digital Sky Survey (top large wedge) [77], Center for Astrophysics Survey (top small wedge) [78], 2dF Galaxy Redshift Survey (left) [79]. The observations and simulation are nigh indistinguishable on similar length scales. Figure from [80].

galaxy survey results in Fig. 1.7. On comparable length and time scales, the simulation and observation are indistinguishable.

This discussion has assumed that the non-baryonic matter was non-relativistic during the beginning of structure formation. However, one could also envision a relativistic dark matter candidate, which is termed hot dark matter (HDM). One potential HDM example is a neutrino with mass of a few tens of eV. Simulations of a neutrino dominated universe [81] find that the resulting large scale structure disagrees with observations because the relativistic neutrinos inhibit small-scale perturbation growth [82]. This then necessitates that structure formation begins with the largest objects and proceeds downwards in scale, which disagrees with the most distantly observed galaxies [83]. The effect of HDM would also be profound on the CMB power spectrum which is not observed [84]. The results of these simulations indicate that in order to reproduce the observed late universe LSS, the early universe must have been dominated by a CDM component, or at most a "warm" dark matter (WDM) which has intermediate velocities.

The final measurement from LSS to be discussed here is that of the baryon acoustic oscillation (BAO) peak. As previously mentioned, before the baryons decoupled from radiation, they were oscillating. When decoupling occurred, all of the oscillatory modes were frozen in their cycle and transforming back to position space gives a baryon over density at a specific distance: the sound crossing horizon. The scale of this over density
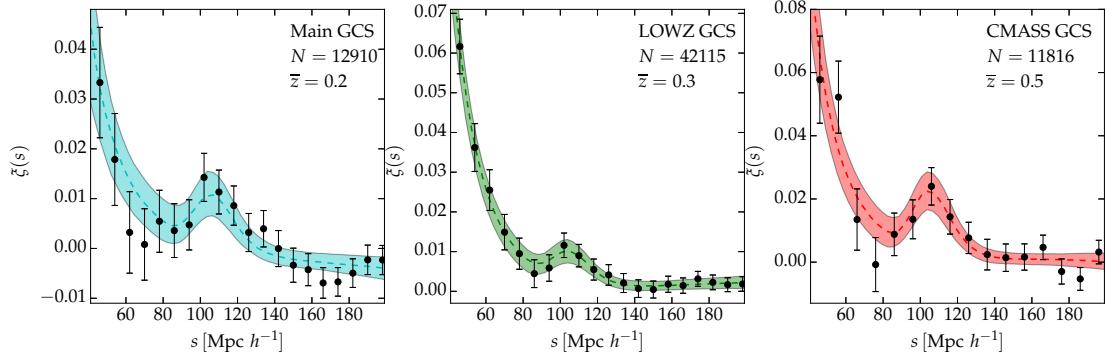
Figure 1.8: Two point correlation function ξ as a function of comoving galaxy separation distance s for three galaxy surveys with N samples and various mean redshifts $\bar{z}$. A best fit curve with 68 % uncertainty band is given for each. The BAO feature is observed in each at $s \sim 100 \text{ Mpc} \, h^{-1}$. Figure from [87].

provides a standard ruler to be used in any epoch of the universe, and how it evolved is indicative of the content of the universe.

This length scale can be observed in the late universe by mapping the locations of thousands of galaxies and computing the two-point correlation function ξ between them. The two-point correlation function asks the question, "Given the location of arbitrary object A, what is the probability for arbitrary object B to be at distance C?" If there were no oscillations, i.e. no baryons, ξ is expected to be smooth and featureless. With oscillations, a peak is expected at a distance corresponding to sound horizon evolved to the present epoch. Such a feature was first observed in 2005 by SDSS [85] and 2dFGRS [86]. More recent results are shown in Fig. 1.8, fitting the correlation function to three different galaxy surveys, including the recent Baryon Oscillation Spectroscopic Survey (BOSS, a dedicated survey of SDSS), with different mean redshifts [87]. The BAO feature is clear in each sample at a comoving separation distance $s \sim 100 \text{ Mpc} \, h^{-1}$. The fits to the correlation data are non-trivially related to the energy content of the universe [88], and are typically done assuming a baryon content and fitting a total mass content. Assuming a flat universe and the Planck CMB $\Omega_{\text{B}} = 0.049$, the most recent results fit $\Omega_{\text{M}} = 0.33^{+0.24}_{-0.16}$ [87]. The BAO feature indicates a matter content greater than that of just Baryons, necessitating dark matter.

1.4   A Picture for Dark Matter

The astrophysical and cosmological evidence presented in Sec. 1.3 paints a picture of a missing component to the universe whose properties must satisfy several constraints. The most widely accepted solution is a particulate one: dark matter is either a single or combination of elementary particles. The necessary properties that such particles must have are summarized here [89].

Stability: The dark matter content of the universe is observed in the present day, and thus any dark matter theory must provide a stable (on cosmological time scales) solution which does not decay into standard model particles.

Relic Density: From the latest CMB fits, the density parameter (relic density) of dark matter is $\Omega_{\mathrm{CDM}} = 0.259 \pm 0.003$. Any suitable dark matter solution must account for this contribution to the universe's energy budget.

Non-relativistic: LSS simulations disfavor hot, relativistic, dark matter in comparison to the observed universe. This requires that a dark matter solution is cold, or at most warm, with most solutions investigating a strictly non-relativistic particle.

Neutral: Galaxy and cluster dynamics indicate that dark matter must be electrically neutral, or else it would interact with photons and be observable to standard astronomy observational techniques.

Elemental abundances: The light elements are produced in BBN, with mostly good agreement with observations, and the heavier elements in stars. A dark matter candidate must not change these well computed and understood results such that they no longer agree with observations. Disallowed effects include modifying freeze-out physics in BBN, or providing another method for stars to radiate energy such that they would die too young.

Self-Interactions: Clusters such as the bullet cluster indicate a near-collisionless dark matter. Any dark matter candidate must only not interact with the electromagnetic force, but it must not interact with itself through any known force up to bounds provided by cluster observations.

Chapter 2

Identifying Dark Matter

The astrophysical evidence for dark matter could generally be stated as, "astronomers do not observe enough visible matter to account for the measured gravitational effects." This presents two approaches to solving the problem: either they do not observe all of the matter or the current understanding of gravity is lacking on large scales. The cosmological evidence for dark matter indicates a discrepancy between the baryonic and total matter content and favors the first solution.

Identifying a non-baryonic particle which meets all criteria for dark matter has proven a challenge as no known elementary particle satisfies the requirements. This has lead to an exploration of "beyond-the-standard-model" theories (BSM) of various types which provide a wide range of dark matter candidates. Most BSM theories are developed to solve other particle-physics problems and the fact that some happen to also provide a dark matter candidate increases their attractiveness. Figure 2.1 demonstrates the breadth of parameter space spanned by a few of these candidates. This figure, along with most dark matter search plots, compares the dark matter particle's mass m_χ to its cross section for interacting with regular matter. The available parameter space spans a large $\sim$30 orders of magnitude in each dimension.

The most studied class of potential dark matter candidates are weakly interacting massive particles (WIMPs). WIMPs have compelling motivation from early universe thermal freeze-out calculations (Sec. 2.1), can be found in numerous BSM theories (Sec. 2.2), and can be detected using multiple approaches (Sec. 2.3). Although WIMP particles are the most studied dark matter candidate, other solutions to the missing
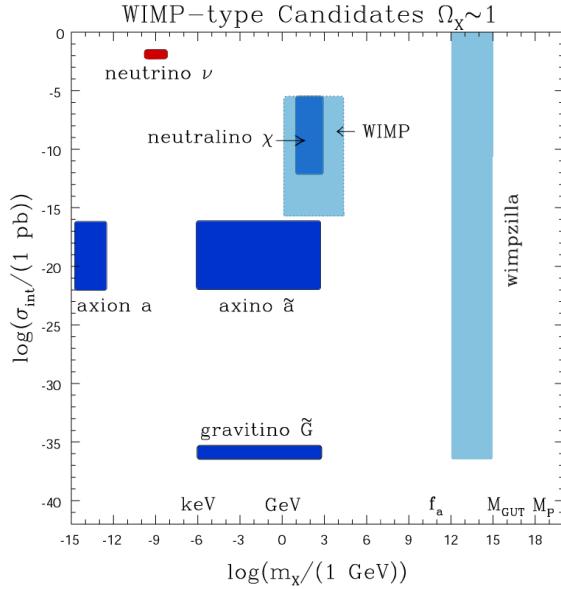
Figure 2.1: Regions of parameter space generally spanned by select dark matter candidates. The parameter space is defined by the particle's mass and generally cross section for interacting with standard matter. The neutrino is the only standard model particle and would be hot dark matter, while the others are cold. Figures from [90].

matter problem have also been proposed, with several remaining open areas of study (Sec. 2.4).

2.1 WIMP Paradigm Motivation: Thermal Production

A compelling motivation for WIMP dark matter is that it can be cosmically produced through a process known as thermal freeze-out. In the early universe, the ambient temperature was high enough that elementary particles were in contact via a thermal bath and thermal-equilibrium dynamics are appropriate. The number density, energy density, and pressure of a particle species in thermal equilibrium are given as

$$
n = \begin{cases} \frac{g_1 \zeta(3)}{\pi^2 (\hbar c)^3} \left(k_{\mathrm{B}} T\right)^3 & \text{Relativistic} \\ g \left(\frac{mc^2 k_{\mathrm{B}} T}{2\pi (\hbar c)^2}\right)^{3/2} e^{-mc^2/k_{\mathrm{B}} T} & \text{Non-Relativistic} \end{cases} \tag{2.1}
$$

$$
\rho c^2 = \begin{cases} \frac{g_2 \pi^2}{30 (\hbar c)^3} \left(k_{\mathrm{B}} T\right)^4 & \text{Relativistic} \\ n m c^2 & \text{Non-Relativistic} \end{cases} \tag{2.2}
$$

$$
p = \begin{cases} \rho c^2/3 & \text{Relativistic} \\ n k_{\mathrm{B}} T & \text{Non-Relativistic} \end{cases} \tag{2.3}
$$

where the evaluation in the relativistic $(k_\mathrm{B}T \gg mc^2)$ and non-relativistic $(k_\mathrm{B}T \ll mc^2)$ regimes differ, T is the temperature of the thermal bath, m is the particle mass, and $\zeta(3)$ is the Riemann zeta function. For bosons $g_1 = g_2 = g$ while for fermions $g_1 = 3g/4$ and $g_2 = 7g/8$, with g as the number of internal degrees of freedom for the given species.

The universe was radiation dominated at this time, and its overall dynamics governed by all relativistic species in equilibrium. The total energy and entropy densities for these species are

$$\rho_\mathrm{R} c^2 = \frac{g_* \pi^2}{30 \left(\hbar c\right)^3} \left(k_\mathrm{B} T_\gamma\right)^4 \tag{2.4}$$

$$s_\mathrm{R} = \frac{2\pi^2 k_\mathrm{B} g_{*S}}{45 \left(\hbar c\right)^3} \left(k_\mathrm{B} T_\gamma\right)^3 , \tag{2.5}$$

where T_γ is the equilibrium temperature of the γ's and the entropy density is calculated from $s = \left(\rho c^2 + p\right)/T$. The summed degrees of freedom are given by

$$g_* = \sum_i g_2 \left(T_i/T_\gamma\right)^4 \tag{2.6}$$

$$g_{*S} = \sum_i g_2 \left(T_i/T_\gamma\right)^3 , \tag{2.7}$$

where T_i is the equilibrium temperature of the ith species. It can be shown (see, e.g. [66]) that the total entropy $S = sV$ in a comoving volume V is conserved. This implies that $s \propto T^3 \propto V^{-1}$ which means that the number of particles of a given species i in a comoving volume is $Y_i \equiv n_i/s$.[1] Combining Eqs. 2.1 and 2.5 gives

$$Y = \begin{cases} \frac{45\zeta(3)}{2\pi^4 k_\mathrm{B}} \frac{g_1}{g_{*S}} & x \ll 3 \\ \frac{45}{2\pi^4 k_\mathrm{B}} \left(\frac{\pi}{8}\right)^{1/2} \frac{g}{g_{*S}} x^{3/2} e^{-x} & x \gg 3, \end{cases} \tag{2.8}$$

where $x \equiv mc^2/k_\mathrm{B}T$.

Two changes can occur to a particle species as the universe cools, they can become non-relativistic and they can leave equilibrium.[2] A species can leave equilibrium only if there are number-changing processes, such as creation and annihilation. The equilibrium

---

[1] It additionally implies that $T \propto a^{-1}$, again showing that the universe was hotter while smaller.
[2] The values of g_* and g_{*S} decrease when either occurs. For all but the coolest temperatures, it is

temperature determines whether creation processes are allowed, while annihilation can occur at any temperature. Species which remain in equilibrium as the universe cools will become non-relativistic and their particle density will fall as they annihilate.

The universe is also expanding, however, and eventually it becomes improbable that two particles meet to annihilate. When this occurs, the particle number ceases to change, an event called "freeze-out". The dynamics of this process are governed by the Boltzmann equation

$$\frac{\mathrm{d}n}{\mathrm{d}t} = -3Hn - \langle \sigma_A v \rangle \left(n^2 - n_{\mathrm{eq}}^2 \right),$$ (2.10)

where $\langle \sigma_A v \rangle$ is the thermally-averaged annihilation cross section times velocity. The first term on the right hand side is due to dilution from the expansion of the universe, the n^2 term accounts for annihilation processes which decrease the density, and the n_{eq}^2 term accounts creation processes which increase the density. Equation 2.10 can be rewritten in a suggestive form as

$$\frac{x}{Y_{\mathrm{eq}}} \frac{\mathrm{d}Y}{\mathrm{d}x} = -\frac{\Gamma_A}{H} \left[\left(\frac{Y}{Y_{\mathrm{eq}}} \right)^2 - 1 \right],$$ (2.11)

where $\Gamma_A \equiv n_{\mathrm{eq}} \langle \sigma_A v \rangle$ is the annihilation interaction rate. Remembering that, for this radiation dominated period, $T \propto t^{-1/2}$, and thus $x \propto t^{1/2}$, the change in particle number as a function of time becomes small once $\Gamma_A/H < \mathcal{O}(1)$, i.e. a particle freezes-out when its interaction rate becomes less than the expansion rate of the universe. The observable density parameter today, called the relic density Ω_0, is

$$\Omega_0 = \frac{\rho}{\rho_c} = \frac{mc^2 n_0}{\rho_c} = \frac{mc^2 \left(k_{\mathrm{B}} T_0 \right)^3}{\rho_c} \frac{n_0}{\left(k_{\mathrm{B}} T_0 \right)^3}.$$ (2.12)

Once the particle species freezes out, the values at freeze out, denoted by subscript f, are the same as those observable today. $n_0/s_0 = Y_0 = Y_f = n_f/s_f$ gives that

appropriate to take $g_* \approx g_{*S}$ with rough values of

$$g_* \approx g_{*\mathrm{S}} \sim \begin{cases} 100 & k_{\mathrm{B}} T \gtrsim 300 \text{ MeV} \\ 10 & 100 \text{ MeV} \gtrsim k_{\mathrm{B}} T \gtrsim 1 \text{ MeV} \\ 1 & k_{\mathrm{B}} T \lesssim 1 \text{ MeV}. \end{cases}$$ (2.9)

$n_0/T_0^3 = (g_{*S,0}/g_{*S,f})\, n_f/T_f^3$ and

$$\Omega_0 = \frac{mc^2 \left(k_{\mathrm{B}}T_0\right)^3}{\rho_c} \frac{g_{*S,0}}{g_{*S,f}} \frac{n_f}{\left(k_{\mathrm{B}}T_f\right)^3}. \tag{2.13}$$

The exact solution of the Boltzmann equation, which gives n_f and x_f at freeze-out, depends upon whether the given species was relativistic or not at freeze-out. Large-scale structure simulations favor a cold particle m_χ, for which numerical solutions are needed for the Boltzmann equation. An estimate can be computed instead using the rough statement of freeze-out occurring when $\Gamma_A \sim H$. The freeze-out number density is then approximated as

$$n_f \sim \frac{T_f^2}{M_{\mathrm{P}} \left\langle \sigma_A v \right\rangle}, \tag{2.14}$$

where the Planck mass is $M_{\mathrm{P}} = \sqrt{\hbar c/G_{\mathrm{N}}}$ $(H^2 = 8\pi\hbar c\rho/3M_{\mathrm{P}}^2)$, and $\rho \propto T^4$ during this radiation dominated period. Substituting this expression into Eq. 2.13 yields

$$\Omega_\chi \sim \frac{x_f T_0^3}{\rho_c M_{\mathrm{P}}} \left\langle \sigma_A v \right\rangle^{-1} \tag{2.15}$$

$$\sim \left(3 \times 10^{-27} \ \mathrm{cm}^3\,\mathrm{s}^{-1}\right) \left\langle \sigma_A v \right\rangle^{-1}, \tag{2.16}$$

where the second line is an approximation using typical values. For stronger annihilation cross sections, the relic density is smaller as more of the population annihilates prior to freeze-out. The freeze-out and relic density generation process is shown in Fig. 2.2 for a 100 GeV/c^2 particle.

The thermally averaged cross section can be parameterized on dimensional grounds with an expansion in v^2 as [89, 91]

$$\left\langle \sigma_A v \right\rangle \sim \frac{g_c^4}{m_\chi^2} \left(1 + v^2 + \ldots\right), \tag{2.17}$$

where g_c is the gauge coupling for the force responsible for the annihilation. With this parameterization, the relic density dependence is

$$\Omega_\chi \sim \frac{m_\chi^2}{g_c^4 \left(1 + v^2\right)}. \tag{2.18}$$
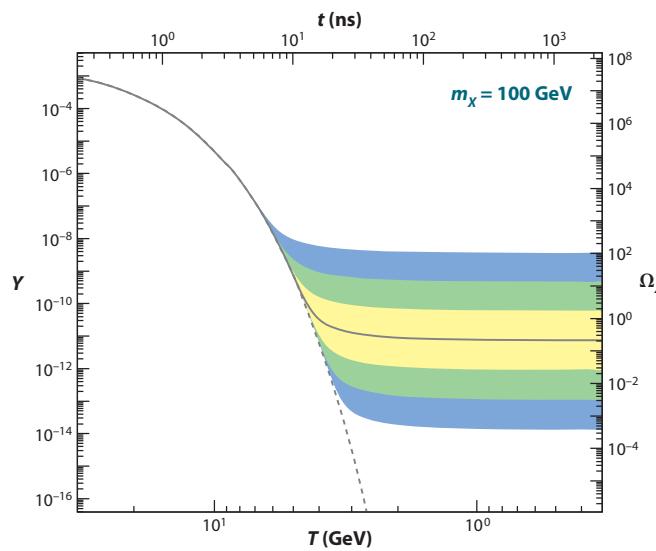
Figure 2.2: Demonstration of freeze-out for particle m_χ. While in equilibrium (dash line), the number of particles in a comoving volume Y and the relic density Ω_χ decrease as a functions of temperature T and time t. When freeze-out occurs, the abundance ceases to change and departs equilibrium (solid line). The central curve is the annihilation cross section which gives a relic density equal to that of cold dark matter, while the bands differ by 10, 10^2, and 10^3 from this value. Figure from [91].

A thermally produced dark matter candidate should have mass and coupling such that $\Omega_\chi = \Omega_{\mathrm{CDM}} = 0.259 \pm 0.003$ [28]. A remarkable observation is that this equality holds for WIMPs, which interact through the weak force $g_c \simeq 0.65$ and have a typical weak-scale mass of $m_\chi \sim 100$ GeV$/c^2$. This is the so-called "WIMP Miracle" which provides enticing evidence for a WIMP dark matter candidate.

2.2   WIMP Candidates

2.2.1   Supersymmetry

By far the most popular class of theories for beyond-the-standard-model physics over the past few decades is supersymmetry (SUSY) [92–94]. The development of SUSY had many motivations, one of which was to solve the hierarchy problem: the radiative corrections the Higgs mass should cause it to be much larger than is observed, unless there is extreme fine-tuning. SUSY introduces new physics at the TeV energy level which cancels these corrections and provides a natural energy scale between that of the electroweak force (10^3 GeV) and the Planck scale (10^{19} GeV), where a quantum theory of gravity is expected.

SUSY also provides another desirable features in a BSM theory, unification of the
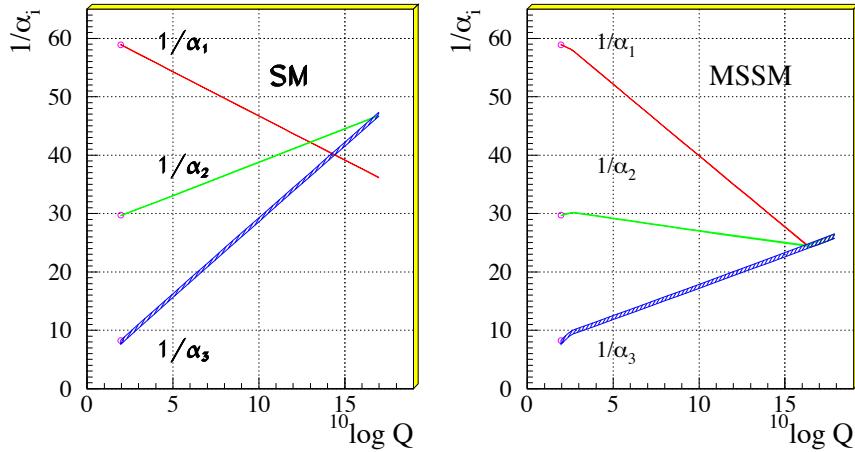
Figure 2.3: Demonstration of the running of coupling constants in the standard model (left) and supersymmetry (right) as functions of interaction energy Q in GeV. The couplings do not unify in the SM. With new SUSY physics at the TeV scale, the running slopes change and the couplings unify at $\sim 10^{16}$ GeV. Figure from [93].

physical forces at high energy. This unification is theoretically enticing and has precedence in the unification of the electromagnetic and weak forces. To demonstrate this, consider the gauge couplings $a_{1,2,3}$ for the standard model (SM) $U(1)$, $SU(2)$, and $SU(3)$ groups respectively. The couplings determine the strength of the electromagnetic, weak nuclear, and strong nuclear forces and it is experimentally observed that their values change with interaction energy Q (termed "running of the coupling constants"). α_1 is anti-correlated with Q while $\alpha_{2,3}$ are correlated. As shown in Fig. 2.3, the SM gives the unification of α_2 and α_3, but α_1 "misses". Including effects of the minimal supersymmetric standard model (MSSSM)[3] gives a unification of all three at the "grand unification theory" (GUT) scale of 10^{16} GeV.

The base addition SUSY makes to the SM is a spin-statistics symmetry whose operator changes the spin of a particle by 1/2. Such a symmetry allows for fermions to become bosons and vice versa. Allowing for the spin-2 graviton (gauge boson for gravity) to unify with the spin-1 SM bosons motivates such an operator. Incorporating this symmetry into SM quantum field theory results in a spectrum of new particles such that the fermionic/bosonic SM particles have corresponding bosonic/fermionic superpartners

---

[3] As it's name implies, the MSSM includes only the minimum additions to the SM through several simplifying assumptions.

with spins differing by 1/2. As these superpartners have not been experimentally observed, the symmetry must be spontaneously broken at some higher energy level pushing the superpartner masses to higher values.

Since SUSY provides a spin-changing operator, it also naturally provides mechanisms to break baryon- and lepton-number conservation. The most important example of this is the decay of the proton via several channels: $p \to e^+\pi^0$, $\mu^+\pi^0$, $\nu\pi^+$, etc. For a SUSY breaking scale of $\mathcal{O}(100 \text{ GeV}/c^2)$, the proton lifetime would be $\ll 1$ s compared to the measured lower limits of $>10^{29}$ years [29]. This rather large discrepancy can be avoided by imposing a discrete symmetry called R-parity

$$R = (-1)^{3B+L+2s}, \tag{2.19}$$

where B and L are the particle's baryon and lepton number and s its spin. Superpartners have $R = -1$ while SM particles have $R = +1$. Conservation of R implies that heavier supersymmetric particles can only have decays which include lighter supersymmetric particles. A corollary of this is the prediction of a lightest supersymmetric particle (LSP) which is stable and is a WIMP dark matter candidate [95]. In the constrained MSSM (CMSSM), the LSP is typically identified as the lightest neutralino χ_1^0, a linear combination of the superpartners of the neutral gauge bosons [96].

SUSY has not been observed in the Large Hadron Collider (LHC) [97], which places tight bounds on the CMSSM. This has lead to extensions, such as the next-to-minimal model (NMSSM) [98] and phenomenological MSSM (pMSSM) [99]. Fitting all of the available null evidence to the CMSSM, gives the best-fit expectation in the m_χ and $p-\chi$ interaction cross section plane as shown in Fig. 2.4: the preferred mass is $m_\chi \sim 1$ TeV.

2.2.2   Universal Extra Dimensions

The concept that there are more than three spatial dimensions was first proposed by Kaluza in 1921 [101] as a (classical) attempt to unify general relativity and electromagnetism. Klein expanded on this idea in 1926 [102] by proposing that any extra dimensions are compactified to a small scale, explaining why they are not observed in normal space-time measurements. Extra dimensional theories are now generally called Kaluza-Klein theories. Compactification can be understood through the example of an
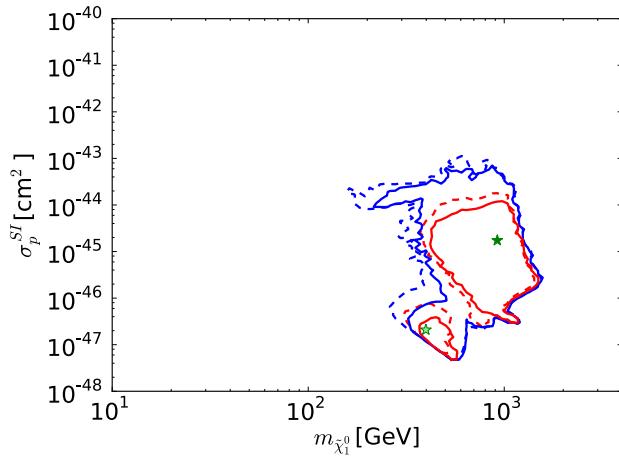
Figure 2.4: Best-fit (green filled star) with 68 % (red) and 95 % (blue) contours of the neutralino mass and spin-independent elastic scattering cross section with a single proton from a global likelihood hit of the CMSSM to null collider and dark matter detection results. The dashed lines, along with unfilled star, are from an alternative parameter model. Figure from [100].

ant traveling along a piece of string: from a far-away observer's perspective, the ant has only a single flat dimension along which to travel (down the string length), whereas from the ant's perspective, there is an additional compactified dimension (around the string). The ideas of Kaluza and Klein had several issues at the time and the concept of extra dimensions was mostly neglected during the middle of the 20th century. In more recent times, Kaluza-Klein theories have been proposed to be able to solve many of the same outstanding problems as SUSY, including gauge coupling unification [103] and the hierarchy problem [104].

The theory of Universal Extra Dimensions (UED) [105] is particularly interesting for dark matter physics. UED elevates all SM fields to the compactified extra dimension(s) and their momenta in the extra dimension appears to observers in the standard four-dimensions as additional mass, i.e. heavier particles. Due to the compactification, the extra-dimensional momentum of any given particle field is quantized yielding tree-level masses for additional particles of

$$m_n^2 = \frac{n^2}{R^2} + m_0, \tag{2.20}$$

where R is the length scale of the compactification, n is the quantum number of extra-dimensional momentum, and m_0 is the SM mass of the particle. Radiative corrections break the degeneracies between SM particles with the same mass . In order for the zeroth-excitation particles to match the SM particles, compactification must be done

on an orbifold, which leads to a discrete symmetry called KK-parity

$$P = (-1)^n .$$ (2.21)

This parity implies that a single extra-dimensional particle cannot decay to only SM particles: the lightest Kaluza-Klein particle (LKP) is stable and a viable dark matter candidate [106]. In the minimal extension of UED, the LKP is the $n = 1$ excitation of the B^0 gauge boson. The non-detection of extra-dimensions at the LHC [107] implies that $R \lesssim 2 \times 10^{-19}$ m, which in turn gives LKP masses of $m_{\mathrm{LKP}} \gtrsim 1$ TeV.

2.2.3   Dark Sector Models

Many theories have been proposed to explain dark matter as a component of some dark sector (also called a hidden sector) which does not interact via the SM gauge fields. These theories have been particularly successful in hypothesizing lower-mass dark matter in contrast to the heavier WIMPs predicted by SUSY and UED. One approach is to postulate a new force of nature mediated by of a dark $U(1)$ gauge field [108–110]. This dark "photon", the charge of which is only carried by dark matter, can kinematically mix with the SM photon allowing for some interaction with SM particles. The model of Ref. [108] gives a spin-independent proton-interaction cross section of order 10^{-40} for a 10 GeV/c^2 WIMP.

There are also generic models which consider Eq. 2.18 and look for combinations of m and g_c which are not of the typical weak scale but still satisfy the relic density requirement. These models have been termed WIMPless dark matter [111, 112]. A characteristic model of WIMPless dark matter is gauge-mediated supersymmetry breaking, which breaks SUSY into the MSSM plus a hidden sector with some connection between. The LSP is now found in the hidden sector and relieves the MSSM from tight experimental constraints [111].

Asymmetric dark matter (ADM) is a collection of models, all of which propose an asymmetry between the dark matter and its antiparticle which is physically related to the measured baryon/anti-baryon asymmetry [113–116]. The models originated out of the observation that $\Omega_{\mathrm{CDM}} \approx 5\Omega_{\mathrm{B}}$. This relation is a coincidence in standard WIMP

theories, whereas ADM proposed that it is a signature of the related asymmetries (usually attributed to $B-L$ asymmetry). Such a mechanism naturally gives that the number densities of dark matter and baryons are related as $n_{\mathrm{DM}} \sim n_{\mathrm{B}}$ which in turn implies

$$\Omega_{\mathrm{CDM}} \sim (m_{\mathrm{DM}}/m_{\mathrm{b}}) \, \Omega_{\mathrm{B}}. \tag{2.22}$$

Taking the proton mass as m_{B}, this yields $m_{\mathrm{CDM}} \sim 5$–15 GeV/c^2 [117]. As Refs. [114] and [117] demonstrate, there are many such models which fit under this umbrella, including versions of SUSY and dark forces. It is possible, though not always required, that the relic density is generated through thermal freeze-out. The interaction of ADM with SM particles is not guaranteed, but it could proceed through the same mechanisms which annihilate the dark matter, or generate the original asymmetry, if those processes interact with the SM. Depending on how the interaction proceeds, the spin-independent proton-interaction cross section ranges from 10^{-41}–10^{-45} cm^2 [115, 117].

The methodology of a dark sector is taken to an extreme in mirror dark matter scenarios [118]. The dark sector is here a "mirror" of the SM, in that the SM group $G = SU(3)_c \otimes SU(2)_L \otimes U(1)_Y$ is mirrored into the dark sector such that the full group is $G_{SM} \otimes G_{DM}$. The SM and DM can interact via gravity and either a mixing of the photon and mirror-photon or between the Higgs and mirror-Higgs. The mirror sector cannot be completely identical to the SM, since the difference in Ω_{SM} and Ω_{DM}, amongst other differences, must be explained [118]. In this scenario, dark matter is composed primarily of mirror baryons, H and He, generated in a mirror BBN-type process.[4] Having similar masses as the SM counterparts, the mass of dark matter is $\mathcal{O}\left(15 \text{ GeV}/c^2\right)$.

2.2.4   Other WIMP Models

Little Higgs models postulate an extended electroweak symmetry breaking at the TeV energy scale to alleviate the hierarchy problem. This breaking gives a lighter mass Higgs along with several new particles [119–122]. Some little Higgs theories contain a conserved "T-Parity" (T for TeV scale), such the heavy particles from the extended symmetry breaking are odd and the lighter SM particles are even. Similarly to $R-$ and

---

[4] LSS formation would imply that the temperature of the mirror CMB is less than the SM CMB, such that mirror decoupling occurs earlier to allow for the mirror density perturbations to begin growing before the SM perturbations.

KK-parity, this provides a stable particle, the lightest T-odd particle (LTP), as a dark matter candidate with a mass $\mathcal{O}\big(\mathrm{TeV}/c^2\big)$ [123].

SuperWIMP theories postulate that the current dark matter relic density is made up of super-weakly interacting massive particles (superWIMPs) [124, 125]. In this models, WIMPs are thermally produced through freeze-out with the appropriate relic density, but then later decay to superWIMPs which have much smaller interaction strengths. Assuming one superWIMP per WIMP decay, the density of superWIMPs Ω_{SWIMP} is related to that of the WIMPs Ω_{WIMP} via

$$\Omega_{\mathrm{SWIMP}} = \frac{m_{\mathrm{SWIMP}}}{m_{\mathrm{WIMP}}}\Omega_{\mathrm{WIMP}}, \tag{2.23}$$

where the superWIMP density is a fraction of the WIMP density and determined by the ratio of their masses. SuperWIMPs can be found in many frameworks, including the Gravitino of SUSY [126, 127], UED excitations of the graviton [128], and generic scaler/vector fields added to the SM [129]. In general the interaction strength of super-WIMPs make their likely detection to be through effects on cosmic evolution, though some specific couplings were found in [129] which enhance the strength, allowing for other means of detection.

2.3   Detecting WIMPs

The true nature of the dark matter WIMPs cannot be identified until they, or a clear signature of them, are detected in a dedicated search. There are three complementary methods of detecting WIMPs, each arising from the cartoon Feynman diagram given in Fig. 2.5. These methods are generalized by considering two initial particles i_1, i_2 and two final particles f_1, f_2 such that $i_1 i_2 \rightarrow f_1 f_2$. Any of these particles can be either a standard model particle ψ or a WIMP χ. The direction of time in the diagram indicates which detection method is under consideration.

Collider Production $\psi\psi \rightarrow \chi\chi$: Two SM particles collide at high energy, recreating the environment of the early universe, and WIMPs are created from the decay of strongly-produced particles. The dark matter is inferred from a reconstruction of decay particles and missing energy.
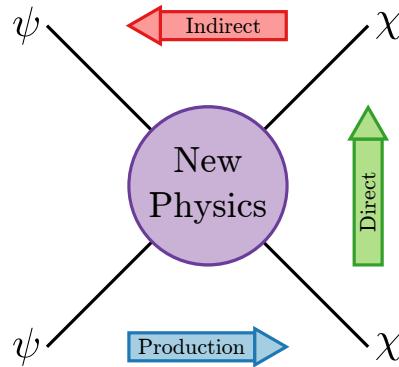
Figure 2.5: Cartoon Feynman diagram involving two standard model particles ψ and two WIMPs χ with some new physical interaction at the center. If time flows from left to right, the method is collider production, from right to left, the method is indirect detection, from bottom to top, the method is direct detection.

Indirect Detection $\chi\chi \to \psi\psi$: Two WIMPs, which can be own antiparticles, or a WIMP and anti-WIMP, annihilate and create SM particles. The SM annihilation products, which could be neutrinos, charged particles, or γ's, are then detected in satellites and the parent dark matter inferred.

Direct Detection $\chi\psi \to \chi\psi$: A WIMP scatters off normal matter. The reaction of the SM particle is directly observed, and recoil kinematics used to infer the scattering WIMP.

The first two methods are described in the remainder of this section while direct detection, being more central to this thesis, is the subject of the next chapter.

2.3.1   Collider Production

Searches for dark matter in colliders are performed by searching for missing transverse energy E_T. Since the initial momentum of the collision is entirely along the direction of the beam, all momentum in the final products transverse to the beam must sum to zero. If $\sum E_T \neq 0$ for the detected products, this indicates that products were created which escaped the detector. Such an escaped particle could be dark matter. If the mass of the WIMP-SM mediator is larger than the typical collision energy scale, a "contact" interaction can be assumed and searches for missing E_T take place in an effective field theory framework [130]. In this framework, limits are placed for particular coupling types (scalar, vector, etc.). If the WIMP-SM mediator is lighter, it can be produced in the LHC and an s-wave interaction must be assumed. WIMP-search limits from colliders are highly model dependent.

(a) CMS Results   (b) ATLAS Results
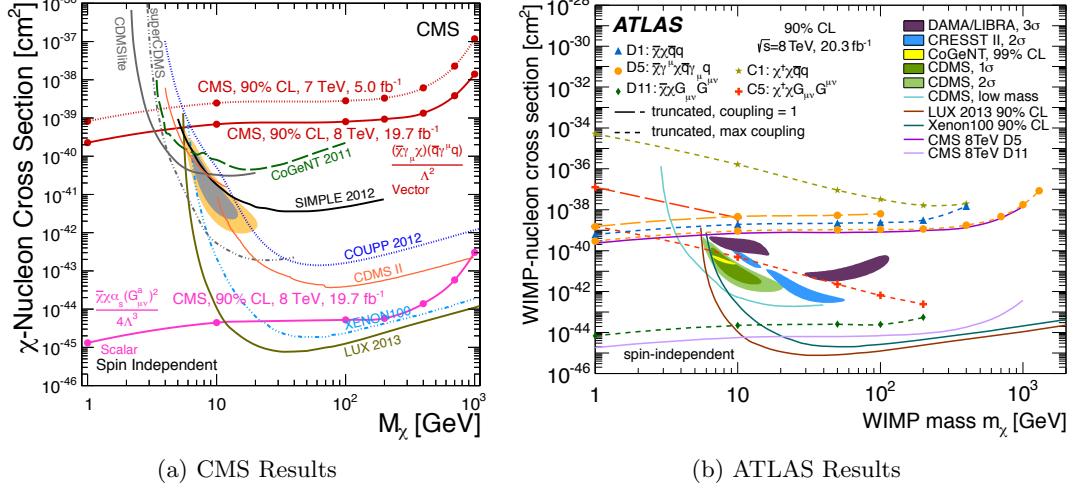
Figure 2.6: Limits on the spin-independent WIMP-nucleon scattering cross section, assuming a contact interaction, as a function of WIMP mass from the CMS (a) and ATLAS (b) experiments for various couplings. Figures from [131, 132].

The two general purpose detectors at the LHC, CMS and ATLAS, have both conducted searches for dark matter with monojets [131, 132]. Using the first LHC run, with a center-of-mass energy of 8 TeV, they set limits on the spin-independent WIMP-nucleon cross section, assuming a contact interaction, as a function of WIMP mass as seen in Fig. 2.6. The limits are compared to direct detection limits and it is seen that, depending on the operator, the collider sensitivity is comparable to the direct detection experiments. Colliders do not have low-energy thresholds and can typically reach lower WIMP masses then direct detection experiments. The amount of energy available for the collision limits the sensitivity at higher WIMP masses. CMS and ATLAS plan to continue looking for signatures of dark matter in future runs of the LHC at higher energy [97].

2.3.2   Indirect Detection

Indirect detection searches look for signatures of dark matter annihilation/decay in the universe using astrophysical techniques. The inherent difficulty with indirect searches is claiming with certainty that a signal is not caused by some other astrophysical source. Cataloging every type of possible source, and understanding the different radiation

given off by each, is a continual task which makes it difficult to claim a WIMP signal with strong confidence. A dark matter signal could arise in several different detection channels, since the exact annihilation or decay process is unknown. Searches in three such channels, γ rays, neutrinos, and anti-matter, are discussed below.

γ Rays

A γ-ray signal from dark matter could arise from WIMPs annihilating or decaying to SM particles.[5] There could be direct channels to all γ's, such as $\chi\chi \to \gamma\gamma$ or a mixed signal $\chi\chi \to \gamma X$, where χ is a WIMP or anti-WIMP and X is some heavy SM particle. Even without direct channels, a γ signal could be seen, either through the subsequent decay of heavier SM particles or the creation of cosmic rays which produce γ rays. Regardless of the channel, an excess of γ's compared to standard astrophysical sources would be created and could be detected by γ ray observatories such as the Fermi Large Area Telescope (Fermi-LAT, or Fermi for short) [133].

The expected γ-ray flux from dark matter of mass m_χ as a function of energy $\mathrm{d}\Phi/\mathrm{d}E$ is [134]

$$\frac{\mathrm{d}\Phi}{\mathrm{d}E} = \frac{1}{4\pi} \underbrace{\frac{\langle \sigma_A v \rangle}{2m_\chi^2 c^2} \frac{\mathrm{d}N}{\mathrm{d}E}}_{\text{Particle Physics}} \times \underbrace{\int_{\Delta\Omega} \mathrm{d}\Omega' \int_{\text{los}} \rho_\chi^2 \, \mathrm{d}l(r, \theta')}_{\text{Astrophysics}}, \qquad (2.24)$$

where $\mathrm{d}N/\mathrm{d}E$ is the expected γ flux from the annihilation, $\Delta\Omega$ is the solid angle of the sky observed, and ρ_χ is the density of dark matter which is integrated over the line-of-sight (los). Typically, areas of the sky with a high expected WIMP density are studied such as dwarf spheroidals, galaxy clusters, the Galactic Center (GC), and the diffuse isotropic γ ray background (IGRB). Limits on the velocity-averaged annihilation cross section $\langle \sigma_A v \rangle$ as a function of WIMP mass, from Fermi, looking at these sources for a specific annihilation channel are shown in Fig. 2.7. For lower WIMP masses, the limits are approaching to the annihilation cross section expected from the observed relic density.

There have been several claims of dark matter signals coming from the γ ray data.

---

[5] Whether the WIMPs are their own antiparticle (Majorana) or have a separate anti-particle (Dirac) depends on the theory. As an interesting example, due to the matter-antimatter asymmetry assumed in asymmetric dark matter models, a Dirac WIMP would not give an annihilation signal due to a lack of remaining antiparticles.
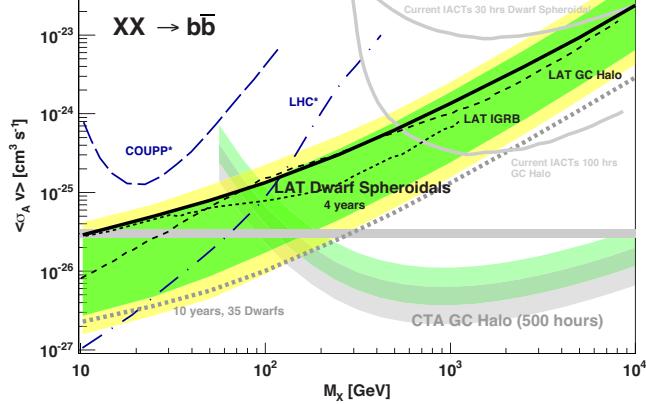
Figure 2.7: γ-ray satellite limits on the thermally-averaged annihilation cross section $\langle \sigma_A v \rangle$ for annihilation of WIMPs χ with mass M_χ to $b\bar{b}$. Fermi-LAT limits are from observing various sources. The horizontal band near $\langle \sigma_A v \rangle \sim 3 \times 10^{-26}$ is the expected cross section to match the relic density. Figure from [134].

However, as stated above, the astrophysical backgrounds are difficult to exhaustively model which makes these claims, by themselves, tenuous at best. γ ray excesses in the IRBG near the GC, which is very difficult to model, have been interpreted as dark matter ranging from 7–10 GeV/c^2 [135], 36–51 GeV/c^2 [136], or 10–50 GeV/c^2 [137]. Early Fermi data also showed evidence of a peak near $\sim$130 GeV/c^2 [138, 139], however, later scrutiny reduced the significance of the peak [140, 141].

Neutrinos

Another avenue of indirectly observing dark matter is through neutrinos. In particular, as the Sun travels through the galaxy's WIMP halo, it can sweep up dark matter by gravitationally binding WIMPs to itself. Over the course of the Sun's lifetime, enough WIMPs may have been bound such that the probability for annihilation is high. Most SM products of the annihilation, such as γ's, would be trapped in the sun, however neutrinos would escape. The spectrum of neutrinos $\mathrm{d}N/\mathrm{d}E$ from WIMP annihilation to some final state $X\bar{X}$ is [142]

$$\frac{\mathrm{d}N}{\mathrm{d}E} = \frac{1}{2} \int_{E/\gamma(1+\beta)}^{E/\gamma(1-\beta)} \frac{1}{\gamma\beta} \frac{\mathrm{d}E'}{E'} \left(\frac{\mathrm{d}N}{\mathrm{d}E}\right)^{\mathrm{rest}}_{X\bar{X}}, \qquad (2.25)$$

where neutrino oscillations has been ignored, $\gamma = m_\chi/m_X$, $\beta = \sqrt{1 - \gamma^{-2}}$, and $(\mathrm{d}N/\mathrm{d}E)^{\mathrm{rest}}_{X\bar{X}}$ is the neutrino spectrum created by the $X\bar{X}$ pair at rest. Neutrino telescopes, such as IceCube [143] and Super-Kamiokande [144] have looked for a neutrino
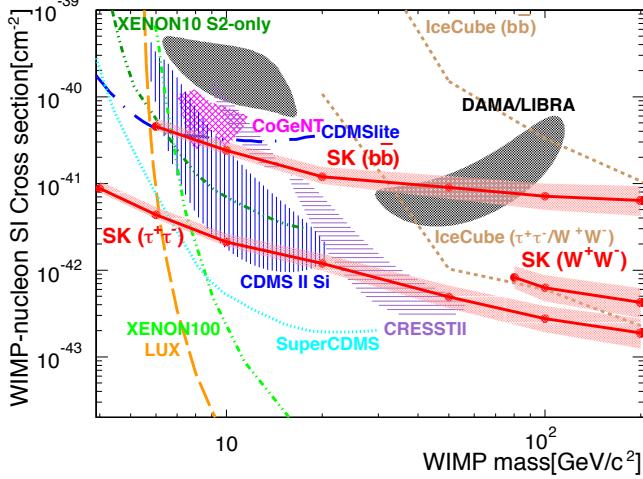
Figure 2.8: 90 % confidence level limits on the spin-independent WIMP-nucleon elastic scatter cross section from Super-Kamiokande (red with 68 % uncertainty bands) and IceCube (brown dotted) for various annihilation channels compared to direct detection experiments at lower WIMP masses. Figure from [144].

excess following this spectrum. There is minimal astrophysical uncertainty/modeling in these results, however they are strongly model dependent on the assumed initially-produced SM particle pair. As can be seen in Fig. 2.8, these limits are comparable with direct detection results for at low masses if the interaction is spin-independent and the model correct.

Antimatter

Finally, indirect detection could also proceed through antimatter. Antimatter could be produced by annihilating WIMPs which create heavier secondaries that decay to antimatter. There would then be an excess of antimatter compared to other astrophysical sources. Such an excess has been observed in positrons by the HEAT [145], PAMELA [146], and AMS-02 [147] experiments which can be attributed to heavy WIMPs ($m_\chi > 1$ TeV/c^2) [148]. However, the dark matter interpretation is strained when trying to reconcile the AMS-02 excess, Fermi observations of dwarf galaxies [149], and luminosities of galaxy clusters [150]. Some examples of these constraints are shown in Fig. 2.9 where the best-fit AMS-02 points are compared to limits derived from Fermi observations. In most decay channels, the Fermi limits rule-out the AMS-02 points. As with γ-rays, non-WIMP explanations for the excess have also been studied, notably using pulsars, which can also reproduce the excess [151, 152].
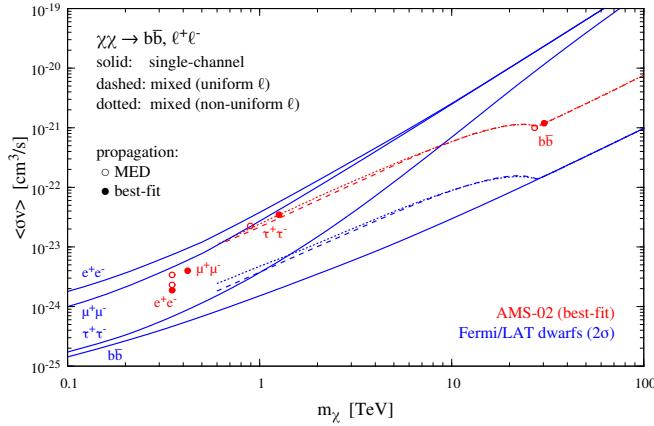
Figure 2.9: Comparison of AMS-02 positron excess best-fit points (red circles) to Fermi dwarf galaxy constraints (blue curves) for different lepton annihilation channels. The Fermi constraints for $\tau^+\tau^-$ and $b\bar{b}$ rule-out the AMS-02 points, while those from e^+e^- and $\mu^+\mu^-$ do not but are poor overall fits. Figure from [149].

2.4 Other Solutions

Numerous solutions to the missing matter problem have been proposed outside of the WIMP paradigm. Some of these solutions are justified by Occam's razor: find a solution using known particles before postulating new ones. Others do postulate a new particle, but in a manner different than standard WIMPs.

2.4.1 Modified Newtonian Dynamics

Just as discrepancies in the Newtonian treatment of Mercury's orbit became an avenue by which Newton's law of universal gravitation was superseded by Einstein's general theory of relativity, perhaps the discrepancies in gravity which are attributed to the presence of a dark matter are simply an indication that general relativity must be superseded by yet another formalism of gravity. The most studied alternative gravitational theory is generally termed MOND, for MOdified Newtonian Dynamics. MOND was first proposed by Milgrom in 1983 [153] where he postulated that at small enough accelerations (or large enough distances from a massive body) the acceleration $\boldsymbol{a}$ due to a Newtonian potential Φ is modified as

$$\tilde{\mu}\left(\frac{|\boldsymbol{a}|}{a_0}\right)\boldsymbol{a} = -\nabla\Phi, \tag{2.26}$$

where a_0 is the acceleration scale at which MOND becomes important and $\tilde{\mu}(x)$ is a monotonic function such that

$$\tilde{\mu}(x \gg 1) \approx 1 \qquad \tilde{\mu}(x \ll 1) \approx x. \tag{2.27}$$

Using this expression to compute the orbital velocity at large radius from a massive body gives a constant $v = (G_{\mathrm{N}} M a_0)^{1/4}$, which would explain the flat rotation curves observed in galaxies [154].

The MOND paradigm is able to explain the discrepancies at the galactic level, however the true proving ground for the paradigm is that of cluster dynamics and gravitational lensing. To enter this realm, the empirical formalism above requires a physical model which is the non-relativistic limit of a fully-covariant theory. The most popular relativistic formalism of MOND is called the Tensor-Vector-Scalar theory (TeVeS) [155], which non-relativistically reduces to aquadratic Lagrangian theory (AQUAL) [156]. Fits to the Bullet Cluster using TeVeS [157–159] conclude that an invisible matter contribution is still required, suggesting that a 2 eV/c^2 neutrino would suffice. However, since a particulate solution has difficulty explaining the Abel 520 cluster, where there is no separation between the lensing and x-ray emissions, which is easily explainable in MOND, cluster dynamics cannot definitely prove or disprove either solution. The question of MOND remains open, although there are still unanswered objections [53].

2.4.2   MACHOs

Massive compact halo objects (MACHOs) are standard astrophysical objects which emit very little, if any, radiation, making them difficult to observe using standard telescopes. These could be black holes, neutron stars, brown dwarfs, or Jupiter type planets which are remnants of earlier generations of stars. MACHOs can be detected by microlensing as these objects pass in front of known background stars [160, 161]. The primary difficulty with a MACHO explanation of dark matter is the tight constraints on the baryonic content of the universe by BBN, CMB, and LSS studies. Thus, if measurements of MACHOs show that they do compose dark matter, it would require drastic shifts in cosmological theory.

Efforts to measure the MACHO content of the Milky Way were undertaken by the

MACHO Collaboration [162] and the EROS-2 Survey [163] by considering lensing of the Large Magellanic Cloud. The nearby galaxy M31 ha also been studied by the Wendelstein Calar Alto Pixellensing Project [164]. Additionally, the Kepler mission [165] has been used to look for primordial black holes [166]. These surveys give MACHO mass fractions of the Galactic halos as being $\lesssim$8–30 % of the total. Although the results from individual surveys can differ by appreciable amounts, the general conclusion is the same: MACHOs cannot account for the majority of the necessary dark matter.

2.4.3 Light Neutrinos

The SM contains a single family of non-baryonic particles which are WIMPs in the technical sense and could be dark matter: neutrinos. Although originally conceived of as massless, oscillation experiments give definitive proof that neutrinos do have finite, if small, masses [29]. However, there are two constraints, both from a result of how neutrinos froze-out, which make them less viable as the primary component of dark matter.

The cosmic neutrino background decoupled when $\bar{\nu} + \nu \to \bar{\ell} + \ell$ became improbable at $k_{\mathrm{B}}T \sim 3$ MeV ($t \sim 1$ s). The neutrinos were relativistic at this time and thus formed a hot relic. The first constraint is that large-scale structure disfavors hot dark matter (Sec. 1.3.5).

The relic density for the relativistic neutrinos is found by combining Eqs. 2.1 and 2.13 to give

$$\Omega_{\nu,0}h^2 = \frac{\sum_i^N (g_i/2)m_i c^2}{94 \text{ eV}}, \tag{2.28}$$

where N is the number of neutrino species and $g_i = 4, 2$ for Dirac and Majorana neutrinos. Constraints from the CMB give the sum of neutrino masses as <0.194 eV/c^2 and the number of neutrino species as consistent with the 3 SM generations [28]. This then gives

$$\Omega_{\nu,0}h^2 < \begin{cases} 0.0021 & \text{Dirac} \\ 0.0042 & \text{Majorana.} \end{cases} \tag{2.29}$$

The second constraint is that the neutrino relic density is an order of magnitude too small to account for all of the non-baryonic matter in the universe.

2.4.4   Sterile Neutrinos

The simplest neutrino addition to the SM is a right-handed neutrino which does not interact through the weak force. Such "sterile" neutrinos have right-handed chirality, complimenting the left-handed SM neutrinos [167]. These neutrinos could mix with the SM neutrinos and participate in Higgs or new physical interactions.

Both Majorana and Dirac masses are allowed in the Lagrangian for sterile neutrinos, which allows for an unequal distribution of masses between the left- and right-handed neutrinos (the "see-saw" mechanism). The observable masses are found by considering the mass matrix $\mathcal{M}$ resulting from the mixing of SM and sterile neutrinos. For simplicity, a single neutrino of each type gives the matrix

$$\mathcal{M} = \left[\begin{array}{cc} 0 & m_D \\ m_D & m_R \end{array} \right] \tag{2.30}$$

where m_D and m_R are the Dirac and Majorana masses of the sterile neutrino and $m_R \gg m_D$. The observable masses for the sterile M_s and SM $M_{\rm SM}$ neutrinos correspond to the eigenvalues of $\mathcal{M}$. These eigenvalues are disproportional, in that the larger is $M_s \approx m_R$ and the lighter $M_{SM} \approx m_D/m_R$.[6] This simultaneously explains the light masses of the SM neutrinos and the necessary heavier mass of the sterile neutrino. The neutrino minimal standard model (νMSM) takes the sterile neutrino mass in the keV/c^2–GeV/c^2 range, making it (or, if there are more than one sterile neutrino, the lightest one) a viable dark matter candidate [168–170].[7]

The sterile neutrino N can decay through a dominant channel as $N \to \nu\nu\bar{\nu}$ and through a subdominant channel as $N \to \nu\gamma$. The latter decay channel indicates that dark matter wouldn't be entirely dark and should be detectable using standard astronomical methods. Recent observations from the Fermi Large Area Telescope searching for this flux give the lifetime of the N as $\gtrsim 10^{19}$ yr for $20 < M_s < 50$ keV [172]. Although N is not strictly stable, it would be so on the scale of the age of the universe. Other astrophysical observation methods are possible, which restrict N as dark matter

---

[6] The second eigenvector technically has a negative sign, but that is naturally accounted for in the Lagragian to give a positive mass.

[7] In this mass range, the sterile neutrino is a warm dark matter candidate, and bounds on its mass can be found via large-scale structure arguments [171].

to masses $1 < M_s < 50$ keV/c^2 [170].

2.4.5   Axions

The Lagrangian which describes quantum chromodymamics (QCD), the theory of strong interactions between quarks and gluons, includes a term which permits QCD to violate charge-parity (CP) symmetry. The proportionality constant $\bar{\theta}$ for this CP-violating term is naively expected to be of order of unity. One consequence of this violation is to endow the neutron with an electric dipole moment; experimental searches for this dipole yield a bound of $\bar{\theta} \lesssim 10^{-10}$ [173]. This small bound, and questions of its naturalness, is termed the strong CP problem.

A solution to the strong CP problem was proposed by Peccei and Quinn [174, 175] who introduced a global abelian symmetry called PQ symmetry. They assume that PQ symmetry is spontaneously broken and thus produces a pseudo-Nambu-Goldsone boson, called the axion A^8 [176, 177]. The potential for the axion naturally cancels out the unwanted CP-violating term in the Lagrangian, solving the strong CP problem.

The mass of the axion m_A is given by [178]

$$m_A \simeq 6 \ \mu\text{eV} \frac{10^{12} \ \text{GeV}}{f_A},\tag{2.31}$$

where f_A is called the axion decay constant. Axions can couple to two γ's with a Lagrangian term of

$$\mathcal{L}_{A\gamma\gamma} = G_{A\gamma\gamma} \mathbf{E} \cdot \mathbf{B} \phi_A,\tag{2.32}$$

where $G_{A\gamma\gamma}$ is the coupling coefficient, $\mathbf{E}$ and $\mathbf{B}$ are electric and magnetic fields and ϕ_A is the axion field. For the Peccei-Quinn axion, $G_{A\gamma\gamma} \propto m_A$, however a class of particles called axion-like particles (ALPs), where the coupling strength is not dependent on the mass, are also considered. The coupling above provides an additional method by which stars can radiate energy. Considerations of stellar lifetimes leads to a first-order limit on the mass of $m_A < 10^{-2}$ eV/c^2 [179]. As also indicated in Fig. 2.1, the mass of the axion is significantly smaller than standard WIMPs.

Cosmologically produced axions are a dark matter candidate. Axions due to thermal

---

[8] Both A and a are used to denote the axion in the literature.
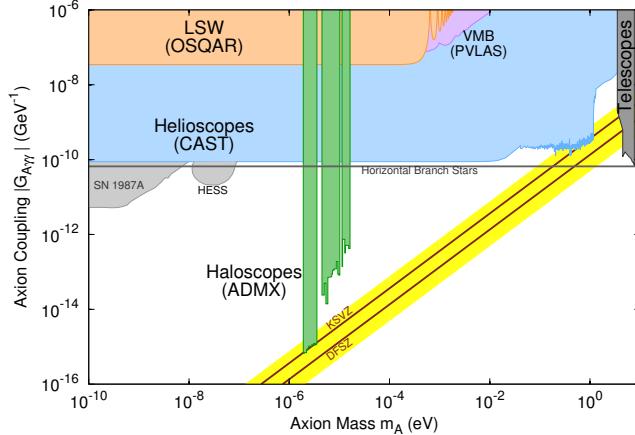
Figure 2.10: Axion-like particle parameter space, particle mass m_a versus two photon coupling coefficient $G_{A\gamma\gamma}$, and exclusion limits from a variety of sources. An axion which is also cosmic dark matter would reside in the yellow band, with two popular theories indicated (KSVZ and DFSZ). Figure from [29].

freeze-out are relativistic and incur the restriction of HDM [29]. However, there are several ways by which cold axions can also be produced [180]. The energy density of cold axions varies depending upon how they were produced and whether PQ symmetry breaking occurs before or after inflation, but the value is typically

$$\Omega_A h^2 \sim \left(\frac{f_A}{10^{12} \text{ GeV}} \right)^{7/6}. \tag{2.33}$$

Combining with Eq. 2.31, the axion could account for the cold dark matter density if $m_A \sim \mathcal{O}\left(10 \ \mu\text{eV}/c^2\right)$.

Bounds on axions and ALPs come from numerous experimental sources and mostly focusing on the $A\gamma\gamma$ coupling (bounds can also be placed on the Aee coupling [181]). A selection of these limits are shown in Fig. 2.10 in the m_A versus $G_{A\gamma\gamma}$ plane. A common experimental method is to use the $A\gamma\gamma$ interaction by converting either solar (helioscopes) or cosmic (haloscopes) axions to photons in strong fields [182]. Although small portions of the cosmologically interesting parts of the plane have begun to be probed, the vast majority of this space is still unexplored.

Chapter 3

Direct Detection of Dark Matter

The premise for a direct detection experiment is that the galaxy is embedded in a WIMP halo, and therefore the Earth is traveling through the dark matter. Direct detection experiments are particle physics detectors which attempt to detect individual WIMPs that scatter off the detector's target, assuming that gravity is not their sole interaction. More specifically, because the WIMPs interact through the weak force, detectable interactions will be with the nuclei in the detector's target. Such an interaction is called a nuclear recoil (NR), as opposed to an electron recoil (ER), defined as interactions with the atomic electrons in the target.

The rate for these interactions is small (Secs. 3.1–3.3), requiring extensive measures to reduce backgrounds (Sec. 3.4), and a variety of experiments participate in the field (Sec. 3.6).

3.1 Direct Detection Rate

The number of observed events N with recoil energy E_r in some energy range $E_1 \to E_2$ is [183]

$$N = \int_{E_1}^{E_2} \frac{\mathrm{d}N}{\mathrm{d}E}\,\mathrm{d}E = \int_{E_1}^{E_2} \frac{\mathrm{d}R}{\mathrm{d}E_r}\mathcal{E}(E)\,\mathrm{d}E_r, \qquad (3.1)$$

where $\mathrm{d}R/\mathrm{d}E$ is the differential recoil rate per detector mass and exposure time and $\mathcal{E}(E_r)$ is the effective exposure of the experiment (how large is the detector, how long is the run, and how efficient is it at correctly identifying NRs). Determining the differential

rate starts with the differential number density of WIMPs in the neighborhood of the detector [184, 185]

$$\mathrm{d}n = n_0 \frac{f(\boldsymbol{v}, \boldsymbol{v}_E)}{k} \, \mathrm{d}^3 \boldsymbol{v}, \tag{3.2}$$

where the mean WIMP number density is $n_0 \equiv \rho_0/m_\chi$, with ρ_0 as the local mass density of WIMPs of mass m_χ, $\boldsymbol{v}$ is the velocity of the WIMPs, and $\boldsymbol{v}_E$ is the Earth's velocity relative to the dark matter halo. $f(\boldsymbol{v}, \boldsymbol{v}_E)$ is the velocity distribution function of the halo, with respect to the Earth, with normalization k such that

$$n_0 = \int_0^{v_{\mathrm{esc}}} \mathrm{d}n, \tag{3.3}$$

with $v = |\boldsymbol{v}|$ and v_{esc} as the local escape velocity of the galaxy. The differential event rate per mass on a target with N_T nuclei per unit mass is

$$\mathrm{d}R = N_T v \, \mathrm{d}\sigma \, \mathrm{d}n = N_T n_0 \, \mathrm{d}\sigma \frac{v f(\boldsymbol{v}, \boldsymbol{v}_E)}{k} \, \mathrm{d}^3 \boldsymbol{v}, \tag{3.4}$$

where $\mathrm{d}\sigma$ is the differential WIMP-nucleus interaction cross section.

WIMPs have non-relativistic velocities $\mathcal{O}(10^{-3}c)$. Thus, a WIMP with velocity v and energy $E = \frac{1}{2}mv^2$, will impart a recoil energy E_{r} to the nucleus of mass m_T of

$$E_{\mathrm{r}} = \frac{\mu_T^2 v^2}{m_T} \left(1 - \cos\theta \right), \tag{3.5}$$

where θ is the recoiling angle in the center of mass frame and $\mu_T = m_\chi m_T / (m_\chi + m_T)$ is the reduced mass of the WIMP-nucleus system.[1] There is thus a range of WIMP energies, and therefore WIMP velocities, which can create a specific E_{r} value. The minimum being

$$v_{\mathrm{min}} = \sqrt{\frac{m_T E_{\mathrm{r}}}{2\mu_T^2}}, \tag{3.6}$$

while the maximum v_{max} is related to the Galactic escape velocity v_{esc} and the Earth's motion in the halo. Note also that for a specific WIMP velocity, Eq. 3.5 gives the

---

[1] The average recoil energy is $\langle E_{\mathrm{r}} \rangle = \mu_T^2 v^2/m_T = E_\chi \left(2\xi/(1+\xi)^2 \right)$ with $\xi = m_T/m_\chi$. For a 100 GeV/c^2 WIMP with $v = 10^{-3}c$ scattering on a Germanium nuclei ($m_T \sim 67$ GeV/c^2), the recoil is $\langle E_{\mathrm{r}} \rangle = 24$ keV. For the same WIMP scattering with an electron ($m_T = 511$ keV/c^2), the recoil is $\langle E_{\mathrm{r}} \rangle = 0.5$ eV, below modern detector technology reach. This is the justification for only searching for NRs from WIMPs.

maximum possible recoil as $E_{\mathrm{r}}^{\max} = 2\mu_T^2 v^2/m_T$. The differential rate, with respect to recoil energy, $\mathrm{d}R/\,\mathrm{d}E_{\mathrm{r}}$ must therefore account for all WIMP velocities $v_{\min} \leq v \leq v_{\max}$ which can impart E_{r} to the nucleus as well as the changing value of the cross section with E_{r}

$$\frac{\mathrm{d}R}{\mathrm{d}E_{\mathrm{r}}} = n_0 N_T \int_{v_{\min}}^{v_{\max}} \frac{\mathrm{d}\sigma}{\mathrm{d}E_{\mathrm{r}}} \frac{v f(\boldsymbol{v}, \boldsymbol{v}_E)}{k} \,\mathrm{d}^3\boldsymbol{v}. \tag{3.7}$$

3.2 WIMP-nucleon Cross Sections

For a given WIMP theory, the specific value of the interaction cross section can be computed from first principles. However, since the true nature of dark matter is as yet unknown, a more general approach is taken. The WIMP-nuclei interaction is typically categorized as either being spin-independent (SI) or spin-dependent (SD) [186], although a more general effective field theory approach is actively being investigated by many groups [187–190]. This section considers the two canonical interactions and demonstrates how they relate to the total rate.

3.2.1 Spin-Independent Interaction

The SI interaction typically arises from scalar couplings between WIMPs and quarks in the Lagrangian.[2] In the non-relativistic limit, the general scalar term is [191, 192]

$$\mathcal{L} \supset \alpha_q^S \bar{\chi}\chi\bar{q}q, \tag{3.8}$$

where α_q^S is a coupling constant and χ and q are the WIMP and quark fields respectively. The cross section is usually considered in terms of the momentum transferred in the scatter $q^2 \equiv |\boldsymbol{q}|^2 = 2m_T E_{\mathrm{r}}$. In the zero-momentum $(q \to 0)$ limit, the above interaction term gives the differential cross section [95]

$$\left.\frac{\mathrm{d}\sigma_{\mathrm{SI}}}{\mathrm{d}q^2}\right|_{q\to 0} = \frac{f_{p/n}}{\pi v^2}, \tag{3.9}$$

---

[2] Vector interactions are also possible, such as for a Dirac fermion. See, e.g. [95, 191–193] for details.

where v is the relative velocity of the WIMP to a nucleon, and the proton/neutron couplings are

$$\frac{f_{p/n}}{m_{p/n}} = \sum_{q=u,d,s} \frac{\alpha_q^S}{m_q} f_{Tq}^{(p/n)} + \frac{2}{27} f_{TG}^{(p/n)} \sum_{q=c,b,t} \frac{\alpha_q^S}{m_q}, \tag{3.10}$$

where $f_{Tq}^{(p/n)}$ give the contributions of the light mass quarks to the nucleon mass $m_{p/n}$ while $f_{TG}^{(p/n)} = 1 - \sum_{q=u,d,s} f_{Tq}^{(p/n)}$ gives the gluon contribution. In the $q \to 0$ limit, the interaction is coherent between nuclei in a nucleus (A, Z) giving the total nuclear cross section as a sum over all of the nuclei

$$\left. \frac{d\sigma_{\mathrm{SI}}}{dq^2} \right|_{q \to 0} = \frac{1}{\pi v^2} \left[f_p Z + (A - Z) f_n \right]^2. \tag{3.11}$$

As the energy of the recoil increases, $q > 0$, the WIMP begins to probe the internal structure of the nucleus and the interaction loses coherence. This loss is parameterized by a nuclear form factor $F_{\mathrm{SI}}(q)$, where $F_{\mathrm{SI}}(q = 0) = 1$ and

$$\frac{d\sigma_{\mathrm{SI}}}{dq^2} = \frac{1}{\pi v^2} \left[f_p Z + (A - Z) f_n \right]^2 F_{\mathrm{SI}}^2(q). \tag{3.12}$$

A standard cross section σ_0^{SI} is defined as the total cross section in the zero momentum limit [95]

$$\sigma_0^{\mathrm{SI}} = \int_0^{4\mu_T^2 v^2} \left. \frac{d\sigma_{\mathrm{SI}}}{dq^2} \right|_{q \to 0} dq^2$$
$$= \frac{4\mu_T^2}{\pi} \left[f_p Z + (A - Z) f_n \right]^2, \tag{3.13}$$

where $4\mu_T^2 v^2$ is the momentum transfer at $E_{\mathrm{r}} = E_{\mathrm{r}}^{\mathrm{max}}$. Combining Eqs. 3.12 and 3.13 gives[3]

$$\frac{d\sigma_{\mathrm{SI}}}{dq^2} = \frac{1}{4\mu_T^2 v^2} \sigma_0^{\mathrm{SI}} F_{\mathrm{SI}}^2(q) \tag{3.14}$$

$$\frac{d\sigma_{\mathrm{SI}}}{dE_{\mathrm{r}}} = \frac{m_T}{2\mu_T^2 v^2} \sigma_0^{\mathrm{SI}} F_{\mathrm{SI}}^2(q). \tag{3.15}$$

When the wavelength of the scatter h/q is comparable to the radius, the effective

---

[3] Note that the fraction given in the second expression is equivalent to $1/E_r^{\mathrm{max}}$.
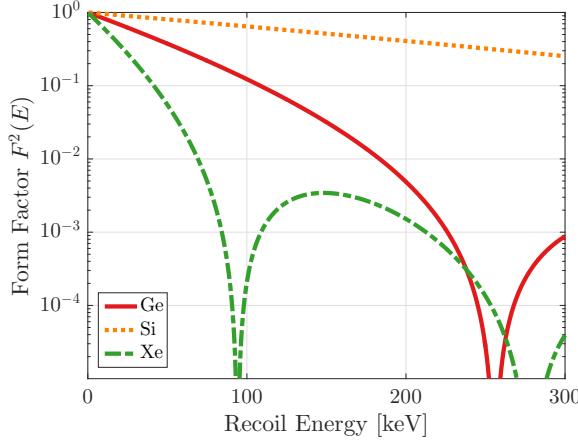
Figure 3.1: Helm form factors as a function of nuclear recoil energy for three elements used as direct detection experimental targets: Ge (red solid), Si (tan dotted), and Xe (green dashed-dot).

cross section begins to decrease, i.e. $F_{\mathrm{SI}} < 1$. Although there are several analytical and theoretical models for the form factor [194], the one most commonly used in the direct detection community is that of Helm [195][4]

$$F_{\mathrm{SI}}(q) = 3\frac{j_1(qr_n)}{qr_n}e^{-\frac{1}{2}(qs)^2} \tag{3.16}$$

$$= 3\frac{\sin(qr_n) - qr_n\cos(qr_n)}{(qr_n)^3}e^{-\frac{1}{2}(qs)^2}, \tag{3.17}$$

where j_1 is the spherical Bessel function of the first order, s is a measure of the nuclear skin thickness, and r_n is a measure of the nuclear radius. There are several methods of parameterizing these values, with Ref. [184] preferring

$$r_n^2 = c^2 + \frac{7}{3}\pi^2 a^2 - 5s^2 \tag{3.18}$$

$$c \simeq 1.23A^{1/3} - 0.60 \text{ fm} \tag{3.19}$$

$$s \simeq 0.9 \text{ fm} \tag{3.20}$$

$$a \simeq 0.52 \text{ fm}. \tag{3.21}$$

The squares of the Helm form factors for various target nuclei are shown in Fig. 3.1.

Further assumptions and normalizations are typically used in the direct detection

---

[4] This distribution is similar, but not identical to, the Fourier transform of a Woods-Saxon parameterized nuclear density distribution, and, as such, some authors label it the Woods-Saxon form factor [95, 196].

field. Most models use an isospin-conserving WIMP interaction, which treats protons and neutrons the same ($f_n = f_p$). Equation 3.13 then yields

$$\sigma_0^{\text{SI}} = \frac{4\mu_T^2}{\pi} A^2 f_p^2. \tag{3.22}$$

Targets with higher atomic mass receive an A^2 enhancement of the cross-section. For Xe, Ge, and Si this is $A^2 \sim 16900$, 5000 and 800 respectively. Additionally, since different experiments have different detector targets, results are computed on the WIMP-proton cross section $\sigma_p^{SI} = \sigma_0^{\text{SI}}(A = 1)$, as opposed to that of the WIMP-nucleus given above. Since f_p is the same for both expressions, a rearrangement gives

$$\sigma_0^{\text{SI}} = \left(\frac{\mu_T}{\mu_p} A\right)^2 \sigma_p^{\text{SI}}, \tag{3.23}$$

where μ_p is the reduced mass of the WIMP-proton system. Since a WIMP model enters through f_p, quoting limits on σ_p^{SI} is model independent and detector target agnostic.

3.2.2 Spin-Dependent Interaction

The SD interaction does not have the coherence advantage of the SI case. Nucleons with opposite spin interfere destructively meaning that the interaction is dominated by unpaired nucleons. The number and species of unpaired nucleons varies even between isotopes of the same material. Additionally, this interference occurs even in the zero-momentum transfer limit, meaning that the separation into a point-like interaction and form factor, as was done in the SI case, is not strictly possible. This also implies that different detector compositions have widely different sensitivities depending on whether or not they have have an unpaired proton or neutron.

The SD contribution to the cross section is typically assumed to come from the axial current coupling to quarks. For fermionic WIMPs, such as the lightest supersymmetric particle, the Lagrangian component is

$$\mathcal{L} = \alpha_q^A \left(\bar{\chi}\gamma^\mu\gamma_5\chi\right)\left(\bar{q}\gamma_\mu\gamma_5 q\right). \tag{3.24}$$

For non-fermionic WIMPs, such as the spin-1 lightest Kaluza-Klein particle and lightest

T-odd particle, the interaction is slightly different [191, 193]. The differential cross section [196–199] for the full nucleus is

$$\frac{\mathrm{d}\sigma_{\mathrm{SD}}}{\mathrm{d}q^2} = \frac{8G_{\mathrm{F}}^2}{(2J+1)\,v^2} S_T(q),$$
(3.25)

where G_{F} is the Fermi coupling constant, J is the total nuclear spin, and the spin-structure function for the target nucleus is

$$S_T(q) = a_0^2 S_{00}(q) + a_1^2 S_{11}(q) + a_0 a_1 S_{01}(q).$$
(3.26)

The isoscalar (S_{00}), isovector (S_{11}), and interference (S_{01}) functions are determined either by experiment or nuclear modeling. The isoscalar and isovector couplings $a_0 = a_p + a_n$ and $a_1 = a_p - a_n$ are related to the proton/neutron couplings a_p/a_n defined as

$$a_{p/n} = \sum_{q=u,d,s} \frac{\alpha_q^A}{\sqrt{2}G_{\mathrm{F}}} \Delta_q^{(p/n)},$$
(3.27)

where $\Delta_q^{(p/n)}$ are related to the matrix elements of the axial-vector current in the nucleon as $\langle p, n| \, \bar{q}\gamma_\mu\gamma_5 q \, |p, n\rangle = 2s_\mu^{(p/n)}\Delta_q^{(p/n)}$ with $s_\mu^{(p/n)}$ as the nucleon spin [95]. Results are often presented in the proton- or neutron-only basis defined as $a_1 = a_0 = 1$ (proton only) and $a_1 = -a_0 = 1$ (neutron only). The spin-structure functions for the proton- and neutron-only bases for several isotopes are shown in Fig. 3.2 using the recent computations of [198] compared to the older calculations of [200–202]. All of the isotopes shown have an odd neutron, resulting in larger neutron-only structure functions.

Equation 3.25 can be massaged into a form similar to Eq. 3.14 by normalizing the spin-structure function to unity at $q = 0$ as [95, 184]

$$\frac{\mathrm{d}\sigma_{\mathrm{SD}}}{\mathrm{d}q^2} = \frac{8G_{\mathrm{F}}^2}{(2J+1)\,v^2} S_T(0)F_{\mathrm{SD}}^2(q),$$
(3.28)

(a) Proton-Only Coupling   (b) Neutron-Only Coupling
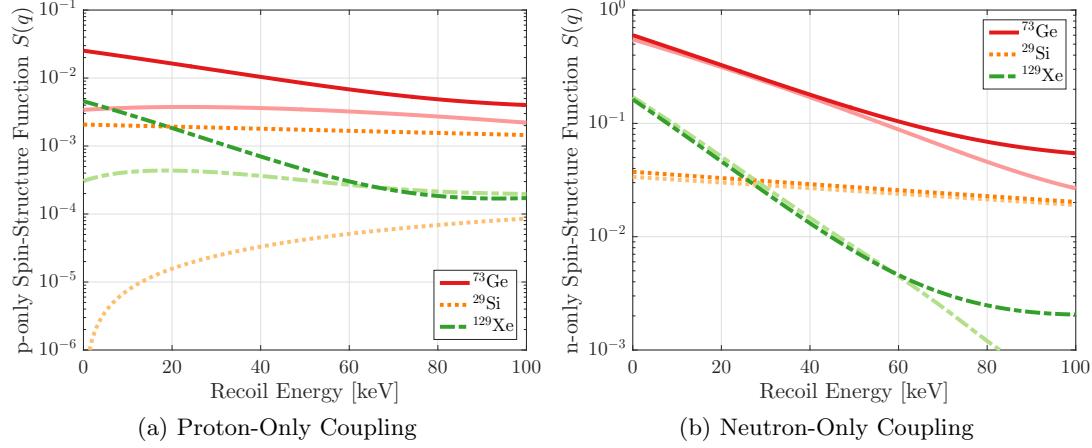
Figure 3.2: Spin-structure functions for the proton-only (a) and neutron-only (b) spin-dependent interactions as a function of nuclear recoil energy for nucleon-odd isotopes found in Ge (red solid curves), Si (orange dotted curves), and Xe (green dashed-dot curves). For Ge and Si, the only nucleon-odd isotopes are ^{73}Ge and ^{29}Si while Xe has two isotopes, ^{129}Xe and ^{131}Xe, with similar abundances and structure functions, only one of which is shown here. The newer, two-body, computations [198] are given by darker curves while older [200–202] computations are lighter curves.

where $F_{\mathrm{SD}}^2 \equiv S(q)/S(0)$. The zero-momentum structure function is [198]

$$S_T(0) = \frac{(2J+1)(J+1)}{4\pi J}\left|\left(a_0 + a_1'\right)\langle S_p\rangle + \left(a_0 - a_1'\right)\langle S_n\rangle\right|^2 \tag{3.29}$$

$$\approx \frac{(2J+1)(J+1)}{\pi J}\left|a_p\langle S_p\rangle + a_n\langle S_n\rangle\right|^2, \tag{3.30}$$

where $\langle S_{p/n}\rangle$ are the spin expectation values of the proton/neutron groups within the nucleus. The isovector coupling $a_1' = a_1\left(1 + \delta a_1(0)\right)$ includes two-body currents in the δa_1 term. Two-body currents represent a WIMP interacting with two nuclei through chiral effective field theory as computed using the nuclear model of [198]. Including two-body currents is a recent development, and the second line above gives the more widely used expression in older literature with only single-body currents. The difference between including, or not including, two-body currents is shown in Fig. 3.2 where the even nucleon group (protons for each of the elements shown) receives a boost by a factor of $\sim$10 towards low recoil energies. When two-body currents are included, the new contribution makes it such that the odd-nucleon type determines the structure function

for both proton and neutron dependent scattering [198]. Note also that, even without two-body currents, computations of the spin-expectation values give $\langle S_{n/p} \rangle \neq 0$ in odd-proton/-neutron nuclei due to polarization effects, although $\langle S_p \rangle \gg \langle S_n \rangle$ for proton-odd nuclei and vice versa for neutron-odd nuclei.

A standard cross section σ_0^{SD} is again defined by integrating the cross section in the zero momentum limit [95, 203]

$$\sigma_0^{\text{SD}} = \frac{32}{2J+1} G_{\text{F}}^2 \mu_T^2 S_T(0) \tag{3.31}$$

$$= \frac{8(J+1)}{\pi J} G_{\text{F}}^2 \mu_T^2 \left| (a_0 + a_1') \langle S_p \rangle + (a_0 - a_1') \langle S_n \rangle \right|^2. \tag{3.32}$$

The differential cross section is written in terms of σ_0^{SD} as

$$\frac{\text{d}\sigma_{\text{SD}}}{\text{d}q^2} = \frac{1}{4\mu_T^2 v^2} \sigma_0^{\text{SD}} F_{\text{SD}}^2(q) \tag{3.33}$$

$$\frac{\text{d}\sigma_{\text{SD}}}{\text{d}E_{\text{r}}} = \frac{m_T}{2\mu_T^2 v^2} \sigma_0^{\text{SD}} F_{\text{SD}}^2(q). \tag{3.34}$$

Similarly to the SI case, results on the standard cross section are normalized to that of a free nucleon, either a proton σ_p^{SD} or neutron σ_n^{SD}. Unfortunately, due to the differences in spin states between the nuclei, the scaling from nucleus to nucleon is not as clean. The cross section of the nucleus in terms of that of a proton/neutron is

$$\sigma_0^{\text{SD}} = \frac{2}{2J+1} \left(\frac{\mu_T}{\mu_{p/n}} \right)^2 \frac{S_T(0)}{S_{p/n}(0)} \sigma_{p/n}^{\text{SD}} \tag{3.35}$$

$$= \frac{1}{3} \frac{J+1}{J} \left(\frac{\mu_T}{\mu_{p/n}} \right)^2 \frac{|(a_0 + a_1') \langle S_p \rangle + (a_0 - a_1') \langle S_n \rangle|^2}{a_{p/n}^2} \sigma_{p/n}^{\text{SD}}, \tag{3.36}$$

where in the free proton/neutron scattering $\langle S_{p/n} \rangle = 1/2 = J$, $\langle S_{n,p} \rangle = 0$, and $\delta a_1(0) = 0$ (i.e. there cannot be two-body scattering in the free nucleon case). This expression is significantly more complicated than the corresponding SI case (Eq. 3.23) and, unless two-body currents are neglected, it cannot be simplified to remove all dependence on the model parameters $a_0/a_1 \to a_p/a_n$.

3.2.3 Cross Sections and Rate

The results of the previous two sections are combined with Eq. 3.7 to separate the nuclear and particle physics inputs from the astrophysical input. The complete differential WIMP-nucleus cross section is a sum of the SI and SD components

$$\frac{\mathrm{d}\sigma}{\mathrm{d}E_{\mathrm{r}}} = \frac{\mathrm{d}\sigma_{\mathrm{SI}}}{\mathrm{d}E_{\mathrm{r}}} + \frac{\mathrm{d}\sigma_{\mathrm{SD}}}{\mathrm{d}E_{\mathrm{r}}} \tag{3.37}$$

$$\frac{\mathrm{d}\sigma}{\mathrm{d}E_{\mathrm{r}}} = \frac{m_T}{2\mu_T^2 v^2} \left[\sigma_0^{\mathrm{SI}} F_{\mathrm{SI}}^2(q) + \sigma_0^{\mathrm{SD}} F_{\mathrm{SD}}^2(q) \right], \tag{3.38}$$

where Eqs. 3.15 and 3.34 were used in the second line and the values for the standard cross sections and form factors are found in the above sections. Placing this into Eq. 3.7 along with substituting $n_0 = \rho_0/m_\chi$ gives[5]

$$\frac{\mathrm{d}R}{\mathrm{d}E_{\mathrm{r}}} = \underbrace{\frac{N_T m_T}{2 m_\chi \mu_T^2}}_{\text{Detector}} \cdot \underbrace{\left[\sigma_0^{\mathrm{SI}} F_{\mathrm{SI}}^2(E_{\mathrm{r}}) + \sigma_0^{\mathrm{SD}} F_{\mathrm{SD}}^2(E_{\mathrm{r}}) \right]}_{\text{Particle and Nuclear}} \cdot \underbrace{\rho_0 \int_{v_{\min}}^{v_{\max}} \frac{1}{k} \frac{f(\boldsymbol{v}, \boldsymbol{v}_E)}{v} \, \mathrm{d}^3 \boldsymbol{v}}_{\text{Astro}}. \tag{3.39}$$

3.3 Standard Halo Model

The astrophysical contribution to the direct detection rate is

$$\mathcal{I} = \frac{\rho_0}{k} \int_{v_{\min}}^{v_{\max}} \frac{f(\boldsymbol{v}, \boldsymbol{v}_E)}{v} \, \mathrm{d}^3 \boldsymbol{v}, \tag{3.40}$$

where the specific value of $\mathcal{I}$ depends upon the dark matter halo velocity distribution, the local mean density, and specific velocities describing the galaxy and the Earth's motion through it. The first piece requires assumptions and model building while the latter two pieces come from astrophysical measurements.

The Standard Halo Model (SHM) accepted for use in the direct detection community assumes the dark matter halo is an isothermal, isotropic, and non-rotating sphere.[6] For a collection of particles in this situation, the phase space distribution function $f(\boldsymbol{x}, \boldsymbol{v})$

---

[5] The portion labeled astrophysics does have some detector dependence in $v_{\min}$ as from Eq. 3.6.

[6] A rotating halo would flatten, similarly to the luminous disk, which is counter to the scale height of HI gas in the Milky Way (see Sec. 1.3.1). Note that rotating, or counter-rotating, models have been considered in [185].

is that which solves the collisionless Boltzmann equation

$$\frac{\mathrm{d}f}{\mathrm{d}t} = \frac{\partial f}{\partial t} + \boldsymbol{v} \cdot \frac{\partial f}{\partial \boldsymbol{x}} - \frac{\partial \Phi}{\partial \boldsymbol{x}} \frac{\partial f}{\partial \boldsymbol{v}} = 0, \tag{3.41}$$

where Φ is the Newtonian potential. For a self-gravitating isothermal sphere, the solution is found via Maxwell-Boltzmann statistics as

$$f(\boldsymbol{x}, \boldsymbol{v}) = C \exp\left(-E/k_{\mathrm{B}}T\right), \tag{3.42}$$

where C is a normalization constant and the energy is given by $E = \frac{1}{2}m_\chi v^2 + m_\chi \Phi(\boldsymbol{x})$. The velocity distribution function is required for computed $\mathcal{I}$ and is found by integrating over the spatial coordinates

$$\begin{aligned}
f(\boldsymbol{v}) &= \int f(\boldsymbol{x}, \boldsymbol{v}) \, \mathrm{d}^3\boldsymbol{x} \\
&= C \exp\left(-m_\chi v^2/2k_{\mathrm{B}}T\right) \int \exp\left(-m_\chi \Phi(\boldsymbol{x})\right) \mathrm{d}^3\boldsymbol{x} \\
&= C' \exp\left(-m_\chi v^2/2k_{\mathrm{B}}T\right) \\
&= C' \exp\left(-v^2/2\sigma_v^2\right),
\end{aligned} \tag{3.43}$$

where the spatial integral over the potential is absorbed, along with other proportionality constants, into C' (for Eq. 3.41, the distribution at the Earth's location, where the potential is a constant, is needed and justifies this combination) and $\sigma_v^2 \equiv k_{\mathrm{B}}T/m_\chi$. This is a Maxwellian velocity distribution with radial velocity dispersion σ_v.[7] The temperature of the dark matter halo cannot be measured, however σ_v can otherwise be related to measurable astrophysical quantities.

Poisson's equation for this system is

$$\frac{1}{r^2}\frac{\mathrm{d}}{\mathrm{d}r}\left(r^2\frac{\mathrm{d}\Phi}{\mathrm{d}r}\right) = 4\pi G_{\mathrm{N}}\rho. \tag{3.44}$$

Integrating Eq. 3.41 over velocities instead of positions gives the density as $\rho \propto$

---

[7] The definition of σ_v in the literature is inconsistent. The one-dimensional dispersion is used here while others use the three-dimensional dispersion. The two are related as $\sigma_v^2 \to \sigma_v^2/3$ transforming from the one- to three-dimensional case.

$\exp\left(-\Phi/\sigma^2\right)$ allowing for 3.44 to be rewritten as

$$\frac{\mathrm{d}}{\mathrm{d}r}\left(r^2\frac{\mathrm{d}\ln\rho}{\mathrm{d}r}\right) = -\frac{4\pi G_{\mathrm{N}}}{\sigma_v^2}r^2\rho. \tag{3.45}$$

Solving Eq. 3.45 yields the density

$$\rho(r) = \frac{\sigma_v^2}{2\pi G_{\mathrm{N}}r^2}, \tag{3.46}$$

which has the desired r^{-2} behavior to give flat rotation curves. The circular velocity v_c is related to the dispersion by $v_c = \sqrt{2}\sigma_v$. This solution, called the singular isothermal sphere, has infinite density at the origin and a change of coordinates is required to avoid the singularity (see [204] for a full derivation). In the new coordinates, $v_c(r)$ is non-constant, but is such that $v_c(r \to \infty) \equiv v_0 = \sqrt{2}\sigma_v$, where v_0 is called the characteristic velocity. The dispersion σ_v is thus related to the measurable v_0.

In using Eq. 3.43 in Eq. 3.40, the velocity distribution must be boosted from the halo frame to the lab (Earth) frame. This boosting is done by

$$\boldsymbol{v} \to \boldsymbol{v} + \boldsymbol{v}_E = \boldsymbol{v} + \boldsymbol{\Theta}_0 + \boldsymbol{v}_\odot + \boldsymbol{v}_\oplus, \tag{3.47}$$

where $\boldsymbol{\Theta}_0$ is local standard of rest (LSR). This corresponds to the Galactic circular rotation at the Earth's radius R_0. $\boldsymbol{v}_\odot$ is the sun's peculiar velocity with respect to neighboring stars and $\boldsymbol{v}_\oplus$ is the Earth's orbital velocity around the sun. The galactic rotation curve is fairly flat between 4–18 Kpc [185]. With the Earth at $R_0 \approx 8.5$ Kpc, the SHM assumes the rotation curve of the galaxy has already reached its asymptotic value at R_0 giving $v_0 = \Theta_0$.[8] The motion of the Earth around the Sun changes the kinetic energy of the impinging WIMPs over the course of a year. The orbital velocity is small compared to $\boldsymbol{v}_0 + \boldsymbol{v}_\odot$ and is typically assumed to be averaged out over a year.[9] The value given for $v_\odot$ is the component of the Solar peculiar velocity in the direction of the galactic rotation, which is, for simplicity, the only component ordinarily used giving the yearly averaged $v_E = v_0 + v_\odot$ along the galactic rotation. The numerical values used in the SHM, and their associated uncertainties, are studied in Sec. 12.6.

---

[8] By this argument, the most probable velocity of the WIMPs is identical to the LSR in the SHM.
[9] Some searches use this known motion to their advantage, in which case it is accounted for.

Absorbing all integration constants together as $1/k$, the value of k is found via Eq. 3.3. The normalization integral gives then

$$k = \int_0^{2\pi} \mathrm{d}\phi \int_0^{v_{\mathrm{esc}}} \int_{-1}^{+1} \exp\left(-|\boldsymbol{v} + \boldsymbol{v}_E|^2 / v_0^2\right) \mathrm{d}(\cos\theta) v^2 \, \mathrm{d}v$$

$$= \left(\pi v_0^2\right)^{3/2} \left[\mathrm{erf}(z) - \frac{2}{\sqrt{\pi}} z e^{-z^2}\right] \tag{3.48}$$

$$\equiv k_0 \left[\mathrm{erf}(z) - \frac{2}{\sqrt{\pi}} z e^{-z^2}\right], \tag{3.49}$$

where $z = v_{\mathrm{esc}}/v_0$.

Lastly, the integral over velocities in Eq. 3.40 is evaluated. The pure Maxwellian velocity distribution extends to infinite velocities, but in a physical picture the distribution will be cut off at some maximum velocity. In the frame of the halo, this maximum velocity is the Galactic escape velocity, however, in the lab frame, care must be taken due to the movement of the Earth [185, 205, 206]. For particular choices of v_{min} (i.e. WIMP mass, detector material), using $v_{\mathrm{max}} = v_{\mathrm{esc}}$ can lead to negative rates which are nonphysical. The proper approach is to consider that the maximum velocity is bounded as

$$|\boldsymbol{v} + \boldsymbol{v}_E| \leq v_{\mathrm{esc}}, \tag{3.50}$$

which gives the relation

$$v_{\mathrm{max}}(\cos\theta) = \sqrt{v_{\mathrm{esc}}^2 - v_E^2 \left(1 - \cos^2\theta\right)} - v_E \cos\theta, \tag{3.51}$$

where θ is the scattering angle in the galactic rest frame. The integral is then

$$\mathcal{I} = \frac{\rho_0}{k} \int_0^{2\pi} \mathrm{d}\phi \int_{-1}^{+1} \int_{v_{\mathrm{min}}}^{v_{\mathrm{max}}(\cos\theta)} v \exp\left(-\frac{v^2 + 2v v_E \cos\theta + v_E^2}{v_0^2}\right) \mathrm{d}v \, \mathrm{d}(\cos\theta). \tag{3.52}$$

There are three distinct cases for the relationship between v_{min} and $v_{\mathrm{max}}(\cos\theta)$ which

lead to different results (the details of the integrations can be found in [205])

$$
\mathcal{I} \;=\; \frac{k_0}{k}\frac{\rho_0}{2yv_0}
\begin{cases}
\operatorname{erf}(x+y) - \operatorname{erf}(x-y) - \frac{4}{\sqrt{\pi}} y e^{-z^2} & 0 < x < z - y \\[2mm]
\operatorname{erf}(z) - \operatorname{erf}(x-y) - \frac{2}{\sqrt{\pi}}\left(y+z-x\right) e^{-z^2} & z - y < x < y + z \quad (3.53) \\[2mm]
0 & y + z < x,
\end{cases}
$$

where $x = v_{\min}/v_0$, $y = v_E/v_0$, z is defined above, and the last case artificially sets the rate to zero to avoid unphysically negative results.[10]

These final astrophysical results are combined with the differential rate given in Eq. 3.39 to obtain the final elastic scattering WIMP rate. A selection of such rates are given in Figs. 3.3 and 3.4 for the SI and SD interactions respectively. Both figures give the rates for the same target with various WIMP masses and for the same WIMP mass with different targets. The spectra are featureless exponentials with a cut-off which depends on m_χ and m_T and a normalization which depends on cross section.

3.4 Background Considerations

The differential rate spectra shown in Figs. 3.3 and 3.4 indicate that WIMPs in the 1–100 GeV/c^2 mass range create recoils in the $\mathcal{O}\left(10^{-1} – 10^2 \text{ keV}\right)$ range. In a germanium target, the total scattering rate above a 2 keV threshold for both a $\left(m_\chi = 50 \text{ GeV}/c^2, \sigma_p^{SI} = 10^{-43} \text{ cm}^2\right)$ and a $\left(m_\chi = 5 \text{ GeV}/c^2, \sigma_p^{SI} = 10^{-41} \text{ cm}^2\right)$ WIMP is $R \approx 0.05$ [kg day]$^{-1}$. WIMP scatterings are rare and occur at rates well below typical background radiation rates. Direct detection experiments must therefore operate in a low background environments, by choosing appropriate operating location and shielding, and/or have methods by which to distinguish between WIMP and background events.

---

[10] The above procedure sharply truncates the pure Maxwellian distribution and is equivalent to multiplying Eq. 3.43 by the Heaviside step function $\Theta(v_{\text{esc}} - v)$. This is also likely unphysical and other, still *ad hoc*, approaches have been proposed which smoothly bring the distribution to zero at $v = v_{\text{esc}}$. Two such modifications are $f(\boldsymbol{v}) = f_{\text{SHM}}(\boldsymbol{v}) \cdot e^{-z^2}$ [207] and $f(\boldsymbol{v}) = f_{\text{SHM}}(\boldsymbol{v}) - e^{-z^2}$ [208], where $f_{\text{SHM}}(\boldsymbol{v})$ is the pure Maxwellian as given by Eq. 3.43. Note that the value of k must be computed afresh for each case, using Eq. 3.3 with the given distribution function.

(a) Germainum Target

(b) 10 GeV/c^2 WIMP
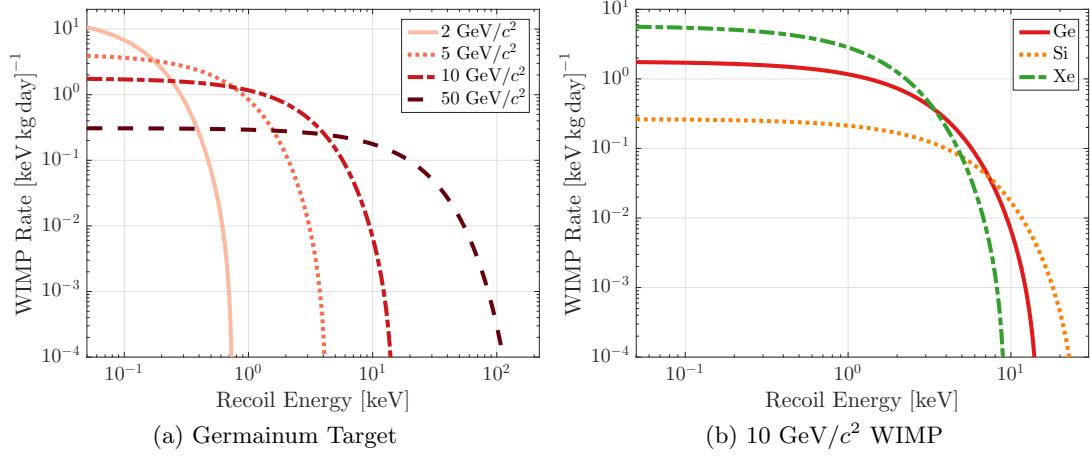
Figure 3.3: Differential WIMP elastic scattering rate for a spin-independent WIMP-proton cross section $\sigma_p^{\mathrm{SI}} = 1 \times 10^{-41}$ cm^{-2} and different WIMP masses on a germanium target (a) and different targets for a 10 GeV/c^2 mass WIMP (b). For (a), the WIMP masses considered are 2 (solid), 5 (dotted), 10 (dashed-dot), and 50 (dashed) GeV/c^2. For (b), the material targets are germanium (red solid), silicon (orange dotted), and xenon (green dashed-dot).

(a) Germainum Target

(b) 10 GeV/c^2 WIMP
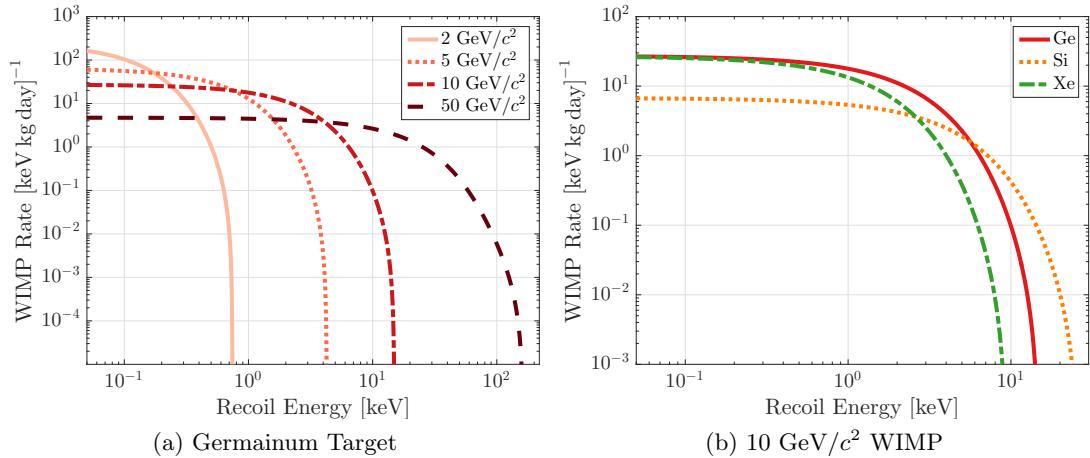
Figure 3.4: Differential WIMP elastic scattering rate for a spin-dependent (proton-only coupling) WIMP-proton cross section $\sigma_p^{\mathrm{SD}} = 1 \times 10^{-33}$ cm^{-2} and different WIMP masses on a germanium target (a) and different targets for a 10 GeV/c^2 mass WIMP (b). For (a), the WIMP masses considered are 2 (solid), 5 (dotted), 10 (dashed-dot), and 50 (dashed) GeV/c^2. For (b), the material targets are germanium (red solid), silicon (orange dotted), and xenon (green dashed-dot).

3.4.1   Background Sources

There are three categories which backgrounds can fall under: (1) prompt secondary particles and long-lived isotopes created by cosmic rays, (2) products from the decays of long-lived isotopes in and around the experimental apparatus, and (3) detector-dependent backgrounds. The first two can be generally discussed for any experiment.

Cosmogenics

Cosmic rays are high energy particles, mostly protons, which impinge on the atmosphere and create multi-particle showers which reach the surface. A major component consists of high-energy muons which can traverse large amounts of material, such as rock in the Earth's crust, before interacting and creating lower-energy secondary particles. Secondary neutrons are particularly dangerous since neutrons scatter from the nucleus of a detector, creating NRs which mimic WIMPs.

In order to avoid these cosmogenic backgrounds, direct detection experiments are commonly located in underground laboratories. The muons themselves typically deposit $\mathcal{O}(1 \text{ MeV})$ of energy in the detector, well above the typical WIMP range, and are eliminated by imposing an appropriate energy range for a WIMP search. The secondary neutrons, however, are energetic enough to penetrate shielding and produce recoils appropriate for a WIMP search, thus producing a significant background. This background can be reduced by going to a deeper underground laboratory or by installing an active veto system. The primary muon and secondary neutron fluxes as a function of overburden depth are given in Fig. 3.5 with several laboratories marked [209]. The muon flux data points are measurements, while the neutron flux data points are derived from a simulation. The depth is measured is kilometer-water-equivalent (km.w.e.) to normalize differences in densities and shape of overburden rock at the varying global locations.

In addition to the direct background from cosmic rays and muon-induced neutrons, cosmic rays can also create radioactive isotopes in the detector material. These internal isotopes cannot be shielded and efforts must be made to reduce their presence. This is achieved by limiting the amount of time the detector material is exposed to cosmic rays prior to running the experiment (fabricating and/or storing underground)
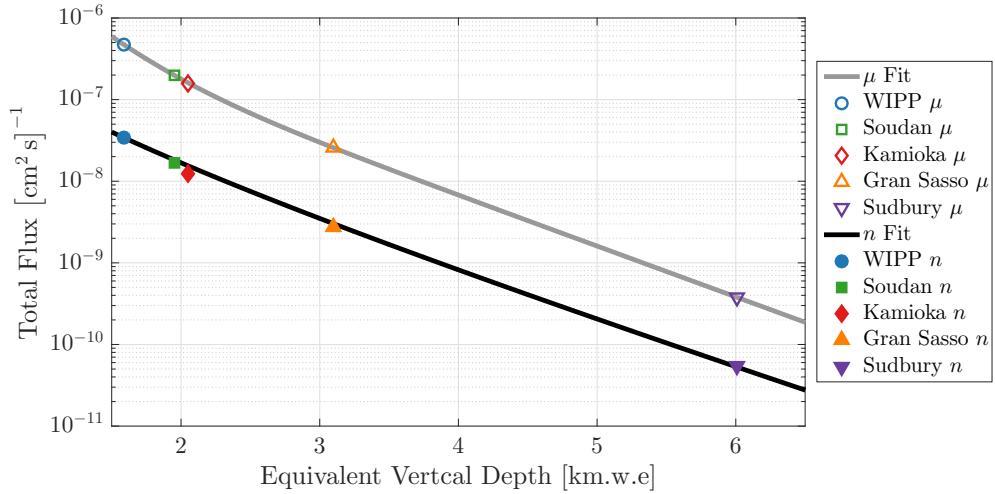
Figure 3.5: Cosmic muon and neutron fluxes for various underground laboratories at different overburden depths. Muon flux data points are measurements while neutron flux data points are computations based on simulation and the measured muon fluxes. Depth is measured in km-water-equivalent. Models are fit to each data set. Data and fits from [209].

or by removing the cosmogenic isotopes via distillation or absorption (for noble liquid detectors).

Radiogenics

Ambient radiation from long-lived radioactive isotopes is ubiquitously present at low levels in the environment. These isotopes were created either in the formation of the Earth (halflives $>10^9$ yr) or from high-energy cosmic rays interacting with the material. The subsequent radioactive decays create γ's and $\beta' s$, which create ER scatters and neutrons which create NR scatters. Electromagnetically-interacting particles are well shielded by high electron-density materials, such as lead and copper, while neutrons are well shielded by hydrogenous materials, such as polyethylene or water. However, the trace amounts of radiation present in the shielding can turn the shielding itself into a source of backgrounds. Understanding the effect from this background requires modeling the contamination and simulating the expected background.

3.4.2   Background Discrimination Approaches

Although comprehensive measures are taken to either avoid or reduce backgrounds in detectors no experiment can completely avoid them. There are several approaches to discriminate background events from WIMP events, as outlined below.

Annual Modulation

The motion of the Earth around the Sun causes a modulation in the kinetic energy of the impinging WIMPs. Some detectors make specific use of this motion and the associated modulated rate above threshold. Accounting for this motion, the Earth's velocity relative to the halo, in units of km/s, is approximately

$$v_E = v_0 + v_\odot + v_\oplus \cos\gamma \cos\left(\frac{2\pi\,(t - t_0)}{T}\right), \tag{3.54}$$

where $t_0 \approx 150$ days, $T = 1$ year, and $\gamma = 60°$ is the angle of inclination between the Earth's solar motion and the Sun's galactic motion. This modulation gives a corresponding variation to the differential recoil rate as [191]

$$\frac{\mathrm{d}R}{\mathrm{d}E_\mathrm{r}} \approx \left\langle \frac{\mathrm{d}R}{\mathrm{d}E_\mathrm{r}} \right\rangle \left[1 + A(E_\mathrm{r})\cos\left(\frac{2\pi\,(t - t_0)}{T}\right)\right], \tag{3.55}$$

where $\left\langle \frac{\mathrm{d}R}{\mathrm{d}E_\mathrm{r}} \right\rangle$ is the average rate and $A(E_\mathrm{r})$ is the modulation amplitude. The portion of the distribution above a given experimental threshold then also modulates: the total number of counts above threshold modulates and the magnitude of the modulation depends upon the threshold. This is demonstrated in Fig. 3.6, where for higher thresholds the modulation peaks in June (when the relative velocity between the Earth and halo is maximized) and troughs in December. For lower thresholds, the modulation sign reverses. Since the differences in rate are small, and the effect is largest at lower energies, experiments with long continual exposures and low thresholds are best suited for this type of search. Regardless of their overall background levels, these experiments statistically look for variations on top of their background with a period of a year.
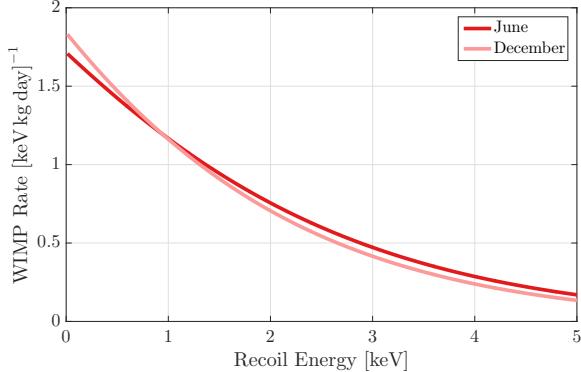
Figure 3.6: Differential recoil rate for a $10 \text{ GeV}/c^2$ WIMP with $\sigma_p^{\text{SI}} = 10^{-41} \text{ cm}^2$ on a Ge target in June (dark) and December (light) accounting for the Earth's orbit around the Sun. The relative Earth-WIMP velocity is maximum in July and minimum in December. Note the point at ~ 1 keV where the sign of the modulation changes.

Directional Dependence

Similar to the annual modulation approach, the directional dependence approach utilizes the fact that the Earth-borne detector has a predictable motion relative to the Galactic WIMP "wind". The angular differential rate for WIMP scattering is [191, 210]

$$\frac{\mathrm{d}R}{\mathrm{d}E_{\mathrm{r}}\,\mathrm{d}(\cos\gamma)} \propto \exp\left[-\frac{((v_0 + v_\odot)\cos\gamma - v_{\min})^2}{v_0^2}\right], \tag{3.56}$$

where γ is the direction between the recoiling WIMP and the mean direction of the Sun's motion relative to the halo. Background events are expected to be isotropic while the WIMP recoils are peaked in the direction of the motion of the Earth relative to the WIMP. The Earth's rotation about its own axis will also cause a varying signature to the angular distribution, with a shift in mean recoil angle every 12 sidereal hours. If a non-isotropically distributed signal is detected, and it matches the Galactic expectation, it would only take $\mathcal{O}(10\text{--}100)$ events to statistically claim a detection above some isotropic background [211]. This relative ease in claiming a signal is offset by technical challenges in measuring the angle of recoil.

Event-by-Event Discrimination

In the keV energy range, WIMPs scatter as NRs while most backgrounds scatter as ERs. Due to the larger mass and charge of a nucleus, it will traverse a much shorter distance in its recoil than an electron given the same recoil energy: an NR has a denser energy deposition than an ER, which can in turn lead to differences in detector response
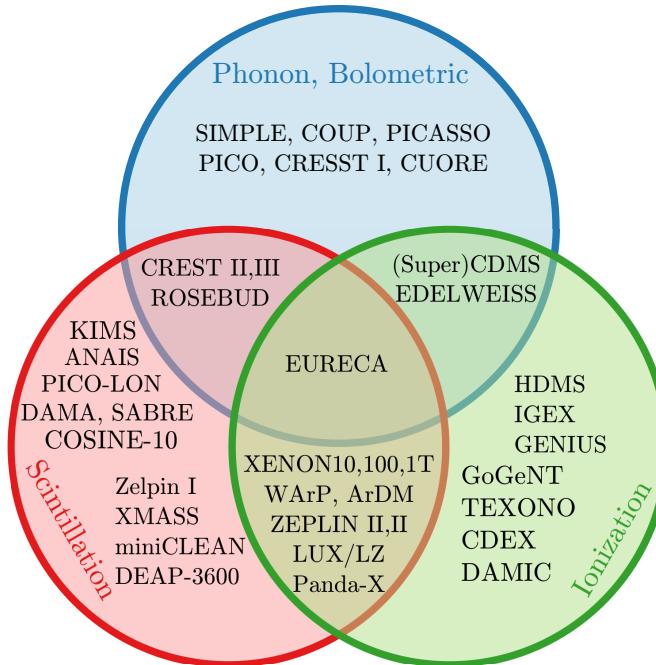
Figure 3.7: Summary of direct detection experiments based upon the different read-out channels used. The top circle includes any heat read-out, including threshold detectors and cryogenic crystals. Several of the single-read-out experiments use pulse-shape, threshold, or statistical discrimination techniques. Figure modified from [213].

between the two [212]. Common detector energy-collection techniques include phonons, ionization, and scintillation, which differ in the amount of nuclear recoil energy required to create a quanta: a few meV per phonon, $\sim$10 eV per charge carrier, and $\sim$100 eV per scintillation photon [203]. These different responses, and the ratios between them, allow for the discrimination of each individual event as either ER or NR. Another type of detector, the so-called "threshold detector", simply eliminates ER response altogether. Event-by-event discrimination allows an experiment to remove almost all ER backgrounds. NR backgrounds cannot be removed using such a technique, making neutrons a particularly dangerous background.

Direct detection experiments in the field can be categorized based upon what collection techniques are used to read out energy as given in Fig. 3.7. Event-by-event discrimination typically requires two read-out techniques, though some targets, notably argon, can do so with only one. Other single-read-out experiments use the statistical discrimination approaches given above.

3.5 Sensitivity

How sensitive an experiment is to a WIMP signal depends on how large the background is and whether that background can be removed. To understand the general sensitivity to backgrounds, consider a hypothetical experiment with background rate B and signal rate S over some exposure MT. N events which pass all discrimination cuts are observed by the experiment. The observed events are some combination of signal events, which pass the discrimination with efficiency α, and background events, which are not rejected with some inefficiency β. The measured rate, N/MT is then statistically compared to the expected signal rate $\alpha S_{\exp}$ to set a limit. The $90\,\%$ upper limit on the number of signal events $N_{90} = \alpha S_{90} MT$ is found by computing the inverse cumulative distribution function (CDF) $F^{-1}(C; N)$ at the $C = 0.9$ level. Limits on the rate are then translated to limits on the interaction cross-section by Eq. 3.39, where a high limit on the rate implies a higher limit on the cross section. The probability density function (PDF) integrated over in the CDF is Poissonian, due to the low statistics of the events, with PDF of $f(n; \nu) = \frac{\nu^n}{n!} e^{-\nu}$. The upper limit on the signal events is then

$$N_{90} = F^{-1}(0.9; N) = \left\{ \eta \colon \int_0^{\eta} f(\nu; N) \mathrm{d}\nu = 0.90 \right\}. \tag{3.57}$$

At large enough statistics, a Poisson distribution can be approximated as Gaussian distribution with $\mu = \nu = \sigma^2$. The Gaussian distribution has PDF of $f(x; \mu, \sigma) = \frac{1}{\sqrt{2\pi\sigma^2}} \exp\left[-\frac{(x-\mu)^2}{2\sigma^2}\right]$.

Three sensitivity regimes are identified based upon the background level:

1. **Background Free:** If there are zero observed events, which is possible for small enough exposures for a given shielding, then $N_{90} = F_{\mathrm{Poiss}}^{-1}(0.9; 0) = 2.3$ and the $90\,\%$ limit on the signal $S_{90} = 2.3/(\alpha MT)$. In this regime, the sensitivity increases as the inverse of the exposure and will continue until the experiment begins to observe background events.

2. **Background Limited:** When the experimental exposure is large enough such that events are observed, the sensitivity dependency changes. If the backgrounds cannot be discriminated against and are not well understood, then all observed events must be treated as signal. In this case, N is sufficiently large to use the

Gaussian approximation for the underlying distribution. The $90\,\%$ point of a Gaussian CDF is at $\mu + 1.28\sigma$ which then gives $N_{90} = N + 1.28\sqrt{N}$ and a limit on the signal of

$$S_{90} = \frac{N + 1.28\sqrt{N}}{\alpha MT} = \frac{\beta B}{\alpha} + \frac{1.28}{\alpha}\sqrt{\frac{\beta B}{MT}}, \tag{3.58}$$

where the second equality is in the limit where $B \gg S$ such that $N \approx \beta BMT$. In the presence of this background, the sensitivity increases with the inverse of $\sqrt{MT}$ and asymptotically approaching a fixed value dependent on the overall background rate. Once that plateau is reached, further exposure does not yield better sensitivity.

3. **Background Subtracted:** If the sources of backgrounds are understood well enough, they can be modeled and subtracted from the observed spectrum. Such modeling predicts the number of expected background events passing all discrimination cuts N_{bkgd}, the rate of which can be subtracted from the background limited sensitivity $S_{90}^{(\text{Lim})}$ given by Eq. 3.58

$$S_{90} = S_{90}^{(\text{Lim})} - \frac{N_{\text{bkgd}}}{\alpha MT} = \frac{1.28}{\alpha}\sqrt{\frac{\beta B}{MT}}, \tag{3.59}$$

where the second equality is again taken in the $B \gg S$ limit such that $N = N_{\text{bkgd}}$. In this regime, better sensitivity can be reached, without a plateau, but it will increase only as the inverse of $\sqrt{MT}$.

For event-by-event discriminating detectors, there is statistical variance associated with the discriminating cut. In the high background limit, this variance is [214]

$$(\delta S_{\text{stat}})^2 = \left(\frac{\beta\,(1-\beta)}{(\alpha-\beta)^2}\right)\frac{B}{MT} = Q\frac{B}{MT}, \tag{3.60}$$

where Q is the background rejection quality factor. This variance weakens the sensitivity, but can be reduced by improving Q, i.e. making a cleaner discrimination, or with larger exposure. The systematic variance on α and β also weaken the sensitivity, and their size ultimately determines the sensitivity reach of a discrimination experiment [212].

The generic shape of sensitivity curves in the WIMP mass vs. cross section plane (whether it is an SI or SD interaction is irrelevant) can be understood by simple approximations to the differential rate Eq. 3.39. Assuming that $v_{\rm esc} = \infty$ and $v_E = 0$, the velocity and normalization integrals become simple and the rate can be written as

$$\frac{{\rm d}R}{{\rm d}E_{\rm r}} \propto \frac{N_T m_T}{m_\chi \mu_T^2 v_0} \sigma e^{-v_{\rm min}^2/v_0^2} \approx \frac{N_T m_T}{m_\chi \mu_T^2 v_0} \left(\frac{\mu_T}{\mu_p}\right)^2 \sigma_p e^{-\frac{E_{\rm r} m_T}{2\mu_T^2 v_0^2}}, \qquad (3.61)$$

The sensitivity on σ_p is found by inverting this equation to solve for σ_p and using the 90 % upper limit on the differential rate ${\rm d}R/\,{\rm d}E_{\rm r}|_{\rm UL}$ as the rate in the expression.

If $m_\chi \gg m_T$, $\mu_T \sim m_T$ and $\mu_p \sim m_p$ and the upper limit on the WIMP-nucleon cross section $\sigma_{\rm UL}$ is

$$\sigma_{\rm UL} \sim \frac{m_\chi m_p^2 v_0}{N_T m_T} \left.\frac{{\rm d}R}{{\rm d}E_{\rm r}}\right|_{\rm UL} e^{\frac{E_{\rm r}}{2m_T v_0^2}}. \qquad (3.62)$$

For higher mass WIMPs with a given detector, the limit on the cross section increases as $\sigma_{\rm UL} \propto m_\chi$. This can also be understood as a consequence of the fact that $\rho_0 = m_\chi n_0$ is measured and constant. Thus, increasing m_χ implies that the number density must decrease and the probability for an interaction similarly decreases. Additionally, a higher m_T leads to a lower limit, i.e. heavier detectors are better for heavy mass WIMPs.

In the opposite limit, where $m_\chi \ll m_T$, $\mu_T \sim \mu_p \sim m_\chi$ and the sensitivity is

$$\sigma_{\rm UL} \sim \frac{m_\chi^3 v_0}{N_T m_T} \left.\frac{{\rm d}R}{{\rm d}E_{\rm r}}\right|_{\rm UL} e^{\frac{E_{\rm r} m_T}{2m_\chi^2 v_0^2}}. \qquad (3.63)$$

Experimentally, recoil energies cannot be arbitrarily small and have some lower threshold $E_{\rm r} = E_{th}$. For a given threshold and detector, the limit goes as $\sigma_{\rm UL} \propto m_\chi^3 \exp\left(E_{th}/m_\chi^2\right)$ and sharply increases at low WIMP masses. The limit can be lowered by decreasing the detector threshold or decreasing the nuclear target mass, i.e. lighter mass detectors with lower thresholds are better for light mass WIMPs. The same detector is then not ideal for searching for both lighter and heavier WIMP masses.

3.6 Status of the Field

At the 2013 "SNOWMASS on the Mississippi" meeting, the American dark matter community came together and took stock of the current and future directions of the
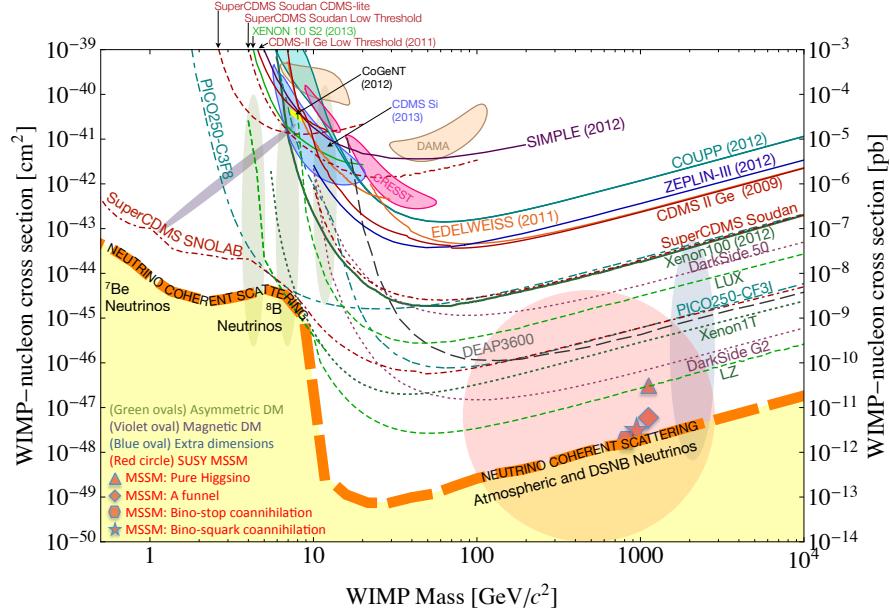
Figure 3.8: Status and vision of the direct detection field as summarized at the SNOW-MASS on the Mississippi meeting. 90 % upper limit results (solid curves) and sensitivity projections (non-solid curves) on the spin-independent WIMP-nucleon cross section. Closed contours are the 90 % confidence regions from experimental excess from the labeled result. The region at low cross section is the region where coherent neutrino scattering from solar neutrinos become a background. Rough, theoretically-predicted, parameter spaces are given by non-bordered regions and specific supersymmetry predictions are given by the markers. Figure from [215].

direct detection field [215]. The summary of this discussion can be seen in Fig. 3.8 showing exclusion limits and projections at the time compared to rough parameter space predicted by various theoretical models. Although somewhat outdated, the status and vision of the field is still correctly described by the very comprehensive plot.

For heavier mass WIMPs, $\gtrsim 10$ GeV/c^2, there has been no experimental evidence which is attributable to WIMPs. This mass range is dominated by large liquid noble detectors. Notably, the LUX [216, 217], XENON [218], PandaX [219], and ZEPLIN [220] experiments use liquid xenon, while DarkSide [221, 222] uses liquid argon. The liquid noble detectors can scale to large detector masses, and therefore exposures. Background modeling has kept them from becoming background limited, allowing for the deep limits into the regions of the historically preferred WIMP theories, like supersymmetry and

universal extra dimensions. Cryogenic crystals, such as CDMS [223, 224] (Ge and Si targets) and EDELWEISS [225] (Ge targets) have historically been competitive at higher WIMP masses, but they have more difficulties scaling to large masses and have become sub-dominant in this region. Similarly, superheated bubble detectors COUPP [226], PICASSO [227], PICO [228–230], and SIMPLE [231] (CF_3I, C_4F_{10}, C_3F_8, and C_2ClF_5 targets) are less competitive at higher WIMP masses due to lower target mass and exposure (note, however, that the fluorine in these detectors gives excellent sensitivity to WIMP-proton spin-dependent interactions).

The story is somewhat different a lower WIMP masses, $\lesssim 10$ GeV/c^2. Four experiments have observed an excess of events above background which, when interpreted as a WIMP signal, give the four different contoured regions seen in Fig. 3.8. These excesses were observed by the event-by-event discriminating experiments of CRESST [232] ($CaWO_4$ targets) and CDMS [233] (Si target analysis) and by the annual modulation searches of CoGENT [234] (Ge target) and DAMA/LIBRA [235, 236] (NaI(Tl) targets).

Of these results, the most significant, and most perplexing to the rest of the field, is that of DAMA/LIBRA. The most recent results of the DAMA/LIBRA experiment are shown in Fig. 3.9, where a clear modulation cycle is observed in the data with a phase consistent with the expected Galactic halo signal. Combining the DAMA/LIBRA signal with that of its predecessor, DAMA/NAI, gives a total exposure of 1.33 ton yr over 14 yearly cycles and yields a rejection of the non-oscillatory background model at the 9.2σ level. In the standard interpretation of a WIMP, the DAMA/LIBRA contours, along with those of the other excesses, are in tension with the limits of other experiments, such as LUX or CDMS-Ge. This has spawned great interest in the low-mass dark matter regime in attempts to verify/refute the excess signals [237–240], find an alternative explanation of the observed modulation signals [241], or propose an alternative model for dark matter which resolves the tension. Several of the models discussed in Sec. 2.2.3 were developed based on these results and alternatives in the dark matter halo have also been considered to resolve the tension (see ,e.g. [183]).

In response to these excesses and low-mass dark-matter theories, new dedicated low-mass WIMP searches have been undertaken. Many traditionally high-mass-search experiments have adjusted analysis techniques in order to reach lower thresholds and the sensitivity to low-mass WIMPs that allows. This includes searches
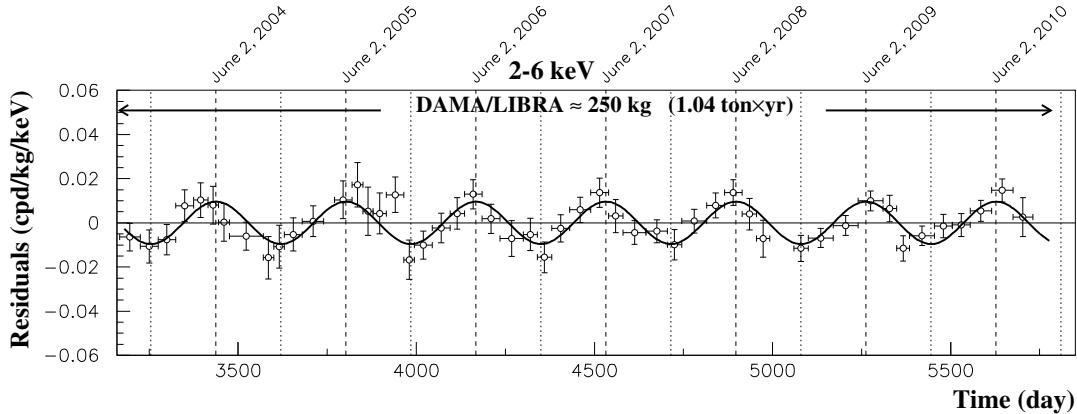
Figure 3.9: Annual modulation results from 7 years of data from the DAMA/LIBRA experiment. The residual modulation is well fit by a sinusoidal modulation as expected from the dark matter halo, ruling out a modulation free signal at the 9.2σ level. Figure from [242].

by CDMS/SuperCDMS [243–246], EDELWEISS [247, 248], XENON [249–251], and XMass [252, 253]. Other experiments with sensitivity in this region include the superheated bubble detectors described above, CDEX/TEXONO (Ge ionization detectors) [254–256], DAMIC (silicon CCDs) [257], and more recent runs of CRESST [258, 259]. Additionally, an alternative operating mode of a SuperCDMS detector, called CDMSlite [260], drastically lowers the SuperCDMS threshold and gives access to lower mass WIMPs.

The dark matter direct detection field can be summarized as: possible hints of a signal at lower masses, which are in tension with other exclusion limits, with no evidence of signal at higher masses, which tightly constrains traditional WIMP theories. This motivates the continued push in the field for both mass regimes, and the different and complementary detector technologies required for each region.

Chapter 4

ZIP Detector Technology

The dark matter direct detection experiment named the Cryogenic Dark Matter Search (CDMS) took data at the Soudan Underground Laboratory (SUL, or Soudan for short) for the last 15 years. It comprised two generations of the experiment: CDMS II and SuperCDMS Soudan. The heart of CDMS is a technology called the Z-sensitive Ionization and Phonon (ZIP) detectors. Between the two generations, the basic ZIP technology was the same even though the exact type of detector improved.

A ZIP is a semi-conducting device where a scattering particle will create electron-hole (e/h) pairs in addition to lattice phonons (heat). A potential bias is applied across the detector and the energy used to create the e/h pairs inferred through an ionization signal. The phonons are absorbed as they scatter off the surfaces of the detector and their energy inferred through a phonon signal. Electron and nuclear recoil (ER and NR) discrimination is possible as the relative amount of energy recorded in each of these two channels is different by recoil type.

In last few years, SuperCDMS also developed alternative operating mode for a ZIP, called the CDMS low ionization threshold experiment (CDMSlite), which operated at much higher biases and exchanged the ER and NR discrimination for lower energy thresholds. This thesis focuses on data taken with the CDMSlite mode using a Super-CDMSdetector, however the historical CDMS II data are used for background studies, necessitating a description of all detector types.

(a) oZIP   (b) iZIP

Figure 4.1: Photographs of an oZIP (a) used in CDMS II and an iZIP (b) used in SuperCDMS Soudan. Detectors are shown in their respective copper housings.

4.1 Physical Characteristics and Array Descriptions

The CDMS II experiment used original-ZIPs (oZIPs) while the SuperCDMS Soudan experiment used interleaved-ZIPs (iZIPs);[1] photos of these are seen in Fig. 4.1. Both styles of ZIPs were roughly cylindrical in shape with a diameter of 76 mm, heights of 10 mm (oZIP) and 25 mm (iZIP), and composed of ultra-pure crystals of germanium (impurity levels $\sim 10^{10}$ cm^{-3}) or silicon (impurity levels $\sim 10^{16}$ cm^{-3}). The germanium/silicon oZIPs had masses of $\sim 250/100$ g while the germanium iZIPs had masses of ~ 600 g. The actual masses and impurity levels varied by individual crystal. The applied biases were -3 V (Ge oZIP), -4 V (Si oZIP), ± 2 V (Ge iZIP), ~ 70 V (Ge CDMSlite). For the iZIP, the different biases were applied on the top/bottom faces giving a total $V_b = -4$ V.

Read-out electrodes and sensors for measuring the ionization and phonon signals were photolithographically patterned onto the top and bottom surfaces of the crystals. For oZIPs, one side contained two charge electrodes arranged as a central circular electrode and an outer annulus which were read out separately. These were referred to as the inner and outer charge channels. The opposite oZIP face contained phonon sensors arranged in a grid with each quadrant of the grid read out separately and labeled as A–D. The size and orientation of all of the channels can be seen in the Fig. 4.2(a).

---

[1] Note that until the creation of non-oZIPs, the oZIPs were simply called ZIPs and appear in the literature as such.

(a) oZip Channels   (b) iZIP Channels
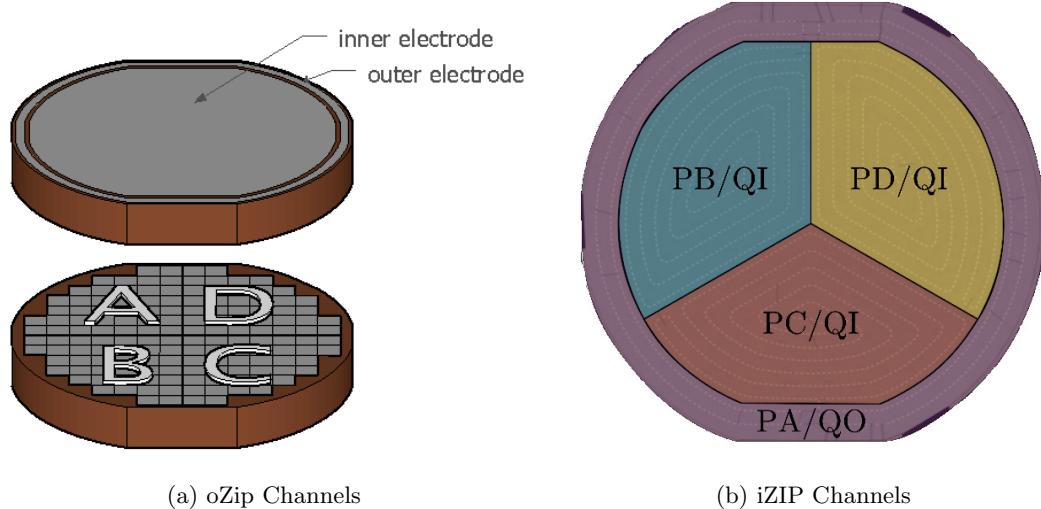
Figure 4.2: Type and location of ionization and phonon read-out channels for the oZIP
(a) and iZIP (b). The oZIP had inner and outer charge electrodes (top) on one face and
four phonon channels (A–D), split in quadrants on the opposing face (bottom). The
iZIP had two ionization and four phonon channels on each face (one face shown) with
the read-out sensors interleaved. One phonon (A) and ionization (O) channel covered
an outer ring, while three phonon channels (B–D) and one ionization channel (I) covered
the inner area, with the phonon channels split into three wedges. The opposing face
was rotated by 60 degrees. Subfigure (a) from [224] and (b) from B. Shank, with
modifications.

The "interleaved" name of the iZIPs was derived from the change in charge and phonon
sensors arrangement compared to oZIPs: there were charge and phonon sensors on both
the top and bottom faces with sensors for the two alternating. The charge electrodes
were read out as one inner and one outer channel. The phonon sensors were read out as
four channels, however the shape and positions of each were different compared to an
oZIP: channel A was an outer ring and channels B–D were three inner wedges. A single
iZIP face with the channels highlighted is shown in Fig. 4.2(b). The top and bottom
faces had the channels rotated by 60 degrees to give finer position information.

At its largest payload, CDMS II deployed an array of 30 oZIP detectors, arranged
into five towers of six detectors each. The layout of these towers is given in Fig. 4.3(a),
where the yellow detectors are Si and the brown detectors are Ge. There were 11 Si

(a) CDMS II Array
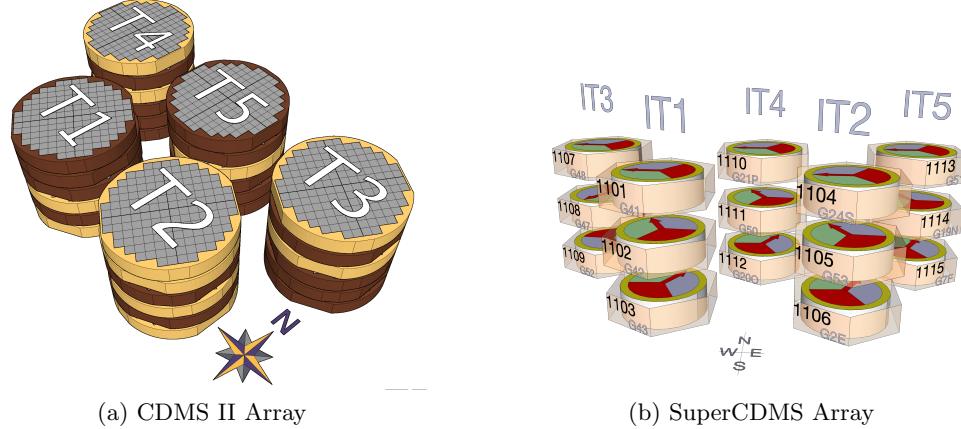
(b) SuperCDMS Array

Figure 4.3: Layout of the detector arrays of CDMS II (a) and SuperCDMS Soudan (b). CDMS II used 11 Si (yellow) and 19 Ge (brown) oZIPs while SuperCDMS Soudan used 15 Ge iZIPs. In both cases, the detectors were arranged into five towers with detectors in the same tower rotated with respect to one another. Left figure from [224].

detectors, for a total Si payload of ∼1.1 kg and 19 Ge detectors, for a total Ge payload of ∼2.75 kg. The two detector types were analyzed separately during CDMS II analyses. SuperCDMS Soudan also deployed five towers, but each tower contained only three of the thicker Ge iZIPs detectors. The layout is given in Fig. 4.3(b). The 15 total detectors had a payload of ∼9 kg. Individual detectors were labeled based upon their tower and position within the stack position, numbered from the top. For example, T1Z4 for CDMS II and iT3Z1 for SuperCDMS Soudan.

4.2 The Ionization Measurement

In general, when a particle scatters in a ZIP detector, a portion of its deposited energy goes towards the promotion of valence electrons from their bound states into the conduction band. This requires the deposited energy to be much greater than the band gap of the crystal ($E_{\mathrm{gap}} = 0.74/1.17$ eV for Ge/Si [261]). The initially-freed electrons can have sufficient momentum to liberate other electrons, which would create a cascade ending in many low momentum electrons near the deposition site (so-called "charge cloud"). Even though the band gap is $\mathcal{O}(\mathrm{eV})$, a greater amount of energy is required to liberate a single electron/hole pair. For an electron recoil, it requires $\epsilon_\gamma = 3.0/3.8$ eV to liberate

one electron-hole pair in Ge/Si [262, 263]. This means that $\sim$25–30 % of the deposited energy is expended in driving electrons across the band gap, while the rest is shed as optical phonons due to momentum conservation during the pair creation process [264]. It is easier for recoiling nuclei to transfer energy to phonons, meaning that $\epsilon_{\mathrm{NR}} < \epsilon_\gamma$ and fewer charge carriers are generated for an NR, an effect called "quenching".

A potential difference V_b is applied across the crystal to drift the free electrons and holes to the opposite polarity faces. The dynamics of electron and hole propagation differ due to holes having an isotropic effective mass while electrons have an anisotropic effective mass, which is expressed as a tensor [265]. Hence, hole propagation mostly follows the field lines while electron propagation occurs obliquely to the field lines, implying that the electrodes which are sensitive to holes will give more accurate information with regards to the initial scatter location. This effect is more pronounced in Ge compared to Si due to the differences in the natures of the crystals.

Image charges are created in the ionization electrodes in response to the drifting charge carries. The amount of image charge created is derived via Ramo theory [266], which gives the image charge Q due to a drifting charge q as

$$Q = q\varphi_0(\boldsymbol{x}), \tag{4.1}$$

where $\varphi_0(\boldsymbol{x})$ is the weighting potential at position $\boldsymbol{x}$. The weighting potential effectively gives the induced charge as the created charge weighted by the distance the charge travels through the crystal. If the field is uniform and an electron and hole each drift to opposite side electrodes, they each create an image charge and $Q_{\mathrm{tot}} = q$. This process is colloquially referred to as "collecting electrons/holes", even though it is the induced image charge which is actually read-out.

If a scatter occurs close to an electrode on a surface, the initial charge cloud can reach the surface of the detector and be collected immediately by whichever electrode is present since self-shielding within the cloud masks the true potential of the electrode. Due to this, events close to the surface (in the so-called "dead layer") cannot be properly characterized by the read-out information and analysis. A thin layer of amorphous silicon is placed between the electrode and the crystal, which is found to reduce this back-diffusion of charge [267]. Electrons incident on the surface (e.g. β decays) have a

high probability to scatter in the dead layer and are problematic.

Impurities in a crystal can be left with net charge when the detector is cooled to the low temperatures used by CDMS. As charge carries drift across the detector, they can be attracted to the impurities instead of the electrodes (see [268] for a detailed discussion). This reduces the amount of signal collected by the electrodes and causes the energy of the scatter to be incorrectly estimated. Light emitting diodes (LEDs) are mounted on the detector housings and the detectors ares periodically exposed to the LED light ("flashing" or "baking" in CDMS jargon), whose photons create excess electron/hole pairs which neutralize the net charge of the impurity sites.

The ionization signal is read out through a JFET (Junction gate Field-Effect Transistor) charge amplifier circuit as shown in Fig. 4.4, where the detector is denoted as having capacitance C_d. The induced charge in the circuit is quickly collected into the feedback capacitor C_f (the parasitic capacitance of the circuit), which causes a voltage spike in the output V_o. The capacitor then drains through the feedback resistor R_f with a time constant $\tau = R_f C_f$. A large biasing resistor R_b is placed between the biasing source and the detector to prevent the induced current of the signal from shorting. The feedback loop is protected from the biasing source via a coupling capacitor C_c. C_s is any stray capacitance. During the quick rising edge, R_b and R_f in the circuit can be ignored, which gives $V_o = Q/C_f$. The shape of this rising edge depends on the propagation of charges in the detector, which occurs on the timescale of $\mathcal{O}(\text{ns})$. Compared to the digitization rate, the rising edge is recorded as near-instantaneous. Since the decay constant is set by the circuit ($\tau \approx 40~\mu$s), the only variable is the amplitude of the peak, which is directly proportional to the induced charge collected.

For both oZIPs and iZIPs, the signal was digitized at a rate of 1.25 MHz (0.8μs per sample). 2048 samples were stored for each event, with the rising edge of the trace centered, for total trace lengths of $\sim$1.6 ms. An example event's ionization pulses from a single side are shown in in Fig. 4.5. This recoil had $\sim$511 keV of energy in an iZIP and occurred mostly in the inner channel.

The amplitude of the charge pulse is a measure of the image charge, and, by proxy, the number of electron/hole pairs $N_{\text{e/h}}$ created in the recoil. This is used to compute a quantity termed the "ionization energy" E_{Q}, which is defined as the recoil energy
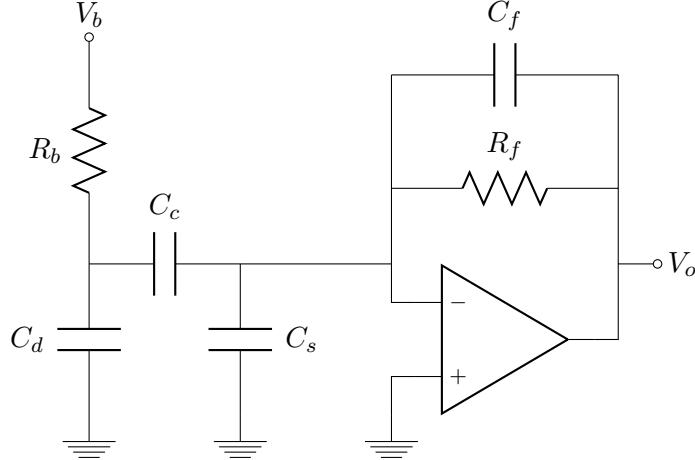
Figure 4.4: Simplified read-out circuit for a single ionization channel. The detector is given by $C_d \approx 50$ pF, which is biased by V_b through a biasing resistors $R_b = 40$ MΩ. The channel is coupled through a coupling capacitor $C_c = 300$ pF to the feedback loop consisting of the amplifier, feedback resistor $R_f = 40$ MΩ, feedback capacitor $C_f \approx 1$ pF, and any stray capacitance $C_s \approx 75$ pF. The final output voltage is then V_o.
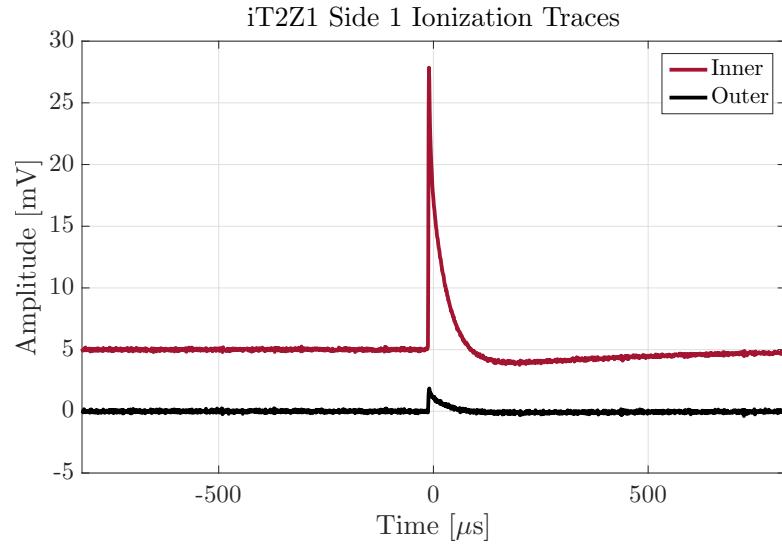
Figure 4.5: Inner and outer ionization traces from side 1 of iT2Z1 for an example event of ∼511 keV recoil energy. The inner channel's trace is shifted upwards by 5 mV for clarity.

inferred from $N_{e/h}$ by assuming the event is an ER with 100 % charge collection efficiency

$$E_Q = N_{e/h}\epsilon_\gamma. \tag{4.2}$$

From the definition, the true initial recoil energy $E_r = E_Q$ for completely collected ERs. For NRs, the quenching effect is accounted for via a recoil-energy-dependent quantity called the "ionization yield" (or simply "yield" for short) $Y(E_r) \equiv E_Q/E_r$. For an ER with complete charge collection efficiency, $Y(E_r) = 1$, while for NRs, or ERs with incomplete charge collection efficiency, $Y(E_r) < 1$. Using the definition of the yield in Eq. 4.2 and rearranging gives an expression which quantifies quenching via NRs producing fewer electron/hole pairs

$$N_{e/h} = Y(E_r)E_r/\epsilon_\gamma. \tag{4.3}$$

The measured yield is used to discriminate between NRs and ERs.

4.3 The Phonon Measurement

In a crystal, the thermal average number of phonons (lattice vibrations) for a given angular frequency mode ω is given by the Bose-Einstein distribution as

$$\langle n \rangle = \frac{1}{\exp(\hbar\omega/k_B T) - 1}. \tag{4.4}$$

The temperature of the crystal T determines the properties of this distribution, with the peak being at $\hbar\omega = 2.8k_B T$. At the cryogenic operating temperatures of CDMS, $\sim$50 mK, the peak is at $\hbar\omega = 12.1\ \mu$eV: only phonons which are extremely out of equilibrium (athermal), such as those generated by a scattering particle, are detectable.[2] When a particle scatters off an electron or nucleus in the crystal, $\gtrsim$70 % of the deposited energy is transmitted as phonons.

---

[2] This is a motivation for operating at cryogenic temperatures.

4.3.1   Primary and Relaxation Phonons

The "primary" phonons generated by the initial scatter are termed primary phonons and are created near the Debeye energy: $\mathcal{O}(10\text{ THz})$ for Ge and Si [261]. The subsequent interaction of these phonons is termed quasi-diffusion and is determined by two processes. Anharmonic decay occurs when a single phonon of frequency ν splits into two phonons of lesser frequency (and energy). The decay rate goes as $\tau_D \propto (1\text{ THz}/\nu)^5$ with the proportionality constant $\mathcal{O}(\mu s)$ [269]. Phonons also undergo elastic isotope scattering, which is a result of the lattice being inhomogeneous due to the mix of isotopes present in an element's natural abundance. The scattering rate goes $\tau \propto (1\text{ THz}/\nu)^4$ [270], with the proportionality constant being dependent on the dominant isotope mass and fraction, with a value of 0.41 μs for Si as an example [269]. Due to these processes, primary phonons have quick decay rates and correspondingly short mean-free-paths. Quasi-diffusion endures for a few μs until the mean-free-path becomes of the order of the size of the detector, $\nu \lesssim 1$ THz. At these energies the phonons become "ballistic" and scatter between the crystal surfaces. It is primarily during this ballistic scattering that the detector's sensors, located on the flat surfaces, collect the phonons.

Another source of phonons is due to the fact that the ionization sensors collect image charges and not the liberated charge carriers themselves. Once the carriers have drifted across the detector and reach the surface, energy conservation requires that the energy expended in driving these charges across the band band E_{gap} return to the crystal. This occurs when the charges downscatter near the surface and relax back to the Fermi level. Any remaining kinetic energy of the carriers E_{KE} is also transferred to the lattice. The energy is released as high-energy "relaxation" phonons (compared to the $\mathcal{O}(\text{meV})$ primary phonons). As they are near the surface, they quickly interact with the surface-based sensors.

The energy in the primary E_P and relaxation E_R phonons is

$$E_P = E_{\text{r}} - N_{\text{e/h}}E_{\text{gap}} \tag{4.5}$$

$$E_R = N_{\text{e/h}}E_{\text{gap}} + E_{KE}. \tag{4.6}$$

Their sum is the initial recoil energy in addition to the total carrier kinetic energy

$$E_P + E_R = E_\mathrm{r} + E_{KE}. \tag{4.7}$$

4.3.2 Neganov-Trofimov-Luke Phonons

Neganov-Trofimov-Luke (NTL) phonons [271, 272] are created by drifting the electric charges across the crystal. Once liberated, the charge carriers are quickly accelerated by the applied field and jump between lattice sites. However, due to conservation of momentum, some amount of energy is transfered to the lattice in this process. The charge carriers reach a terminal velocity and additional work from the electric field is transfered to the lattice, i.e. phonons. These NTL phonons are the crucial factor for CDMSlite and are discussed in detail.

To help understand this phonon generation, a single charge carrier lattice interaction is explored in Fig. 4.6. Momentum conservation for this interaction requires that $\boldsymbol{k} - \boldsymbol{k}' = \boldsymbol{q}$, where $\boldsymbol{k}$ is the wave vector of the incoming charge carrier, $\boldsymbol{k}'$ is the wave vector of the outgoing charge carrier, and $\boldsymbol{q}$ is the wave vector of the generated phonon. The initial velocity $\boldsymbol{v}$ of the charge carrier is related to $\boldsymbol{k}$ by

$$\boldsymbol{v} = \hbar \boldsymbol{k} / m_c, \tag{4.8}$$

where $\hbar$ is the reduced Planck constant, and m_c is the effective carrier mass. Its velocity after the interaction $\boldsymbol{v}'$ is similarly related to $\boldsymbol{k}'$. The initial energy of the charge carrier is

$$\epsilon = \frac{(\hbar \boldsymbol{k})^2}{2m_c}, \tag{4.9}$$

and the energy after the interaction is similarly related by $\boldsymbol{k}'$. Conservation of energy requires

$$\frac{\hbar \left(\boldsymbol{k}^2 - \boldsymbol{k}'^2 \right)}{2m_c} = \omega, \tag{4.10}$$

where $k = |\boldsymbol{k}|$, $k' = |\boldsymbol{k}'|$, and ω is the angular frequency of the phonon. The dispersion relationship for the phonon is $\omega = c_s q$, where c_s is the speed of sound in the crystal. Using this relationship with the conservation of energy and momentum equations, the
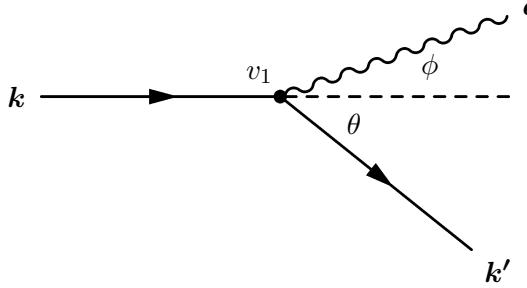
Figure 4.6: Minimalistic diagram showing a charge carrier scattering off a lattice point in the lab frame where the lattice point v_1 is initially at rest. The charge carrier enters with wave vector $\boldsymbol{k}$ and exits with wave vector $\boldsymbol{k'}$ at an angle θ to $\boldsymbol{k}$. An NTL phonon is created with wavevector $\boldsymbol{q}$ at an angle ϕ to $\boldsymbol{k}$.

magnitude of $q = |\boldsymbol{q}|$ is found as [273, 274]

$$q = 2\left(k\cos\phi - c_s m_c/\hbar\right). \tag{4.11}$$

Comparing Eqs. 4.8 and 4.11 shows that the minimum velocity of the charge carrier required to a create an NTL phonon is the speed of sound, making NTL phonons an analogy of Cerenkov radiation. The analogy continues in requiring $\phi < \pi/2$, meaning the phonons are created in the forward-going hemisphere in relation to the charge carrier.

The charge carriers are accelerated due to the electric field such that

$$\hbar\frac{\mathrm{d}\boldsymbol{k}}{\mathrm{d}t} = e\boldsymbol{E}, \tag{4.12}$$

where e is the elementary charge and $\boldsymbol{E}$ is the applied electric field. However, due to interactions which create phonons, the charge carrier cannot be accelerated to arbitrarily large velocities. For a germanium crystal at $\sim$40 mK with a 1-100 V/cm strength electric field, the terminal velocity is $10-100$ km/s [265] which is around the speed of sound [274]. When the charge carrier reaches this point, there is a competition between the injection of energy due to the electric field and the loss of energy due to the emission of phonons. For a typical field of $\mathcal{O}\left(10\right)$ V/cm drifting a carrier over $\mathcal{O}\left(1\right)$ cm, the work done is $\mathcal{O}\left(10\right)$ eV. This is compared to the kinetic energy of the charge carrier at a limiting velocity of $\sim$100 km/s of $\epsilon \sim 30$ meV.[3] Thus, the majority of the energy imparted by

---

[3] This entire argument, adapted from [275], glosses over much semiconductor physics, but the conclusions are still valid. In fact, holes and electrons behave differently, partially due to the electron's

the electric field is shed as phonons, and in particular as NTL phonons as this process dominates for carrier energies $\lesssim 30$ meV [264].

The energy shed as NTL phonons from a single charge carrier q traversing some distance d_q in the detector is

$$E_q = eEd_q - E_{KE;q}, \tag{4.13}$$

where $E = |\boldsymbol{E}|$ and $E_{KE;q}$ is the kinetic energy of the carrier as some amount of the work done is used in the initial acceleration of the carrier. The total NTL-phonon energy from all carriers is then

$$E_{\mathrm{NTL}} = \sum_q E_q = q \sum_q Ed_q - E_{KE}, \tag{4.14}$$

where E_{KE} is the total kinetic energy in the carriers, which is returned to the crystal during the relaxation of the carriers. In the bulk of the detector, the electric field is constant giving $E = V_b/d_0$, where d_0 is the thickness of the detector. This allows Eq. 4.14 to be written as

$$E_{\mathrm{NTL}} = eV_b \sum_q \frac{d_q}{d_0} - E_{KE}. \tag{4.15}$$

The remaining summation is the number of carriers weighted by their drift distances, which, recalling Ramo theory (Sec. 4.2), is equal to the image charges detected by the ionization electrodes $N_{\mathrm{e/h}}$ giving

$$E_{\mathrm{NTL}} = eV_b N_{\mathrm{e/h}} - E_{KE}. \tag{4.16}$$

---

effective mass being an anisotropic tensor, which changes how electrons propagate through the crystal. Although Eq. 4.12 gives that the rate of change in momentum aligns with the applied field, treating the derivative of Eq. 4.8 carefully with a tensor mass finds that the rate of change of velocity does not align with the electric field. This requires a transformation into momentum space for proper accounting, see [264, 265, 273, 274] for details.

4.3.3 Total Phonon Energy Scales

The total phonon energy detected in the system E_t is a sum of all three phonon sources: primary, relaxation, and NTL

$$E_t = E_P + E_R + E_{\text{NTL}} \tag{4.17}$$

$$= E_r - N_{\text{e/h}} E_{\text{gap}} + N_{\text{e/h}} E_{\text{gap}} + E_{KE} + eV_b N_{\text{e/h}} - E_{KE} \tag{4.18}$$

$$= E_r + eV_b N_{\text{e/h}}, \tag{4.19}$$

Using Eq. 4.2 gives

$$E_t = E_r + \frac{eV_b}{\epsilon_\gamma} E_Q, \tag{4.20}$$

which demonstrates how the total phonon signal, ionization signal, and initial recoil energy are all related and is valid regardless of recoil type. Using instead Eq. 4.3 with the ionization yield gives

$$E_t = E_r \left(1 + Y(E_r) g(V_b)\right) \tag{4.21}$$

$$= E_r \mathcal{A}(V_b), \tag{4.22}$$

where two short-hand variables are introduced with $g(V_b) \equiv eV_b/\epsilon_\gamma$ as the NTL-gain and $\mathcal{A}(V_b) \equiv (1 + Y(E_r) g(V_b))$ as the total amplification. This last expression demonstrates the primary advantage of operating at larger bias potentials, such as with CDMSlite: amplification of the recoil-energy signal through the phonon channel.

Equation 4.21 defines three different energy scales with corresponding units based upon the known or assumed recoil type.

Total Phonon Energy: No recoil type is assumed. The measured E_t is reported with units of keV_t.

Electron Equivalent Energy: An ER is assumed. The yield is assumed to be unity and the electron-equivalent recoil energy $E_{r,ee} = E_t/\left(1 + g(V_b)\right)$ is reported with units of keV_{ee}.

Nuclear-Recoil Equivalent Energy: An NR is assumed. The nuclear-recoil equivalent recoil energy $E_{r,nr} = E_t/\left(1 + Y(E_{r,nr}) g(V_b)\right)$ is reported with units of keV_{nr}.

4.3.4   Phonon Detection

The phonon sensors consist of Quasiparticle-trap-assisted Electrothermal-feedback Transition-edge-sensors (QETs) which are affixed to a flat surface of the detector. The QETs consist of aluminum fins, photolithically mounted to the germanium, which are connected to strips of tungsten. The detector is cooled such that the aluminum ($T_c = 1.2$ K) and tungsten ($T_c \sim 80$ mK) are superconducting, with the tungsten being held at its conduction/superconducting transition by electrothermal feedback. This results in a very sensitive phonon sensor.

Quasiparticle trapping was first proposed by Booth in [276] and a cartoon schematic of its implementation in a CDMS QET is shown in Fig. 4.7. If a phonon in the detector hits a bare Ge/Si surface, it will be reflected back into the detector. If, instead, it hits the surface where an aluminum fin is positioned, it will enter the fin: ballistic phonons will continue to reflect from the surfaces until entering a fin. If the energy of the phonon is greater than the superconducting gap energy of aluminum $2\Delta_{\text{Al}} = 340$ μeV (or alternatively $\nu \gtrsim 82$ GHz, below the $\sim$1 Tz ballistic threshold frequency), the phonon will break up a copper pair and create quasiparticles. This process can also create lower energy phonons, which, if they are energetic enough, will break up more cooper pairs. If, instead, they have $E < 2\Delta_{\text{Al}}$, they cannot create more quasiparticles and return to the detector: their energy is lost to the sensor.

The edge of the Al fin overlaps with the W strip in what is called the "bi-layer". As the T_c of W is less than that of Al, so too is the gap energy required to break up cooper pairs with $2\Delta_{\text{W}} \sim 20$ μeV. Due to the proximity to W in the bi-layer, the gap in this region is $2\Delta_{\text{W}} < 2\Delta_{\text{Bi}} < 2\Delta_{\text{Al}}$. Quasiparticles created by the phonon interaction diffuse through the Al, with a time scale of 1–2 μs, until they reach the bi-layer. During the diffusion, they can shed phonons which either create more quasiparticles or are lost depending on their energy. Once the quasiparticles enter the bi-layer, if they interact and lose energy, they will be trapped and cannot reenter the Al only portion of the fin. This energy loss is through either electron-electron scattering or shedding of a phonon, which is guaranteed to have $E < 2\Delta_{\text{Al}}$ and is lost energy. The trapped quasiparticles then diffuse into the W with minimal probability for energy loss in the process. Once in the W, the quasiparticles continue to scatter and lose energy, however since the W only layer has an even smaller gap energy, the particles are trapped in the W. In the W,
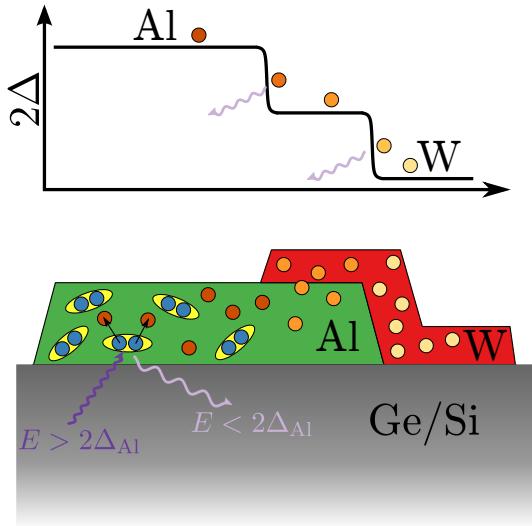
Figure 4.7: Cartoon demonstrating the physics behind quasiparticle trapping in a QET. Phonons entering the superconducting aluminum fins with $E > 2\Delta_{Al}$ (dark purple) can break up cooper pairs (blue circles joined by yellow oval) to create quasiparticles (dark orange). It is possible here and later for phonons to be created with $E < 2\Delta_{Al}$ (light purple) which is lost energy. Quasiparticles diffuse from areas of higher energy to lower energy, as represented by the top graph ($2\Delta_{Al} = 340$ μeV, $2\Delta_W \sim 20$ μeV). Gradients of orange indicate the relative energy of the quasiparticles (dark is more energetic).

electron-electron scattering is about one hundred times more probable than electron-phonon scattering, and thus there is minimal energy lost once they reach this point.

The phonon energy signal is converted to an electronic signal in the tungsten portion of the QET. The tungsten is voltage biased at 0 V (it is used as the ground for the electric field) and, due to Joule heating, is held at its transition edge between superconducting and normal conducting. This system is called a transition-edge-sensor (TES). The electronic signal resulting from the crystal's phonons acts as an external power source on the TES and, as such, increases the temperature of the tungsten. Since the tungsten is at the transition between conductivities, this increase in temperature pushes the TES to have normal resistance. The Joule-heating power provided by the power supply is $P_J = V_b^2/R$, and thus an increase in resistance leads to a decrease in Joule power. This change in power at the operating point of the TES, given by $R = R_0 \approx 100$–200 mΩ, is

$$\left.\frac{\mathrm{d}P_J}{\mathrm{d}T}\right|_{R_0} = -\alpha \left.\frac{P_J}{T}\right|_{R_0} \quad : \quad \alpha \equiv \left(\frac{T}{R}\frac{\partial R}{\partial T}\right)_{R_0}, \tag{4.23}$$

where α characterizes how sensitive the TES is to shifts in temperature and can be $>10^3$. An increase in temperature due to an event's signal leads to a decrease in Joule heating, which in turn causes the TES to cool back to its operating point. This interchange is known as electrothermal feedback (ETF) [270, 277]. The cooling of the TES follows
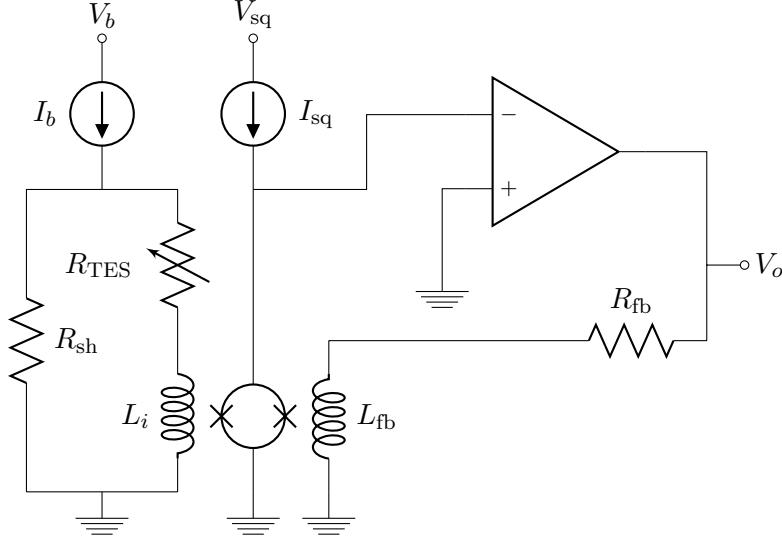
Figure 4.8: Simplified read-out circuit for a single phonon channel. The TES $R_{\text{TES}} \approx$ 100–200 mΩ is voltage biased from V_b and $R_{\text{sh}} \approx 25$ mΩ and receives current I_b. When an event occurs, R_{TES} increases which changes the current through $L_i = 250$ nH which is felt by the squid array and the similarly coupled $L_{\text{fb}} = 0.1L_i$. The array is biased by V_{sq} with I_{sq}. The current through L_{fb} is read-out through the feedback resistor $R_{\text{fb}} = 1$ kΩ as output voltage V_o with amplification from the amplifier.

an exponential with some time constant $\tau_{\text{ETF}} \sim 50/100$ μs for oZIPs/iZIPs [270, 275]. Since the ballistic phonons scatter multiple times before their energy is reduced below $2\Delta_{\text{Al}}$, the measured decay time is several times longer than this.

Since the bias voltage is held constant, the decrease in P_J is accompanied by a decrease in biasing current. This change in current is indirectly read out by the phonon electronics chain which is given in Fig. 4.8. The TES is voltage biased with a shunt resistor R_{sh} and draws current I_b. When the resistance of the TES increases, the current changes via the above mechanism and so too changes the current through the SQUID-array-coupled input inductor L_i. SQUIDs, for superconducting quantum interference devices, are very sensitive magnetometers and the array detects the change in magnetic flux from L_i. The change in bias of the SQUIDs causes a current in the feedback inductor L_{fb}. The feedback resistor R_{fb} lets the change in current be amplified and read out through the output voltage V_o, which is digitized.

The geometry of the QET placement differed between oZIPs and iZIPs. In the oZIPs,

(a) Charge and QET interleaved channels

(b) Photo of a single QET. Light green corresponds to aluminum fins and the tungsten is highlighted in red.

(c) Schematic of a QET chain. Blue is aluminum, red is tungsten, and green is amorphous silicon.
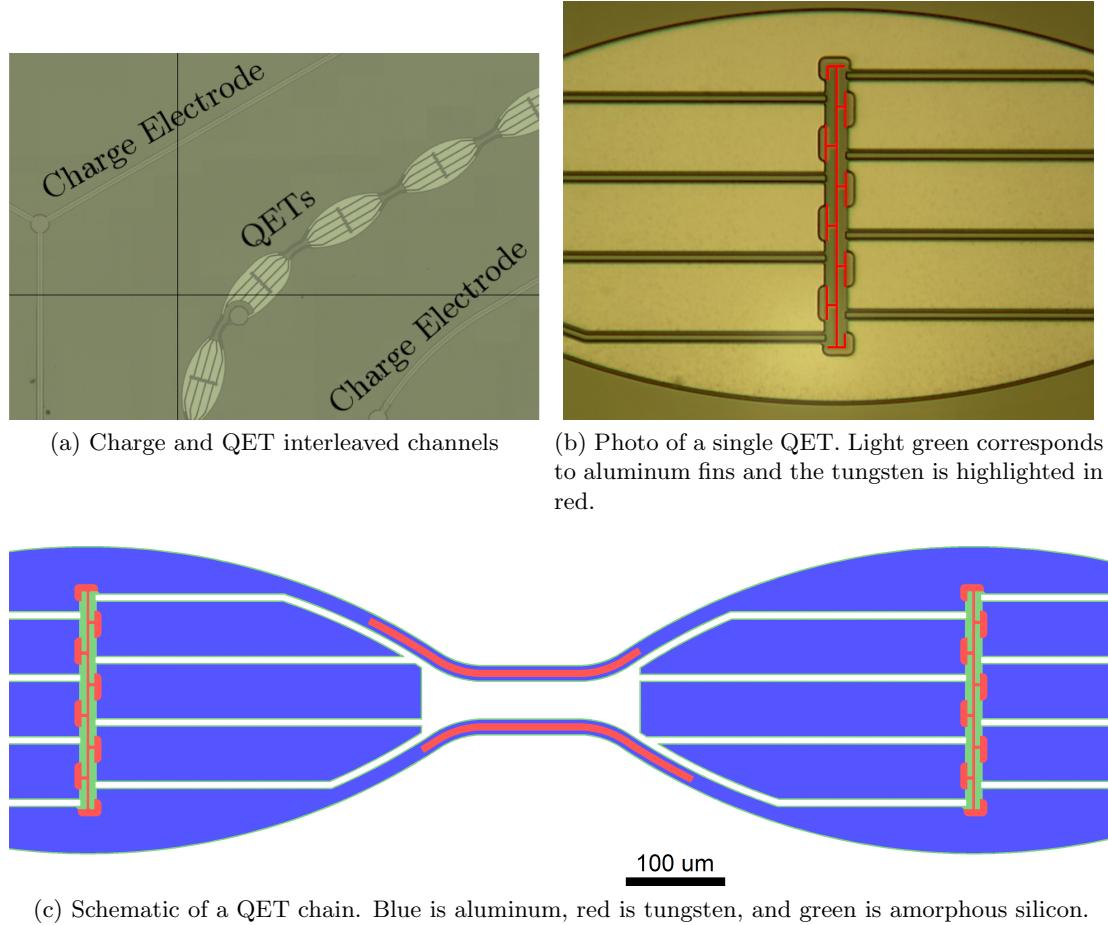
Figure 4.9: Various depictions of the QET geometry used with iZIPs.

there were with 4144 QETs per detector covering approximately 82 % of the detector face with aluminum [267, 278]. For the iZIPs, a chain of QETs were interleaved with charge sensors as shown in Fig. 4.9(a). An individual QET is photographed in Fig. 4.9(b) while a schematic of two connected QETs is given in Fig. 4.9(c). In this design, the eight aluminum fins made on ovular shape with the tungsten in the middle of the oval. The QETs were connected by more aluminum and tungsten in series along the thread. There were 1820 QETs per face covering a reduced ∼5 % on the face [277].

An example event's phonon pulses are shown in Fig. 4.10. The scatter occurred in an iZIP detector, which were digitized at a rate of 0.625 MHz (1.6 μs per sample).
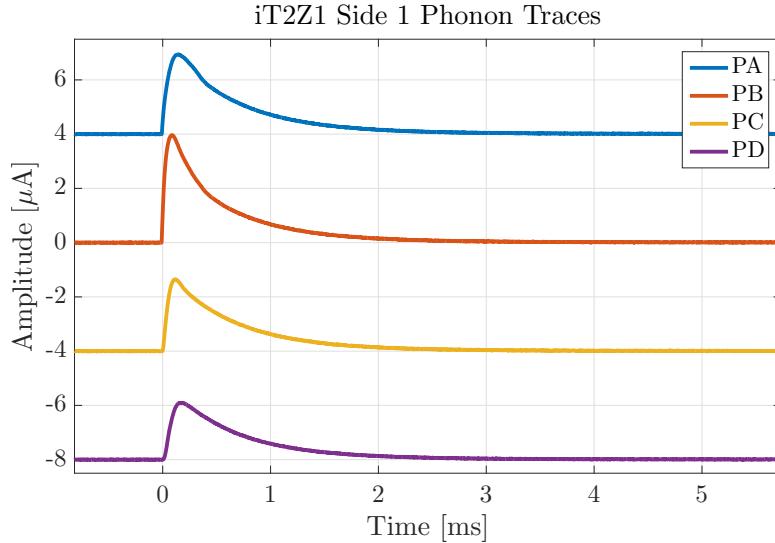
Figure 4.10: Phonon output traces from the four channels on side 1 of iT2Z1 for an example event with ~511 keV recoil energy. The four channels are vertically shifted by 4 nA for clarity.

The trace lengths were shorter in CDMS II, due to increased TES coverage, and the digitization rate was the same as for the ionization traces. With 4096 digitized bins, the total trace lengths were 3.28/6.55 ms for CDMS II/SuperCDMS.

Unlike the charge traces, the phonon traces can show considerable position dependence. This is a direct result of the different types of phonons created by an event. The diffusive phonons created by the initial recoil are absorbed by whichever channel is closest in proximity and this occurs on a short timescale before the phonons become ballistic. If the scatter is deep enough in the detector to become ballistic before hitting a surface, the closest channel is the first to be hit by the resulting ballistic phonons. The ballistic phonons scatter between surfaces until they are absorbed or are not energetic enough to be so. Due to the small surface area coverage of Al (particularly in an iZIP), it can take up to 100 scatters for all ballistic phonons to reach one of those states: this is a longer process and all channels participate equally in the energy absorption. An event caused by a particle scatter has a trace with two distinctive characteristics: a sharp peak which gives localization information and a slow decay which gives energy information.
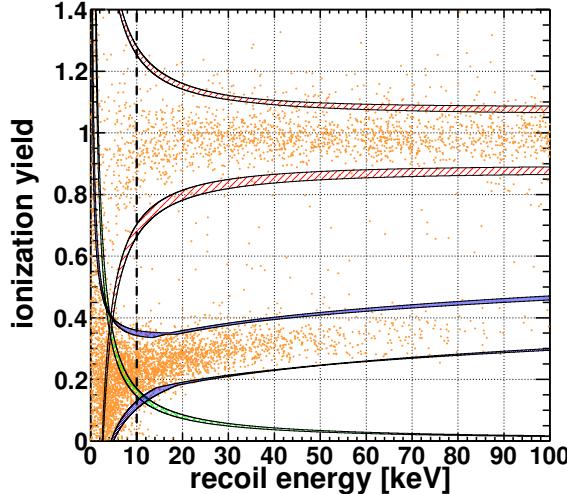
Figure 4.11: Ionization yield as a function of recoil energy for ^{252}Cf calibration data (yellow points) taken with an oZIP. ERs populate a band at $Y(E_r) \sim 1$ (red band) while NRs populate a band near $Y(E_r) \sim 0.3$ (blue band). A typical charge threshold is also shown (green band). The width of the band definitions comes variations of the band definition by time and are tuned on known-recoil-type calibration data. Figure courtesy of A. Villano.

4.4 Ionization Yield Discrimination

The ionization yield defined in Sec. 4.2 allows the ZIP technology to discriminate between ERs and NRs. The yield is the ratio between the charge energy E_Q and true recoil energy E_r and, through a combination of the ionization and phonon measurements, can be determined for any given event. Rearranging Eq. 4.20 for E_r gives the yield as

$$Y(E_r) = \frac{E_Q}{E_t - \frac{eV_b}{\epsilon_\gamma} E_Q}. \tag{4.24}$$

An example yield versus recoil energy plot is given in Fig. 4.11 from an oZIP detector and calibration data. Photons and other ERs populate a band straddling $Y(E_r) = 1$ while nuclear recoils (from neutrons in this data) populate a band at $Y(E_r) \sim 0.3$. The bands are defined by fitting the populations of known recoil type from calibration data. A typical charge threshold is also shown, which has a $1/E_r$ behavior from Eq. 4.24. There are two other notable features in this plot. First, the ER and NR bands flare out at lower recoil energies due to increased noise in the measurements. Below $\sim$10 keV the separation between the bands decreases rapidly and at $\sim$5 keV they overlap at the 3σ level. This implies that, for low recoil energies, the discrimination power of $Y(E_r)$ decreases. Traditional CDMS searches have set a threshold of $E_r = 10$ keV to avoid this region, which sacrifices sensitivity to low-mass WIMPs.
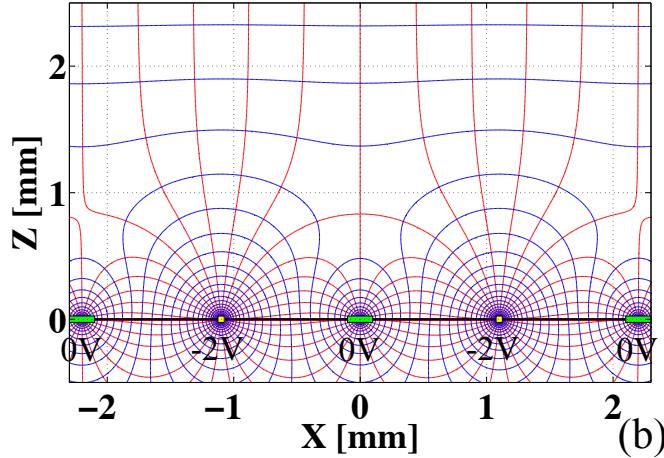
Figure 4.12: Electric field (red lines) and equipotential lines (blue lines) near an in-strumented surface of an iZIP detector. The phonon sensors were held at 0 V (green) while the charge sensors were held at -2 V (yellow). The opposite face had a similar configuration, but with the charge sensors held at $+2$ V. Scatters in the bulk of the detector see a uniform field and electron/hole pairs drift to different sides. Scatters near a surface see the more complex surface field, and both charge carriers drift to the same surface. Figure from [279].

The second notable feature is that there are events between the NR and ER bands. These are ER events with reduced E_Q due to scattering in the dead layer. Incoming β particles are the most likely cause of these so-called "surface events". In CDMS II, surface events were the primary background and were removed using the fact that scatters closer to the surface have sharper phonon-pulse rising edges than scatters in the bulk of the detector. Such a differentiation based on phonon pulse shape is called a "timing cut".

It was to better reject surface events that the SuperCDMS collaboration developed the iZIP technology. The electric field close to an instrumented surface of an iZIP detector is shown in Fig. 4.12. Phonon sensors were biased at 0 V while charge sensors were biased at -2 V. The opposing face had similar instrumentation but with the charge sensors biased to $+2$ V. This formed a total bias of 4 V in the bulk of the crystal. Electron/hole pairs created in the bulk drifted to, and were collected on, opposite faces of the detector. Near the instrumented surfaces, a more complex potential existed. Electron/hole pairs created at the surface drifted to the same face and were collected
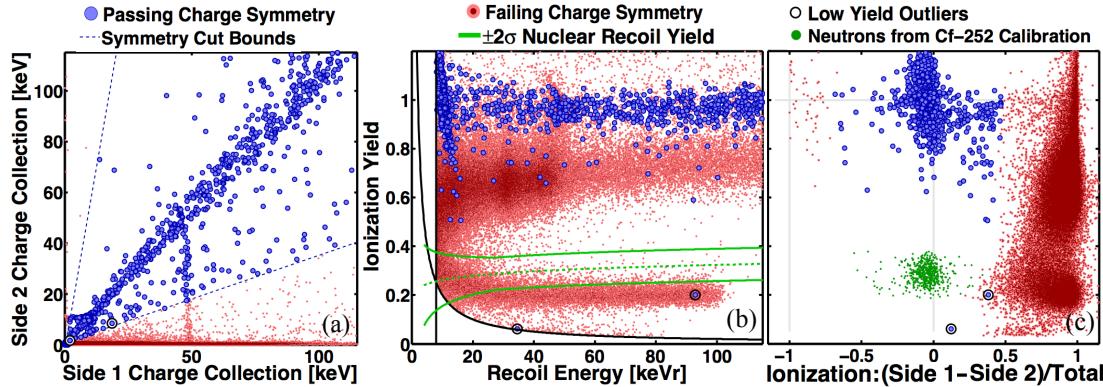
Figure 4.13: Data from ∼900 live hours for detector iT3Z1, which had a ^{210}Pb source on side 1. (a) Ionization signal on both sides of the detector showing the charge symmetry cuts (dash lines). Blue events pass the symmetry cut while red events do not. The source on side 1 is clearly visible including a 46.7 keV γ line. (b) Recoil energy versus ionization yield with coloring the same as before. The green lines define the NR band, within which there are no blue events. Two low yield outliers (circled) are present, but not in the NR band itself. (c) Yield versus charge partition ([S1-S2]/total), now including green neutron events from calibration data used to defined the NR band. NR signal-like events show a symmetric signal as evidenced by partition values of ∼0. Figure from [279].

there. Approximately equal charge energy was collected on both sides of the detector for bulk events while only one side of the detector had signal for surface events. A discrimination cut, called a charge symmetry cut, was made by requiring signals on both sides of the detector.

In order to test the performance of iZIP detectors, two surface sources were installed during SuperCDMS running. These sources were silicon wafers implanted with ^{222}Rn, which quickly decayed to ^{210}Pb. They were mounted on the top of iT3Z1 and the bottom of iT3Z3. The ^{210}Pb decay chain creates low-energy γ's, β's and recoiling nuclei (see Sec. 6.1.2), and, since the wafers were only on a single side of the detector, these all created surface events. These data are shown in Fig. 4.13, where no surface events were found to be within the NR band region, and an upper limit on the surface-event leakage fraction (percentage of surface events passing the symmetry cut and being within the NR band) set at 1.7×10^{-5}.

4.4.1 Yield at High Bias

The ionization-yield discrimination power diminishes as the bias potential is increased due to the inherent noise of the read-out signals. The uncertainty on the estimated yield can be found from the uncertainties σ_t and σ_Q on the measured E_t and E_Q. Using standard uncertainty propagation, this uncertainty σ_Y is

$$
\begin{aligned}
\sigma_Y^2 &= \left(\frac{dY}{dE_t}\right)^2 \sigma_t^2 + \left(\frac{dY}{dE_Q}\right)^2 \sigma_Q^2 \\
\sigma_Y^2 &= \left[\frac{-E_Q}{(E_t - E_Q g(V_b))^2}\right]^2 \sigma_t^2 + \left[\frac{E_t}{(E_t - E_Q g(V_b))^2}\right]^2 \sigma_Q^2 \\
\sigma_Y^2 &= \left(\frac{E_Q}{E_t - E_Q g(V_b)}\right)^2 \left(\frac{E_t}{E_t - E_Q g(V_b)}\right)^2 \left[\left(\frac{\sigma_t}{E_t}\right)^2 + \left(\frac{\sigma_Q}{E_Q}\right)^2\right].
\end{aligned}
\tag{4.25}
$$

The first term is the yield itself while the second term is E_t/E_r, i.e. the total amplification $\mathcal{A}(V_b)$. The final expression is then

$$
\frac{\sigma_Y}{Y} = \mathcal{A}(V_b) \left[\left(\frac{\sigma_t}{E_t}\right)^2 + \left(\frac{\sigma_Q}{E_Q}\right)^2\right]^{1/2},
\tag{4.26}
$$

which shows the percent uncertainty on the yield linearly increasing with bias. The read-out noise does not increase with bias, meaning $\sigma_t/E_t \to 0$ at high bias and the primary contributor the yield uncertainty is the amplification of the charge noise. A broader yield band means a higher probability of ER events leaking into the NR band, which weakens the overall discrimination power.

The broadening effect is demonstrated with simulated data in Fig. 4.14. 50 keV NR events are simulated assuming $Y = 0.3$ and adding typical Gaussian noise to the phonon ($\sigma_t = 0.15$ keV) and charge ($\sigma_Q = 0.4$ keV) signals. 10^5 events are simulated at every 0.5 V from 0–100 V with the median and central 68 % confidence band of the yield distribution at each bias shown. Although the median gives the expected $Y = 0.3$, the width of the distribution increases by $\sim$10$\times$ over the bias range. Simulating ERs with $Y = 1$ shows similar broadening.

The broadening is an issue for all ZIP operations and is why the standard operating biases are so low. For CDMSlite-mode, not only are the biases higher but the target
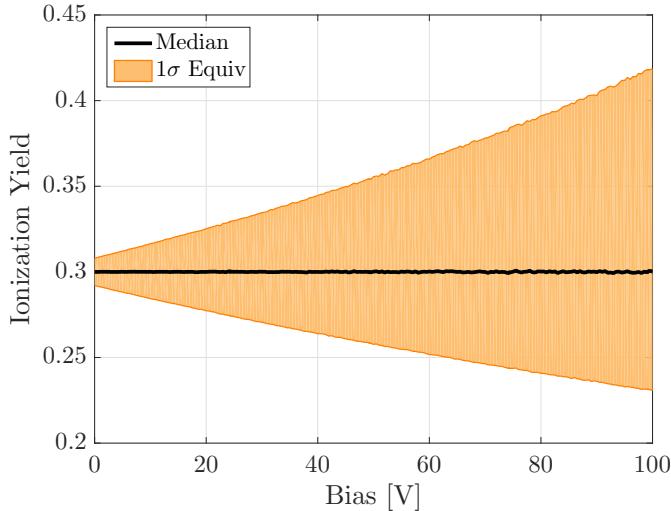
Figure 4.14: Simulated ionization yield bands for $E_r = 50$ nuclear-recoil events ($Y = 0.3$) at increasing bias potentials. For each bias potential, 10^5 events are simulated, adding noise, and the median (black line) and central 68 % confidence band (yellow shaded) computed. The yield band width increases by $\sim10\times$ over the range.

recoil energies lower. This combination presents a second problem. Taking the limit that $E_r/g(V_b) \to 0$, and correspondingly $E_Q/g(V_b) \to 0$, and writing the expression for yield including the read out uncertainties gives

$$Y = \frac{E_Q \pm \sigma_Q}{(E_r + E_Q g(V_b)) \pm \sigma_t - E_Q g(V_b) \mp \sigma_Q}$$

$$Y = \frac{E_Q \pm \sigma_Q}{E_r \pm \sigma_t \mp \sigma_Q g(V_b)} \to \frac{\pm \sigma_Q}{\pm \sigma_t \mp \sigma_Q g(V_b)} \to \frac{-1}{g(V_b)}. \tag{4.27}$$

The measurement of the yield departs from the expected value and asymptotes to zero as the bias is increased. Stated differently, in this limit, the primary-phonon component to E_t is so small that $E_t \to E_Q g(V_b)$: the two previously independent read-out measurements become degenerate, and the detector looses its discrimination ability.[4] The primary disadvantage of CDMSlite-mode detectors is their inability to distinguish NRs and ERs.

---

[4] Differences in hardware also make the charge signal less useful in CDMSlite. This technical issue further complicates measuring the yield.

Chapter 5

CDMS at Soudan

At the Soudan Underground Laboratory (SUL), the CDMS II experiment took science data from 2003–2008 and SuperCDMS Soudan took science data from 2012–2015 using the same infrastructure and electronics as the earlier experiment. Additionally, CDMSlite data was taken during parts of 2013–2015. This chapter describes these Soudan experiments, with more emphasis on SuperCDMS: their physical description, how they took data, how the data were processed, and a selection of their most recent WIMP-search results.

5.1 Experimental Infrastructure and Shielding

5.1.1 The Soudan Mine

The Soudan mine opened in 1882 as an open-pit iron ore mine with operations moving underground in the early 20$^{\text{th}}$ century. Located in northern Minnesota, the environment is beautiful in the summer, frigid in the winter, and a constant 60° year round underground. The mine ceased operations in 1962 and shortly thereafter ownership was transferred to the Minnesota Department of Natural Resources who converted the mine into a state park, which is its status to the present day.

Scientific endeavors at Soudan began with the Soudan 1 proton decay experiment located on the 23$^{\text{rd}}$ level of the mine (590 m below ground) in the early 1980's. Its success motivated a larger experiment, Soudan 2, which operated in a newly excavated

Figure 5.1: Computer rendering of the Soudan Underground Laboratory. White indicates open space while black indicates rock. The Soudan 2 and MINOS caverns are the large rectangular blocks on the right and left respectively. They are connected to each other and the historical tunnels by small access tunnels. The historical drift is the rough-edged tunnel which leads off to the right. The angled vertical tunnel is the shaft to the surface. The CDMS experiments were housed in the Soudan 2 cavern.

cavern on the lowest 27th level (713 m below ground) and ran from the late 1980's to the early 2000's. The laboratory was then expanded to a second new cavern to house the Main Injector Neutrino Oscillation Experiment (MINOS) and the Soudan 2 cavern was re-purposed to house CDMS and other experiments. CDMS started its first science run at Soudan in 2003 as part of the CDMS II experiment and concluded its final run in 2015 as part of the SuperCDMS Soudan experiment. A rendering of the SUL is given Fig. 5.1, indicating the Soudan 2 and MINOS caverns and their relation to the shaft to the surface and the original mining tunnels (the "drift").

5.1.2 Experimental Facility

The CDMS experimental site in Soudan is diagrammed in Fig. 5.2 and described in detail in [280]. The experiment proper was situated in a radio-frequency shielded room, simply known as the RF room. In addition to being shielded from electromagnetic signals, the RF room was a clean enclosure, measured to be a class-10,000 clean room during working hours and as a class-1,000 clean room when unoccupied. There was also an attached room (called the ante-room), which was not RF shielded but was still clean and used for detector preparations. Inside the RF room, the detectors sat in a copper
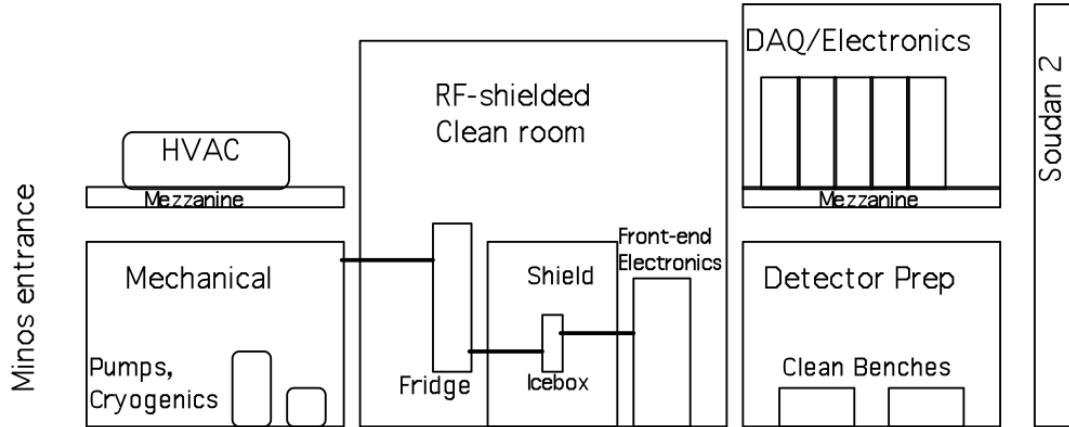
Figure 5.2: Schematic of the CDMS experimental installation at Soudan. The RF room, cryo-pad, and ante-room were on the ground level while the air handling equipment, electronics room, and office were on a second level termed the mezzanine. The entire installation abutted the former Soudan 2 enclosure. Figure from [203].

cryostat, known as the icebox, which was surrounded by concentric layers of shielding and attached to a dilution refrigerator. A rack of front-end electronics boards was also located in the RF room. The RF room was penetrated for both cryogenic systems control and electronics cables. The fridge control led to a mechanical area known as the cryo-pad, which contained the dewars of cryogens, pumps, and necessary controls, most of which had been automated over the years. The electronics cabling led to a room on a second level mezzanine called the electronics room. The electronics room housed more of the detector control electronics as well as the data acquisition (DAQ) computers. On the other side of the RF room, opposite the electronics room, on the mezzanine was an area where HVAC systems maintain the atmosphere and temperature in the RF room. A controller's office was also located on the mezzanine for those physically on site to use.

A cross section of the icebox, fridge, and their connections is shown in Fig. 5.3. The cryostat consisted of six axially concentric cans which were held at 300 K, 77 K, 4 K, 600 mK, 50 mK, and 10 mK (base temperature) respectively. Each stage was connected via a copper tube to the corresponding temperature stage of the dilution refrigerator to transfer heat from the cryostat. The nested tubes of the cold stem (C stem) penetrated the shielding. The refrigerator was a Kelvinox 400-S ^{3}He-^{4}He dilution

refrigerator, rated at 400 μW at 100 mK cooling power. It achieved a base temperature of $\lesssim$ 10 mK with no additional payload. A gap above the inner three cans provided room for the 4 K stage detector electronics. Read-out cabling from these detector electronics ran through a second set of nested tubes in the electronics stem (E stem) to the front-end electronics outside the shield. A secondary cooling system was installed during the CDMS II experiment, mounted to the E stem opposite the fridge, to reduce the live time loss from liquid helium transfers to the refrigerator. This cooling system was a Giffords-McMahon cryocooler which provided 1.5 W of cooling power at 4 K. The cryocooler was driven by the expansion and contraction of helium gas by a mechanical piston.

5.1.3   Shielding

The shielding for CDMS was designed to reject external backgrounds from cosmic rays and cavern rock radioactivity, as well as internal radioactive decays from the experimental apparatus itself. The Soudan mine overburden itself provided shielding from cosmic rays. The 713 m of stable greenstone rock reduced the muon flux in the laboratory by a factor of 5×10^4. Although this shielding greatly reduced muons, secondary particles produced by the remaining flux were still unacceptably large. An active muon veto layer surrounded the experiment to further reject cosmogenic backgrounds. The veto consisted of forty, 5 cm thick, panels of Bicron BC-408 ($H_{11}C_{10}$) plastic connected to photomultiplier tubes. The panels were arranged in an overlapping pattern to eliminate any direct line-of-sight to the detectors. Coincidence with any of the veto panels was used to reject events in the analysis at high efficiency (Sec. 11.4.2). The veto panels are represented by the blue rectangles connected to white photomultiplier tubes surrounding the rest of the shielding in Fig. 5.4.

Inside the veto panels were alternating layers of neutron and gamma shielding. The hydrogenous outer layer moderated neutrons. It was made from 40 cm thick polyethylene (H_2C_1 chains). Electromagnetically interacting particles, primarily γ's, were shielded by two sequential layers of lead. Together, these layers provided 22.5 cm of shielding with the inner 4.5 cm composed of ancient lead. The isotope ^{210}Pb is found in trace amounts in natural lead, has a half life of 22.3 yr, and its decay products can create substantial bremsstrahlung. The ancient lead was recovered from a ballast from
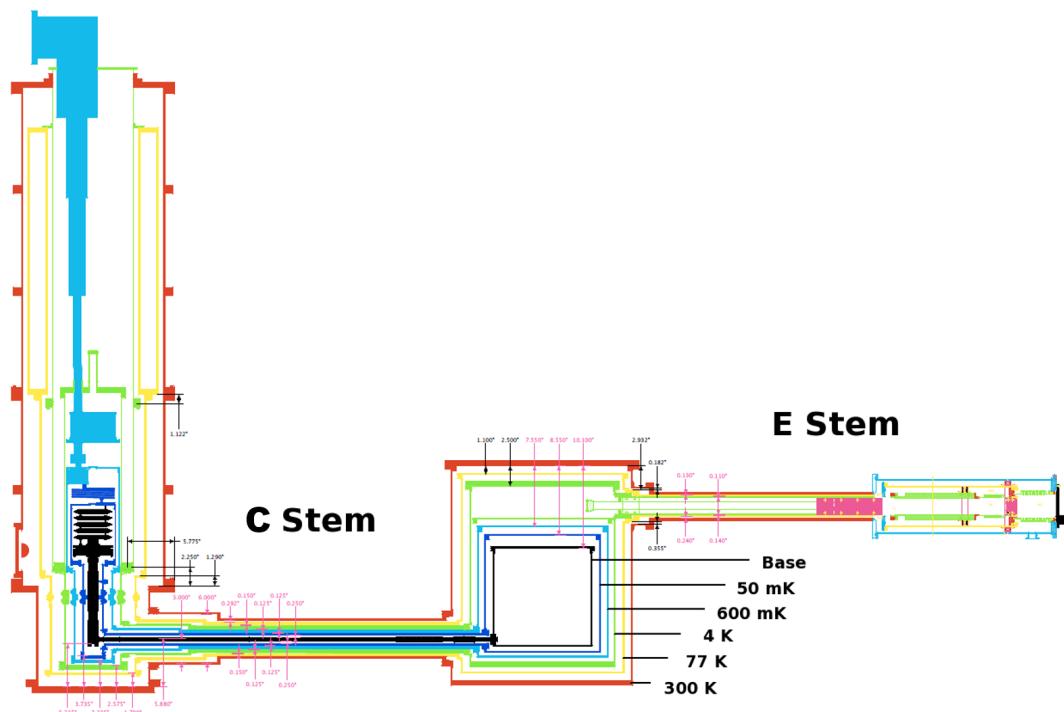
Figure 5.3: Schematic of the CDMS cryogenic system. The dilution refrigerator (left) and interior temperature stages were connected to the icebox through the C stem. The six icebox cans were held at 300 K, 77 K, 4 K, 600 mK, 50 mK, and 10 mK (base temperature) respectively. The detector payload was suspended in the center can (not shown). Detector electronics fed from above the payload at the 4 K stage through the E stem (right). Figure from [281].

CDMS Shielding and Veto

(a) Top View

(b) Side View
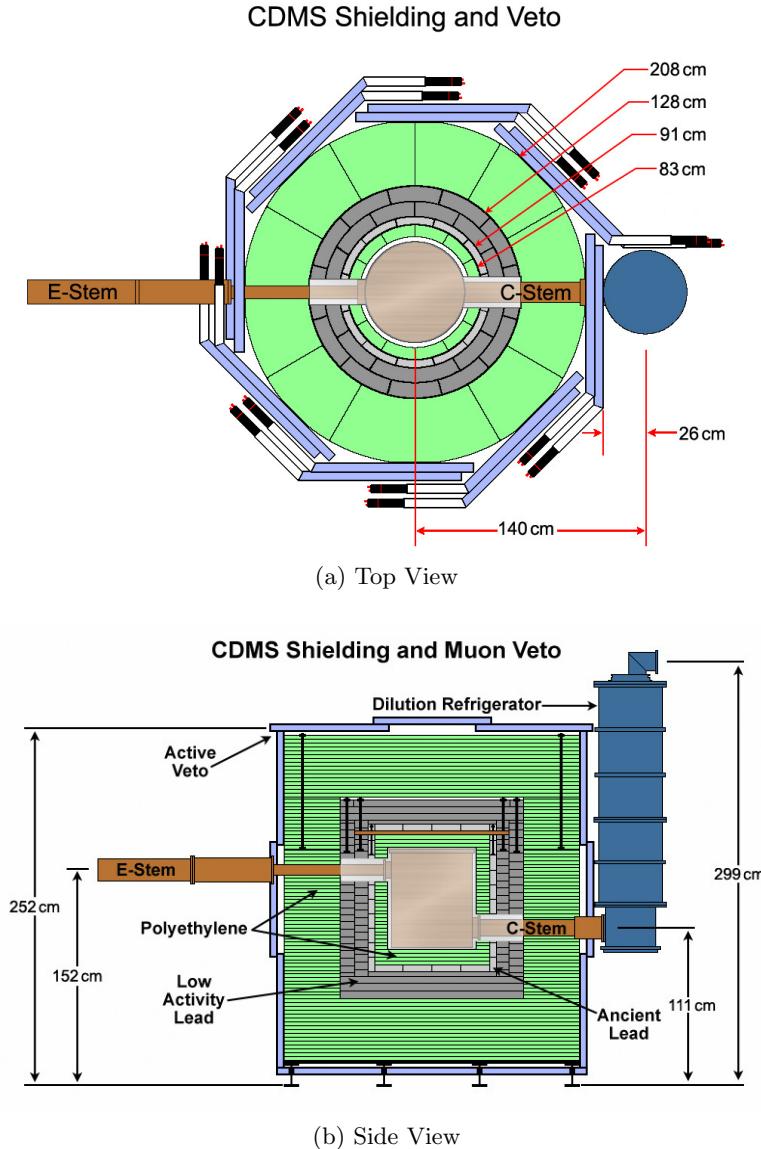
Figure 5.4: Cross-section diagrams of the CDMS shielding as seen from above (a) and the side (b). The outermost layer was the muon veto scintillating panels (light blue) connected to photomultiplier tubes (white and black). The subsequent layers consisted of (from the outermost to the innermost): 40 cm of polyethylene (green), 18 cm of lead (dark grey), 4.5 cm of ancient lead (light grey), and 10 cm of polyethylene (green). The cryostat (light tan) provided, on average, ∼1.9 cm of copper shielding. Also shown are the E-stem and C-stem penetrations (brown) and the relative size and location of the dilution refrigerator (dark blue). Figures courtesy A. Villano and J. Sanders.

a sunken Roman ship in the Mediterranean and was depleted of ^{210}Pb. It was located inside the regular lead, to act as shielding for the bremsstrahlung from the regular lead. An inner layer of polyethylene was located between the lead shield and the cryostat to provide 10 cm of shielding against neutrons created in the outer polyethylene and lead shields. A 0.381 mm thick mu-metal (81 % Ni, 19 % Fe) shield was located inside the inner polyethylene to block any magnetic fields which could interfere with detector electronics operations. The air layer between the mu-metal shield and the outermost cryostat can was purged with "old air" to reduce the content of the radioactive ^{222}Rn naturally found in the atmosphere. The old air was stored in cylinders for at least two weeks to allow the ^{222}Rn, half life 3.82 d, and its immediate daughters to decay. The icebox cans were each 0.125 in thick, providing an additional ∼1.9 cm of γ and β shielding.

5.2   Data Divisions

A period of data taking during which the cryogenics were continuously stable was called a "run". Interruptions in the cryogenics, such as a need to warm the experiment, would end a run. Analysis data sets were typically defined as being over a set of runs. Of importance for this thesis are the last set of data runs during CDMS II, runs 125–128, and the three data runs of SuperCDMS, runs 133–135. The CDMS II runs are collectively known as c58 (combined 125–128) and were taken from 2006–2008. Run 133 was the first science run of SuperCDMS and ran from early-2012 to mid-2013. The run ended when a ^{133}Ba source became trapped inside the shield, requiring a warm-up and partial deconstruction of the shield to retrieve the source. Run 134 started in mid-2013 and ended in mid-2014 to perform standard maintenance on the cryocooler. Run 135 was the last run of SuperCDMS Soudan, and ran from late-2014 to mid-2015 for decommissioning. Three CDMSlite runs, labeled runs 1–3, occurred during run 133 (Run 1), runs 134–135 (Run 2), and run 135 (Run 3).

The basic unit of stored data was a data series (or series, for short). The length of a series was determined by how long the detectors could maintain sufficient neutralization for the full collection of the charge signal. Neutralization was "lost" when impurity traps attracted enough charge carriers to significantly reduce the ionization signal [267]. For

SuperCDMS, neutralization became compromised after ~3 hours while in CDMS II it could take up to ~12 hours. Series lengths in SuperCDMS, as used in Part III, were 3 hours long, after which an LED flash and a 10 minute cool down period were required. Due to the high rate during calibration data (below), a three-hour long calibration series was broken in six blocks of 25 minutes of data taking each followed by an LED flash and 5 minute cool down.

There were three primary data types taken by both CDMS II and SuperCDMS, two of which utilized radioactive sources:

1. **Low-Background/WIMP-Search:** These were the primary data used for determining science results, i.e. used to look for dark matter recoils. No intentional sources were deployed and only ambient background and signal events were expected. The majority of the data were taken in this mode to maximize WIMP-search exposure.

2. **^{133}Ba Calibration:** For these data, two ^{133}Ba sources were placed in source tubes which extended along the E and C stems and ended at the edge of the cryostat. This located the sources inside the polyethylene and lead shields. The ^{133}Ba decayed to ^{133}Cs via γ and conversion electron channels. The four most prominent peaks from the decay were at 356.0, 302.8, 383.8, and 276.4 keV [282]. These lines were generally used for energy scale calibration and defining the ER band in the yield versus recoil energy plane. The β's created by the decay were also used to study surface events. On average, five ^{133}Ba data series were taken over the course of a week for SuperCDMS.

3. **^{252}Cf Calibration:** For these data, a single ^{252}Cf source was inserted alternatively between the two source tubes. The source primarily decayed by α emission, which subsequently generated γs, but it also underwent spontaneous fission with $\sim 3\,\%$ probability. The fission process produced 3–4 neutrons per decay with energies of up to 10 MeV, and a most probable energy at ~1 MeV [283]. These neutron data were used for the NR calibration to define the NR band in the yield versus recoil energy plane. ^{252}Cf data were taken only occasionally, a few times during a calendar year, with a handful of series taken each time, to avoid neutron activation of the crystals.
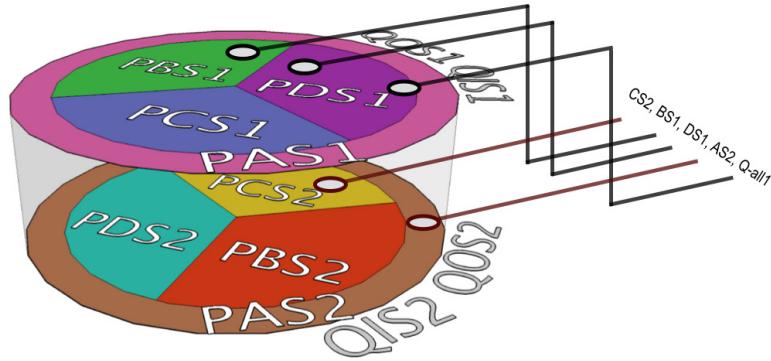
Figure 5.5: Schematic drawing of an iZIP detector with charge and phonon read-out channels labeled and the wire connections for a single DIB indicated. A single DIB connected to channels on both sides of the detector. Wire connections of DIB-1 are indicated with side 1 connections in black and side 2 connections in brown. Channel labeling uses P/Q for phonon/charge channels and S1/2 for the different sides. Figure from [275].

5.3   Electronics

The read-out electronics were originally designed for the CDMS II oZIPs and full descriptions can be found in Refs. [278, 284]. The same system was used for SuperCDMS and CDMSlite, although some modifications were required for the later detector types. The base of the system was a chain of electronics boards that started with an interface board connected to the ZIP, which connected to a circuit board at the 4K stage of the cryocooler, before connecting to a room temperature biasing and amplification board in the RF room, and ending with a trigger-control board in the electronics room. The trigger-control boards for all detectors were then connected to the data acquisition system (DAQ) for user control.

The detector interface boards (DIBs) were able to read out all the channels of an oZIP: four phonon channels and two charge channels. The iZIPs had twice as many of each type of channel and two DIBs were required per iZIP. Each DIB was connected to channels on both sides of the detector (determined by proximity to the connectors) as shown in Fig. 5.5.

The front-end boards (FEBs) contained the amplifiers and biasing sources needed

for the charge and phonon read-out circuits. However, they could only apply biases up to 10 V which were too low for CDMSlite operations. Additionally, for CDMSlite operations, all channels on a single side were grounded while all channels on the opposing side were connected to a high-voltage power supply (HVPS). The CDMSlite adapter board, as diagrammed in Fig. 5.6, took as input the connections from the two DIBs attached to a detector, disentangled the channel lines associated with the two sides, and connected one side to the HVPS and the other to a single FEB and hence the DAQ for read-out. The HVPS was controlled by a separate LabVIEW program. See Appendix A of Ref. [275] for circuit diagram details of the adapter board. Note that in this biasing configuration, only half of the detector's phonon channels were read out.

5.4 Triggering

The detector triggering was controlled based upon five user-controlled settings: charge low/high (Qlo/Qhi), phonon low/high (Plo/Phi), and phonon ultra low (Pwhisper). Each trigger-control board, which had access to four phonon and two charge channels, performed an analog sum of the individual charge/phonon traces and compared the total traces to the user-set values for each trigger setting. The user also defined a trigger condition to determine when to record the current data. Exceeding the Plo value in the phonon traces was almost exclusively used as the trigger condition. If this condition was met, a "detector trigger" occurred and the current detector traces saved. A detector's efficiency at triggering on low energy events determined the lowest possible energy threshold used for that detector in analysis. For a given event, more than one detector could surpass their trigger settings. The first detector to do so issued what was called the "global trigger". The recorded traces in all detectors were aligned such that the global-trigger time was always in the same bin. If a detector trigger was issued during low-background running, the entire ZIP array was read out. During calibration running, only the tower which contained the initiating trigger was read out to conserve data-storage space.

For SuperCDMS, there were two trigger-control boards per detector and hence two Plo values. These could be adjusted individually depending on whether all channels were functioning properly. The trigger condition for any detector was by default set
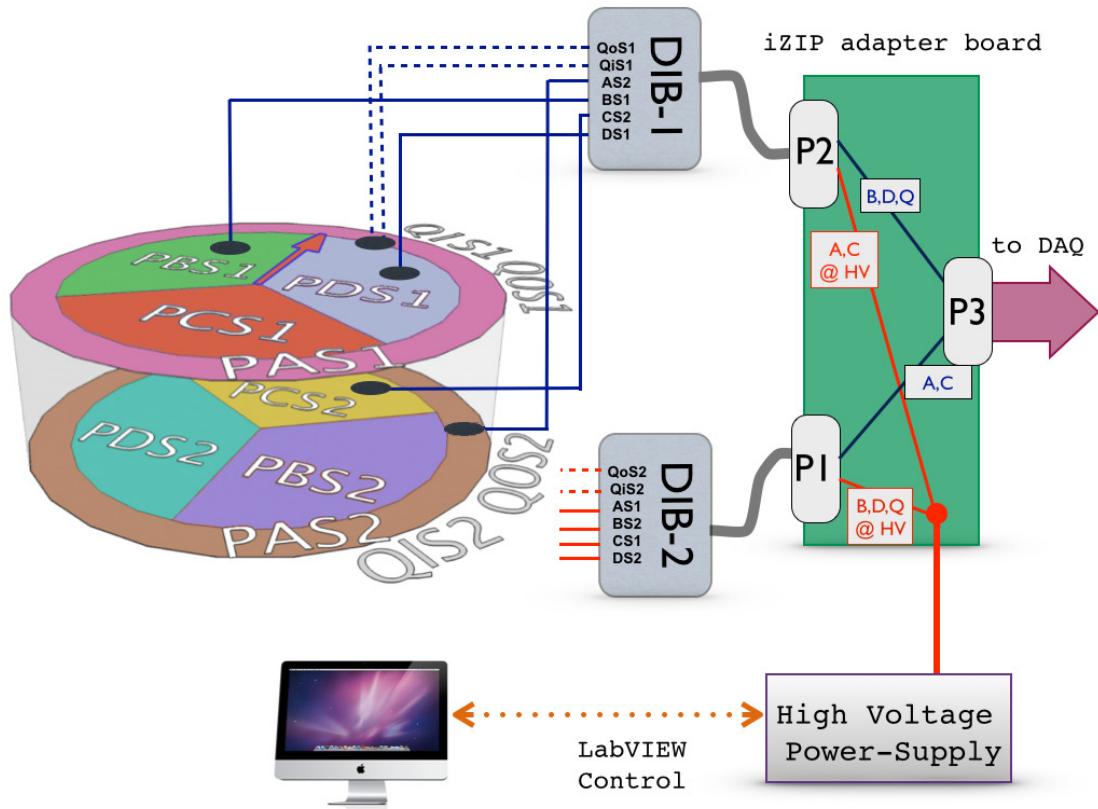
Figure 5.6: Cartoon schematic of the CDMSlite iZIP adapter board. The two DIBs connected to a single detector were connected to the board. The board disentangled the side 1 (S1) and side 2 (S2) channels from the incoming DIB connections. Channels on S1 were grouped together and connected to a single FEB, which in turn connected to the usual DAQ. Channels on S2 were grouped together and connected to a high-voltage power-supply which was control separately with a LabVIEW interface. Figure adapted from [275].

as a logical OR of the two Plo values. However, during the course of running, several detector channels became problematic requiring utilization of a logical AND between the Plo values. The overall rate of detector triggers was also used as a measure of experimental health. During Run 133, a low-background series had an overall trigger rate of $\mathcal{O}(1\ \mathrm{Hz})$ while, towards the end of Run 134, the rate was more than 10 times this, indicating a new background trigger source.

A second type of trigger, a random trigger, was initiated by a signal from the DAQ and recorded the current channel traces, regardless of their content. Assuming there was no particle event occurring, the recorded traces were used as a good indicator of the mostly electronic noise in the detectors. Random triggers, also known as "randoms", were taken in three different modes for SuperCDMS:

- **Beginning-/End-of-Run Randoms:** At the start and end of each series, 500 random triggers were taken in succession. In analysis, these randoms give an indication of the noise health before and after a series.

- **In-Run Randoms:** After every detector trigger during a data series, a uniform random number from 0–1 was drawn by the DAQ. If that number was <0.1, a random trigger was issued. In-run randoms thus occurred approximately every tenth event, but not strictly so. In analysis, in-run randoms give an indication of the noise health throughout the data series.

5.5   Data Processing and Calibration

The raw data saved by the experiments primarily consisted of the traces from the various charge and phonon channels along with other information of the experimental condition at the time of the event. In analysis, all of the information about the initial event scatter, most importantly the recoil energy, is gleaned from these raw traces. Variables describing these quantities are computed by processing the raw data. These variables are given two names by CDMS, reduced quantities (RQs) and relational-reduced quantities (RRQs). RQs are the direct result of running some algorithm on the raw traces, such as the amplitude of a charge pulse in V, while RRQs come from either calibrating RQs to physical units, converting V to keV, or from relationships between RQs, such as the relative energy in any given channel as a measure of the location of the event.

5.5.1 Energy Reconstruction

The maximum height of a pulse and the integral of a pulse are computationally simple measures of the energy of the pulse. However, the energy estimates obtained from these algorithms have too poor resolution for careful analysis, although it is sufficient to determine the data quality. During data taking, these quick algorithms were used to obtain a real-time measure of data quality.

More robust energy reconstruction comes from later processing which performed several optimal-filter fits of signal templates to data traces. In general, the optimal filter algorithms model a signal trace $S(t)$ as a linear combination of a template $A(t - t_0)$, which can be shifted by some time delay t_0, and Gaussian noise $n(t)$

$$S(t) = aA(t - t_0) + n(t), \tag{5.1}$$

where the template is scaled by some amplitude a, whose optimal value is desired. The "optimal" fit is performed in frequency space to better avoid time-domain correlations with non-white noise. The need for a Fourier transformation, however, makes the algorithms computationally slower. The frequency-domain goodness-of-fit χ^2 for each fit depends upon the amplitude of the template and the time delay. Computationally, t_0 is scanned over and the best-fit amplitude and χ^2 computed at each delay. The delay, and therefore amplitude, which gives the lowest χ^2 value is taken as the global best-fit. All three quantities are returned by the algorithms. The χ^2 is used to remove pulses with poor goodness-of-fit, such as if the signal trace is significantly different from the template, i.e. a non-physical event. The amplitude primarily gives energy information and the delay gives information about the position of the event in the detector. The basic algorithm fits a single template to a single trace, however more complicated algorithms can also be used. These algorithms are reviewed in Appendix A.

The various algorithms used by SuperCDMS were:

OF: The basic optimal filter algorithm fits a single template to a single trace. This was used for the phonon traces from each individual channel, as well as the total pulse formed after normalizing (see the next section) and summing the channels. For iZIPs a sum of each side was fit as well as the sum of both sides. A single template was created by averaging the total pulse of many high-quality events.

The time-delay scan-window was $[-200, +100] \, / \, [-50, +10] \, / \, [-25, +10] \; \mu$s around the global trigger time for SuperCDMS Ge/CDMS II Ge/CDMS II Si detectors.

OFX: For the ionization signal, there was $\sim 1\,\%$ and $\sim 5\,\%$ capacitive crosstalk between the inner and outer channels in SuperCDMS and CDMS II respectively. This crosstalk was accounted for by computing four templates and performing a joint fit between the channels. The four templates were: primary inner, primary outer, crosstalk in inner due to outer, crosstalk in outer due to inner. The templates were generated by finding a population of pure inner (outer) events, averaging their pulses in the inner (outer) channel for the primary template and then in the outer (inner) channel for the crosstalk template. The time window over which the time delay was scanned was $[-100, +10] \, / \, [-50, +10] \; \mu$s around the global trigger time for Ge/Si detectors in either experimental generation.

NSOF: In CDMS II, the position dependence in the phonon traces was removed by an arduous "position correction" procedure as described in [285]. For SuperCDMS, a new procedure was instead developed. The non-stationary optimal filter (NSOF) was the primary method to remove the position dependence of the OF fit. In the NSOF, the initial peaky/nonpeaky portion of the pulse was treated as non-stationary noise. These portions were deweighted in the fit which gives greater governance of the fit to the long-decay tail. The same templates and time-delay scanning window as the OF fit were used in addition to a noise "template" describing the peaky portion of the traces. The ^{133}Ba 356 keV line is shown in Fig. 5.7 for the regular OF and NSOF algorithms to demonstrate the improvement in resolution due to the NSOF. The sole purpose of the NSOF was energy reconstruction and it was only run on the total phonon trace. For pulses with sufficiently small amplitude, i.e. just above or in the noise, the OF and NSOF gave near-identical results. To preserve processing time, a cut in energy was placed below which the NSOF was not run and the OF value used instead.

2T-Fit: A second approach to remove the phonon position dependence was developed by the CDMS group at Queen's University and the analysis in this thesis is the first to benefit from its use. This method fit a single trace to two templates, where the two templates attempted to model the fast initial portion and slow ballistic tail
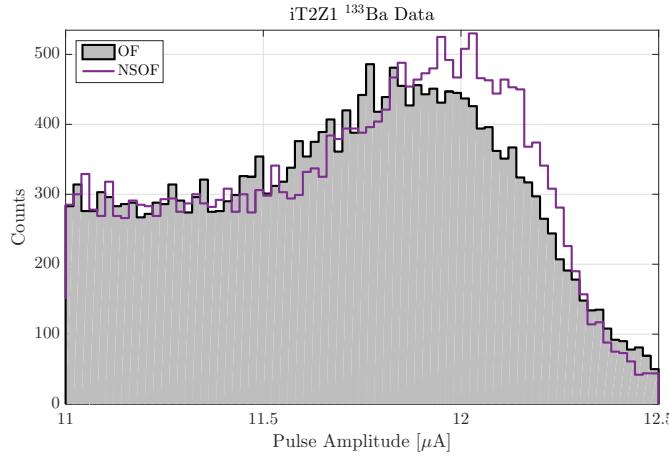
Figure 5.7: Uncalibrated phonon-pulse-amplitude distribution for the same data processed with the standard OF (grey filled) and NSOF (purple line). The data is ^{133}Ba-calibration data and the peak at $\sim$12 μA is the 356 keV peak. The resolution improves using the NSOF fitting algorithm.

separately. The results gave both energy and position information of the event. See Sec. 10.1.2 for further details on the 2T fitting.

OF0/NSOF0: In the analysis, the reconstructed energies found from random triggers are used as an estimate of the noise resolution of the detectors. A naive expectation for the distribution of randoms is for it to be centered at 0 keV with some Gaussian spread. However, since the OF and NSOF algorithms were set to find either the minimum χ^2 or maximum amplitude in a time window, the fits always picked a noise fluctuation within the scanned timing window and were biased towards non-zero amplitudes. To estimate the true resolution, OF and NSOF fits were performed with the time delays forced to be zero. This zero-delay fit was used only to estimate the baseline resolution due to electronics noise. The OF0 algorithm was run on both charge and phonon traces and the NSOF0 run on the phonon traces.

5.5.2   Calibration

The outputs of any of the OF-fitting algorithms were the amplitude(s) of the template(s) in arbitrary ADC units which was converted to the physically read out units of volts

(ionization) and amperes (phonon) given the specific read-out circuits. These outputs were stored as RQs. A calibration was used to covert from units of circuits to units of recoil energy, keV specifically. The calibration of the different signals was done using the higher statistics ^{133}Ba calibration data, which gave electron recoils peaks that were easy to identify and have known recoil energy. The calibration proceeded sequentially, with each step usually depending on the previous one, in the following order: inner charge, outer charge, relative phonon, total phonon.

1. **Inner Charge:** The inner charge channel covered most of the surface area of a detector's face and this was large enough to fully collect γ events from the calibration source. The most prominent peaks (356, 303, and 384 keV) were usually identifiable in the spectrum. Gaussian fits were performed to give the peak position and width in units of volts and compared to the known keV energy values. A line was fit to the three points with the slope of that line indicating the proper calibration.

2. **Outer Charge:** The outer charge channel covered too small of a surface area of the detector face for the method used with the inner channel. Its calibration was based on shared events with the previously calibrated inner channel. Peak events which were fully collected between the two charge channels populate a negatively sloped diagonal band in the inner- versus outer-charge plane. Since the inner channel was already calibrated, a fit to this band should cross the inner channel axis at the calibrated energy. The outer channel calibration was set such that the fit crossed the outer channel axis at the appropriate energy. The prominent 356 keV peak was used for this process.

3. **Relative Phonon:** The first step in calibrating the phonon energy scale was to look at the calibration between all of the phonon channels. The raw output could differ between the channels due to physical differences in the TESs, such critical temperatures or saturation points. Since the ballistic phonon tail for an event illuminated all channels equally in the detector, the tails of the individual traces were used for relative calibration. The energy absorbed by the channels in the ballistic tails should be the same, and thus the power (integral of the tail) should also be the same. Relative calibration constants were derived with respect to a

single channel on the detector (typically channel D on side 2 for SuperCDMS[1])
by scaling the power of the other channels' tails to the power of that tail.

4. **Absolute Phonon:** The total phonon energy was constructed using the OF fit
   information of the channels in two ways: applying the OF to the individual channel
   traces and then summing the resulting OF values, or adding the raw traces, after
   applying relative calibrations, and running the OF or NSOF on the total trace.
   The latter method gave better resolution and was typically the energy quantity
   used. The absolute energy-scale calibration was performed in the same manner for
   both methods. The ^{133}Ba peaks used were primarily γ decays, and as such should
   have had an ionization yield of unity. Using the γ assumption, the total phonon
   energy would be $E_\mathrm{t}^\gamma = E_\mathrm{Q}\left(1 + eV_b/\epsilon_\gamma\right)$. In CDMS II, the basis for calibrating
   the true energy scale was to calculate E_t^γ for the peak events using the calibrated
   charge quantities and then enforce that $E_\mathrm{t}^\gamma = E_\mathrm{t}$, where E_t is the measured phonon
   quantity. Calibrating in this way also roughly centered the ER yield band at the
   expected $Y(E_\mathrm{r}) = 1$. In SuperCDMS, this procedure was found to be deficient
   in that the total phonon calibration depended on the temperature of the towers.
   This also caused the ionization yield to have temperature dependence. The total
   calibration was instead performed by considering the ratio of $E_\mathrm{t}/E_\mathrm{t}^\gamma$ as a function
   of temperature. A quadratic fit was performed and the calibration constants found
   by making the ratio flat and have a mean value of unity based upon that fit.

5.6   Recent Results

The CDMS II and SuperCDMS Soudan experiments were very successful over their
years at Soudan. The data produced there led to many results and a selection of the
most recent are briefly reviewed. In addition to providing background leading up to the
analysis presented in Part III, the background estimates described in Part II were used
in these analyses.

---

[1] Studies have been done to look at the variation in calibration due to picking a different base channel
with results showing ∼15 % variation in the relative constants. The total phonon pulse constructed next,
however, changes very little with the different relative calibrations [286].

5.6.1   CDMS II c58R

The last WIMP-search data set from the CDMS II experiment consisted of runs 125–128 (c58). The initial Ge results from these runs were published in [223], where two bulk-recoil candidate events were found within the NR band. It was later discovered that a time-saving shortcut taken in the data processing resulted in a non-optimal charge energy being used for one of those events. Using the corrected energy caused one of the events to leave the signal region. However, it was unknown whether fixing the data processing would bring other, previously rejected, events into the signal region. To correctly answer this question, the c58 dataset was reprocessed with a fixed algorithm and a reanalysis undertaken. This reanalysis effort was collectively termed c58R.

c58R Si

The data from the Si detectors were never analyzed in the original c58 processing, but their analysis with c58R was published in [233] and was (still is) a rather important result. The c58R Si result analyzed 8 oZIP detectors with a total exposure of 140.2 kg day over an energy range of 7–100 keV. Three candidate events were observed with an expected background of $0.41^{+0.20}_{-0.08}$ (stat)$^{+0.28}_{-0.24}$ (sys) for surface events, <0.13 for neutrons, and <0.08 for ^{206}Pb daughters. A profile likelihood fit was performed to the three data points which showed that there was a 5.4% probability that they were background fluctuations. The preferred region in the spin-independent cross section-WIMP mass plane from this fit is given in Fig. 5.8. The highest likelihood point was at $m_\chi = 8.6$ GeV/c^2 and $\sigma_p^{\rm SI} = 1.9 \times 10^{-41}$ cm^2. This result is often referenced as the CDMS II Si result, but this is a slight misnomer as the Si analysis from the earlier CDMS II combined runs 123–124 (c34) results were published at a similar time in [203, 287]; c34 had no candidate events.

c58R Ge

The initial goal of the reprocessing was for the Ge detectors and the resulting reanalysis was published in [224]. The Ge reanalysis began before the final c58R Si result was known, and it therefore focused exclusively on high-mass WIMPs in the recoil energy range of 10–100 keV. For that analysis, 14 oZIPs were used for a total exposure of
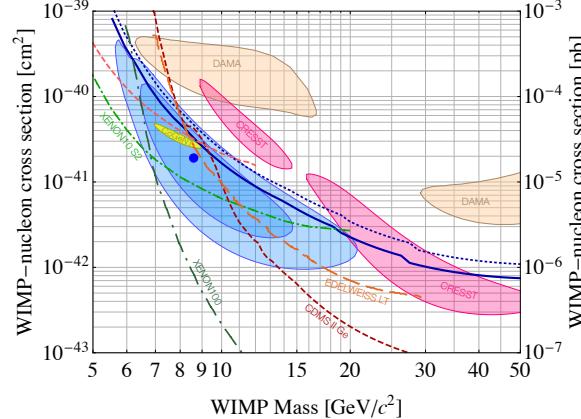
Figure 5.8: Spin-independent WIMP-nucleon cross section vs. WIMP mass plane as presented in the c58R Si result. The 90 % upper limit from that result is shown by the blue dotted line (combining with c34 result gives blue solid line), while the 68 % and 90 % contours are given by the blue shaded regions. The highest likelihood point of $m_\chi = 8.6$ GeV/c^2 and $\sigma_p^{\mathrm{SI}} = 1.9 \times 10^{-41}$ cm^2 is given by the blue dot. The limits and contours are compared to other selected results at the time of publication of [233].

612 kg days. In addition to re-doing the initial analysis, an attempt was made to consider the systematics associated with different timing cuts used to remove surface events. Three different timing cuts were developed: a classic CDMS cut in the same vein as the original c58 analysis, a neutral-network-derived cut, and a five-dimensional χ^2-based discrimination. The results of these three analyses, compared to the initial c58 result, are given in Fig. 5.9(a). The classic cut found two candidate events, the neural network cut found one, and the χ^2-based cut found none and was the primary result in the paper.

The scope of the result was extended after the publication of the c58R Si result as the lower mass region became of greater interest. In order to better probe the Si result, the recoil-energy thresholds on the detectors were lowered to as low as ∼4.5 keV and new results computed in the ∼5–15 keV region. This was called the mid-threshold (MT) analysis. 6 candidates were observed with the Classic timing cut, 16 with the neural network cut, and zero with the χ^2-based cut. The classic timing had the best exposure and sensitivity in this range, as can be seen in the limit curves of Fig. 5.9(b), and was chosen as the primary result.
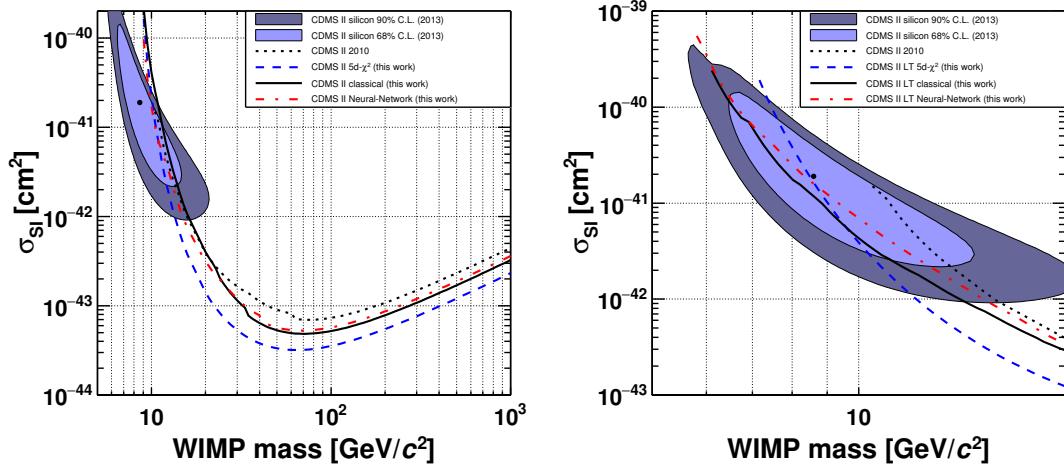
Figure 5.9: 90 % upper limits on the spin-indpendent WIMP-nucleon cross section from the three c58R Ge timing analyses compared to the initial 2010 c58 Ge result. Also shown are the 68 % and 90 % contours and the best fit point from the c58R Si result. The 10–100 keV analysis is shown on the left while the ∼5–15 keV extended analyses are shown on the right. Figures from [224].

5.6.2   SuperCDMS LT

The iZIP analysis strategy for SuperCDMS Soudan was to split the search into two separate analyses: low-threshold (LT) and high-threshold (HT) searches. The LT analysis's goal was to lower the energy thresholds as low as possible to improve sensitivity to low-mass WIMPs. Leakage of background events into the signal region was expected and, as such, the LT analysis was not expected to be background free. Due to this, the LT analysis was conducted first. Conversely, The HT analysis, which set a higher threshold and was expected to be background free, would require the largest possible exposure. Work is still ongoing to analyze the complete SuperCDMS Soudan iZIP data set for the HT search. Additionally, a novel operating mode and analysis type was pioneered which allowed access to the lowest WIMP masses yet: the CDMS low ionization threshold experiment. Given its importance in Part III, the previous result from this method is discussed in Chapter 9.

The SuperCDMS LT (SCDMS LT) analysis, published in [245], used data taken during Run 133 with the seven iZIP detectors with the lowest thresholds, 2–10 keV
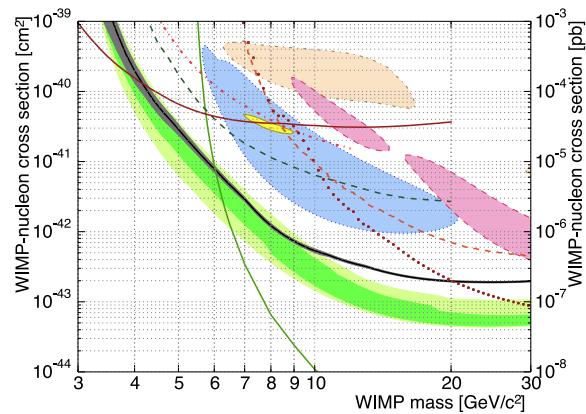
Figure 5.10:   90 % upper limit on the spin-independent WIMP-nucleon cross section from the SCDMS LT analysis compared to other results at the time of publication.   The limit (black with grey uncertainty band) is less restrictive than the sensitivity (green bands) due to three higher energy events in a single detector. The result greatly improves on the CDMS II low-threshold analysis (dotted dark red). Figure from [260].

for nuclear recoils, for a total exposure of 577 kg days. The resulting spin-independent limit is shown in Fig. 5.10. In this background-limited search, the expected background sources were: bulk γ's from Compton scatters and activation peaks in the detectors and the decay products of ^{210}Pb on the detectors and housings. Using these modeled backgrounds, a boosted decision tree (BDT) was trained to rank, in several variables, a given event based upon how "background like" or "signal like" that event appears. A cut was placed in the BDT output score to remove background events (replacing the CDMS II-style timing cut). After this cut, a background of 11 events were observed with an expected background of $6.2^{+1.1}_{-0.8}$ events.

Part II

Radiogenic Background Estimation

Chapter 6

Introduction to Radiogenic Backgrounds

Radiogenic backgrounds in dark matter experiments are non-WIMP events whose origins are radioactive isotopes present in the experimental environment and apparatus. Experiments are designed with sufficient shielding to block close-to-all environmental sources such that the radioactivity of the shielding itself, and other internal materials, becomes the dominant source of these backgrounds. The radiation from these sources can be divided into those which cause electrons recoils (ERs) in the detectors, such as γ's and β's, and those which cause nuclear recoils (NRs) in the detectors, such as neutrons (n's). Four classes of backgrounds rates are of interest for background studies: NR and ER scatters which deposit energy in either a single or multiple detectors. These are abbreviated as NRSS, NRMS, ERSS, and ERMS, where SS and MS indicate single- or multiple-detector scattering events. For experiments with NR/ER discrimination, such as CDMS, NRSS events are particularly dangerous as they are indistinguishable from WIMP scatters in physical data.

The total estimated rate for any of these types of events is computed as

$$\text{Total Rate} = \sum_{\text{Sources}} \text{Rate(Sim.)} \times \text{Yield(Sim.)} \times \frac{\text{Volume(Geom.)}}{\text{Det. Mass(Geom.)}} \times \text{Contam.(Meas.).}$$

(6.1)

The determination of each term in this expression defines the program followed for

each radiogenic background estimate performed. The sum is performed over all sources, where a source is a combination of a geometrical object and radioactive decay. For each source, the rate is determined by simulation as the number of events (of the desired type) per initially simulated particle. The yield converts the rate from the simulation units to physical units, i.e. number of events per contamination level, per time, and per source volume. The yield depends on the material of the source and, for n sources, requires another simulation. The rate is then weighted by the geometrical factors of source volume and payload mass and the measured source-contamination level.

For every background estimate, some of the inputs are the same:

- Relevant radioactive decays

- Yield for each decay

- Simulation toolkit.

These universal components are the subject of the remainder of this chapter. The geometrical factors and contamination levels differ for individual estimates. Chapter 7 describes work done to measure the CDMS Soudan shield's contamination levels and estimate the background rates for multiple Soudan WIMP-search analyses. Chapter 8 describes work done to calculate the projected background rates in the forthcoming SuperCDMS SNOLAB experiment, including on-going material screening to pre-measure contamination levels of building materials and global simulations.

6.1   Sources of Radiogenic Backgrounds

Radiogenic sources have three production mechanisms: primordial, cosmogenic, and anthropogenic [288]. The primordial sources are of most interest as they are the only source of neutrons. The other two production mechanisms provide γ's and β's which are observable in CDMS ER data.

6.1.1   Long-Lived Primordial Sources

Isotopes with half-lives of $\gtrsim 10^9$ yr are present in the Earth's crust as a remnant from its formation. These isotopes are found in all ores mined from the Earth and traces

of them linger in manufactured material. Even if the ore is purified before creating a final product, the manufacturing process itself often re-introduces contaminants. The most important primordial isotopes are the naturally occurring ^{232}Th (99.98 % NA, $\tau_{1/2} = 14.1$ Gyr), ^{238}U (99.27 % NA, $\tau_{1/2} = 4.5$ Gyr), and ^{40}K (0.012 % NA, $\tau_{1/2} = 1.3$ Gyr), where NA stands for "natural abundance" and $\tau_{1/2}$ is the half-life.[1] The average concentrations of these isotopes in the continental upper crust are 850 Bq/kg (^{40}K), 44 Bq/kg (^{232}Th), and 36 Bq/kg (^{238}U) [288].

The simplest of these isotopes is ^{40}K, which undergoes a β decay to ^{40}Ca 89.3 % of the time and electron-capture to ^{40}Ar 10.7 % of the time. The β has an endpoint of 1.32 MeV while the electron-capture is accompanied by a 1.460 MeV γ. Due to the common abundance of natural ^{nat}K in many materials, there are often high levels of ^{40}K which can dominate the γ-radiation background. Since ^{nat}K is found in many common foods, and is essential to the human body, ^{40}K provides a sizable amount of natural radiation to a human. With an activity of $\sim$30 Bq/g for natural K [289], this amounts to $\sim$5 kBq in a typical person, or, somewhat more amusingly, 15 Bq/banana.

The other two long-lived primordial isotopes, ^{238}U and ^{232}Th, decay by α-emission and are the start of long decay chains. These decay chains are given in Fig. 6.1. Each chain contains daughter isotopes with strong γ emissions, the strongest of which are labeled in the figure. The half-lives of all daughter isotopes are significantly shorter than the progenitors, i.e. secular equilibrium of the chain is often assumed, although multiple avenues for the migration of isotopes can break the equilibrium [288]. The highest energy γ is at 2.6 MeV coming from ^{208}Tl, a daughter of ^{232}Th. This 2.6 MeV peak is usually considered the end-point for an environmental γ/β spectrum.[2] The next strongest peak is at 2.2 MeV from ^{214}Bi, a daughter of ^{238}U.

These γ- and β-producing processes are well studied and can be simulated directly. The unit of measure from the simulation for the rate in Eq. 6.1 is, as an example, NRSS per decay. The yields in Eq. 6.1 for these sources only need to account for conversions to match the units of the input contamination and desired exposure. CDMS Soudan typically reported exposures of kg day while SuperCDMS SNOLAB uses kg yr, and the

---

[1] ^{235}U is also naturally occurring, with 0.72 % NA and $\tau_{1/2} = 0.7$ Gyr, but, due to the prevalence of ^{238}U, it is relatively insignificant and is not considered further in this analysis.

[2] ^{208}Tl has several avenues of decay, and the 2.6 MeV γ can be coincident with lower-energy products. If all the products are collected in a single detector, the spectrum can extend beyond 2.6 MeV.
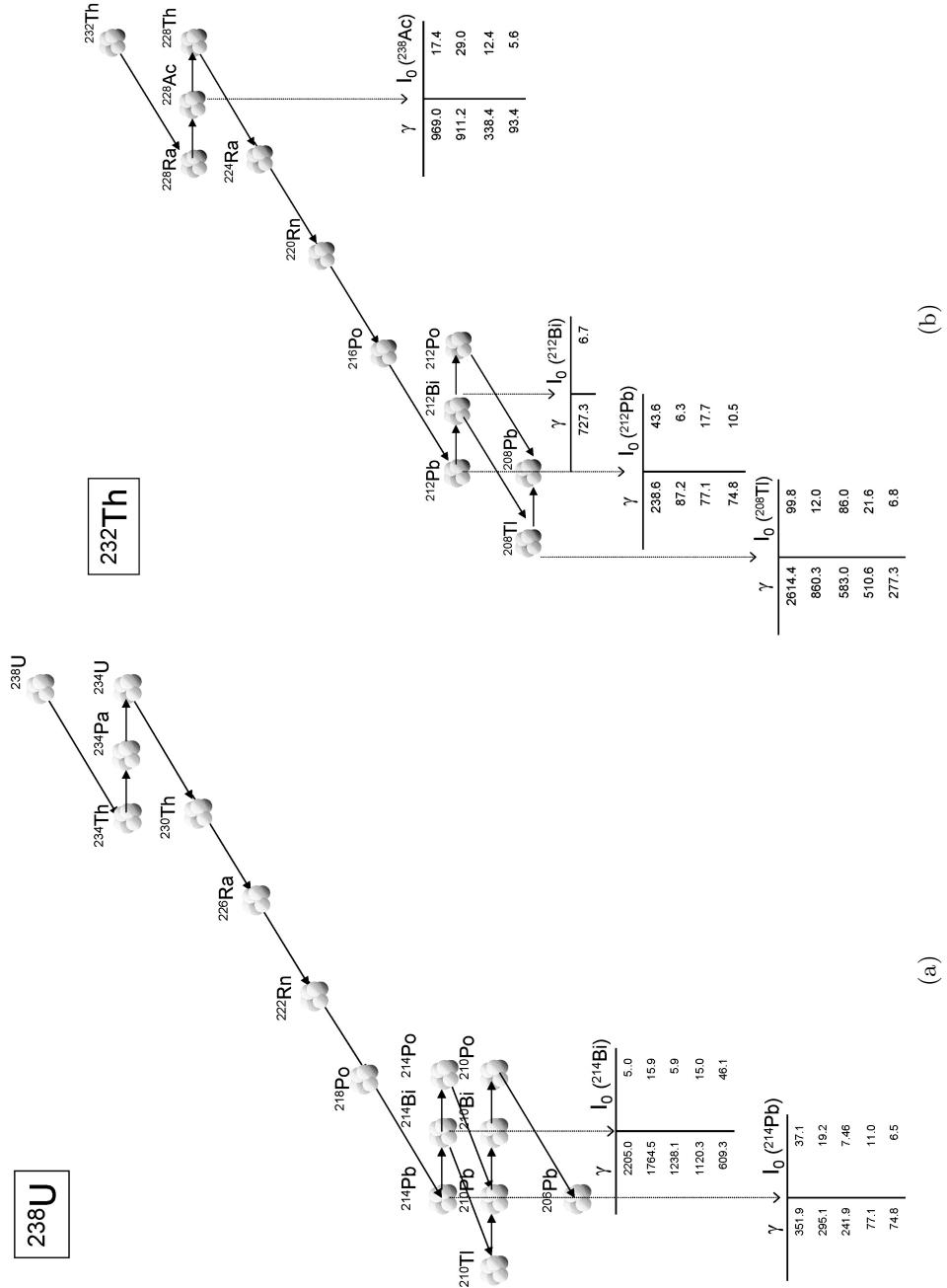
Figure 6.1: ^{238}U (a) and ^{232}Th (b) decay chains with daughter nuclei. The horizontal axis is proton number Z while the vertical axis is atomic mass A. Right arrows ($\rightarrow$) indicate β decays and downward-slanted arrows ($\swarrow$) indicate α emission. The highest intensity γ's from the prominent γ emitting isotopes are indicated by intensities and energy in keV. Figures from [290].

common contamination unit is $\mathrm{mBq\,kg^{-1}}$. The yield thus includes the density of the material and a conversion to days/years.

The presence of ^{238}U and ^{232}Th is particularly dangerous for CDMS since they are also sources of neutrons. There are two n-production mechanisms which occur, spontaneous fission (SF) and (α, n). Briefly reviewing the nuclear physics behind these reactions is helpful to understand how these sources are used in simulation and in the calculation of their yields. The chain progenitors can undergo spontaneous fission (SF). The immediate products of SF are unstable and decay by emitting γ's and n's. This is most prevalent for ^{238}U, where the branching fraction of SF is 5.45×10^{-7} [290], but has also been observed in ^{232}Th with a branching fraction of $\sim 1.2 \times 10^{-11}$ [291]. ^{230}Th and ^{234}U, daughters of ^{238}U, can also undergo SF at low probability. The energies of the SF products do not depend upon the surrounding (matrix) material.

The (α, n) reaction occurs when energetic α's created throughout the decay chains interact with the matrix material. The energies of the possible α's per decay chain are given in Table 6.1. The Q-values needed to undergo (α, n) reactions in CDMS shield components are given in Table 6.2. The primary (α, n) reactions occur within copper and carbon while no α has the energy to initiate the reaction in lead. Since the energies of the decay α's differ between the chains, and the Q-values between materials, the energy of the resulting n's varies between chains and materials.

The probabilities for the n-creating reactions are small such that numerous decays be needed to simulate sufficient n statistics. It is more efficient to simulate individual n's, with the appropriate energies, and use the yield to scale to physical units. The initial-n energy spectra and yields are calculated via simulation with the SOURCES4C package [294, 295]. SOURCES4C simulates the neutron output of each decay chain, accounted for all contributing daughters and processes. Example energy spectra of the resulting n's for SF and (α, n) can be seen in Fig. 6.2. The total yield is taken from these spectra and is given in Table 6.3, where only a conversion to the desired time unit is needed for use in Eq. 6.1.

6.1.2 ^{222}Rn and ^{210}Pb

Isotopes of radon are parts of both the ^{238}U and ^{232}Th decay chains. Since radon is a noble gas, it can diffuse out of the surrounding material and enter the atmosphere.

Isotope	E_α [keV]	Intensitity [%]
^{238}U	4198.0	79.00
	4151.0	21.00
^{234}U	4774.6	71.38
	4722.4	28.42
^{230}Th	4687.0	76.30
	4620.5	23.40
^{226}Ra	4784.3	93.84
	4601.0	6.16
^{222}Rn	5489.5	99.92
^{218}Po	6002.4	99.98
^{214}Po	8686.8	99.99
^{210}Po	5304.3	100.00

(a) ^{238}U Decay Chain

Isotope	E_α [keV]	Intensitity [%]
^{232}Th	4012.3	78.20
	3947.2	21.70
^{228}Th	5423.2	73.40
	5340.4	26.00
^{224}Ra	5685.4	94.92
	5448.6	5.06
^{220}Rn	6288.1	99.89
^{216}Po	6778.3	99.99
^{212}Bi	6050.8	25.13
	6089.9	9.75
^{212}Po	8784.9	100.00

(b) ^{232}Th Decay Chain

Table 6.1: Energies and intensities of α particles created during the ^{238}U (a) and ^{232}Th (b) decay chains. Only decays with intensities $>5\,\%$ are shown. Values from [292].

(a) Spontaneous Fission

(b) (α, n)
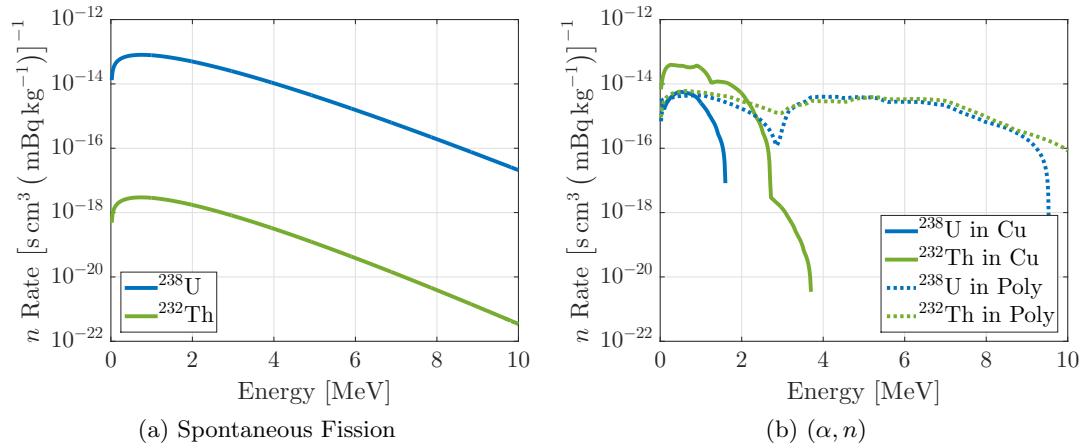
Figure 6.2: Neutron energy spectra resulting from spontaneous fission (a) and (α, n) reactions (b) from the ^{238}U (blue) and ^{232}Th (green) chains in copper (solid) and polyethylene (dot). Units of the rates are neutrons per second per $\mathrm{mBq\,kg^{-1}}$ contamination level per $\mathrm{cm^3}$ of matrix material volume. The spontaneous fission spectra do not depend upon the matrix material while those from (α, n) do.

Isotope	NA [%]	Q-value [keV]
^{63}Cu	69.15	-7501.51
^{65}Cu	30.85	-5823.94
^{204}Pb	1.40	-13610.29
^{205}Pb	Trace	-11946.98
^{206}Pb	24.10	-13065.90
^{207}Pb	22.10	-12145.24
^{208}Pb	52.40	-14962.35
^{210}Pb	Trace	-13721.29
^{1}H	99.98	-23681.00
^{2}H	0.02	-4189.60
^{3}H	Trace	-4783.39
^{12}C	98.90	-8502.01
^{13}C	1.10	2215.61
^{14}C	Trace	-1817.70

Table 6.2: Q-values necessary for the (α, n) reaction to proceed with the naturally occurring isotopes of copper, lead, hydrogen, and carbon. Negative values require that amount of energy to initiate the reaction. For the energies of α's from the primordial decay chains, the reaction occurs with either copper isotope or ^{12}C. No α is energetic enough for the reaction to occur in lead. All values from [293].

Decay Chain	Lead	Polyethylene	Copper
	$\left[\mathrm{s\,cm^3} \left(\mathrm{mBq\,kg^{-1}} \right) \right]^{-1}$		
^{238}U	9.80×10^{-12}	2.10×10^{-12}	1.00×10^{-11}
^{232}Th	3.44×10^{-16}	1.29×10^{-12}	2.33×10^{-12}

Table 6.3: Neutron yields for the primordial decay chains from common experimental materials in units of $\left[\mathrm{s\,cm^3} \left(\mathrm{mBq\,kg^{-1}} \right) \right]^{-1}$: neutrons created per time per volume and contamination level of the source material. The yield for lead is only from SF while those for Polyethylene and Copper are sums of SF and (α, n) processes. Values computed with the SOURCES4C package [294, 295].

^{220}Rn from the ^{232}Th chain has a half-life of 55.6 s [292] and often does not survive to escape the material. ^{222}Rn from the ^{238}U chain, however, has a half-life of 3.82 d [292] and does escape the material in large amounts: the typical contamination level of air in laboratories/dwellings is 40 Bq m^{-3} [288]. Airborne ^{222}Rn can "plate-out", attaching itself to exposed surfaces, and decay. There are thus two effects of the gas: it can break the secular equilibrium of the ^{238}U chain and it creates a source on the surfaces of materials. Radon plate-out on the surfaces of CDMS detectors and housings is particularly problematic.

Although most of the γ and β emitters of the ^{238}U chain occur after ^{222}Rn, almost all of them have short half-lives. These generally short half-lives mean that radon can be removed from air but isolating the gas for several times the half-life of ^{222}Rn, a product called "old-air". Old-air purges are common to reduce radon: CDMS Soudan installed an old-air purge in 2003 as described in Sec. 5.1.3.

^{210}Pb is the most worrisome isotope created by radon sources with a half-life of 22 yr. Once ^{210}Pb is attached to a surface, it will not significantly decrease over the life-span of an experiment. ^{210}Pb is also found in trace amounts in natural lead. This is the motivation for the CDMS ancient-lead layer interior to the standard lead. The inner lead shields the ^{210}Pb products from the normal lead while generating significantly fewer products itself. The decay chain following ^{210}Pb is detailed in Fig. 6.3. The α from ^{210}Po cannot create neutrons, which means the most worrisome product is the β from ^{210}Bi with an endpoint of 1.161 MeV. This β can create substantial bremsstrahlung and characteristic x rays in the surrounding material. For sources on detector surfaces, all non-γ products from the chain are important. The α and the recoiling nuclei, such as the final ^{206}Pb nuclei, will have reduced yield and appear similar to germanium NRs. Additionally, the low-energy β's appear as surface events. When simulating ^{222}Rn and ^{210}Pb sources, the decays are directly simulated and the yields are the same as for other γ and β sources as described above.[3]

---

[3] To use Eq. 6.1 for surfaces sources, the volume must be replaced by the surface area and the units of contamination similarly changed.
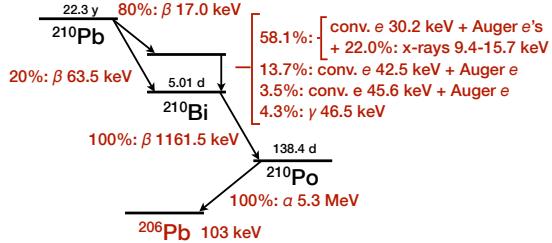
Figure 6.3: Decay chain for ^{210}Pb and its daughters. Figure from [246].

6.1.3 Cosmogenic and Anthropogenic

Non-primordial radiogenic sources are produced in two manners and generally have half-lives of $\mathcal{O}(\text{yr})$.[4] For all of these sources, the decays can be simulated directly, and the yields in Eq. 6.1 are the same as other γ and β sources.

The first production method is anthropogenic (man-made). The most important anthropogenic isotope is ^{137}Cs, with has a half-life of 30.1 yr. ^{137}Cs is a common fission product of ^{235}U, which is used in nuclear weapons and reactors. ^{137}Cs is water soluble, spreads easily, and is found in different materials. It decays via β emission which is accompanied by a 661 keV γ $\sim$95 % of the time.

The second production method is cosmogenic. These sources are created when incident cosmic rays initiate nuclear reactions on naturally present isotopes in the atmosphere or Earth. Many different cosmogenic isotopes are possible (see, e.g. [290]), and only a few which are important to CDMS are discussed here. In particular, the isotopes can be present in the silicon and germanium detector crystals and the surrounded copper.

Silicon detectors can contain ^{3}H and ^{32}Si which β decay with endpoints of 18.6 and 227.2 keV respectively. ^{3}H is a spallation product in the crystal itself while ^{32}Si is created in the atmosphere, migrates through water sources, and becomes present in natural silicon at low levels. Germanium detectors can also contain ^{3}H in addition to numerous isotopes which decay by electron capture and give discrete lines below $\sim$10 keV. Several contaminants are possible in copper with the most important being the semi-long-lived ^{60}Co. It decays with a relatively low-energy β which is almost always followed by two high-energy γ's with 1173 and 1333 keV of energy. All potential

---

[4] All decay information in this section is taken from [292].

Material	Isotope	Half-life	Material	Isotope	Half-life
Germanium	^{3}H	12.32 yr	Silicon	^{3}H	12.32 yr
	^{68}Ge	270.95 d		^{32}Si	153 yr
	^{68}Ga	67.71 min	Copper	^{46}Sc	3.891 hr
	^{65}Zn	243.93 d		^{48}V	15.9735 d
	^{73}As	80.30 d		^{54}Mn	312.20 d
	^{57}Co	271.74 d		^{56}Co	77.236 d
	^{55}Fe	2.744 yr		^{57}Co	271.74 d
	^{54}Mn	312.20 d		^{58}Co	70.86 d
	^{49}V	330 d		^{59}Fe	44.495 d
				^{60}Co	1925.28 d

Table 6.4: Potential cosmogenic contamination sources in silicon, germanium, and copper.

cosmogenic contaminants for the three materials are listed, along with their half-lives, in Table 6.4.

6.2   Geant4 Monte Carlo Simulation

The rate of NRSSs, or any of the other types of events, from an individual source in Eq. 6.1 is determined using the GEANT4 particle simulation toolkit [296, 297]. In GEANT4, the user constructs a geometry consisting of the shape, size, location, and material nature of physical components. Particles are then simulated, where the type, energy, source, etc. are specified by the user. GEANT4 uses a library of physics processes and random-number generation to determine a track for the particle and any additionally created particles during the process. Any part of the geometry may be made "sensitive" such that any particle interactions, including energy depositions, occurring in that volume are recorded for off-line analysis.

Some necessary GEANT4 vocabulary is defined:

- **Event:** An event is the highest level category in GEANT4. An event is created when the user specifies the creation of an initial particle (called the "primary") and all interactions of the primary and any subsequently created particles (called

"secondaries") are grouped under the same event. NRSSs etc. are counted per event, where for γ and β sources, an event is a single decay, while for n sources, an event is a single neutron.

- **Step:** A step is the process used to take a particle from one state to another. What those states are, and how the change occurs, depends upon the physics processes loaded into the simulation. The most common step is to transport the particle some distance between interactions. This involves randomly selecting a direction to travel (based upon any angular dependencies of the previous interaction), how far to transport the particle (based upon the mean-free-path in the surrounding material), and what type of interaction occurs at the end (based upon the physics of the given particle and the surrounding medium). Particle decays, absorptions, scattering, etc. all occur in steps, along with the deposition of energy into the surrounding material.

- **Track:** Particles move along tracks as they traverse and interact with the detector. A track is composed of many individual steps.

- **Sensitive Volume:** When a volume is coded to be sensitive, any particle steps which occur in the volume are stored and can be recorded to external files.

- **Hit:** Each record of a particle interaction, such as depositing energy, which occurs in a sensitive volume is termed a hit. Each hit, or a combination of them, are then recorded.

- **Physics List:** A file designating which physics processes, and their corresponding models, are to be considered in a given simulation. Processes can be turned on/off depending upon the energy range of interest or computing time available. For low energy processes, as would be of interest for dark matter experiments, the commonly used list is called "shielding". This list contains all of the standard electromagnetic processes and low-energy neutron processes which are not typically included for high-energy experiments.

The Soudan- and SNOLAB-related background estimates described in the following two chapters each use specific GEANT4 geometries that are described as needed.

For these simulations, the simulation output requires some processing to better match physical data. The real detectors cannot resolve the timing of individual hits, thus in the simulation the deposited energy for all hits in a given detector for a single event are summed into a single recoil energy. The recoil is classified as an ER or NR based upon the relative amount of energy deposited through electromagnetic E_{EM} and nuclear $E_{\mathrm{Nuc.}}$ processes. A recoil is declared an ER if

$$E_{\mathrm{EM}} > 0.05 E_{\mathrm{Nuc.}}, \tag{6.2}$$

and an NR otherwise. A single scatter is defined as an event in which only one detector has total recoil energy above 2 keV, and all other events are labeled as multiple scatters.

Chapter 7

CDMS Soudan Background Estimates

The radiogenic neutron background for the SuperCDMS Soudan LT and CDMS II c58R WIMP-search analyses are estimated using GEANT4 simulations in two steps: a global gamma simulation to determine shielding contamination values (Sec. 7.1) and several global neutron simulations to determine the NRSS yield (Sec. 7.2). The two are combined for the final NRSS background numbers.

These simulations use the CDMS Soudan geometry as depicted in Fig. 7.1. The detector payload shown in the figure is that from CDMS II, which is changed to that of SuperCDMS Soudan when appropriate. Shield layers are modeled as single monolithic cans instead of the stacks of smaller pieces which were actually present. The detector electronics are not included, while simplified copper tower components are included.

7.1   CDMS II: Global Gamma Monte Carlo

Gamma spectroscopy is a technique where the type and strength of radioactive sources are determined by studying the energy spectrum, in some nearby detector, created by the γ and β decays from the sources [298]. Fully collected γ's appear as peaks in the energy spectrum on top of a mostly-smooth continuum created by β decays and non-fully collected γ's. These peaks are direct indicators of what radioisotopes are present and their relative strength compared to the continuum can indicate the source's
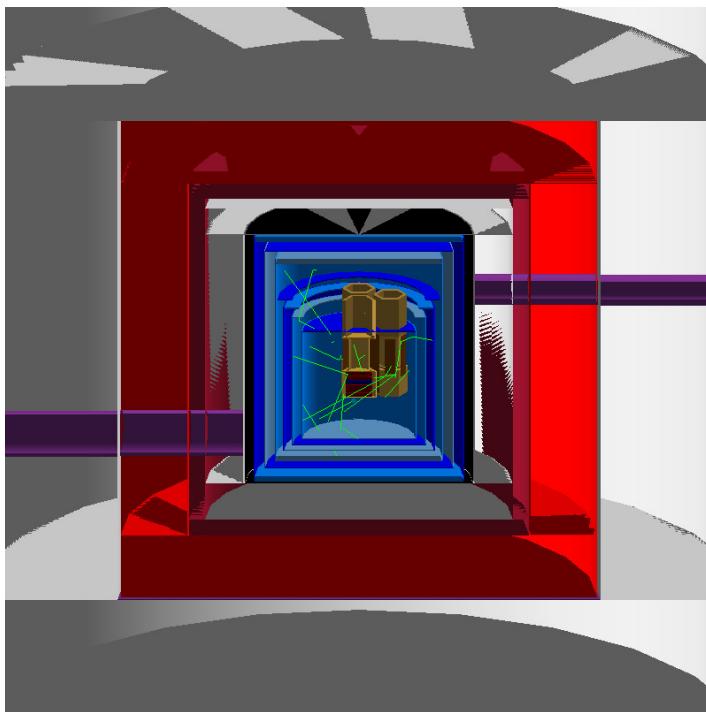
Figure 7.1: Cross-sectional view of the CDMS II geometry simulated in GEANT4. The layers of the shielding are: outer poly (outer gray), outer lead (bright red), inner lead (dark red), inner poly (inner gray), mu metal (black), and cryostat cans (varied blue). Tan and brown tower components are copper. Ge oZIPs are dark red and Si oZIPs are blue. Simplified copper stems penetrate the outer shielding (purple). Simulated γ's from the base can are shown (green lines), some of which hit the ZIPs (blue circles).

location with respect to the detector. Gamma spectroscopy is used in two different ways by CDMS. One approach is to consider the electron-recoil spectrum from low-background data taken with the Soudan experiments. The analysis of this spectrum gives an *in situ* measurement of the Soudan shield's contamination levels and is useful for current Soudan analyses (see below). The second approach uses a separate, dedicated, detector to study the contamination levels of materials under consideration for use in the SuperCDMS SNOLAB experiment (next chapter).

For this thesis, a global gamma Monte Carlo simulation and fit was performed using the reprocessed data from CDMS II Run 125. The premise for a global gamma simulation is to simulate the common radioactive decays in different geometric components of the experimental apparatus (importantly the cryostat, shield, and detector towers) and then fit a combined spectrum to the measured electron recoil spectrum. The combined spectrum is a weighted sum of all the individual spectra, where the weights are free parameters. If there are N decay-geometry combinations (hereafter called "sources") simulated, the fit is N-dimensional over the sources' weights and the best-fit weights

are a measure of the sources' physical contamination levels. This study is described in four steps: selection of physical data, generation of simulated data, execution of the fit, and examination of the results.

7.1.1   Data Selection

This study was one component of the c58R reanalysis campaign to provide updated and better fits compared to previous studies with earlier CDMS II data [280]. In addition to having a larger exposure than the previously used data, some of the shorter-lived isotopes may have substantially decayed away since the first Soudan runs. This fit should be more accurate for use with later CDMS II and SuperCDMS Soudan analyses.

The data used is the total charge energy (sum of inner and outer charge channels) from the reprocessing of Run 125. Only one of the four runs is used because many of the quality cuts applied to the data are tuned individually for each run and these cuts must be also be applied to the simulated data: having a single set of cut values is convenient. Run 125 was the longest individual run, had the highest number of functioning detectors (14 Ge oZIPs), and accounted for $\sim$60 % of the total c58R exposure.

Events are chosen based upon the following criteria: they were in a functioning Ge detector, not electronic glitches, not coincident with the muon veto or NuMI beam, not random triggers, of general good pulse-shape quality, in the ER band, above a charge threshold, and sufficiently within the inner channel (i.e. energy in outer channel is consistent with noise).[1] An energy threshold is applied to the spectrum, only events which deposited $\geq$10 keV in the array are kept, which avoids low energy background sources not simulated for this study. The final data are shown in Fig. 7.2, where the energy in all detectors is summed for each event (a procedure called "co-adding") in order to better reconstruct the high-energy portion of the spectrum. Numerous peaks, with common ones labeled, are on top of a smooth continuum. The data is also presented co-added by tower, instead of by array, for towers 1 and 5. Variation is seen between the towers, in particular with stronger peaks seen in towers 4 and 5 and weaker peaks seen in towers 1 and 2. This is related to the number of usable detectors in each tower but also could be an indication of non-isotropic sources.

---

[1] Each of these cuts were developed previously by others for either the c58 or c58R analyses, seeRefs. [281, 285, 299–301].
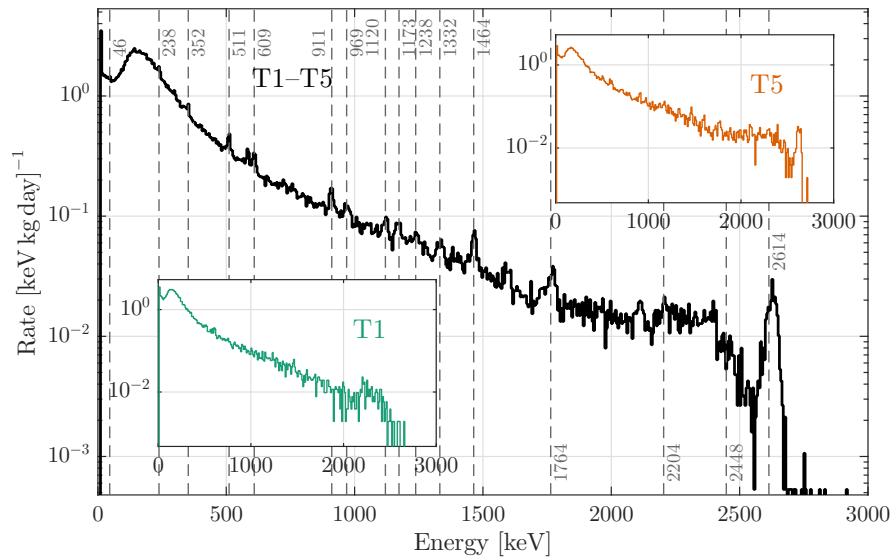
Figure 7.2: Run 125 charge-energy electron-recoil spectrum, co-added across all functioning germanium detectors (main) and within tower 1 (lower left) and tower 5 (upper right). Tower 5 has more prominent lines above the continuum than tower 1, particularly the 2614 keV line from ^{208}Tl, potentially indicating position dependence of the sources. Common decay lines are marked by vertical dash lines with location labels in keV.

7.1.2   Gamma Simulation

To match the data spectrum, common radioactive contaminants are simulated from components of the apparatus which are expected to be contaminated. The decays simulated include the primary γ and β emitters from the ^{238}U and ^{232}Th chains, ^{40}K, and ^{60}Co. The geometrical sources are the inner and outer lead layers, the inner polyethylene, the six copper cryostat cans, and the copper components of the towers and detector housings. For each of these sources, the decays are simulated uniformly throughout the volume. Two surface sources are also included: the outside surface of the outermost cryostat can (OVC can) and the inner surface of the innermost cryostat can (base can). The number of decays for each source in the simulation are given in Table 7.1. Secular equilibrium is assumed for the long chains, meaning the number of primaries simulated match the ratio of decays (1:1 for all except ^{208}Tl, which has a branching fraction of 35.94 %). The low-chain isotopes of the ^{238}U chain have 10× the statistics due to their low-energy products. The cryostat is assumed to have the same contamination between all layers, and the ratio of decays matches the ratio of volumes of the cans.

Three steps of processing are performed on the simulated data before it is compared to the physical data. The first groups similar sources to reduce the number of free parameters in the fit. Sources are first grouped by decay chain, grouping ^{228}Ac, ^{212}Pb, ^{212}Bi, and ^{208}Tl as a single ^{232}Th for each geometry, and similarly for ^{214}Pb, ^{214}Bi, ^{210}Pb, and ^{210}Bi as ^{238}U.[2] A separate chain for ^{222}Rn is made on the outer surface using ^{210}Pb and ^{210}Bi. The second grouping occurs by combining all six cryostat cans into a single source, which is allowed since the same contamination level is assumed throughout. After these groupings, the number of sources reduces from 160 to a more reasonable 43.

The second processing step accounts for the difference in energy resolution between the simulated and physical data: the simulation has perfect resolution while the physical detectors do not (nor do they each have the same resolution). Energy-dependent fits of the resolution were previously performed by D. Moore [302] for 9 of the 14 detectors.

---

[2] The factor of 10 difference in simulated statistics between the upper and lower portions of the ^{238}U chain is accounted for in this combination.

Decay	Outer Lead	Inner Lead	Inner Poly	Outer Surface	OVC Can	Liquid N Can	IVC Can	Still Can	Cold Can	Base Can	Inner Surface	T1–T5
^{228}Ac	1.0E11	1.0E9	1.0E8	1.0E8	1.0E7	5.0E6	5.0E6	2.0E6	2.0E6	1.0E6	1.0E6	1.0E6
^{212}Pb	1.0E11	1.0E9	1.0E8	1.0E8	1.0E7	5.0E6	5.0E6	2.0E6	2.0E6	1.0E6	1.0E6	1.0E6
^{212}Bi	1.0E11	1.0E9	1.0E8	1.0E8	1.0E7	5.0E6	5.0E6	2.0E6	2.0E6	1.0E6	1.0E6	1.0E6
^{208}Tl	3.6E10	3.6E8	3.6E7	3.6E7	3.6E6	1.8E5	1.8E5	7.2E5	7.2E5	3.6E5	3.6E5	3.6E5
^{214}Pb	1.0E11	1.0E9	1.0E8	1.0E8	1.0E7	5.0E6	5.0E6	2.0E6	2.0E6	1.0E6	1.0E6	1.0E6
^{214}Bi	1.0E11	1.0E9	1.0E8	1.0E8	1.0E7	5.0E6	5.0E6	2.0E6	2.0E6	1.0E6	1.0E6	1.0E6
^{210}Pb	1.0E12	1.0E10	1.0E9	1.0E9	1.0E8	5.0E7	5.0E7	2.0E7	2.0E7	1.0E7	1.0E7	1.0E7
^{210}Bi	1.0E12	1.0E10	1.0E9	1.0E9	1.0E8	5.0E7	5.0E7	2.0E7	2.0E7	1.0E7	1.0E7	1.0E7
^{60}Co	1.0E11	-	-	1.0E8	1.0E7	5.0E6	5.0E6	2.0E6	2.0E6	1.0E6	1.0E6	1.0E6
^{40}K	1.0E12	1.0E10	1.0E9	1.0E9	1.0E8	5.0E7	5.0E7	2.0E7	2.0E7	1.0E7	1.0E7	1.0E7

Table 7.1: Number of simulated decays from each decay-geometry source for the global gamma Monte Carlo simulation. The final column gives the number simulated in each of the towers 1–5. A dash (-) indicates the source is not simulated.
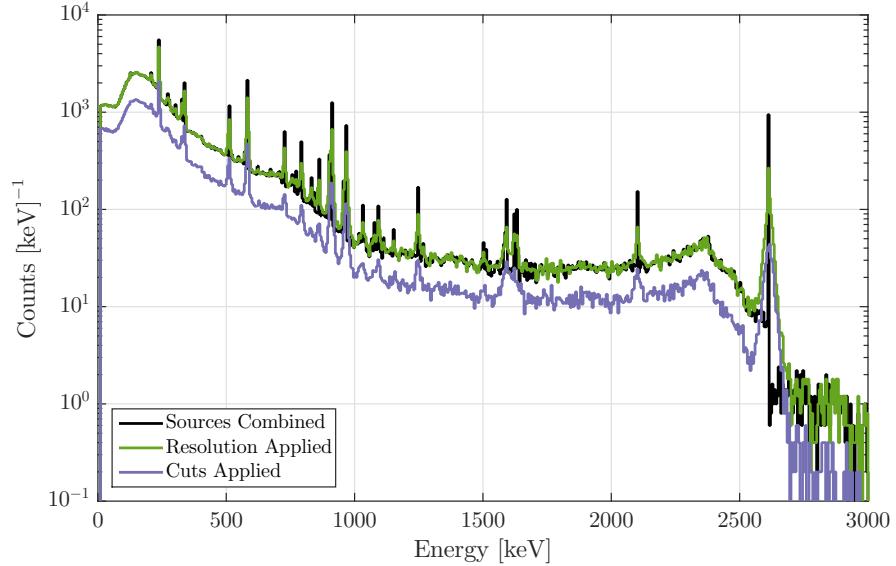
Figure 7.3: Coadded energy spectrum of the simulated ^{232}Th decays in the cryostat cans after sequential processing. The curves give the spectrum after: combining decay chain and cryostat cans sources (black), applying resolution (green), and applying cuts (purple)

His study fit the following model to several measured peak widths

$$\sigma(E) = \sqrt{A_1^2 + A_2^2 E + A_3^2 E^2}, \tag{7.1}$$

where the A_i are the free parameters.[3] The fits found by Moore are used for 7 of the detectors (two of his fits poorly match later data), with appropriate averages of these fits used for the remaining 7. The impact of adding resolution to the simulation is seen in the top two curves of a sample source, ^{232}Th from the cryostat, shown in Fig. 7.3.

The third processing step is to apply the same cuts as the physical data to the simulated data. In particular, a threshold cut on the inner channel and a radial fiducial volume cut on the outer channel are applied. In order to apply these cuts, some measure of charge propagation must be considered. This is implemented using the simulated charge-collection maps shown in Fig. 7.4. These maps were created by S. Hertell [303] and indicate, for a given radius and height of an interaction, what percentage of the

---

[3] The physical motivation behind such a model is discussed in Sec. 12.2.
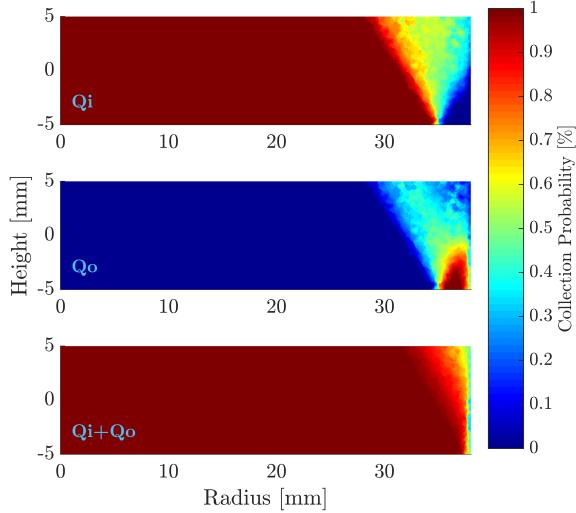
Figure 7.4: Map showing the percentage of energy collected by the inner (top) and outer (middle) charge electrodes for an energy deposition at a given location in a Ge oZIP detector. The sum of the two maps is also given (bottom), showing a high-radius region with $<100\,\%$ collection.

deposited energy is collected by the inner and outer charge channels respectively. The sum of the two is also given, showing how there is a region with incomplete charge collection at high radius. Applying these maps to each simulated energy deposition returns energy quantities for each channel which better match the physical reality. The inner threshold and outer fiducial volume cuts as defined for the physical data are then directly applied to the simulated data. The final simulated spectrum for the sample source, after applying these cuts, is shown by the bottom curve in Fig. 7.3.

7.1.3 Fitting Results

A χ^2-minimization fit is performed between a weighted sum of the 43 sources and the physical data. The weighting is done by binning the spectra in 5 keV bins (the size of bin has little effect on the final fit) and summing the simulation outputs in each bin as

$$\mathrm{MC}_j^{\mathrm{tot}} = \sum_i^{43} \mathrm{MC}_{ij} w_i, \tag{7.2}$$

where MC_{ij} is the number of counts in the jth bin from the ith source and w_i is the weight of that source. The χ^2 quantity is defined between $\mathrm{MC}_j^{\mathrm{tot}}$ and the physical data

in each bin x_j as

$$\chi^2 = \sum_j \frac{\left(\text{MC}_j^{\text{tot}} - x_j\right)^2}{x_j}.$$

(7.3)

The χ^2 is minimized with respect to the w_i to find the best-fit combination of simulated sources to the data.

Some specifics of the fit are: (1) In an attempt to accommodate some position dependence, the fit is performed by simultaneously fitting each of the five towers' coadded spectra. (2) Bounds are placed on the fitting weights. All weights are bounded to be positive, as negative weights are unphysical. The contamination levels of the inner poly and lead layers have been estimated from previous screening measurements and the $\mu + 1\sigma$ level of the measurements are used as upper bounds on the weights for those sources. (3) The effect of the surface sources is tested by performing the fit with and without the inner and outer surfaces. The only surface source included in both is the ^{222}Rn source, which is generally expected. The fitting results are near-identical between the two fits, with the surface sources fit to effectively zero in the full fit: $\chi^2 = 2.1592$ with surfaces and $\chi^2 = 2.1587$ without. Since simulating the proper neutron spectra from surface sources is difficult (see Sec. 7.2), the fit without the surfaces is used as the official result. (4) The physical spectra contain a peak at $\sim$10 keV, which is not included in the simulation: the lowest energy bin (10–15 keV) is not included in the χ^2 sum.

The best-fit results are shown in Fig. 7.5, where the best-fit summed simulated spectra are compared to the measured data on each tower, i.e. in the planes where the fit is performed. As a check, the same best-fit weights are applied to the total coadded spectrum and compared to the data in Fig. 7.6. The contribution to the summed simulation from each of the sources, grouped by geometrical location, are also shown in Fig. 7.6. Lastly, the contamination values corresponding to the best-fit weights for each source are given in Table 7.2.

7.1.4 Discussion

The number of sources fit to zero is unexpected, especially for the copper cans and towers. Previous fits performed with earlier Soudan data (Run 123 [304]) gave values
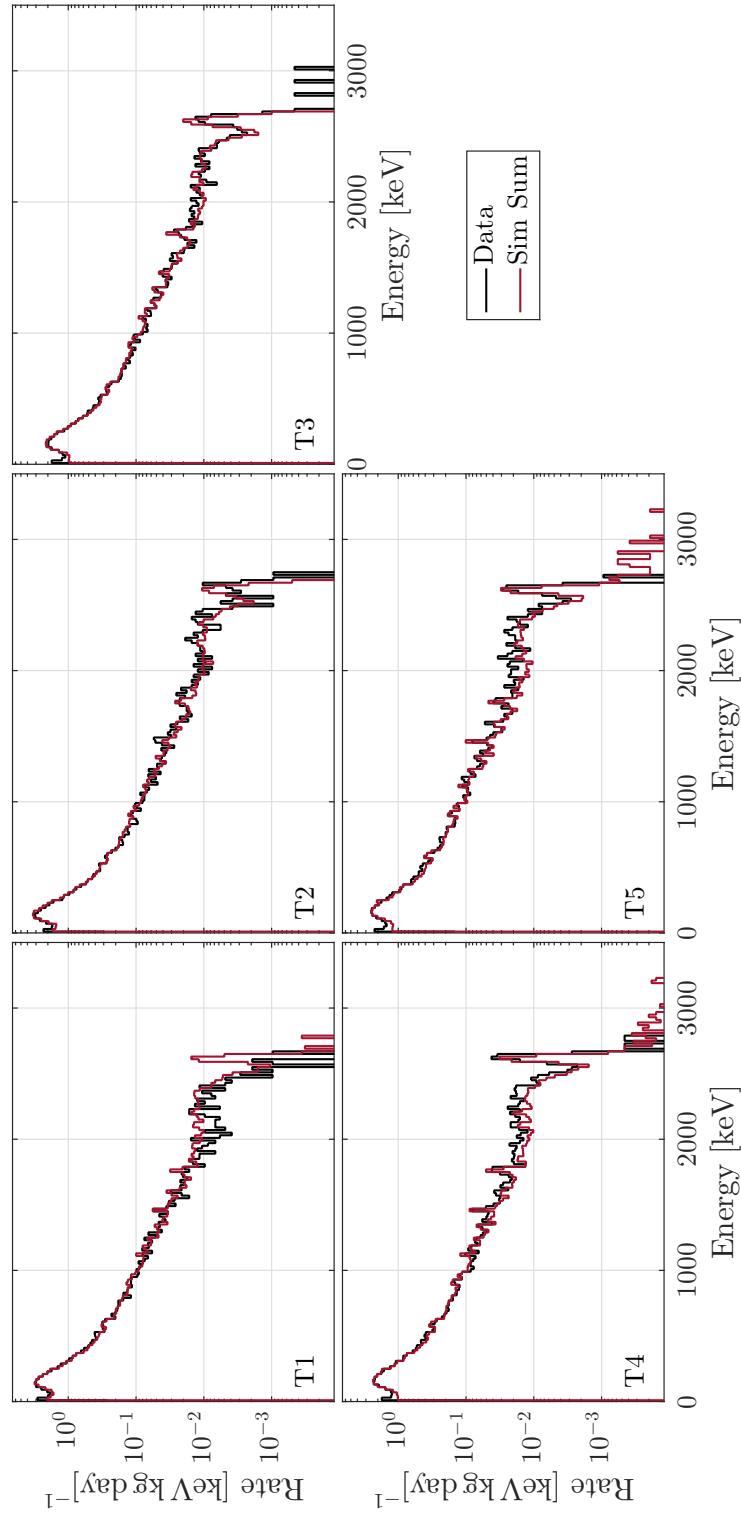
Figure 7.5: Run 125 charge-energy spectrum coadded within each of the five towers (black) compared to the summed simulation spectra in those towers (red). The fit is performed by simultaneously matching all towers; this given fit does not include surface sources (except for ^{222}Rn). The fit visually matches the data well, with the main exception being the lack of a 2.6 MeV peak in the T1 data.
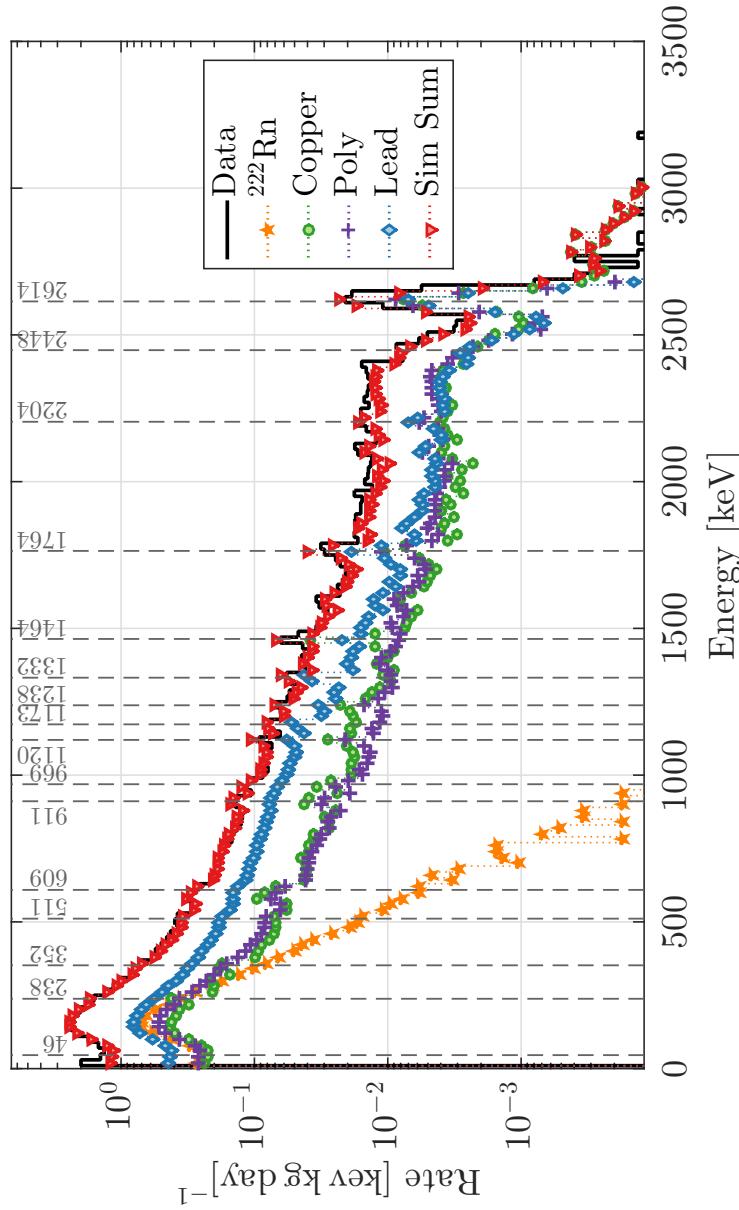
Figure 7.6: Run 125 charge-energy spectrum coadded over all detectors (black) compared to the summed simulated spectrum (red downward triangles). The weights are those found from fitting all towers without surface sources (except ^{222}Rn). The contribution to the summed simulation spectrum from different geometrical sources (summed over decay sources) are also given: ^{222}Rn on the outer surface (orange stars), all copper components (green circles), inner poly (purple cross), all lead sources (blue diamonds). Common decay lines are indicated by vertical dash lines with energy labels in keV.

Decay	Outer Lead	Inner Lead	Inner Poly	Outer Surface	Cans	Inner Surface	Tower 1	Tower 2	Tower 3	Tower 4	Tower 5
^{232}Th	6.9E−3	2.0E+0	4.2E+0	-	0.0E+0	-	1.8E+0	0.0E+0	0.0E+0	1.7E+0	6.9E+0
^{238}U	1.8E−4	5.9E+0	4.1E+0	-	0.0E+0	-	1.9E+0	0.0E+0	0.0E+0	1.6E+0	5.9E+0
^{40}K	1.6E+1	4.6E+0	9.7E−4	-	0.0E+0	-	5.3E+0	0.0E+0	0.0E+0	1.1E+1	2.6E+1
^{60}Co	4.3E+1	-	-	-	0.0E+0	-	0.0E+0	0.0E+0	0.0E+0	0.0E+0	6.1E−2
^{222}Rn	-	-	-	7.4E+1	-	-	-	-	-	-	-
^{232}Th	6.9E−3	1.4E+0	3.2E+0	1.6E−2	0.0E+0	0.0E+0	1.7E+0	0.0E+0	0.0E+0	1.5E+0	6.7E+0
^{238}U	1.8E−4	5.9E+0	4.1E+0	0.0E+0	0.0E+0	0.0E+0	2.0E+0	0.0E+0	0.0E+0	1.6E+0	6.0E+0
^{40}K	1.6E+1	4.1E+0	9.7E−4	0.0E+0	0.0E+0	0.0E+0	5.8E+0	0.0E+0	0.0E+0	1.8E+1	2.6E+1
^{60}Co	4.1E+1	-	-	0.0E+0	0.0E+0	-	0.0E+0	0.0E+0	0.0E+0	0.0E+0	6.1E−2
^{222}Rn	-	-	-	7.4E+1	-	-	-	-	-	-	-

Table 7.2: Contamination values corresponding to the best-fit weights of the global gamma simulation for the fits with (bottom) and without (top) surfaces. Units are $mBq\,kg^{-1}$ for bulk sources and are $mBq\,cm^{-2}$ for surface sources. Entries given by a dash (-) are sources not included in the fit, while those given by zero are set to zero by the fit. The χ^2 values for the two fits are near-identical: $\chi^2 = 2.1587$ without surfaces and $\chi^2 = 2.1592$ with surfaces.

of $\sim$2 mBq kg^{-1} for ^{238}U and ^{232}Th in the cryostat, however that fit did not include either of lead shields and overall yielded a poorer fit. The values found for the outer lead shield are also unexpected, both the low values of ^{232}Th/^{238}U and the high value of ^{60}Co. There is likely degeneracy between the cryostat cans and the lead shield, which should ideally have been broken by the comparison of peak height above the continuum from the source (closer sources have higher peak-to-continuum values). There could additionally be a source of radiation which is not included in the simulations. These concerns are summarized by stating that there is a systematic uncertainty on these results.

Additionally, although the true values of the contaminants are interesting on their own, these results can be considered as secondary to the final NRSS rates (the contamination is only a single component of Eqs. 6.1). The fit is deemed good enough for this main purpose, as long as a systematic uncertainty is estimated on the final NRSS values. This systematic is estimated by refitting the spectra with various priors placed on the fit which impose more physical values on sources. Examples of these priors are: lower bounds of 1 mBq kg^{-1} in all copper sources, removing or placing an upper bound on ^{60}Co from the outer lead, removing all bounds. In computing the NRSS backgrounds in the next section, this systematic is found to be $\mathcal{O}(10\,\%)$.

This fit is published alongside the c58R Ge analysis in [224], however information learned since then provides insight on the final result and decisions made. After the decommissioning of SuperCDMS Soudan, pieces of the lead shields and the inner poly were more accurately measured using a high-purity Ge detector (see Sec. 8.1 and Table 8.2, in particular) giving values of ^{232}Th/^{238}U/^{40}K/^{60}Co for each of: outer lead — $0.24 \pm 0.44/1.12 \pm 0.44/{<}1.07/{<}0.05$ mBq kg^{-1}, inner lead — $0.72 \pm 0.48/0.56 \pm 0.41/1.53 \pm 0.62/{<}0.07$ mBq kg^{-1}, inner poly — $1.51 \pm 0.51/0.59 \pm 0.39/1.87 \pm 1.17/{<}0.13$ mBq kg^{-1}. It is evident that the fit could not break the degeneracy between the two lead shields. The ^{60}Co in the lead is also evidently unphysical, with a more probable source being the cans (which is where the simulation prefers if the lead is disallowed).

A more recent global gamma has been performed by E. Lopez using SuperCDMS data [149]. In that study a gradient in ER rate is observed within a tower stack, with the rate decreasing the further up in the stack a detector is. This indicates a non-isotropic source, such as dust which settled on the bottom on a cryostat can, and his fits prefer

that source when it is included. Such a source was also probably present in the CDMS II data, and could account for the afore-identified systematic in the CDMS II study.

7.2 Radiogenic Background Estimates

The radiogenic NRSS backgrounds expected for the c58R (high-threshold (HT) and mid-threshold (MT) analyses for Ge and Si) and SuperCDMS LT analyses are estimated by summing Eq. 6.1 for each neutron source and then applying the exposures and efficiencies for each analysis. Using the contamination values found in the CDMS II global gamma study, the remaining unknown in Eq. 6.1 is the NRSS yield, which comes from global neutron simulations.

7.2.1 Global Neutron Simulations

For the global neutron simulations, ^{238}U- and ^{232}Th-chain neutrons are simulated from all geometrical locations used in the global gamma simulation, except the surface sources, as given by Table 7.1. The neutron yields given in Table 6.3 are calculated using SOURCES4C specifically for bulk contamination. The (α, n) process in particular depends on where in the material the contamination is and it is unclear exactly how to simulate a surface source with SOURCES4C. This difficulty is mitigated since the difference in best-fits in the global gamma simulation between including or omitting the surface sources is negligible. The only appreciable surface source is the ^{222}Rn on the outer surface which does not generate neutrons. The final NRSS product of the simulation should be unaffected between using the bulk-only or surface fits and thus the simpler bulk-only fit is used.

A set of simulations are run using the CDMS II and SuperCDMS detector configurations. The number of n primaries generated and the NRSS yield from each source is given in Table 7.3. For the counting of NRSS, the specific detectors and energy range used in each analysis is considered. These ranges are (in keV) — c58R Ge HT: 10–100, c58R Ge MT: 2–20, c58R Si HT: 7–100, c58R Si MT: 2–20, r133 LT: 1.5–10.5. The NRSS yield from each each source is computed by dividing out the contamination of Eq. 6.1. Two general conclusions from these results are: (1) The HT and MT rates for the same detector material are comparable, with the MT higher in some cases. This

(a) c58R Ge

(b) c58R Si
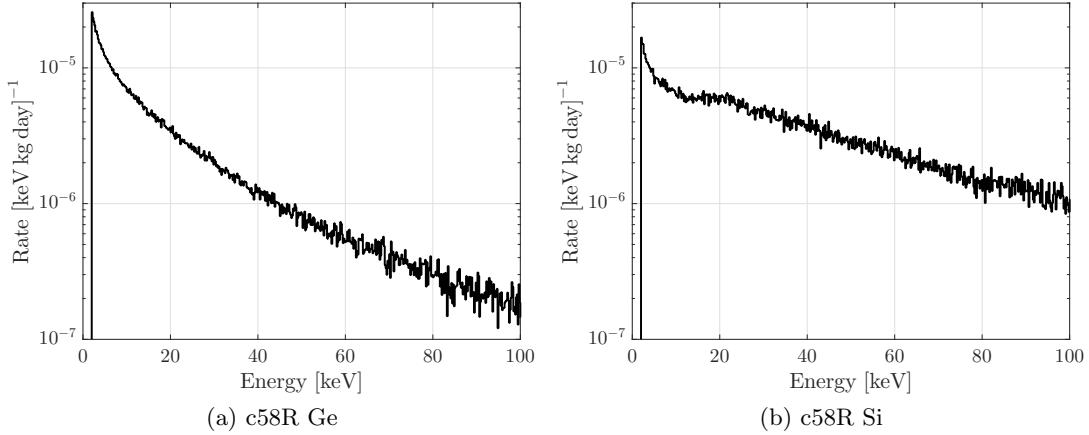
Figure 7.7: Total NRSS rate expected in the c58R Ge (a) and Si (b) detectors due to radiogenic neutron sources. The feature at ~20 keV in the Si spectrum is due to nuclear resonances.

is due to the rising exponential shape of the recoil spectra and the fact that the MT reaches lower energies. (2) The Si rates are higher than the Ge ones for the same source and energy range. This is due to a softer slope of the Si recoil spectrum compared to the Ge one.

The total rate expected in a given analysis is found by summing the individual source rates, weighted by their respective contamination levels found in the global gamma study. The spectra of the total rates in the c58R Ge and Si detectors are shown in Fig. 7.7. The Ge spectrum is a featureless exponential, while the Si spectrum contains a feature at ~20 keV due to nuclear resonances [305]. The integrated rate over the various energy ranges is given in Table 7.4. The uncertainties are statistical, due to the number of NRSS in the simulation, and systematic, based on the systematic associated with the global gamma study. As explained in Sec. 7.1.4, various bounds are placed on the global gamma fitting to determine how much the fit changes. Ten total variations are fit and the total NRSS rate using each of the contamination sets computed. The mean μ and standard deviation σ are computed from this set and the percent uncertainty, σ/μ found. The percent uncertainties for each analysis are — c58R Ge HT:12.32 %, c58R Ge MT: 14.28 %, c58R Si HT: 11.84 %, c58R Si MT: 13.53 %, r133 Ge LT: 9.5 %.

Category	Decay	Outer Lead	Inner Lead	Inner Poly	Cans	Tower 1	Tower 2	Tower 3	Tower 4	Tower 5
Primaries	^{232}Th	5E+8	1E+8	5E+7	1.25E+7	5E+5	5E+5	5E+5	5E+5	5E+5
	^{238}U	5E+8	1E+8	5E+7	1.25E+7	5E+5	5E+5	5E+5	5E+5	5E+5
c58R Ge HT	^{232}Th	3.97E−10	1.77E−10	7.02E−6	7.96E−6	3.05E−6	2.98E−7	3.71E−7	3.67E−7	3.14E−7
	^{238}U	1.21E−5	5.53E−6	1.08E−5	3.35E−5	1.24E−6	1.20E−6	1.49E−6	1.51E−6	1.28E−6
c58R Ge MT	^{232}Th	5.19E−10	2.27E−10	8.56E−6	1.08E−5	3.76E−7	3.67E−7	4.45E−7	4.37E−7	3.86E−7
	^{238}U	1.59E−5	7.05E−6	1.35E−5	3.67E−5	1.24E−6	1.19E−6	1.40E−6	1.40E−6	1.23E−6
c58R Si HT	^{232}Th	9.91E−10	4.49E−10	1.63E−5	2.00E−5	9.37E−7	1.47E−6	7.99E−7	1.18E−6	9.72E−7
	^{238}U	3.02E−5	1.38E−5	2.58E−5	7.70E−5	3.42E−6	5.35E−6	2.96E−6	4.18E−6	3.50E−6
c58R Si MT	^{232}Th	4.65E−10	2.06E−10	7.34E−6	9.13E−6	4.03E−7	6.02E−7	3.23E−7	4.72E−7	4.15E−7
	^{238}U	1.42E−5	6.36E−6	1.18E−5	3.18E−5	1.27E−6	1.89E−6	1.14E−6	1.50E−6	1.33E−6
r133 Ge LT	^{232}Th	3.14E−10	1.45E−10	4.86E−6	1.46E−5	2.64E−7	2.80E−7	1.42E−7	2.85E−7	2.57E−7
	^{238}U	9.50E−5	4.42E−6	7.98E−6	4.93E−5	7.97E−7	8.58E−7	4.59E−7	8.56E−7	7.83E−7

Table 7.3: Results of the global neutron simulations for c58R and r133. Units for "Primaries' rows' are the number of simulation neutrons and units for the analysis rows are NRSS rate $[\text{kg day } (\text{mBq kg}^{-1})]^{-1}$. The sources with the highest rate are the inner poly and cans for ^{238}U. Due to the rising exponential, HT and MT rates are comparable for the same material. Due to the differences in slope of the recoil spectra, the Si rates are higher than Ge in comparable ranges.

Analysis	Total Integrated Rate $[\mathrm{kg\,day}]^{-1}$
c58R Ge HT	$(1.149 \pm 0.004\,(\mathrm{stat}) \pm 0.142\,(\mathrm{sys})) \times 10^{-4}$
c58R Ge MT	$(1.402 \pm 0.004\,(\mathrm{stat}) \pm 0.200\,(\mathrm{sys})) \times 10^{-4}$
c58R Si HT	$(2.979 \pm 0.012\,(\mathrm{stat}) \pm 0.353\,(\mathrm{sys})) \times 10^{-4}$
c58R Si MT	$(1.326 \pm 0.008\,(\mathrm{stat}) \pm 0.179\,(\mathrm{sys})) \times 10^{-4}$
r133 Ge LT	$(8.869 \pm 0.032\,(\mathrm{stat}) \pm 0.845\,(\mathrm{sys})) \times 10^{-5}$

Table 7.4: Total NRSS rates for the c58R and r133 analyses. Statistical uncertainties are Poissonian and systematic uncertainties are due to the uncertainty in contamination values from the global gamma study.

7.2.2   Efficiency Correction

The spectra and results of the previous section give the expected observations if the detectors and analysis had perfect efficiency at detecting neutrons. This is not the case and the spectra must be corrected for the non-perfect efficiency as well as the total exposure of the analyses. The final WIMP-search efficiency and exposure from each of the analyses were provided by the respective analysis groups. The final exposure needed for each calculation is given in Table 7.5. The efficiencies are energy dependent and are convolved with the NRSS spectra. For the c58R analyses, the total efficiency of the entire detector array, weighted by the live time of each detector, was provided: a single convolution is needed for each analysis. The convolved NRSS spectra for these analyses are shown in Fig. 7.8(a), where the three different timing cuts used in the c58R Ge analyses are each shown. For the SuperCDMS LT analysis, the efficiencies were given on a by-detector basis. A convolution is performed for each detector using the same total NRSS spectrum (statistics were poor for individual detectors in the simulation). These convolved spectra are shown in Fig. 7.8(b).

The final results from these studies, the expected background events for the given analyses, is computed by taking the integrated rates from Fig. 7.8 over the appropriate energy range and multiplying by the analyses' exposures. These results are given in Table 7.6. In addition to the integrated rate and background count estimate, the spectrum-averaged neutron efficiency is given. This is the integrated rate after efficiencies compared to the integrated rate before efficiencies (Table 7.4) and is a measure of

Analysis	Exposure [kg day]
c58R Ge	612.17
c58R Si	140.20
r133 iT1Z1	78.87
r133 iT2Z1	81.49
r133 iT2Z2	79.47
r133 iT4Z2	85.78
r133 iT4Z3	82.31
r133 iT5Z2	81.15
r133 iT5Z3	77.87
r133 Total	566.93

Table 7.5: Analysis exposures for the full c58R Ge and Si analyses and for each detector in the r133 LT analysis.

(a) c58R Analyses

(b) SuperCDMS Detectors
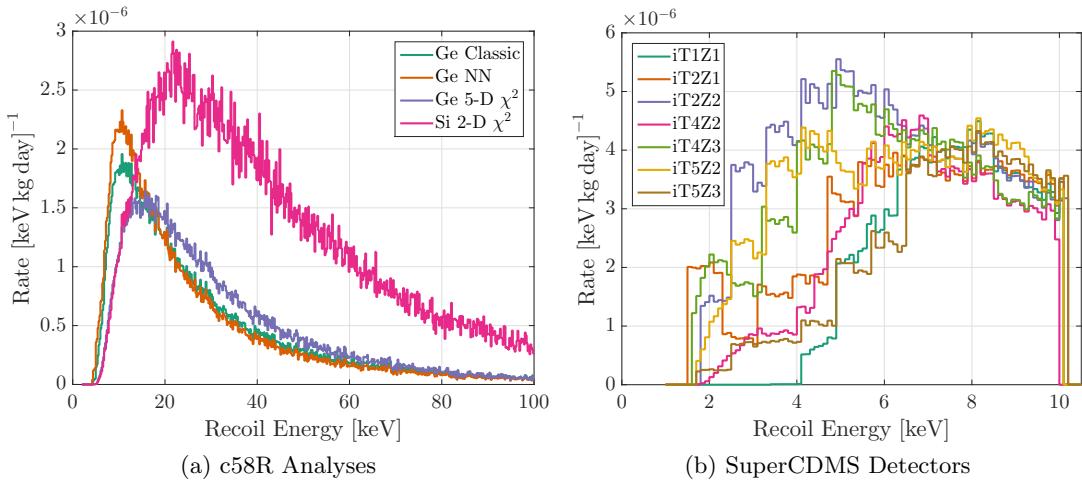
Figure 7.8: NRSS Rate after convolution with analysis efficiencies. Subfigure (a) has the three c58R Ge timing analyses and the c58R Si analysis. The timing cuts were: Ge Classic, Ge Neutral Network (NN), Ge 5-D χ^2, and Si 2-D χ^2. Subfigure (b) has the spectra for individual detectors in the r133 LT analysis. The step-like features in the r133 curves are due to how the boosted-decision tree cut used in that analysis was tuned.

how efficient the analyses are at accepting neutron NRSS. They range from $\sim$15 % to $\sim$40 %. These background numbers are the final values published in [224, 233, 245] for the various analyses.

Analysis	Specification	Integrated Rate $[\text{kg day}]^{-1}$	Total Background [Counts]	Eff.
c58R HT	Ge Classic	$(4.059 \pm 0.014\,(\text{stat}) \pm 0.500\,(\text{sys})) \times 10^{-5}$	$0.0249 \pm 0.0001\,(\text{stat}) \pm 0.0031\,(\text{sys})$	35.33 %
	Ge NN	$(4.005 \pm 0.014\,(\text{stat}) \pm 0.493\,(\text{sys})) \times 10^{-5}$	$0.0245 \pm 0.0001\,(\text{stat}) \pm 0.0030\,(\text{sys})$	34.85 %
	Ge 5-D χ^2	$(4.644 \pm 0.016\,(\text{stat}) \pm 0.572\,(\text{sys})) \times 10^{-5}$	$0.0284 \pm 0.0001\,(\text{stat}) \pm 0.0035\,(\text{sys})$	40.41 %
	Si 2-D χ^2	$(1.135 \pm 0.005\,(\text{stat}) \pm 0.134\,(\text{sys})) \times 10^{-4}$	$0.0159 \pm 0.0001\,(\text{stat}) \pm 0.0019\,(\text{sys})$	38.09 %
c58R MT	Ge Classic	$(2.133 \pm 0.007\,(\text{stat}) \pm 0.305\,(\text{sys})) \times 10^{-5}$	$0.0131 \pm {<}0.0001\,(\text{stat}) \pm 0.0019\,(\text{sys})$	15.21 %
	Ge NN	$(2.421 \pm 0.008\,(\text{stat}) \pm 0.346\,(\text{sys})) \times 10^{-5}$	$0.0148 \pm {<}0.0001\,(\text{stat}) \pm 0.0021\,(\text{sys})$	17.26 %
	Ge 5-D χ^2	$(1.714 \pm 0.005\,(\text{stat}) \pm 0.248\,(\text{sys})) \times 10^{-5}$	$0.0105 \pm {<}0.0001\,(\text{stat}) \pm 0.0015\,(\text{sys})$	12.22 %
	Si 2-D χ^2	$(1.900 \pm 0.012\,(\text{stat}) \pm 0.256\,(\text{sys})) \times 10^{-5}$	$0.0027 \pm {<}0.0001\,(\text{stat}) \pm 0.0004\,(\text{sys})$	14.29 %
SCDMS LT	iT1Z1	$(1.838 \pm 0.007\,(\text{stat}) \pm 0.178\,(\text{sys})) \times 10^{-5}$	$(1.450 \pm 0.005\,(\text{stat}) \pm 0.140\,(\text{sys})) \times 10^{-3}$	20.72 %
	iT2Z1	$(2.424 \pm 0.009\,(\text{stat}) \pm 0.235\,(\text{sys})) \times 10^{-5}$	$(1.975 \pm 0.007\,(\text{stat}) \pm 0.191\,(\text{sys})) \times 10^{-3}$	27.33 %
	iT2Z2	$(3.297 \pm 0.012\,(\text{stat}) \pm 0.319\,(\text{sys})) \times 10^{-5}$	$(2.620 \pm 0.010\,(\text{stat}) \pm 0.254\,(\text{sys})) \times 10^{-3}$	37.17 %
	iT4Z2	$(2.100 \pm 0.008\,(\text{stat}) \pm 0.203\,(\text{sys})) \times 10^{-5}$	$(1.801 \pm 0.007\,(\text{stat}) \pm 0.174\,(\text{sys})) \times 10^{-3}$	23.67 %
	iT4Z3	$(2.938 \pm 0.011\,(\text{stat}) \pm 0.284\,(\text{sys})) \times 10^{-5}$	$(2.418 \pm 0.009\,(\text{stat}) \pm 0.234\,(\text{sys})) \times 10^{-3}$	33.12 %
	iT5Z2	$(2.908 \pm 0.011\,(\text{stat}) \pm 0.282\,(\text{sys})) \times 10^{-5}$	$(2.360 \pm 0.009\,(\text{stat}) \pm 0.228\,(\text{sys})) \times 10^{-3}$	32.79 %
	iT5Z3	$(1.979 \pm 0.007\,(\text{stat}) \pm 0.192\,(\text{sys})) \times 10^{-5}$	$(1.541 \pm 0.006\,(\text{stat}) \pm 0.149\,(\text{sys})) \times 10^{-3}$	22.32 %
	Total	$(2.499 \pm 0.004\,(\text{stat}) \pm 0.093\,(\text{sys})) \times 10^{-5}$	$(1.417 \pm 0.002\,(\text{stat}) \pm 0.053\,(\text{sys})) \times 10^{-2}$	28.17 %

Table 7.6: Final Results of the radiogenic background studies for the c58R and SuperCDMS(SCDMS) LT analyses. The total integrated background rate, total expected background, and spectrum-average neutron efficiency are given. For the c58R analyses, the timing cuts given are: Ge Classic, Ge Neural Net (NN), Ge 5-D χ^2, and Si 2-D χ^2. For the SuperCDMS LT analysis, results are given for individual detectors and the exposure-weighted total.

Chapter 8

SuperCDMS SNOLAB Background Projections

The next stage for the CDMS Collaboration is a larger and more sensitive experiment at SNOLAB in Sudbury, Ontario. The raw materials used in constructing the SuperCDMS SNOLAB experiment must be carefully selected based on their inherent radioactivity to reduce the expected background. A comprehensive material-screening program is used by the collaboration to select the least radioactive materials. The Gopher high-purity germanium detector, located in Soudan, is a vital component of this program and work for this thesis included operating and assisting in the development of sample analysis for the screener. These dedicated contamination-level measurements pair with the *in situ* Soudan measurements using global Monte Carlo simulations (Sec. 7.1). The global simulation efforts were then extended to the background expected for the new experiment at SNOLAB, which will have a new shield. This was the first global background projection for the SuperCDMS SNOLAB experiment.
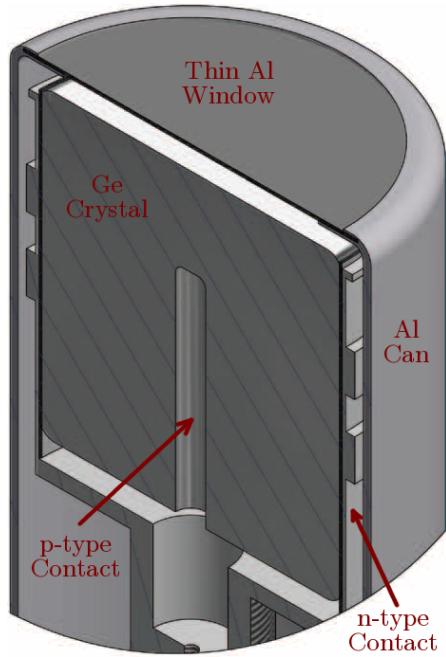
Figure 8.1: Cartoon of a Canberra extended range coaxial Ge detector, such as Gopher. The Ge crystal has an n-type contact on the inner bore, a p-type contact on the outer surface, and a thin-window contact on the top surface. It is surrounded by an Al can, which is thinner (1.6 mm) on the top window. Image adapted from [306].

8.1 Material Screening: Gopher Detector

8.1.1 Physical Description

The University of Minnesota SuperCDMS group operates a high-purity Ge (HPGe) detector located at Soudan called Gopher. The physics behind a HPGe gamma spectrometer is the same as the ionization measurement in ZIP detectors, which gives superior resolution compared to other screening technologies. The p-type Ge crystal in Gopher is a cylinder with a radius of 47.5 mm, height of 55 mm, and mass of 2.075 kg. The detector was fabricated by Canberra Industries Inc. as part of their Extended Range Coaxial Ge Detectors series [306]. A general cartoon of a detector in this series is given in Fig. 8.1. The biasing configuration is such that the inner contact is a p-type ion-implanted boron electrode which is $\sim$0.3 μm thick and negatively biased while the outer contact is an n-type diffused lithium electrode which is $\sim$0.5 mm thick and positively biased. The bias applied to Gopher is $\sim$3500 V. In the extended range detectors, a thin-window contact is used on top of the detector to give better sensitivity to low energies. For Gopher, the detector is housed in a aluminum can, with the top surface (the "window") a thin 1.6 mm of aluminum.

Figure 8.2: Mid-construction photograph of the Gopher shield. The innermost layer is 5.08 cm OFHC copper (brown), next is 5.00 cm of ULA lead (dark gray), last is 25.4 cm of standard lead (light gray). The detector can and crystal are located in the copper cavity with a pipe connected to the cryostat (in back) through the shielding. The protruding stack of lead in the front is a door, which can be lowered to give access to the cavity. Photograph courtesy of M. Epland.

In order to achieve low-background rates, the Gopher detector is surrounded by extensive gamma shielding. A mid-construction image of the shielding, showing each layer of the shield, is given in Fig. 8.2. Immediately around the detector can is the screening cavity, which is an open rectangular prism that is 29.84 cm deep, 24.84 cm high, and 24.84 cm across. The can diameter is 10.5 cm and it is located a small distance from the back of the chamber. The chamber walls are composed of low-background 5.08-cm-thick oxygen-free high thermal conductivity copper (OFHC). The copper box is surrounded by 5 cm of ultra-low activity lead (ULA), which is depleted of ^{210}Pb. This is then surrounded by at least 25.4 cm of regular lead in any direction.

Gopher was originally constructed with a shield consisting of 0.9523 cm of copper and 30.48 cm of lead with the new shield built, with manual-labor assistance from the author, in 2012. The first-shield set-up, construction, characterization, and second-shield design for Gopher was performed by O. Kameav with an assortment of students. The addition of the OFHC copper and ULA lead reduced the background level by a factor of ~10 as shown in Fig. 8.3, which compares the background spectra for the old and new shields.[1] The most prominent component to the background is the β spectrum from the ^{210}Pb daughter ^{210}Bi. Discrete peaks from various contamination sources are seen on top of smooth continuum. The large peaks below 100 keV are atomic x-ray

---

[1] The new shield background was taken with single poly brick in the cavity. This brick is needed to raise small samples to be closer to the detector and is left in the cavity for each sample regardless as part of the background.
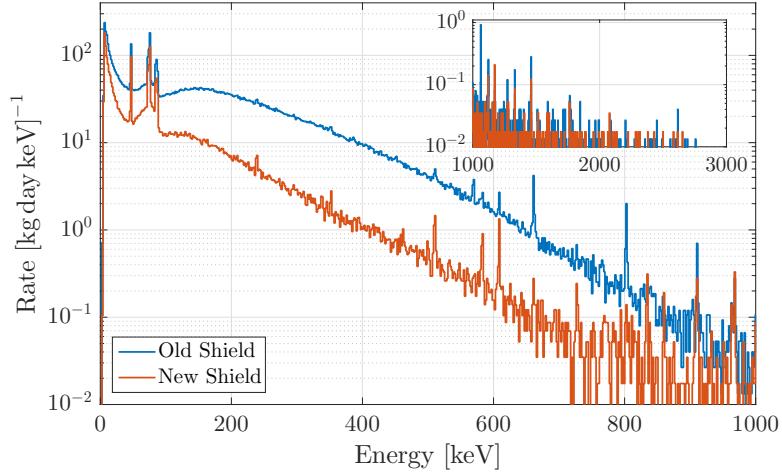
Figure 8.3: Gopher background spectra taken with the original (blue) and upgraded (orange) shielding. The primary component of both spectra is the ^{210}Bi β decay below $\sim$1 MeV, which is reduced by a factor of $\sim$10 with the new shield. Discrete peaks from other contaminants are seen above the continuum in both. The inset shows the sparsely populated high-energy region of the spectra.

transitions.

8.1.2 Sample Analysis

The primary data analysis package for Gopher was also written by O. Kameav. Many additions additions/improvements to this package were added for this thesis:

- Implementation of data preprocessing to remove suspect data from the analysis.

- Identification and removal of additional peaks found near peaks of interest.

- Improvements of the GEANT4 Monte Carlo simulation.

- Development of a Monte Carlo sampling technique to compute upper limits.

To demonstrate the analysis, including these improvements, the Zytel nylon (mass of 477 g) sample analysis is detailed. A photograph of the Zytel nylon sample inside the screening cavity is shown in Fig. 8.4.

Figure 8.4: Zytel nylon (Zytel 101 NC010 Nylon 6,6 Polyamide) sample (stack of white squares) in the Gopher screening cavity. The white brick in front is polyethylene, which is left in the cavity since it was present in the background spectrum run.
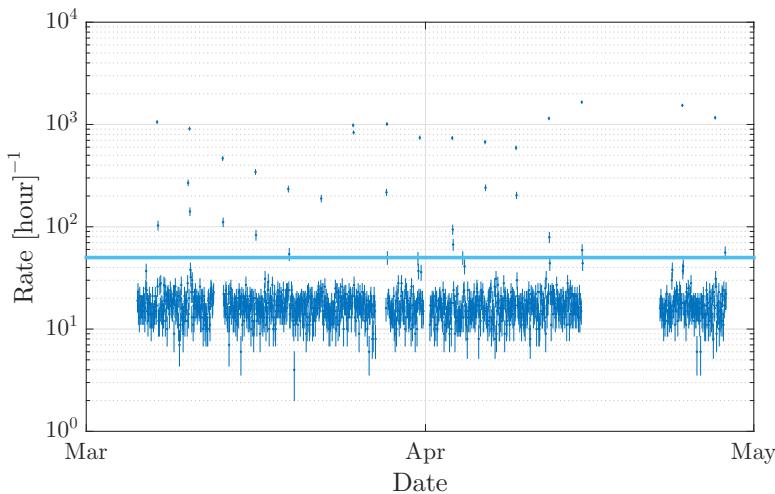
Figure 8.5: Rate of events near 10 keV for each hour-long file from the Zytel nylon sample screening in Gopher. Sharp increases in noise due to the cryostat are removed by a threshold cut (solid line).

Preprocessing

The Ge crystal is cooled by liquid nitrogen via the cryostat shown in Fig. 8.2. The cryostat introduces noise in the detector whenever a nitrogen transfer occurs. The data files containing the additional noise are removed from the analysis and identified by an increase in event rate near ~10 keV. In order to remove the smallest about of live time, each data file is set to be an hour long. The rate of events near 10 keV is computed for each file and a cut placed to remove high-rate files. The rate in this energy range for the Zytel nylon sample is shown in Fig. 8.5 along with the cut used.

The entire Gopher apparatus is continually purged with N_2 gas, contained by a cage surrounding the shield. The purge functions to reduce the atmospheric ^{222}Rn content around the experiment. This reduces the amount of ^{222}Rn which diffuses through any
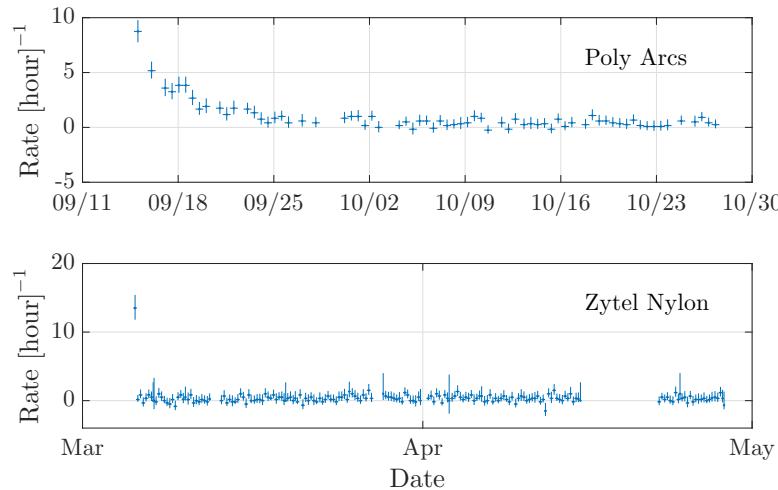
Figure 8.6: Event rate in three common peaks of ^{222}Rn daughters for two samples in Gopher. The poly arcs sample was screened prior to the installation of a nitrogen purge around Gopher while the Zytel nylon (bottom) was screened after. Prior to the purge, the first several days of the data were rejected due to high ^{222}Rn rate, while after the purge only the first few hours need to be removed.

cracks in the shield and the contamination of the atmosphere allowed into the cavity during sample exchanges. The effect of the purge is shown in Fig. 8.6, which compares the Zytel nylon data to that of an older sample screened prior to the use of the purge. The rate of events in three common peaks of ^{222}Rn daughters is given. In order to obtain reasonable statistics, data files are combined until the live time is >6 hours. In the older sample, the rate in these peaks decayed over the course of several days. After the installation of the purge, the rate was elevated for only the first few hours. The data files which have an elevated rate in these peaks are removed from the analysis. This is particularly important as the same peaks used to identify ^{222}Rn are used in the ^{238}U contamination measurement.

The spectrum from the Zytel nylon data after these preprocessing steps is given in Fig. 8.7. In comparison to the background in Fig. 8.3, the spectrum is only slightly elevated above background; an early indicator of low contamination in the sample.
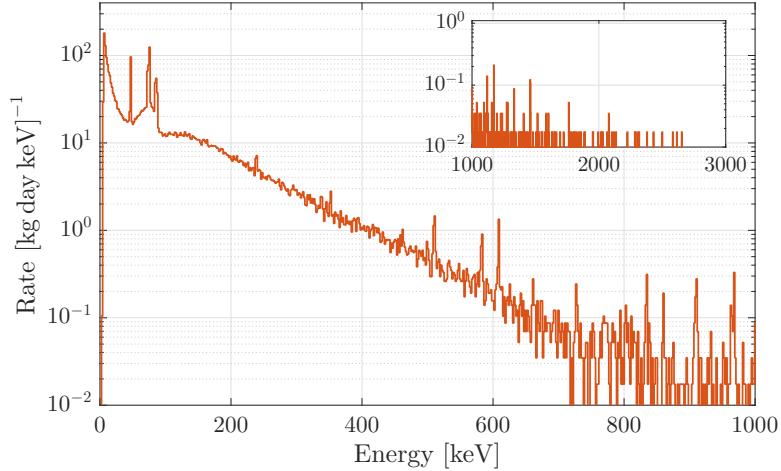
Figure 8.7: Gamma spectrum from the Zytel Nylon screening in Gopher. In comparison to Fig. 8.3, the sample is barely above background rates, common for Gopher screening. Higher energy peaks can be below background rates due to the sample shielding the background.

Peak Analysis

The base component of the main analysis is the fitting of several peaks in the spectrum which have a known decay sources. The intensities of the peaks are directly related to the radioactivity of the given sources in the cavity. The standard peaks used in Gopher analyses are listed in Table 8.1. The curve fitting method is demonstrated with simulated data in Fig. 8.8. The peak, generically labeled α, at 30 keV is on top of a background which decreases linearly with energy. The sum of a Gaussian and line is fit to the data. Two parameters are extracted from the fit: α_t, the total number of events in the central 90 % range of the peak ($\mu \pm 2.36\sigma$) and α_b, the number of events in the central 90 % range due to the linear background, which is extracted from the linear fit. The number of events in the spectrum due to the peak alone is then $\alpha_n = \alpha_t - \alpha_b$. The extracted α_i quantities have Poisson variance of $\sigma_i^2 = \alpha_i$, while α_n is the difference of two Poisson distributions (Skellam distribution) and has variance of $\sigma_n^2 = \alpha_t + \alpha_b$.

In a full analysis, such a fit is performed on three different spectra for each given peak. These are the with-sample spectrum ($\alpha = s$), the sample-free background spectrum ($\alpha = b$), and a GEANT4 simulated spectrum ($\alpha = M$). The data, fits, and α_n values for the 238 keV peak for the Zytel nylon sample and background spectra are given in

Index	Chain	Isotope	Energy [keV]	Index	Chain	Isotope	Energy [keV]
1	^{238}U	^{214}Pb	295	6	^{232}Th	^{228}Ac	911
2			352	7			969
3		^{214}Bi	609	8		^{212}Pb	238
4			1120	9		^{212}Bi	727
5			1765	10		^{208}Tl	583
13	-	^{60}Co	1173	11			860
14			1333	12			2614
15	-	^{40}K	1460	16	-	^{137}Cs	661

Table 8.1: Gamma peaks used in standard Gopher analyses along with their parent isotope and, if applicable, the decay chain to which the parent belongs. The index corresponds to the final result order.
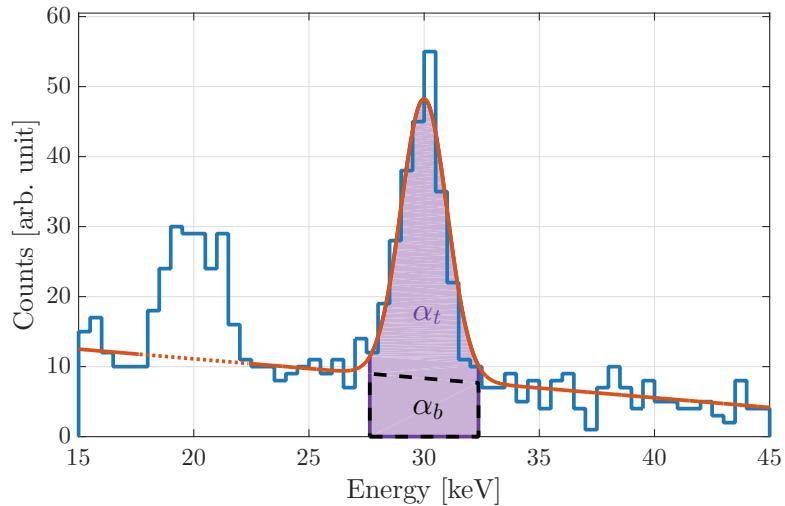
Figure 8.8: Simulated data showing a peak at 30 keV on top of a background which linearly decreases with energy (blue). The sum of a Gaussian and line fit (orange) is shown along with the area under the central 90 % of the peak (purple). The extrapolated linear background under the peak is given by the black dashed outline. The quantities α_t and α_b are derived from these areas. An addition peak is present in the side-band at 20 keV and the energy range excluded from the fit due to this peak shown by dots.

Fig. 8.9. Fitting the background spectrum is required to determine how many of the s_n events are originally from the shield instead of the sample. To calculate the events from the sample itself, s_n and b_n are compared, after normalizing by their respective live times T_S and T_B. The spectrum with the longer exposure is scaled to that of the shorter exposure to give the useful acquisition time as $T_{\text{aqt}} = \min(T_S, T_B)$. The normalized peak counts from each spectra are then

$$S_n = s_n \frac{T_{\text{aqt}}}{T_S} \qquad B_n = b_n \frac{T_{\text{aqt}}}{T_B}, \tag{8.1}$$

and the total number of peak events from the sample is $N = S_n - B_n$. The uncertainties on the live times are negligible and standard uncertainty propagation[2] gives the variance of N to be

$$\sigma_N^2 = T_{\text{aqt}}^2 \left(\frac{s_t + s_b}{T_S^2} + \frac{b_t + b_b}{T_B^2} \right). \tag{8.2}$$

The event rate R for the peak from the sample is the number of events per acquisition time, i.e. $R = N/T_{\text{aqt}}$ and $\sigma_R = \sigma_N/T_{\text{aqt}}$. The 238 keV peak rate from Zytel nylon is $R = (2.61 \pm 1.52) \times 10^{-5} \text{ s}^{-1}$.

It is possible for there to be more than one peak within a fitting region, which typically spans $\mu \pm 15\sigma$ around a given peak. One common example is the 242 keV peak from ^{214}Pb, its third most intense line, which is close to the 238 keV peak used in the analysis. The probability of the 242 keV peak is low (7.5 %) and it is only distinguishable above background for high-levels of ^{214}Pb. Other potential side peaks are also usually low-intensity decays made prominent by high contaminations. When a side peak (or peaks) is identified in the fit, it is removed by excluding $\mu \pm 2\sigma$ around the side peak from the range used in the fit. This prevents unphysical rises in the linear background fit, which would give incorrect estimates of s_n. No side-band peaks are prevalent in the Zytel nylon sample, instead, the effect is shown in the simulated data in Fig. 8.8.

Simulation

The next step in the analysis is to convert the rate to a contamination level C. The rate is the number of detected events coming from the sample per time, however, only

---

[2] i.e. $\sigma_N^2 = N^2 \left(\sum_{\alpha = S_n, B_n} \left[\frac{\sigma_\alpha}{\alpha} \right]^2 \right).$
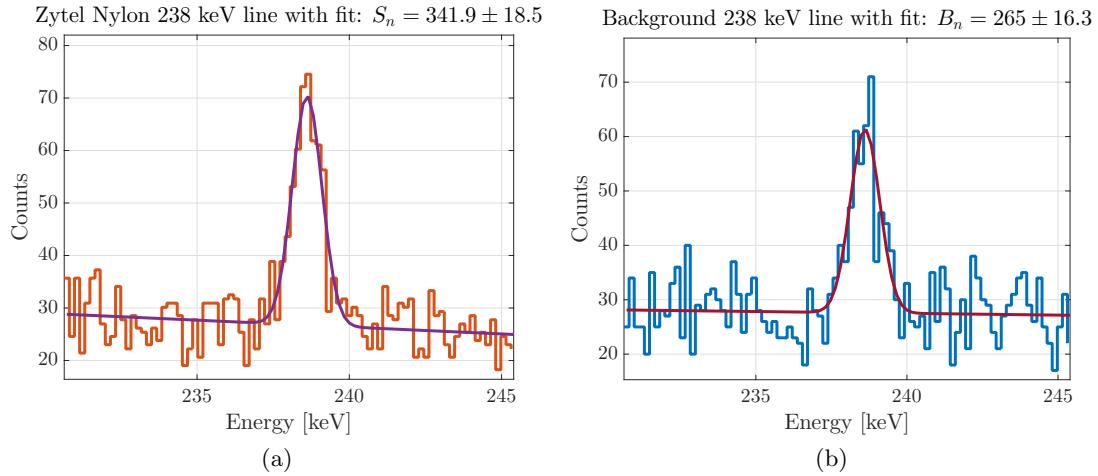
Figure 8.9: Data and fits to the 238 keV peak from the Zytel nylon sample (a) and the background spectrum (b). The normalized number of counts in the peak for each spectra is given in the figure title. The sample counts are scaled to the live time of the background spectrum.

a (typically) small portion of decays from sample reach the detector. This reduction is called the geometrical efficiency $\mathcal{E}$, and is related to the sample size, density, and location/orientation in the cavity. As this changes with each sample, a GEANT4 Monte Carlo is used to simulate each sample's geometry. The Gopher geometry is created in GEANT4 in a compartmentalized way, making it easy to create and place individual samples without adjusting the overall geometry. The Monte Carlo geometry with the Zytel nylon sample in the cavity is shown in Fig. 8.10.

The geometrical efficiency is computed by fitting each peak in the simulated spectrum and calculating

$$\mathcal{E} = M_n/N_p = (M_t - M_b)/N_p \tag{8.3}$$

where N_p is the number of primaries simulated (typically 1×10^6), and M_n and $M_{t/b}$ are defined above. The Gaussian plus line fit is needed even in simulation as lower energy peaks can be on top of the Compton continuum from higher energy peaks in the same decay. The variance of $\mathcal{E}$ is

$$\sigma_{\mathcal{E}}^2 = \mathcal{E}^2 \left(\frac{M_t + M_b}{(M_t - M_b)^2} + \frac{1}{N_p} \right). \tag{8.4}$$
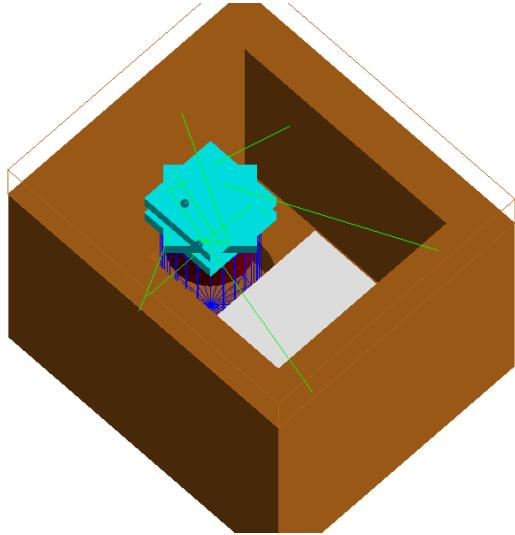
Figure 8.10: GEANT4 Monte Carlo simulation geometry of the Gopher cavity with the Zytel nylon sample. The copper surrounding the cavity is in brown, the aluminum can in blue, the detector in solid red, the sample in cyan, and a poly brick in white. Simulated γ rays are in green. The top of the copper box as well as the aluminum can are given as transparent wire-frames for clarity.

The contamination level and variance in the sample of mass m is then

$$C = \frac{R}{m\mathcal{E}} \tag{8.5}$$

$$\sigma_C^2 = C^2 \left(\left(\frac{\sigma_R}{R} \right)^2 + \left(\frac{\sigma_\mathcal{E}}{\mathcal{E}} \right)^2 \right). \tag{8.6}$$

For the 238 keV zytel nylon line, $\mathcal{E} = (3.46 \pm 0.02) \times 10^{-2}$ and $C = 1.59 \pm 0.92 \, \mathrm{mBq\,kg^{-1}}$.

Contamination Upper Limits

The above procedure gives a value of $C \pm \sigma_C$ for the contamination level of each individual peak. However, for low contamination levels, it is often not statistically justified to claim a signal above the background. In such cases, an upper limit on C is more appropriate. Upper limits on a certain quantity are typically found by studying its PDF. In this case, the PDF for C is needed. C, as given by Eq. 8.6, is described by a combination of seven Poisson random variables (s_t, s_b, b_t, b_b, M_t, M_b, N_p). The statistics are often too low to justify a Gaussian approximation for C and such a combination of Poisson variables is not represented by another well-characterized distribution. Instead, the distribution is created by Monte Carlo sampling. Random values are sampled from the seven Poisson distributions, each described by a mean given by that it's measured value, and combined as in Eq. 8.6. This process is repeated 1×10^4 times per line to
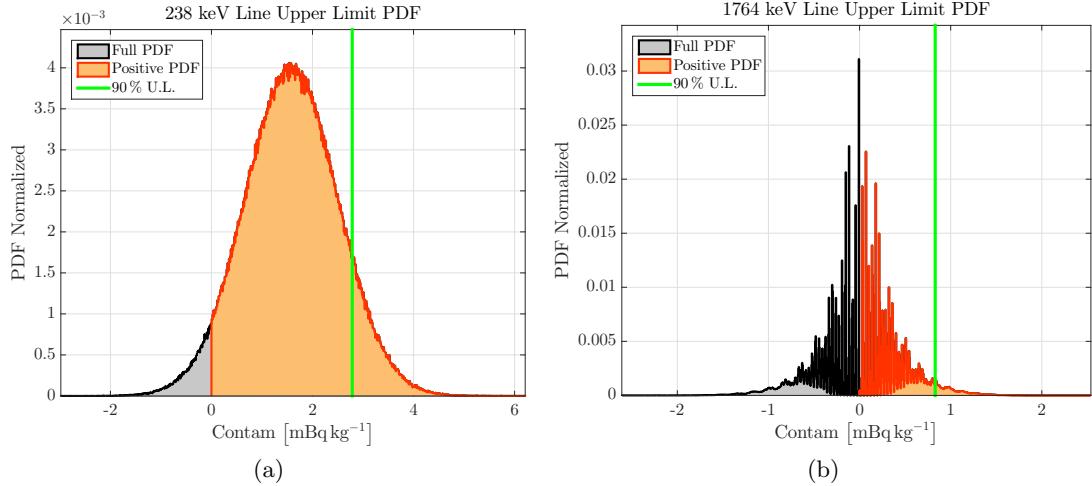
Figure 8.11: Probability distribution functions (PDFs) describing the contamination values for the 238 (a) and 1764 (b) keV lines from the Zytel nylon sample. The distributions are constructed by Monte Carlo sampling of the underlying Poisson distributions. The 238 line has high enough statistics to be approximated as Gaussian, while the 1764 keV line is a hybrid between discrete, low-statistic, Poisson distributions and continuous, high-statistic, Gaussian distributions. The 90 % upper limits (green lines) are computed as the 90th percentile of the positive portions of the distributions (orange).

build the PDFs. The prior information that $C \geq 0$ is used in examining the PDF and the 90 % upper limit $\hat{\nu}$ is found as

$$\hat{\nu} = \left\{ \nu \left| 0.9 = \frac{\int_0^\nu \text{PDF}(s_t, s_b, b_t, b_b, M_t, M_b)}{\int_0^\infty \text{PDF}(s_t, s_b, b_t, b_b, M_t, M_b)} \right. \right\}. \tag{8.7}$$

Two examples of the upper limit procedure for the Zytel nylon sample are shown in Fig. 8.11. The 238 keV distribution has high enough statistics for the PDF to be approximated as Gaussian. Conversely, the higher energy and lower statistics line at 1764 keV shows a hybrid nature of discrete steps with a Gaussian-like envelope — demonstrating a trade-off between the large values, such as Monte Carlo counts, and small values, such as the background and sample fit quantities.

Final Results

The final results for the Zytel nylon-sample screening are given in Fig. 8.12, where the contamination levels and upper limits for each of the considered peaks are shown. The line indexes are given in Table 8.1. For each sample, a final value per decay chain is typically reported and a human decision is required to decide whether that value is an upper limit or central value with uncertainty. The final values, by default, assume secular equilibrium for the long chains. If an upper limit is reported, the highest limit from the group of peaks is chosen. For the Zytel nylon sample, upper limits were reported for ^{238}U, ^{60}Co, and ^{137}Cs. If a central value is reported, a weighted mean and standard deviation, using high-quality lines,[3] are calculated and reported. The mean is computed as

$$\bar{C} = \frac{\sum_{i=1}^{n} C_i \sigma_{C,i}^{-2}}{\sum_{i=1}^{n} \sigma_{C,i}^{-2}}, \tag{8.8}$$

for n high-quality lines. The variance is taken as the maximum of the following two expressions

$$\sigma_{\bar{C}}^2 = \frac{1}{\sum_{i=1}^{n} \sigma_{C,i}^{-2}}, \tag{8.9}$$

$$\sigma_{\bar{C}}^2 = \frac{1}{\sum_{i=1}^{n} \sigma_{C,i}^{-2}} \cdot \frac{1}{n-1} \cdot \sum_{i=1}^{n} \frac{\left(C_i - \bar{C}\right)^2}{\sigma_{C,i}^2} \tag{8.10}$$

where the first computation gives an accurate variance if the individual peaks are consistent with each other and the second computation gives a more accurate variance when they are inconsistent. Such inconsistency implies over-dispersion due to an unknown systematic, and the variance is corrected by the reduced χ^2 value between the measurements and the weighted mean. For the Zytel nylon sample, a central value was reported for ^{40}K and ^{232}Th, where the ^{232}Th value averaged the 238, 583, 911, and 969 keV lines. The ^{232}Th lines are particularly interesting for this sample. Two of the lines, 860 and 727 keV, have negative central values, indicative of the sample screening the background for these lines. The upper limit computed from the sampled PDFs, however, are consistent with the other high-quality lines, which lends credence to the

---

[3] Another human decision.
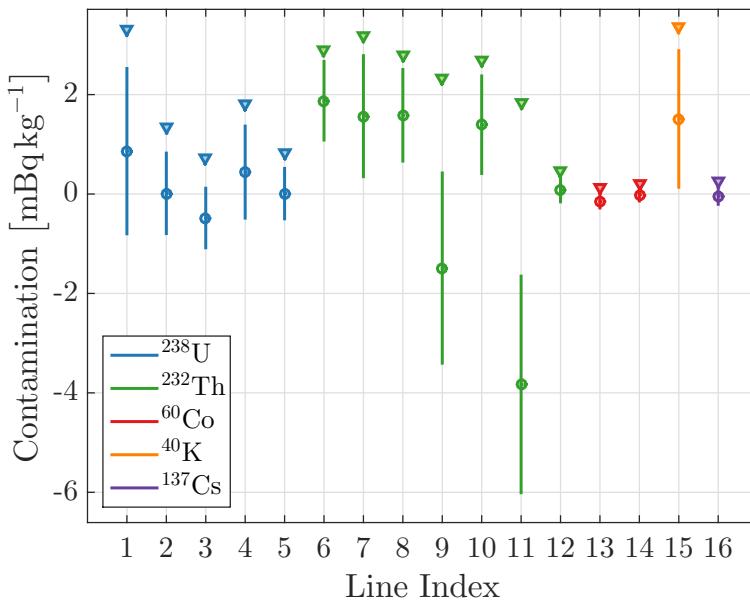
Figure 8.12: Final contamination levels (circles with uncertainty) and 90 % upper limits (downward triangles) for each line considered for the Zytel nylon sample. The line index is given in Table 8.1.

Monte Carlo sampling method.[4]

The final results for all gopher samples screened for this thesis are given in Table 8.2 in chronological order. The correct upper-limit-computation procedure was implemented starting with the Zytel nylon sample; samples screening prior to this did not compute upper limits and fields are left blank where an upper limit would be required. Some samples appear twice, with one entry having a "Purified" label. For these samples, the purified sample underwent specific treatment to reduce contamination levels. These procedures are more expensive and thus both versions were screened to determine if the extra purification, and cost, is truly needed. The "surface steel" sample was screened only for a surface ^{210}Pb source as identified by the 46.6 keV γ from ^{210}Pb. This sample was then screened again after a novel surface-purification technique was applied at Syracuse University, and a large reduction in surface contamination seen [307]. Most samples were screened to determine if they are appropriate for use in the SuperCDMS SNOLAB, though some samples were screened from the SuperCDMS Soudan, Soudan II, and other external experiments. Results for SuperCDMS Soudan samples are useful to inform the *in situ* measurements of contaminations done with CDMS Soudan data (Sec. 7.1).

---

[4] The 2614 keV line almost never has the statistics to perform a reasonable fit. It is never used in determining the final reported value.

Table 8.2: Final contamination values for all samples screened in Gopher for this thesis. Unless otherwise noted, all values are in units of $[\mathrm{mBq\,kg^{-1}}]$. Samples are listed chronologically, starting with the earliest screened.

Sample Name	^{238}U	^{232}Th	^{60}Co	^{40}K	^{137}Cs
Surface Steel[5]					
Surface Steel, Purified[6]					
2020 Graphite, Purified	3.89 ± 0.60	79.63 ± 2.02		4.10 ± 1.65	
Zirconium Oxide	6892 ± 50	1834 ± 17		45.19 ± 8.8	
UF-4S Graphite, Purified		52.03 ± 3.11			
TDK Capacitors[7]	10.46 ± 0.16	1.25 ± 0.06		0.51 ± 0.17	
2020 Graphite	298.14 ± 20.67	1152.52 ± 20.67		13.21 ± 6.00	5.65 ± 1.4
Noryl	1.83 ± 1.58	0.47 ± 0.54		13.99 ± 2.15	
PMMA	<14.12	2.18 ± 2.13			
Delrin	0.74 ± 0.78	2.75 ± 0.83		1.84 ± 2.4	
Vespel SCP-5050	7.72 ± 0.69	9.95 ± 0.72		7.26 ± 2.18	0.48 ± 0.26
Ti (15-3-3-3) Foil	20.40 ± 1.03	7.97 ± 0.89		3.26 ± 2.14	

Continued on next page

---

[5] Only screened for surface ^{210}Pb using the 46.6 keV line. Value of 14620 ± 1340 $\mathrm{mBq\,m^{-2}}$.
[6] Only screened for surface ^{210}Pb using the 46.6 keV line. Value of <1124 $\mathrm{mBq\,m^{-2}}$.
[7] Units are μBq per capacitor.

Table 8.2 – continued from previous page

Sample Name	^{238}U	^{232}Th	^{60}Co	^{40}K	^{137}Cs
IpDIA Capacitors[8]	<5.25	4.87 ± 2.17		15.5 ± 8.4	
Mylar Foil	2.16 ± 0.25	0.35 ± 0.19		0.94 ± 0.45	
ACCU-Mesh Foil	15.76 ± 3.06	18.32 ± 2.48		81.83 ± 9.95	
ZXF-5Q Graphite	<1.88	3.05 ± 0.75		<1.761	
Brass Screws	1.05 ± 0.45	1.47 ± 0.45	2.32 ± 0.61	1.12 ± 0.45	<0.26
Ti (15-3-3-3) Plate	1.80 ± 1.95	7.69 ± 1.95		6.11 ± 4.60	
DragonPlate CFRP	0.82 ± 0.62	2.93 ± 1.60		8.21 ± 2.36	
Sumika MRZ Thermoplastic	8234 ± 97	10990 ± 1574	4.95 ± 2.71	1647 ± 98	79.29 ± 11.05
Sumika SZ Thermoplastic	380.7 ± 15.7	73.8 ± 8.6		99150 ± 2950	
Sumika T/SCZ Thermoplastic	2788 ± 21	29.38 ± 7.32	0.53 ± 0.29	13.17 ± 3.68	
Alpha Solder Paste	5.62 ± 1.56	5.28 ± 1.56	<0.42	154.3 ± 11.3	
Zytel Nylon	<1.34	1.64 ± 0.47	<0.20	1.51 ± 1.38	<0.25
PEEK Pellets, Cleaned	20.53 ± 0.76	11.85 ± 0.78	<0.11	10.90 ± 1.49	<0.13
Sumika PES	1.21 ± 0.36	1.14 ± 0.48	<0.42	1000 ± 30	<0.45
GdB$_6$ Scintillator	6.61 ± 4.72	29.30 ± 7.06	<2.04	<3.09	<2.14

---

[8] Units are μBq per capacitor.

Table 8.2 – continued from previous page

Sample Name	^{238}U	^{232}Th	^{60}Co	^{40}K	^{137}Cs
Gd Isopropoxide Scintillator	<28.31	8.61 ± 3.94	<1.74	<26.60	<1.21
Soudan II Veto Al Frame	9.49 ± 2.43	182.9 ± 10.3	<1.14	17.37 ± 7.78	<2.05
Soudan II Shotcrete	6089 ± 1312	6527 ± 755	<12.26	4489 ± 844	<11.84
Soudan II Veto Preamp[9]	551.1 ± 47.5	297.9 ± 33.3	<0.30	52.62 ± 2.11	<0.51
RuO$_2$ Resistors[10]	<4.79	2.35 ± 0.72	<0.71	<3.90	0.32
PVDF Pellets	<2.49	<2.36	<0.17	<1.49	<0.13
Phosphor-Bronze Wire Loom	0.97 ± 0.67	1.47 ± 0.43	<0.34	5.22 ± 1.51	<0.18
CDMS Ancient Lead	0.56 ± 0.41	0.72 ± 0.46	<0.07	1.53 ± 0.62	<0.23
CDMS Outer Lead	1.12 ± 0.44	0.24 ± 0.44	<0.05	<1.07	<0.26
CDMS Inner Poly	0.59 ± 0.39	1.51 ± 0.51	<0.13	1.87 ± 1.17	<0.19
SuperCDMS Tower 4[11]	<2.07	1.43 ± 0.37	<0.10	<2.11	<0.14
Cirlex	6.33 ± 1.23	<2.24	<0.01	<1.55	<0.01

---

[9] Units are mBq per circuit board.
[10] Units are μBq per resistor.
[11] Assuming all contamination is in the copper components.

There are several potential improvements to the Gopher analysis.

- The fitting could be improved by using a maximum-likelihood estimation technique, which is less biased by zero-count bins than the current least-squared fitting.

- Relieving the burden of the operator to make decisions which could bias the results is desirable. This could be accomplished by devising a proper method to propagate the fitting uncertainties into the total uncertainty. This should inflate the uncertainties on the high-energy lines and bring their reported values into better consistency with higher-count lines. Another approach is to compute goodness-of-fit quantities and only include lines in the final value which pass some threshold on goodness-of-fit.

- Statistical approaches to smoothly transition between an upper limit and a central value with uncertainty exist [308, 309] and could be investigated to remove that decision from a potentially biased operator.

- The resolution of Gopher is non-Gaussian at the higher energies as evidenced by investigating high-energy lines in high-contamination samples; in particular there is a low-energy skew that should be investigated and properly treated.

- Several samples show odd behavior in the ^{238}U lines which questions the validity of the secular-equilibrium and bulk-only-contamination assumptions. The former can be investigated by including the 186 keV ^{226}Ra line into the analysis as ^{226}Ra occurs much earlier in the decay chain (notably above ^{222}Rn). The latter can be investigated by performing a surface-only Monte Carlo simulation and doing either a simple comparison or joint-fit with the bulk-only simulation.

- The overall background of Gopher should be understood through a global-gamma simulation fit. With trusted background contamination levels, the background could be simulated for each sample and used in the analysis. This would correctly account for instances of the sample shielding the crystal from the usual background.

8.2   Initial Global Simulations

The SuperCDMS SNOLAB experiment has been part of the SuperCDMS Collaboration's plan for many years. Proposals were submitted for research and development funding in 2012 to both the Department of Energy (DOE) and National Science Foundation (NSF). For these proposals, radiogenic background estimates were needed based on the preliminary shield and detector-array designs available at the time. Such a study, known as the "passive shielding" study, was undertaken with GEANT4 for this thesis and the final rate estimates were included in those two proposals.

8.2.1   Geometry

The simulation uses a simplistic and preliminary geometry. The concept for the entirely passive shielding is based on a larger, and cleaner, implementation of the Soudan shield. The layers consist of: Outer poly, outer vacuum chamber (OVC), lead, inner poly, load can, shield can, inner vacuum chamber (IVC), still can, cold plate can, mixing chamber can. The last six cans are the components of the copper cryostat. The OVC is aluminum. The layers are axially-concentric hollow cylinders with radial and vertical thicknesses as given in Table 8.3.

   The detectors in the simulation are perfect cylinders of germanium with an individual mass of 1.39 kg, diameter of 100 mm, and height of 33.3 mm. Twelve towers, each consisting of 6 detector, are implemented giving a total payload of 100.8 kg. A hollow cylinder of copper, 0.08 in. thick, surrounds the stack of detectors to represent detector housings. The full geometry of the simulation is shown in in Fig. 8.13, including the arrangement of the 12 towers into a triangular pattern.

8.2.2   Simulation and Results

Sources

The goal of this study is to determine the electron (ER) and nuclear (NR) recoil background rates from all radiogenic sources. The long-lived primordial sources of ^{40}K, ^{238}U, and ^{232}Th are simulated in all components of the geometry. For the long chains, both neutrons and gammas are simulated with the gamma-source isotopes of ^{228}Ac, ^{212}Pb,

Layer	Thickness [in.]	Inner Diameter [in.]	Inner Height [in.]
Outer Poly	40.0	79.25	70.00
OVC	0.25	78.25	69.00
Lead	7.0	62.75	51.50
Inner Poly	4.0	53.75	43.50
Load Can	0.375	53.00	42.75
Shield Can	0.5	47.25	40.31
IVC	0.5	42.25	38.44
Still Can	0.5	37.25	25.25
Cold Plate	0.5	32.25	23.00
Mixing Chamber	0.5	26.00	21.00

Table 8.3: Dimensions of the initial SuperCDMS SNOLAB passive shielding configuration. The layers' inner diameter, height, and thickness are all given. Gaps between layers are vacuum.

(a)   (b)
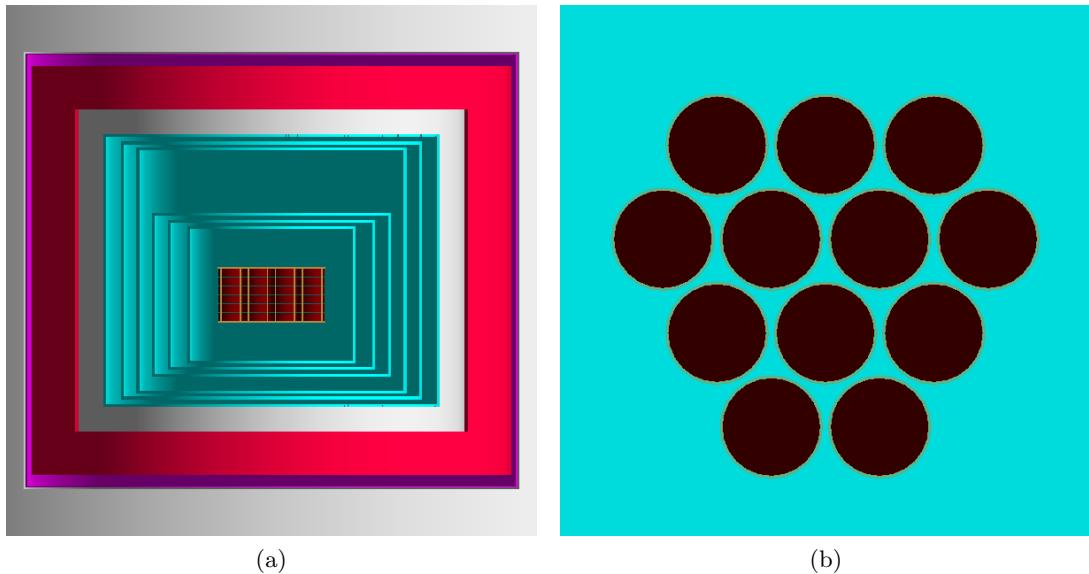
Figure 8.13: GEANT4 geometry for the SuperCDMS SNOLAB passive shielding study. Subfigure (a) shows a cross-sectional side view giving the different shield layers from outermost to innermost of: (mostly off image) outer poly (grey), OVC (magenta), lead (red), inner poly (grey), six cryostat cans (cyan), detector housing (wire-frame brown), Ge detectors (dark red). Subfigure (b) shows a top view of the detector stacks, showing the triangular arrangement of the 12 towers.
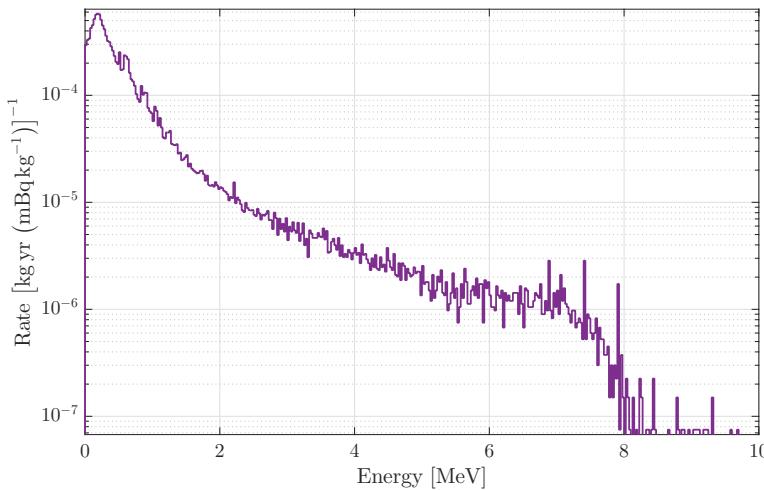
Figure 8.14: Electron recoil spectrum as a result of ^{238}U-sourced neutrons simulated in the mixing chamber in the SuperCDMS SNOLAB passive shielding study. Normalization is per exposure and per contamination level of the source. Discrete lines are observed due to the n-capture on ^{1}H, ^{63}Cu, and ^{65}Cu.

^{212}Bi, ^{208}Tl for ^{232}Th and ^{214}Pb, ^{214}Bi, ^{210}Pb, ^{210}Bi for ^{238}U. The number of primary events simulated for each decay source are: 1×10^7 γ's and 1×10^6 n's from the outer poly, 5×10^6 γ's and 1×10^6 n's from both the lead and inner poly, 1×10^6 γ's and n's from each copper can, and 5×10^5 γ's and n's from each of the tower casings. Recall that, for γ sources, a single primary corresponds to single decay of the chain progenitor and isotopes in the chain are simulated in the proper ratio assuming secular equilibrium. For neutron sources, instead, the normalization yields in Table 6.3 are required to convert from primaries to decays.

The ER spectra from the γ sources and the NR spectra from the neutron sources are very similar to those seen with the Soudan geometry (see, e.g. Figs. 7.3 and 7.7(a)). The ER spectrum from one of the neutron sources, ^{238}U, generated from the mixing chamber can is shown in Fig. 8.14. Several peaks are present due to neutron-capture processes on isotopes found in the shield. Most notable are the 2.2 MeV peak from capture on ^{1}H [310] and the numerous peaks at 6–8 MeV and 1–2 MeV from ^{63}Cu [311] and ^{65}Cu [312]. The smooth continuum is a result of Compton and bremsstrahlung interactions originating from the high energy capture γ's. The ER rate from n primaries is typically $\mathcal{O}(10^{-8})$ smaller than from γ primaries; although this ER rate is included as a result of the n simulation, its contribution is practically negligible.

Decay	Primary	Type	Outer Poly	Lead	Inner Poly	Cryostat Cans	Tower Housings
γ's	^{232}Th	ERSS	$<2.63\,\mathrm{E}+0$	$1.85\,\mathrm{E}+1$	$2.31\,\mathrm{E}+1$	$1.73\,\mathrm{E}+3$	$3.04\,\mathrm{E}+2$
γ's	^{232}Th	ERMS	$<2.63\,\mathrm{E}+0$	$9.77\,\mathrm{E}+1$	$4.92\,\mathrm{E}+1$	$2.90\,\mathrm{E}+3$	$9.41\,\mathrm{E}+2$
γ's	^{238}U	ERSS	$<2.63\,\mathrm{E}+0$	$2.19\,\mathrm{E}+1$	$1.80\,\mathrm{E}+1$	$1.34\,\mathrm{E}+3$	$2.23\,\mathrm{E}+2$
γ's	^{238}U	ERMS	$<2.63\,\mathrm{E}+0$	$5.73\,\mathrm{E}+1$	$3.98\,\mathrm{E}+1$	$2.37\,\mathrm{E}+3$	$7.41\,\mathrm{E}+2$
γ's	^{40}K	ERSS	$<2.63\,\mathrm{E}+0$	$1.68\,\mathrm{E}+0$	$2.34\,\mathrm{E}+1$	$9.94\,\mathrm{E}+1$	$6.48\,\mathrm{E}+1$
γ's	^{40}K	ERMS	$<2.63\,\mathrm{E}+0$	$3.37\,\mathrm{E}+0$	$4.91\,\mathrm{E}+0$	$1.89\,\mathrm{E}+2$	$4.58\,\mathrm{E}+1$
n's	^{232}Th	ERSS	$<1.59\,\mathrm{E}-4$	$1.74\,\mathrm{E}-8$	$1.39\,\mathrm{E}-3$	$1.94\,\mathrm{E}-4$	$7.11\,\mathrm{E}-6$
n's	^{232}Th	ERMS	$1.59\,\mathrm{E}-4$	$6.22\,\mathrm{E}-8$	$3.04\,\mathrm{E}-3$	$1.02\,\mathrm{E}-3$	$8.00\,\mathrm{E}-7$
n's	^{238}U	ERSS	$2.03\,\mathrm{E}-4$	$4.37\,\mathrm{E}-4$	$1.66\,\mathrm{E}-3$	$1.06\,\mathrm{E}-3$	$1.38\,\mathrm{E}-5$
n's	^{238}U	ERMS	$2.03\,\mathrm{E}-4$	$1.78\,\mathrm{E}-3$	$6.37\,\mathrm{E}-3$	$5.68\,\mathrm{E}-3$	$5.75\,\mathrm{E}-6$
n's	^{232}Th	NRSS	$3.19\,\mathrm{E}-5$	$4.04\,\mathrm{E}-8$	$1.52\,\mathrm{E}-3$	$4.20\,\mathrm{E}-3$	$1.89\,\mathrm{E}-4$
n's	^{232}Th	NRMS	$1.28\,\mathrm{E}-4$	$9.18\,\mathrm{E}-8$	$3.62\,\mathrm{E}-3$	$8.34\,\mathrm{E}-3$	$5.05\,\mathrm{E}-4$
n's	^{238}U	NRSS	$4.06\,\mathrm{E}-5$	$1.38\,\mathrm{E}-3$	$1.83\,\mathrm{E}-3$	$1.73\,\mathrm{E}-2$	$7.22\,\mathrm{E}-4$
n's	^{238}U	NRMS	$4.06\,\mathrm{E}-5$	$2.83\,\mathrm{E}-3$	$4.23\,\mathrm{E}-3$	$3.59\,\mathrm{E}-2$	$2.02\,\mathrm{E}-3$

Table 8.4: ERSS, ERMS, NRSS, and NRMS rates, in units of $\left[\mathrm{kg\,yr}\left(\mathrm{mBq\,kg}^{-1}\right)\right]^{-1}$ from the different decay-geometry sources in the SuperCDMS SNOLAB passive shielding study. The rates from the twelve tower housings and the six cryostat cans are each respectively combined into single sources in the table. ERs are generated by both γ and n decays while NRs are generated only by n decays.

Rates

The NR and ER single- and multiple-scatter rates are computed using Eq. 6.1 with an analysis range of 10–100 keV. For multiple scatters, an event is counted if the event-type of consideration has a recoil within the 10-100 range and another detector has any type of recoil above 2 keV. The rate of each event type for each source per exposure and contamination level is given in Table 8.4. The outer poly source had very small, if any statistics, and uncertainties on those rates are $\mathcal{O}(100\,\%)$.

Contamination levels for each of the sources in each of the materials are assumed in order to combine the difference sources. These contamination levels are from a literature search of "reasonably" achievable levels and are given in Table 8.5. The final

Decay	Polyethylene	Lead	Copper
^{232}Th	0.2	0.5	0.02
^{238}U	0.3	2.0	0.1
^{40}K	1.0	7.0	0.04

Table 8.5: Contamination levels, in $\mathrm{mBq\,kg^{-1}}$, assumed for each decay and source combination in the SuperCDMS SNOLAB passive study.

Type	Electron Recoil	Nuclear Recoil
Single Scatters	$(2.81 \pm 0.17) \times 10^{+2}$	$(5.53 \pm 0.20) \times 10^{-3}$
Multiple Scatters	$(6.11 \pm 0.27) \times 10^{+2}$	$(1.17 \pm 0.03) \times 10^{-2}$
Singles/Multiples Ratio	0.46 ± 0.04	0.47 ± 0.02

Table 8.6: Total ERSS, ERMS, NRSS, and NRMS rates from summing all sources in the SuperCDMS SNOLAB passive shielding study. Rates are in units of $[\mathrm{kg\,yr}]^{-1}$. The ratio of the singles and multiples rates is also given and is comparable between the two recoil types. Poisson uncertainties due to the statistics of the simulation are given.

total rates for the different event types are found by summing of all individual source rates, weighted by their respective contamination levels, and are given in Table 8.6. Also presented is the ratio of single scatters to multiple scatters. This ratio is directly related to the number, and positioning, of detectors. Values of ~0.5 are seen here, compared to ~0.8 in CDMS II and ~1 in SuperCDMS Soudan, indicating the benefit of having a larger number of individual detectors.

8.2.3   Secondary Studies

The geometry for the main study was somewhat arbitrarily chosen. Although based on the Soudan passive shield, the necessity of each component and the individual thicknesses were selected without detailed study. Two follow-up studies are also performed to explore those decisions and illuminate later decisions. For these simulations, the geometry is the same as the main study expect for a specific change in each. This implies that vacuum replaced shield materials when the shield components were thinned or removed. These are gaps which would not exist in a final geometry so these results are

very rough. Additionally, in light of the poor statistics in the main study, the number of primary n's from the outer three layers of the shield is increased, which also decreases the final uncertainties. For each decay-source, 1×10^7 n's are simulated from the outer poly and 5×10^6 n's from both the lead and inner poly.

Reduction of Cryostat Thickness: The cryostat cans are 0.5 in. thick in the main study and are the largest contributor, per contaminant, to the NRSS rate as seen in Table 8.4. The advantage to the thicker cans is that copper is a reasonable γ shield. Given the iZIP's rejection ability with ERs, a higher ERSS background could be acceptable if it lowered the NRSS background. To test this effect, the cryostat cans are reduced to be 0.125 in. thick. The final rates in this scenario are given in Table 8.7. As expected, the ER rates increase, by a factor of ~3. The NRSS rate decreases by 16 %, which is significant compared to the 2 % uncertainty.

Removal of Inner Poly Shield The inner poly layer is the second highest source of NRSS events, per contaminant, after the cryostat cans. This study eliminates the inner poly to determine whether it contributes more events than it shields. The final rates in this scenario are given in Table 8.8. The ER rates are statistically identical to the main study, while the NR rates increases by a factor of ~20. The inclusion of the inner poly layer reduces the NR rates significantly.

Type	Electron Recoil	Nuclear Recoil
Single Scatters	$(8.95 \pm 0.51) \times 10^{+2}$	$(4.62 \pm 0.10) \times 10^{-3}$
Multiple Scatters	$(1.99 \pm 0.80) \times 10^{+3}$	$(9.10 \pm 0.13) \times 10^{-3}$
Singles/Multiples Ratio	0.45 ± 0.03	0.51 ± 0.01

Table 8.7: Total ERSS, ERMS, NRSS, and NRMS rates from summing all sources in the SuperCDMS SNOLAB passive shielding study with thin cryostat cans. Rates are in units of $[\text{kg yr}]^{-1}$. Poisson uncertainties due to the statistics of the simulation are given. The thinner cans increases the ER rates by a factor of $\sim$3 while reducing the NRSS rate by 16 %. The singles-to-multiple ratio also increased, implying better multiple scatter rejection efficiency.

Type	Electron Recoil	Nuclear Recoil
Single Scatters	$(2.81 \pm 0.14) \times 10^{+2}$	$(1.02 \pm 0.01) \times 10^{-1}$
Multiple Scatters	$(6.48 \pm 0.26) \times 10^{+2}$	$(2.25 \pm 0.01) \times 10^{-1}$
Singles/Multiples Ratio	0.43 ± 0.03	0.45 ± 0.01

Table 8.8: Total ERSS, ERMS, NRSS, and NRMS rates from summing all sources in the SuperCDMS SNOLAB passive shielding study with no inner poly. Rates are in units of $[\text{kg yr}]^{-1}$. Poisson uncertainties due to the statistics of the simulation are given. The removal of the inner poly has minimal effect on the ER rates but increases the NR rates by a factor of $\sim$20. Without the inner poly, the number of neutrons reaching the detectors greatly increases, which leads to the smaller uncertainty on NR rates compared to other studies.

Part III

CDMSlite Run 2
WIMP-Search Analysis

Chapter 9

CDMSlite Run 2

9.1 Motivation

Several factors motivate searches for dark matter of mass $\mathcal{O}\left(\lesssim 10\right)$ GeV/c^2. The absence of experimental evidence for historically favored theories, such as supersymmetry, has led to the development of many low-mass WIMP theories, such as asymmetric dark matter (Sec. 2.2.3). Additionally, the few observed experimental above-background excesses can all be interpreted as evidence for low-mass WIMPs (see Sec. 3.6). While an experiment's sensitivity to high-mass WIMPs is mainly dependent on its exposure, its sensitivity to low-mass WIMPs is mainly dependent on experimental factors such as target nuclei, threshold, noise resolution, etc. In light of this, the SuperCDMS experiment developed a non-standard operating mode for an iZIP detector, which allowed for significantly lower thresholds to be reached. This operating mode is called the CDMS low ionization threshold experiment (CDMSlite).

CDMSlite utilized the amplification of the recoil energy through Neganov-Trofomiv-Luke (NTL) phonons such that the total phonon signal is (Sec. 4.3.3)

$$E_{\mathrm{t}} = E_{\mathrm{r}}\mathcal{A}(V_b), \tag{9.1}$$

recalling the amplification factor $\mathcal{A}(V_b) = (1 + Y(E_{\mathrm{r}})g(V_b))$. Using NTL phonons to amplify the ionization signal was first demonstrated by Luke in 1988 [272]. Luke showed that an ionization signal could be read out through the thermal sensors on a crystal,

and more importantly that the amplitude of this thermal signal increased by increasing the applied bias potential. Luke later demonstrated that the noise did not depend upon the bias potential [313] (at least until break-down of the crystal was observed), and so also demonstrated that a small recoil signal which was below the noise value for no applied bias could be boosted above the noise value at higher bias potentials due to the NTL-phonon contribution. This in turn led to lower thresholds when considering the initial recoil energy.

This effect is demonstrated using simulated data in Fig. 9.1. Two peaks with initial recoil energies of 0.16 and 1.30 keV are simulated on top of a flat background. The location, and ratio, of the peaks are not arbitrary and correspond to electron-capture decay peaks of ^{71}Ge, activation lines seen clearly with CDMSlite. These peaks are near the typical noise threshold of iZIP detectors and include the sub-keV scale. The total phonon energy at three different bias potentials is simulated using a data-driven model for energy resolution (Sec. 12.2). The relative location of the peaks with respect to the noise increases with bias potential. Of particular interest is the lower energy peak, which is unobservable at the lowest bias potential, is observable but of unknown shape at the intermediate potential, and is fully resolved at the highest potential. This indicates that the effective energy threshold, when converted to recoil energy, is lowered as the potential increases.

The advantage of having a lower recoil threshold in a SuperCDMS detector in looking for low-mass dark matter is demonstrated in Fig. 9.2. This figure shows the expected nuclear recoil spectrum from WIMPs of three different WIMP masses (2, 5, and 10 GeV/c^2) with a fixed spin-independent WIMP-nucleon cross section of $\sigma_p^{SI} = 1.5 \times 10^{-41}$ cm^2 on a germanium target. Two threshold values are also given in the figure, one typical of the standard iZIP configuration ($\sim$1.6 keV) and one typical of the CDMSlite high-voltage[1] configuration (0.5 keV). The lower threshold allows for a significantly larger portion of the 5 and 10 GeV/c^2 WIMP-recoil spectra to be observable. Lighter WIMPs will, in general, deposit less energy per recoil, and, since there is a maximum WIMP velocity, there exists a minimum WIMP mass which is able to deposit a given amount of energy. Decreasing the lower threshold for CDMSlite also gives access to WIMPs

---

[1] Here and further uses of "high-voltage" in the CDMSlite context refer to when $eV_b \gg \epsilon_\gamma$, giving biases of order 10's V. This is opposed to the potentials applied across standard high-purity germanium detectors which are of order kV.
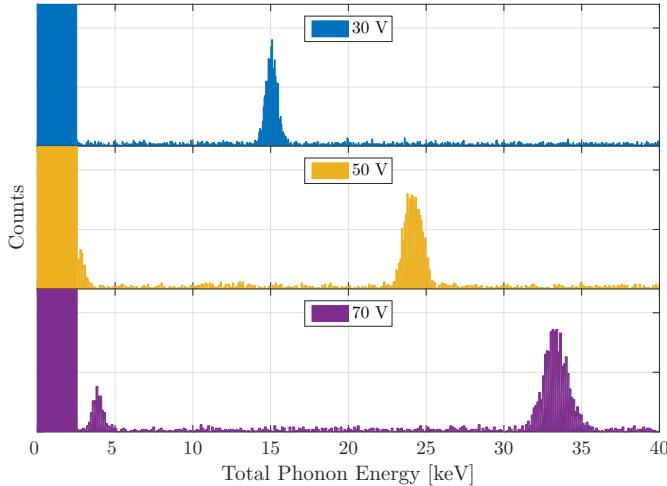
Figure 9.1: Simulated phonon spectra at three different bias potentials demonstrating NTL amplification. Two electron-recoil peaks with recoil energies of 1.30 and 0.160 keV are on top of a flat background with different biases in each plot. The location of the noise does not change with increases in potential, but the lower energy peak is unobservable at the lowest bias potential, is observable but of unknown shape at the intermediate potential, and is fully resolvable for the highest potential.

which are completely unobservable at higher thresholds, such as WIMPs of ~ 2 GeV/c^2 as evidenced in the figure.

The first testing of CDMSlite was performed in test facilities using a CDMS II silicon detector [314, 315]. Further tests with CDMS II germanium and silicon detectors at Soudan, as well as early versions of SuperCDMS iZIP detectors (also germanium), demonstrated the feasibility of stable operations in such a mode [316, 317]. This led to the first science-data to be taken with CDMSlite in 2013, which is called CDMSlite Run 1, or simply Run 1, throughout. The details of the operations and analysis of this run are the subjects of Refs. [260, 275].

A single SuperCDMS iZIP detector (iT5Z2, mass 606.5 g) was used for Run 1 at a nominal bias potential of -69 V.[2] The data was gathered over three short periods in August–September 2013 with a raw run-time of 15.79 days. There were several operational difficulties in this data set which required the removal of a substantial portion of the live time and resulted in a final run-time of only 10.32 days, or an exposure of 6.25 kg days. Minimal data cuts were applied; notably no fiducial volume cut was used. The data obtained can be seen in Fig. 9.3 calibrated to keV$_{ee}$, recalling that the electron-equivalent energy scale assumes unity yield, and corrected for efficiency (except

---

[2] Subsequent studies have called this bias potential into question, see Sec. 10.2.1.
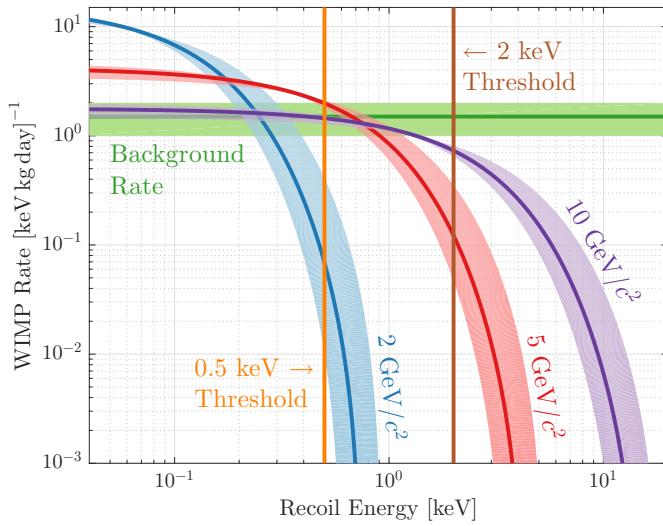
Figure 9.2: Expected recoil spectra for different WIMP masses along with thresholds typical of operating in standard iZIP (brown) and CDMSlite (orange) configurations. The solid recoil curves give the WIMP recoil rate for several WIMP masses each with a WIMP-Nucleon spin-independent cross section of $\sigma_{SI} = 1 \times 10^{-41}$ cm^2. Uncertainty bands are astrophysical. A typical ER background rate is given by green. The CDMSlite threshold increases sensitivity to all three WIMP masses.

trigger efficiency). The ^{71}Ge K- and L-shell electron-capture lines (see Sec. 10.2) are visible at 10.37 and 1.30 keV$_{ee}$ respectively on top of a continuous background.

The analysis threshold used for the analysis of Run 1 was set at 170 eV$_{ee}$. The limiting factor in this determination was the presence of non-electronic low-frequency noise which dominated below $\sim$100 eV$_{ee}$. Converting to the nuclear-recoil equivalent energy scale gave a threshold of 841 eV$_{nr}$ and world-leading upper limits between masses of 2.8–6 GeV/c^2. The 90% upper-limit on the spin-independent WIMP-nucleon cross
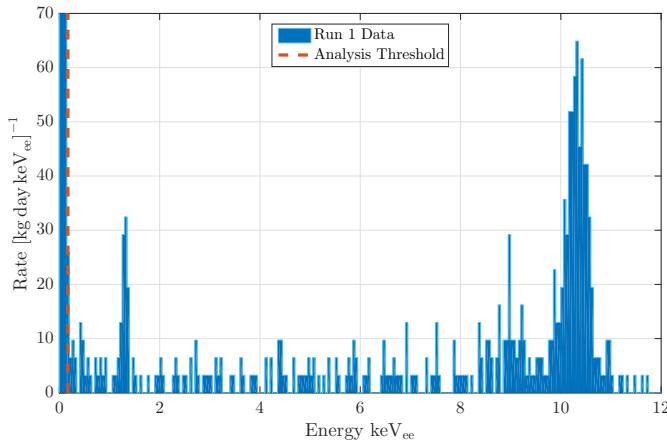
Figure 9.3: Final event spectrum from CDMSlite Run 1 calibrated to keV$_{ee}$ and corrected for efficiency (except trigger efficiency). The ^{71}Ge K-shell (10.37 keV$_{ee}$) and L-shell (1.30 keV$_{ee}$) electron-capture lines on top of a Compton background can be seen. The analysis threshold is shown at 170 eV$_{ee}$ (dashed orange).
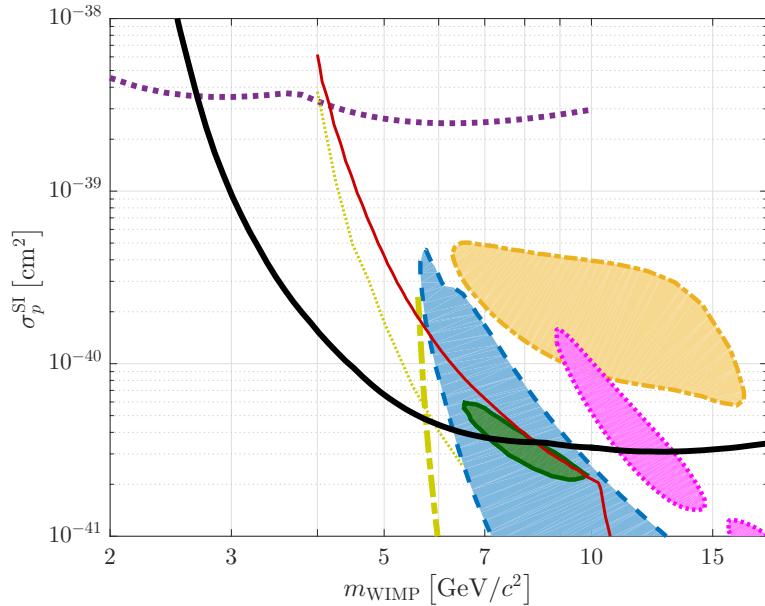
Figure 9.4: Run 1 90% confidence level upper limit on WIMP mass and spin-independent cross section (thick solid black) [260] compared to regions and leading/important limits at the time of the Run 1 result. Closed regions are the CDMS IISi 90% C.L. (blue dashed shaded) [233], CoGeNT 90% C.L. (dark-green solid shaded) [234], DAMA/LIBRA 95% C.L. (tan dashed-dot shaded) [235, 236, 318], and CRESST-II 95% C.L. (magenta dotted shaded) [232]. The other 90% upper-limits shown are CDMS II Ge combined (red thin solid) [223, 244], LUX (dark-yellow thick dashed-dot) [216], XENON10 S2 only (dark-yellow thin dotted) [250], and DAMIC (purple thick dotted) [257]

section set with these data is shown in Fig. 9.4 compared to relevant results at the time of its publication.

The success of the first CDMSlite run motivated the taking of a second CDMSlite data set, hereafter called Run 2, which began commissioning in December 2013 and took science data from February 2014 to November 2014. Several areas were identified to improve upon the Run 1 result and are classified in two categories, those which allow for lower WIMP masses to be achieved and those which allow for lower cross sections to be reached:

Lower WIMP Masses:

- Better reject low-frequency noise
- Lower physical threshold

- Lower attainable threshold

Lower Cross Sections:

- Increase exposure

- Increase duty-cycle

- Reduce backgrounds (fiducial volume)

Many of these improvements were addressed by altering the operational and data-taking procedures during the extended Run 2 commissioning period.

9.2   Commissioning

CDMSlite Run 2 was commissioned starting in mid-December of 2013 and ending at the start of February 2014. This commissioning consisted of modifications to and installation of new CDMSlite adapter boards, selection of a detector, optimization of the applied bias voltage, and investigation of the optimal operating routine.

9.2.1   Electronics Improvements

Using knowledge learned from Run 1, two new CDMSlite-biasing adapter boards (Sec. 5.3) were made for Run 2. In Run 1, the potential across the detector was seen to vary with time as observed by a $\lesssim 10\%$ change in the NTL amplification. This implies that, in addition to the desired circuit across the crystal, there was an alternative route, through some parasitic resistance R_p, which current from the high-voltage power supply (HVPS) could take. The current through this additional circuit branch is labeled the leakage current. The existence of the leakage current reduced the bias applied across the crystal compared to the applied bias, which in turn reduced the NTL amplification.

After Run 1 follow-up tests were done with its adapter board at a test facility (R. Basu Thankur) and humidity was observed to have an effect on the bias current. The new adapter boards for Run 2 were ultrasonically cleaned, baked overnight, and then covered in a humi-seal specifically to reduce the impact of humidity changes on the electronics. Lab bench tests indicated a decrease in leakage current by a factor of ≥ 10 due to this treatment of the boards [275]. The new boards were mounted underneath

the front-end electronics boards at Soudan, where cooling fans are used. Additionally, a dry N_2 purge line was placed inside one of the boards with the same intentions.

Although the leakage current was expected to have less variability in Run 2 than in Run 1 due to the above improvements, steps were also taken to monitor the leakage current in real time. The HVPS maintained a constant voltage V_b, but if the resistance along the circuit were to change, i.e. a time varying R_p, than the HVPS biasing current I_b must also necessarily have changed. For Run 2, I_b was recorded in a database and folded into the data processing so that its time variance could be used in analysis as a proxy for the varying parasitic resistance. Additionally, the total resistance on the adapter board was reduced. In order to protect the coupling capacitor in the charge read-out circuit, a large load resistor R_L was required on the adapter board. For Run 1, $R_L = 400$ MΩ as the maximum bias was as yet unknown. Assuming Run 2 would operate at a similar bias as Run 1, the load resistor was decreased to $R_L = 195$ MΩ on the new boards. A smaller total effective resistance in the circuit, caused by reducing R_L, meant that I_b had to be larger to maintain the same biasing potential. This made I_b easier to monitor and use in the analysis.

9.2.2   Detector Selection

The first step in determining if a detector could be used for CDMSlite was to perform a bias-voltage scan, where the applied potential was increased and the performance of the detector monitored for both detector break-down and any shorts in the electronics. Figures 9.5(a)–(c) show the results of quick bias scans performed on three detectors of interest. iT5Z2 was known to hold high biasing due to Run 1, and iT2Z1 and iT4Z1 were better performing detectors in iZIP mode. The figures show the appliedV_b compared to the steady-state applied I_b. The circuit was Ohmic, as expected, with the linear relationship between the bias and current having a slope of $1/R_{tot}$, where R_{tot} was the total resistance seen by the HVPS.

In the steady-state configuration with no parasitic resistance, one would expect no change in I_b with V_b. The fact that I_b did increase with V_b indicated a short somewhere in the circuit. Tests were performed with the detectors disconnected and I_b did not change with V_b to within the resolution of the ammeter (0.1 nA), indicating that $R_p \gtrsim 10$ GΩ was large. The total resistances seen in Fig. 9.5 are ~ 2 GΩ for iT4Z1 and iT2Z1 and

(a) iT4Z1
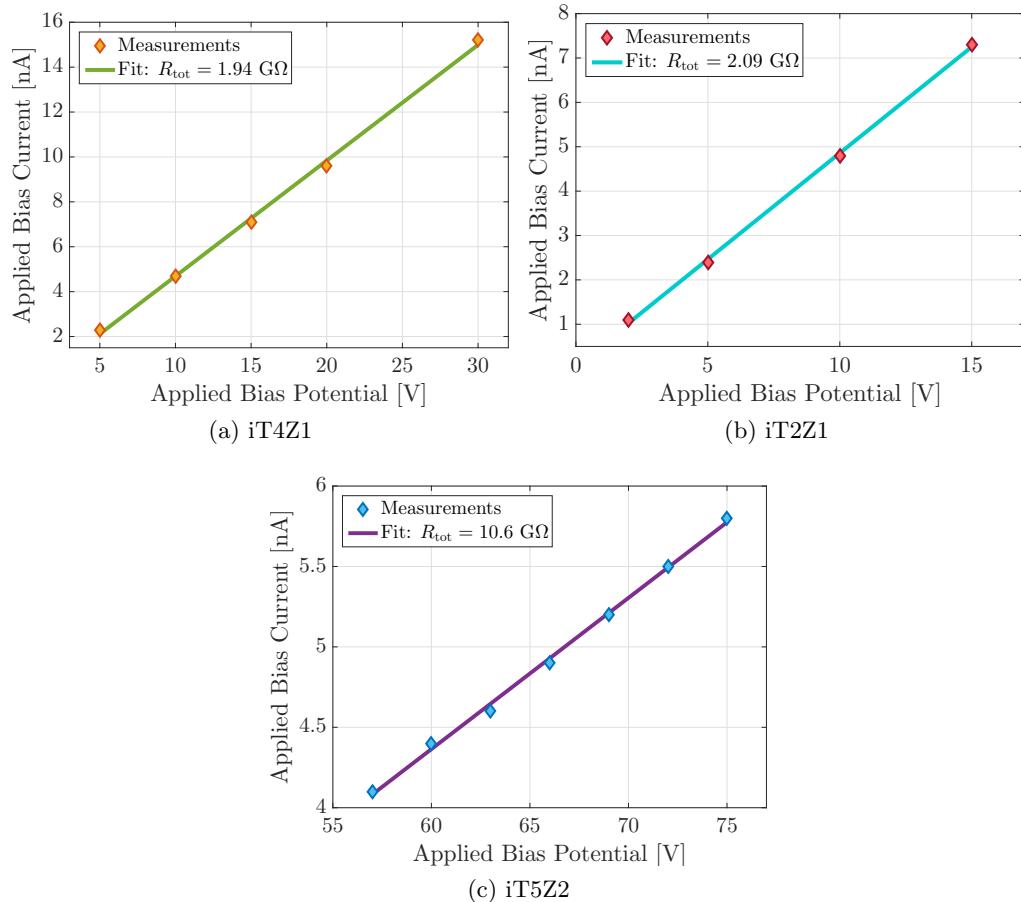
(b) iT2Z1

(c) iT5Z2

Figure 9.5: Voltage scan measurements and linear fit of applied bias vs. applied current for iT4Z1, iT2Z1, and iT5Z2 from the commissioning of CDMSlite Run 2. The inverse of the slope gives the total resistance encountered in the circuit. A smaller resistance indicates poorer detector performance in CDMSlite mode.

$\sim$10 GΩ for iT5Z2. The lower total resistance on the two new detectors indicated some short beyond the adapter board while iT5Z2 was consistent with no short beyond the adapter board.

How such a short, of unknown origin, would effect operating in CDMSlite mode was uncertain at the time of commissioning. Coupled with an urgency to start Run 2, it was decided to again run the same single detector as Run 1, iT5Z2, in CDMSlite mode. This operating mode started in January 2014 and was until the end of the run.

9.2.3   Bias Selection

After the selection of iT5Z2 for use in Run 2, the next commissioning step was to determine an optimal applied bias voltage to operate the detector with. A more detailed bias scan[3] was performed to assist in this decision. The two goals for looking at the bias scan data were to see signs of detector break-down and to optimize the signal-to-noise ratio.

To determine the optimal bias for CDMSlite, the distribution of random triggers for each bias was considered: a sign of detector break-down was an increase in the width of the noise distribution. Figure 9.6 shows the width of the noise distribution at different biases, with three series shown per bias. The series of interest here underwent a process termed "pre-biasing" which reduced the width of the noise distribution (next section). The width was found by computing the CDF of the energy distribution and finding the energy where the CDF crossed 0.84, i.e. the $\mu + \sigma$ Gaussian equivalent value.[4] The width of the noise remained constant with bias voltage (to within the spread of the series) for biases up to $\sim$70 V after which a slight increase was observed. To first order, this indicated that the nominal voltage of 69 V for Run 1 was close to optimal and that such a potential should also be used in Run 2.

The signal-to-noise ratio (SNR) was another metric used to indicate the optimal bias potential for CDMSlite. In order to create a recoil-energy-independent SNR metric, the signal $\mathcal{S}$ and noise $\mathcal{N}$ quantities were defined as ratios compared to a 0 V bias potential.

---

[3] This scan was more "detailed" when compared to the scans done to select the detector as more data was taken at each bias the data were saved and processed.

[4] The OF0 energy estimator was used for these noise studies.
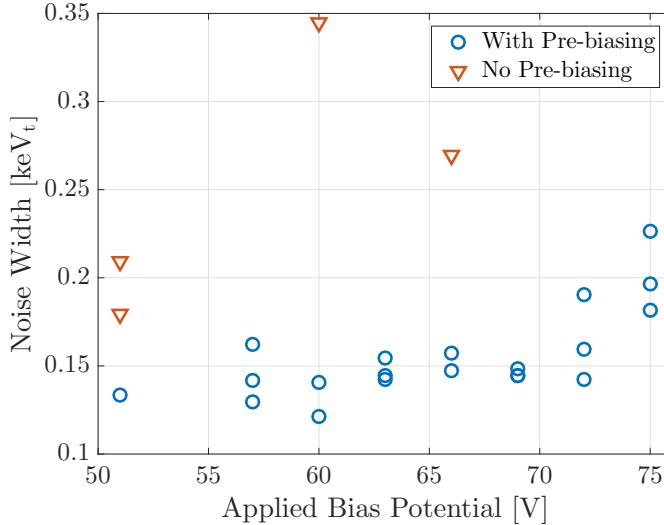
Figure 9.6: Width of the noise distribution at different high-voltage bias potentials for series which were pre-biased (circles) and those which were not (downward triangles). The width of the noise remained mostly constant until biases of $\sim$70 V, where detector break-down was observed. Pre-biasing mitigated the detector-based leakage current observed in Run 1 and reduced the width of the noise distribution.

These ratios were

$$\mathcal{S} = \frac{E_{\mathrm{t}}(V_b)}{E_{\mathrm{t}}(0)} = \mathcal{A}(V_b) \tag{9.2}$$

$$\mathcal{N} = \frac{\sigma(V_b)}{\sigma(0)}, \tag{9.3}$$

where $\sigma(V_b)$ is the measured width of the noise at a given potential and the width at 0 V was assumed to be 110 eV$_{\mathrm{t}}$. The SNR was then only dependent on the bias and scaled by the 0 V noise width as

$$\mathrm{SNR} = \frac{\mathcal{S}}{\mathcal{N}} = \sigma(0) \cdot \frac{\mathcal{A}(V_b)}{\sigma(V_b)}. \tag{9.4}$$

The SNRs for the same series as in Fig. 9.6 are shown in Fig. 9.7. Although there was large variance at each bias, a trend was seen where the SNR increased until biases of $\sim$70 V, where it then decreased. This behavior corroborated the observation of increased noise width at $\sim$70 V.

Initially during the commissioning process, the bias potential was set to 60 V while this optimal-bias study occurred; about 1 month of 60 V data was taken. These studies showed that increasing the bias to 70 V would be better. At the start of February 2014, the bias potential was increased to 70 V, where it remained for the duration of Run 2.
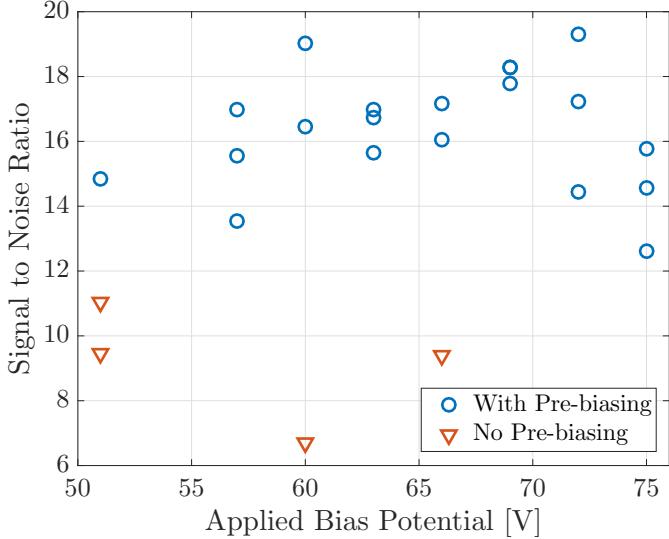
Figure 9.7: Signal-to-noise ratio (SNR) at different high-voltage bias potentials for series which were pre-biased (circles) and those which were not (downward triangles).The SNR increased until biases of ~70 V and and then decreased. Pre-biasing reduced the noise and therefore increased the SNR.

9.2.4   Optimal Operating mode: Pre-biasing

One of the large operational problems with CDMSlite Run 1 was the presence of detector-sourced leakage current observed immediately after the high-voltage bias was applied. This current was accompanied by a high rate of noise events seen in the detector. The rate of these events decayed away quasi-exponentially with time constants of $\mathcal{O}(10 \text{ min.})$. This phenomena was covered extensively by Basu Thakur in Appendix B of [275], with a theoretical explanation proposed based upon trapped charges being released in the presence of a stronger electric field. The detector leakage current (not to be confused with the parasitic-resistance-based leakage current) was again observed in Run 2. An example of the high-rate of noise after the application of the potential is shown in Fig. 9.8 for a single series taken during the commissioning process at $V_b = -66$ V. The energy[5] of events as a function of time since the series started, when the bias was applied, is shown. A higher density of events with higher reconstructed energy near the start of data taking is seen. These events decayed away and were absent by ~20 minutes into the series. In Run 1, a cut was developed which fit the decay rate to an exponential and the first 4 time-constants worth of data was removed. This cut removed ~30 % of each series, greatly reducing the duty-cycle and final live time.

The trapped-charge theory for these events posits that that the probability for a

---

[5] Using the OF0 energy reconstruction.
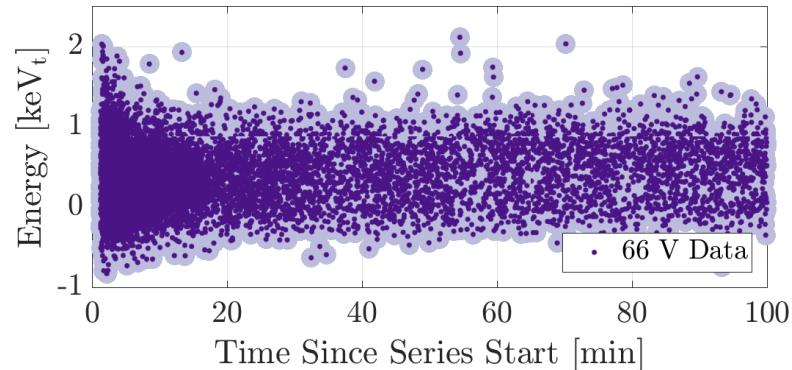
Figure 9.8: Event energy as a function of time since the start of a data series showing a higher density of high-energy events at the start of the series, corresponding to detector-based leakage current. This series was taken during CDMSlite Run 2 commissioning with an applied bias of -66 V.

trapped charge to escape the trapping potential increases as the applied electric field increases, which explains why this effect was prominent in CDMSlite but not in standard iZIP operations. A corollary is that, if a detector is biased to some potential difference V_2, for a long enough time to clear the trapped charges accessible at the corresponding electric field, and then dropped to some potential difference $V_1 < V_2$, then the trapped charges accessible to the electric field at V_1 should already be clear and no leakage current should be observed. This was the basis behind pre-biasing the CDMSlite detector to a larger potential difference prior to each data series.

The operational procedure behind pre-biasing is shown in Fig. 9.9 by considering the applied bias and current from the HVPS as a function of time during the end of one series and lead-up to the next series. The potential difference started at 70 V with a steady current of ~6.4 nA corresponding to the end of a 3 hour long series. This first series ended at 04:38 when the detector was grounded for LED flashing. After the LED flash, a ten minute cool-down period was required to return the experiment to base temperature. During these ten minutes, when no data was taken, the detector was biased to a potential difference of 80 V. The detector-based leakage current was then observable by a sharp increase and decay in the HVPS current which then reached a steady state by the end of the ten minutes. After the cool-down, the detector was reconfigured for data taking and the applied bias was reduced to the data-taking difference of 70 V. The next
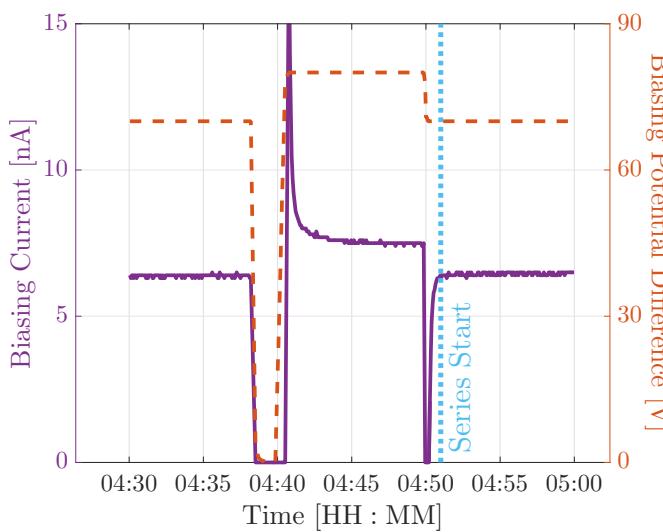
Figure 9.9: Operational procedure for pre-biasing the CDMSlite detector demonstrated through the HVPS applied current (purple solid on left axis) and bias (orange dashed on right axis) over time. Between the end of one series and the start of another (blue dotted line), both biased at 70 V, the bias was held at 80 V. When the potential difference was increased, the current sharply increased, mirroring the detector-based leakage current noise seen in the detector, and decayed to a constant ∼7.5 nA. The steady state current at a 70 V bias was ∼6.4 nA, which was lower than while at 80 V and indicative of some total parasitic resistance.

series started at 04:51, at which point the current was constant at the same ∼6.4 nA value as the steady-state current with no indications of leakage current. Note also the difference in steady-state currents at 70 and 80 V, indicative parasitic resistance.

The proof that this procedure produced higher quality data is apparent from Fig. 9.10 for a series which was pre-biased prior to taking data. This was another Run 2 commissioning series which was taken 19 hours apart from, and at the same potential as, the non-pre-biased series in Fig. 9.8. The higher density of high-energy events is now absent from the beginning of the run, as was desired.

The quantitative improvement due to pre-biasing is seen by comparing the noise widths in Figs. 9.6 and 9.7. Series which were not pre-biased are shown as downward triangles and those that were pre-biased are shown are blue circles. The series which were not pre-biased had a significantly larger noise width, driven by the leakage-current events at the start of the series, which in turn led to reduced SNR. It should also be noted that the two series highlighted in Figs. 9.8 and 9.10 are also used in Figs. 9.6 and
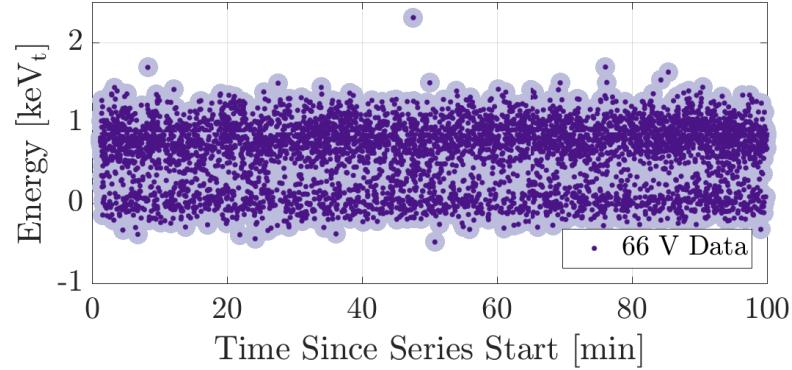
Figure 9.10: Event energy as a function of time since the start of the data series for a series which was pre-biased. The higher density of high-energy events at the beginning of the run, i.e. the detector leakage current, was not seen due to the pre-biasing. This series was from the CDMSlite Run 2 commissioning period taken 19 hours apart from at the same applied bias, -66 V, as the non-pre-biased series shown in Fig. 9.8.

9.7.

   To conclude, pre-biasing was a major operational improvement for CDMSlite Run 2. In eliminating the detector-based leakage current, no series-by-series live-time cut was required (increased duty-cycle), and the noise environment greatly improved, giving reduced noise distribution width (decreased threshold) and increased signal-to-noise (improved resolution).

9.3   Noise Monitors

The noise observed in the analysis of SuperCDMS data can be broken down into three categories: electronic σ_{elec}, vibrational σ_{vib}, and detector-based σ_{det}. The total noise σ_{tot} is then

$$\sigma_{\mathrm{tot}}^2 = \sigma_{\mathrm{elec}}^2 + \sigma_{\mathrm{vib}}^2 + \sigma_{\mathrm{det}}^2. \tag{9.5}$$

Reducing the noise in the experiment is particularly important for near-threshold searches, where the noise and true events become confused. The pre-biasing procedure reduced σ_{det}. To reduce σ_{vib} and σ_{elec}, eight new sensors were installed in Soudan to monitor potential sources of noise and look for correlations between events in the detectors and activity elsewhere in the experiment. The names and locations of these

Name	Type	Location	Panel
Setra	Voltage Driven Acc.	Cryocooler	(i)
COUPP	Piezoelectric Acc.	E stem exterior	(ii)
Acc0	Constant Current Acc.	C stem/Fridge Bottom	(iii)
Acc1	Constant Current Acc.	Fridge Top	(iv)
Acc2	Constant Current Acc.	LH E stem, outside shield	(v)
Acc3	Constant Current Acc.	LH E stem, inside shield	(vi)
Ground	Wire to Rack Ground	Electronics Room Rack	(vii)
60 Hz	Transformer to Rack Power	Electronics Room Rack	$(viii)$

Table 9.1: Name, type, and location of each of the eight noise monitor sensors. The first six sensors monitor vibrational noise sources while the last two monitor electronic noise sources. The "Acc." in the second column is short for accelerometer. The Acc3 sensor was nonfunctional after installation. "LH" stands for the 4 K, i.e. Liquid Helium, stage of the cryocooler (interior of the E stem). The last column gives the panel number corresponding to Fig. 9.11 [319–322].

eight sensors are given in Table 9.1. The first six were meant to monitor vibrational noise sources while the last two were meant to monitor electronic noise sources. Unfortunately, the accelerometer inside the shield on the 4 K stage of the E-stem was found to be non-functional after installation. The last column of the table gives numbers corresponding to the traces in Fig. 9.11 which shows example outputs from the monitors for two events.

The threshold for Run 1 was set at 170 eV$_{ee}$, mainly due to the high rate of low-frequency noise (LF-noise) below $\sim$100 eV$_{ee}$. The zero-energy noise width (σ_{elec}) of Run 1 was significantly less than 100 eV$_{ee}$, which implied that emphasis should first go towards reducing σ_{vib}. There had long been suspicions that this LF-noise was correlated with the cryocooler, implying that LF-noise was vibrational in nature.

The accelerometers attached to the fridge showed very little sign of vibration while those attached to the cryocooler and E stem showed significant activity. This is unsurprising since the mechanical action of Gifford-McMahan cryocoolers, such as the one used in Soudan, is known to create vibrations of $\mathcal{O}(20~\mu\text{m})$ at the cooled sample [323]. This made the cryocooler the prime suspect for the creation of the LF-noise and the Setra and COUPP sensors the most important to monitor as shown in Fig. 9.11. The
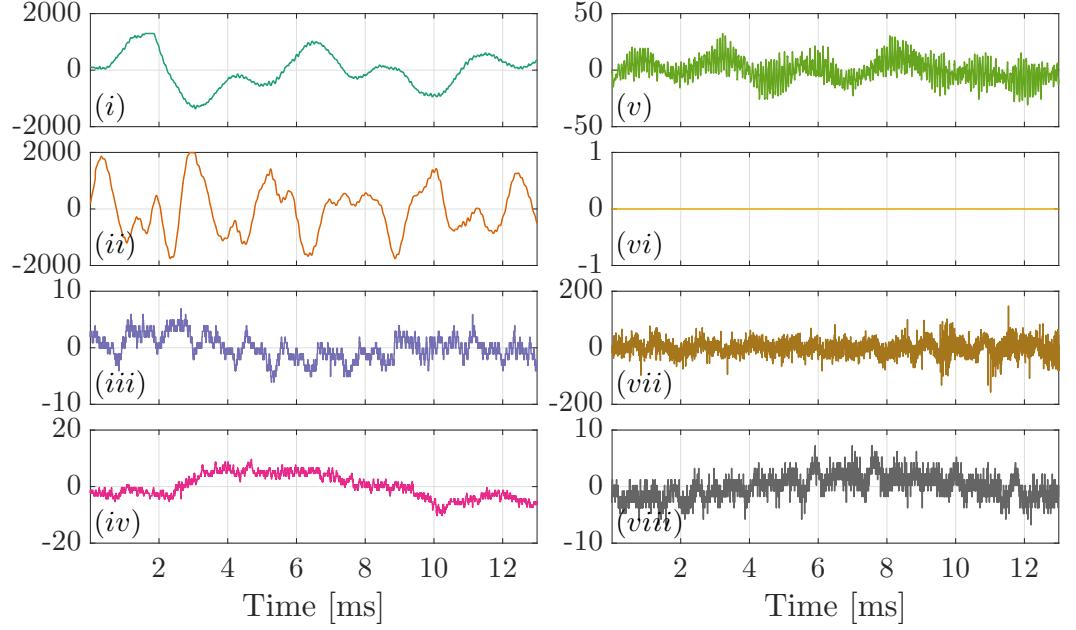
(a) Active Portion
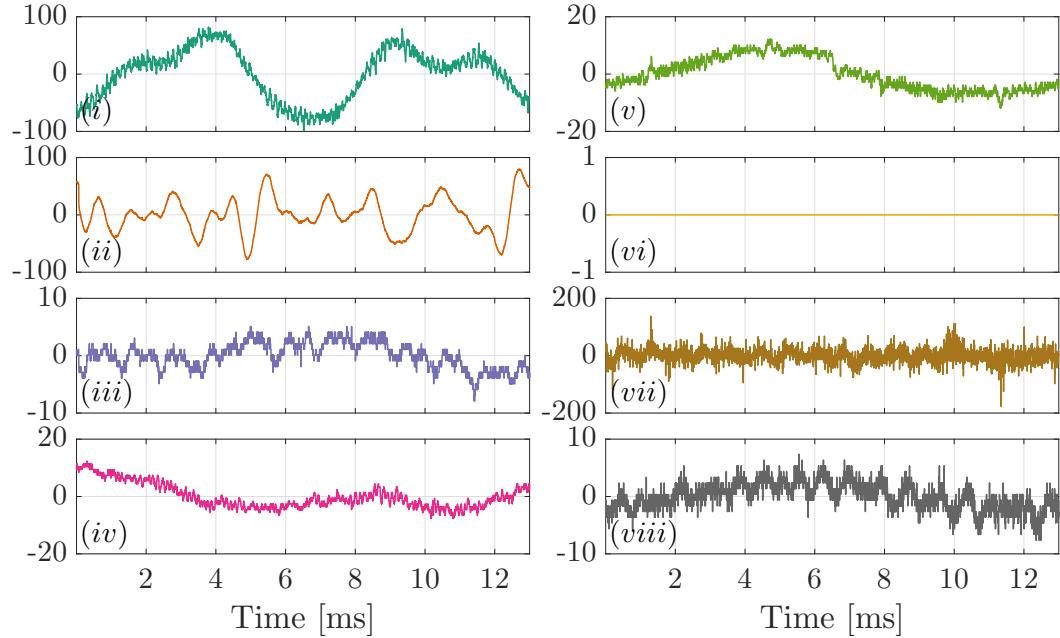
(b) Passive Portion

Figure 9.11: Noise monitor output traces for two events, occurring the during active (top) and passive (bottom) portions of the cryocooler cycle. The eight panels correspond to the eight sensors with roman numerals assigned in Table 9.1. The vertical scale of any given monitor is arbitrary, but the same between the two events. The 20× increase in scale for the Setra (i) and COUPP (ii) traces between the figures indicated their sensitivity to the cryocooler.
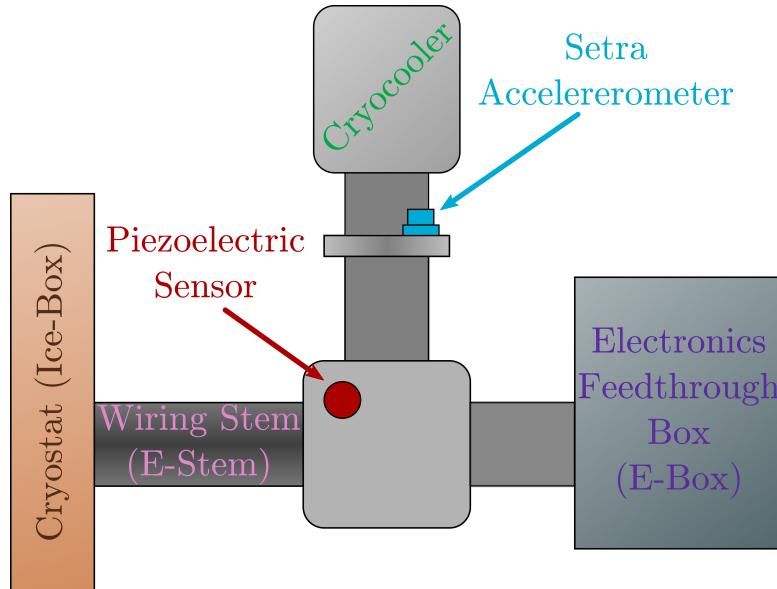
Figure 9.12: Cartoon showing the locations of the Setra accelerometer and COUPP piezoelectric sensor relative to the cryocooler, cryostat, and electronics feed-through box. Figure adapted from [275].

specific locations of these two monitors on the cryocooler are shown in Fig. 9.12.

The read-out system for these sensors was designed to give two types of signals; the first being a digitized trace of the sensor output and the second being a NIM pulse to be used as a time stamp for certain noise sources. A custom transducer box, designed by R. Basu Thakur, was used to accomplish this [319–321]. The vibration sensors' signals were fed into the box, where they were first amplified (5–50 driver gain [321]) and then cleaned via a low pass filter (characteristic frequency of 50 kHz (Setra) or 10 kHz (others) [324]). The trace signals were then sent to a digitizer from the muon veto electronics and fed into the standard data stream. The rack ground and 60 Hz transformer outputs were fed directly to the digitizer. In the transducer box, the signals from the Setra and COUPP sensors were split prior to digitization with the second copy of the signal being sent to a threshold discriminator. Over the course of installation, the Setra was identified as the more sensitive of the two redundant sensors and a NIM pulse was generated when the maximum of the Setra trace was above a 1–2 V threshold [321]. This NIM pulse was smoothed through a gate generator (10 ms width) to ensure a single

NIM pulse per cryocooler cycle. The smoothed pulse was fed into the time-stamp unit used for the muon veto panels, which was also fed into the data stream. The output is summarized as seven digitized traces and one time-stamp indicating the time of largest vibration in the cryocooler cycle. The timing information is particularly important for use in analysis.

9.4   Run 2 Data Periods

The commissioning period of Run 2 occurred during December of 2013 and January of 2014, and science data officially started on February 4, 2014 when the operational configuration of 70 V applied potential difference with pre-biasing at 80 V was finalized. A timeline of all data periods relevant to Run 2 is given in Fig. 9.13. The run was split into two main pieces and contained both WIMP-search and calibration data.

CDMSlite Run 2 started during SuperCDMS Run 134. The installation of the noise monitor program gave high hopes for the discrimination against cryocooler-induced LF-noise and the Plo trigger threshold was set at 10.5 mV (compared to 12.5 mV in Run 1). Due to rounding in the conversion from decimal to hexadecimal in the DAQ system, this actually corresponded to 10.7 mV [325].

Although the noise monitoring program allowed for better characterization of LF-noise, the realities of the age of the cryocooler were eventually too severe to be handled in analysis. The cryocooler had been employed since 2005, and it thus had close to 10 years of near-continual operations, longer than the recommended maintenance length, for the data used in Run 2. The cold-head of the cryocooler deteriorated throughout the run, leading to a higher rate of LF-noise induction. The effect of the deterioration was seen by monitoring the overall trigger rate such as in Fig. 9.14, which shows the trigger rate, by series, for the first part of Run 2. For the majority of the run, the trigger rate was ∼1 Hz, with occasional, short-lived, increases. However, at the end of June, the rate systematically increased prompting an increase to the trigger threshold to 11.0 mV. This increase initially decreased the rate, however it greatly increased again in July. This final increase prompted the end of data taking for maintenance and the experiment was warmed to room temperature for cryocooler maintenance. The cryostat was not opened nor was any work done on the detectors themselves. This warm-up
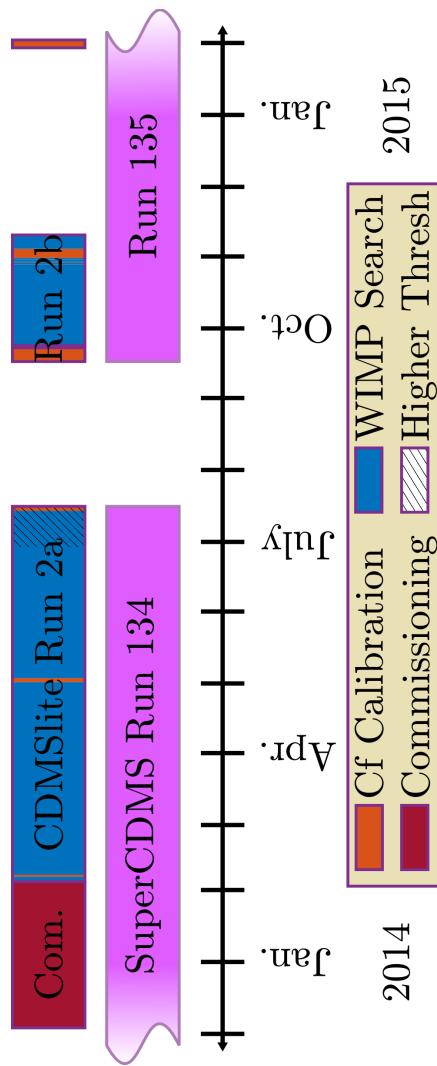
Figure 9.13: Timeline of CDMSlite Run 2 showing data periods and calibration data. Commissioning (dark red) occurred during December 2013 and January 2014. The run officially began on February 4, 2014. Blue indicates Wimp-search data while orange indicates ^{252}Cf-calibration data. Run 2 began during the general SuperCDMS Run 134 (magenta). Due to the deterioration of the cryocooler cold-head, and the corresponding increase in trigger rate, Run 134 ended in July 2014. After maintenance on the cryocooler, data taking resumed in September for SuperCDMS Run 135. CDMSlite Run 2 data taking also resumed in Run 135. Run 2 data taken during Run 134 is labeled as Run 2a while that taken during Run 135 is labeled as Run 2b. At the end of Run 2a, the trigger threshold was slightly increased to combat the rising trigger rate (gray shading). ^{252}Cf-calibration data was taken periodically during the run, with the notable exception being the data taken in January 2015 specifically to measure the Run 2b trigger efficiency.
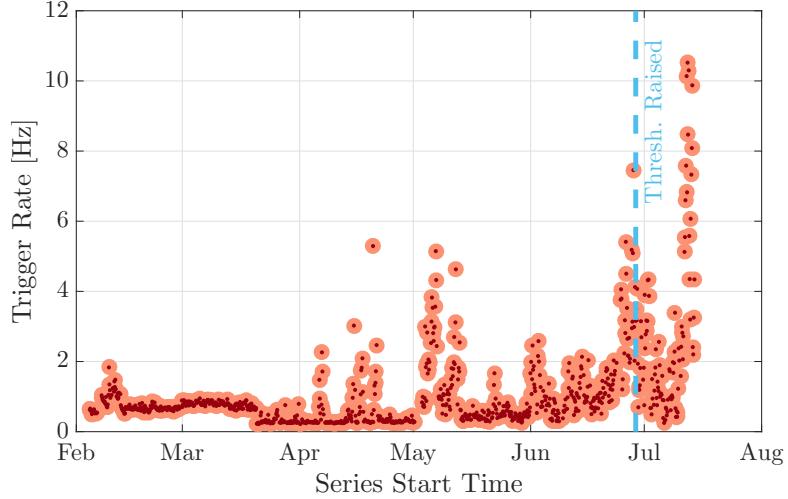
Figure 9.14: Trigger rate for each series in CDMSlite Run 2a. The rate increased starting in June due to the deterioration of the cryocooler cold-head. The trigger threshold was increased slightly to combat this increase (blue dashed line), but the rate continued to increased in July. This prompted the end of SuperCDMS Run 134 for maintenance of the cryocooler. The mean uncertainty on the trigger rate was 1.28 %.

ended Run 134; CDMSlite data taken during Run 134 was designated as Run 2a.

Operations resumed in September during SuperCDMS Run 135 and iT5Z2 was returned to the Run 2 operating state. The data taken during Run 135 was designated as Run 2b. The maintenance of the cryocooler gave expectation of a better LF-noise environment and the trigger threshold was set even lower at 8.0 mV. After the conclusion of Run 2b, it was discovered that the noise monitors had not been configured correctly in September when Run 135 started: the cryocooler monitoring information was not available for the Run 2b data. The noise monitors were correctly configured again in January 2015 and ^{252}Cf calibration data taken with the Run 2b configuration.

The dates, labels, live times, and trigger threshold settings for the pieces of Run 2 are given in Table 9.2. The majority of the run, 99.41 raw live-days, was taken during the 10.5 mV trigger threshold period of Run 2a. The remaining 32.82 live-days was split between the increased trigger period of Run 2a (10.87 live-days) and Run 2b (21.95 live-days) for a grand-total raw exposure of 132.23 live-days.

The increase in trigger threshold in June 2014 during Run 2a was inadvertently not taken into account for a majority of the data analysis. The official analysis proceeded

Time Span [YY/MM/DD]	Label	Raw Live Time [days]	DAQ Trigger [V]	Projected Trigger [mV]
14/02/04–14/06/28	Run 2a	99.41	0.0105	10.7
14/06/28–14/07/14		10.87	0.0110	11.2
14/09/23–14/11/10	Run 2b	21.95	0.0080	7.8

Table 9.2: CDMSlite Run 2 data divisions giving the labels, raw live time, and trigger settings for each. The DAQ Trigger value is the threshold set by the user in decimal. The actual threshold setting occurs in hexadecimal, and the conversion/rounding between bases means the user set value is not the true threshold value, which is given by the Projected Trigger column [325].

assuming that Run 2a could be described as a single, 10.5 mV, entity. The effect of this slightly higher threshold was later checked (Sec. 12.5.4) and compared to the uncertainties presented with the official result.

The ^{252}Cf calibration data periods are given in the timeline as they are very important for CDMSlite. Neutrons can capture of natural ^{70}Ge and create ^{71}Ge which subsequently decays by electron-capture. The peaks created by the calibration data were visible in the CDMSlite spectra and are useful for energy calibration (Sec. 10.2). Two calibrations were performed during Run 2a, February and May. Numerous calibrations were performed during Run 2b, including a dedicated CDMSlite calibration in January 2015 using the noise monitors.

In conclusion, the second run of CDMSlite lasted from February to November 2014 and operated a single iZIP detector, iT5Z2, at a 70 V potential difference. The sensitivity to WIMP mass was increased by installing noise monitors on the cryocooler (to reject LF-noise), decreasing the physical threshold, and operating at a larger bias potential. The sensitivity to cross section was improved by operating for a longer exposure ($\sim$10$\times$ longer) and increasing the duty-cycle via pre-biasing.

Chapter 10

Processing Improvements and Energy Scale

The first step in the the analysis of the CDMSlite Run 2 data involves taking the raw data and interpreting them correctly. The standard iZIP-mode processing and calibration required modifications due to the peculiarities of CDMSlite. In particular, the optimal filter template generation procedure was modified, the novel two-template fitting was implemented, and the total phonon energy scale calibrated using internal activation peaks.

10.1   Pulse Fitting Improvements

The basic concepts of the SuperCDMS data processing is given in Sec. 5.5.1 and applies to the CDMSlite data which were processed along with the data from the iZIP detectors There were a few modifications and additions to the data processing specifically for Run 2 as dictated by hardware differences and by new analysis techniques. In general, pulse-shape provides the primary description of an event and the optimal filter (OF) and non-stationary OF (NSOF) algorithms (Sec. 5.5.1 and Appendix A), which find the best fit of a template to the given trace, were used in SuperCDMS processing to describe the pulse. As a reminder, after an OF fit to a pulse, three variables are returned: (1) the time between the global trigger and the start of the pulse (delay), (2) the amplitude of the pulse, and (3) the goodness-of-fit χ^2. For this analysis, a new template was required

for the OF and NSOF and the specifics of the CDMSlite mode required changes in how the template was defined compared to iZIP templates. Additionally, the two-template OF algorithm (2T-fit) was used for the first time, requiring a detailed description of that fit.

10.1.1   Template Generation Pulse Alignment

In general, OF templates are created by averaging over many individual pulses, which serves to average-out the electronics noise and position-dependence. Since pulses can start at different times in the read-out trace, i.e. small delays in triggering due to the location of the event in the detector along with delays between detectors, an early step in the averaging procedure is to align all of the pulses such that their start times are equal. The definition of "start time" is ambiguous and must be determined from the traces themselves or by first processing with older templates. For all of the SuperCDMS processing, templates created from previous runs were used as an educated guess for initial processing and the delay from this initial fit used to refine the alignment for future template generation.

To aid in describing a pulse, the RTFT Walk algorithm was also used. The variables created by the RTFT walk were the time, relative to the start of digitization, at which the pulse reached the nth % of it's eventual maximum. These times were given for both when the pulse was increasing (rising edge) and decreasing (falling edge). For analysis, combinations of these walk parameters can be used to describe how peaky a pulse is. A standard phonon pulse shape is given in Fig. 10.1(right) with a zoom in on the rising edge in Fig. 10.1(left) and some of the quantities from the OF and RTFT Walk algorithms are visually demonstrated.

For a standard iZIP detector, the start time for alignment is generally taken as the delay specified by the OF fit of the charge trace. The charge trace has a near-instantaneous rising edge, Fig. 10.1(right), which gives an accurate measure of the start of the event. Using the charge information for the start time is problematic for CDMSlite. The biasing configuration (Sec. 5.3) for CDMSlite placed all channels on the read-out face at ground and charge carriers were thus equally likely to be collected by phonon and ionization sensors. The ionization channels for CDMSlite were practically useless and could not be used to determine the pulse start time.
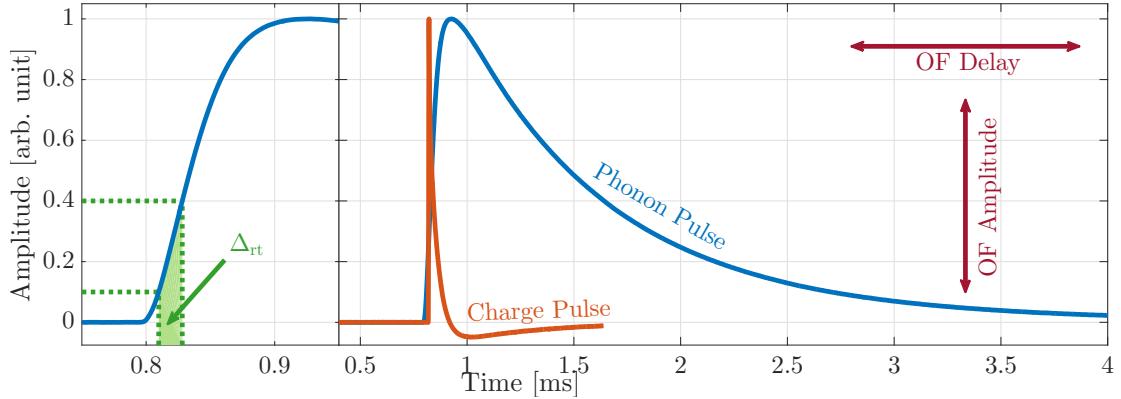
Figure 10.1: (right) Phonon (blue) and charge (orange) pulse templates demonstrating the typical pulse shape for iT5Z2 with a (left) zoom of the rising edge. The 10 % and 40 % RTFT Walk points on the rising edge are highlighted in dotted green with their difference, the rise time Δ_{rt}, as the time spanned by the light green area. The rise time of the charge pulse is significantly smaller than in the phonon pulse. When the templates are fit to a trace with the OF, they can be shifted in time, the delay, and scaled vertically, the amplitude.

This required the development of an alignment algorithm based solely on the total phonon trace. The primary assumption of this new algorithm was that the trace is linear near the rising edge. A linear fit to the early portion of the trace was used to extrapolate back in time to when the amplitude was zero, i.e. the x-intercept of the fit. If only two points were used, the extrapolated start time was

$$t_0 = \left(f t_{f'} - f' t_f \right) / \left(f - f' \right), \tag{10.1}$$

where f and f' are the fraction of the pulse height at the two points and t_f and $t_{f'}$ are the times at which those fractions are reaches, i.e. the RTFT Walk output. True fits were performed with greater than two points, but the linearity assumption breaks down further up the trace. Several combinations of the 10, 20, 30, and 40 % points were investigated with little difference observed in the final alignment. The slight differences indicated better behavior using a two-point alignment with the 10 % and 20 % points and this algorithm was implemented. For these two rise-time points, Eq. 10.1 reduces to

$$t_0 = \left(2 t_{0.10} - t_{0.20} \right). \tag{10.2}$$

With this new alignment method, OF templates specifically for Run 2 were generated following six steps:

1. Baseline Subtraction: Subtract means of pre-pulse baselines.

2. Alignment: Align with Eq. 10.2.

3. Normalize: Divide by integrals of pulse tails.

4. Preliminary Average: Average, on a per-bin basis, over all pulses.

5. Quality Cut: Calculate χ^2 compared to preliminary average, keep best 80 % of pulses.

6. Final Average: Average using traces passing previous step.

7. NSOF: Compute residual between template and pulses in time and frequency space for use in NSOF.

Since the primary energy information of a trace is in the long tail, normalizing to equal tail-area was equivalent to normalizing the traces by energy. Steps 1, 2, 3, and 6 of this process are shown in Fig. 10.2, with the final template given by the bright-green line in the lower left subfigure. Events from the ^{71}Ge K-shell activation peak from the 7 days immediately following the February ^{252}Cf-calibration data were used for the template creation process.

The NSOF algorithm required the frequency-space covariance matrix of the non-stationary "noise" created by the position dependence in the initial part of the traces. This needed to only be computed once, as it depends on the detector and not the event, and was created as another piece of the template. The difference between the new-found template and the many pulses used to create it are given in Fig. 10.3. These difference are known as "residual" traces. Since the power in the tail of the pulse is the same between the template and traces, the residuals contain only the position-dependence in the peakier (or not) early part of the trace. The Fourier space equivalent of the residuals was used as the NSOF covariance template.
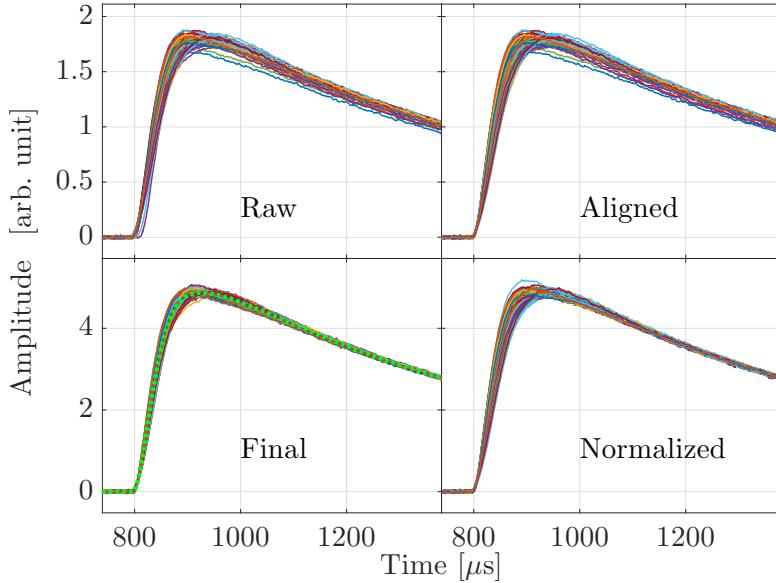
Figure 10.2: Four steps of the phonon OF-template creation process. Starting in the upper-left and proceeding clockwise, the subplots show: raw total-phonon traces, after alignment, after normalization, and after removal of the worst 20 %, with that final template (green dotted).
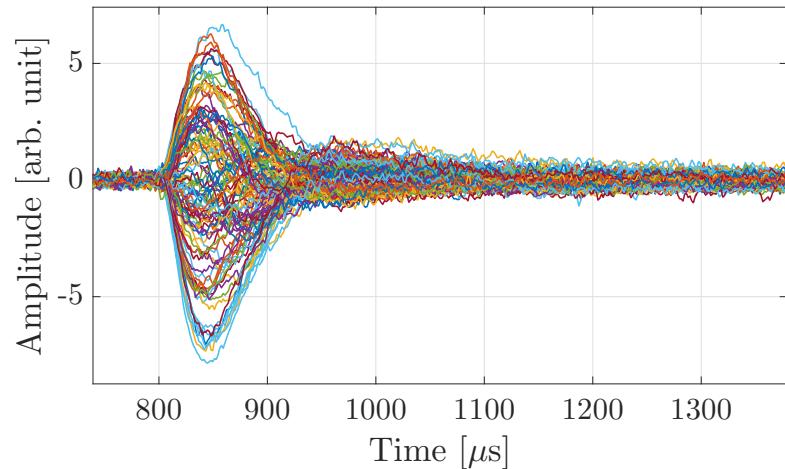
Figure 10.3: Residual traces after subtracting the OF template from a collection of total phonon traces. The sharp peak (positive or negative) observed between 800–900 μs corresponds to the position dependence of the trace. The Fourier-space equivalent of these residuals are used for the covariance template. The fast/residual template used in the two-template OF fitting algorithm is derived by averaging such residuals after flipping those traces with a negative initial pulse.
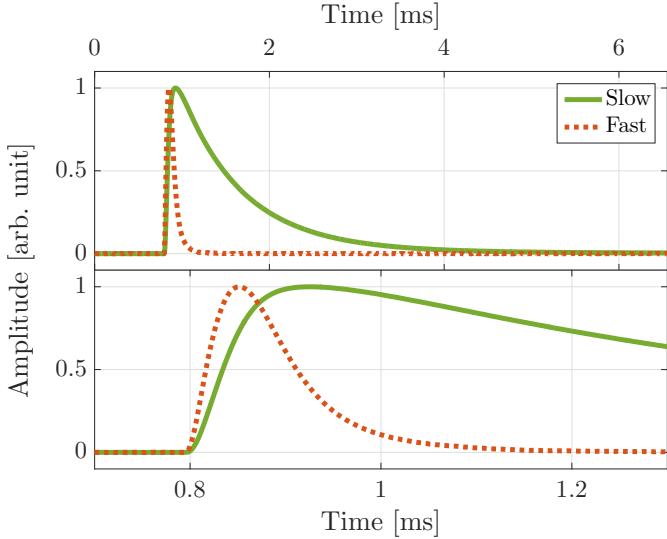
Figure 10.4: Templates used in the two-template OF-fitting algorithm. The top panel shows the full length of the trace while the bottom is a zoom around the rising edge. The slow template (green solid) is the regular OF-fit total phonon template while the fast/residual template (orange dot) is derived from residual traces such as seen in Fig. 10.3.

10.1.2 Two-Template Fitting

Since the NSOF deweights the position-dependent peakiness found in the traces, it was the primary energy estimator used by SuperCDMS in general, and the CDMSlite Run 2 analysis in particular. The NSOF was only used to reconstruct event energy and was only run on the total phonon trace, which has the least position dependence. The NSOF outputs were therefore not useful for deriving position information of the event.

A novel fitting technique was developed by the Queen's University research group and implemented for this analysis. This two-template OF fitting (2T fitting) characterizes both the energy and position information of the pulses. The method fits each trace $S(t)$ to a time-delayed t_0 linear combination of two templates and noise $n(t)$ as

$$S(t) = \sum_{i=s,f} a_i A_i(t - t_0) + n(t). \tag{10.3}$$

$A_s(t)$ is the standard OF template with fitted amplitude a_s and $A_f(t)$ is a new template with fitting amplitude a_f. The standard OF template and the new template have relatively slow and fast rise- and fall-times respectively. This new template was derived by averaging the residual pulses, such as those seen in Fig. 10.3, after inverting those with negative peaks. The two templates used are shown for comparison in Fig. 10.4 and are interchangeably known as the fast/slow or residual/OF templates.
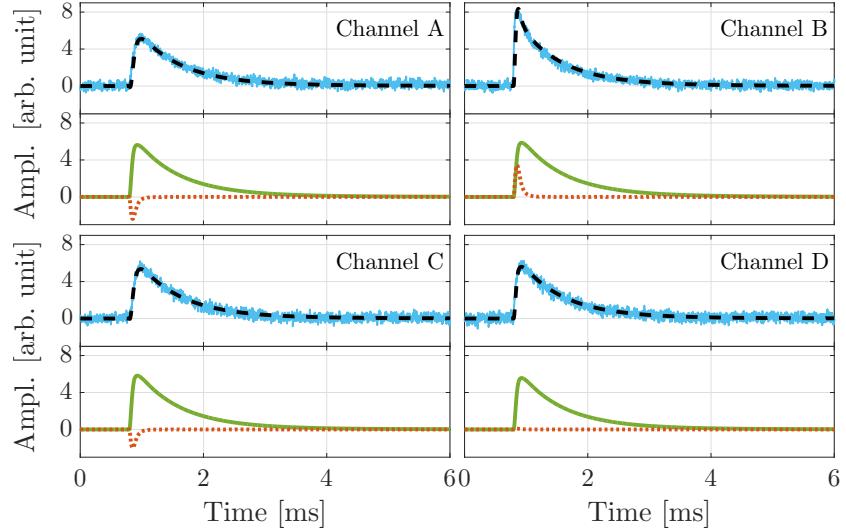
Figure 10.5: Two-template OF fitting results for all phonon channels for an example event from the *L*-shell activation peak. The raw trace (light-blue solid) is compared to the final fit (black dash) which is a sum of the slow (green solid) and fast (orange dot) templates. The arbitrary units of the vertical axes are the same for all channels, i.e. relative height differences in the channel traces are physical. A more positive fast template indicates that channel's closer proximity to the interaction location, while a more negative indicates that channel's further proximity. In particular, this event occurred closest to channel B and furthest from channels A and C.

The 2T-fitting algorithm was run on each individual channel's trace in addition to the total trace. For each trace, the OF delay was set to be equal between the two templates which gave four output parameters: the single delay, the amplitudes of both templates, and the χ^2. The amplitude of the slow template on the total trace gave energy information[1] while the relative amplitudes of the fast templates between the channels gave position information. An example event is given in Fig. 10.5, where each of the four channel fits are shown.

10.2   Calibration

Since CDMSlite cannot determine the ionization yield (Sec. 4.4.1), calibrating the total phonon energy scale to a physical recoil- energy scale was performed in three steps. The

---

[1] The energy resolution from this fit was comparable, but slightly worse than, the NSOF resolution.

keV$_\text{t}$ energy scale was first studied and compared to expectations (Sec. 10.2.1). This was then calibrated using a known ER source to the keV$_\text{ee}$ scale (Sec. 10.2.2) and then converted to keV$_\text{nr}$ using a yield model (Sec. 12.2.2). The usual ER calibration source for SuperCDMS was ^{133}Ba and its peak at 356 keV. However, this was prohibitively high for CDMSlite due to the saturation of the phonon read-out TESes at $\sim$500 keV$_\text{t}$ ($\sim$30 keV$_\text{ee}$). Using an external source with a decay $\lesssim$30 keV$_\text{ee}$ was also not feasible given the shielding from the copper cryostat cans. A low-energy source internal to the detector was instead used.

The neutrons from the ^{252}Cf calibration data could capture on the natural ^{70}Ge in the detector and create unstable ^{71}Ge, which decays by electron-capture (EC) with a half-life of 11.43 days [326]. The entire process is

$$^{70}\text{Ge} + n \longrightarrow {}^{71}\text{Ge}$$
$$^{71}\text{Ge} + e \longrightarrow {}^{71}\text{Ga} + \nu_e + \gamma\text{'s}, e\text{'s}.$$
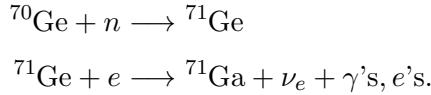
The energy released by the X rays and Auger electrons after the EC process depends on which shell the captured electron was originally in. These energy levels correspond to the binding energy of ^{71}Ga and are given in Table 10.1 along with a summary of the resultant decay products for each shell. See Appendix B for the full details of the capture and decay processes. The ^{252}Cf calibrations provided CDMSlite with two very clear peaks (K and L shells) for calibration. At 70 V, the M-shell peak was also visible above threshold. These peaks were used to compare the keV$_\text{t}$ scale to the theoretical expected and then to calibrate to keV$_\text{ee}$. Any general references to the "K-/L-/M-shell" peaks refer to these ^{71}Ge EC peaks.

10.2.1 Experimental keV$_\text{t}$ Scale

The theoretically expected keV$_\text{t}$ energy scale is defined by Eq. 9.1 as $E_\text{t} = E_\text{r}\mathcal{A}(V_b)$. Even though only one side of the CDMSlite detector was read out, the phonon sensors on the non-read-out side still absorbed phonons. The expected experimentally observed energy scale is then half of the theoretical

$$E_\text{obs} = \frac{E_\text{r}}{2}\left(1 + Y(E_\text{r})g(V_b)\right). \tag{10.4}$$

Capture Shell	Probability [%]	Decay Product	Probability [%]	Energy [keV]
K-Shell	87.57	Auger-e-cascade	42.30	10.37
		Ga-K$_\alpha$+cascade	39.52	9.25+1.12
		Ga-K$_\beta$+cascade	5.76	10.26+0.11
L-Shell	10.43	Auger-e-cascade	10.43	1.30
M-Shell	1.78	Auger-e-cascade	1.78	0.160

Table 10.1: ^{71}Ge electron-capture decay products. The total energy is the ^{71}Ga binding energy of the shell from which the e was captured from. See Appendix B for details of cascades.

The validity of this energy scale was determined by comparing the observed K-shell peak to its expected value as shown in Fig. 10.6. For these data, and all subsequent Run 2 data, there were two base criteria: a bias potential of $V_b = -70$ V[2] and only using non-randomly triggered events. Unless otherwise stated, the energy estimator is that from the NSOF algorithm.

At $V_b = -70$ V, the theoretical NTL amplification factor for electron recoils is $(1 + 70/\epsilon_\gamma)/2 = 12.17$. For the K-shell at 10.37 keV$_{ee}$, the expected location of the peak was 126 keV$_t$. A simple fit to the peak in Fig. 10.6 gave a mean of 154 keV$_t$, $\sim$22 % higher than expected. As a check, the peak was also fit in the 60 V commissioning data, giving a mean at 135 keV$_t$ compared to the expected 109 keV$_t$, $\sim$24 % higher than expected.

The mis-calibration of the keV$_t$ energy scale was a result of applying the 4 V, iZIP-derived, calibration constants to the 70 V data. At low fields, it is possible for charges to not reach the electrodes leading to <100 % collection of charge carriers. This could be due to residual traps, other local electric fields, and/or charges never leaving the charge cloud due to self-shielding. The efficiency of collecting ionization in an iZIP-style detector is shown in Fig. 10.7 [268, 299]. Electrons/holes have $\sim$80/90 % efficiency respectively at the iZIP-applied field of $\sim$1.6 V cm^{-1} and $\sim$100 % efficiency at the CDMSlite-applied field of $\sim$27.6 V cm. This means that the 4 V constants are over-calculated when used with CDMSlite data. This over-calibration is the inverse of

---

[2] This cut officially defined the Run 2 exposure.
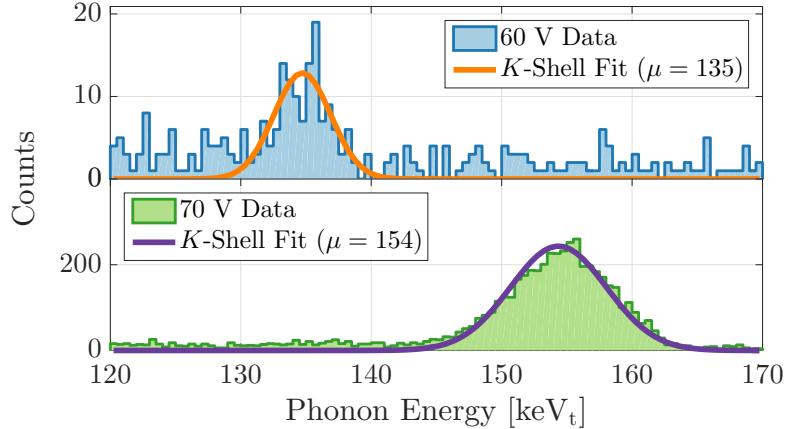
Figure 10.6: Location and simple fit to the ^{71}Ge K-shell capture line for Run 2 at both 60 V (top) and 70 V (bottom) bias potentials. The mean of the peaks are at 135 and 154 keV$_t$ which are $\sim24\,\%$ and $\sim22\,\%$ higher than the expected locations of 109 and 126 keV$_t$ for 60 and 70 V respectively.

the efficiency at 4 V or $\sim1/0.85 = 1.18$ which roughly matches the $\sim20\,\%$ observed excess.[3]

There is one difficulty, however, with this explanation for the keV$_t$ energy scale. The total phonon energy scale in Run 1 *did* match the theoretical gain for $V_b = -69$ V. The K-shell peak was at 124.8 ± 2.4 keV$_t$ compared to the expected 124.4 keV$_t$. The electronics improvements for Run 2, such as monitoring the biasing current, and reducing the size of the adapter board load resistor (Sec. 9.2.1) gave more confidence in the Run 2 measurement. This implies that Run 1 was *not* at 69 V and the apparent energy scale match was a (cruel) coincidence. The implications of this hypothesis are shown in Fig. 10.8, which gives the measured K-shell peak location at the different known bias potentials. The two points from Run 2 are used to fit a detector scaling factor $\mathcal{D}$ to the total energy to give the energy scale seen in the analysis as

$$E_t^{\text{Analysis}} = \mathcal{D} \times E_r \mathcal{A}(V_b)/2. \tag{10.5}$$

The fit gives $\mathcal{D} = 1.23$, implying the calibration scaling increased the energy scale by

---

[3] More recent work by A. Phipps indicates that accounting for impact ionization, where drifting charges release previously trapped charge and increases the ionization signal, leads to $>100\,\%$ collection efficiency at CDMSlite strength fields [327].
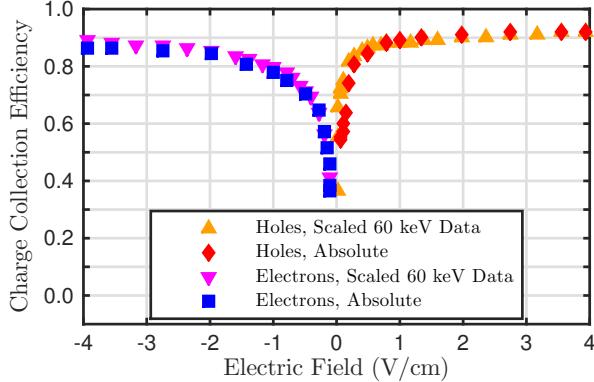
Figure 10.7: Charge collection efficiency as a function of bias potential for a 2.54 cm thick Ge iZIP detector. The blue squares and purple downward triangles show the efficiency for collecting electrons while the red squares and orange upward triangles show the efficiency for collecting holes. Figure from [327], see [268] for information on the two different normalizations.
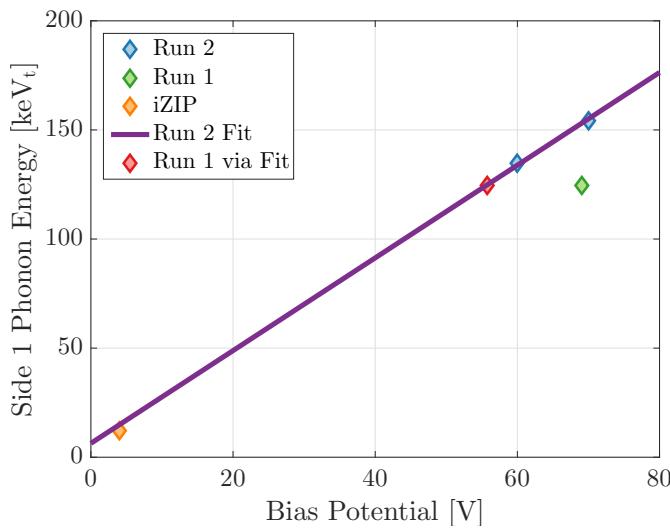
Figure 10.8: Observed location of the K-shell peak in total phonon energy compared to the applied bias potential. Observed values include the two potentials in Run 2 (blue), Run 1 (green), and standard iZIP mode (yellow). A model (purple) is fit to the Run 2 data giving a factor of 1.23 compared to the standard NTL amplification and implying a potential difference for Run 1 of 56 V (red). The model is 22 % greater than the 4 V data.

23 % when compared to theory. The model then infers, by considering the measured mean of the peak, that the actual potential difference at the detector for Run 1 was ~56 V. As a cross-check, when extrapolating the fit down to 4 V, where the calibration constants were derived, the model gives the expected 22 % above theory. The implicates of this change in bias for Run 1 are discussed in Refs. [275, 328].

10.2.2 Final keV$_{ee}$ Calibration

Converting from keV$_t$ to keV$_{ee}$ is performed by using the measured E_t location of the K-shell peak and the known recoil $E_r = 10.37$ keV$_{ee}$. A simple mean of the peak was
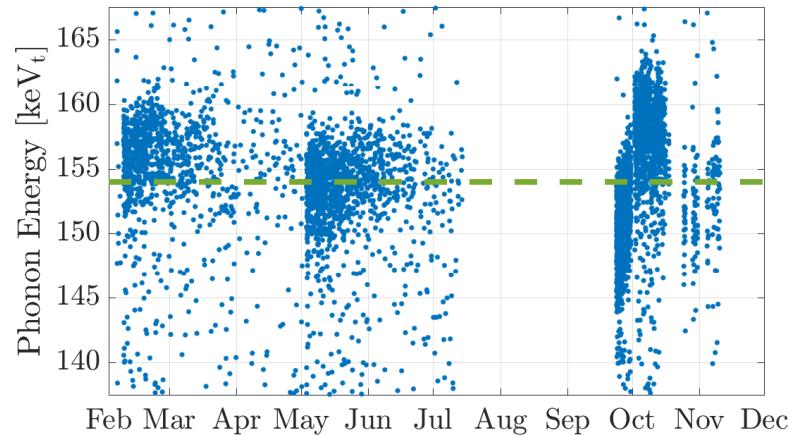
Figure 10.9: Raw location of the K-shell activation line as a function of time throughout Run 2. The density of the peak in February, May, and October indicate proximity to the ^{252}Cf calibrations. The amplification of the line is not constant throughout the run, as evidenced by the shifting of the dense population in time. The overall mean of the line (green-dashed) as found in Fig. 10.6 does not adequately describe the whole run, necessitating a time-dependent correction.

not used for the conversion because the location of the peak varied with time as shown in Fig. 10.9. Thus, in addition to converting to keV$_{ee}$, a time-dependent gain correction is used to improve the overall resolution of the line. This correction contained four components with each step of the calibration shown in Fig. 10.13 at the end of the section. During each step of correction, the absolute value of the keV$_t$ scale was taken as arbitrary and the final step is to use the new mean of the K-shell peak as a scaling factor to the correct keV$_{ee}$ value. The following discussions were first investigating by Y. Ricci with later development by W. Rau [329].

Leakage Current Adjustment

If the electronics were ideal, after applying the high voltage there would be a constant (small) current measured from the High-Voltage Power-Supply (HVPS). However, the HVPS recorded a varying current implying a time-varying parasitic resistance R_p. The parasitic resistance responsible for the leakage current contributed to a drop in the potential difference across the detector which reduced the NTL gain. The total
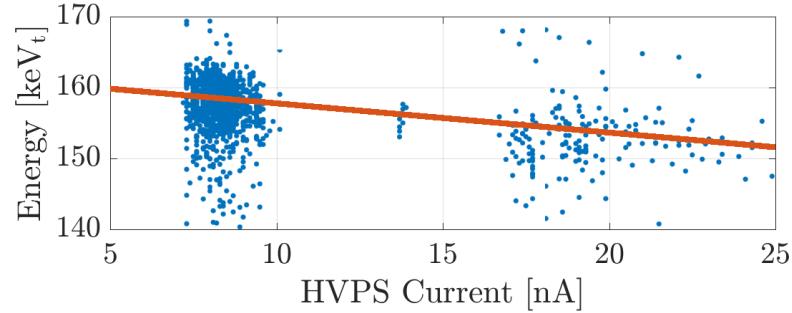
Figure 10.10: High-Voltage Power-Supply (HVPS) current compared to total phonon energy of the K-shell, showing a linear dependence. The fit to this population was used to correct the energy scale for the voltage drop due to leakage current, which led to reduced NTL gain. The slope indicated the resistance the leakage current encounters, and was consistent with the load resistor on the iZIP adapter board.

amplification with the leakage current correction and assuming an ER is

$$\mathcal{G} = 1 + e\left(V_b - I_b R\right)/\epsilon_\gamma, \tag{10.6}$$

where I_b is the HVPS current and R is the resistance through which the current flows. In order to determine the value of R, the relationship between the measured phonon energy and the I_b was fit linearly with the slope indicating R. Figure 10.10 show this relationship with a fit slope of -0.825 keV/nA. This corresponds to $R = 194$ MΩ as the resistance encountered by I_b. This is, to within uncertainty, equal to the adapter-board load resistor of $R_L = 195$ MΩ. The correction assumed the current passed through the load resistor, $R = R_L$. Stated differently, $R_p \gg R_L$ such that only a negligible (but still non-zero) current went through R_p.

The event-by-event corrected E_t^{Corr} energy scale was the ratio between the total amplification expected with no voltage drop and that which was observed with the measured I_b for the given event

$$\begin{aligned} E_t^{\mathrm{Corr}} &= E_{\mathrm{t}} \cdot \frac{\mathcal{A}\left(V_b, Y = 1\right)}{\mathcal{G}(R = R_L)} \\ &\quad E_{\mathrm{t}} \cdot \frac{1 + eV_b/\epsilon_\gamma}{1 + e\left(V_b - I_b R_L\right)/\epsilon_\gamma}. \end{aligned} \tag{10.7}$$

This correction is seen in the second panel of Fig. 10.13. For the recorded $I_b \sim 10$ nA,
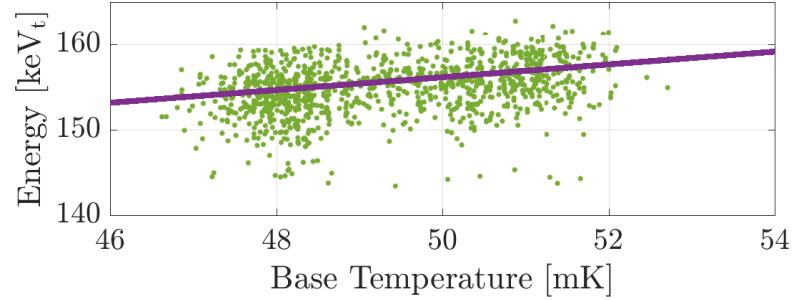
Figure 10.11: Experiment base temperature compared to total phonon energy of the K-shell, showing a linear dependence. The fit to this population was used to correct the energy scale for the change in detector response due to temperature.

the correction was ~2 %.

Base Temperature Adjustment

The next correction was due to variation in the experiment's base temperature. Previous analyses have demonstrated that the base temperature affects the calibration [330]. The base temperature was also stored in the data stream and Fig. 10.11 shows that a linear fit describes the energy scale's dependence on the temperature. The slope from this fit, along with an arbitrary reference point, was used to remove the dependence on base temperature as shown in the third panel of Fig. 10.13. The base temperature was measured as 47–52 mK, which gave corrections of ~3 %.

Discrete Shifts Correction

After applying the first two corrections, discrete shifts were observed in the energy scale as shown in the third panel of Fig. 10.13. An empirical correction was applied by fitting the means of the two Run 2b distributions and scaling them to match the Run 2a distribution's mean. This correction is shown in the fourth panel of Fig. 10.13, where the two Run 2b shifts were 0.81 % and 2.87 % respectively.

Position Dependence Correction

The final correction used information from the new 2T-fitting algorithm. Figure 10.12 shows the amplitude of the residual-template fit compared to the NSOF total-energy fit,
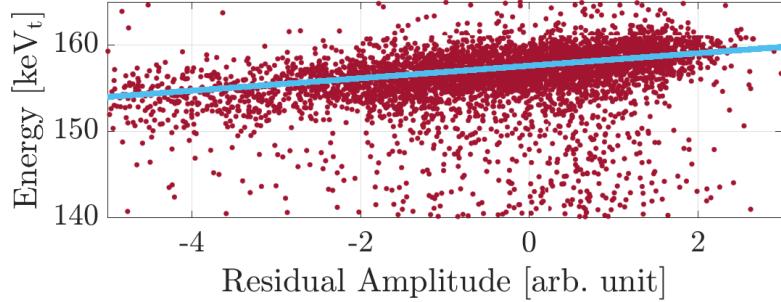
Figure 10.12: Amplitude of the residual template fit compared to total phonon energy of the K-shell, showing a linear dependence. The fit to this population was used to correct the energy scale for position dependence (peakiness) in the traces.

where a dependence is observed with peakier pulses (larger residual template amplitude) reconstructed to higher NSOF total-energy values. This dependence indicated that the NSOF did not remove all of the position dependence of the pulse during the fit. This small failure of the NSOF fit was likely more true for CDMSlite- than iZIP-mode since only one face of the detector was read out. The position dependence was removed by fitting the distribution and correcting by the slope. This correction was 0–5 keV$_\text{t}$ for any given event. The final distribution in keV$_\text{t}$ can be seen in the fifth panel of Fig. 10.13.

Electron-Equivalent Energy Scaling

After correcting the time-dependence in the NTL gain, the final calibration step was to determine the conversion from the keV$_\text{t}$ to the keV$_\text{ee}$ energy scale. The mean of the new keV$_\text{t}$ K-shell distribution was used to scale to the known recoil energy of 10.37 keV$_\text{ee}$. There could be concern that any of these corrections are over-correcting the energy scale, i.e. correcting on features of the K-shell which were specific that that energy. Overcorrection was checked by also considering the L-shell peak at 1.30 keV$_\text{ee}$. If the corrections were general to the whole spectrum, they should also improve the resolution of the L-shell. The keV$_\text{ee}$ spectrum of the K- and L-shell peaks with each correction applied are shown in Fig. 10.14. The improvement in K-shell resolution is obvious and the resolution of the L-shell also increases after each step, verifying the global nature of the corrections.
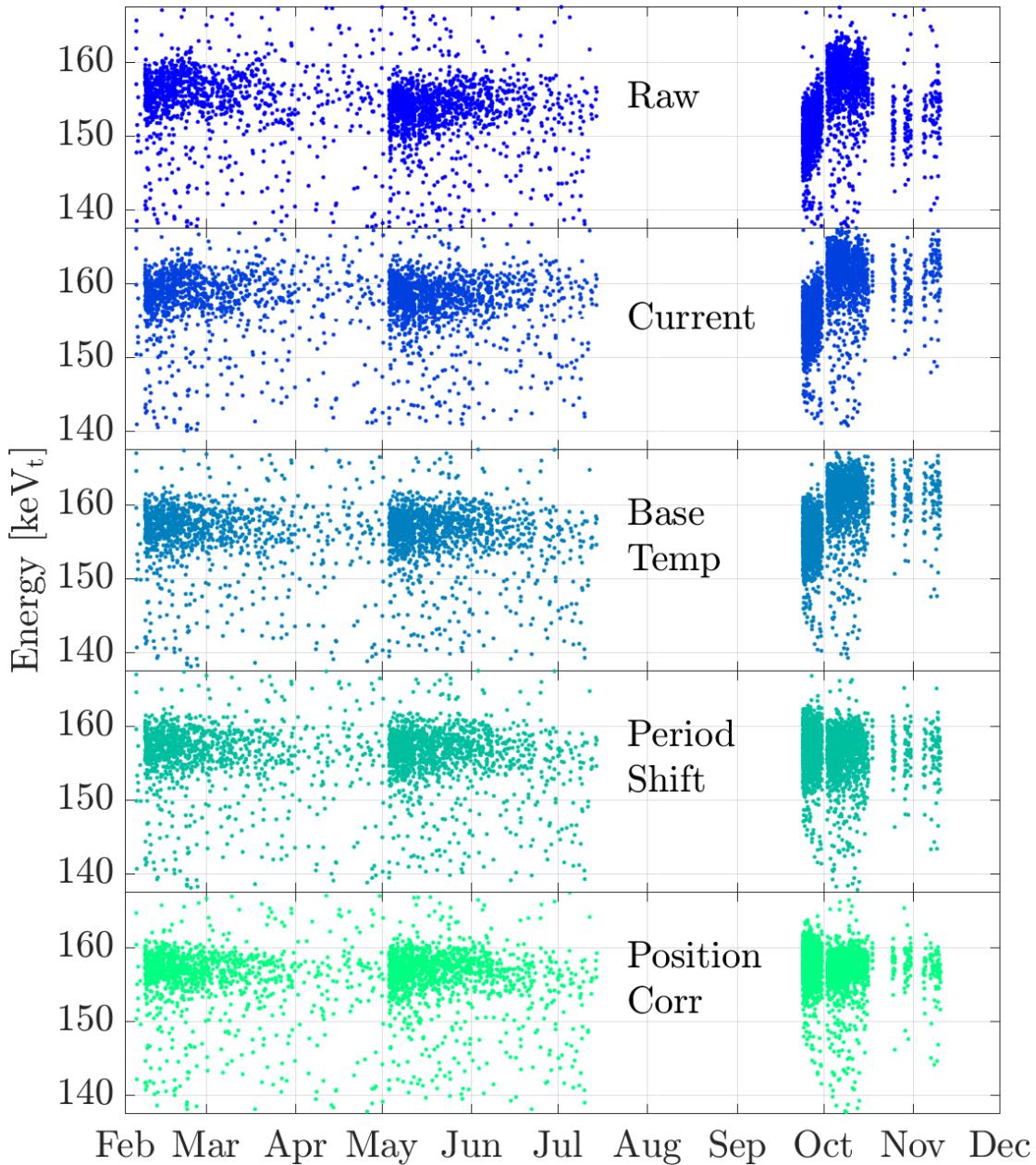
Figure 10.13: K-shell energy over the course of Run 2 showing the raw energy estimate (first panel) and subsequent corrections to the energy scale. These corrections included gain variations due to HVPS leakage current (second panel), experiment base temperature (third panel), discrete period shifts (fourth panel), and position dependence (fifth panel). Each correction improved the resolution of the peak.
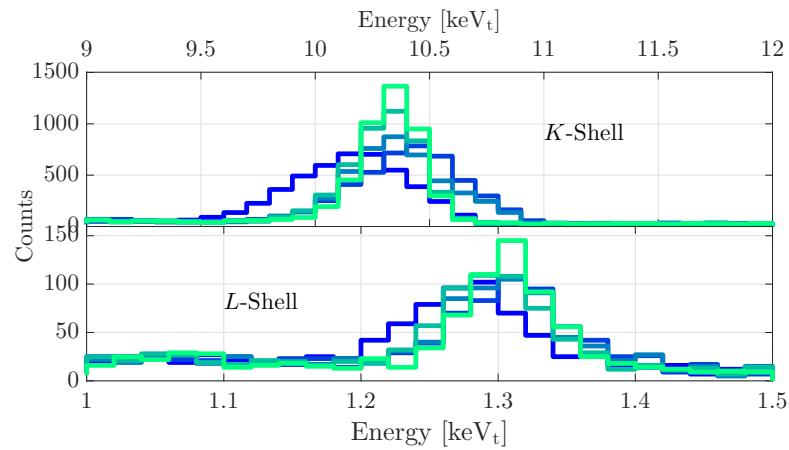
Figure 10.14: Resolution of the K shell (top) and L shell (bottom) after each of the corrections shown in Fig. 10.13. These corrections were, going from dark blue to light green, HVPS leakage current, experiment base temperature, discrete period shifts, and position dependence. The scaling from keV_t to keV_{ee} for all peaks was achieved using the mean of the final K-shell peak. The location of the L-shell at the expected $1.30\,keV_{ee}$ verified that the final scaling was correct.

Chapter 11

Event Selection and Efficiency

The goal of any dark matter search is to analyze the data set for events caused by dark matter interacting in the detector. Doing so requires sifting through the data to remove both non-physical events and physical events which do not correspond to dark matter[1]. This chapter details the event selection process used to achieve this for the CDMSlite Run 2 data set. In particular, it describes the use of various selection criteria to reject non-physical events. such as low-frequency noise, the implementation of a fiducial volume cut for the first time in CDMSlite for the removal of physical background events, and the determination of the low-energy threshold reached. The final live time remaining and the acceptance efficiencies for each of the criteria are are discussed.

11.1   General Philosophy

The criteria applied to the data to ensure that only high-quality, WIMP-like, events are selected are enforced by a series of cuts which remove events thought not to be caused by WIMPs. These cuts fall into two broad categories:

1. **Quality Cuts:** These cuts remove events which were not caused by the interaction of an particle in the detector or have other external, i.e. non-physical, reasons for

---

[1] At least events which either could not be caused by a vanilla-WIMP model or which would only be caused by such a model at very low probability

being removed. This includes various electronically caused glitches, erroneously recorded variables in the databases, or events with poor pulse-shape.

2. **Physics Cuts:** These cuts remove events which appear to be caused by a particle interaction in the detector, but which do not match the signal expected of a standard WIMP. This includes coincidence with known sources, multiple scattering in the detector array, and fiducial volume considerations.

In addition to removing evens, each cut must also be accounted for in the final result in either one of two ways:

1. **Live Time:** For cuts in this category, the live time associated with the rejected data is removed from the total exposure. This assumes that the underlying reason for the cut indicates uncertainty in the integrity of the experiment, and thus removing the time prior to the event is a conservative choice.

2. **Efficiency:** For cuts in this category, the probability that a WIMP-like event would be removed by the given cut is computed. This assumes that the experiment was operating correctly and the possibility of a true WIMP event occurring must be considered.

After computing all of the cuts, the live time and efficiencies for them are addressed. The live time loss is given in Sec. 11.6 and the various efficiencies computed in Sec. 11.7.

11.2 General Quality Cuts

11.2.1 Bad Base Temperature, HVPS Current, or 2T-Fit

This cut is a direct consequence of the energy correction and calibration described in Sec. 10.2.2. The base temperature of the experiment, the high-voltage power supply (HVPS) current, and the 2T-fitting results are all used to correct the energy scale. The corollary to this is that events for which any of these quantities are missing or suspect cannot be accurately calibrated. This cut removes events whose base temperature is missing or exceptionally high, whose HVPS current is exceptionally high (and therefore

not caused by the usual electronics chain, e.g. sudden environmental changes), and for whom the 2T-fitting algorithm failed for any reason.[2]

11.2.2 Bad GPS Timing Information

The DAQ system has two methods of recording the time of an event. The first is a custom time stamp module fully incorporated in the data taking process which records a time for each trigger and stores this information in the history buffer for the computation of timing parameters such as the live time. This is the primary timing information used in the analysis. The second is a Symmetricom GPS time stamp module which was added to the system after the initial DAQ design [284]. This system was added for coincidence studies with the NuMI neutrino beam utilized by the MINOS experiment [331], which uses GPS time. In the development of the NuMI coincidence cut (Sec. 11.4.3), it was discovered that, for a small minority of events, the two methods of recording the event time information could disagree by appreciable amounts [332, 333]. The reasons for the disagreement are not understood and these events are removed.

11.2.3 Asymmetric Multiply-Triggered Glitches

A glitch is defined as an event whose rise- and fall-times are exceptionally fast and unphysical. Glitch events arise from voltage spikes in the TES-biasing lines, directly heating them, which generates pulses. The physical source(s) of the voltage spikes remains unknown. If the voltage spike is large enough, multiple channels will receive a pulse which leads to a large multiplicity of triggers. In contrast, consider the desired event generated by a particle interacting in the detectors. If the energy of the event is sufficiently above the trigger thresholds of a detector, both the phonon and charge channels should trigger. When considering how many detectors issue a trigger, there should be rough consistency between the number of phonon and charge triggers in a given event. If there is a large discrepancy between the number of charge and phonon triggering detectors, than such an event is most probably a glitch.

The proper plane to identify glitches with high trigger multiplicity is shown in Fig. 11.1, which compares the number of trigger-control boards with a charge or phonon

---

[2] One such failure is if the physical start time of the pulse is outside the window which the OF algorithm scans over.
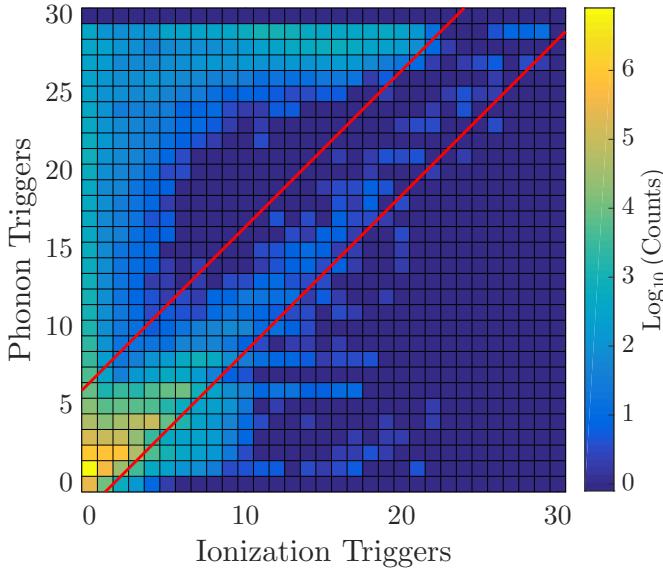
Figure 11.1: Number of trigger-control boards containing either an ionization or phonon trigger within ± 0.1 ms of the global trigger. Events caused by an interacting particle in the detector are roughly along the diagonal while glitch events are in the off-diagonal populations. The cut is shown by the red lines.

trigger for Run 2 data.[3] As expected for physical events, there is a population of events near the diagonal along with various populations on the off-diagonals — glitches. A cut was developed by R. Bunker [334] which removes these off-diagonal populations as shown in the figure by the red lines. This cut was developed using early SuperCDMS commissioning data from 2012 and applied as-is for Run 2. It removes events where $[(n_p - n_q) > 6] \vee [(n_q - n_p) > 1]$, where n_p and n_q are the number of trigger-control boards with a phonon and charge trigger respectively.

If the glitch-generating voltage spike is small enough, the resulting traces may fall below the trigger thresholds on some detectors and effectively allow glitches to pass this cut. Since glitches have faster rise and fall times, a discrimination based upon pulse shape can be be made to remove these residual glitches (Sec. 11.3.3).

11.2.4   Non-triggered Ionization Glitches

Previous studies of the noise environment in the SuperCDMS detectors identified that the outer charge channel of iT5Z2 used for CDMSlite had intermittent irregularities [335]. The cause of these irregularities is a peculiar type of glitch event with extremely sharp rise and falls times, large amplitudes, and potentially multiple peaks.

---

[3] Recall that iZIPs were connected to two trigger-control boards which could separately issue a trigger.
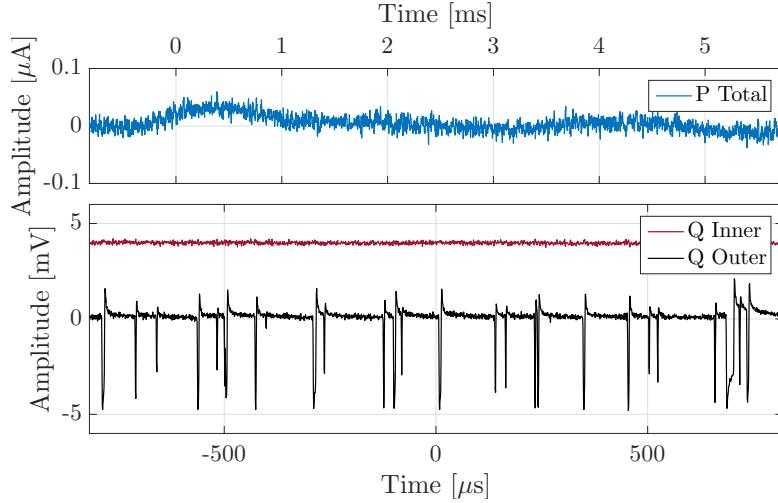
Figure 11.2: Total phonon (top) and inner/outer ionization (bottom) traces correspond-ing to a non-triggered charge-glitch event. The glitch behavior is evident in the outer charge channel (black), with multiple large amplitudes, which did not issue a charge trigger. The inner charge channel is shifted upwards by 4 mV for clarity and times "0" on both horizontal scales are the same global time.

These glitches also do not always cause a ionization trigger. An example of such a glitch can be seen in the outer charge trace in Fig. 11.2. This event highlights the trouble with these glitches: there is a low energy phonon event, which triggered the experiment, and the erratic glitch behavior in the outer charge channel. This event had one total phonon trigger and no ionization trigger: this event passes the asymmetrically-triggered glitch cut . These glitch events were not unique to iT5Z2 as they occasionally occurred across the entire array simultaneously, still issuing no charge trigger and thus passing the previous glitch cut. As the source of these glitches is unknown, similar to other types of glitches, these events are removed from the analysis.

CDMSlite is general does not typically consider the charge channels. This is for several reasons: (1) the charge signal is not amplified by the NTL effect meaning low-energy events are lost in the noise, (2) the ionization yield is generally not useful at high voltages, and (3) the biasing configuration places the charge and phonon sensors at the same bias: drifting charges are as likely be end on the phonon sensors as the charge sensors. However, in order to identify these charge glitches, the standard charge-data processing was used in Run 2.
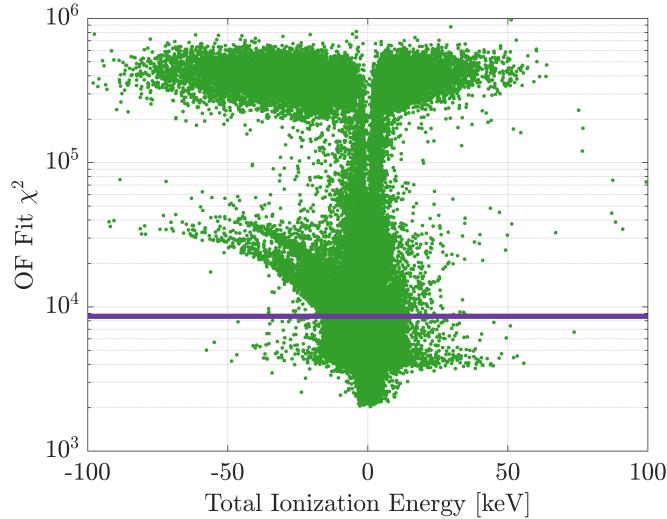
Figure 11.3: Total ionization energy compared to the OF-fit χ^2 value after application of the cuts against bad base temperature, HVPS current, 2T-fit, GPS timing, and triggered glitches. Charge glitches have any number of sharp spikes and thus have poor χ^2 values; since the template has a single peak those traces with multiple peaks appear at higher χ^2 values. The cut rejecting these glitches is shown by the solid line.

Since these glitches do not look like a usual charge pulse, they are expected to be a poor fit for the OF template and be identifiable in the charge χ^2 versus energy plane. The total (inner+outer) ionization energy is plotted vs. the outer channel's χ^2 fit value in Fig. 11.3 after applying the previous cuts, including the triggered glitch cut. There is a surprisingly large amount of structure in the plane, including multiple populations at high χ^2, with the general rule being that the higher in χ^2 an event is, the more peaks in the charge trace is present. A cut is tuned to reject 95 % of the random triggers in Run 2a and is shown by the line in the figure.

There are several series for which an appreciable amount of live time is lost due to these glitches. Those series for which >4 % of the live time is lost are declared "bad" series and a separate cut created to remove the entire series (Sec. 11.2.6).

11.2.5 Good Phonon Baseline Noise

Phonon traces were digitized with 4096 bins with the first 512 of them being prior to the global trigger bin. These pre-pulse bins can be used to characterize the baseline noise environment prior to the event. If the baseline has any oddities in it,[4] it will cause issues with properly fitting the template, which has a flat baseline. There is inherent Gaussian electronics noise in the traces and so, for a "flat" pre-pulse, the distribution

---

[4] Such as unexpected noise, elevation due to the tail of a previously occurring event (so-called pile-up event), or low-frequency noise.
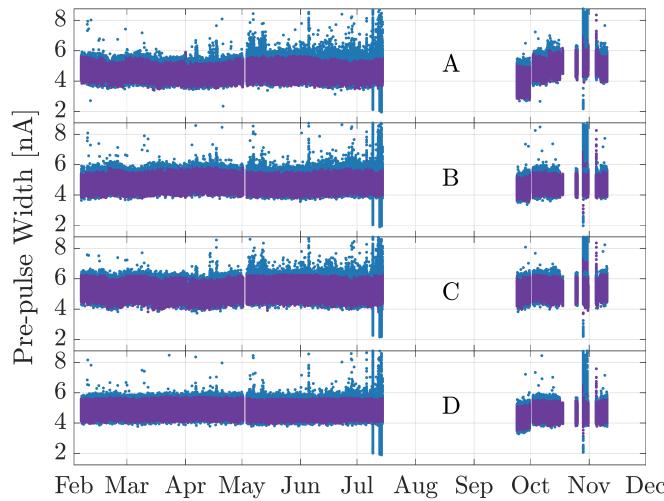
Figure 11.4: Width of the 512 digitizers bins prior to the global trigger on each of the four phonon channel for random triggers over the course of CDMSlite Run 2. The good baseline cut fits this distribution by series and removes events further than 4σ from the mean (blue events) in any channel.

of digitizer bin values should be Gaussian. The standard deviation of the pre-pulse distribution is computed during processing and this is taken as a measure of how well behaved the baseline was for that event. Randomly triggered events are also a measure of the noise environment in the experiment: the pre-pulse width of randoms provides a distribution by which to judge the pre-pulse width of non-random events.

To define a cut, the distribution of widths from the random triggers for each individual series is fit to a Gaussian (a reasonable fit for almost all series). Events are removed if their pre-pulse widths are greater than 4σ from the mean of randoms distribution. The cut is computed on a series-by-series basis, as the noise could shift between series. Since the baseline varies by individual channel, the fits and cut are tuned on each of the four phonon channels separately. An event is removed if it fails the cut on any channel.

The definition of the cut can be seen in Fig. 11.4, which shows the pre-pulse width of random triggers across Run 2 for each of the four phonon channels. There are a few series where the randoms distribution has very long tails. These correspond to three series in July which had extreme trigger bursts, which shifted the pre-pulse distribution, and five series in November which evidently were not pre-biased properly (the tail is due to detector-based leakage current). These problematic series are added to bad series cut (Sec. 11.2.6).

11.2.6 Bad Data Series

During the development of the charge glitch and phonon baseline noise cuts, several series were identified as being particularly problematic. These series are removed in their entirety from the analysis and a loss in live time accepted. The "bad series" diagnosis comes from one of three reasons:

1. If $>4\,\%$ of the live time of a series is removed by the ionization glitch cut; removes 112 series.

2. If the series contains an extreme trigger burst as identified by the phonon baseline cut; removes 3 series.

3. If the series was not prebiased; removes 5 series.

120 out of 1209 total series are removed with a live time loss of 12.66 days. This cut is the single largest reduction of live time. However, since CDMSlite is background limited, such a loss in live time does not significantly affect the final sensitivity.

11.3 Phonon Pulse-Shape Based Quality Cuts

The following three criteria are all explicitly based on the shape of an event's total phonon pulse. This is implemented by considering the distributions of the goodness-of-fit χ^2 values of the OF fit using three different templates. These templates correspond to different event types, two of which are background to be rejected. Recall that the OF is only "optimal" if the topology of the event matches the template being fit. A corollary is that fitting to different templates shows how much a given pulse resembles one template versus another. The three templates, and the corresponding notation for their respective goodness-of-fit parameters, are: (1) standard physics event ($\chi^2_{\mathrm{NF/OF}}$ for OF/NSOF fits respectively), (2) low-frequency noise (χ^2_{LF}), and (3) electronic glitch (χ^2_{Gl}).

11.3.1 Phonon Pulse Quality

The NSOF fit to the total phonon pulse is the primary energy estimator used in this analysis. Given its primacy, it is important that the estimator is accurate and a good fit

to the traces: events with abnormally high χ^2_{NF} values are removed. The most common type of event with high χ^2_{NF} are "pile-up" events, where more than one pulse is present in the recorded trace. These events have >1 peak in the trace while the template has single peak, giving poor fit quality. Another common pathology is TES saturation, where the peak of the pulse is flattened. These, and any other odd pathology present, are removed by cutting on χ^2_{NF}.

The cut is set in the energy versus χ^2_{NF} plane using the higher statistics calibration data. For Run 2a, this includes a combination of ^{232}Cf and ^{133}Ba data while for Run 2b, only ^{252}Cf data is used. The ^{252}Cf data used to set the cut for Run 2a can be seen in Fig. 11.5. For lower energies, the distribution is flat near $\sim$4100 and starts to increases above $\sim$200 keV$_t$. The cut threshold is set by binning the χ^2_{NF} in bins of 15 keV$_t$ and determining the width of each bin's distribution. A quartic polynomial in energy is fit to the $\mu + n\sigma$ level from each bin. The specific algorithm was slightly different between the two parts of the run. For Run 2a, the distribution in each bin was fit to a Gaussian to determine the width. The polynomial was then fit to the maximum $\mu + 3.5\sigma$ values in each bin between ^{133}Ba and ^{252}Cf data. For Run 2b, the width was instead determined by an iterative method which removes outliers from the distribution. Due to the removal of outliers, the distribution widths are smaller and the polynomial fit to the $\mu + 5\sigma$ values from the ^{252}Cf data. The value of n is essentially arbitrary, as long as events below the cut are high quality events. The cut threshold as a function of keV$_t$ is given by the curve in Fig. 11.5.

11.3.2   Low-Frequency Noise

The energy threshold for Run 1 was set at 170 keV$_{ee}$ in part because of the presence of low-frequency noise (LF-noise). This source of noise was again present in Run 2, as seen in Fig. 11.6(a). At the lowest energies, a second noise distribution was present, shifted to a higher reconstructed energy than the expected electronics noise distribution, which covered the lowest-energy portion of the spectrum. An example trace from an event in this distributions is shown in Fig. 11.6(b). After applying a low-pass filter, a comparison with the OF-template emphasizes the difference in pulse-shape between LF-noise and a standard event. Notably, the LF-noise trace has slower rise and falls times and oscillates in the tale.
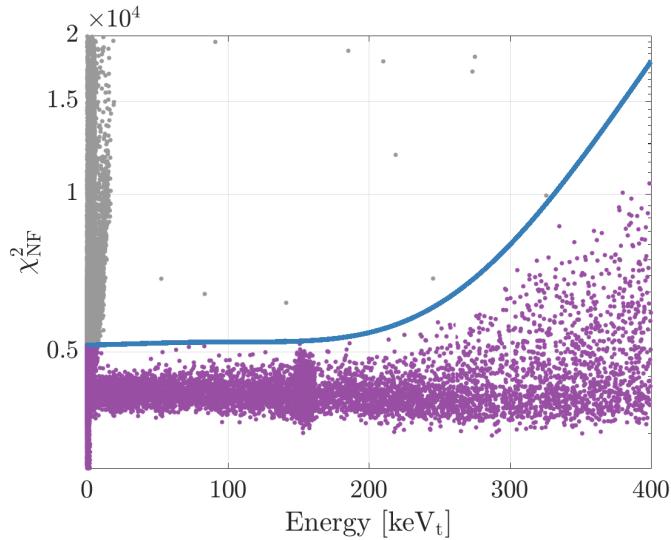
Figure 11.5: Total phonon NSOF-fit χ^2 goodness-of-fit value as a function of energy for ^{252}Cf events in Run 2a, including the definition of the cut in this plane (blue line). Events below the cut (purple) are retained while those above (grey) are rejected.

(a)

(b)
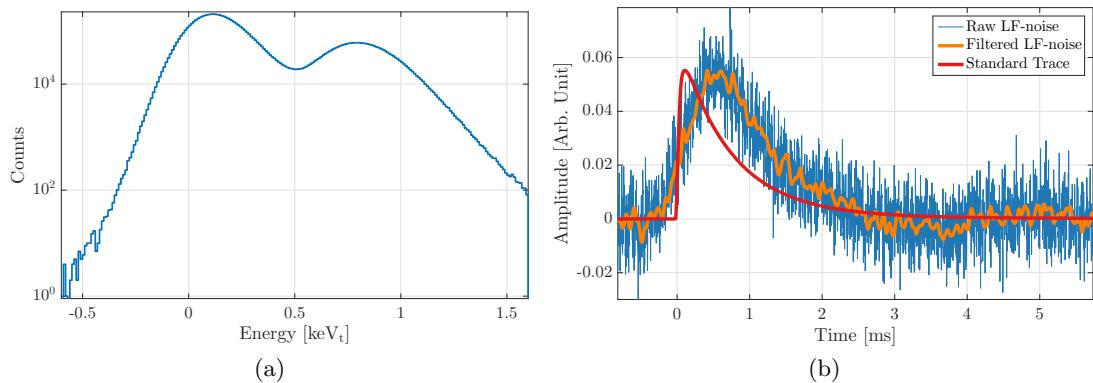
Figure 11.6: Run 2 noise distribution (a) showing the expected electronics noise width at $\sim$0 keV$_t$ and the LF-noise distribution at $\sim$0.75 keV$_t$ along with a sample trace (b) from the LF-noise distribution. The raw trace is shown in blue with the orange being smoothed with a low-pass filter. Comparing to the red OF template demonstrates the poor pulse-shape of the LF-noise event.

In an effort to better track and reject this source of non-physical background, vibrational sensors were installed in and around the experiment (Sec. 9.3). Much of the vibration monitoring work was initiated by R. Basu Thakur and much credit is due to him for this work. Although initial attempts to reject the LF-noise were made using only the vibrational information, on its own such a cut was ultimately unsuccessful. Instead, a cut is made which uses the phonon pulse-shape in addition to the noise monitor information. The full study first considers the cryocooler timing information, then defines a correlated noise metric using that timing information, and finally defines a pulse-shape based cut. This is organized as

(1): Cryocooler Timing

(2): Correlated Noise Metric

(3): $\Delta\chi^2_{\mathrm{LF}}$ Pulse-Shape Cut

(1) Cryocooler Timing

Of the multiple noise monitors installed on the experiment, the Setra accelerometer located on the cryocooler was the most sensitive to the cryocooler-generated vibrations, and it is selected as the primary noise monitor for the analysis. The outputs from the sensor, recorded with every event in the experiment, are twofold: a 13 ms digitized trace of its measured acceleration and the time of the event compared to the start time the cryocooler cycle. The "start" is defined based on the threshold discriminator output of the monitor, i.e. the last time the acceleration exceeded a set value. These outputs are processed with the data and are manifest in four variables:

- $t_- \equiv t_{\mathrm{last}} - t_{\mathrm{global}}$, where t_{global} is the global trigger time of the current event and t_{last} is the most recent threshold discriminator time. This is the time since the start of the immediately preceding cryocooler cycle (time-since).

- $t_+ \equiv t_{\mathrm{next}} - t_{\mathrm{global}}$, t_{next} is the next occurring threshold discriminator time. This is the time until the next start of a cryocooler cycle (time-until).

- μ_s The mean of the ADC values from the digitized trace.

- σ_s The standard deviation of the ADC values from the digitized trace.
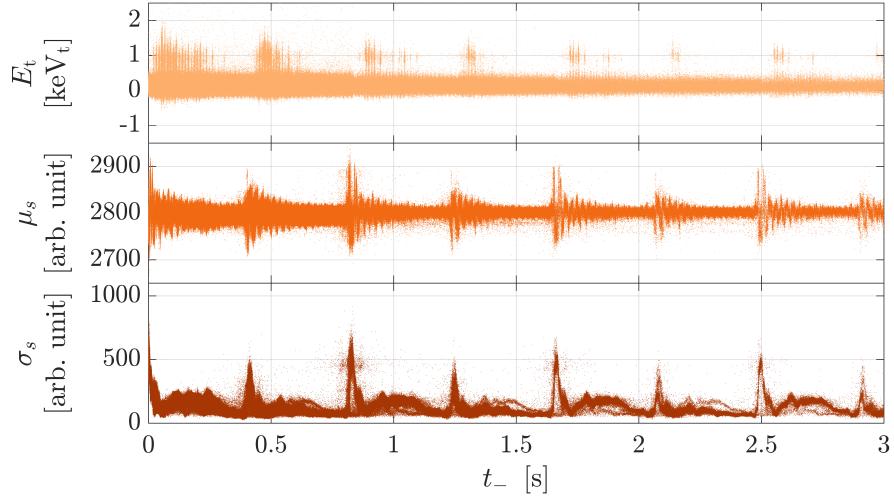
Figure 11.7: Energy (top) and the mean (μ_s, middle) and standard deviation (σ_s, bottom) of the Setra accelerometer trace as a function of time-since the previous cryocooler cycle (t_-). Only times up to 3 s are shown, however the distribution continues out to $\mathcal{O}(100\text{ s})$ with decreasing statics at larger times. The peaks in the Setra quantities appear to correlate with the LF-noise seen in the energy plane ($\sim$1 keV$_\text{t}$).

The cryocooler causes a response in the detector as opposed to the converse and thus t_- is the time of interest. The energy of events near the noise threshold in Run 2[5] as well as the two Setra-trace variables are compared to the time-since quantity in Fig. 11.7.

As can be seen from the figure, the timing distribution goes well beyond the roughly one second cryocooler period. There are also obvious times when the accelerometer detected stronger vibrations and these appear to correlate, with some time delay, with the LF-noise (clusters at $E_\text{t} \sim 1$ keV$_\text{t}$).

The extension beyond a single cryocooler cycle is understood by recognizing that the non-linear nature of the noise means that some cycles do not reach the threshold necessary to generate a time stamp. These cycles are "missed" in the data. The probability to miss a cycle should decrease with time, which is observed in Fig. 11.7. In the processing, if there is not a Setra time-stamp in the history buffer, then t_- is derived by finding t_- of the preceding event and adding the time between the events.

---

[5] For the entirety of the LF-noise discussion, the ptOF estimate of E_t is used to avoid any artifacts due to the NSOF fit low-energy cut-off.
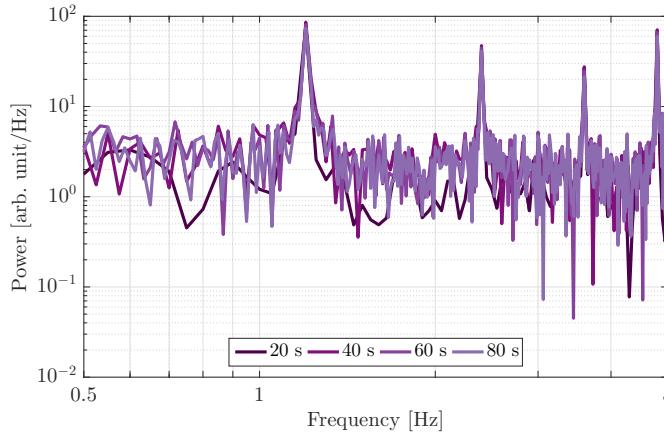
Figure 11.8: Fourier transformation of the standard deviation of the Setra accelerometer (σ_s) distribution, binned by 2 ms, for different bandwidths. The first two peaks are at frequencies of 1.2 and 2.4 Hz which correspond to timings of 830 and 420 ms respectively. These are the frequency of the chirp and thump, which gives the total period of the cryocooler as $t_c = 830$ ms. Figure adapted from [337].

As each cycle should be identical, the distributions above can be simplified by taking a modified time-since $\hat{t}_- \equiv t_-$ (mod t_c), where t_c is the period of the cryocooler. The period is measured by binning σ_s in bins of 2 ms (the resolution of t_- [336]) and performing a Fourier transformation as seen in Fig. 11.8, where multiple sharp peaks in the spectrum are seen. The first two occur at f=1.2 and 2.4 Hz respectively, giving times of 830 and 420 ms and corresponding to the two LF-noise clusters per cycle. The first (and largest) is termed the "chirp" while the second the "thump" after the sensorial characteristics one would observe while standing next to the experiment in Soudan. Since the chirp is the strongest portion of the vibrational cycle, it is what triggers the time-stamp and is therefore the de-facto "start" of the cycle. This gives $\hat{t}_- = 830$ ms.

With t_c measured, Fig. 11.9 gives the distributions of energy and Setra quantities as a function of cycle time. The clustering of events observed above is now more easily discussed. The bye-eye correlation between the accelerometer and LF-noise is again observed, with a delay in $\hat{t}_-$ between the setra and detector measurements. The strength of this correlation, and the size of the delay, is computed by considering the cross-correlation, with temporal shift τ, between the energy distribution and σ_s [338]

$$R(\tau) = \frac{\int_0^{t_c} \frac{dt}{t_c} x(t) W_{t_c}\{s(t-\tau)\}}{\sqrt{\int_0^{t_c} \frac{dt}{t_c} x^2(t) \int_0^{t_c} \frac{dt}{t_c} s^2(t)}} \tag{11.1}$$
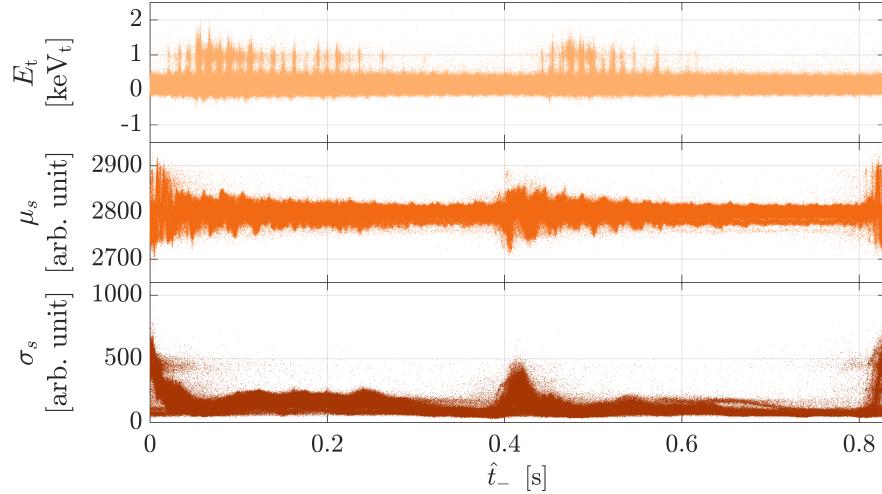
Figure 11.9: Energy (top) and the mean (μ_s, middle) and standard deviation (σ_s, bottom) of the Setra accelerometer trace as a function of the modulo, over the period $t_c = 830$ ms, time-since the previous cryocooler cycle ($\hat{t}_-$). For each cycle, there are two clusterings of events, with the clusters in energy delayed compared to the Setra quantities.

where, for t_k bins, $x(t_k) = \mu_k^x + 3\sigma_k^x$, with μ_k^x and σ_k^x as the mean and standard deviation of the noise distribution in the kth bin, $s(t_k) = \mu_k^s + 3\sigma_k^s$, with μ_k^s and σ_k^s as the mean and standard deviation of σ_s in the kth bin, and W_{t_c} wraps the distribution around the t_c period of the cryocooler. The distributions of $x(t_-)$ and $s(t_-)$ are shown in the top panel of Fig. 11.10 and $R(\tau)$ is shown in the bottom.

The maximum value of $R(\tau)$ is 0.93 at $\tau = 54$ ms, meaning a strong correlation with a delay of 54 ms. The delay is a combination of the time needed for the vibration to propagate to the detector, the dispersion of the vibration as it travels, and general filtering lags. The two clusters in energy, and hence, the LF-noise, are decisively shown to correlate to the chirp and thump in the cryocooler.

(2): Correlated Noise Metric

A quantitative metric is developed to identify periods of correlated noise, i.e. LF-noise, using the cryocooler timing information. The basis of this metric is to bin by time and assign a score to each bin based upon how "bad" the noise is in that bin. The score is then adjusted by how poor the neighboring bins score.
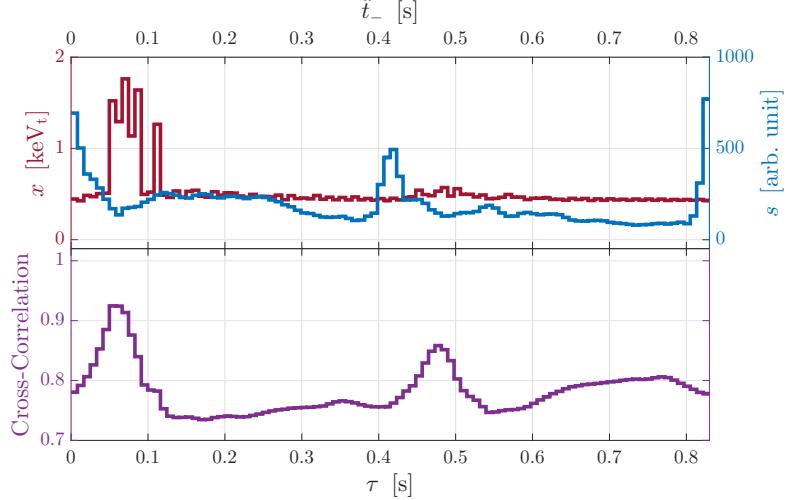
Figure 11.10: Metrics of the upper edge of the noise distribution (x) and the standard deviation of the Setra trace (s) over modulo cycle time $(\hat{t}_-)$ (top) and the cross-correlation between them for variable timing delays (τ) (bottom). The strongest peak is at a delay of $\tau = 54$ ms with a correlation of 0.93. The secondary peak at $\tau \sim 450$ ms is the cross-correlation between the chirp and the thump. Figure adapted from [336].

The increased trigger rate which ended Run 2a was due to LF-noise induced throughout the entire cryocooler cycle. To include this change in cryocooler behavior, the metric is developed in the plane of time-since, calendar time, and event count This 2-D plane is seen in Fig. 11.11 for the whole of Run 2a. The color axis is the number of events, per bin, between -5–17.5 keV$_t$ with a trigger in iT5Z2. The binning is arbitrary (as long as the thump and chirp are separate) for $\hat{t}_-$ at $\Delta t = 10$ ms, while for calendar time it is chosen as short enough, at $\Delta T = 1.2$ hr, to identify periods when no data were taken (e.g. calibration data). The utility of working in this plane is evident as the calendar-time-varying "strength" of the chirp and thump is evident and is explicitly usable.

The involved development of the noise score is detailed in Appendix C. The final score $s^{(3)}$ is calculated for the ith and j^{th} bin as

$$s_{ij}^{(3)} = \left(\prod_{m=i-N}^{i+N} \prod_{n=j-N}^{j+N} \left(s_{ij}^{(0)} \right)^{w_d(i,j;m,n)} \right)^{1/\sum_{m,n} w_d}, \qquad (11.2)$$
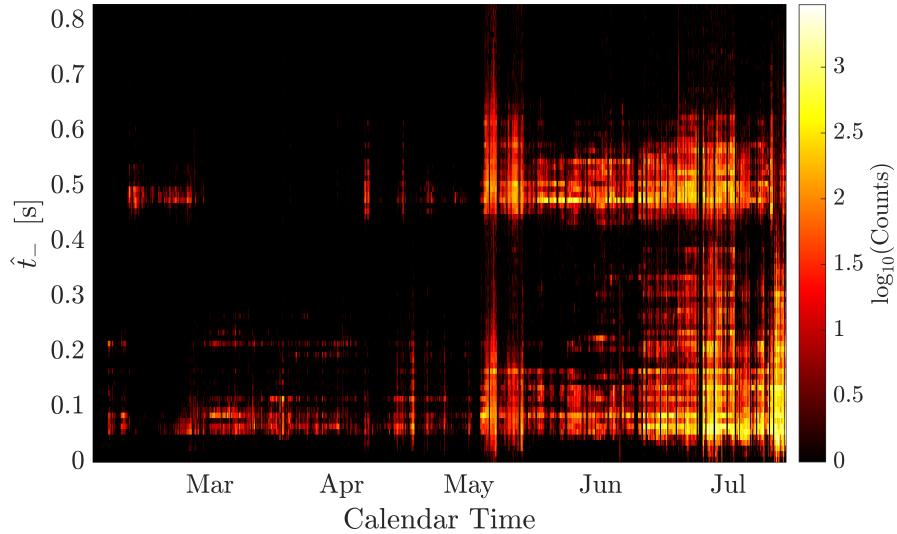
Figure 11.11: Number of triggered events for Run 2a between -5–17.5 keV$_t$ in the two dimensional plane of modulo cryocooler time, $\hat{t}_-$, and calendar time. The color scale is logarithmic with empty bins mapped to the lowest color. The thump and chirp identified in the one-dimensional plane are seen as horizontal bands near $\hat{t}_- \sim 0.1, 0.5$.

where N is the number of adjoining bins to correlate over, $w_d = (1 - \alpha)^d$ is the correlation weight with shaping parameter α and inter-bin distance $d = \sqrt{(i - m)^2 + (j - n)^2}$. The initial score $s_{ij}^{(0)}$ is a Poisson CDF with mean ξ, where ξ is a filter parameter to be tuned, defined for the ith and j^{th} bins as

$$s_{ij}^{(0)} = \text{CDF}_{\text{Poiss}}(n_{ij}; \xi). \tag{11.3}$$

In essence, a single bin is correlated to a $N{+}1 \times N{+}1$ square centered on itself with the strength of those correlations controlled by two factors: the distance d (closer bins exert stronger effect) and the overall strength α, where, as $\alpha \to 1$, the correlation disappears $\left(s^{(3)} \to s^{(0)}\right)$.

The correlated score is an a-causal (correlating forward and backwards in time) geometric low-pass filter with several parameters: ΔT, Δt, ξ, N, and α. An example score is shown in Fig. 11.12 with the same time bins as before, $\Delta T = 1.2$ hr and $\Delta t = 10$ ms, $\xi = 3$, $N = 3$, and $\alpha = 0.2$. The choice of these parameters requires some explanation. The choices of ΔT, Δt, and N are related as both increasing N and
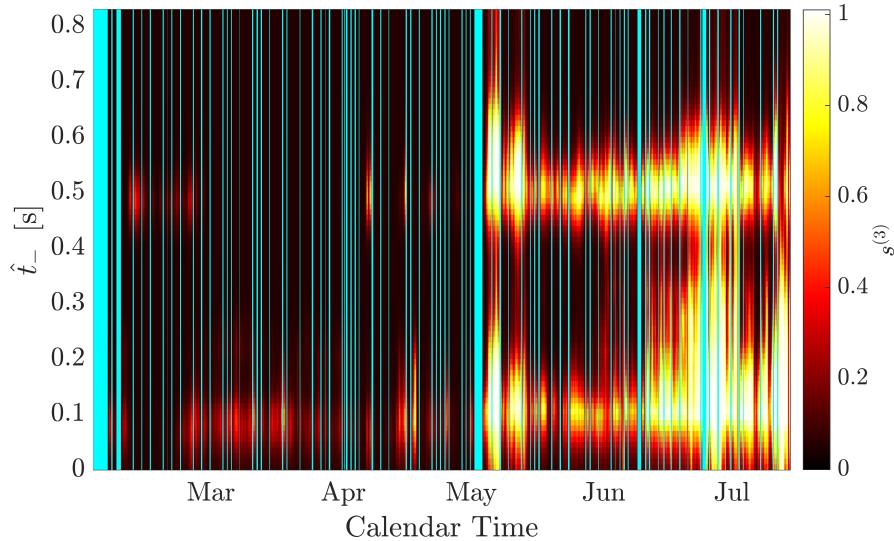
Figure 11.12: Correlated noise score $s^{(3)}$ for Run 2a based on the number of counts per two-dimensional time bin (Fig. 11.11) after applying an a-causal geometric low-pass filter (Eq. 11.2). Times when no data were taken, e.g. calibration data, are shown in cyan and not used for the correlation. Scores closer to unity indicate periods of high LF-noise induction.

increasing the time bins implies correlating over longer stretches of time. The score should not be correlated with empty time periods, such as calibration data, and hence the choice of 1.2 hr as shorter than a typical series length ($\sim$3 hours). A series length is also a reasonable time-scale to correlate over, hence $N = 3$. Bye-eye studies indicate that a shaping parameter of $\alpha = 0.2$ is reasonable to adequately smooth over single bin fluctuations while leaving true correlations identifiable. See Appendix C for details of these choices.

One use of the correlated score could be to remove LF-noise by directly cutting on score value. This was the initial intent of developing the score, where periods with $s^{(3)} < \eta$, for some tuned η threshold, were removed and the cut treated as a live time cut. Several attempts were made to optimize the cut using both η and ξ as free parameters. These attempts gave values in the range of $\xi \in [2, 3]$ and $\eta \in [0.054, 0.15]$ with the variables anti-correlated (Appendix C). However, these optimization attempts removed a large portion of the live time, 57.3–78.9 %, which was cause for concern and
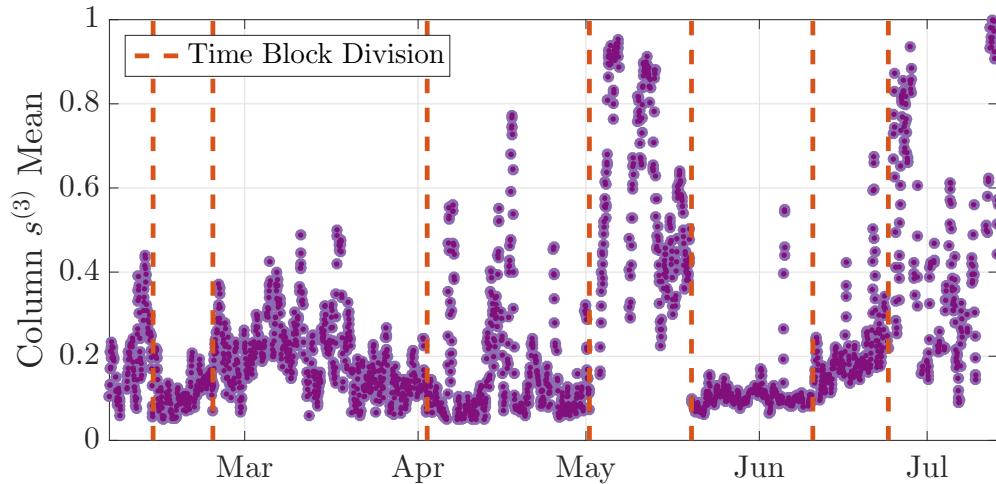
Figure 11.13: Average correlated-noise score $s^{(3)}$ (purple points) over all events in each of the 1.2 hr calendar time bins and the divisions of the eight time blocks (dashed lines) defined for Run 2a.

ultimately led to the abandonment of using the score in this manner.[6] This choice was further confirmed when it was learned that the noise monitor information is not available for Run 2b and hence no such cut is possible for those data.

The strategy ultimately used for LF-noise removal was to use the correlated score to define time blocks of similar-LF-noise activity and then create a pulse-shape based cut which is tighter/looser depending on the cryocooler activity. For Run 2a, these time blocks are defined by considering the average score, over individual events, for each calendar time bin. This average is shown in Fig. 11.13 and it tracks the expected behavior based on Fig. 11.12 reasonably well. Run 2a is split into eight different blocks, also seen in the figure, based on trends in this average.

For Run 2b, the score cannot cannot be used to define time blocks. However, there are discrete jumps in energy scale during Run 2b. Changes in the noise environment, or at least the reconstructed energy of the noise, is also expected with these jumps and thus they naturally define time blocks: Run 2b is split into four time blocks based on these changes. The start and end times of each of the 12 total time blocks are given in Table 11.1.

---

[6] The unwieldy number of free parameters to optimize, and no clear path on how to do this without bias, was also a factor in this decision.

Time Block	Start Time [MM/DD HH:MM]	End Time [MM/DD HH:MM]
1	02/04 19:58	02/12 14:28
2	02/12 14:28	02/23 07:15
3	02/23 07:15	04/02 14:23
4	04/02 14:23	01/05 15:32
5	05/01 15:32	05/19 21:30
6	05/19 21:30	06/10 13:03
7	06/10 13:03	06/24 01:02
8	06/24 01:02	07/14 13:00
9	09/23 06:41	10/02 00:31
10	10/02 00:31	10/23 00:00
11	10/23 00:00	11/02 00:00
12	11/02 00:00	11/10 14:13

Table 11.1: Start and end times for the 12 time blocks of Run 2. The first eight are in Run 2a and defined via the correlated noise score. The last four are in Run 2b and are defined based on discrete changes in the environment. The year for all dates is 2014.
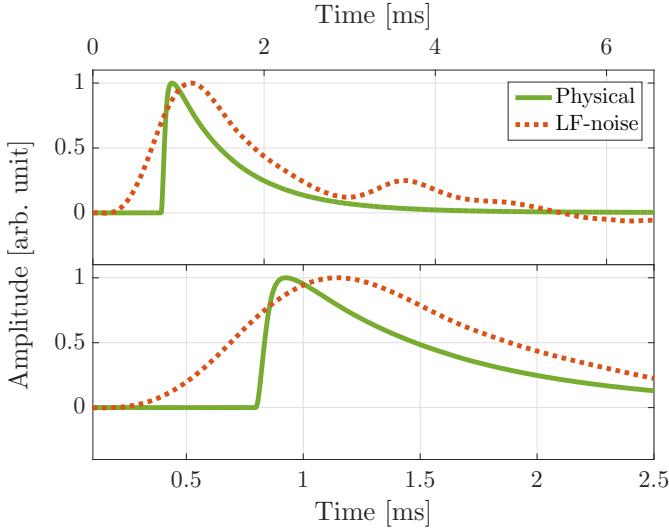
Figure 11.14: Optimal filter templates for a standard phonon pulse (green solid) and background LF-noise (orange dot). The full trace (top) and zoom around rising edge (bottom) are shown. The LF-noise trace has longer rise- and fall-times and multiple peaks compared to the phonon trace.

(3) $\Delta\chi^2_{\mathbf{LF}}$ Pulse-Shape Cut

Within each each time block defined above, a cut based upon the total-phonon pulse-shape of individual events is defined similarly to the cuts of this kind which were pioneered in the SuperCDMS LT analysis. The general approach is, for a given background, (1) identify a "clean" population of background events, (2) define a template for the background by aligning and averaging the background population's traces, (3) perform an OF fit using the background template during the data processing, (4) compare the OF-fit χ^2 values from the fits to the standard template and the background template.

The LF-noise template used for the Run 2 analysis is the same as was used for the LT analysis. The details of creating this template are described in Appendix A of Ref. [187]. This template is compared to the standard event template in Fig. 11.14, where it is seen that the pulse-shapes are quite different. Notably, the LF-noise template has longer rise- and fall-times and multiple peaks.

After processing the data with the LF-noise template, this template's fit is compared to the fit of the standard phonon template by considering the difference of χ^2 values $\Delta\chi^2_{\mathrm{LF}}$

$$\Delta\chi^2_{\mathrm{LF}} \equiv \chi^2_{\mathrm{OF}} - \chi^2_{\mathrm{LF}}. \tag{11.4}$$

The regular OF fit (as opposed to NSOF) is used because the LF-noise fit is done with the OF algorithm. The typical distribution of $\Delta\chi^2_{\mathrm{LF}}$ can be seen in Fig. 11.15 for both
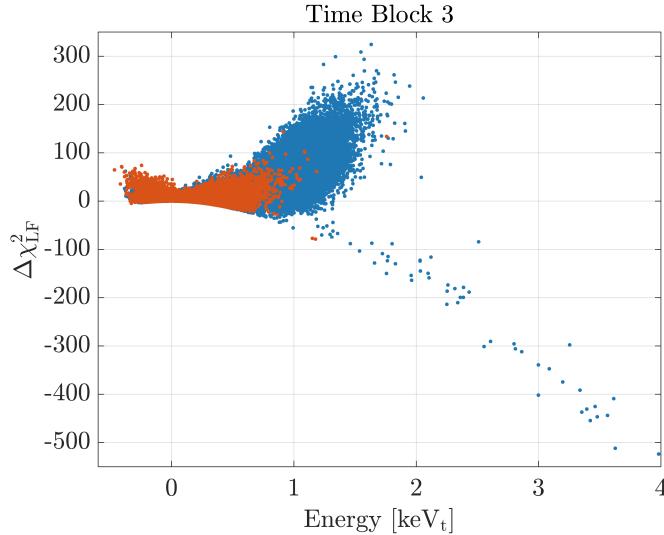
Figure 11.15: $\Delta\chi^2_{\mathrm{LF}}$ as a function total phonon energy for time block 3 for random (orange) and nonrandom (blue) triggered events. Events which are more LF-noise-like have positive $\Delta\chi^2_{\mathrm{LF}}$ and cluster near 1 keV$_t$ while those similar to standard pulses have negative $\Delta\chi^2_{\mathrm{LF}}$ and fall along a downward parabola.

random and non-random triggers of time block 3 after applying all of the previously defined cuts.[7] Events which are better fit by the standard template are negative while those better fit by the LF-noise template are positive. High quality traces fall along a downward parabola, which is intuitively understood given the quadratic dependencies of the χ^2 on pulse amplitude (Appendix A), while LF-noise clusters near 1 keV$_t$ with some outliers. The LF-noise portion is not a parabola as LF-noise events have considerable pulse-shape variation.

A tripart cut is defined in this plane, where the type of cut is the same across all time blocks but the tightness, i.e. how strict is it in rejecting LF-noise, varies by block depending on how noisy (high LF-noise rate) or quiet (low LF-noise rate) the period is. This also necessitates that the cuts be tuned on the low-background data itself, to best capture the differences in the noise environment. The cut consists of a flat portion, a parabolic portion, and a contoured portion.

The flat portion is defined by considering the randomly triggered events. The flat-cut threshold is set using a "symmeterized" randoms distribution as the randoms can also be contaminated by LF-noise. This distribution is found by taking the randoms distribution with negative $\Delta\chi^2_{\mathrm{LF}}$ (which is hypothetically LF-noise free) and reflecting it to positive $\Delta\chi^2_{\mathrm{LF}}$ values. The randoms distributions for time block 7 are shown in

---

[7] A rough cut against pulse shape glitches (Sec. 11.3.3) is also applied for clarity. The rough cut is the same as used in Run 1.
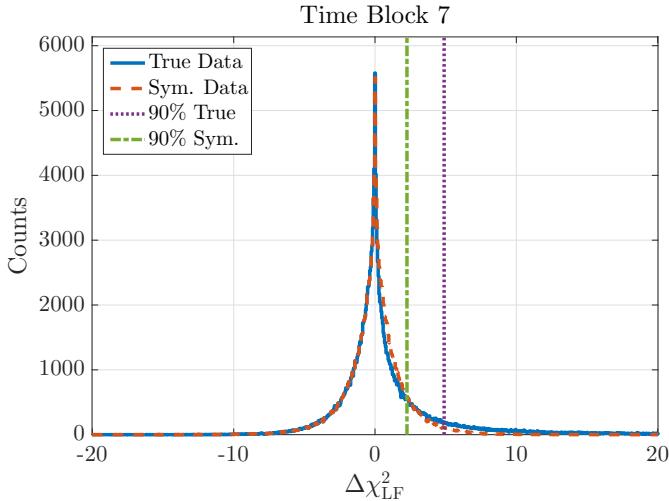
Figure 11.16: Distributions of random triggers in $\Delta\chi^2_{\text{LF}}$ for time block 7 showing the true (blue) and symmeterized (orange dashed) data along with the 90$^{\text{th}}$ percentile of each (purple dot-dashed and green dashed respectively). The LF-noise cut rejects events which fall above the 90% point of the symmeterized distribution.

Fig. 11.16. This portion of the cut primarily removes events at the lowest energies and the symmeterization places a stricter cut, in general, for each time block.

The parabolic portion is defined by fitting the high-energy parabolic arm. The fitting is done in multiple steps. A parabola is first fit to the event population itself to find a central fit. Next, the data is binned in 40 keV$_{\text{t}}$ bins. Within each bin, a Gaussian is fit to a shifted $\Delta\chi^2_{\text{LF}}$ distribution. This shifted distribution takes, for each event, the $\Delta\chi^2_{\text{LF}}$ of the event and subtracts the value of the central parabola at that event's energy. The shifting best captures the expected Gaussian white noise. The cut itself is fit as a second parabola to the $\mu + 5\sigma$ points from each bin, where μ is the value of the central parabola at the bin's center and σ is the width of the shifted distribution fit. An additional constraint is placed on the y-intercept of the cut to ensure the cut is tight enough at low energy. The components of the parabola fitting, along with the final cut, for time block 2 are shown in Fig. 11.17.

The final component of the cut is tuned on the LF noise itself using a kernel density estimate (KDE). A KDE is an estimate of the underlying, and unknown, PDF of the data. Given N observations $\boldsymbol{X}$ from an unknown two-dimensional probability density function, the Gaussian multivariate KDE $\hat{f}(\boldsymbol{x}; \boldsymbol{H})$ is defined as

$$\hat{f}(\boldsymbol{x}; \boldsymbol{H}) = \frac{1}{N} \sum_{i=1}^{N} \phi(\boldsymbol{x}, \boldsymbol{X}_i; \boldsymbol{H}), \tag{11.5}$$
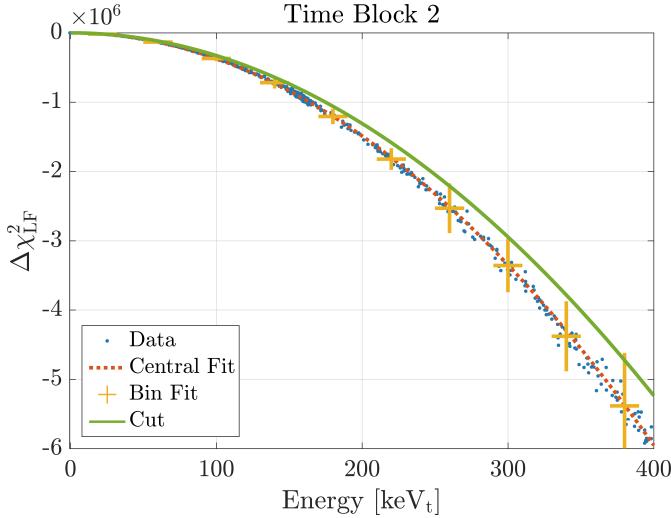
Figure 11.17: $\Delta\chi^2_{\mathrm{LF}}$ as a function of total phonon energy for time block 2 showing the good-event parabola (blue) and the parabolic LF-noise cut (green). The data are binned by energy and a Gaussian fit to the $\Delta\chi^2_{\mathrm{LF}}$ distribution shifted by the central fit parabola (orange dotted). The cut is fit to the $\mu + 5\sigma$ points (yellow) of each bin and events above the parabola are rejected.

where

$$\phi(\boldsymbol{x}, \boldsymbol{X}_i; \boldsymbol{H}) = \frac{1}{2\pi} |\boldsymbol{H}|^{-1} e^{\left(-\frac{1}{2}(\boldsymbol{x}-\boldsymbol{X}_i)^\intercal \boldsymbol{H}^{-1}(\boldsymbol{x}-\boldsymbol{X}_i)\right)} \tag{11.6}$$

is a multi-variate Gaussian PDF with mean $\boldsymbol{X}_i$ and covariance $\boldsymbol{H}$ (with determinant $|\boldsymbol{H}|$). The covariance of the Gaussian kernel is also called the bandwidth of the KDE. The choice of bandwidth is often a difficult question and the resulting KDE highly depends on this choice. For the use here, an algorithm which dynamically determines the optimal bandwidth in each dimension, assuming $\boldsymbol{H}$ is diagonal, is used [339]. In each time block, a KDE is computed using events in the LF-noise energy range which also issued a trigger, i.e. $\boldsymbol{X}_i = \left(E_{\mathrm{t},i}, \Delta\chi^2_{\mathrm{LF},i}\right)$.

The cut is a convex hull around the largest $n^{\mathrm{th}}\sigma$ contour where n is defined separately for each time block. The cut removes events which fall inside this contour. The components of the KDE definition and the resulting cut for time block 4 is shown in Fig. 11.18, where, for this particular time block the cut is set using the largest 2.5σ contour.

The final cut removes events which fall above the flat or parabolic portions or within the KDE contour. Two examples of the final cut are shown in Fig. 11.19 for time block 2 (a relatively quite block) and time block 7 (a relatively noisy block). The differences between the two show the strength of the time block formalism, specifically block 2 retains efficiency down to the lowest energy, while block 7 has zero efficiency (as indicated by the entire population being removed) close to the LF-noise cluster. How
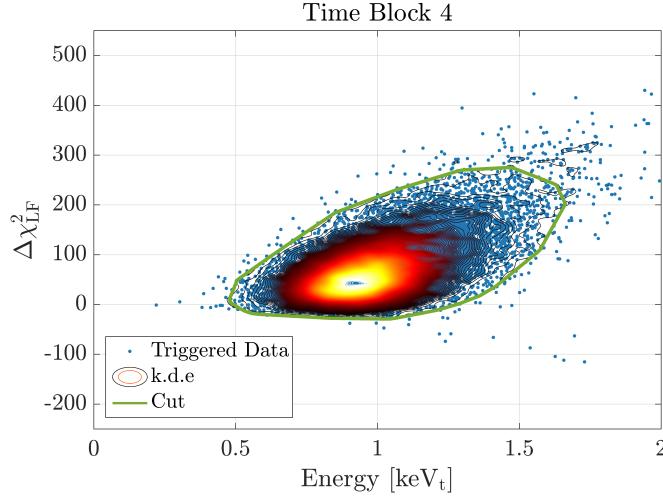
Figure 11.18: $\Delta\chi^2_{\mathrm{LF}}$ as a function of total phonon energy for time block 4 showing triggered events near the LF-noise cluster (blue) along with the corresponding kernel density estimate (contours) and contour cut (green). The cut is defined as a convex hull around the largest 2.5σ (for this time block) contour of the KDE and rejects events within the contour.

loose or tight a given time block is tuned is determined by surveying events near the border and discerning whether they are LF noise by considering their individual pulse shape.

11.3.3 Pulse-Shape Glitches

Glitches are removed by two other cuts, the asymmetric multiply-triggered glitches (Sec. 11.2.3) and non-triggered ionization glitches (Sec. 11.2.4). However, there is a population of low-energy phonon glitches which are below the trigger threshold on some detectors and do not trigger more than a single detector and therefore pass both of these cuts. These glitches are removed by pulse-shape discrimination as, by definition, a glitch has unphysically sharp rise and fall times.

This cut is defined in the same manner as the LF-noise pulse-shape cut. A glitch-trace template was defined by R. Bunker in Ref. [334] for general use is SuperCDMS analyses. That template is used without change in this analysis and can be seen in Fig. 11.20; the rise and fall times are noticeably shorter compared to the standard pulse.

As with the LF-noise cut, all events are fit to the glitch template in the processing using the OF-algorithm and the the difference of goodness-of-fit quantities is used to define $\Delta\chi^2_{\mathrm{Gl}}$ as

$$\Delta\chi^2_{\mathrm{Gl}} \equiv \chi^2_{\mathrm{OF}} - \chi^2_{\mathrm{Gl}}. \tag{11.7}$$

(a) (b)
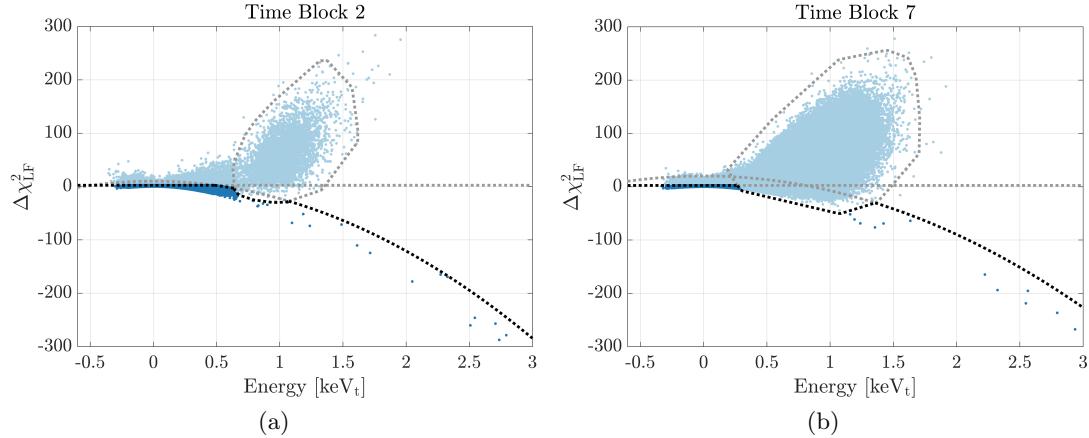
Figure 11.19: $\Delta\chi^2_{\text{LF}}$ as a function of total phonon energy for time blocks 2 (a) and 7 (b) showing the three portions of the cut (dotted) with the active portion at any given energy darkened. Events above the flat or parabolic portions or within the contour portion are rejected (light blue) while any others are retained (dark blue). Time block 2 is a relatively quite block while time block 7 is relatively noisy. The contour portion of the cut is tuned looser in block 2 (2.5σ) than in block 7 (5σ) due to the changing LF-noise environment throughout the run.
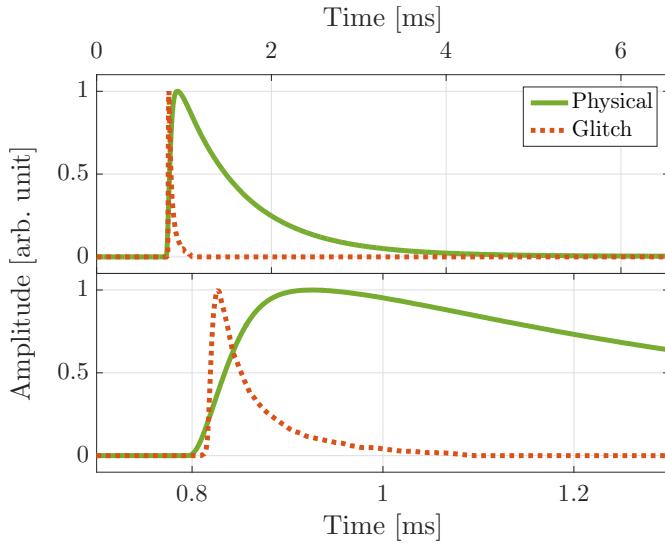
Figure 11.20: Optimal filter templates a the standard phonon pulse (green solid) and electronic glitch (orange dot). The full trace (top) and a zoom around the rising edges (bottom) are shown. The glitch template has significantly smaller rise- and fall-times.
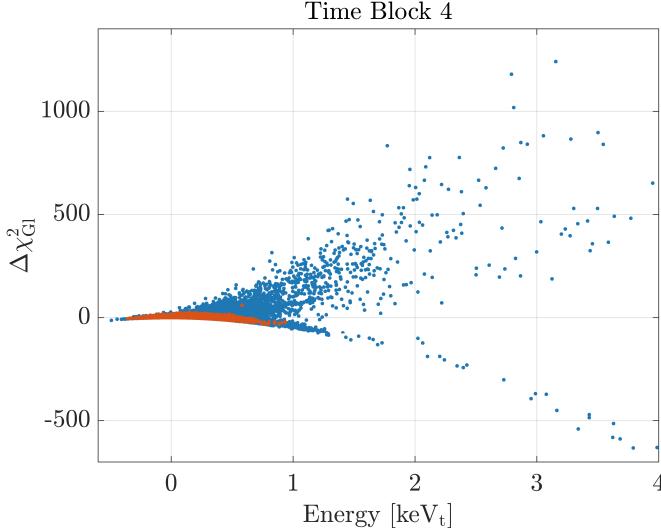
Time Block 4

Figure 11.21: $\Delta\chi^2_{\mathrm{Gl}}$ as a function of total phonon energy (OF) for time block 4 for random (orange) and nonrandom (blue) triggered events. Events which are more glitch-like have positive $\Delta\chi^2_{\mathrm{Gl}}$ and occupy a roughly-parabolic region. Events similar to standard pulses have negative $\Delta\chi^2_{\mathrm{Gl}}$ and occupy a downward facing parabola.

Events which fit the glitch template better have positive $\Delta\chi^2_{\mathrm{Gl}}$ while those which fit the standard template better are negative and fall along a parabola. The positive population is more parabolic than the similar population in $\Delta\chi^2_{\mathrm{LF}}$ as glitches have more consistent pulse shape. Due to the similarities between this cut and the LF-noise cut, the same time-block structure is used. The $\Delta\chi^2_{\mathrm{Gl}}$ versus total phonon energy (again using the standard OF-estimated energy for consistency) is seen in Fig. 11.21 for time block 4. Glitches populate the positive regions of the plane with sparse density.

A cut was made in Run 1 in this plane keeping events below an energy independent threshold of $\Delta\chi^2_{\mathrm{Gl}} < 10$. This is a rough cut which was used for much of the previously described analysis. The energy-independent thresholds for the Run 2 cut, tuned by time block, are found by finding the tighter cut between the Run 1 threshold and the 99th percentile of the random trigger $\Delta\chi^2_{\mathrm{Gl}}$ distribution. An example distribution of random triggers, for time block 4, is shown in Fig. 11.22.

A a parabolic portion of the cut is also required since a small population of glitch events passes the flat threshold. The parabolic cut is defined identically to its counterpart in the LF-noise cut: a parabola is fit to the good events distribution, the data are binned in 40 keV$_{\mathrm{t}}$ bins, in each bin, a shifted $\Delta\chi^2_{\mathrm{Gl}}$ distribution is fit to a Gaussian, a parabola is fit to the $\mu + 5\sigma$ points for each bin with a bound on the y-intercept to ensure a tight cut at low energy. This last parabola is the cut threshold. Each of these components are shown in Fig. 11.23 for time block 4. The parabolic portion of the
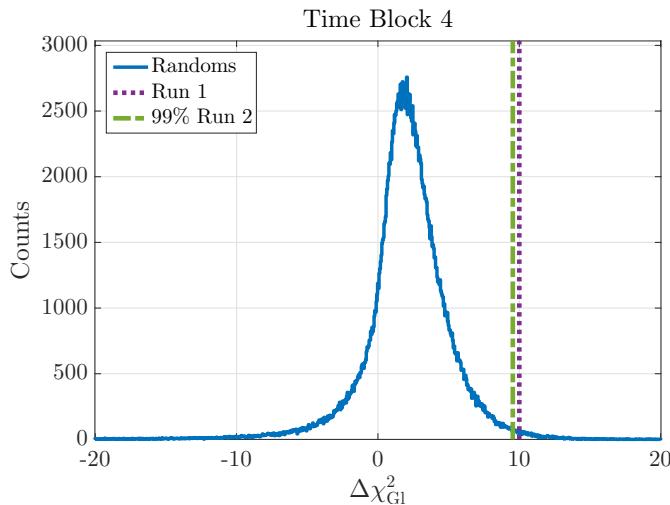
Figure 11.22: Distribution of random triggers in $\Delta\chi^2_{\mathrm{Gl}}$ for time block 4 along with the 99th percentile point (green dashed) and the Run 1 glitch cut threshold (purple dotted). In each time block, the glitch cut rejects events above the minimum of these two; for this time block it is the 99th percentile point.

cut removes outliers at high energy as well as the tails of the glitch distribution at low energies.

The final glitch cut removes events above either portion's threshold in each time block. This is shown for time block 4 in Fig. 11.24. Variations between the time blocks in this cut are due more to discrete shifts in the experimental noise conditions than changes in the glitch population itself.

11.4 Simple Physics Cuts

The cut criteria for removing high-quality pulses which do not match the standard WIMP profile, or for which there are other physical reasons for rejection, are split into two categories. Those cuts which have been used, in one form or another, by CDMS for many previous analyses are described in this section. The more complicated fiducial volume cut, which was developed specifically for this analysis, is covered in the following Sec. 11.5.

11.4.1 Multiple Scatters

Dark matter has such a small interaction cross-section that the probability for a single WIMP to interact in more than one iZIP detector in the same event (termed a multiple scatter) is negligibly low. Multiple scatter events are removed from the WIMP-search
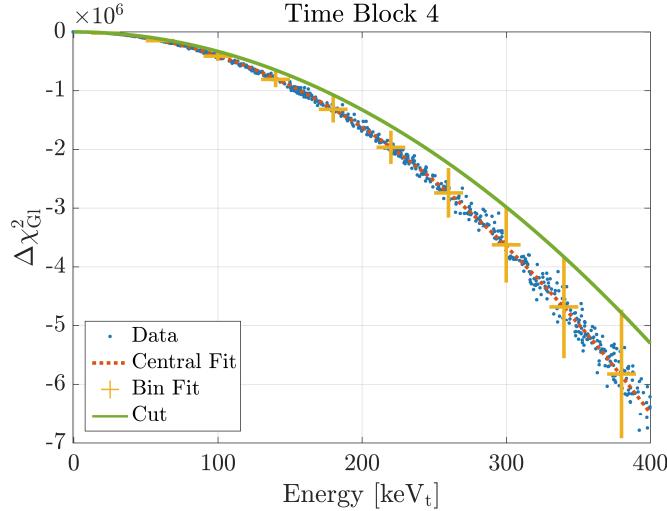
Figure 11.23: $\Delta\chi^2_{\text{Gl}}$ as a function of total phonon energy for time block 4 showing the good event parabola (blue) and the parabolic glitch cut (green). The data are binned by energy and a Gaussian fit to the $\Delta\chi^2_{\text{Gl}}$ distribution shifted by the central fit parabola (orange dotted). The cut is fit the $\mu + 5\sigma$ points (yellow) of each of the bins and events above the parabola are rejected.
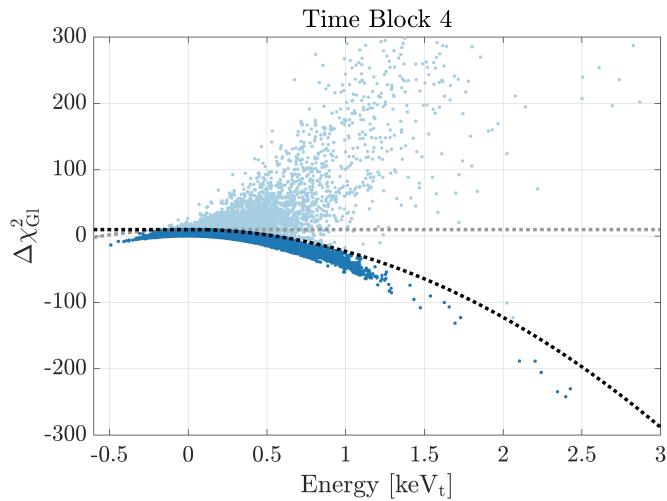
Figure 11.24: $\Delta\chi^2_{\text{Gl}}$ as a function of total phonon energy for time block 4 showing the two portions of the cut (dotted) with the active portion at any given energy darkened. Events above any portion of the cut are rejected (light blue) while those below are retained (dark blue).

data set to effectively lower the background. This is particularly important for CDMSlite since the dominant background are electron recoils, which have a higher probability for multiply scattering. A cut to identify multiple scatters, by necessity, must involve the other iZIPs in the detector array and such a cut was developed by B. Welliver for the general SuperCDMS analyses and adopted for Run 2 analysis [340].

The general strategy for this cut is as follows: to identify a multiple scatter on detector D, examine the other detectors (vetoing detectors) and determine whether the trace in any vetoing detector is above some energy threshold. This classifies the event as a multiple scatter candidate for detector D. The event is classified as a true multiple scatter if the trace in detector D is not noise, i.e. is also above an energy threshold. Consideration is also taken for whether the trace in the vetoing detector is identified as LF-noise or a pulse-shape glitch or if the entire event is classified as a triggered glitch; if so, then the event is not a multiple candidate. This allows for a tight multiples definition, and conversely a loose singles definition when taking the logical negation of the cut.

A CDMSlite specific cut was also considered based solely on the number of triggers in the experiment. Such a cut would have classified events where only iT5Z2 issued a trigger as a single scatter. However, given the special considerations for LF-noise, glitches, and additional detector specific dependencies built into the energy based cut, that cut is still used.

11.4.2   Muon Veto Coincidence

A dark matter candidate event should have no activity in the veto system which surrounds the experiment. This ensures that the event was not caused by cosmic rays or ambient radiation in the cavern.[8] "Activity" in the veto system is defined in two ways. First, a digital time history of veto panels exceeding hardware thresholds is recorded and if a veto panel exceeds its threshold (typically 1–2 MeV) less than 50 μs before or during the event, then the event is rejected. Second, the amplitude of the trace in each panel is read out with each event triggered in the experiment (185 μs before the trigger until 20 μs after). If the amplitude of any trace is above a specified threshold, then that

---

[8] The probability for ambient radiation to penetrate the entire shield is very small, but the possibility should still be accounted for in the analysis.

event is rejected.

11.4.3   NuMI Beam Coincidence

The MINOS experiment [331] was also located at Soudan, where it detected neutrinos created by the NuMI beam at Fermi National Accelerator Laboratory (FNAL). Although the probability for these neutrinos to interact in the SuperCDMS payload is small,[9] events which occur during a NuMI beam dump are removed to be conservative. The NuMI beam dumps are recorded by a GPS time stamp at FNAL and compared to the Symmetricom GPS time stamp unit in the SuperCDMS DAQ. The NuMI beam arrival time at Soudan is provided by the MINOS collaboration and events whose GPS based trigger time is within 200 μs these times are rejected.[10] The number of events removed is consistent with the expected accidental coincidence rate based on the rate of low background events.

11.5   Radial Fiducial Volume

11.5.1   Motivation

The energy spectra remaining for Run 2a and Run 2b after applying the quality and the simple-physics cuts are given in Fig. 11.25. The K- and L-shell lines are prominent in both periods and there is a hint of the M-shell in Run 2a. These spectra are not scaled by their respective live time and hence the inter-peak statistics are less in Run 2b. The activation peaks, however, show comparable statistics due to having performed more ^{252}Cf calibration in Run 2b. There are two features of the spectrum to consider: (1) In Run 2b, there is a very large peak at the lowest energies which completely covers the M-shell's location. The relative rate between the three peaks seen in Run 2a indicates that this peak in Run 2b is not the M-shell peak. (2) The activation peaks are expected to be Gaussian in shape, however there is a noticeable skew to lower energies (most visible in the K shell) which gives the peaks low-energy tails.

---

[9] The estimated number of NuMI neutrino coincidence events in the Run 2 exposure is $\mathcal{O}\left(10^{-5}\text{--}10^{-1}\right)$ where the large uncertainty is due to the uncertain absolute neutrino flux [333].

[10] The 200 μs is a combination of the length of a NuMI spill and the size of the OF-delay search window.
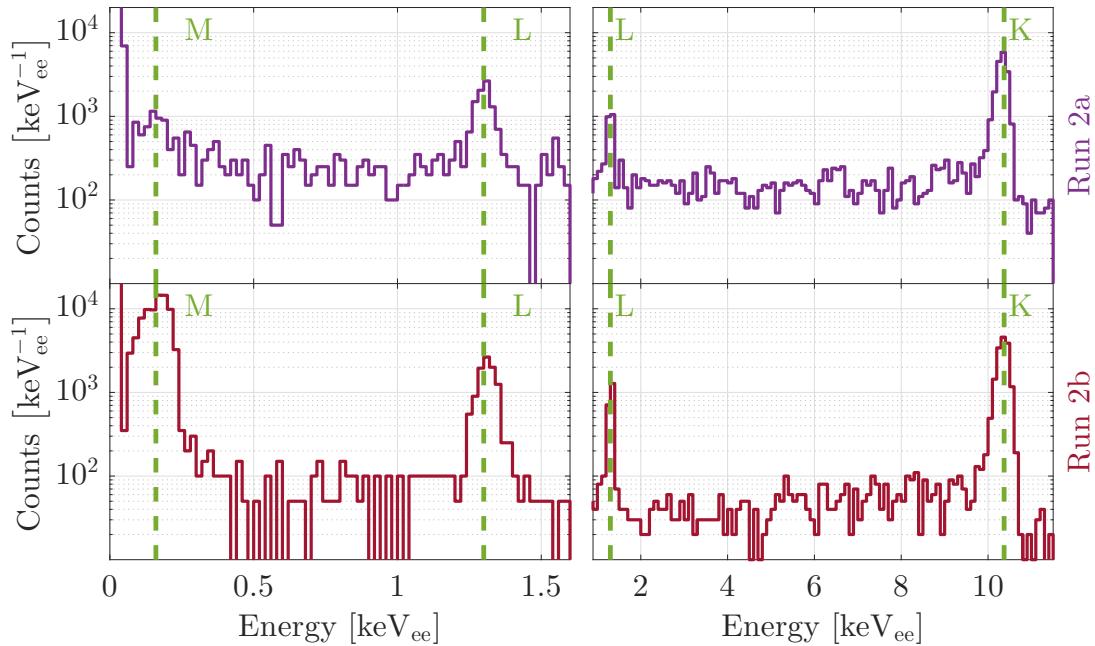
Figure 11.25: Energy spectra of events passing all quality and simple-physics cuts for Run 2a (top) and Run 2b (bottom) for two energy ranges. Vertical lines indicate the locations of the 10.37 (K), 1.30 (L), and 0.16 (M) keV$_{ee}$ activation peaks. The difference in statistics between the peaks between the two runs is due to the difference in live time between Run 2a and Run 2b. Unexpectedly, there is a large peak at $\sim$200 eV$_{ee}$ in Run 2b and the K-shell peaks are skewed to low energies.

Both of these features can be investigated by considering the position distributions of the events. One method to estimate a Cartesian-like location of an event is to consider how the energy is partitioned between the three inner-channels, based on the OF-fit amplitude of each, and normalizing the sum of the three. Knowing that their centers are rotated by 120° from each other, the estimates X_{OF} and Y_{OF} are

$$X_{\mathrm{OF}} = \frac{\cos\left(30°\right)\mathrm{D}_{\mathrm{OF}} + \cos\left(150°\right)\mathrm{B}_{\mathrm{OF}} + \cos\left(270°\right)\mathrm{C}_{\mathrm{OF}}}{\mathrm{B}_{\mathrm{OF}} + \mathrm{C}_{\mathrm{OF}} + \mathrm{D}_{\mathrm{OF}}} \tag{11.8}$$

$$Y_{\mathrm{OF}} = \frac{\sin\left(30°\right)\mathrm{D}_{\mathrm{OF}} + \sin\left(150°\right)\mathrm{B}_{\mathrm{OF}} + \sin\left(270°\right)\mathrm{C}_{\mathrm{OF}}}{\mathrm{B}_{\mathrm{OF}} + \mathrm{C}_{\mathrm{OF}} + \mathrm{D}_{\mathrm{OF}}}, \tag{11.9}$$

where N_{OF} is the OF-fit amplitude to the Nth channel. These quantities are called the X and Y partitions and they create a so-called "triangle plot" (with each corner corresponding to a single channel's dominance) as seen in Fig. 11.26 for Run 2b data. In this plot, events which have energy between 50 and 330 $\mathrm{eV}_{\mathrm{ee}}$, i.e. the general location of the additional peak, are highlighted in orange. These peak events have a suspiciously localized distribution above channel B. Although the position distribution is questionable, the pulse-shapes of these events appear to be of high quality leading to hypotheses of some form of short which draws charge through the crystal and mimics a real signal.[11] An initial approach to remove these events was to generate a KDE using the highlighted events and remove events within some $n\,\%$ contour, but these events can be more efficiently removed by considering the radial position distribution.

There are two standard methods which SuperCDMS uses to estimate the radial location of an event, both of which involve comparing the values of certain metrics between the three inner and one outer phonon channels. The first is based on the partitioning of the OF-fit amplitudes (the radial partition), where the radius is the ratio between the outer channel's amplitude and the sum of all four channels' amplitudes; values closer to 1 indicate larger radius. The second is based on the RTFT walk 20 % rise time points of the channels (the delay radius), where the radius is the difference between the primary[12] inner channel's and the outer channel's rise time. The units are

---

[11] The ultimate cause of this spot is, as yet, unknown. One idea is that debris settled on the detector face, acting like a source, during the inter-run warm-up, though the cryostat was never opened. Another is a local short through the crystal between read-out channels. In any case, this type of spot have been previously observed in test-facility data [317, 341].

[12] The primary inner channel is defined as the inner channel with the largest Of-fit amplitude.
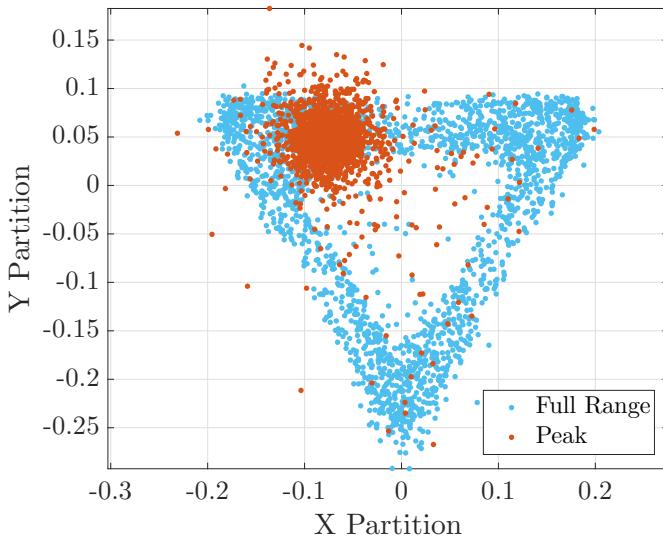
Figure 11.26: X- versus Y-partition space for Run 2b with events between 50 and 330 eV$_{ee}$ highlighted in orange. Each corner of the plot represents the dominance of a single inner phonon channel. The low-energy peak is localized into a spot above channel B.

in μs and larger differences indicate larger radius. Both of these quantities are plotted in Fig. 11.27. Although the timing radius appears to have less energy dependence and better separation between inner and outer events, the shared generalities of both inform the features seen in Fig. 11.25. The spot from Fig. 11.26 has a distribution centered at larger radius, though with significant leakage to smaller radius in both of these planes. There is also a dense horizontal band in each (at $\sim$0.25 in radial partition and $\sim$0 μs in the delay radius) which is denser near the vertical clusters, which are the K- and L-shell activation peaks. This indicates that the low-energy tails of the activation peaks are due to high-radius events. A strategy which removes high-radius events can serve to significantly clean up the spectrum by reducing the spot and removing the tails of the peaks. The physical cause of the latter is investigated in Sec. 11.5.2 while the final approach for a radial cut is given in Sec. 11.5.3.

11.5.2   E-field Simulation

The physical cause for the low-energy skew of the activation peaks is the electric-field configuration of the detector. The calculated field for the CDMSlite biasing configuration, assuming a perfect cylinder and bias potentials of $+70$ V and 0 V on the top and bottom faces respectively, is shown in Fig. 11.28. The field lines given in green are those which terminate on the outer wall of the detector as opposed to the bottom face.
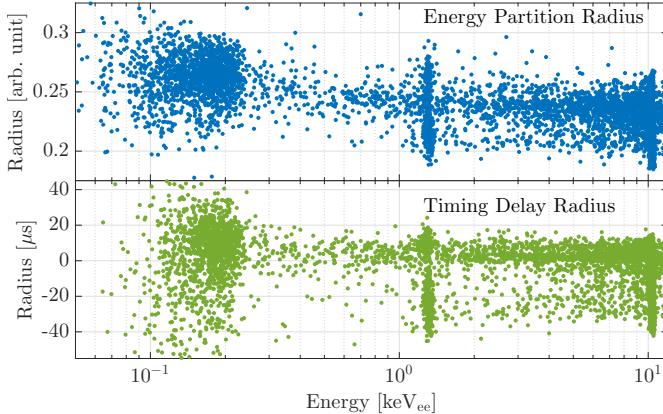
Figure 11.27: Standard radial parameters used by SuperCDMS as functions of energy. The radial partition (top) is based on the relative energy in each channel while the delay radius (bottom) is based on the rise times of the traces. In both plots, higher radial values correspond to larger radii. Both estimators show the Run 2b spot ($\sim$100 eVee) generally at higher radii and a horizontal band of a events at larger radii connected to the activation peaks (vertical clusters).

This presents a problem because there is a small gap between the edge of the detector and the grounded detector housing. The presence of this gap implies that the potential difference along the green lines is less than the full 70 V and that events created in this region have reduced NTL gain.

The relationship between the high-radius electric field and reduced-energy events, i.e. tails on the activation peaks, is solidified by performing a multi-step simulation of a mono-energetic and uniform source in the detector. The first step of the simulation is done in GEANT4, where a simplified post-electron-capture ^{71}Ga de-excitation is simulated uniformly throughout the detector. GEANT4 simulates where and how the γ's deposit energy but it does not simulate the detector response and read-out. The detector response is handled by a second simulation called the SuperCDMS Detector Monte Carlo (DMC) which has been developed in Matlab [274]. The DMC simulates the propagation of phonons and charge, including the generation of NTL phonons, and the absorption in and read out of the different channels. The ultimate goal of the DMC is to simulate events which completely mimic (up to electronics noise) the true data and can be used to inform the cuts set in the analysis. Although, the incarnation used here does not quite meet that goal, it is close enough to inform general conclusions.

The outputs of the DMC are noiseless phonon traces for each detector channel from the simulated TESes. These traces are processed by adding experimental noise

Electric Field for V$_{top}$ = 70 V and V$_{bot}$ = 0 V
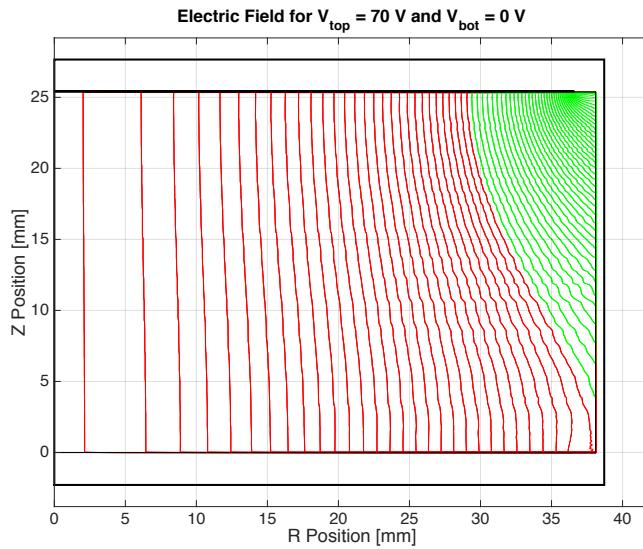
Figure 11.28: Calculated electric-field configuration for the CDMSlite biasing mode assuming a simple cylinder with a +70 V bias on the top face and a grounded bottom face. Field lines in green terminate on the side wall of the detector. A gap between the edge of the detector and the grounded detector housing implies that potential differences along the green field lines is <70 V which in turn leads to reduced NTL gain for events in that region. Figure courtesy of B. Cabrera.

to mimic the true data and running the OF algorithm. Comparing the GEANT4 input "true" position and energy to the DMC output OF-fit quantities informs the accuracy of the position estimators under discussion. The OF-processed DMC energy as a function of GEANT4 position[13] is given in Fig. 11.29 for K-shell events. As expected, events near the outer edge of the detector have reduced total phonon energy, with the lowest energy events near the top/bottom of the detector corresponding to where the read-out interfaces connect and cause further disturbances to the field. These lower energy events should correspond to the observed tail on the K-shell peak, as verified by making a radial cut in the DMC. The DMC radial partition is given in Fig. 11.30 as a function of true position showing that this estimator does correspond to the outer-edge events. Making a crude partition cut proves that a radial cut does remove the low-energy tail as seen in Fig. 11.31. These simulations give strong motivation to apply a radial fiducial-volume cut to the physical data.

---

[13] The possibility of multiple GEANT4 hits in a single event, and thus multiple "true" positions, is handled by constructing an energy-averaged position of the event

$$\bar{\boldsymbol{x}} = \frac{\sum_i^N \varepsilon_i \boldsymbol{x}_i}{\sum_i^N \varepsilon_i} \tag{11.10}$$

over the N total hits, where ε_i energy is deposited at the $\boldsymbol{x}_i$ location for the ith hit.
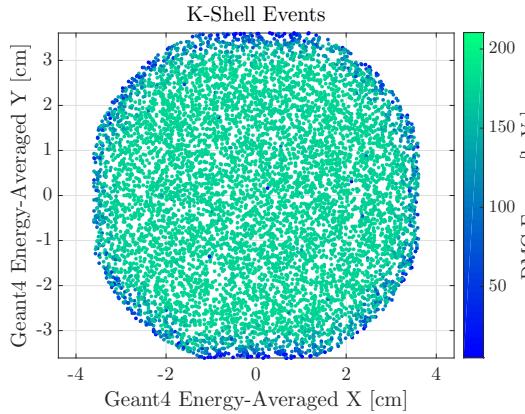
Figure 11.29: DMC OF-processed total phonon energy as a function of the true GEANT4 event location[13] for mono-energetic K-shell events. Events near the edge of the detector have reduced energy due to the electric field configuration.
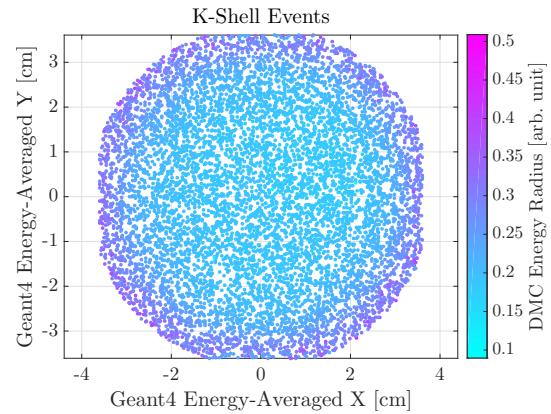
Figure 11.30: DMC OF-processed radial partition as a function of the true GEANT4 event location[13] for mono-energetic K-shell events. The radial partition corresponds the edge of the detector, allowing for a cut to be made to remove high-radius events.
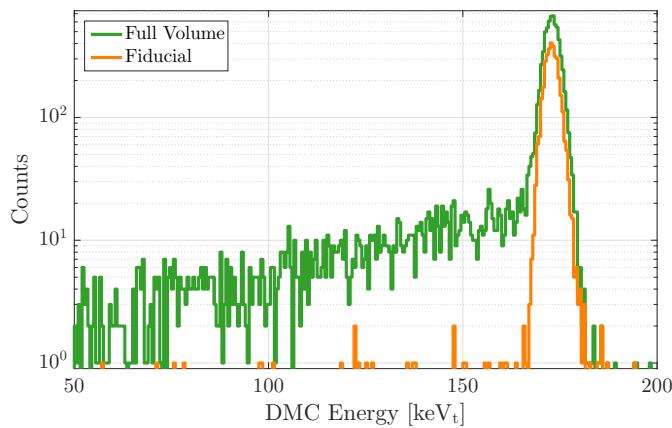
Figure 11.31: K-shell peak from a DMC simulation with (orange) and without (green) a cut on the radial partition of 0.2. The low-energy tail of the peak, caused by the electric field configuration, is removed to a high percentage by such a fiducial volume cut.

11.5.3 Radial Cut

Implementing a radial fiducial-volume cut is an important improvement for CDMSlite analyses. Without the yield discrimination, CDMSlite becomes background-limited due to ERs rather rapidly. Defining a fiducial volume decreases the overall background rate, by removing reduced-NTL gain events and ^{222}Rn daughters, and correspondingly pushes the WIMP sensitivity to lower cross sections. The final radial parameter and cut were developed by W. Rau [342], but given the importance of this cut the process is described in detail.

Radial Parameter and Threshold

The two traditional radial estimators used by SuperCDMS, shown in Fig. 11.27, are based on the standard OF-fit and the RTFT-walk algorithms respectively. However, the new 2T-fitting algorithm implemented for this analysis can also be used to extract position information. The radial partition uses the difference in amplitude between channels while the delay radius uses the difference in timing between the channels. The new 2T-based radial parameter uses both of these concepts in the fast-template amplitude and OF delay of each channel.[14] The derivation of the radial parameter is mostly empirical, i.e. corrections are made based on observations of the data and what would make a cleaner radial parameter, using the following steps:

1. For the Nth channel, correct the energy scale, using the energy-carrying slow-template amplitude, in the same manner as described in Sec. 10.2.2 for the total phonon trace. Derive the corrected fast amplitude N_f^{Corr} applying these same correction factors to the fitted fast-template amplitude.

2. For the Nth channel, construct a corrected delay parameter $\Delta_{N;2\text{T}}^{\text{Corr}}$ which is the difference in 2T-delay between that channel $\delta_{N;2\text{T}}$ and the total phonon pulse $\delta_{\text{tot};2\text{T}}$, shifted by a ratio which indicates how peaky that channel is

$$\Delta_{N;2\text{T}}^{\text{Corr}} = \delta_{N;2\text{T}} - \delta_{\text{tot};2\text{T}} - \xi_{N;2\text{T}} \cdot N_f^{\text{Corr}}/E_{\text{r,ee}}, \qquad (11.11)$$

---

[14] The physics of the fast channel carrying the position information and the slow channel the energy information implies that the start time of channels and total traces should not contain position information. However, there is some degeneracy in low energy pulses such that a lower fast amplitude but short delay pulse can look like a larger fast amplitude long delay pulse.

where $\xi_{N;2\mathrm{T}}$ is the slow-template relative calibration factor and $E_{\mathrm{r,ee}}$ is the total energy of the event, in keV$_{\mathrm{ee}}$, as defined in Sec. 10.2.2.

3. Construct Cartesian estimators $X_{2\mathrm{T}}$, $Y_{2\mathrm{T}}$ in the same manner as the numerators of Eqs. 11.8–11.9 using $\Delta^{\mathrm{Corr}}_{N;2\mathrm{T}}$ instead of the OF-fitted amplitudes N_{OF}.

4. Construct a preliminary radial parameter $R_{0;2\mathrm{T}}$, recalling that A is the outer channel, as

$$R_{0;2\mathrm{T}} = \min\left(\Delta^{\mathrm{Corr}}_{B;2\mathrm{T}}, \Delta^{\mathrm{Corr}}_{C;2\mathrm{T}}, \Delta^{\mathrm{Corr}}_{D;2\mathrm{T}}\right) - \Delta^{\mathrm{Corr}}_{A;2\mathrm{T}}. \qquad (11.12)$$

5. Derive the final radial parameter $R_{2\mathrm{T}}$ by correcting the preliminary radial parameter using the angle $\phi_{2\mathrm{T}}$ derived from the triangle plot of 2T-position estimators.

The justification for the final correction is shown in the 2T-based triangle plot in Fig. 11.32 which has $R_{0;2\mathrm{T}}$ in the color highlight. Events towards the inner portion of the triangle have a higher $R_{0;2\mathrm{T}}$ (common for delay-based radial estimators), however the inner corners have somewhat smaller $R_{0;2\mathrm{T}}$ compared to the inner edges. This is even more evident when directly comparing $R_{0;2\mathrm{T}}$ to $\phi_{2\mathrm{T}}$ as in Fig. 11.33. Fitted lines to the distribution are used to correct to the final $R_{2\mathrm{T}}$. Also note that the final parameter truly has arbitrary units, being a combination delay and amplitude measurements, and is scaled, by a factor of 10^5, to more convenient values.

The final radial parameter as a function of energy is given in Fig. 11.34 for Run 2a and Run 2b. As with other radial estimators, there is a dense horizontal band for the outermost events, however the separation between this band and the inner events is larger in the new parameter. Also note that the spot in Run 2b is more densely clustered at high radial value than in previous estimators.[15] The radial cut consists of a energy-independent threshold in each period, even though some flaring at low energy in seen in the radial distribution. The flaring indicates that increased leakage is expected at lower energies, particularly in Run 2b. The values of the thresholds are set at -4 and -5 for the two periods to remove the outer events while keeping a large fraction of inner event, guided by the separation of these populations seen in the L shell. The lower threshold value in Run 2b is motivated by two factors: (1) The radial distribution of

---

[15] It is important to note that at no point in the derivation of the radial parameter is the spot used, i.e. its tightly clustered location at high radius is an unexpected benefit and not a calculated result.
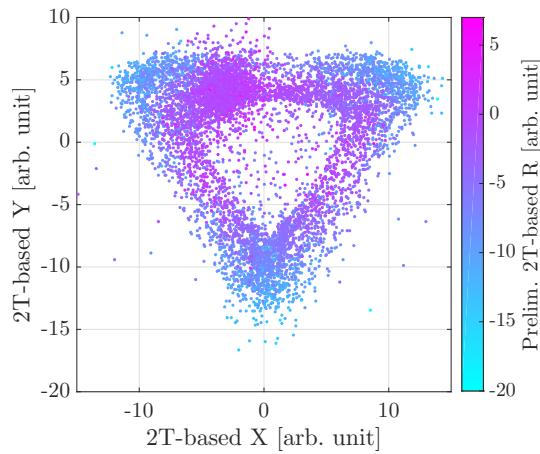
Figure 11.32: 2T-fit based Cartesian position estimators (X_{2T}, Y_{2T}) compared to the preliminary 2T-based radial parameter $(R_{0;2T})$. Higher radial events are towards the center of the triangle with the inner edge events having higher radii compared to the inner corners. Figure adapted from [342].
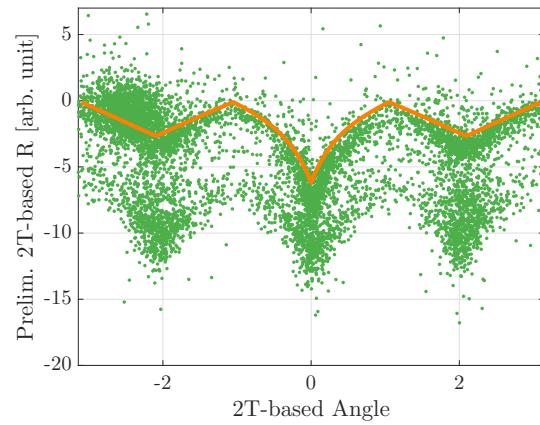
Figure 11.33: Preliminary 2T-based radial parameter $(R_{0;2T})$ as a function of 2T-based angle (ϕ_{2T}) which is computed using the 2T-based Cartesian position estimators. The distribution is corrected to form the final 2T-based radial parameter using the fitted curves (orange). Figure adapted from [342].
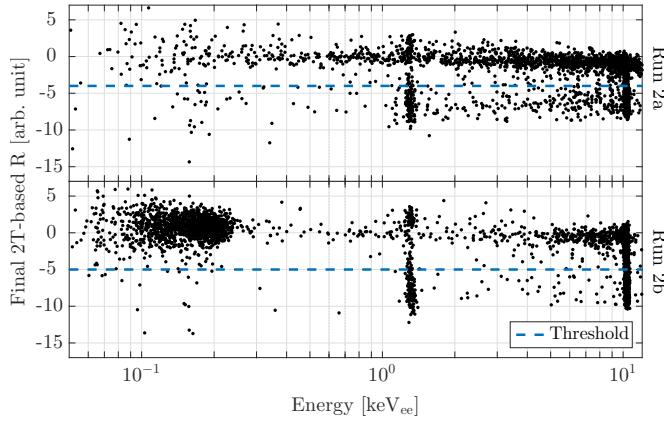
Figure 11.34: Final 2T-based radial parameter $(R_{2\mathrm{T}})$ as a function of energy for Run 2a (top) and Run 2b (bottom). The dashed lines indicate the radial cut thresholds. The densely populated horizontal band corresponds to high radii events. The distribution in radius shifted slightly between periods, which, in addition to the high radius spot, motivated a lower threshold in Run 2b.

events is slightly shifted downward in Run 2b (thus a lower threshold gives a comparable efficiency between the periods) and, (2) the presence of the additional background in Run 2b at low energies would give a higher leakage in that period if the thresholds were equal.

11.6   Live time

The total raw live time for Run 2 is 132.32 d, 110.28 d in Run 2a and 21.95 d in Run 2b. The final live time is given after the application of all live-time-removing cuts. These cuts are listed in Table 11.2 along with the amount and percentage of the run removed by each. The time blocks defined for the LF-noise and pulse-shape glitch cuts are a convenient binning to observe the time dependence of these cuts. The live time remaining in each bin after subsequent application of the cuts is shown in Fig. 11.35. The bad series cut removes the most live time, at $9.58\,\%$ of the whole, with particularly strong effect in time blocks 5, 8, and 9. The final total live time is 115.60 d, split between 97.87 d in Run 2a and 17.78 d in Run 2b.

Cut Name	Live Time Removed	Percentage of Total
HVPS, Temp, 2T-Fit	0.31 d	0.23 %
Asym. Glitches	0.82 d	0.60 %
Charge Glitches	1.30 d	0.98 %
Phonon Baseline	2.60 d	1.97 %
Bad Series	12.66 d	9.58 %
NuMI Beam	10.34 min	<0.01 %

Table 11.2: Live time removed by cut along with the percentage of the total exposure. The phonon baseline and charge glitch values are after application of the bad series cut. Other values are computed independently from each other.
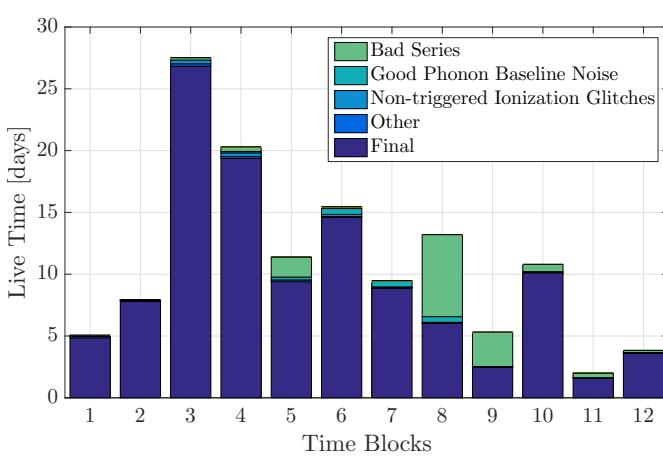
Figure 11.35: Live time remaining after application of subsequent live time cuts for the different time blocks on Run 2. The color in the legend indicates the live time removed by that particular cut. The "Other" cuts are the asymmetrically triggered glitch cut, NuMI coincidence cut, bad GPS time cut, and bad base temperature etc. cut. The bad series cut removes the most live time.

11.7   Efficiency

11.7.1   Energy Independent Efficiency

The efficiencies for the multiple-scatter and muon-veto-coincidence cuts are computed using random triggers. Random triggers should be a population of zero-energy single-scatter events which are uncorrelated with muon veto activity. The efficiency for correctly identifying single scatters is one minus the fraction of random triggers which are mis-identified as a multiple scatters: the single scatter efficiency is $98.27 \pm 0.01\,\%$. The efficiency for the muon veto cut is an estimate of the number of accidental coincidences between the random triggers and the muon veto: the muon veto efficiency is $98.77 \pm 0.01\,\%$. There is a large number of random triggers which gives the small statistical uncertainties.

11.7.2   Pulse-Shape based Cuts Efficiency

The three phonon pulse-shape-based cuts (phonon pulse quality, LF-noise, pulse-shape glitches) are strongly energy dependent due to the the fact that the LF-noise and glitch cuts have different threshold-setting techniques at different energies and since they vary by time block. In the past, the efficiency of similar cuts was found by considering high-statistics calibration data.[16] There are two main issues in doing so: (1) quality cuts, the selection of which could bias the estimate, must be applied to the calibration data to identify a "clean" sample and (2) the experimental conditions fluctuate throughout the run, such as the LF-noise contribution, and thus calibration data taken at specific instances may not accurately represent the entire data set. An alternative method for estimating the efficiency is to generate, and process, a fake data set by simulating individual pulses, and finding the fraction of the fake events which pass the cut. The simulated events are constructed using a noiseless template, which eliminates the need to apply quality cuts, and a random-triggered noise event from the actual data set, which tracks the changing experimental environment. Both problems of using calibration data are thus avoided using the simulated data set.

---

[16] ^{252}Cf neutron-data mostly, to best mimic a WIMP interaction.

The ith fake-event trace t of the kth population is constructed as

$$t_{ijk} = \frac{n_j}{\alpha\beta\gamma} + \frac{a_i}{\delta} \times T_k,\tag{11.13}$$

where n_j is the jth noise trace (units of ADC), a_i is an arbitrary amplitude (units of keV$_t$), T_k is the template for the population type (normalized to unity amplitude), α is the number of ADC bins per volt, β is the read-out circuit feedback gain (units of Ohms), γ is the read-out circuit driver gain (dimensionless), and δ is the calibration from keV$_t$ to Amperes. The number of noise traces available, i.e. the maximum of j, is the number of randomly-triggered events in the data set. The number of events simulated, i.e. the limit of i, is, in principle, unlimited[17] but is practically set to be the same of j, i.e. one simulated event per recorded noise trace in the experiment. If the statistics of the noise traces are wanting, then the noise traces could be reused, however this is unnecessary for this analysis. The efficiency is calculated using all in-run randoms.[18] The arbitrary amplitudes are chosen to span 0–25 keV$_t$. This range encompasses the L-shell activation peak ($\sim$20 keV$_t$) and the efficiency is expected to be 100 % at higher energies.

The remaining component needed is the number and type of the event populations k. Recall that events close to a surface have sharper peaks, i.e. quicker rise time, than those in the bulk and that the standard OF-fitting template T_{OF} averages these differences to create a general template. However, the new 2T-fitting algorithm allows for a characterization of the position dependence in the total phonon pulse.

This characterization is accomplished by considering the ratio of the fitted amplitudes of the fast and slow templates for the K-shell activation peak, which is seen in Fig. 11.36. As shown there, the distribution of ratios for the peak ($\sim$150 keV$_t$) is bound by $\sim\pm0.125$, with the peakier pulses having a positive ratio and less-peakier pulses a negative ratio. Two new templates, named the "peaky" and "nonpeaky" templates, are created by a linear combination of the fast and slow templates which have ratios

---

[17] By choosing different combinations of n_j and a_i.

[18] The beginning-of-run randoms can be biased due to their proximity to the initial biasing of the detector. The end-of-run randoms were considered, but the in-run random simulation gave more conservative results.
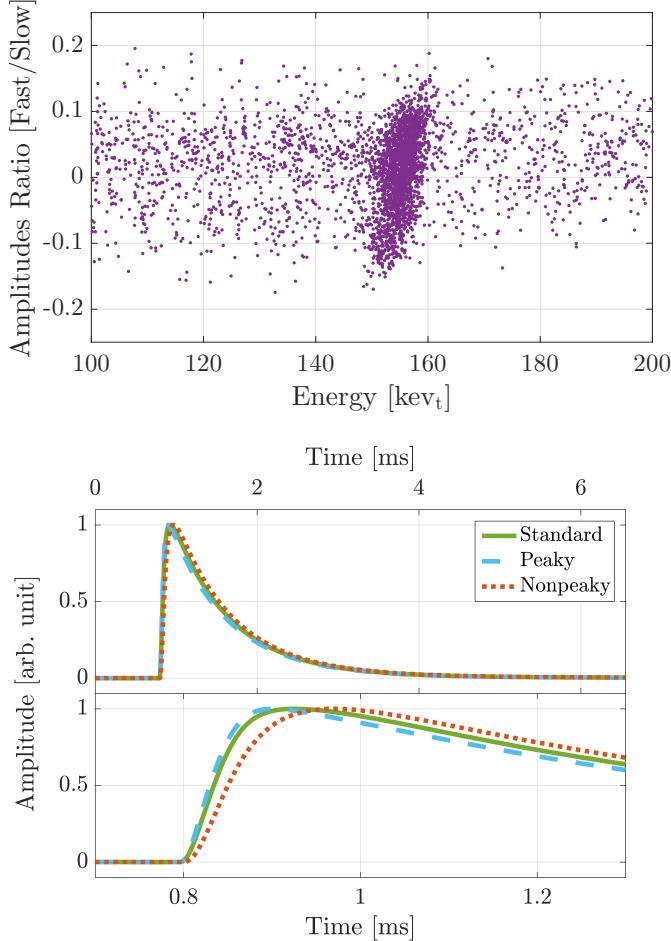
Figure 11.36: Ratio of the fitted two-template fast and slow amplitudes near the K-shell activation peak ($\sim$150 keV$_\text{t}$). The bounds of ± 0.125 on the peak are used to generate peaky and nonpeaky templates.

Figure 11.37: Standard (green solid), peaky (orange dot), and nonpeaky (blue dash) templates used in the pulse simulation to generate three populations of events to encompass differences in pulse shape. The peaky and nonpeaky templates are created by combining the two-template fit fast and slow templates (Fig. 10.4) using the bounds of the distribution in Fig. 11.36.

matching these bounds

$$T_\text{peaky/nonpeaky} = T_\text{slow} \pm 0.125 \cdot T_\text{fast}, \tag{11.14}$$

where $T_\text{fast/slow}$ are the fast and slow templates as seen in Fig. 10.4. The templates used for the three event populations in the simulation are the standard OF template and the new peaky and nonpeaky templates, all of which are shown in Fig. 11.37.

The binned efficiency of all three cuts is found by calculating the fraction of simulated events passing the cuts in any given bin. A single efficiency is computed, as opposed to three individual efficiencies, because an event with particularly poor pulse-shape can fail more than one cut and would be counted more than once if individual efficiencies
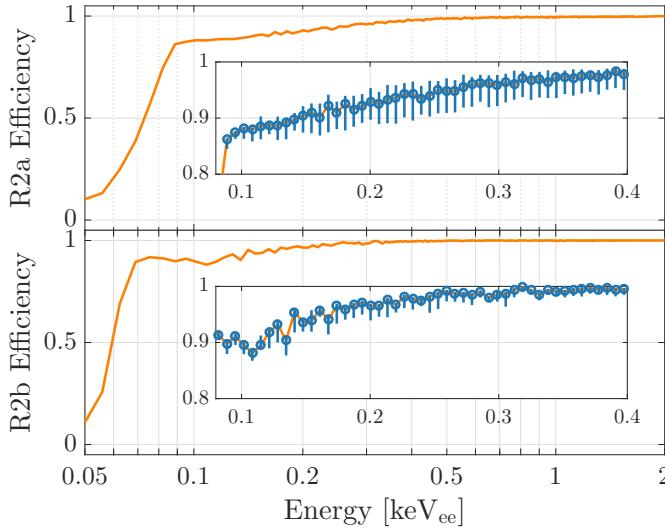
Figure 11.38: WIMP-signal efficiency of the phonon pulse-shape based cuts estimated from pulse simulation for Run 2a (top) and 2b (bottom). The efficiency is binned by 0.1 keV$_t$, scaled to keV$_{ee}$, with assumed 100 % efficiency above 1.6 keV$_{ee}$. The mean statistical uncertainty per bin is 1.2 %. Insets: zooms of the $\mathcal{O}(100\ eV_{ee})$ regions with blue error bars showing the systematic uncertainty due to the different templates used in the simulation. This uncertainty is negligible outside of these regions.

were used. Symbolically, for each efficiency ε_i, $\varepsilon_{ABC} \neq \varepsilon_A \otimes \varepsilon_B \otimes \varepsilon_B$. Also note that the energy estimator for the efficiency must match the primary estimator used in the analysis, the NSOF estimate scaled to keV$_{ee}$, which is different from the plane in which the LF-noise and glitch cuts are defined. This implies that "sharp" thresholds in the definition may not translate to similarly sharp thresholds in efficiency.

The efficiency for the three cuts is shown in Fig. 11.38, split between Run 2a and 2b. The sharp drop in efficiency near 60–80 eV$_{ee}$ corresponds to the contour portions of the LF-noise cut. The mean statistical uncertainty at each bin is 1.2 %. The difference between the central efficiency values for each template's curve is treated as a systematic uncertainty (Sec. 12.3), is most prominent in the $\mathcal{O}(100\ eV_{ee})$ region, and is shown in the figure by error bars representing the maximum/minimum of the standard, peaky, and nonpeaky curves at each bin.

11.7.3 Maximum Likelihood Estimation

The efficiencies for the radial fiducial volume cut and for triggering on low-energy events are both calculated using, in part, the maximum likelihood estimation (MLE) technique to fit some model to the data. This method is explained in theory [343] before considering its use in those calculations.

Suppose an experiment measures a quantity x according to some PDF n times yielding the collection of measurements $\mathbf{x} = (x_1, \ldots, x_n)$. If the functional form of the PDF is known as $f(\boldsymbol{x}; \boldsymbol{\theta})$, but at least one of the parameters $\boldsymbol{\theta}$ of the PDF is not known, the MLE method uses the observed data to find estimated values of $\boldsymbol{\theta}$, termed $\hat{\boldsymbol{\theta}}$. The probability for observing the ith data point in the interval $[x_i, x_i + dx_i]$ is $f(x_i; \boldsymbol{\theta})\mathrm{d}x_i$. Since each measurement is independent, the probability for observing the full collection of measurements is $\prod_i^n f(x_i; \boldsymbol{\theta})\mathrm{d}x_i$. If the hypothesized PDF and $\boldsymbol{\theta}$ are correct, the probability should be high for the measured values. Conversely, if the hypothesized parameters $\boldsymbol{\theta}$ are incorrect, the probability should be low. Since the $\mathrm{d}x_i$ do not depend upon $\boldsymbol{\theta}$, the same argument applies to the likelihood function $\mathcal{L}(\boldsymbol{\theta})$

$$\mathcal{L}(\boldsymbol{\theta}) = \prod_i^n f(x_i; \boldsymbol{\theta}). \tag{11.15}$$

With this motivation, the vales of $\boldsymbol{\theta}$ which give the PDF best describing the data, i.e. the best fit values $\hat{\boldsymbol{\theta}}$, will be those which maximize $\mathcal{L}$

$$\left.\frac{\partial \mathcal{L}}{\partial \theta_i}\right|_{\theta_i = \hat{\theta}_i} = 0. \tag{11.16}$$

Since the logarithmic function is monotonically increasing, $\hat{\boldsymbol{\theta}}$ also maximizes $\ln(\mathcal{L})$ which can be easier to work with as it converts the product to a sum

$$\ln(\mathcal{L}(\boldsymbol{\theta})) = \sum_i^n f(x_i; \boldsymbol{\theta}). \tag{11.17}$$

In situations where the number of measurements is itself a Poisson random variable with mean value ν, i.e. an experiment counting events such as CDMSlite, the Poisson probability for finding n measurements $P(n; \nu)$ must also be included in the likelihood function. This is called the extended maximum likelihood function $\mathcal{L}(\nu, \boldsymbol{\theta})$, where

$$\begin{aligned}
\mathcal{L}(\nu, \boldsymbol{\theta}) &= P(n; \nu) \cdot \mathcal{L}(\boldsymbol{\theta}) \\
&= \frac{\nu^n e^\nu}{n!} \cdot \prod_i^n f(x_i; \boldsymbol{\theta}).
\end{aligned} \tag{11.18}$$

and the logarithm is

$$\ln\left(\mathcal{L}(\nu,\boldsymbol{\theta})\right) = -\nu + \sum_i^n \ln\left(\nu f(x_i;\boldsymbol{\theta})\right). \tag{11.19}$$

In the case where ν is independent of $\boldsymbol{\theta}$, $\partial\mathcal{L}(\nu,\boldsymbol{\theta})/\partial\nu = 0$ when $\hat{\nu} = n$. The extended MLE approach appropriately adds additional statistical uncertainty in the final estimators.

There are several methods by which to estimate the uncertainty on the $\hat{\boldsymbol{\theta}}$ parameters, termed $\Delta\hat{\boldsymbol{\theta}}$. One method, employed in Run 2 analysis, is to report a confidence interval or region[19] based upon the Bayesian Posterior PDF given as

$$p(\boldsymbol{\theta}|\boldsymbol{x}) = \frac{\mathcal{L}(\boldsymbol{x}|\boldsymbol{\theta})\pi(\boldsymbol{\theta})}{\int \mathcal{L}(\boldsymbol{x}|\boldsymbol{\theta}')\pi(\boldsymbol{\theta}')d\boldsymbol{\theta}'}, \tag{11.20}$$

where $\pi(\boldsymbol{\theta})$ is the prior PDF containing information about $\boldsymbol{\theta}$, such as when values are physical, i.e. $\pi(0 \le \theta_i \le 1) = 1$ and zero otherwise if θ_i is a percentage. The confidence intervals or regions on either the joint or marginal posterior distributions are then used to give $\Delta\hat{\boldsymbol{\theta}}$.

11.7.4   Radial Cut Efficiency

The efficiency for the radial cut is determined using two basic facts about the ^{71}Ge electron-capture peaks: they uniformly illuminate the detector and have a known half life of 11.43 days [326]. The uniform illumination is similar to the coverage of a dark matter signal, meaning the activation peaks are an appropriate proxy for calculating the signal efficiency, while the known half life allows for the activation signal to be identified compared to a time-independent background and WIMP signal. A cartoon of what a mono-energetic and homogeneous source, such as an activation peak, looks like in the radius versus energy plane is given in Fig. 11.39 and is used to illustrate the different steps of the efficiency calculation.

The cartoon distribution is first divided into two populations, events with reduced NTL-amplification (R) and those in the primary peak (P). The low-energy edge of R is given by considering an event with no NTL-amplification ($E_\mathrm{t} = E_\mathrm{r}$) converted to

---

[19] Formally known as the credible interval or region.
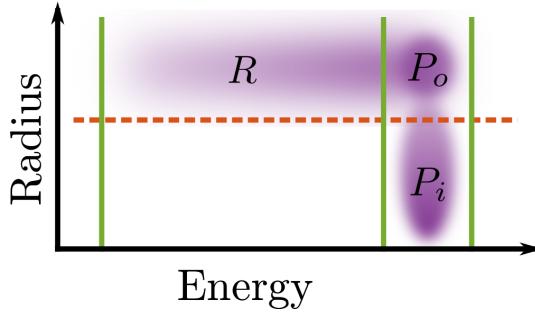
Figure 11.39: Cartoon showing the morphology of a mono-energetic and homogeneous peak in the radius versus energy plane. The distribution is split (green lines) into those events with reduced NTL-amplification (R) and those in the peak (P). The peak is further broken into those which pass (P_i) and fail (P_o) the radial cut (orange dash). The final signal efficiency is $\mathcal{E} = P_i / (P_i + P_o + R)$.

$E_{\mathrm{r,ee}}$ using same the calibration as the peak. The peak events are further split into two subpopulations $P = P_i + P_o$, "inner" events that pass the radial cut (P_i) and "outer" event that do not (P_o). The efficiency of an event passing the cut is then

$$
\begin{aligned}
\mathcal{E} &= \frac{P_i}{R + P} \\
&= \frac{P}{R + P} \cdot \frac{P_i}{P} \\
&\equiv \mathcal{E}_E \cdot \mathcal{E}_P,
\end{aligned}
\tag{11.21}
$$

where $\mathcal{E}_E$ is defined as the energy efficiency, the probability that the event has the full NTL-amplification, and $\mathcal{E}_P$ is defined as the peak efficiency, the probability that an event with full NTL amplification passes the radial cut. These two terms are individually estimated by separate methods. The full radial cut efficiency was computed by K. Page and R. Underwood from Queen's University but, given the importance of the radial cut for this analysis, the calculation is given with detail. The calculation is organized as

(1): Efficiency To Have Full NTL Amplification: $\mathcal{E}_E$

    (1.A): Alignment of Post-Cf Periods

    (1.B): Exponential Fitting

(2): Efficiency at Full NTL Amplification: $\mathcal{E}_P$

(1) Efficiency To Have Full NTL Amplification: $\mathcal{E}_E$

The probability for an event to have full NTL-gain is directly related to the geometry of the electric field (Fig. 11.28). As the effect is geometrical, it is independent of energy. The efficiency is calculated with the high-statistics K-shell peak and applied to the entire energy range.

In the data, the K shell is not isolated since it occurs on top of other sources, namely the Compton-scatter-dominated background and the L-shell peak.[20] This complicates the division of the radius vs. energy plane and the R bin is split into many sub-bins as shown in Fig. 11.40. The goal of the energy-efficiency calculation is to determine the K-shell contribution in each bin to use in computing $\mathcal{E}_E$. In terms of the new bins and the K-shell contribution in each, the energy efficiency is

$$\mathcal{E}_E = \frac{K_i + K_o}{K_i + K_o + K_o^1 + K_i^1 + L_{o;K} + L_{o;K}^2},\qquad(11.22)$$

where the last two terms in the denominator are the K-shell contribution in bins which also contain L-shell events. Also note that the radial cut threshold, here chosen as -4, is used as a tool to define bins, but the specific location of the threshold is irrelevant up to the negligible K-shell contributions in L_i and L_i^2. The $\mathcal{E}_E$ calculated with the current bins is applicable to the entire run even though the threshold differs between Run 2a and 2b.

Separating the different components to determine the K-shell strength in each bin was performed by K. Page, with assistance from R. Underwood, in [344, 345]. The separation was attained in two steps: (A) aligning the three post-Cf data periods based upon the strength of the K shell and (B) within each bin, fitting the events' rate to an exponential decay with the known ^{71}Ge half live plus a constant (in time) background. The exponential contribution to the fit corresponds to the K-shell portion of each bin.

(1.A) Alignment of Post-Cf Periods

Since the activation events decay with a known half life, and the background is constant in time, these components are separated by performing a fit in time relative the end of the previous ^{252}Cf calibration. There are three post-Cf periods (post-February, post-May, post-September) and, to increase the statistical significance of the fit, they are

---

[20] But not, however, the M shell as the end point of the K shell tail is $\sim$400 eV$_{ee}$.
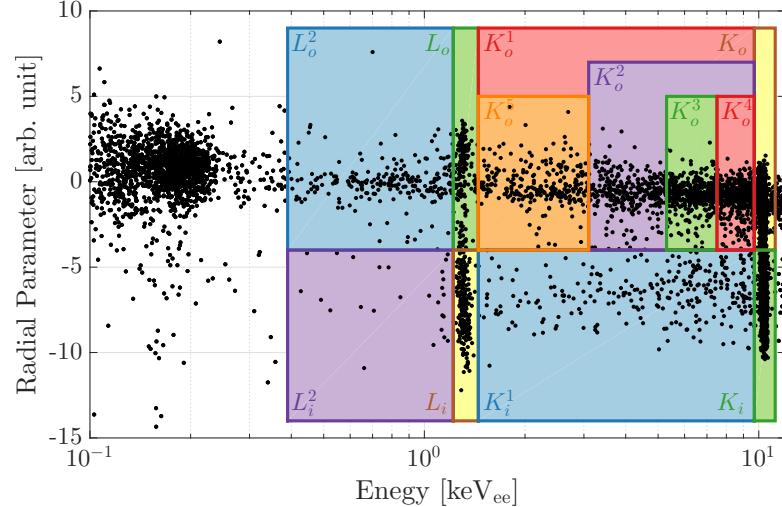
Figure 11.40: Energy versus radial parameter plane showing the different two-dimensional bins used in the computation of the energy efficiency. The K_o^2 and K_o^5 bins are sub-bins of K_o^1, with the former having further sub-bins of K_o^3 and K_o^4.

combined. However, the length of each ^{252}Cf exposure differed and the strength of the activation is correspondingly different for each post-Cf period. The three periods must then be shifted in time such that the strength of each decay aligns. The new shifted time scale is called "aligned time" t' and is such that $t' = 0$ immediately following the strongest calibration exposure (post-September). The concept is shown by the cartoon in Fig. 11.41. The time shift for the first two periods to align with the third are $t_I = 21.76$ d (post-February) and $t_{II} = 15.60$ d (post-May) [346]. For any given event occurring at calendar time t, t' is then calculated as

$$t' = \begin{cases} t - t(t_1 = 0) + t_I & \text{if } t \in \text{post-Feb.} \\ t - t(t_2 = 0) + t_{II} & \text{if } t \in \text{post-May.} \\ t - t(t_3 = 0) & \text{if } t \in \text{post-Sep.} \end{cases} \qquad (11.23)$$

where the $t_i = 0$ are the first events following each post-Cf period. The aligning of periods with the data is shown in Fig. 11.42. The alignment shifts $t_{I/II}$ come from an MLE fit of an exponential and flat distributions convolved with the duty cycle of the experiment, which explains the apparent disagreement between the data and fit in
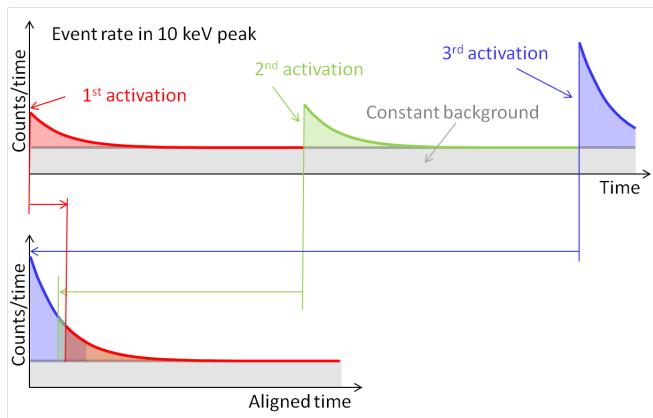
Figure 11.41: Cartoon demonstrating the alignment of post-Cf calibration periods by the strength of the K-shell peak. The signal is a combination of activation events, which decay away with a known half life, and a constant background. The first two periods are shifted to align, by decay strength, with the third period in the time "aligned time" scale. Figure courtesy W. Rau.

Fig. 11.42.

(1.B) Exponential Fitting

To determine the ^{71}Ge contribution in each radial bin, a likelihood function which describes the exponential and flat components, both in the aligned time scale, is required. Using the extended MLE formalism, the likelihood is

$$\mathcal{L}(\nu, r) = P(n; \nu) \cdot \mathcal{L}(r)$$
$$= \frac{\nu^n e^{-\nu}}{n!} \cdot \prod_i^n \frac{r f_s(t_i') + (1 - r) f_b(t_i')}{r I_s + (1 - r) I_b}, \tag{11.24}$$

where t_i' are the aligned times for the events, n is the total number of measured events in the bin, $f_s(t_i')$ is an exponential in t', with half life τ and unity magnitude, convolved with the duty cycle of the experiment, $f_b(t_i')$ is the flat distribution, with unity magnitude, convolved with the duty cycle, and I_s and I_b are the integrals over f_s and f_b respectively. The parameters over which $\mathcal{L}$ is maximized are

$$r = N_s / (N_s + N_b) \tag{11.25}$$
$$n = N_s I_s + N_b I_b, \tag{11.26}$$

where N_s is the magnitude of the ^{71}Ge decay exponential, and N_b is the magnitude of the flat background. Since n is independent of r, $\hat{\nu} = n$ and $\hat{r}$ is found by maximizing $\mathcal{L}(r)$. The K-shell contribution is $\hat{N}_s$, found by inverting $\hat{r}$ and $\hat{n}$. The uncertainty on
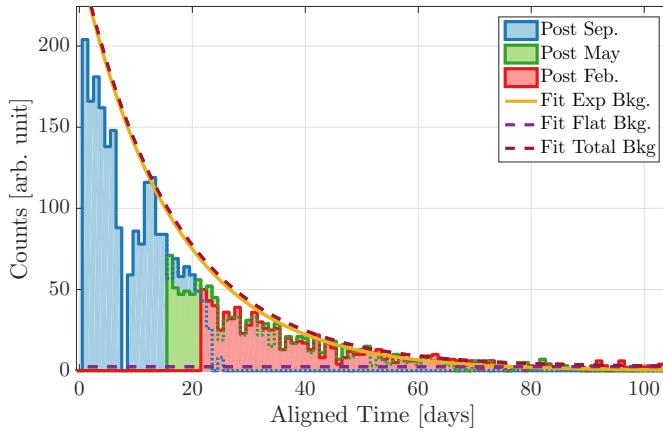
Figure 11.42: Events in the K-shell peak range for the three post-Cf periods as a function of aligned time. The post-May (green) and post-Feb. (red) periods are shifted such that their fitted exponential strength (yellow) matches that of the post-Sep. (blue). The decay occurs on top of a constant background (purple dash) to give the total fitted counts (red dash). The difference between the fit and the data is due to the duty cycle of the experiment. Figure adapted from [347].

$\hat{N}_s$ is found by constructing the posterior distribution, assuming a flat priors or n and r.

The MLE fit separates the ^{71}Ge decay products from the time-independent background, but it does not separate the K- and L-shell contributions from each other. The two decaying components overlap in bins L_o and L_0^2 and only the K-shell contributions in those bins should be used in computing the energy efficiency. The two components are separated using the fact that the ratio of rates between the peaks is well known and the "shape" of the smearing is independent of energy.

A distribution and final value of $\mathcal{E}_E$ are created by sampling the posterior distributions of N_s for each bin and combining them using Eq. 11.22. This distribution is very Gaussian (due to the high statistics limit of these distributions) with a $\mu \pm \sigma$ value of $86.4 \pm 0.9\,\%$.

(2) Efficiency at Full NTL Amplification: $\mathcal{E}_P$

The peak efficiency $\mathcal{E}_P$ represents the probability that an event with full NTL amplification passes the radial cut. It is energy dependent and must be separately estimated at various energies. The threshold of the radial cut affects $\mathcal{E}_P$ and it is computed separately for the Run 2a and Run 2b thresholds.

At the K shell, $\mathcal{E}_P$ is computed directly from the data by taking the fraction of events passing the cut over all events in the peak. In the outer portion of the peak, the non-peak background is first removed, where it is calculated by interpolating the outer rate above and below the peak.[21] The peak efficiency derived from the data is

$$\mathcal{E}_{P,\text{data}} = \frac{N_i}{N_i + N_o - N_b}, \tag{11.27}$$

where $N_{i/o}$ are the number of events passing/failing the cut, and N_b is the interpolated number of background events. The efficiency at 10.37 keV$_{\text{ee}}$ is $54.5 \pm 1.9\,\%$ and $49.8 \pm 1.7\,\%$ for the two periods respectively.

For lower energies, a pulse simulation is used. The simulated was run and analyzed by R. Underwood, is detailed in [346], and summarized here. In addition to simulating a specific energy, the fake events must have a proper radial parameter distribution. This is accomplished by constructing templates from real activation-peak events and using the 2T-fit. For a given peak trace, a template $T_{2\text{T}}$ with unique pulse-shape is constructed as

$$T_{2\text{T}} = (a_s A_s + a_f A_f)/E_{\text{t}}, \tag{11.28}$$

where A_i are the fast and slow templates, a_i are the amplitudes from the fitted data trace, and E_{t} is the NSOF total phonon energy from the event. For each event, there is a template for each of the four channels. These templates are scaled to an arbitrary energy, summed with measured experimental noise, and processed. The radial parameters for the fake events are then constructed in the same manner as the real data. 12 discrete energies are simulated, with the entire peak population scaled to each energy.

Initially, the K-shell peak was used to generate the templates due to the its larger statistics, however the simulated population at 1.3 keV$_{\text{ee}}$ using the K-shell-based templates did not match the observed L-shell peak. The difference is because the residual amplitude population in the outer channel saturates between the two energies as shown in in Fig. 11.43. The distribution of the residual amplitudes flares to large positive values at higher energies for channels B–D while the flaring in channel A ceases after ~ 2 keV$_{\text{ee}}$. The source of this saturation is not well understood, though likely related to

---

[21] The rate below the peak is the background component in that bin from the energy efficiency calculation.
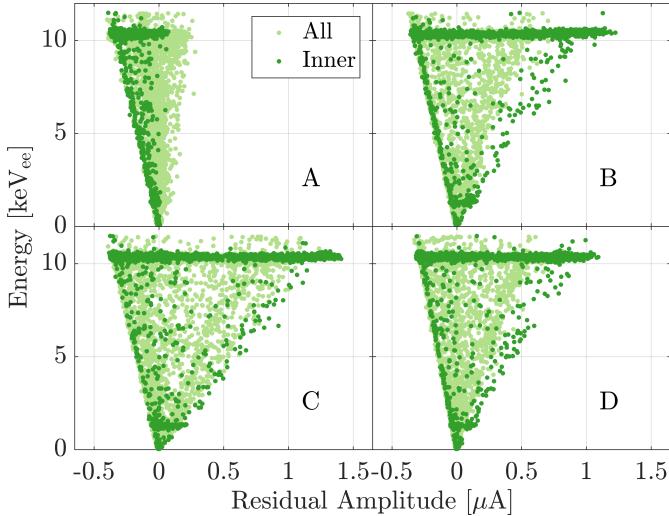
Figure 11.43: 2T-fit residual amplitude for each of the four phonon channels, showing all events (light green) and inner events (dark green), compared to the events' total energy.

the difference is shape between the channels. The K-shell population is not a representative population at lower energies and the L shell peak events are used as the basis for the templates.

There are two corrections required for calculating the peak efficiency from the simulation $\mathcal{E}_{P,\mathrm{sim}}$. (1) The original sample of L-shell events also contains background (non-peak) events and (2) there may be good "inner" events which fail the cut at any given energy due to the non-optimal energy independence of the cut. For correction (1), the number of background events in the initial selection is estimated by interpolating bins on either side of the peak. Using different adjoining bins varies the correction, and a systematic uncertainty of 2.0 % and 0.2 % for Run 2a and Run 2b respectively is given by those differences. For correction (2), the distribution of background events, in the radial parameter, for the adjoining bins is used to infer the distribution of background in the peak. This is used to assign a signal probability weight ω_i to each event based on the inferred background rate at that event's radial value. The final efficiency at each simulated energy with n events is

$$
\begin{aligned}
\mathcal{E}_{P,\mathrm{sim}} &= \frac{\sum_i^n \omega_i}{N_s + N_{sb} - N_b} \\
&= \frac{N_{si} + N_{sbi} \cdot (1 - N_b/N_{sb})}{N_s + N_{sb} - N_b},
\end{aligned}
\tag{11.29}
$$

where N_s and N_{sb} are the number of events in the initial L-shell selection in the radial
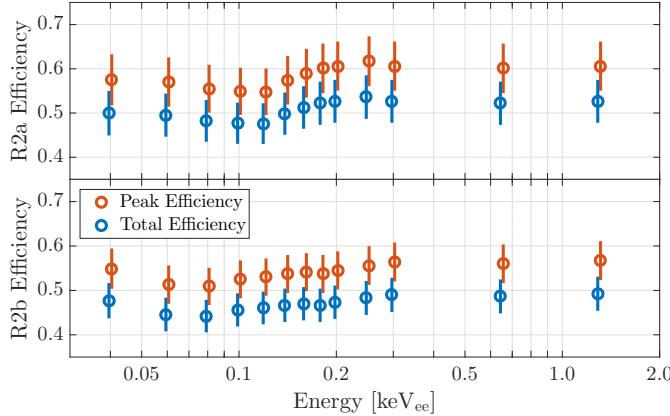
Figure 11.44: Peak ($\mathcal{E}_P$, orange) and total ($\mathcal{E}_E \cdot \mathcal{E}_P$, blue) efficiencies of the radial fiducial volume cut for the lowest energies of Run 2a (top) and Run 2b (bottom). The peak efficiency has a mild energy dependence while the energy efficiency is a constant $\mathcal{E}_E = 86.4\pm0.9\,\%$. Peak and total efficiency points are off-set from each other for clarity.

regions of pure signal ($\omega_i = 1$) and mixed signal and background ($\omega_i = 1 - N_b/N_{sb}$) respectively. N_{si} and N_{sbi} are the number of simulated events, using templates based upon initial events from each of those regions, which pass the radial cut, and N_b is the interpolated number of background events.

The uncertainty on $\mathcal{E}_{P,\mathrm{sim}}$ is found by usual propagation methods given the variance of each N_i used in the calculation.[22] The peak-alone and peak-energy-combined efficiencies for each of the 12 simulated energies are given in Fig. 11.44.

11.7.5   Trigger Efficiency

The lower energy threshold of the analysis is dictated by the experiment's ability to trigger on low energy events. Recalling that there were three different trigger threshold settings, the efficiency for issuing triggers, as a function of energy, is computed separately for each.

The general method for estimating the trigger efficiency is:

1. Gather a set of high quality and high statistics calibration data.

2. Find "good" events which issued a trigger on a non-iT5Z2 detector.

3. Determine, as a function of energy on iT5Z2, the fraction of good events which also issued a trigger in iT5Z2.

---

[22] i.e. $(\Delta\mathcal{E}_{P,\mathrm{sim}})^2 = \sum_i (\partial\mathcal{E}_{P,\mathrm{sim}}/\partial N_i \cdot \Delta N_i)^2$, where $(\Delta N_i)^2$ is the binomial or Poisson variance for the given N_i.

The data set used for the different trigger efficiency estimates are: the February and May ^{252}Cf data for Run 2a data with a 10.65 mV hardware threshold (called simply Run 2a in this section), the July ^{252}Cf data for Run 2a with an 11.0 mV hardware threshold (called Run 2a July in this section), and the January 2015 ^{252}Cf data for Run 2b. The ^{252}Cf data taken concurrently with Run 2b is not used as the noise monitors did not record data during that period. Since calibration data is read out in "selective read out mode," only iT5Z1 and iT5Z3 are be available in step 2 above.

The definition of a "good" event is determined using some of the official cuts and several impromptu cuts. Of the official cuts, the phonon and charge pulse quality cuts, glitch cuts (asymmetrical triggered and pulse quality), and bad GPS timing cut are applied. For Run 2b, the initial KDE-based cut is used to remove the region of the "spot" background.[23] Traces with multiple events are mitigated by the phonon pulse quality cut, but any remaining such events are removed by requiring non-zero live time and non-zero time between the current and preceding event. A cut against phonon baseline noise is made by setting a threshold on the sum of all four channels' pre-pulse variance. To avoid noise-induced cross-talk in the CDMSlite detector, both at higher and lower energies, an energy range cut is applied to iT5Z1 and iT5Z3. Noise multiples, such as could be caused by LF-noise, are mitigated by limiting the number of phonon triggers. LF-noise is directly removed using both the $\Delta\chi^2_{\mathrm{LF}}$ variable and the cryocooler time variable. A flat strict $\Delta\chi^2_{\mathrm{LF}}$ threshold is used. Two periods of cryocooler time are removed for Run 2a at $\hat{t} \in [0.05, 0.25]$ and $\hat{t} \in [0.45, 65]$ s while only the first period is removed for Run 2b.[24] In order to avoid noise in the non-CDMSlite detectors, the event issuing the trigger in those detectors must have greater than 10 keV$_{\mathrm{t}}$ of total phonon energy. These criteria are, in several instances, stricter than the final cuts used in the analysis and the result is a reduction in statistics and a corresponding increase in uncertainty.

For this analysis, "issuing" a trigger is defined as having an exceeded Plo trigger bit in a time window of 300 μs before to 300 μs after the global trigger of that event.

---

[23] No direct evidence is seen for the spot in the calibration data but it could be masked by the higher event rate. The cut to remove that region of the detector is applied to be conservative by assuming the spot, and its unknown origin, is still present.

[24] The maintenance on the cryocooler gave better behaved LF-noise and only the first period is seen to induce noise in the January ^{252}Cf data.

The fraction of good events which triggered iT5Z2 in addition to a different detector is shown, as a function of iT5Z2 energy, in Fig. 11.45 for each of the three trigger periods. Above energies of ~1.5 keV$_t$ the fraction is 100 % for each of the three periods. The energy range over which the efficiency drops from 100 % to 0 % is smaller in the Run 2a periods. The location and width of these "turn-ons" in the efficiency is best characterized by performing a fit to the data.

The fit is performed using the MLE technique. The log-likelihood function used is

$$\ln\left(\mathcal{L}(\mu,\sigma)\right) = \sum_i^{N_+} f_+(E_i;\mu,\sigma) + \sum_j^{N_-} f_-(E_j;\mu,\sigma), \tag{11.30}$$

where $N_\pm$ are the number of events passing/failing the trigger condition on iT5Z2 and

$$f_\pm(E_i;\mu,\sigma) = 0.5\left(1 \pm \operatorname{erf}\left(\frac{E_i - \mu}{\sqrt{2}\sigma}\right)\right), \tag{11.31}$$

where μ is the 50 % point, σ the width of the error function $\operatorname{erf}(x) = \frac{2}{\sqrt{\pi}}\int_0^x \exp\left(-t^2\right)\mathrm{d}t$, and E_i is the total phonon energy of the ith event.[25]

A Markov chain Monte Carlo (MCMC) is used to sample the posterior distribution using a flat prior on μ and a log-normal prior on σ. The prior on σ is needed to prevent the width from becoming unphysically small for Run 2a and is centered at the approximate width of the noise distribution. These simulations were run by J. Wilson. The prior- and marginalized-posterior distributions for μ and σ for the Run 2a fit are given in Fig. 11.46. The two-dimensional posterior distributions from the MCMC are given in the top row of Fig. 11.45 for each of the periods. The 68 % and 95 % regions with highest posterior density are given by the closed curves with the highest *a posteriori* point ("best fit") given by the cross. The best fit curves with uncertainty bands defined by the two-dimensional regions are given by the bottom row of Fig. 11.45.

Finally, the efficiency curves are checked against the WIMP-search events which do and do not trigger iT5Z2. This comparison is shown in Fig. 11.47 for Run 2a and Run 2b. As given in the figure, there are no non-triggering events above the 50 %

---

[25] Initial fits were also performed with a third free parameter: the amplitude A, which multiplies all of $f_\pm$. The value of A is the maximum reached by the function, and, as expected, the fits gave the amplitude as unity with small uncertainty.
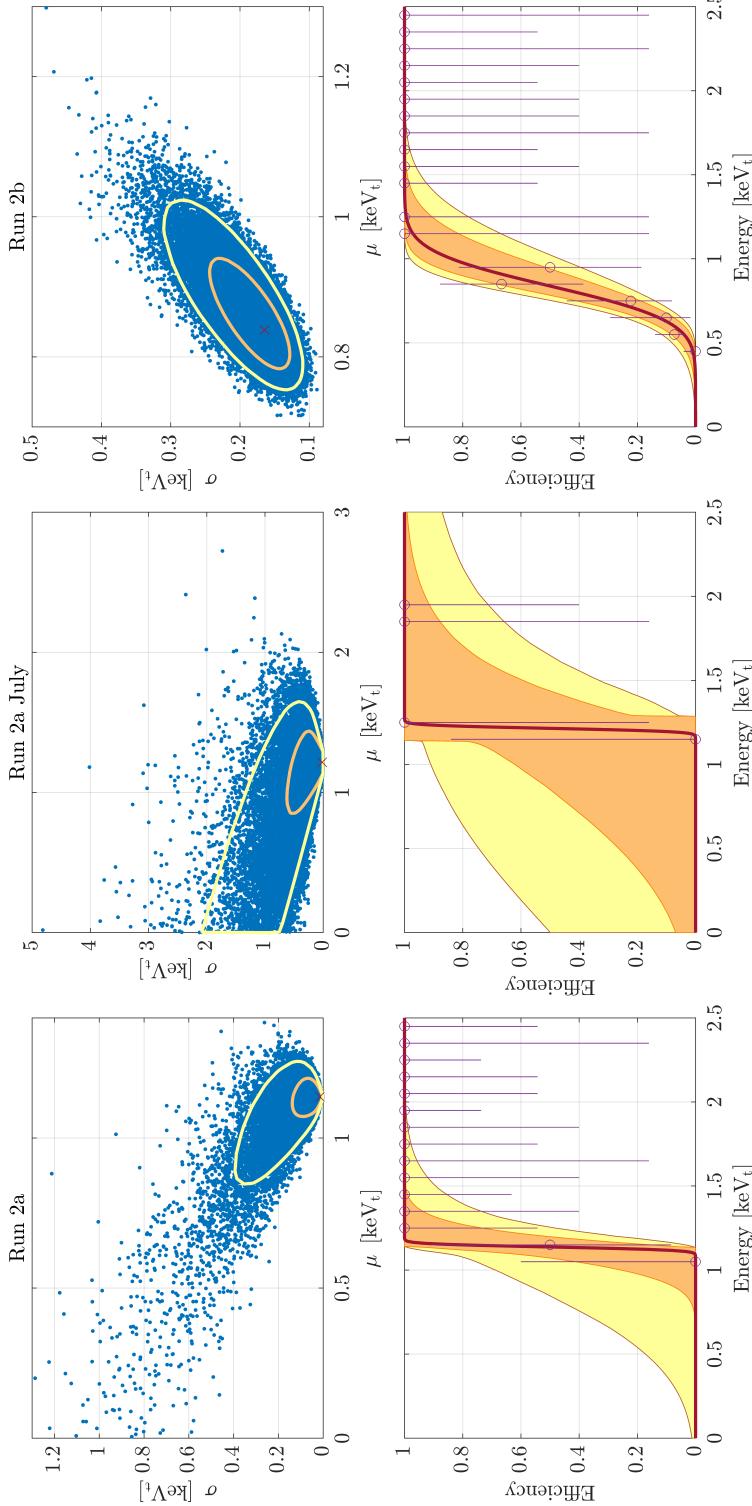
Figure 11.45: Trigger efficiency data and fit information for Run 2a (left), Run 2a July (middle), and Run 2b (right). The top figures show the two-dimensional posterior distribution resulting from the MCMC sampling of the 50 % point (μ) and width (σ) of the efficiency turn-on region. The 95 % (yellow) and 68 % (orange) confidence regions are given by the solid lines while the maximum *a posteriori* point (best fit) is given by the cross. The bottom figures show the binned efficiency (purple points with error bars), the curve created using the best-fit point parameters (black), and regions encapsulating the curves created using parameters in the 95 % (yellow) and 68 % (orange) confidence regions from the top figures.
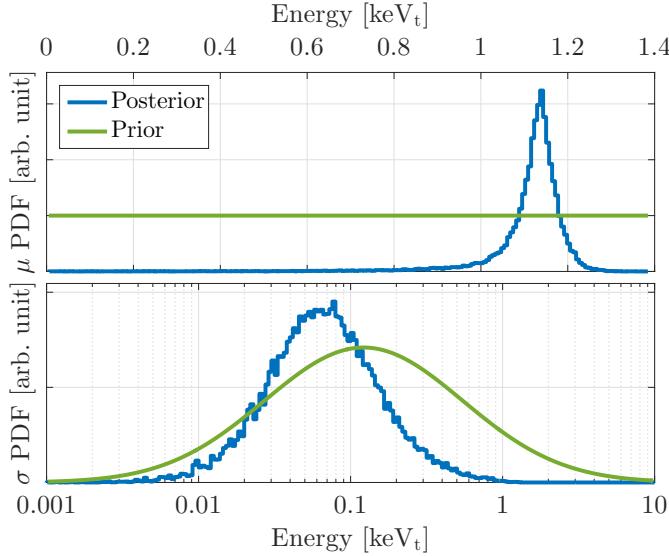
Figure 11.46: Marginal posterior probability density distributions (blue) of μ (top) and σ (bottom) for Run 2a along with the prior distributions (green) used in the MCMC. The prior for μ is flat while the prior for σ is log-normal and centered at 0.144 keV$_t$, approximately the zero energy resolution.

Period	μ [keV$_t$]	μ [eV$_{ee}$]
Run 2a	$1.138^{+0.061}_{-0.066}$	$74.7^{+4.0}_{-4.3}$
Run 2a July	$1.225^{+0.223}_{-0.364}$	$79.8^{+14.7}_{-23.9}$
Run 2b	$0.838^{+0.102}_{-0.055}$	$55.1^{+6.7}_{-3.6}$

Table 11.3: 50 % trigger efficiency point for the different periods of Run 2 given by the maximum *a posteriori* value of the Markov chain Monte Carlo. The Monte Carlo simulation is performed in the keV$_t$ energy scale and the output is scaled to keV$_{ee}$.

efficiency points for each part of the run. There are, however, triggered events below this point. These events are in the noise and represent a noise pathology which triggers; these events should not be included in the final spectrum. To impose this, the 50 % trigger points (best-fit μ from the fits) are explicitly taken as the lower thresholds in the final spectra. These 50 % values are given in Table 11.3. The fits are performed in the keV$_t$ energy scale with the 50 % points converted to keV$_{ee}$ using the final scaling of the usual calibration. The 55 eV$_{ee}$ threshold in Run 2b is the lowest yet attained by SuperCDMS.
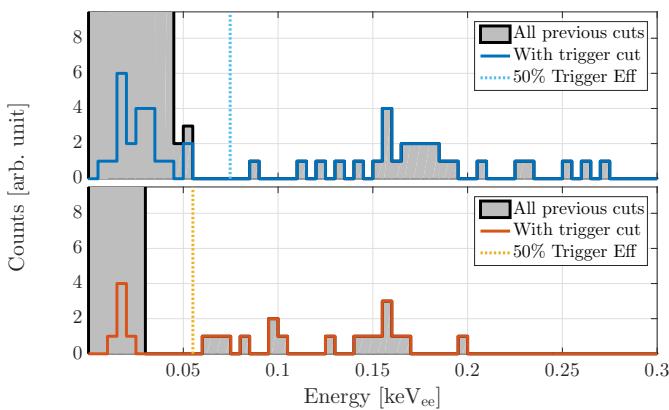
Figure 11.47: Events passing all cuts (grey fill) and those which additionally trigger in iT5Z2 (solid lines) compared to the 50 % trigger efficiency points (dotted lines) for Run 2a (top) and Run 2b (bottom). There are no non-triggering events above the 50 % points. A noise pathology triggers at lower energies; these events are removed by imposing a threshold at the 50 % points.

Chapter 12

WIMP-Search Results

The final result of a dark matter search experiment asks the question of what do the observed events imply about the underlying WIMP physics. In general, producing such a result is model, experiment, and analysis dependent. Recall that the total number of events N observed in an experiment is given by

$$N = \int_{E_1}^{E_2} \frac{\mathrm{d}N}{\mathrm{d}E_\mathrm{r}} \; \mathrm{d}E_\mathrm{r} = \int_{E_1}^{E_2} \frac{\mathrm{d}R}{\mathrm{d}E_\mathrm{r}} \mathcal{E}(E_\mathrm{r}) \; \mathrm{d}E_\mathrm{r}, \tag{12.1}$$

where $[E_1, E_2]$ defines the energy range in recoil energy E_r over which one is looking for dark matter and $\mathcal{E}(E_\mathrm{r})$ is the effective exposure over that range. The differential event rate per unit mass is

$$\frac{\mathrm{d}R}{\mathrm{d}E_\mathrm{r}} = \frac{N_T m_T}{2 m_\chi \mu_T^2} \sigma_0 F^2(E_\mathrm{r}) \mathcal{I}(\mathbf{v}_E, v_\mathrm{esc}), \tag{12.2}$$

where N_T is the number of nuclei per target unit mass, m_T is the mass of the target nucleus, m_χ is the mass of the WIMP, μ_T is the reduced mass of the WIMP-nucleus system, σ_0 is the standard zero-momentum WIMP-nucleus cross section, F is the nuclear form factor and the astrophysical integral $\mathcal{I}$, which depends on the velocity of the Earth relative to the dark matter halo $\mathbf{v}_E$ and the Galactic escape velocity v_esc is given by Eqs. 3.40 and 3.53 with numerical values for astrophysical measurements investigated in Sec. 12.6. A result is calculated by comparing the observed event spectrum, $\mathcal{N}$ or $\mathrm{d}\mathcal{N}/\mathrm{d}E_\mathrm{r}$, with that expected from Eq. 12.1 and inferring information about dark matter; usually an upper limit in the σ_0-m_χ plane. The components, and their sources,

Component	Name	Source
σ_0	WIMP-nucleon cross section	Particle and Astrophysics
$F^2(E_{\mathrm{r}})$	Nuclear Form Factor	Nuclear Physics
$\mathcal{I}(\mathbf{v}_E, v_{\mathrm{esc}})$	Integral over velocity distribution	Astrophysics
$[E_1, E_2]$	Thresholds	Analysis
$m_T,\ N_T$	Target nuclear mass and density	Experiment
$\mathcal{E}(E_{\mathrm{r}})$	Effective Exposure	Experiment and Analysis
$\mathrm{d}\mathcal{N}/\mathrm{d}E_{\mathrm{r}}$	Observed Spectrum	Analysis

Table 12.1: Different components, and their sources, required for computing a WIMP-search result. Some sources come from the experiment and analysis while others are assumptions for basic physics.

for computing a limit are summarized in Table 12.1.

The CDMSlite Run 2 analysis goal is to set upper limits on the spin-independent and spin-dependent WIMP-nucleon cross sections. Using the energy range, effective exposure, and energy spectrum from the analysis, final limits are set using the optimum interval method. The uncertainties associated with the analysis are also propagated to the final result and various cross-checks performed, including understanding the uncertainty from the astrophysical assumptions.

12.1   Analysis Range and Effective Exposure

The lower E_1 and upper E_2 energy thresholds used for Run 2 limits are both dictated by empirical observations of the analysis. The lower energy threshold comes directly from the trigger efficiency curves. There is a population of noise events which issue a trigger in the CDMSlite detector at an energy where the efficiency curve is $\sim 0\,\%$. To avoid this population, an explicit cut-off is placed at the respective $50\,\%$ trigger efficiency values for Run 2a (74.7 keV$_{\mathrm{ee}}$) and Run 2b (55.1 keV$_{\mathrm{ee}}$) such that events below these values are not considered. The upper threshold is chosen based upon the derivation of the radial cut efficiency. Recall that, in the efficiency calculation, the K-shell peak events could not be used for the pulse simulation as the K-shell population did not accurately reproduce the radial distribution seen at lower energies. This is related to the outer

WIMP Parameters: $m_\chi = 4.25$ GeV$/c^2$, $\sigma_p^{\text{SI}} = 1.25 \times 10^{-40}$ cm^2
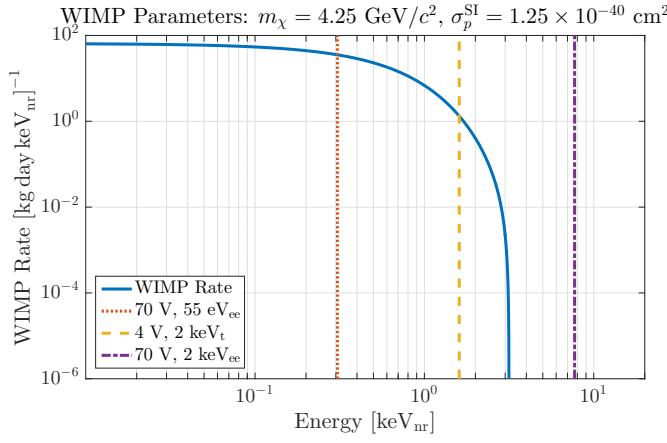
Figure 12.1: Differential interaction rate for a WIMP with mass of 4.5 GeV$/c^2$ and spin-independent cross section of 1.25×10^{-40} cm^2 (blue) along with the lower (orange dot) and upper thresholds (purple dot) for the Run 2 analysis and the lower threshold for the SuperCDMS LT analysis (yellow dash). The threshold for the LT analysis is below the upper threshold of Run 2: it is more sensitive in energy ranges above the Run 2 upper threshold.

channel (channel A) fast-template amplitude saturating above ~ 2 keV$_{\text{ee}}$. As the reason for this saturation is not fully understood, an upper threshold of 2 keV$_{\text{ee}}$ is placed on the spectrum. A check on this threshold is performed in Fig. 12.1, where these thresholds are compared to a spin-independent WIMP spectrum near where the CDMSlite Run 1 and SuperCDMS LT limits cross. As seen there, the lower limit from the LT result is below the 2 keV$_{\text{ee}}$ upper limit for this analysis: the Run 2 result could not do better than the LT result going to higher energies.

The effective exposure combines the detector mass $\mathcal{M}$, the live time $\mathcal{T}$, and the nuclear-recoil efficiency $\epsilon(E_{\text{r}})$ as

$$\mathcal{E}(E_{\text{r}}) = \mathcal{M}\mathcal{T}\epsilon(E_{\text{r}}). \tag{12.3}$$

For iT5Z2, $\mathcal{M} = 606.5$ g and the final live time is $\mathcal{T} = 115.59$ d. The total exposure is then $\mathcal{M}\mathcal{T} = 70.10$ kg day.

The total efficiency of the analysis is the product of all the individual cut efficiencies. The total is calculated separately for Run 2a ϵ_a and Run 2b ϵ_b and then combined by weighting by the respective live times of each $\mathcal{T}_{a/b}$

$$\epsilon = \frac{\epsilon_a \mathcal{T}_a + \epsilon_b \mathcal{T}_b}{\mathcal{T}_a + \mathcal{T}_b}. \tag{12.4}$$
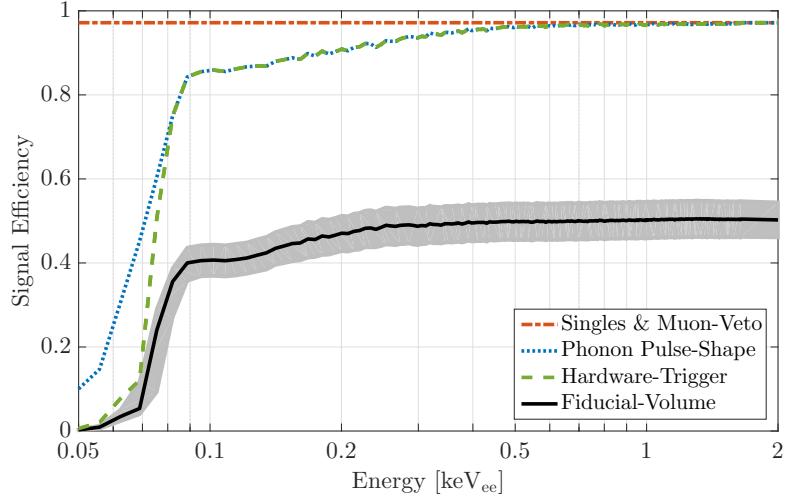
Figure 12.2: Binned total efficiency after sequential application of the singles and muon veto cuts (orange dot dash), phonon pulse-shape cuts (blue dot), hardware-trigger cut (green dash), and radial fiducial volume cut (black solid). The uncertainty (gray band) around the final curve shows the combined uncertainty, at 68 % confidence, of all efficiencies.

The efficiency after sequential application of different cuts in the relevant energy range is given in Fig. 12.2. The largest loss of efficiency is due to the radial fiducial volume cut, which brings the maximum efficiency to ∼50 %. The uncertainty band around the final curve contains the uncertainty, at 68 % confidence, from all of the cuts. This is dominated by the radial fiducial volume efficiency at most energies, with the trigger efficiency having a strong presence below ∼100 eV$_{ee}$. The trigger efficiencies cause the asymmetric uncertainty at those energies as well as the sharp corners (due to cutting-off those efficiencies below their 50 % values). The drop in the phonon pulse-shape cut efficiency near ∼80 % is due to the contour portion of the LF-noise cut.

12.2   Final Spectrum

Obtaining the final spectrum in energy $d\mathcal{N}/dE_r$ directly is difficult for CDMSlite, as the recoil energy depends on whether the event is an NR or ER. As this differentiation cannot be made with CDMSlite, all events in the final spectrum must be assumed to be WIMP-like NRs, even though the vast majority are known to be ERs (activation peaks,

Compton scatters, etc.). Obtaining the final spectrum in appropriate units, then takes two steps:

$$\frac{\mathrm{d}\mathcal{N}}{\mathrm{d}E_{\mathrm{r}}} = \frac{\mathrm{d}\mathcal{N}}{\mathrm{d}E_{\mathrm{r,nr}}} = \left(\frac{\mathrm{d}\mathcal{N}}{\mathrm{d}E_{\mathrm{r,ee}}}\right)\left(\frac{\mathrm{d}E_{\mathrm{r,ee}}}{\mathrm{d}E_{\mathrm{r,nr}}}\right). \tag{12.5}$$

Since the final recoil energy needed is $\mathrm{keV_{nr}}$, the calibrated $\mathrm{keV_{ee}}$ spectrum must be converted using a model. The electron-equivalent spectrum is first characterized and then converted to nuclear-recoil equivalent energy.

12.2.1 Electron-equivalent Spectrum Characterization

The final measured spectrum in $\mathrm{keV_{ee}}$, shown up to above the K-shell peak, is given Fig. 12.3. The spectrum is normalized by the efficiency, accounting for both the exposure and the efficiency, to give a true rate. The trigger efficiency is not a part of the correction to show where the noise begins, however the 50% points are indicated in the inset figure. The K-, L-, and M-shell $^{71}\mathrm{Ge}$ lines are prevalent at 10.37, 1.30, and 0.16 $\mathrm{keV_{ee}}$ respectively. Other activation peaks are known in this energy range, including $^{65}\mathrm{Zn}$ (8.89 (K), 1.10 (L), and 0.12 (M) $\mathrm{keV_{ee}}$), $^{68}\mathrm{Ga}$ (9.66 (K), 1.20 (L), and 0.14 (M) $\mathrm{keV_{ee}}$), and $^{68}\mathrm{Ge}$ (same energy as $^{71}\mathrm{Ge}$). These isotopes are created by cosmic ray activation of the material before the detectors were brought underground in 2011 and they have been decaying since with typical half live of $\mathcal{O}(100\ \mathrm{d})$ [292]. When Run 2 data were taken in 2014, the rates for these isotopes were small and no distinct peaks are visible in the spectrum. $^{3}\mathrm{H}$ β decays with an endpoint of 18.6 $\mathrm{keV_{ee}}$ and a half life of 12.32 yr and is also likely present in the spectrum.

The background rates for different energy ranges, avoiding the primary activation lines, are given Table 12.2 for Run 2a and Run 2b individually as well as combined. The difference in rate above and below the K-shell peak can be attributed to the aforementioned unresolved activation peaks, tritium, and the small amount of reduced-gain events from the peak which pass the radial fiducial volume cut. The rates between the K- and L-shell peaks as well as between the M- and L-shell peaks are consistent, to within statistical error, across the periods at $\sim 1\ [\mathrm{keV_{ee}\,kg\,day}]^{-1}$. The rates between the thresholds and M-shell peak, however, is larger and inconsistent between Run 2a and Run 2b. In general, more backgrounds leakage, such as LF-noise and glitches, is expected at lower energies. The difference between the run periods is attributed to the
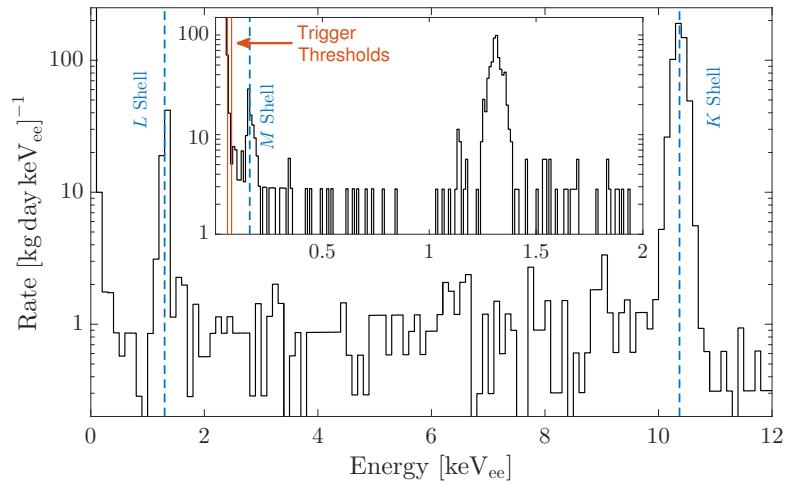
Figure 12.3: Final Run 2 spectrum after applying all cuts and correcting for the efficiency, except the trigger efficiency. The prominent features are the ^{71}Ge electron capture peaks at 10.37 keV$_{ee}$ (K shell), 1.30 keV$_{ee}$ (L shell), and 0.16 keV$_{ee}$ (M shell) and labeled by vertical blue dash lines. Inset: a magnification of the lowest energy region of the spectrum which is used for determining the low-mass WIMP sensitivity. The 50 % trigger efficiency points (orange vertical lines) indicate the lower energy thresholds for the analysis.

Energy $[\text{keV}_{\text{ee}}]$	Run 2a Rate $[\text{keV}_{\text{ee}}\,\text{kg}\,\text{day}]^{-1}$	Run 2b Rate $[\text{keV}_{\text{ee}}\,\text{kg}\,\text{day}]^{-1}$	Run 2 Rate $[\text{keV}_{\text{ee}}\,\text{kg}\,\text{day}]^{-1}$
0.056–0.14	2.52 ± 1.27	$26.15^{+10.13}_{-9.95}$	$16.33^{+8.18}_{-7.97}$
0.2–1.2	1.11 ± 0.19	0.98 ± 0.44	1.09 ± 0.18
1.4–10	0.98 ± 0.06	1.16 ± 0.17	1.00 ± 0.06
11–20	0.30 ± 0.04	0.30 ± 0.09	0.30 ± 0.03

Table 12.2: Average rate between the ^{71}Ge activation peaks after application of all cuts and correcting for the efficiency. The difference in rate above and below the K-shell peak (10.37 keV$_{\text{ee}}$) is attributed to unresolved activation peaks, tritium, and reduced-gain events leaking pass the fiducial volume cut. The difference in rate below the M-shell peak (0.16 keV$_{\text{ee}}$) is attributed to more background leakage at lower energies and the presence of additional background in Run 2b.

Peak	Location $[\text{keV}_{\text{ee}}]$	Resolution $[\%]$	Resolution $[\text{eV}_{\text{ee}}]$
Base line	0.0	N/A	9.7 ± 0.1
M Shell	0.16	11.4 ± 2.8	18.6 ± 4.2
L Shell	1.30	2.36 ± 0.15	31 ± 2
K Shell	10.37	0.974 ± 0.009	101 ± 1

Table 12.3: Resolution of the baseline noise and ^{71}Ge capture peaks. Resolutions are given as a percentage of the mean (μ/σ) as well as in energy.

additional background "spot" in Run 2b, and the fact that the threshold in that portion of the run is lower.

The energy resolution of the experiment is determined by applying Gaussian fits to the three activation lines [348] and considering the width of the noise distribution for the baseline electronics noise σ_0. The noise distribution, computed using randomly triggered events and the zero-delay OF fit, is shown in Fig. 12.4. The distribution is non-Gaussian and slightly offset from zero keV$_{\text{ee}}$. The width is taken as half the distance from the $\mu \pm \sigma$ Gaussian-equivalent percentiles, 84.13 % and 15.87 %. The width is $\sigma_0 = 9.25 \pm 0.11$ eV$_{\text{ee}}$, which is the lowest measured by SuperCDMS. The resolution of the three activation peaks is found in Table 12.3.
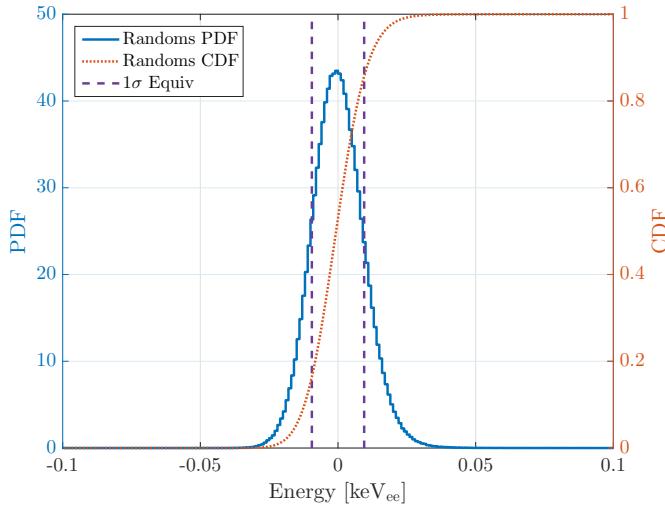
Figure 12.4: Distribution of randomly triggered events in energy using the zero-delay OF fit (blue solid, left vertical axis) normalized as a PDF along with the corresponding CDF (orange dot, right vertical axis). Due to the non-Gaussian shape of the distribution, the width of the noise is taken as half the distance from the $\mu \pm \sigma$ Gaussian-equivalent percentiles, 84.13% and 15.87% (purple dash). The width is 9.25 ± 0.11 eV$_{\mathrm{ee}}$.

An energy-dependent model for the total resolution of the detector $\sigma_{\mathrm{T}}(E_{\mathrm{r,ee}})$ is

$$\sigma_{\mathrm{T}} = \sqrt{\sigma_{\mathrm{E}}^2 + \sigma_{\mathrm{F}}^2(E_{\mathrm{r,ee}}) + \sigma_{\mathrm{PD}}^2(E_{\mathrm{r,ee}})}, \tag{12.6}$$

where σ_{E} is the baseline width due to the electronics noise, $\sigma_{\mathrm{F}}(E_{\mathrm{r,ee}})$ is due to Fano statistics, and $\sigma_{\mathrm{PD}}(E_{\mathrm{r,ee}})$ is broadening due to position dependence. The σ_{F}^2 term comes from U. Fano [349], where he found that for N produced electron-hole pairs in an interaction, the variance of N is $\sigma_N^2 = FN$, where F is termed the Fano factor. Since, for an ER, $N = E_{\mathrm{r,ee}}/\epsilon_\gamma$, this implies a variance in energy of $\sigma_N^2 \epsilon_\gamma^2$. The Fano broadening in Eq. 12.6 then

$$\sigma_{\mathrm{F}}^2(E_{\mathrm{r,ee}}) = \sigma_N^2 \epsilon_\gamma^2 = FN\epsilon_\gamma^2 = FE_{\mathrm{r,ee}}\epsilon_\gamma \tag{12.7}$$

$$\equiv BE_{\mathrm{r,ee}}. \tag{12.8}$$

The Fano factor for Ge has been measured as $F = 0.13$ [350] and is generally considered to be energy independent although this is unchecked at the low energies of CDMSlite. The broadening due to position dependence is assumed to be quadratic with energy as $\sigma_{\mathrm{PD}}^2(E_{\mathrm{r,ee}}) = (AE_{\mathrm{r,ee}})^2$, giving the total resolution as a function of energy as

$$\sigma_{\mathrm{T}} = \sqrt{\sigma_E^2 + BE_{\mathrm{r,ee}} + (AE_{\mathrm{r,ee}})^2} \tag{12.9}$$
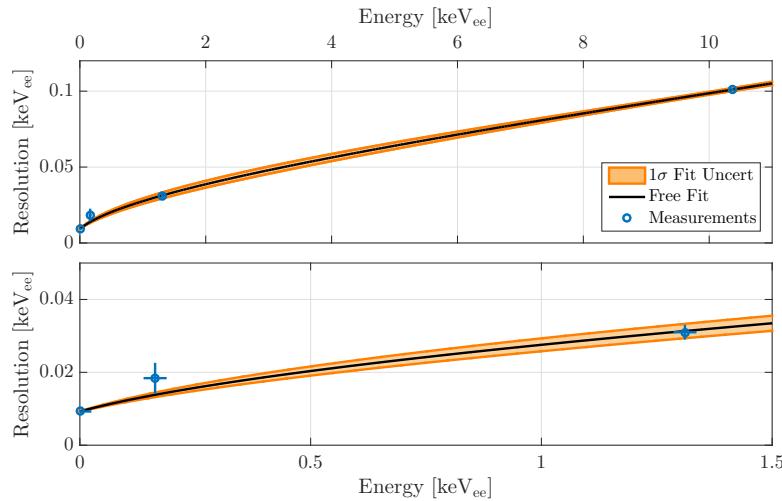
Figure 12.5: Measured resolutions (blue points) along with a fit to (black curve) and the uncertainty (orange shaded) of the model in Eq. 12.9 with all parameters free and the fit is weighted by the uncertainty on each point. The full energy range (top) and enlargement of the lowest energies (bottom) are both given.

Prior knowledge gives the expectation that $\sigma_E = \sigma_0$ and $B = 0.39$ eV$_{ee}$.

This model is fit to the four measured resolution points in Fig. 12.5. The fit has three free parameters, σ_E, B, and A, and is performed by weighting each measurement by its uncertainty. Given how small the uncertainty is on the baseline resolution, it is unsurprising that the fit value is equivalent to the measurement at $\sigma_E = 9.26 \pm 0.11$ eV$_{ee}$. The Fano coefficient is fit to $B = 0.67 \pm 0.11$ eV$_{ee}$, which is higher than the expectation at the 2.3σ level. The position-dependence coefficient is fit to $A = (5.68 \pm 0.94)$. B and A are strongly anti-correlated with a Persons product-moment correlation coefficient of $\rho_{AB} = -0.984$. They are effectively uncorrelated with σ_E with the correlation coefficients of $\rho_{AE} = 0.0167$ and $\rho_{BE} = -0.0189$. Repeating the fit with $B = 0.39$ eV$_{ee}$ fixed to the expectation, gives $A = (7.73 \pm 0.13) \times 10^{-3}$ with slightly worse goodness-of-fit. The uncertainty on the M-shell width is comparably large, giving it a low weight and explaining its relatively poor match to the best-fit curve.

The resolution fits of the activation lines can be used to compute the number of activation events in each peak. The ratio of rates for the activation lines is well known (Appendix B) and a comparison between the measured and expected ratios gives validity to the spectrum. These ratios are given in Table 12.4, where good agreement between the measurement and theory is seen.

For the WIMP-search limit, only events within the energy thresholds defined in

Ratio	Measurement	Theory
M/L	0.16 ± 0.03	0.17
M/K	0.018 ± 0.003	0.020
L/K	0.11 ± 0.01	0.12

Table 12.4: Comparison of the measured and theoretically expected ratio of events in the different ^{71}Ge activation lines. To within the statistical uncertainty on the measurement, the values agree for all ratios. Theoretical values from Appendix B.
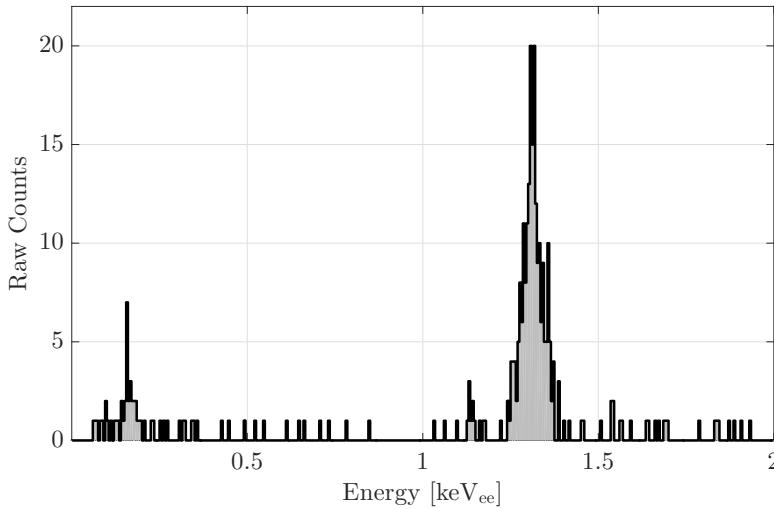
Figure 12.6: Events between $55.1/74.7$ eV$_\text{ee}$ and 2 keV$_\text{ee}$ for Run 2a/b respectively which are used to compute the final WIMP-search result. There are 318 total events in these energy ranges.

Sec. 12.1 are required. The 318 total events between $55.1/74.7$ eV$_\text{ee}$ and 2 keV$_\text{ee}$ for Run 2a/b respectively are shown in Fig. 12.6.

12.2.2 Conversion to Nuclear Recoil Equivalent Energy

In order to set limits on possible WIMP (NR) interactions, the spectrum must be converted to nuclear-recoil equivalent energy. This is accomplished by comparing the definitions of the $E_\text{r,ee}$ and $E_\text{r,nr}$ and assuming the same E_t

$$E_\text{t}[\text{keV}_\text{t}] = E_\text{r,ee}[\text{keV}_\text{ee}]\left(1 + g(V_b)\right) \tag{12.10}$$

$$E_\text{t}[\text{keV}_\text{t}] = E_\text{r,nr}[\text{keV}_\text{nr}]\left(1 + Y(E_\text{r,nr})g(V_b)\right) \tag{12.11}$$

$$E_\text{r}[\text{keV}_\text{nr}] = E_\text{r}[\text{keV}_\text{ee}]\left(\frac{1 + g(V_b)}{1 + Y(E_\text{r,nr})g(V_b)}\right). \tag{12.12}$$

The only unknown is the ionization yield $Y(E_{\mathrm{r,nr}})$, which cannot be directly measured by a CDMSlite detector.[1] This mandates the use of a model.

Several attempts have been made in the community, including by CDMS II [244, 305], to directly measure the ionization yield of Ge as a function of nuclear recoil energy [351–362]. As seen in Fig. 12.7, there is a large spread to the data, which was taken at various temperatures and operating biases. Also, only the data of [351–354] extend below 1 keV$_{\mathrm{ee}}$, the energy range of interest for this analysis. Although more recent models have been proposed [353, 354, 363], the Lindhard model [364] is the most common in the field. The ionization yield in the Lindhard model is

$$Y(E_{\mathrm{r,nr}}) = \frac{k \cdot g\,(\varepsilon)}{1 + k \cdot g\,(\varepsilon)}, \tag{12.13}$$

where $g\,(\varepsilon) = 3\varepsilon^{0.15} + 0.7\varepsilon^{0.6} + \varepsilon$, $\varepsilon = 11.5 E_{\mathrm{nr}}(\mathrm{keV})Z^{-7/3}$, and Z is the atomic number of the material. In the standard Lindhard model, $k = 0.157$ for Ge, however the original authors state that the model is less certain at lower energies: this analysis takes an uncertainty of $k \in [0.1, 0.2]$. The Lindhard model curves for the standard k value and the bounding values are also shown in Fig. 12.7. The bounding values on the Lindhard model encompass a majority of the data points. The thresholds of the analysis $[0.055, 2.0]$ keV$_{\mathrm{ee}}$ correspond to $[0.397, 10.119]$ keV$_{\mathrm{nr}}$ for $k = 0.1$, $[0.304, 7.763]$ keV$_{\mathrm{nr}}$ for $k = 0.157$, and $[0.263, 6.754]$ keV$_{\mathrm{nr}}$ for $k = 0.2$.

12.3   Propagation of Uncertainty

There are several sources of uncertainty in the analysis which are propagated into the final limit curve. The uncertainty propagation uses a Monte Carlo sampling technique to build a distribution of limits from which the final curve and uncertainty are obtained. For each iteration of the sampling procedure, the measured energy spectrum and thresholds, in keV$_{\mathrm{ee}}$, remain the same while the efficiency curve and Lindhard k

---

[1] Here as for the whole analysis, the bias voltage is always assumed to be the full -70 V that was nominally applied to the detector. This is not strictly true, as the high-voltage power supply current indicates that there are slight drops in voltage throughout the run. The current could be used to compute those drops in bias and each individual events' bias used when it is convert to keV$_{\mathrm{nr}}$, however the difference in the final result between doing this and using the full bias for all is $\lesssim 1\,\%$.
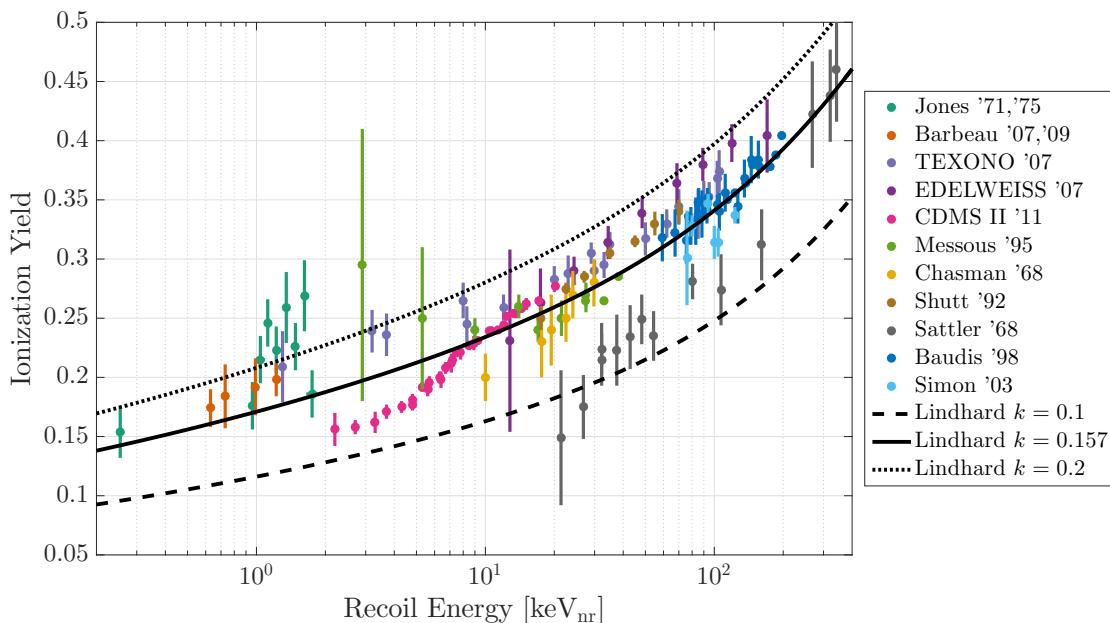
Figure 12.7: Experimental measurements of the ionization yield as a function of NR energy along with Lindhard model curves for the best fit $k = 0.1574$ (solid curve), lower bound $k = 0.1$ (dash curve), and upper bound $k = 0.2$ (dot curve). Experimental data comes from [244, 351–362]. Figure adapted from [363] with assistance from D. Barker.

Title	Source	Type
Energy-Independent Efficiency	Muon Veto Cut	Statistical
	Multiple Scatters Cut	
Trigger Efficiency	Triggered Events	Statistical
Phonon χ^2-based Efficiency	Phonon pulse quality Cut	Statistical, Systematic
	LF-noise Cut	
	Pulse-shape Glitch Cut	
Fiducial Volume Efficiency	Radial Cut	Statistical, Systematic
keV$_{\mathrm{ee}}$ to keV$_{\mathrm{nr}}$ Conversion	Lindhard Theory k	Systematic

Table 12.5: Categories, sources, and types of uncertainty propagated into the Run 2 final result. There is statistical uncertainty in the muon veto and multiple scatters efficiency, trigger efficiency, phonon χ^2-based efficiency, and fiducial volume efficiency. There is systematic uncertainty in the phonon χ^2-based efficiency, fiducial volume efficiency, and Lindhard theory k value.

value are sampled using appropriate posterior probability distributions for each uncertainty. Recall from that the Bayesian posterior is the distribution PDF multiplied by a prior, which is taken to be flat unless specified, and properly normalized.

The different sources and types of uncertainty to be propagated are given in Table 12.5. The majority are statistical uncertainties, though there are systematics in the χ^2-based cuts (phonon pulse quality, LF-noise, pulse-shape glitches), radial cut, and conversion to keV$_{\mathrm{nr}}$. Each of these uncertainties, and their corresponding distributions, are discussed next.

Energy-Independent Efficiency

The uncertainty on the muon veto and multiple scatter cuts is small, and probably could be neglected. However, it provides a simple introduction for the latter, more complicated, uncertainties. A Bernoulli trial is when a single experiment has one of two outputs, success or failure, where the probability of success is p. If a series of N independent Bernoulli trials are performed, the resulting distribution span the range of $[0, 1]$ and can be characterized by the probability of success p. This is the binomial

distribution, where the probability of getting exactly n successes from the N trials is

$$f_B(n; N, p) = \frac{N!}{n!\,(N-n)!} p^n\,(1-p)^{N-n}\,. \tag{12.14}$$

The mean is $\mu = pN$, the variance is $\sigma^2 = Np\,(1-p)$, and in proper limits the distribution can be approximated by a Gaussian.[2] Such a distribution describes a standard efficiency function, which expresses the probability of a nuclear recoil successfully passing the given cut.

For the muon-veto and multiple-scatter cuts, the number of sample draws is the total number of random triggers N_0, the number of successes is the number of randoms passing the cuts n_0 and the best-fit efficiency is the ratio of the two $p_0 = n_0/N_0$. The posterior distribution on the efficiency p with a flat prior is then

$$P(p; n_0, N_0) = f_B(pN_0; N_0, p_0) \tag{12.15}$$

100 samples each from the Run 2a and Run 2b posterior distributions are shown in the top panels of Fig. 12.8 along with the best fit efficiency and 68 % uncertainty on that value using an independent estimate via a simple MLE.

Trigger Efficiency

The trigger efficiency function's best-fit parameters are found by running a Markov chain Monte Carlo (MCMC) to sample the posterior distribution. The MCMC already samples the posterior distribution and its outputs are used directly to propagate the uncertainty. Each MCMC output has the same probability of being selected, with their density dictating the most/least probable regions of the posterior distribution. A sample of these random draws is shown in the second row of Fig. 12.8. Recall that the lower energy thresholds for the analysis periods are defined as the best-fit 50 % trigger efficiency point. The cut-off is imposed regardless of which random curve is drawn, which is particularly important in Run 2a, which has very large uncertainty, allowing for significantly lower 50 % points.

---

[2] If $\mu \pm 3\sigma \in [0, 1]$, or equivalently $N > 9 \cdot \max(p, (1-p))/\min(p, (1-p))$ [365].
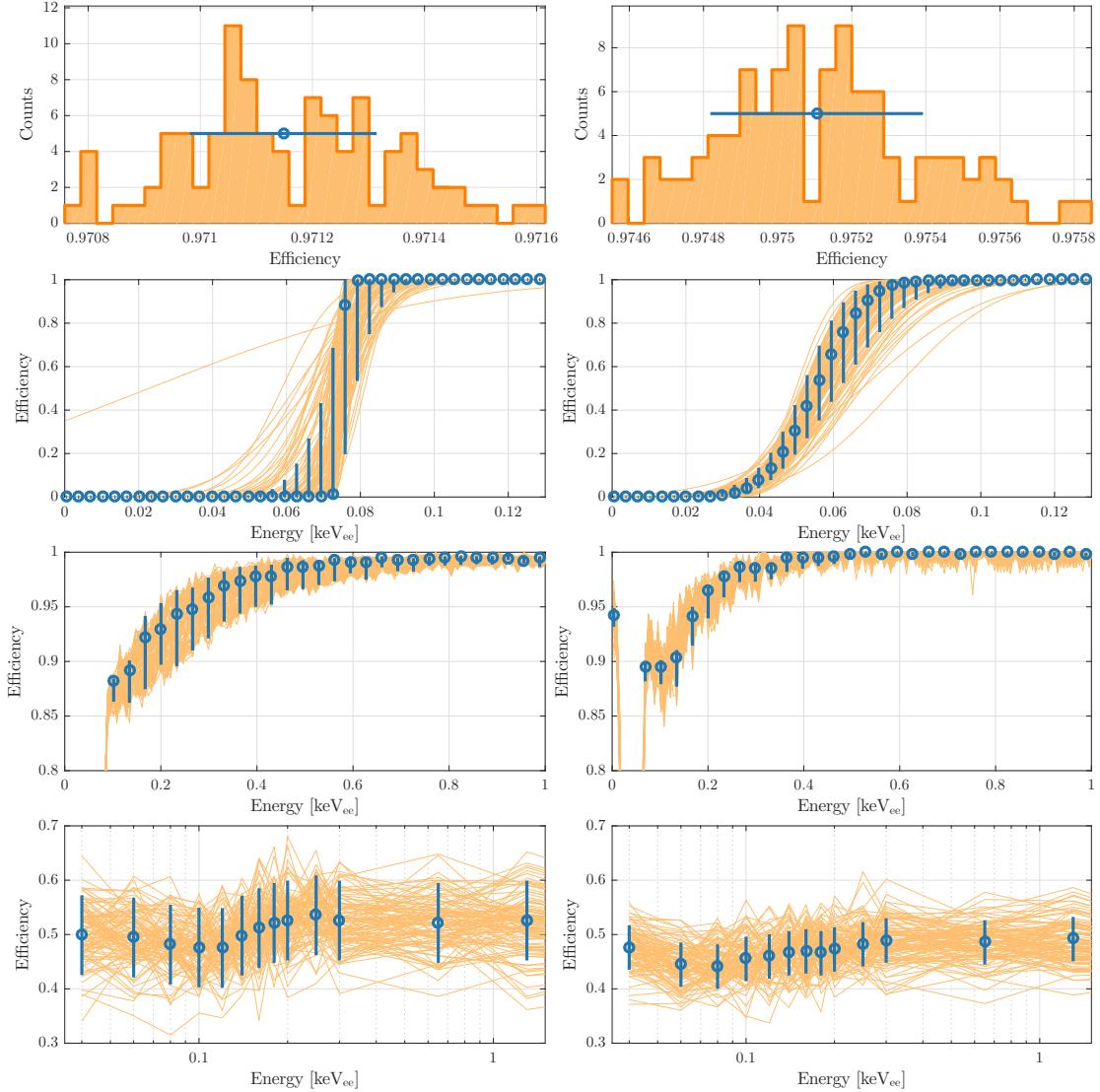
Figure 12.8: 100 randomly draw efficiency samples from posterior probability distributions (orange) for Run 2a (left) and Run 2b (right) for the energy-independent efficiency (first row), trigger efficiency (second row), phonon χ^2-based efficiency (third row), and fiducial-volume efficiency (fourth row). Also shown is the best-fit efficiency with 68 % uncertainties from independent estimates (blue). The best-fit bins for the trigger efficiency and phonon χ^2-based efficiency are down sampled by a factor of 5 for clarity. The best fit of the energy-independent efficiency has arbitrary vertical placement.
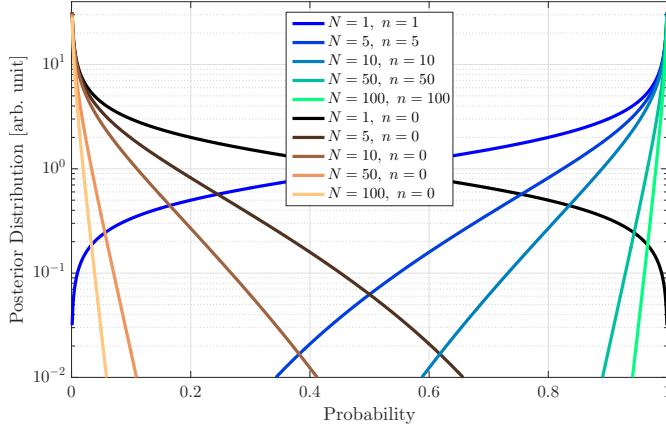
Figure 12.9: Posterior probability distribution used for the phonon χ^2-based efficiency uncertainty propagation when the best-fit efficiency is unity (blue–green curves) or zero (black–tan curves) for different numbers of total events. The distributions use the binomial distribution with Jeffreys prior and are peaked at either one or zero with decreasing variance with event count.

Phonon χ^2-based Efficiency

The efficiency on the phonon χ^2-based cuts, as calculated by a pulse simulation, has both statistical and systematic uncertainties. The source of the statistical uncertainty on the ith bin is related to the total number of events in the pulse simulation in that bin N_i and the number which pass all three cuts in that bin n_i. The result is described by a binomial distribution with probability $p_i = n_i/N_i$. Bins where $p_i = 0$ or $p_i = 1$ require special attention since the variance for each of these cases is $\sigma^2 = 0$, giving uni-valued distributions which cannot be sampled. This problem is circumvented by applying a non-flat prior. The non-informative Jeffreys prior [366] for a Bernoulli trial, and thus a binomial distribution, is $\pi(p) = 1/\sqrt{p\,(1-p)}$ giving a distribution

$$P_i(p; n_i, N_i) = \pi(p) f_B(pN_i; N_i, p_i) \tag{12.16}$$

Some examples of this posterior distribution are given in Fig. 12.9 for the $p_i = 1$ or 0. The distributions are peaked at the expected $p = 1$ or 0 with a tail to lower/higher probabilities. The variance of the distribution decreases as N increases, maintaining the naively expected binomial behavior.

The systematic uncertainty in the efficiency is due to the different pulse-shape templates (standard, peaky, nonpeaky) used in the simulation. This uncertainty is sampled by uniformly drawing between the minimum and maximum efficiencies (of the three

templates) in each given bin. A single random draw is made and used across all bins, i.e. for a random draw of 20 %, all bins will take the value which is 20 % between their minimum and maximum efficiencies, even though the size of the gap varies by bin. The statistical and systematic uncertainties are sampled separately and then linearly combined for the final total efficiency as can be seen in the third row of Fig. 12.8.

Fiducial Volume Efficiency

Recall that the radial fiducial volume efficiency is a product of the energy efficiency $\mathcal{E}_E$ and the peak efficiency $\mathcal{E}_P$, each of which have uncertainty. The energy efficiency is computed by several MLE fits, the uncertainty of which are combined for a total posterior distribution on $\mathcal{E}_E$. The resulting distribution is very Gaussian with $\{\mu, \sigma\} = \{0.864, 0.009\}$ and sampled as such. A single draw from the energy efficiency distribution is used for all energy bins since that portion of the efficiency is energy-independent.

The peak efficiency is computed using a pulse simulation and has three sources of uncertainty. The measured events in the L-shell peak are used to construct the pulse templates, and the first uncertainty component is the statistical uncertainty due to the limited number of such events. The number of L-shell events input to the simulation is large enough ($\mathcal{O}(100)$) that the underlying Poisson distribution is approximated and sampled as Gaussian with $\mu = N$ and $\sigma = \sqrt{N}$ for N total events. Since the same L-shell events are used in the simulation at each energy bin, this uncertainty is correlated between the bins with a single percentile sample and applied to all bins.

The second component to the peak efficiency uncertainty is the statistical error associated with the output of the pulse simulation, such as the number of simulated events passing/failing the radial cut. Since a separate simulation is performed for each energy bin, and different events pass/fail the cut in each, this uncertainty is uncorrelated between bins.[3] The post-simulation numbers are described by a binomial distribution and the individual terms have small enough statistics that Gaussian approximation would be questionable. However, when the three components to $\mathcal{E}$ are combined, a Gaussian approximation and sampling is more reasonable and any difference is small.

---

[3] This is not true in the strictest sense, since events close the cut boundary in the initial L-shell sample have a higher probably of crossing the boundary in every simulation, but this small effect is ignored here.

The third component to the peak efficiency uncertainty is a systematic uncertainty in estimating the assumed non-peak background value under the L-shell peak. The background is an interpolated value which can be estimated by multiple approaches, none of which is obviously better than the others. The efficiency is computed using each method and the difference between the maximum and minimum final uncertainty taken as a systematic uncertainty. For Run 2a, this is $\pm 2\,\%$ and for Run 2b, this is $\pm 0.2\,\%$. The difference in size of the systematic is due to the fact that the background-to-L-shell ratio is significantly smaller in Run 2b and therefore the effect of that background value is reduced. This uncertainty is sampled with a flat prior, added to the statistical uncertainty, and is correlated between all energy bins.

A selection of curves which sample all four uncertainties in the fiducial volume efficiency calculation are shown in the fourth row of Fig. 12.8.

keV$_{\mathrm{ee}}$ to keV$_{\mathrm{nr}}$ Conversion

The final uncertainty is the systematic uncertainty associated with the Lindhard model when converting from keV$_{\mathrm{ee}}$ to keV$_{\mathrm{nr}}$. This uncertainty is taken on the Lindhard model k-value with a flat distribution between $k = 0.1$–0.2 (best fit is $k = 0.157$). All energy variables used in computing the limit are converted: the measured event energies, the upper and lower thresholds, and the efficiency scale. For each iteration, a single k-value is sampled and applied to all conversions.

100 sample conversions of the spectrum and lower energy thresholds are given in Fig. 12.10. Although the k-value is sampled uniformly, a single keV$_{\mathrm{ee}}$ value is not converted to a uniform distribution in keV$_{\mathrm{nr}}$ due to the nature of the Lindhard model. The best-fit energy is not guaranteed to correspond to either the mean, median, or mode of the sampled distribution. This indicates that a uniform sampling is conservative compared to the true underlying distribution of k-values.

A demonstration of the full sampling (efficiencies plus Lindhard) of efficiency curves is shown in Fig. 12.11. Sampling the efficiency functions gives vertical variations while sampling the Lindhard k-value gives horizontal variations.
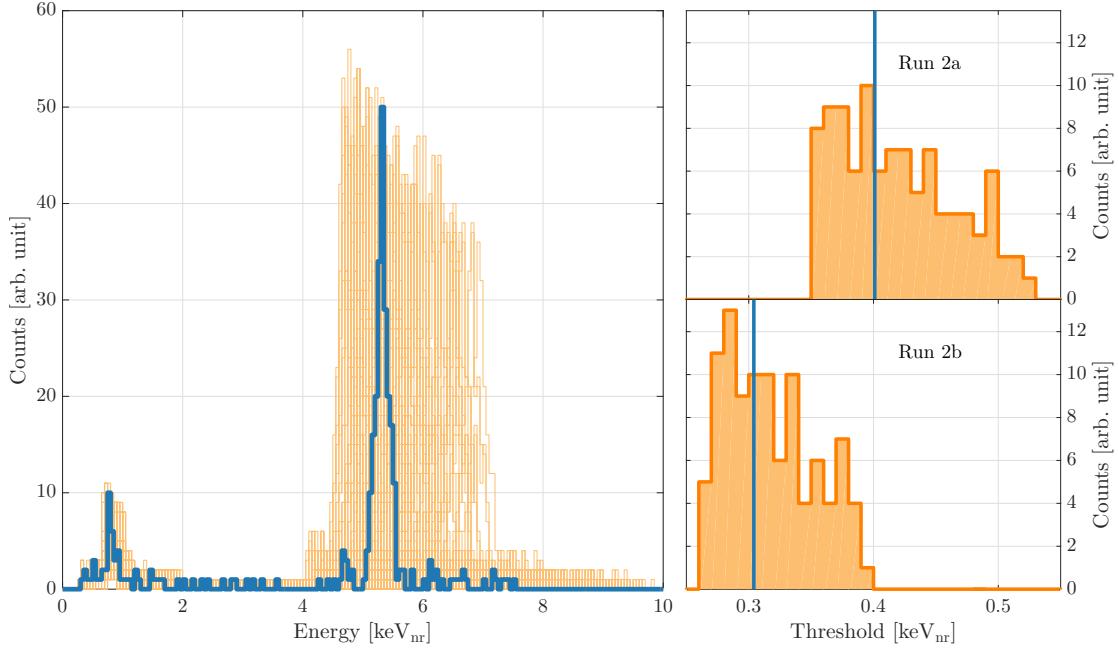
Figure 12.10: The final Run 2 spectrum (left) and lower energy thresholds (right) converted to nuclear-recoil equivalent energy using the Lindhard model and the best-fit model k-value (blue) and 100 randomly drawn k-values (orange). The thresholds are 74.7 keV$_{ee}$ (Run 2a) and 55.1 keV$_{ee}$ (Run 2b) and although the k-values are sampled uniformly, the nature of the conversion gives a non-uniform final distribution.
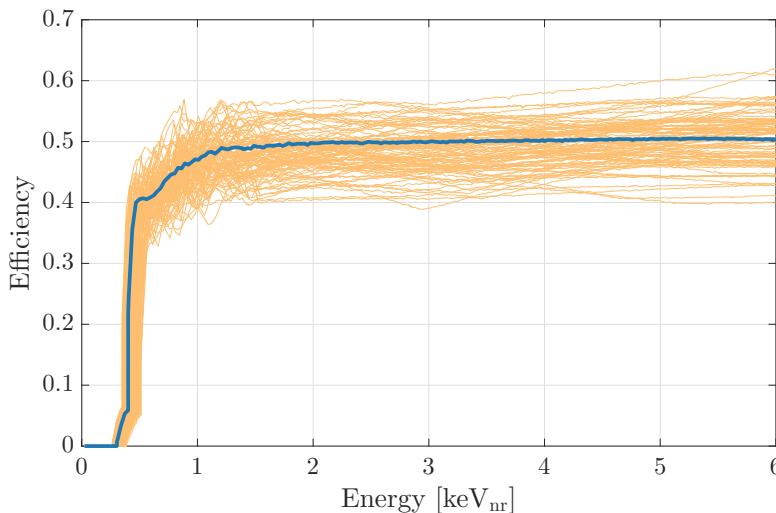
Figure 12.11: Final, live time weighted, Run 2 efficiency (blue) and 100 fully sampled curves (orange) in keV$_{nr}$. Sampling the efficiency functions gives vertical variations while sampling the Lindhard k-value gives horizontal variations.

12.4   Spin-Independent Limit from CDMSlite Run 2

12.4.1   The Optimum Interval Method

In order to compute a WIMP-search limit, the measured spectrum $\mathrm{d}\mathcal{N}/\mathrm{d}E_{\mathrm{r,nr}}$ is statistically compared to the expected spectrum $\mathrm{d}N/\mathrm{d}E_{\mathrm{r,nr}}$. Various statistical methods exist to do this. One family of methods is based on the likelihood of the signal and various backgrounds. Confidence intervals in m_χ and σ_0 are constructed using either the Feldman and Cousins [308] or Bayesian [233] approaches. The likelihood based methods, however, require that all backgrounds be known and their PDFs well understood. If there is an unknown background, the likelihood associated with that background is similarly unknown and these methods cannot be used to compute a final result. For this analysis, there are several known backgrounds (activation lines, Compton scattering of higher energy γ rays, surface decay of ^{222}Rn daughters, tritium) but the specific shape of those spectra at low energies are not well understood, making a likelihood based result untenable.[4]

If there are unknown backgrounds, or the spectral shape of the known backgrounds is not understood, then the most conservative approach is to assume that all measured events could be due to signal. Only an upper limit on σ_0 can be computed with this approach as opposed to a full confidence interval. The simplest method to set an upper limit is using Poisson statistics. In this framework, for a given m_χ, a σ_0 giving an expected mean number of events in the energy range μ is ruled out at the C confidence level if $C\,\%$ of random experiments would expect more than the $\mathcal{N}$ observed events.[5] This method does not account for the distribution of the events, which contains information, and is open to bias from the choice of the energy internal over which the events are counted.

The optimum interval method of Yellin [367] is an approach for finding an upper limit

---

[4] The choice to set an upper limit instead of a full confidence interval was made at the start of the analysis to avoid bias.

[5] The expected number of events for these random experiments are drawn from a Poisson distribution of mean μ. The upper limit on μ, which then translates to σ_{SI}, is then

$$\mu_C = \left\{ \mu \colon \int_0^\mu \frac{t^{\mathcal{N}}}{\mathcal{N}!} e^{-t} \mathrm{d}t = C \right\} \tag{12.17}$$

with an unknown background which avoids the weaknesses of the Poisson method. The optimum interval method requires the energies of the individual measured events, thus accounting for their distribution, and the expected signal rate $dN/dE_{\mathrm{r,nr}}$. The general method proceeds as follows. For a measured spectrum of $\mathcal{N}$ events with energies E_i in some analysis range E_{lo} to E_{hi}, construct all intervals bounded by some $E_a, E_b \in \{E_i, E_{\mathrm{lo}}, E_{\mathrm{hi}}\}$ which contain n events, where $0 \leq n \leq N$. For an observed $\mathcal{N}$ events, there are $(\mathcal{N}+1)(\mathcal{N}+2)/2$ such intervals. For each of these intervals, compute the expected WIMP signal $\langle n \rangle = \int_{E_a}^{E_b} dN/dE_{\mathrm{r,nr}}$, compare this to the observed events in the intervals, and compute a probability $C_n(\langle n \rangle)$ that the expected signal would produce more events in that interval than are observed. The assumed σ_0 is excluded at $C_{\mathrm{max}}\,\%$ confidence, where C_{max} is the maximum probability over all of the intervals. Setting a 90 % upper limit is typical in the dark matter field, so for each m_χ, σ_0 is adjusted until $C_{\mathrm{max}} = 0.90$.

In less quantitative terms, the optimum interval seeks the least probable gap in the measured event spectrum and uses it to set a limit on the expected WIMP parameters. The least probable interval will have low event counts compared to the expected signal, and thus the method naturally avoids regions of high background. In order to account for the large statistics in the Run 2 final spectrum, which has 50086 intervals, the high-statistics extension of the optimum internal is used [368].

12.4.2   Result

The final CDMSlite Run 2 spin-independent WIMP-search limit is derived by computing 1000 optimum-interval 90 % upper-bound limits, where each limit is computed using randomly sampled realizations of the efficiency curve and Lindhard k-value for conversion to keV$_{\mathrm{nr}}$. This gives a distribution of cross-section limits for each WIMP mass, and the official result is taken as the median cross section in each mass bin with the 68 % and 95 % confidence regions defined by the one and two σ Gaussian-equivalent percentiles for each mass: 15.9–84.1 % and 2.5–97.5 % respectively. The upper limit cross section distribution for three selected WIMP masses are shown in Fig. 12.12 with the median and uncertainty regions highlighted. The limits are computed for WIMP masses between 1–20 GeV/c^2 and the median and uncertainty bands over these masses can be seen in Fig. 12.13. These results are published in [369].
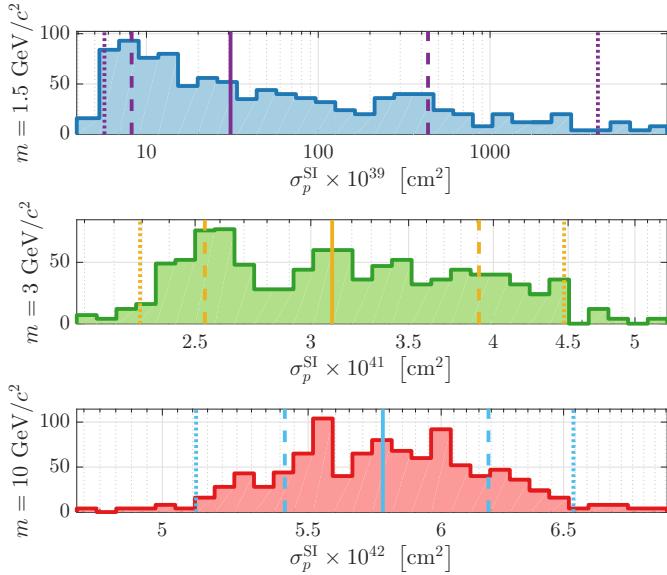
Figure 12.12: Distribution of 1000 limits using randomly sampled efficiencies and conversions to keV_{nr} for WIMP masses of 1.5 (top), 3 (middle), and 10 (bottom) GeV/c^2. The median (solid lines), 68 % confidence interval (dash lines), and 95 % confidence interval (dot lines) are also indicated for each WIMP mass slice.

The smallest WIMP mass accessible for a sampled limit is directly related to the lower energy threshold of the spectrum; this is the Run 2b threshold converted to keV_{nr}. Each of the 1000 limits has a different threshold and reaches a different lowest WIMP mass. If a WIMP mass is below the kinematically accessible region for a given limit, the sensitivity is infinite and treated as such in the computation of percentiles. The number of limits with non-infinite sensitivity at the lowest WIMP masses is shown in the inset of Fig. 12.13. The median, i.e. official, limit becomes infinite when 50 % of the limits are infinite, which occurs below $\sim$1.3 GeV/c^2. The lowest mass for which any of the limits had sensitivity, and defines the lower edge of the confidence intervals, is at $\sim$1.2 GeV/c^2. All 1000 limits have non-infinite sensitivity for masses $\gtrsim$1.5 GeV/c^2.

This result is compared to other relevant results in the low-mass region in Fig. 12.14. The uncertainty band presented here, and in later figures, is the 95 % confidence interval. New parameter space is excluded by Run 2 between WIMP masses of 1.6 and 5.5 GeV/c^2, where CRESST [258] gives stronger constraints for masses below this and the SuperCDMS Low-Threshold [245] and LUX [216] results give stronger constraints for masses above this. The threshold of the CRESST result [258] is comparable at $\sim$300 eV_{nr}, however the presence of lighter mass nuclei in the target ($M_{Ca} = 40$ a.u., $M_O = 16$ a.u.) allows for lower WIMP masses to be reached. The improvements over
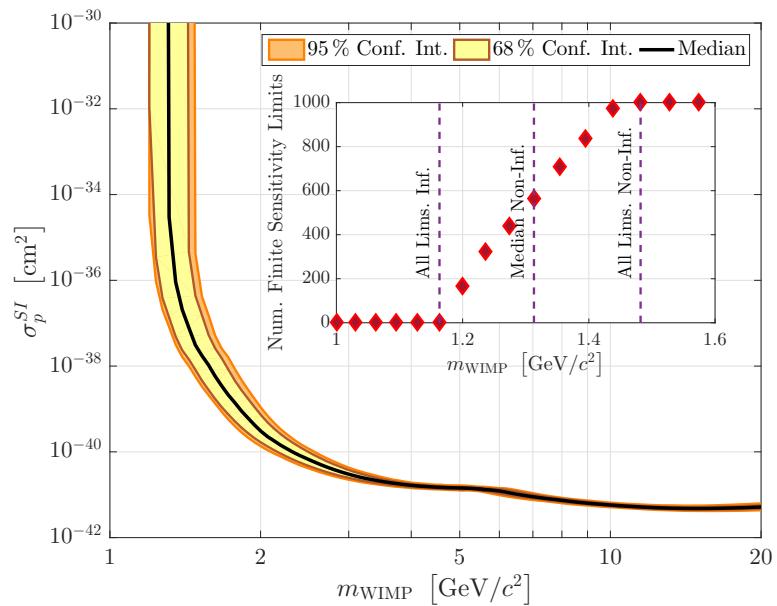
Figure 12.13: Official Run 2 spin-independent limit (median, black curve) with the 68 % (orange shaded) and 95 % (yellow shaded) confidence intervals derived from the 1000 sampled limits. The kink in the limit at 5–6 GeV/c^2 is an effect f the M-shell peak at 160 eV$_{ee}$. Inset: Number of sampled limits, out of 1000 total, which have finite sensitivity for the lowest WIMP masses. The lowest WIMP mass with any non-infinite limits, i.e. the lowest possible sensitivity, is at $\sim$1.2 GeV/c^2. The median of the limits, i.e. the official limit, becomes non-infinite when 50 % of limits are non-infinite, which occurs above $\sim$1.3 GeV/c^2. All 1000 limits have non-infinite sensitivity above $\sim$1.5 GeV/c^2.
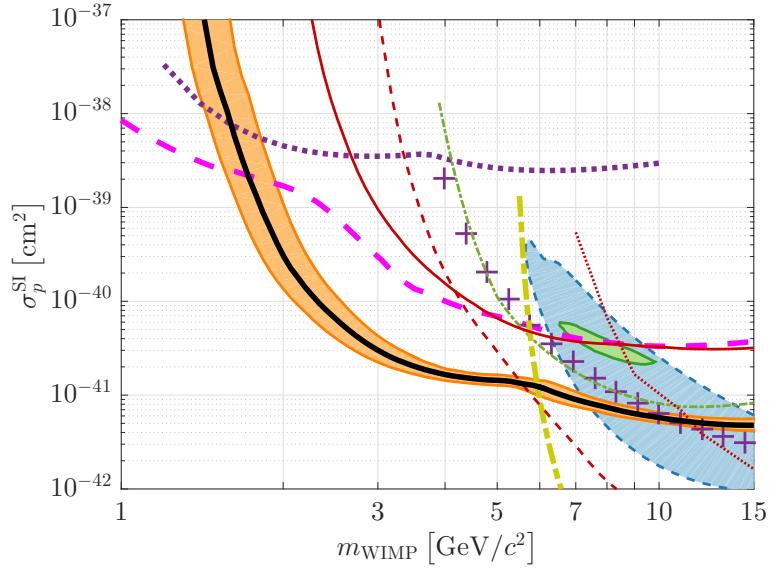
Figure 12.14: CDMSlite Run 2 median (90 % C.L.) and 95 % confidence interval (thick black solid curve surrounded by orange band) compared to other recent and relevant results. Other 90 % upper liits shown are from the first CDMSlite run (thin red solid curve) [260], SuperCDMS (thin red dash curve) [245], EDELWEISS-II (thin red dot curve) [247], CDEX-1 (thin green dot-dash curve) [255], PICO-2L (purple crosses) [228], LUX (thick yellow dot-dash curve) [216], CRESST (thick magenta dash curve) [258], and DAMIC (thick purple dot curve) [257]. Closed regions shown are the CDMS II 90 % C.L. (blue dash shaded region) [233], and CoGeNT 90 % C.L. (green solid shaded region) [234].

the first CDMSlite run are the lower thresholds (55 eV$_{ee}$ vs. 170 eV$_{ee}$) which gives access to lower WIMP masses and lower backgrounds (mainly the fiducial volume cut) which gives access to lower interaction cross-sections. At WIMP masses of 3 GeV/c^2 and 5 GeV/c^2 this result is 33.3× and 4.3× lower in cross section than the Run 1 result, respectively.

12.5   Cross-Checks on the Limit

This section examines several cross-checks of the official limit and uncertainty. These checks explain features of the official curve or validate decisions made in the analysis. In summary, the official limit is consistent to within uncertainties with all cross-checks

12.5.1   Official Limit vs. Expected Sensitivity

The ^{71}Ge activation lines are an essential tool in this analysis, however the location of the M-shell peak is potentially problematic. The lower energy threshold of Run 1 was 170 eV$_{ee}$, which is above the 160 eV$_{ee}$ location of the M-shell. This expected feature raises the background level in the exact energy range which is most interesting to the Run 2 result. To assess the effect of the M shell, a sensitivity study is done which simulates a spectrum consisting of a flat background and M-shell events with varying live time. Limits are computed with the simulated spectra to study how the sensitivity changes with variable M-shell strengths.

For the radial cut efficiency, the three post-Cf periods (post-February, post-May, all of Run 2b) were aligned based upon the relative strength of the ^{71}Ge K shell peak. The aligned-time scale can be used to predict the number of M-shell events as a function of live time. Given that all of Run 2b is close to a ^{252}Cf calibration, the initial simulation focuses on Run 2a. The M-shell estimation proceeds as

1. Inversely order each data series by aligned time, i.e. start with those furthest from a ^{252}Cf calibration.

2. Compute the live time and number of K-shell events in each series.

3. Derive a cumulative K-shell curve as a function of aligned time.

4. Scale this curve by the theoretical ratio of the M/K peaks to estimate the M-shell event rate.

5. For each simulation, find the desired number of M-shell events along the cumulative curve and simulate the live time at the same series position.

The different stages of this computation are given Fig. 12.15. This procedure can be understood visually as starting at the right-hand side of Fig. 11.42 and moving towards the left, progressively gaining K-shell and M-shell statistics, starting with the series with lowest activation strength.

The simulation assumes a simplified version ofRun 2a with the following parameters: energy thresholds of $[0.1, 1.1]$ keV$_{ee}$, chosen to encompass the M-shell without the L-shell and to cut-off before the efficiency drastically decreases, a flat efficiency
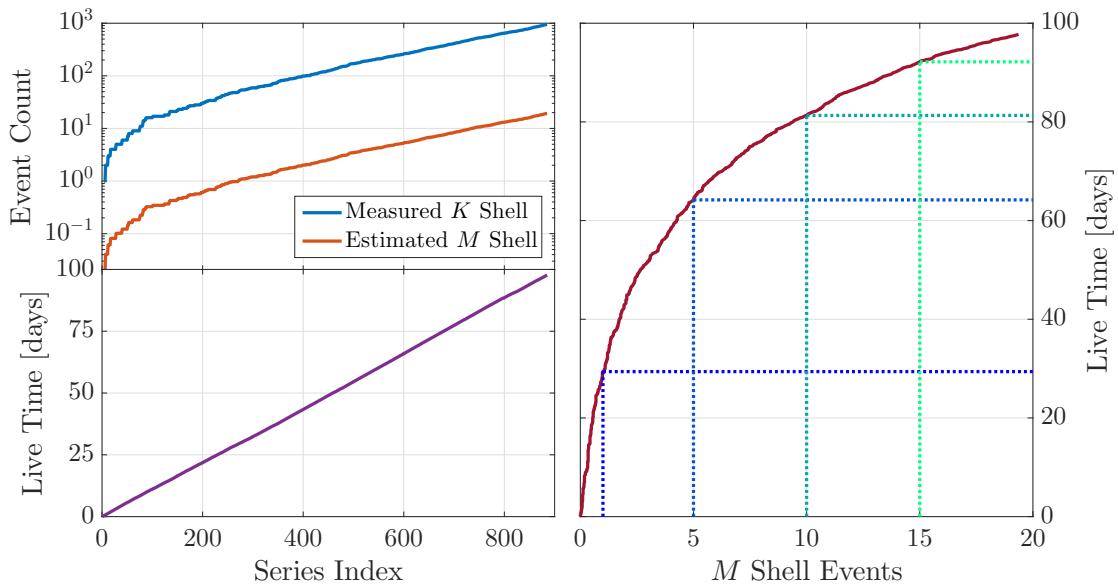
Figure 12.15: Left: cumulative measured K-shell events and estimated M-shell events (top) and cumulative live time (bottom) as a function of Run 2a series index, where index 1 is the series furthest from a ^{252}Cf calibration according to aligned time. The estimated M-shell curve is found by multiplying the measured K-shell curve by the theoretical ratio of 0.02. Right: live time as a function of estimated M-shell events. For a given number of M-shell events (1, 5, 10, 15 shown with dotted lines), the corresponding live time is simulated.
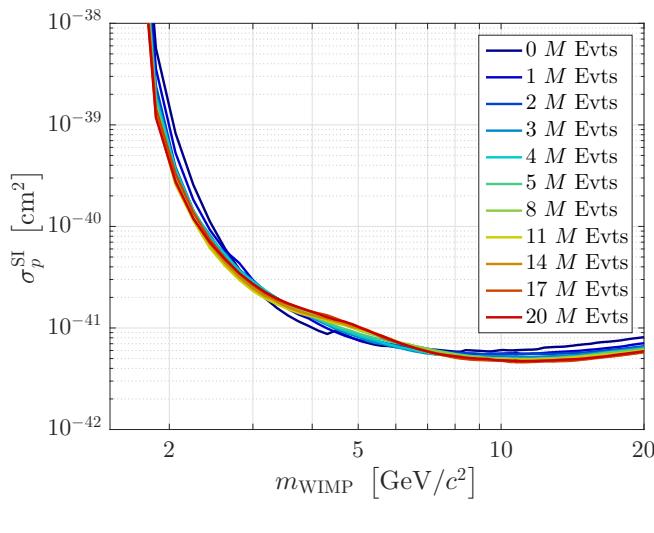
Figure 12.16: WIMP sensitivity as a function of the expected number of M-shell peak events, and therefore live time of Run 2, as estimated from Fig. 12.15. For each number of M-shell events, 100 simulations are performed with an energy range of $[0.1, 1.1]$ keV$_{ee}$ with a background rate and efficiency representative of Run 2a. The median of the 100 simulations is given for each M-shell value. The effect of the M-shell is observed as a kink in the limit curve peaking ~ 5 GeV/c^2.

of 50 %, and a non-efficiency-corrected and non-peak flat background rate of 0.43 ± 0.09 $[\text{keV}_{ee} \, \text{kg} \, \text{day}]^{-1}$, derived from the average Run 2a rate between $[0.2, 1.1]$ keV$_{ee}$. The spectrum is converted to keV$_{nr}$ using the standard Lindhard $k = 0.157$ value. For each iteration, a number of M-shell events are chosen from a Gaussian distribution representative of the peak. The live time corresponding to that M-shell statistic is then used to create a flat background spectrum and an optimum interval 90 % upper limit on the SI WIMP-nucleon cross section computed. For each M-shell value, 100 simulations are performed with the median of this set shown in Fig. 12.16. For the zero M-shell case, the live time corresponding to 0.5 events in Fig. 12.15 is used.

The effect of the M-shell peak on the sensitivity is a kink in the curve, peaking at ~ 5 GeV/c^2, which becomes more pronounced with exposure. These sensitivity curves also indicate, unsurprisingly, that CDMSlite Run 2 is still background limited after the radial cut: the sensitivity initially increases on either side of the kink but saturates above ~ 10 M-shell events.

To compare the sensitivity to the final limit, the simulation parameters are expanded to the full exposure. The expected number of M-shell events is found by counting K-shell events in the full exposure and scaling by the theoretical ratio, giving 36 M-shell events. The average background rate is computed using the full spectrum, giving
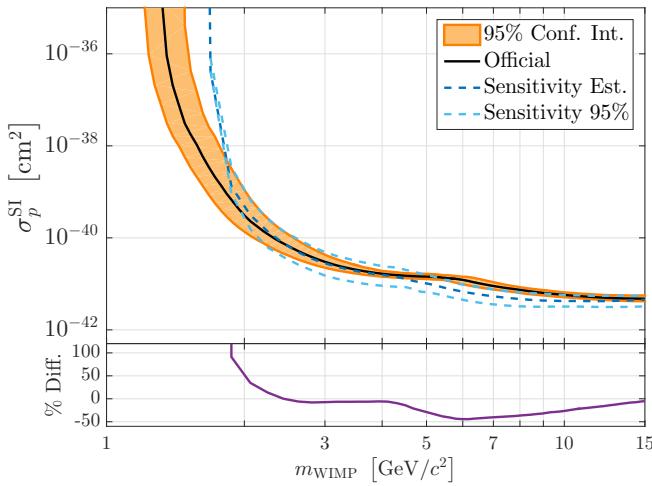
Figure 12.17:   Comparison of the estimated sensitivity median (dark blue dash) and 95 % uncertainty (light blue dash) with the official limit (black solid) and 95 % uncertainty (orange shaded) along with the percent difference between the two medians (bottom panel).   The sensitivity gives an up to 50 % stronger limit above $\sim$4 GeV/c^2 due to a higher background below the M-shell peak in the data compared to the sensitivity simulation.

0.43 ± 0.08 [keV$_{ee}$ kg day]$^{-1}$ which is consistent with the Run 2a-only number. The total exposure is 70.10 kg day. The thresholds of the study are kept the same, i.e. computing the limit using events between $[0.1, 1.1]$ keV$_{ee}$ using the standard Lindhard conversion. 100 simulations are performed and the median and 95 % intervals are reported in Fig. 12.17 compared to the official limit.

The sensitivity and official limit are only comparable above $\sim$2 GeV/c^2 due to the fact that threshold for the sensitivity study is much higher than the official result. The most striking difference between the two is the location of the M-shell-sourced kink, which is at $\sim$4.5 GeV/c^2 in the sensitivity curve and $\sim$6 GeV/c^2 in the official result. This difference is understood by recalling that the average background rate below (and potentially under) the M-shell peak is higher than between the M-shell and L-shell peaks, which is where the simulated-background estimate is derived from. This higher background at lower energies in the data can weaken the resulting limit, by up to 50 %, as indicated by the percent difference curve, and push the kink to a higher WIMP mass. Additionally, the 95 % uncertainty bands for the two minimally overlap over that mass range, making them still marginally consistent results.
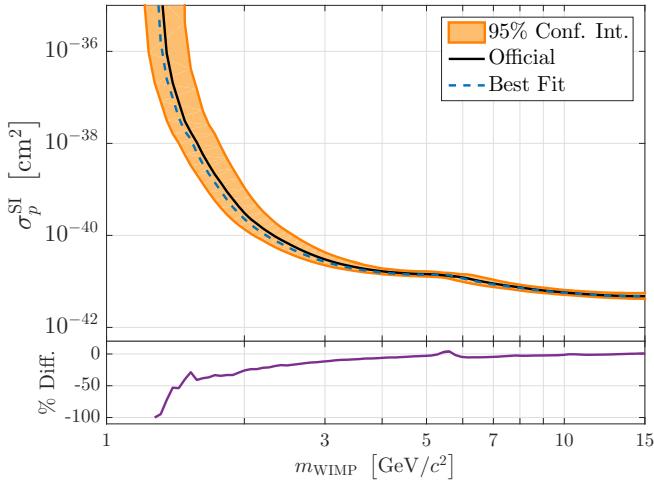
Figure 12.18: Comparison of the best-fit limit (blue dash) with the official limit (black solid) and 95 % uncertainty (orange shaded) along with the percent difference between the two (bottom panel). The best-fit limit increasingly becomes lower than the official limit for masses below $\sim$4 GeV however it remains well contained by the uncertainty of the official limit.

12.5.2   Official Limit vs. Best-Fit Limit

An alternative to the uncertainty-sampling approach is to set a limit using the best-fit efficiency and conversion to keV$_{\rm nr}$. This is how the Run 1 limit was computed and, as such, is a better direct comparison between Run 2 and Run 1. The best-fit[6] efficiency is the final black curve in Fig. 12.2 while the spectrum, threshold, and efficiency using the best-fit conversion to keV$_{\rm nr}$ are shown as the blue curves in Figs. 12.10 and 12.11.

This single limit is shown in Fig. 12.18 along with the percent difference between it and the official limit. The best-fit curve is comparable with the official curve for higher masses but becomes increasing lower below $\sim$4 GeV/c^2. This is understood by recalling the asymmetric shape of the limit distributions at low masses and that the best-fit Lindhard conversion giving limits closer to the peak of the distribution than the median. The limit distributions become more asymmetric with lowering mass which explains why the percent difference increases at lower masses. These differences, however, are well contained in the 95 % uncertainty of the official limit.

12.5.3   Official Limit vs. Loose Radial Cut Limit

The radial cut threshold is set at -4 for Run 2a and -5 for Run 2b. The motivations for the different threshold values are a shift in the radial parameter distribution between

---

[6] The name "best-fit" is a slight misnomer as no fitting is occurring. It is simply the central value of the efficiency curve.
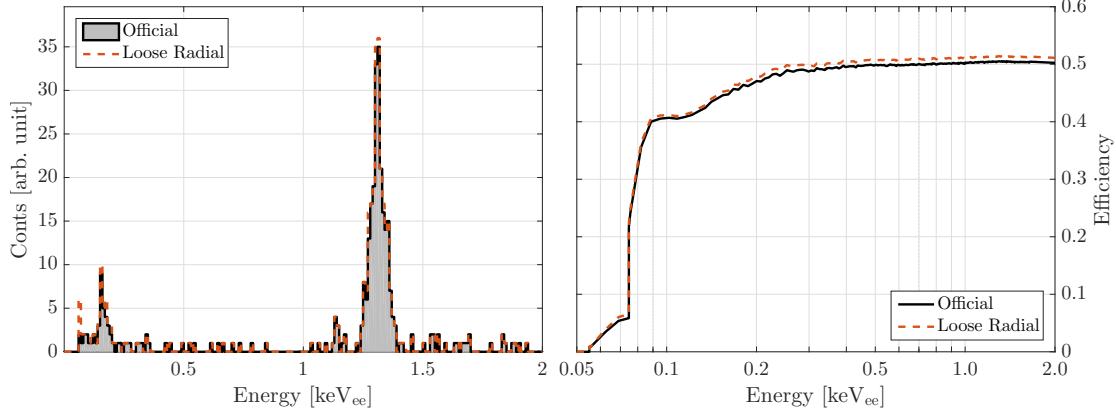
Figure 12.19: Comparison of the official (black solid) and loose-radial-threshold (blue dot) final event spectrum (left) and efficiency (right). The looser radial cut leads to slightly more efficiency and additional events, particularly near threshold.

the runs and the additional background at low energies in Run 2b. The validity of setting different thresholds between the periods is confirmed by calculating what the final limit would be if an identical threshold of -4 were used for the entire run. This looser threshold changes the final spectrum, passing more events, and the final efficiency, raising the Run 2b contribution to the efficiency. The new spectrum and efficiency curve are compared to the official ones in Fig. 12.19. Most importantly, an additional "peak" of events is now present just above threshold. This "peak" is likely leakage from the low-energy background in Run 2b.

The loose radial cut limit is computed in an identical manner as the official limit by sampling, 1000 times, the efficiency and conversion to keV_{nr} uncertainties and computing a limit. The radial-cut efficiency uncertainty is changed to those values appropriate for the new threshold. The median and 95 % confidence intervals of the official and loose radial limits are shown in Fig. 12.20. The largest difference, giving up to 40 % difference between the medians, is the presence of a second kink in the limit at $\sim$1.6 GeV/c^2. This kink is a result of the new "peak" above threshold. The difference between the loose radial cut median and the official limit, however, are well contained in the official uncertainty.
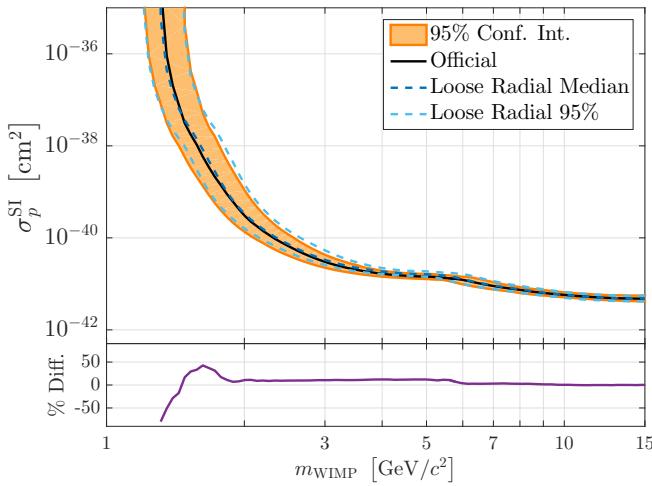
Figure 12.20: Comparison of the official limit (solid black) and 95 % uncertainty (orange shaded) with the median (dark-blue dash) and 95 % uncertainty (light-blue dash) limit using a looser radial cut. A second kink is seen in the loose radial limit at $\sim$1.6 GeV/c^2 which is a result of additional events creating a peak-like structure in the spectrum near the threshold. This difference is well contained in the official uncertainty, however.

12.5.4   Official Limit vs. July-Trigger-Efficiency-Corrected Limit

For 10.87 raw days (4.22 days after applying live time cuts) in July, at the end of Run 2a, the hardware trigger threshold was increased. This change in threshold went unnoticed until after the completion of the final Run 2 result. For all other portions of the analysis, it is assumed that these 4.22 days had the same 75 eV$_{ee}$ threshold as the rest of Run 2a. The effect of this error must be considered to verify that the official limit is not incorrect in a major way.

The 50 % efficiency point for this July period is computed in Sec. 11.7.5 to be $79.8^{+14.7}_{-23.9}$ eV$_{ee}$. This is slightly higher than the main Run 2a 50 % point of $74.7^{+4.0}_{-4.3}$ eV$_{ee}$ and the uncertainty is large enough to fully encompass the Run 2a trigger efficiency curve. There are 5 events passing all cuts and in the limit setting energy range in this July period, however none of them are between 74.7 and 79.8 eV$_{ee}$ having energies of $[1.31, 1.31, 1.45, 1.57, 1.87]$ keV$_{ee}$.

Two approaches are taken to understand the effect of the July trigger-period. The first includes the July exposure and trigger efficiency curve (assuming the efficiency for all other cuts is the same as in Run 2a during this period) while the second completely excludes the July exposure and events. These are termed "with July" and "without July" respectively. In the first approach, no additional events are removed, while in the second the 5 July events are removed. Both approaches have new, live-time-weighted,
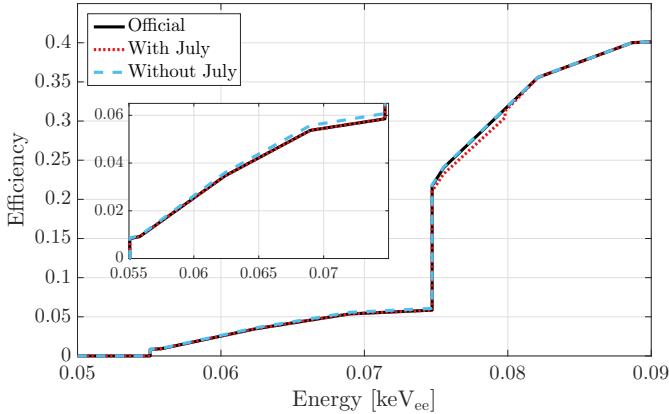
Figure 12.21: Comparison of the final live-time weighted efficiencies in the official (purple solid), with-July (orange dot), and without-July (green dash) schemes. The with-July scheme has a sharp drop at the July trigger 50 % efficiency point of 79 eV$_{\text{ee}}$. Inset: enlargement of the range below the Run 2a cutoffs showing the increase in efficiency in the without-July scheme due to a larger weighting of Run 2b.

efficiency curves $\epsilon_{\text{w/J}}$ (with July) and $\epsilon_{\text{w/oJ}}$ (without July) given by

$$\epsilon_{\text{w/J}} = \frac{\epsilon_a \mathcal{T}_a + \epsilon_b \mathcal{T}_b + \epsilon_J \mathcal{T}_J}{\mathcal{T}_a + \mathcal{T}_b + \mathcal{T}_J} \tag{12.18}$$

$$\epsilon_{\text{w/oJ}} = \frac{\epsilon_a \mathcal{T}_a + \epsilon_b \mathcal{T}_b}{\mathcal{T}_a + \mathcal{T}_b}, \tag{12.19}$$

where $\epsilon_{a/b/J}$ and $\mathcal{T}_{a/b/J}$ are the efficiencies and live times of Run 2a without the July period (93.59 days), Run 2b (17.78 days), and the July period (4.22 days) respectively. In this notation, the efficiency of the official result ϵ_{Off} is

$$\epsilon_{\text{Off}} = \frac{\epsilon_a \left(\mathcal{T}_a + \mathcal{T}_J \right) + \epsilon_b \mathcal{T}_b}{\mathcal{T}_a + \mathcal{T}_b + \mathcal{T}_J}. \tag{12.20}$$

These three efficiencies are compared in Fig. 12.21 and the differences between them are very small. For the with-July scheme, the main difference is a slight drop in efficiency at the July 50 % trigger point. For the without-July scheme, the main difference is the efficiency below the Run 2a 50 % cutoff is slightly higher due to the weight of Run 2a being reduced compared to Run 2b.

The changes in efficiency and spectra are small, and within the official uncertainties, such that the effect on the final limit should also be small. The limits are computed using the best-fit efficiencies and Lindhard k-value and compared to the best-fit with the
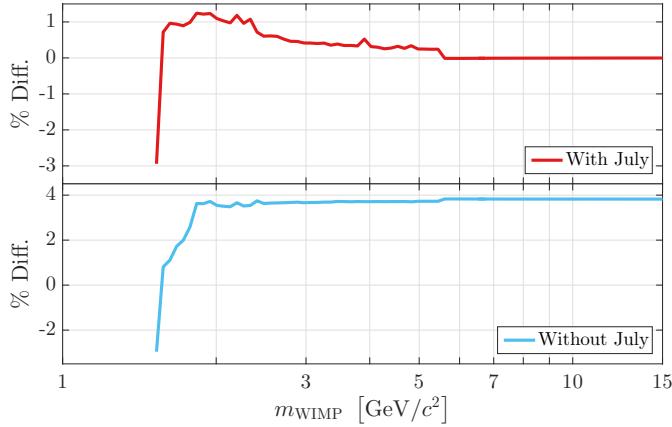
Figure 12.22: Percent difference between the best-fit limit and the with-July (top) and without-July (bottom) limits. The with-July limit is up to $\sim 1\,\%$ weaker below masses of ~ 5 GeV/c^2. The without-July limit is $\sim 4\,\%$ weaker for all masses.

official efficiency (Sec. 12.5.2). The percent differences between the limits are shown in Fig. 12.22. The with-July limit is $\sim 1\,\%$ weaker between 1.5–5.5 GeV/c^2. The without-July limit is $\sim 4\,\%$ weaker over the entire mass range. This study concludes that although neglecting the July trigger-threshold change was a mistake in the analysis, the impact of that mistake is negligible and well within the uncertainties of the official result.

12.6   Uncertainty from the Standard Halo Model

The official limits are computed using the standard halo model (SHM) as the astrophysical input to Eq. 12.2. The SHM (Sec. 3.3) assumes an isothermal, isotropic, and non-rotating sphere for the dark matter distribution, a Maxwellian velocity distribution, and an agreed-upon set of measured astrophysical quantities. The astrophysical quantities are the local dark matter density ρ_0, the Galactic escape velocity v_{esc}, the Solar peculiar velocity $v_\odot$, the Galactic rotational velocity at the Sun's radius Θ_0, and the Earth's orbital velocity $\boldsymbol{v}_\oplus$. The Maxwellian velocity distribution, boosted to the Earth's frame, is

$$f(\boldsymbol{v}, \boldsymbol{v}_E) \propto \begin{cases} e^{-(\boldsymbol{v}+\boldsymbol{v}_E)^2/v_0^2} & v < v_{\mathrm{esc}} \\ 0 & v \geq v_{\mathrm{esc}} \end{cases}, \tag{12.21}$$

with the earth's velocity as $\boldsymbol{v}_E = \boldsymbol{\Theta}_0 + \boldsymbol{v}_\odot + \boldsymbol{v}_\oplus$. The characteristic velocity v_0 is identical to Θ_0 in the SHM. The values of these astrophysical measurements adopted in the SHM are given in Table 12.6. The orbital velocity is usually assumed to average out over a

Constant	Symbol	SHM Value	Source
Characteristic Velocity	v_0	220 km s^{-1}	[370]
Solar Peculiar Velocity	$v_\odot$	12.2 km s^{-1}	[371]
Earth Orbital Velocity	$v_\oplus$	29.8 km s^{-1}	[183]
Galactic Escape Velocity	v_{esc}	544 km s^{-1}	[372]
Local Dark Matter Density	ρ_0	$0.3 \text{ GeV} \, c^{-2} \text{ cm}^{-3}$	[29]

Table 12.6: Astrophysical constants and their values in the Standard Halo Model.

year and neglected in all but annual modulation searches.

As with any astrophysical measurement, there are uncertainties associated with the values in Table 12.6 and the SHM assumptions. The reviews by McCabe [208] and Green [207] provide overviews of the uncertainties on these parameters and their effects on dark-matter direct-detection experiments. They provide a basis for the following discussion on the uncertainty in the Run 2 result from the SHM.

The least certain astrophysical value is the local dark matter density ρ_0, which is usually quoted as having an uncertainty of a factor of 2 or 3 [29]. However, the ultimate source for this canonical value is unclear [373] and measuring the local density has many difficulties as detailed in [374, 375]. Several recent estimates of ρ_0 can be found in Table 12.7. There are reasonably large differences between the measurements, with one contribution to this being differences in the assumed dark matter halo. Since ρ_0 is a proportionality constant in the WIMP rate calculation, changing ρ_0 by some factor scales the limit by that factor (a larger ρ_0 gives more dark matter particles to interact with at the detector, making a non-detection give a stronger limit by the same factor). Knowing that such a shift is possible for all limits, the canonical value of $\rho_0 = 0.3 \text{ GeV} \, c^{-2} \text{ cm}^{-3}$ is still used.

The SHM measurement for the galactic escape velocity v_{esc} comes from the 2007 RAVE Survey. That measurement uses a marginalized MLE fit to the survey data, giving a median value of 544 km s^{-1} with a 90% uncertainty of $498 < v_{\text{esc}} < 608 \text{ km s}^{-1}$ [372]. In 2014, the RAVE collaboration released a more recent result [384], where a similar MLE fit was performed with a median value of 533 km s^{-1} and 90% uncertainty of $492 < v_{\text{esc}} < 587 \text{ km s}^{-1}$. The posterior distribution from which these

Author	Year	$\rho\left[\text{GeV}\,c^{-2}\,\text{cm}^{-3}\right]$	Source
Widrow *et al.*	2008	0.30 ± 0.05	[376]
Weber and de Boer	2010	0.3 ± 0.1	[377]
Catena and Ullio	2010	0.39 ± 0.03	[378]
Salucci *et al.*	2010	0.43 ± 0.15	[373]
Garbari *et al.*	2011	$0.11^{+0.34}_{-0.27}\text{--}1.25^{+0.30}_{-0.34}$	[379]
Garbari *et al.*	2012	$0.85^{+0.57}_{-0.50}\text{--}0.95^{+0.53}_{-0.49}$	[380]
Nesti and Salucci	2013	$0.49^{+0.08}_{-0.09}$	[381]
Bienaymé *et al.*	2014	0.54 ± 0.04	[382]
Lavalle and Magni	2015	$0.08\text{--}0.42$	[383]

Table 12.7: Recent estimates of the local dark matter halo density. Due to the large systematic differences between the results, including in assumed halo profiles, the canonical value of $\rho = 0.3 \text{ GeV}\,c^{-2}\,\text{cm}^{-3}$ is still used. The Garbari *et al.* sources give a range of models.

values are taken from are given in Fig. 12.23 for both the 2007 and 2014 results. Although fits to Galactic parameters, such as those done to determine v_0, also provide values of v_{esc}, the direct measurements from the RAVE Survey are considered more accurate. The 2007 RAVE value is still the standard for use in the field, however the adoption of the 2014 result would likely be more accurate.

The Solar velocity with respect to neighboring stars, the peculiar velocity $v_\odot$, used in both the dark matter and astrophysical fields have come from one of two direct
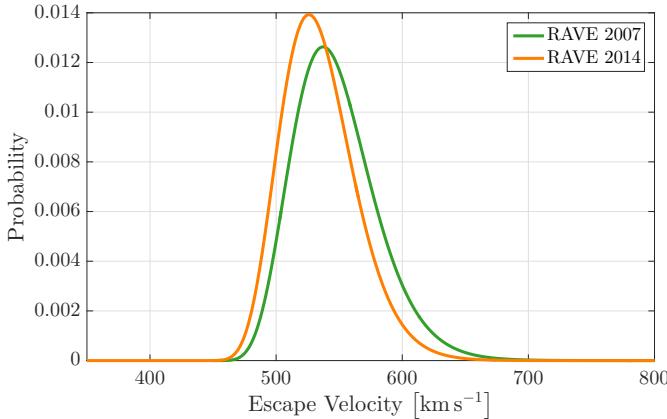
Figure 12.23: Marginalized posterior probability distributions of the Galactic escape velocity from the RAVE survey 2007 [372] (green) and 2014 [384] (orange) results. Curves courtesy of M. Smith, T. Piffl, and M. Steinmetz.

measurements. The total peculiar velocity is parameterized as $(U_\odot, V_\odot, W_\odot)$, where $U_\odot$ is the radial velocity towards the Galactic Center, $V_\odot$ is the velocity in the direction of the Galactic rotation, and $W_\odot$ is the upward vertical velocity. In 1998, Dehnen and Binney found $(10.00 \pm 0.36, 5.23 \pm 0.62, 7.17 \pm 0.38)$ km s^{-1} [385] which was used until it was superseded by Schönrich, Binney, and Dehnnen in 2010 with values of $(11.0 \pm 1.2, 12.24 \pm 2.1, 7.25 \pm 1.1)$ km s^{-1} [371]. The SHM takes $\boldsymbol{v}_\odot = (0, V_\odot, 0) = (0, 12.24, 0)$ km s^{-1}.

Assuming the Galactic rotation curve has reached its asymptotic value at the Solar radius R_0, the characteristic velocity v_0 is identical to the Galactic circular velocity at R_0 in the SHM. This Galactic velocity is labeled in the literature both as the circular velocity (Θ_0, V_c, v_c) or the local-standard-of-rest velocity (Θ_{LSR}, V_{LSR}, v_{LSR}). There are numerous estimates of this parameter using various approaches, a selection of which are given in Table 12.8. The large, and inconsistent, spread of values indicates likely systematics between measurements. One source of this uncertainty is the various Galactic modeling employ with another being that Θ_0 and $V_\odot$ are strongly correlated [386] and thus the choice of prior on $V_\odot$ (usually between the two values quoted above, or $V_\odot$ can be a free parameter in a Galactic fit) can affect the reported vale of Θ_0. The canonical value is an older recommendation and a newer value is likely more accurate. The smallest allowed value from these measurements is 196 km s^{-1} from McMillan and Binney [387]. The largest allowed value is 270 km s^{-1} from the 2009 Reid *et al.* result [388].

All of the astrophysical measurements are interrelated and values of different parameters are correlated. As already stated, $V_\odot$ and Θ_0 are correlated with Reid *et al.* finding a Pearson product-moment correlation coefficient of -0.796 [386]. Θ_0 is also correlated to v_{esc}, with the RAVE survey performing two different fits and finding $v_{\mathrm{esc}}(\Theta_0) = 533^{+54}_{-41}/511^{+48}_{-35}$ km s^{-1} for $\Theta_0 = 220/240$ km s^{-1} respectively [384]. Lastly, Θ_0 and ρ are both correlated to measurements of R_0 (Reid *et al.* finds a correlation coefficient between Θ_0 and R_0 of 0.465) and hence each other. If $\Delta\Theta_0 \approx \pm 30$ km s^{-1}, then $\Delta\rho/\rho \approx \mp 20\%$ [208]. Any approach to estimating the uncertainty in a dark matter limit by considering the different astrophysical measurements independently will inherently over-estimate the total uncertainty due to these correlations.

Building an updated complete model accounting for these correlates was initiated

Author	Year	$\Theta_0 \left[\mathrm{km\,s^{-1}}\right]$	Source
Kerr and Lynden-Bell	1986	220 ± 20	[370]
Reid *et al.*	2009	254 ± 16	[388]
Bovy *et al.*	2009	236 ± 13	[389]
McMillan and Binney	2010	225 ± 29	[387]
Koposov *et al.*	2010	221 ± 18	[390]
Bobylev and Bajkova	2010	248 ± 14	[391]
McMillan	2011	239 ± 5	[392]
Bovy *et al.*	2012	218 ± 16	[393]
Carlin *et al.*	2012	232 ± 14	[394]
Honma *et al.*	2012	238 ± 14	[395]
Reid *et al.*	2014	240 ± 8	[386]
Reid *et al.*	2014	243 ± 6	[386]
Bobylev and Bajkova	2016	230 ± 12	[396]

Table 12.8: Measurements of the Galactic circular velocity at the Sun's location Θ_0. The canonical value is the Kerr and Lynden-Bell recommendation of $220 \ \mathrm{km\,s^{-1}}$. Systematics, notably differing model assumptions made by the authors, are evident between all of the measurements. The two values from the 2014 Reid *et al.* result assume different priors.

by Lavalle and Magni [383]. They start with the 2014 RAVE result and then incorporate the 2014 Reid *et al.* result as it makes similar prior assumptions to the RAVE paper. Specifically, an alternative fit by Reid *et al.* assumes the solar peculiar velocity from [371], same as the RAVE paper, and gets $\Theta_0 = 243 \pm 6$ km s^{-1} with similar goodness-of-fit as their primary result 240 ± 6 km s^{-1} [386]. A new, more consistent, and unified halo parameterization could perhaps then be to use $V_\odot = 12.24$ km s^{-1} from [371], $v_{esc} = 533$ km s^{-1} from [384], and $\Theta_0 = 243$ km s^{-1} from [386]. Lavalle and Magni also note that such a model would indicate $\rho = 0.37$–0.57 GeV$/c^2$ cm^{-3} at the 2σ level.

For the present study, the uncertainties on v_{esc} and $v_0 = \Theta_0$ are propagated into the Run 2 limit as uncorrelated. The uncertainty on $v_\odot$ is small in comparison and is neglected while the uncertainty on ρ_0 is understood as a scaling factor (neglecting correlations). The two uncertainties are propagated in a similar fashion as the analysis uncertainties, where uncertainty distributions for each are defined and sampled 1000 times, with the final uncertainty bands being drawn from the resulting 1000 limits. For v_0, wary of unknown systematics between the many measurements in Table 12.8, a conservative flat distribution is used between $196 < v_0 < 270$ km s^{-1} to encompass all of the measurements. For v_{esc}, the posterior distribution from the 2014 paper which gives the $v_{esc} = 533$ km s^{-1} value is directly used. It would be technically more consistent with the SHM to use the 2007 RAVE distribution, but changing which median value has an almost negligible effect on the Run 2 limit. This justifies using the more precise 2014 likelihood distribution. For these halo-mode- uncertainty studies, the best-fit analysis parameters, as described in Sec. 12.5.2, are used such that the only uncertainty is from the astrophysical measurements.

Before combining the two uncertainty distributions, their individual effects are studied. Figure 12.24 shows the effect of varying v_0 while keeping all other SHM parameters constant. The three curves shown give the Run 2 limit using the bounds of the v_0 distribution along with the canonical value. Varying v_0 has two effects: (1) the dispersion of the Maxwellian distribution changes, which shifts where the most sensitive part of the curve is, where larger v_0 gives more sensitivity to lower WIMP masses and (2) the boost from the dark matter to lab frame changes, affecting which WIMP velocities create recoils above threshold, where, again, a higher v_0 gives more sensitivity to lower
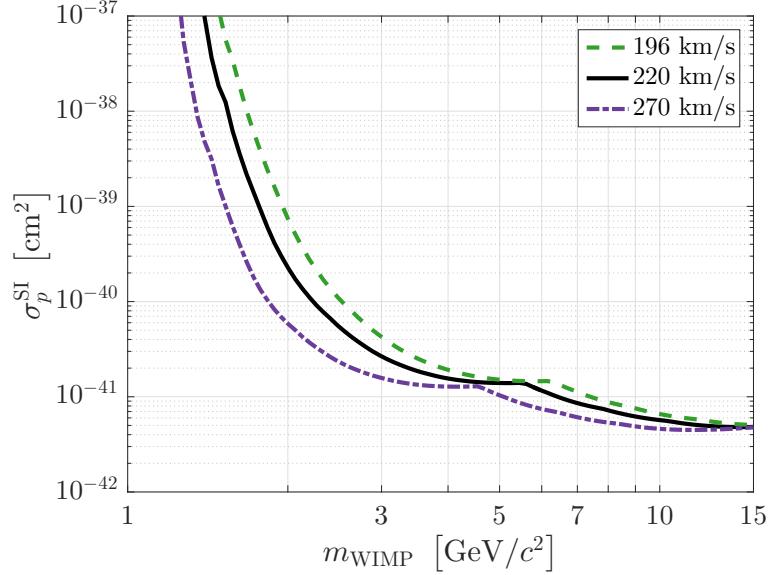
Figure 12.24: Effect on the Run 2 best-fit limit from varying the characteristic velocity in the SHMl v_0 while keeping all other parameters constant. Curves shown are for the SHM value of 220 km s^{-1} (black solid), and the upper and lower bounds of the measured values at 270 km s^{-1} (green dash) and 196 km s^{-1} (purple dash-dot). Varying v_0 changes where the most sensitive part of the curve lies in addition to slight changes in the lowest accessible WIMP mass.

WIMP masses. Figure 12.25 shows the effect of varying v_{esc} alone. The medians from both RAVE papers and the 90% uncertainty limits from the 2014 fit are given. The difference between the median values is $\lesssim 1\%$, which justifies using the 2014 fit's smaller uncertainty. Having a larger v_{esc} allows for the higher velocity tail of the distribution to be sampled, which in turn allows lower-mass WIMPs, by having a higher velocity, to create recoils above thresholds.

The effect of propagating the v_0 and v_{esc} uncertainties simultaneously is shown in Fig. 12.26 by the 68% and 95% confidence bands from the 1000 limits. The best-fit curve substituting the 2014 RAVE v_{esc} value for the 2007 SHM value is also shown. The uncertainty band from the astrophysical uncertainties is of comparable width to the band derived from the analysis uncertainties.

The SHM assumption of a Maxwellian velocity distribution is also uncertain. Physically motivated alternatives or adjustments have been used in attempts to reconcile
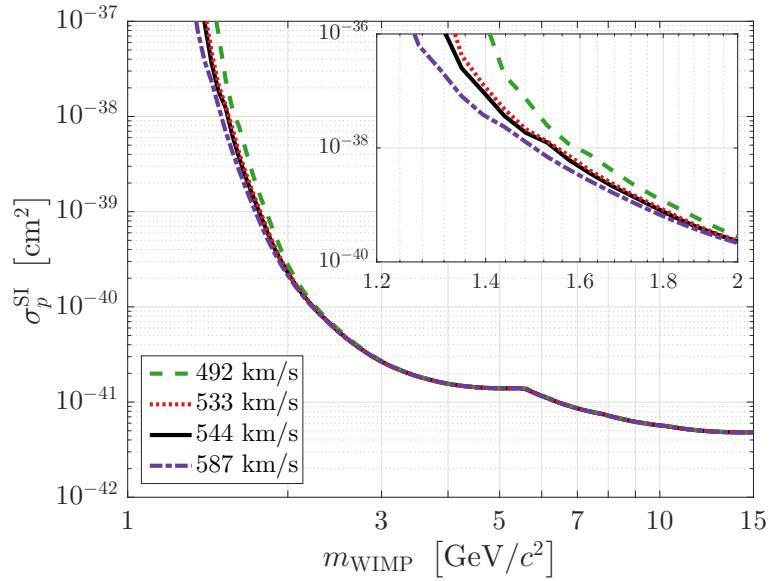
Figure 12.25: Effect on the Run 2 best-fit limit from varying the Galactic escape velocity in the SHM v_{esc} while keeping all other parameters constant. Curves shown are the median values of the 2007 and 2014 RAVE Survey results at 544 $\mathrm{km\,s}^{-1}$ (black solid) and 533 $\mathrm{km\,s}^{-1}$ (red dash) respectively, as well as the 90 % confidence bounds of the 2014 result at 492 $\mathrm{km\,s}^{-1}$ (green dash) and 587 $\mathrm{km\,s}^{-1}$ (purple dash-dot). The inset shows an enlargement below WIMP masses of 2 GeV/c^2. Varying v_{esc} changes the lowest WIMP mass that can produce recoils above threshold and hence gives access to lower/higher masses. The difference between the median-value curves is minimal.
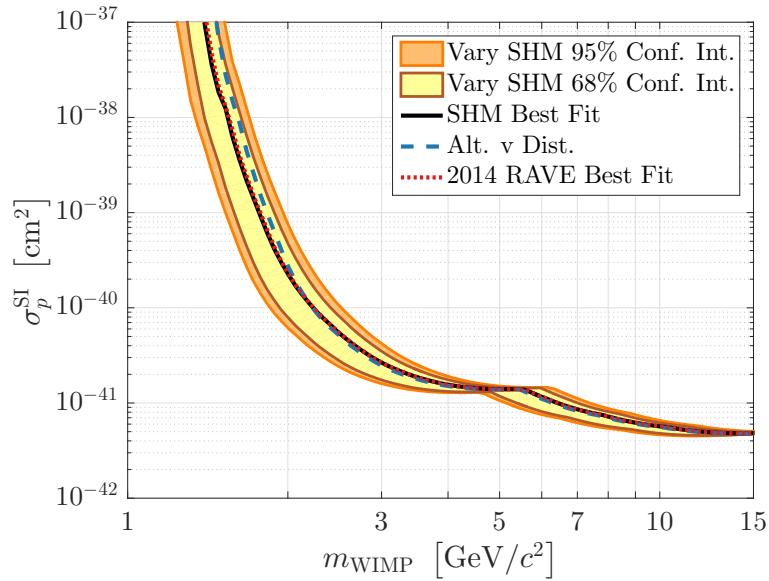
Figure 12.26: 68 % (yellow) and 95 % (orange) uncertainty bands on the best-fit Run 2 spin-independent limit (black) due to the uncertainties in most probable WIMP velocity (v_0) and Galactic escape velocity (v_{esc}) used in the Standard Halo Model (SHM). The uncertainty bands are found by computing 1000 different limits, each time sampling the distributions for v_0 and v_{esc}, and finding the desired confidence intervals in the resulting distribution. The 2014 RAVE survey v_{esc} distribution is sampled and thus the best-fit curve substituting the 2014 median value into the SHM is given for consistency (red dot). The best-fit limit computed using an alternative velocity distribution [397, 398] is also presented (blue dash).

experimental discrepancies [183, 207, 399]. Cosmological simulations also suggest that the isothermal assumption of the halo is not accurate [400]. Many empirical models of the velocity distribution have been built and fit to these simulations [401]. One such model is that of Mao *et al.* [397] which gives a velocity distribution in the rest frame of the dark matter of the form

$$f(v) \propto e^{-v/v_a} \left(v_{\mathrm{esc}}^2 - v^2 \right)^p, \tag{12.22}$$

where v_a, and p are parameters of the model. One desirable characteristic of this model is that it smoothly goes to zero at the escape velocity as compared to the artificial cut-off needed in the SHM. A fit of this model to a Milky Way-like simulation, with baryons, gives $p = 2.7$ and $v_a/v_{\mathrm{esc}} = 0.6875$ [398], where v_{esc} is taken from the 2007 RAVE result. This distribution is boosted to the lab frame via $v \to |\boldsymbol{v} + \boldsymbol{\Theta}_0 + \boldsymbol{v}_\odot + \boldsymbol{v}_\oplus|$, where $\Theta_0 = 220$ km s^{-1} is taken as the canonical circular velocity. The Run 2 limit using this alternative velocity distribution and the best-fit efficiency is also shown in Fig. 12.26. The limit is steeper at lower masses due to the more natural cut-off at the escape velocity.

12.7   Spin-Dependent Limits

While SuperCDMS, including CDMSlite, is most sensitive to the spin-independent WIMP-nucleon cross section, the presence of neutron-odd ^{73}Ge (7.73 % natural abundance) gives sensitivity to spin-dependent interactions. Even though ^{73}Ge is an odd-neutron nuclei, recall that polarization and two-body currents also give sensitivity to WIMP-proton interactions. The WIMP-nucleus standard cross section for spin-dependent interactions is written in terms of the WIMP-nucleon cross section as (Sec. 3.2.2)

$$\sigma_0^{\mathrm{SD}} = \frac{1}{3} \frac{J+1}{J} \left(\frac{\mu_T}{\mu_{p/n}} \right)^2 \frac{|(a_0 + a_1') \langle S_p \rangle + (a_0 - a_1') \langle S_n \rangle|^2}{a_{p/n}^2} \sigma_{p/n}^{\mathrm{SD}}, \tag{12.23}$$

where J is the total nuclear spin, a_0 is the isoscalar coupling, $a_1' = a_1 \left(1 + \delta a_1 \left(0 \right) \right)$ is the isovector coupling including two-body currents $\delta a_1 \left(0 \right)$, μ_T is the reduced mass between

the WIMP and the nucleus, $a_{p/n}$ are the proton/neutron couplings, $\mu_{p/n}$ the WIMP-proton/-neutron reduced mass, and $\sigma_{p/n}^{\mathrm{SD}}$ the WIMP-proton/-neutron cross section. The isoscalar/isovector couplings are related to the proton/neutron couplings as $a_0 = a_p + a_n$ and $a_1 = a_p - a_n$. Given the dependencies of this expression, there is no single two-dimensional plane in which spin-dependent results are compared. Two projections which are considered here are: (1) pick a generic model for the couplings and set upper limits as a function of WIMP mass and (2) pick a WIMP mass and set a limit on the coupling coefficients a_p and a_n.[7]

For the first approach, two special models are chosen: the proton-only ($a_0 = a_1$) and neutron-only ($a_0 = -a_1$) bases. In these two bases, the WIMP-proton/-neutron cross sections $\sigma_{p/n}^{\mathrm{SD}}$ are written in terms of the total-nucleus cross section σ_0^{SD} by re-arranging Eq. 12.23 and substituting the coupling values. The 90 % upper limits in the two planes, WIMP mass vs. WIMP-proton/-neutron cross section, from the Run 2 analysis are given in Figs. 12.27 and 12.28 compared to other experimental limits. The limits are computed in an identical manner as the spin-independent limit by sampling the analysis uncertainty distributions 1000 times at each WIMP mass and presenting curves based on the resulting limit distributions. The limit on σ_n^{SD} is ∼1 order of magnitude more restrictive than that on σ_p^{SD}, which is expected since ^{73}Ge is neutron-odd. For both models, this result sets the most stringent limit for $m_{\mathrm{WMP}} \lesssim 4$ GeV/c^2.

These limits are computed with the Klos *et al.* structure function [198] which includes two-body currents. For comparison, they are also computed using the older Dimitrov *et al.* [200] structure function, which does not include two-body currents. For simplicity, the comparison is done using the best-fit analysis parameters. These curves are given in Fig. 12.29. The neutron-only limit is only slightly better with two-body currents while the proton-only limit is ∼1 order of magnitude better. Note that the SuperCDMS LT and Run 1 curves used in Figs. 12.28 and 12.27 use the older Dimitrov *et al.* structure function.

The second limit-setting approach is, for any given WIMP mass, to set a two-dimensional exclusion curve in the a_p-a_n plane. This is most easily done by recasting the coupling coefficients in polar coordinates as $a_n = a \cos \theta$ and $a_p = a \sin \theta$. The

---

[7] A third option exists: computing the coupling parameters from a specific WIMP model. Since the field is no longer focused on any particular model, this method is not considered further.
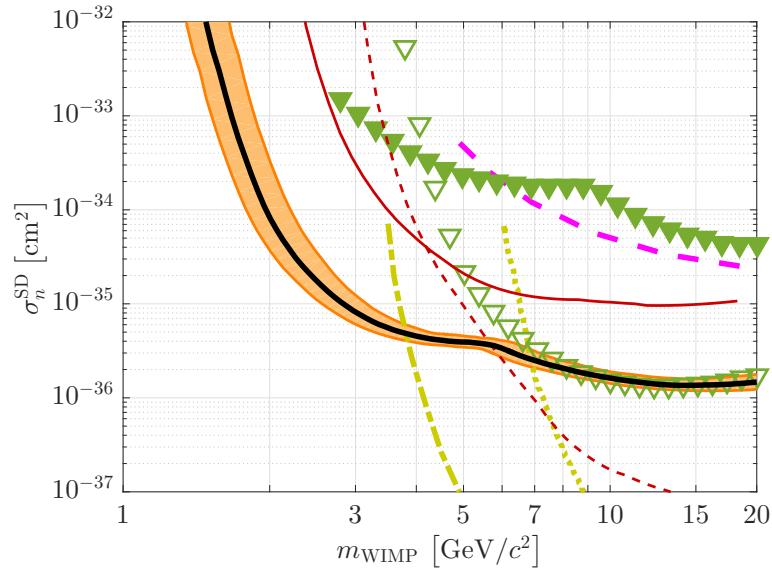
Figure 12.27: Spin-dependent (100 % neutron interaction) upper limit from CDMSlite Run 2 median (90 % C.L) and 95 % confidence interval (thick black solid curve surrounded by orange band) compared to other limits from the first run of CDMSlite (thin red solid curve) [275], SuperCDMS (thin red dash curve) [402], LUX (thick yellow dot-dash curve) [217], XENON100 (thick yellow dot curve) [403], PICASSO (thick magneta dash curve) [404], CDEX-0 (filled green triangles) [405], and CDEX-1 (open green triangles) [406].
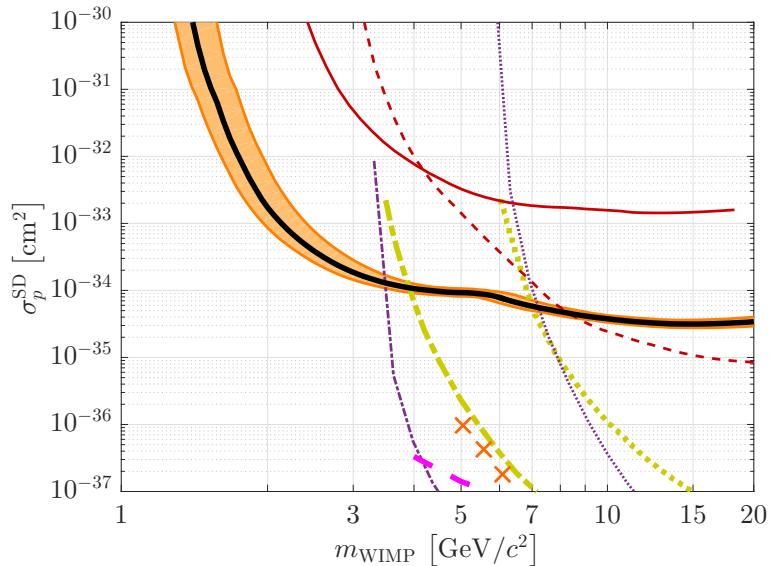
Figure 12.28: Spin-dependent (100 % proton interaction) upper limit from CDMSlite Run 2 median (90 % C.L) and 95 % confidence interval (thick black solid curve surrounded by orange band) compared to other limits from the first run of CDMSlite (thin red solid curve) [275], SuperCDMS (thin red dash curve) [402], LUX (thick yellow dot-dash curve) [217], XENON100 (thick yellow dot curve) [403], PICO-60 (thin purple dot curve) [230], and PICO-2L (thin purple dot-dash curve) [229], PICASSO (thick magenta dash curve) [227], and SIMPLE (orange crosses) [231].

(a) Proton-Only Coupling (b) Neutron-Only Coupling
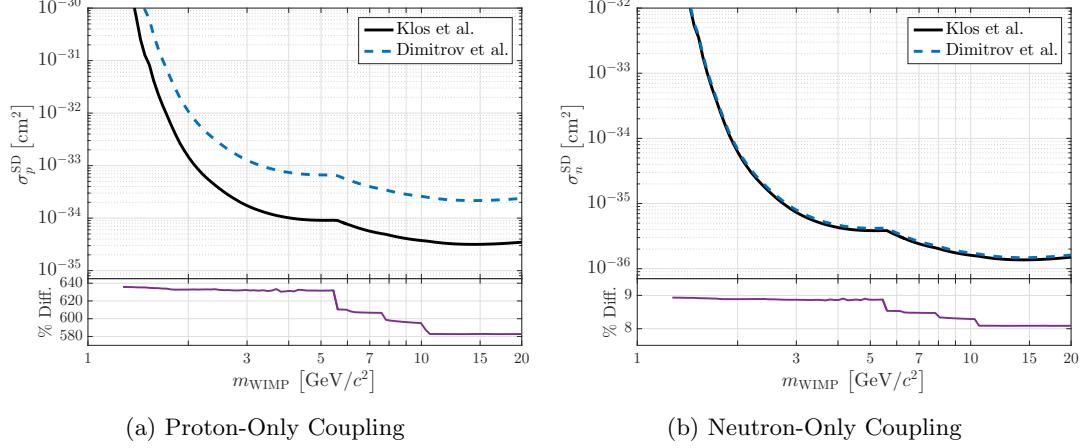
Figure 12.29: Comparison of the best-fit SD limits computed using structure fuctions from Dimitrov *et al.* (blue dash) and Klos *et al.* (black solid) for the proton- (a) and neutron-only (b) interactions. The neutron-only limits have an ∼8 % percent difference between the two while the proton only limit are different by a factor of ∼7.

proton-/neutron-only interactions above are recovered by taking $\theta = \pi/2$ and $\theta = 0$ respectively. In the polar coordinates, the spin-structure function $S(q)$ is then

$$S(q) = a^2 \left[(1 + \sin 2\theta) \, S_{00}(q) + \cos 2\theta S_{10}(q) + (1 - \sin \theta \cos \theta) \, S_{11}(q) \right]. \qquad (12.24)$$

A factor of a^2 similarly factors out of $S_T(0)$. For a given θ, a limit is set on the total-nucleus cross section, as given by Eq. 3.32, which directly translates to a limit on the radius parameter a^2. For consistency, the free-proton in the proton-only scattering is used as a normalization for all limits

$$\sigma_p^{\text{SD}} = \frac{24}{\pi} G_{\text{F}}^2 \mu_p^2 a_p^2 = \frac{24}{\pi} G_{\text{F}}^2 \mu_p^2 a^2. \qquad (12.25)$$

The mechanics for creating a contour are, for a chosen WIMP mass, scan over θ and compute the upper limit on a^2 for each θ value. The 90 % upper limits for WIMP masses of $m_{\text{WIMP}} = 2, 5, 10, 20 \text{ GeV}/c^2$ using Run 2 data are shown in Fig. 12.30. Regions outside of the ellipses are excluded. These limits are set using the analysis uncertainty sampling method and the 68 % and 95 % uncertainty bands from the 1000 samples, at each angle, are also given in the figure. The ellipses are rotated slightly from vertical

due to the order of magnitude difference in sensitivity to a_n over a_p.

An alternative procedure for setting limits in the a_p-a_n plane was proposed by Tovey *et al.* in [407]. In that work, the authors derived a simple expression relating the allowed values of a_p and a_n given the proton- and neutron-only limits

$$\frac{\pi}{24G_{\mathrm{F}}^2\mu_p^2} \geq \left[\frac{a_p}{\sqrt{\sigma_p^L}} \pm \frac{a_n}{\sqrt{\sigma_n^L}}\right]^2, \tag{12.26}$$

where $\sigma_{p/n}^L$ are the limits on the proton-/neutron-only cross sections for a given mass, the small difference between μ_p and μ_n is ignored, and the sign of the addition is the same as the sign of the ratio $\langle S_n\rangle / \langle S_p\rangle$. This expression gives limits in the form of parallel lines in the coupling-constants plane which are easy to compute once the proton- and neutron-only limits are computed.

The Tovey result was derived before two-body currents were considered in the interaction. Including two-body currents into their derivation, done here for the first time, shows a significantly more complicated relationship. The derivation starts with the obvious observation that the allowed total-nucleus cross section is less than the limit set upon it, i.e. $\sigma_0^{\mathrm{SD}}/\sigma_0^L \leq 1$, where σ_0^L is the limit on the total-nucleus cross section. The total cross section is then split into terms proportional to $\langle S_p\rangle$ and $\langle S_n\rangle$. Under the term proportional to $\langle S_p\rangle$, σ_0^L is written in terms of σ_p^L via Eq. 12.23, while under the term proportional to $\langle S_p\rangle$ it is similarly written in terms of σ_n^L. The resulting expression is

$$\frac{\pi}{24G_{\mathrm{F}}^2\mu_p^2} \geq \left[\frac{|a_0 + a_1\left(1 + \delta a_1(0)\right)|}{\sqrt{\sigma_p^L}}\frac{|\langle S_p\rangle|}{|[2 + \delta a_1(0)]\langle S_p\rangle - \delta a_1(0)\langle S_n\rangle|}\right.$$
$$\left.\pm \frac{|a_0 - a_1\left(1 + \delta a_1(0)\right)|}{\sqrt{\sigma_n^L}}\frac{|\langle S_n\rangle|}{|-\delta a_1(0)\langle S_p\rangle + [2 + \delta a_1(0)]\langle S_n\rangle|}\right]^2, \tag{12.27}$$

which reduces to Eq. 12.26 when $\delta a_1(0) \to 0$. The sign is now determined by the sign of the ratio $(a_0 - a_1')\langle S_n\rangle / (a_0 + a_1')\langle S_p\rangle$. The derivation could continue by writing a_0 and a_1 is terms of a_p and a_n, but there is no general property of absolute values which allows for the sum of the coupling terms to be separated. Deriving a limit would
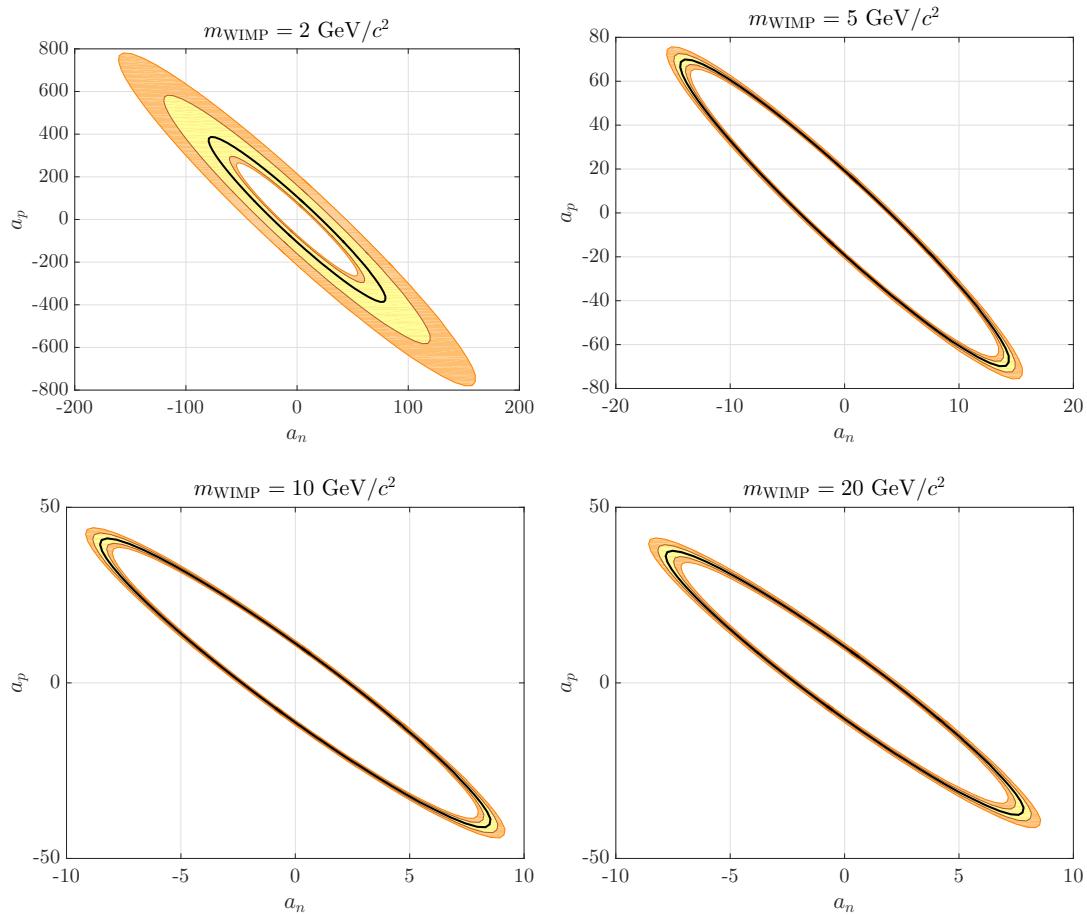
Figure 12.30: Upper limits on the spin-dependent WIMP-proton/-neutron coupling coefficients a_p/a_n for WIMP masses of $m_{\mathrm{WIMP}} = 2$, 5, 10, 20 GeV. Limits are at the 90 % confidence level with the median (thick black), 68 % (yellow band), and 95 % (orange band) uncertainty intervals given.

require numerical sampling and evaluation of (a_p, a_n) pairs. This limit-setting method is more complicated now than it was without two-body currents. Specifically, not only do σ_p^L and σ_n^L depend on the nuclear physics model (which they did before as well), but how they are related to each other now also depends on the nuclear model; a new and undesirable property. This fact, and the added complexity of the expression, yields preference to the polar coordinates method used in the main result.

Part IV

Conclusion

Chapter 13

Future Outlook

The power of the CDMSlite operating mode is apparent given the strong upper limits set by the second SuperCDMS Soudan run. These limits are world-leading below WIMP masses of $\sim$4 GeV/c^2 on both the spin-independent and various spin-dependent WIMP-nucleon cross sections. In light of this success, the SuperCDMS Collaboration has put renewed focus and study into the method. This includes a third, and final, CDMSlite run at Soudan with special calibration and plans for deployment in the next experiment: SuperCDMS SNOLAB. It is largely due to the high-voltage operating mode that SuperCDMS SNOLAB is extremely compelling as an experiment. Both of these efforts should yield ever-stronger low-mass sensitivity.

13.1 Soudan Photo-neutron and CDMSlite Run 3 Data

SuperCDMS Soudan Run 135 was the final data-taking run at Soudan and ran from early-fall 2014 to late-fall 2015. The 2015 portion of the run was dedicated to two data sets: $\sim$3 months of CDMSlite WIMP-search data and $\sim$6 months of photo-neutron calibration data. For the latter data, a beryllium wafer was exposed to one of two radioactive sources, ^{88}Y or ^{124}Sb, which emitted γ's that subsequently impinged on the ^{9}Be (100 % natural abundance) and created neutrons. The γ's released these so-called "photo-neutrons" in a narrow energy range. The 1.84 MeV γ's from ^{88}Y produced 148–156 keV n's while the 1.69 MeV γ from ^{124}Sb produced 21–25 keV n's, where the

energy range corresponds to the outgoing angles of the n's.[1] The goal of the photo-neutron data analysis is to use these neutrons with a known energy range to calibrate the nuclear-recoil equivalent energy scale. This is generally important as the data at low-recoil-energy are sparse in Fig. 12.7 and they do not extend to such low energies. It is particularly important to help inform CDMSlite analyses in converting from keV_{ee} to keV_{nr}. At minimum, it should allow for a better evaluation of the systematic uncertainty taken in that conversion. Other low-energy nuclear recoil calibration methods are being considered and will hopefully be measured at test facilities in the near future.

CDMSlite Run 3 ran from Feb.–May 2015. In most aspects, Run 3 was similar to Run 2 as it used a single detector with the same biasing and read-out electronics. The most notable difference between them is that Run 3 used iT2Z1 instead of iT5Z2. The change in detector was motivated by the lower LF-noise and threshold achieved in the SuperCDMS LT analysis for that detector. The biasing potential difference was also different, increased by 5 V to $V_b = 75$ V. Both of these changes were made with the goal of lowering the analysis threshold compared to Run 2.

Preliminary studies by W. Page show that the $50\,\%$ trigger efficiency point reached as low as 50 eV_{ee} throughout the run [408]. The phrase "as low as" has more meaning in this context than stating "as low as 55 eV_{ee}" in Run 2. This is because the leakage current, due to parasitic resistance, was significantly more variable in Run 3. Midway through the run, the air-handler which supplied fresh air to the RF room was turned off, after which the power-supply current stabilized. The response to this change indicates more sensitivity to the atmosphere (although the CDMSlite adapter board was the same between runs, the front-end electronics board was different) and could also be related to the lower parasitic resistance indicated by Fig. 9.5. While Run 2 has a $\sim 2\,\%$ correction to the keV_t energy scale due to the leakage current, Run 3 has an up to $\sim 33\,\%$ correction. This means that, prior to the stabilization, the threshold was as high as ~ 75 eV_{ee}. The entire run was below the Run 2a threshold and approximately 40 (raw) days were spent in the stable configuration, which is significantly longer than Run 2b. This larger effective exposure at lower thresholds, coupled with the expected reduction in LF-noise rate, means that Run 3 should be more sensitive than Run 2

---

[1] A single outgoing angle corresponds to a single energy, and thus a mono-energetic source is obtained at any given angle. The uncertainty on the incoming γ's energy and how the ^{8}Be nucleus is modeled can also affect the resulting energy. Calculations courtesy of private communication with A. Villano.

below WIMP masses of 3–5 GeV/c^2. The overall lowest WIMP mass accessible should also decrease slightly, to $\sim$1.24 GeV/c^2 compared to $\sim$1.29 GeV/c^2 in Run 2.[2]

A planned improvement to the Run 3 analysis is the implementation of a background model and a corresponding fit to the energy spectrum. The components expected in the spectrum are: electron-capture lines (both ^{71}Ge and cosmogenic activation), Compton scatters, tritium, and ^{210}Pb surface decays. Detailed study is required to understand how each of these backgrounds behave at such low energies. An example of the detail needed is shown by D. Barker, who considered the Compton scatter background [409]. The Compton scatter spectrum is commonly considered to be flat at low energies, but, as the energy of the incoming γ becomes lower than the electron-binding energies of the material, this flat behavior is no longer valid: i.e. in order to scatter and remove a bound electron, the incoming γ must have energy greater than the binding energy. There are thus fewer available bound electrons to scatter with as the γ's energy decreases, creating step-like behavior in the observed spectrum. The magnitudes of these steps are related to the electron-shell geometry. As an example, an incoming 8 keV γ cannot release a K-shell electron in Ge, with a binding energy of $\sim$11 keV, and therefore only 30 of the 32 bound electrons are available for Compton scattering and the overall rate is reduced compared to above the K shell. These steps have been observed in calibration data and should be included in any spectral fitting of either run's spectrum.

An estimate of the Run 3 sensitivity, again computed by W. Page [410], is given in Fig. 13.1. This calculation assumes the same inter-peak background level as Run 2a,[3] a flat 50 % efficiency based on the radial cut efficiency in Run 2, and a live time representative of the later portion of Run 3, when the trigger threshold is lowest and most stable. The model is sampled 100 times, using standard Lindhard to convert to keV$_{nr}$, and the 90 % confidence level upper limit computed using the optimum interval method. The median, with the 95 % uncertainty band, is presented and, in comparison to the Run 2 limit, a reasonable increase in sensitivity below $\sim$3 GeV/c^2 is expected. The implementation of a MLE-style fit should also increase the sensitivity even further.

---

[2] Both estimated using the standard Lindhard conversion (Sec. 12.2.2).

[3] The presence of the high-radius background in Run 2b gives a, likely-unphysical, high background rate below the M-shell line in that part of the run and subsequently increases the overall average rate (Table 12.2). In general, such a background is not expected in Run 3, justifying the use of the Run 2a-only rate.
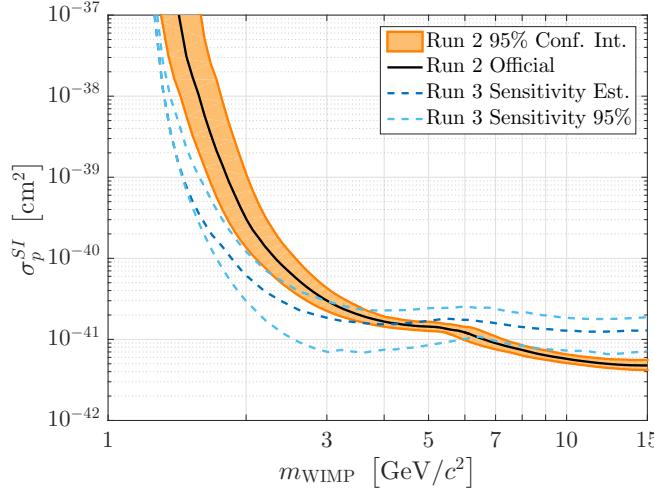
Figure 13.1: Projected sensitivity for CDMSlite Run 3 assuming a 50 keV$_{ee}$ analysis threshold for an 18 kg d exposure. Background rates are the same as Run 2a and a flat 50 % efficiency is assumed. 100 simulations are performed, using standard Lindhard in converting to keV$_{nr}$, and the median (dark blue dash) and 95 % confidence band (light blue dash) are given. Improvement over the Run 2 official limit (black solid with orange band) is expected below $\sim$4 GeV/c^2 in WIMP mass. Figure adapted from [410].

13.2   SuperCDMS SNOLAB Project

The next stage of the SuperCDMS Collaboration is building a larger and more sensitive experimental apparatus at SNOLAB in the Creighton mine in Sudbury, Ontario. SuperCDMS SNOLAB should be superior to the Soudan experiments in almost every way, notably in larger and better performing detectors and in reduced backgrounds. Research and development work for these improvements have been occurring for a number of years, with initial funding proposals submitted in 2012 and 2013 and the final decision by the agencies to fund the experiment in 2014 as part of the "Second Generation" dark matter direct detection program put forth by the Department of Energy and National Science Foundation in the United States. The power of the high-voltage detector mode was one of, if not the, primary reason the experiment was chosen. The mandate from the funding agencies upon selection was that SuperCDMS SNOLAB is to focus on exploring the low-mass-WIMP parameter space. This shift from high-mass WIMPs to low-mass WIMPs, and the correspondingly necessary shift in analysis parameters, changes the backgrounds and sensitivities compared to the initial simulations in Sec. 8.2. The sensitivity estimates of the more mature planned SuperCDMS SNO-LAB experiment are published in [411], and the description in the following sub-sections

(a) iZIP Detector   (b) HV Detector
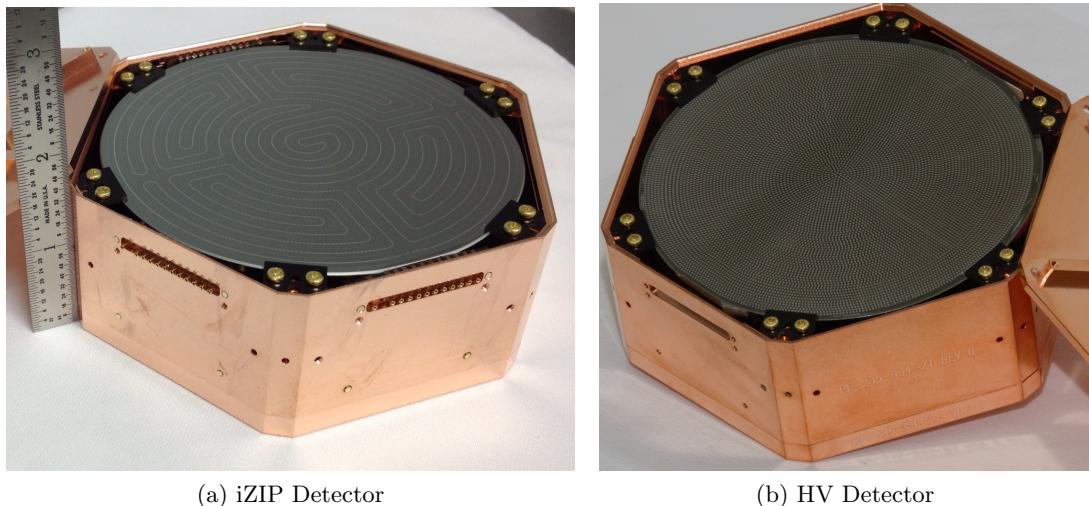
Figure 13.2: iZIP- (a) and high-voltage- (b) type detectors to be used in the SuperCDMS SNOLAB experiment. The crystals are 33.3 mm in radius, 100 mm in diameter, and have a mass of 1.39 kg. The iZIP detector has interleaved phonon and ionization sensors while the HV detector only has phonon sensors which cover a larger percentage of the face's area.

follows the discussion therein.

13.2.1 Physical Description

The detector technology is the heart of SuperCDMS and it has improved with each generation of the experiment. Two detector designs will be used in SuperCDMS SNO-LAB are shown in Fig. 13.2. For both designs the detectors will be larger than those used in Soudan, with a height of 33.3 mm, a diameter of 100 mm, and a total mass of 1.39/0.61 kg for Ge/Si detectors. The first detector type, iZIP, interleaves the ionization and phonon sensors and has 6 phonon and 2 ionization channels per side. The second detector type, high voltage (HV), was designed specifically for CDMSlite-style operating and contains only phonon sensors, with a higher percentage of the surface covered by TESes, with six channels per side. In addition to being larger, the energy resolution and other detector characteristics will improve over the Soudan detectors. Both germanium and silicon detectors will be used. The inclusion of silicon detectors will allow a direct cross-check of the c58R Si result and generally give access to lower-mass WIMPs.

	iZIP		HV	
	Ge	Si	Ge	Si
Number of detectors	10	2	8	4
Expected Exposure [kg d]	56	4.8	44	9.6
Phonon Resolution [eV]	50	25	10	5
Ionization Resolution [eV]	100	110	-	-
Bias Voltage [V]	6	8	100	100

Table 13.1: Planned characterization of the four types of SNO-LAB detectors: Ge iZIP, Si iZIP, Ge HV, Si HV. The HV detectors do not have ionization sensors. The arrangement will be 4 towers of 6 detectors each. Table reproduced from [411].

The number of, and expected parameters for, the four different types of detectors are given in Table 13.1. The four types correspond to the two detector materials and the two sensor layouts. The HV-style detector is expected to have phonon noise of $\lesssim 10$ eV$_{\text{t}}$, which corresponds to $\lesssim 1$ eV$_{\text{ee}}$ at the planned 100 V. Such a baseline noise value will be an improvement of $10\times$ over the CDMSlite-Soudan runs. Note that as SuperCDMS SNOLAB is to be a low-mass WIMP experiment, the initial payload will be significantly smaller than that proposed in 2012 (4 instead of 12 towers): low-energy searches become background limited more quickly. The cryostat will be larger than is needed for this payload, allowing for upgrades in the future. In particular, if a signal consistent with a WIMP of mass 10–30 GeV/c^2 is observed in a different, high-mass focused, experiment, the SuperCDMS SNOLAB cryostat could be filled with iZIP-style detectors to validate the signal. Complementarity between material types is also important to study a positive signal as multiple targets are required to fully characterize such a detection.

The experimental apparatus is shown in Fig. 13.3. The shielding, to first order, follows the initial proposals' geometry in that it is entirely passive. The outer-neutron shield will consist of 60 cm of water (top and sides) or polyethylene (bottom). Inside of the outer-neutron shielding will be a ^{222}Rn shield, inside of which will be continuously purged by N$_2$ gas to mitigate atmospheric ^{222}Rn. The inner shielding will consist of 23 cm of low-activity lead, for γ shielding, and 40 cm of polyethylene for additional neutron shielding. The cryostat will contain six copper cans, each 0.325 in. thick, and space for up-to 31 towers of six detectors each. The operating temperature is designed to be 15–30 mK, cooler than the 50–60 mK at Soudan, which allows for better resolution
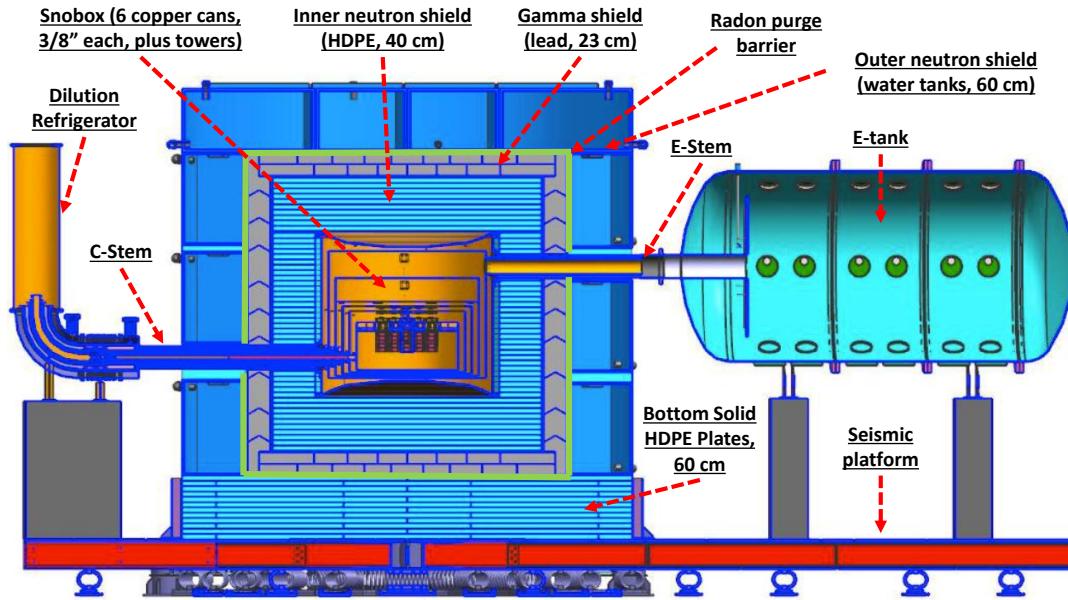
Figure 13.3: Apparatus planned for the SuperCDMS SNOLAB experiment. Shielding consists of, from outer to inner: 60 cm of water (top and side) or high-density polyethylene (HDPE, bottom), 23 cm lead, 40 cm HDPE, and six 0.325 in. copper cryostat cans (Snobox). Cans are thermally connected to the stages of the dilution refrigerator through the C-stem (left) and electronics from the towers are fed through the E-stem to the E-tank (right). The entire apparatus is seismically isolated from the cavern floor as the mine is active and there is occasional blasting. Figure from [411].

in the detectors.

13.2.2 Backgrounds

The advantage of moving to the SNOLAB site is found from comparing the cosmogenic-background fluxes. The fluxes of cosmogenic muons and neutrons are reduced by approximately 2.5 orders of magnitude between Soudan and Sudbury, which relieves the necessity of a specific muon veto layer. The iZIP detectors are estimated to have cosmogenic-neutron rates of 73–77×10^{-6} $[\mathrm{kg\,yr\,keV}]^{-1}$.

In addition to cosmogenic neutrons and the bulk contamination of the shield, the background model includes the cosmogenic $^3\mathrm{H}$, $^{32}\mathrm{Si}$, and numerous electron-capture sources in the detector crystals, bulk contamination from components of the read-out
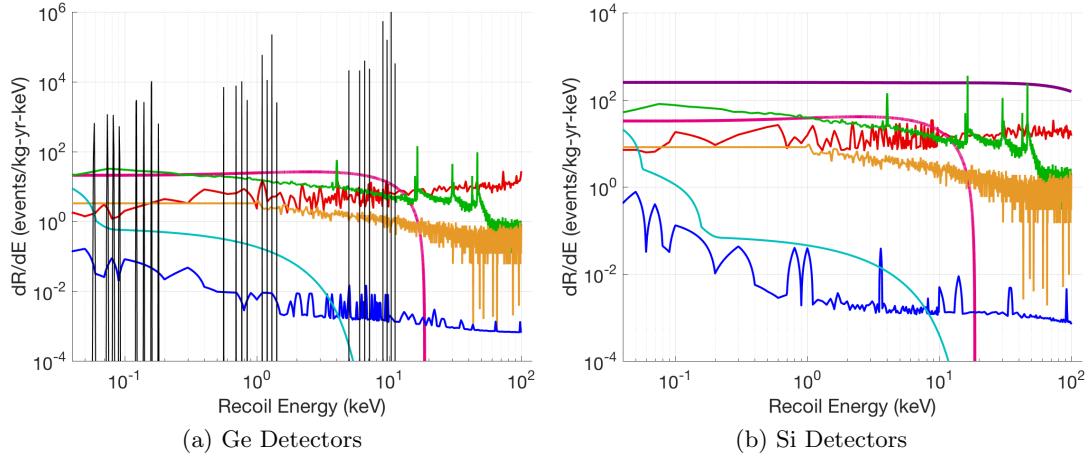
Figure 13.4: Differential rates for the expected backgrounds in the Ge (a) and Si (b) SuperCDMS SNOLAB detectors. Backgrounds are: ^{3}H (pink), ^{32}Si (purple), Ge activation lines (black), Compton scatters (red), surface β's (green), surface ^{206}Pb (orange), neutrons (blue), and coherent neutrino scattering (cyan). The neutron spectrum appears to have a peaky structure, which is due to poor statistics on the cosmogenic neutron simulation. Figures from [411].

electronics, surface sources resulting from ^{222}Rn, cavern-sourced radiation, and coherent neutrino interactions due to solar neutrinos. The differential rates from each of these backgrounds in the Ge and Si detectors are given in Fig. 13.4. The ^{3}H and ^{32}Si in the crystals are expected to be the dominant backgrounds.

13.2.3   Sensitivity Projection

An analytical model is developed in [411] to represent the detector responses to the input background spectra and analysis cuts. This model is applied to the backgrounds in Fig. 13.4 to generate spectra usable for estimating the WIMP-search sensitivities, assuming no WIMPs are present, of the four detector types. For the HV detectors, a radial fiducial volume cut is applied, while for the iZIP detectors, radial and vertical-depth fiducial-volume cuts and an NR/ER discriminating ionization-yield cut are all applied. The energy ranges used for each of the four detector types are given in Table 13.2. Although the noise resolution, in eV$_t$, given in Table 13.1 would indicate lower thresholds for the HV detectors, the ionization yield has not been measured at such

Detector Type	E_{Low} [eV$_{\mathrm{nr}}$]	E_{High} [keV$_{\mathrm{nr}}$]
Ge HV	40	25
Si HV	78	25
Ge iZIP	166	120
Si iZIP	272	120

Table 13.2: Energy ranges used in the SuperCDMS SNOLAB sensitivity estimate for the four different detector types. Values taken from [411].
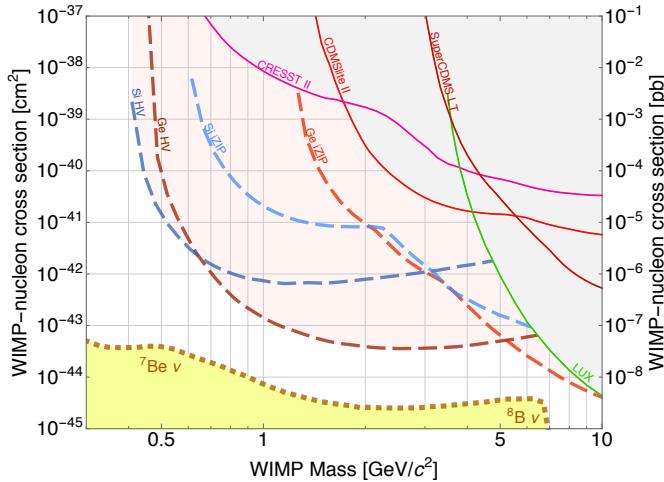
Figure 13.5: Expected sensitivity of the SuperCDMS SNOLAB experiment on the spin-independent WIMP-nucleon cross section from Ge HV (dark red dash), Ge iZIP (light red dash), Si HV (dark blue dash), and Si iZIP (light blue dash) detector types. These are compared to current exclusion limits given by solid curves. Figure from [411].

low energies and therefore a conservative upper bound is taken. With more low-energy calibration studies, these thresholds could be lowered.

The expected sensitivity reach of the SuperCDMS SNOLAB experiment for the spin-independent WIMP-nucleon cross section is given in Fig. 13.5. The curves for each of the detector types are calculated by sampling from the background model to create a pseudo-experiment-spectrum and using the optimum interval to find the 90 % confidence level limit for that sample. Numerous pseudo-experiments are simulated and the median of the collection is given in the figure. SuperCDMS SNOLAB is expected to greatly increase in sensitivity over current results below WIMP masses of $\sim$5 GeV/c^2, mainly due to the Ge HV detectors. These sensitivities are calculated using the conservative optimum interval. Using a likelihood-fitting approach will likely improve the sensitivity and the collaboration is actively investigating such a method, both in these sensitivity studies and in the CDMSlite Run 3 result.

13.3 Finale

The dark matter direct detection field has evolved considerably since the early experiments of the 1990's. Evidence for historically favored solutions to the dark matter problem, such as the supersymmetric neutralino, has been lacking, both from dark matter experiments and from colliders. Confronted with this, and with no firm and/or verified detection signals, the field has been forced to broaden its search parameters and to consider alternatives. In the United States, this has taken the form of a set of second generation experiments. In addition to SuperCDMS SNOLAB, this includes LUX-ZEPLIN (LZ) [412] and ADMX [413]. The three experiments are targeted at low-mass WIMPs, high-mass WIMPs, and axions, respectively. This program is also strengthened by non-US-based efforts, with the general classification of crystal experiments pushing to lighter masses and liquid-noble detectors searching at heavier masses. The CDMSlite high-voltage technique will play a crucial role in in the upcoming low-mass portion of this global push.

This global effort, however, has a potential stopping point ahead: the coherent neutrino scattering (CNS) background [414]. CNS, in which neutrinos elastically scatter with the nucleus, is a prediction of the standard model which has yet to be experimentally verified. In a direct detection experiment, these events would be nuclear recoils and indistinguishable from dark matter. The sun provides a constant flux of neutrinos, from various nuclear reactions, which could interact with a dark matter detector in this way. This has both positive and negative consequences for the field. The positive is that observing CNS would be a discovery of new physics. Precision measurements of the interaction cross section would be another check of the standard model, and, as neutrinos are one promising avenue for beyond-the-standard-model physics, such a verification is of general interest. The negative is that when CNS is detected, it will be an irreducible background in dark matter searches; hence the "floor" moniker. Spectral-shape fitting will be required to push below this level, which requires analyses to be background subtracted. The curves given in the sensitivity plots are the dark-matter equivalent (i.e. from interpreting CNS events as WIMPs) mass-cross section pairing for the predicted standard model interaction.

The future of the dark-matter direct-detection field is thus extremely exciting. Hopefully the upcoming experiments will observe a detection signal. If this is the case, a new generation of experiments will be needed to hone in on that signal and tease out the properties of dark matter, which is the first step to building an adequate theory and discerning all the potential new physics therein. If the upcoming searches do not detect a signal, the study of CNS will still be fruitful and the excitement shifts to looking at new theories, paradigms, and other potential new physics. Approximately 25 % of the universe consists of unknown matter, and the physics community will not stop until the nature of this dark matter has been illuminated.

References

[1] T. Jacobsen, "Enuma Elish-"The Babylonian Genesis"," in *Theor. Universe*, edited by M. K. Munitz (The Free Press, New York, 1965) pp. 8–20.

[2] H. Kragh, "Ancient Cosmological Thought," in *Conceptions Cosm. From Myth. to Accel. Universe A Hist. Cosmol.* (Oxford University Press Inc., New York, 2007) Chap. 1.1, pp. 6–17.

[3] "Genesis," in *New Am. Bible Revis. Ed.* (Saint Benedict Press, Charlotte, 2010).

[4] A. Einstein, "Über die von der molekularkinetischen Theorie der Wärme geforderte Bewegung von in ruhenden Flüssigkeiten suspendierten Teilchen," Ann. Phys. **322**, 549–560 (1905).

[5] H. Kragh, "The Greek Cosmos," in *Conceptions Cosm. From Myth. to Accel. Universe A Hist. Cosmol.* (Oxford University Press Inc., New York, 2007) Chap. 1.2, pp. 18–32.

[6] Ptolemy, *Almagest*, edited by G. J. Toomer (Springer-Verlag, New York, 1984).

[7] Aristotle, *On the Heavens* (Generic NL Freebook Publisher, Raleigh, 2007).

[8] N. Copernicus, *On The Shoulders of Giants*, edited by S. Hawking (Running Press, Philadelphia, 2002).

[9] O. Gingerich, "Did Copernicus Owe a Debt to Aristarchus," J. Hist. Astron. **16**, 37 (1985).

[10] J. Kepler, *New Astronomy*, edited by W. Donahue (Cambridge University Press, New York, 1992).

[11] G. Galilei, "Dialogue Concerning the Two Chief World Systems," in *Theor. Universe*, edited by M. K. Munitz (The Free Press, New York, 1965) pp. 190–197.

[12] I. Newton, *On The Shoulders of Giants*, edited by S. Hawking (Running Press, Philadelphia, 2002).

[13] I. Newton, "Four Letters to Richard Bently," in *Theor. Universe*, edited by M. K. Munitz (The Free Press, New York, 1965) pp. 211–219.

[14] H. Kragh, "Enlightenment Cosmologies," in *Conceptions Cosm. From Myth. to Accel. Universe A Hist. Cosmol.* (Oxford University Press Inc., New York, 2007) Chap. 2.2, pp. 75–89.

[15] F. Bessel, "Bestimmung der Entfernung des 61sten Sterns des Schwans," Astron. Nachrichten **16**, 65–96 (1839).

[16] I. Kant, *Theor. Universe*, edited by M. K. Munitz (The Free Press, New York, 1965) pp. 231–249.

[17] W. Herschel, "On the Construction of the Heavens," in *Theor. Universe*, edited by M. K. Munitz (The Free Press, New York, 1965) pp. 264–270.

[18] H. Kragh, "The Via Lacta," in *Conceptions Cosm. From Myth. to Accel. Universe A Hist. Cosmol.* (Oxford University Press Inc., New York, 2007) Chap. 2.5, pp. 110–124.

[19] A. Einstein, "Die Feldgleichungen der Gravitation," Sitzungsberichte der Königlich Preußischen Akad. der Wissenschaften (Berlin), Seite 844-847. (1915); A. Einstein, "Die Grundlage der allgemeinen Relativitätstheorie," Ann. Phys. **354**, 769–822 (1916); A. Einstein, "Kosmologische Betrachtungen zur allgemeinen Relativitätstheorie," Sitzungsberichte der Königlich Preußischen Akad. der Wissenschaften (Berlin), Seite 142-152. (1917).

[20] A. Friedmann, "On the Curvature of Space," Gen. Relativ. Gravit. **31**, 1991–2000 (1922); A. Friedmann, "Über die Möglichkeit einer Welt mit konstanter negativer Krümmung des Raumes," Zeitschrift für Phys. **21**, 326–332 (1924).

[21] G. Lemaître, "Un Univers homogène de masse constante et de rayon croissant rendant compte de la vitesse radiale des nébuleuses extra-galactiques," Ann. la Société Sci. Bruxelles , 49–59 (1927).

[22] H. P. Robertson, "On The Foundations Of Relativistic Cosmology," Proc. Natl. Acad. Sci. **15**, 822–829 (1929); H. P. Robertson, "Kinematics and World-Structure," Astrophys. J. **82**, 284 (1935); H. P. Robertson, "Kinematics and World-Structure II," Astrophys. J. **83**, 187 (1936); H. P. Robertson, "Kinematics and World-Structure III," Astrophys. J. **83**, 257 (1936).

[23] A. Walker, "On Milne's theory of world structure," Proc. London Math. Soc. **s2-42**, 90–127 (1937).

[24] J. Stephan, "Über die Beziehung zwischen der Wärmestrahlung und der Temperatur," Sitzungsberichte der Math. Cl. der Kais. Akad. der Wissenschaften **79**, 391 (1879).

[25] L. Boltzmann, "Ableitung des Stefan'schen Gesetzes, betreffend die Abhängigkeit der Wärmestrahlung von der Temperatur aus der electromagnetischen Lichttheorie," Ann. Phys. **258**, 291–294 (1884).

[26] A. G. Riess *et al.*, "Observational Evidence from Supernovae for an Accelerating Universe and a Cosmological Constant," Astron. J. **116**, 1009–1038 (1998).

[27] S. Perlmutter *et al.*, "Measurements of Ω and Λ from 42 High-Redshift Supernovae," Astrophys. J. **517**, 565–586 (1999).

[28] P. A. R. Ade *et al.* (Planck Collaboration), "Planck 2015 results: XIII. Cosmological parameters," Astron. Astrophys. **594**, A13 (2016); P. A. R. Ade *et al.* (Planck Collaboration), "Planck 2013 results. XVI. Cosmological parameters," Astron. Astrophys. **571**, A16 (2014).

[29] K. Olive *et al.*, "Review of Particle Physics," Chinese Phys. C **38**, 090001 (2014).

[30] V. C. Rubin and J. Ford, W. Kent, "Rotation of the Andromeda Nebula from a Spectroscopic Survey of Emission Regions," Astrophys. J. **159**, 379 (1970).

[31] V. C. Rubin, N. Thonnard, and J. Ford, W. K., "Extended rotation curves of high-luminosity spiral galaxies. IV - Systematic dynamical properties, Sa→Sc," Astrophys. J. **225**, L107 (1978).

[32] Y. Sofue and V. Rubin, "Rotation Curves of Spiral Galaxies," Annu. Rev. Astron. Astrophys. **39**, 137–174 (2001).

[33] P. M. Kalberla and J. Kerp, "The HI Distribution of the Milky Way," Annu. Rev. Astron. Astrophys. **47**, 27–61 (2009).

[34] A. K. Drukier, K. Freese, and D. N. Spergel, "Detecting cold dark-matter candidates," Phys. Rev. D **33**, 3495–3508 (1986).

[35] A. Klypin, A. V. Kravtsov, O. Valenzuela, and F. Prada, "Where Are the Missing Galactic Satellites?" Astrophys. J. **522**, 82–92 (1999).

[36] M. Mateo, "Dwarf Galaxies Of The Local Group," Annu. Rev. Astron. Astrophys. **36**, 435–506 (1998).

[37] L. E. Strigari, J. S. Bullock, M. Kaplinghat, A. V. Kravtsov, O. Y. Gnedin, K. Abazajian, and A. A. Klypin, "A Large Dark Matter Core in the Fornax Dwarf Spheroidal Galaxy?" Astrophys. J. **652**, 306–312 (2006).

[38] L. E. Strigari, J. S. Bullock, M. Kaplinghat, J. D. Simon, M. Geha, B. Willman, and M. G. Walker, "A common mass scale for satellite galaxies of the Milky Way." Nature **454**, 1096–7 (2008).

[39] V. Belokurov *et al.*, "A Faint New Milky Way Satellite in Bootes," Astrophys. J. **647**, L111–L114 (2006).

[40] D. B. Zucker *et al.*, "A New Milky Way Dwarf Satellite in Canes Venatici," Astrophys. J. **643**, L103–L106 (2006).

[41] B. Willman, J. J. Dalcanton, D. Martinez-Delgado, A. A. West, M. R. Blanton, D. W. Hogg, J. C. Barentine, H. J. Brewington, M. Harvanek, S. J. Kleinman, J. Krzesinski, D. Long, E. H. Neilsen, Jr., A. Nitta, and S. A. Snedden, "A New Milky Way Dwarf Galaxy in Ursa Major," Astrophys. J. **626**, L85–L88 (2005).

[42] J. D. Simon and M. Geha, "The Kinematics of the Ultra-faint Milky Way Satellites: Solving the Missing Satellite Problem," Astrophys. J. **670**, 313–331 (2007).

[43] K. Bechtol *et al.* (DES Collaboration), "Eight New Milky Way Companions Discovered In First-Year Dark Energy Survey Data," Astrophys. J. **807**, 50 (2015).

[44] S. E. Koposov, V. Belokurov, G. Torrealba, and N. W. Evans, "Beasts Of The Southern Wild: Discovery Of Nine Ultra Faint Satallites In The Vicinity Of The Magellanic Clouds," Astrophys. J. **805**, 130 (2015).

[45] A. Drlica-Wagner *et al.* (DES Collaboration), "Eight Ultra-Faint Galaxy Candidates Discovered In Year Two Of The Dark Energy Survey," Astrophys. J. **813**, 109 (2015).

[46] E. Luque *et al.*, "Digging deeper into the Southern skies: a compact Milky Way companion discovered in first-year Dark Energy Survey data," Mon. Not. R. Astron. Soc. **458**, 603–612 (2016).

[47] F. Zwicky, "Republication of: The redshift of extragalactic nebulae," Gen. Relativ. Gravit. **41**, 207–224 (2008).

[48] F. Zwicky, "On the Masses of Nebulae and of Clusters of Nebulae," Astrophys. J. **86**, 217 (1937).

[49] S. Smith, "The Mass of the Virgo Cluster," Astrophys. J. **83**, 23 (1936).

[50] G. M. Voit, "Tracing cosmic evolution with clusters of galaxies," Rev. Mod. Phys. **77**, 207–258 (2005).

[51] A. Vikhlinin, A. Kravtsov, W. Forman, C. Jones, M. Markevitch, S. S. Murray, and L. Van Speybroeck, "Chandra Sample of Nearby Relaxed Galaxy Clusters: Mass, Gas Fraction, and Mass Temperature Relation," Astrophys. J. **640**, 691–709 (2006).

[52] A. Vikhlinin, A. V. Kravtsov, R. A. Burenin, H. Ebeling, W. R. Forman, A. Hornstrup, C. Jones, S. S. Murray, D. Nagai, H. Quintana, and A. Voevodkin, "Chandra Cluster Cosmology Project III: Cosmological Parameter Contraints," Astrophys. J. **692**, 1060–1074 (2009).

[53] Y. Mellier, "Gravitational lensing and dark matter," in *Part. Dark Matter Obs. Model. Searches*, edited by G. Bertone (Cambridge University Press, New York, 2010) pp. 56–82.

[54] D. Clowe, M. Bradač, A. H. Gonzalez, M. Markevitch, S. W. Randall, C. Jones, and D. Zaritsky, "A Direct Empirical Proof of the Existence of Dark Matter," Astrophys. J. **648**, L109–L113 (2006).

[55] M. Markevitch, "Chandra observation of the most interesting cluster in the Universe," arXiv:0511345 [astro-ph] .

[56] S. W. Randall, M. Markevitch, D. Clowe, A. H. Gonzalez, and M. Bradač, "Constraints on the SelfInteraction Cross Section of Dark Matter from Numerical Simulations of the Merging Galaxy Cluster 1E 065756," Astrophys. J. **679**, 1173–1180 (2008).

[57] M. Bradač, S. W. Allen, T. Treu, H. Ebeling, R. Massey, R. G. Morris, A. von der Linden, and D. Applegate, "Revealing the Properties of Dark Matter in the Merging Cluster MACS J0025.41222," Astrophys. J. **687**, 959–967 (2008).

[58] M. J. Jee, H. Hoekstra, A. Mahdavi, and A. Babul, "Hubble Space Telescope /Advanced Camera For Surveys Confirmation Of The Dark Substructure In A520," Astrophys. J. **783**, 78 (2014).

[59] M. Markevitch and D. Clowe, "Chandra :: Photo Album :: 1E 0657-56 :: 21 Aug 06," (2016).

[60] R. Cyburt, "The NACRE thermonuclear reaction compilation and big bang nucleosynthesis," New Astron. **6**, 215–238 (2001); R. H. Cyburt, B. D. Fields, and K. A. Olive, "An update on the big bang nucleosynthesis prediction for ^{7}Li: the problem worsens," J. Cosmol. Astropart. Phys. 2008 (2008) 012.

[61] K. Jedamzik and M. Pospelov, "Particle Dark Matter and Big Bang Nucleosynthesis," in *Part. Dark Matter Obs. Model. Searches*, edited by G. Bertone (Cambridge University Press, New York, 2010) Chap. 27, pp. 547–564.

[62] R. H. Cyburt, B. D. Fields, K. A. Olive, and T.-H. Yeh, "Big bang nucleosynthesis: Present status," Rev. Mod. Phys. **88**, 015004 (2016).

[63] M. Fukugita and P. J. E. Peebles, "The Cosmic Energy Inventory," Astrophys. J. **616**, 643–668 (2004).

[64] D. J. Fixsen, "The Temperature Of The Cosmic Microwave Background," Astrophys. J. **707**, 916–920 (2009).

[65] R. Adam *et al.* (Planck Collaboration), "Planck 2015 Results," Astron. Astrophys. **594**, A1 (2016).

[66] E. W. Kolb and M. S. Turner, *The Early Universe* (Addison-Wesley, New York, 1990).

[67] W. Hu, N. Sugiyama, and J. Silk, "The physics of microwave background anisotropies," Nature **386**, 37–43 (1997).

[68] C.-P. Ma and E. Bertschinger, "Cosmological Perturbation Theory in the Synchronous and Conformal Newtonian Gauges," Astrophys. J. **455**, 7 (1995).

[69] N. Sugiyama, "Introduction to temperature anisotropies of Cosmic Microwave Background radiation," Prog. Theor. Exp. Phys. **2014**, 6B101 (2014).

[70] P. A. R. Ade *et al.* (BICEP2 Collaboration), "Detection of B-mode polarization at degree angular scales by BICEP2." Phys. Rev. Lett. **112**, 241101 (2014).

[71] A. H. Guth, "Inflationary universe: A possible solution to the horizon and flatness problems," Phys. Rev. D **23**, 347–356 (1981).

[72] A. Linde, "A new inflationary universe scenario: A possible solution of the horizon, flatness, homogeneity, isotropy and primordial monopole problems," Phys. Lett. B **108**, 389–393 (1982).

[73] A. Albrecht and P. J. Steinhardt, "Cosmology for Grand Unified Theories with Radiatively Induced Symmetry Breaking," Phys. Rev. Lett. **48**, 1220–1223 (1982).

[74] P. Coles and F. Lucchin, *Cosmology : The Origin and Evolution of Cosmic Structure*, 2nd ed. (Wiley, Chichester, 2002).

[75] L. Anderson *et al.* (SDSS Collaboration), "The clustering of galaxies in the SDSS-III Baryon Oscillation Spectroscopic Survey: baryon acoustic oscillations in the Data Release 9 spectroscopic galaxy sample," Mon. Not. R. Astron. Soc. **427**, 3435–3467 (2013).

[76] V. Springel *et al.*, "Simulations of the formation, evolution and clustering of galaxies and quasars." Nature **435**, 629–36 (2005).

[77] D. G. York *et al.* (SDSS Collaboration), "The Sloan Digital Sky Survey: Technical Summary," Astron. J. **120**, 1579–1587 (2000).

[78] M. J. Geller and J. P. Huchra, "Mapping the universe." Science **246**, 897–903 (1989).

[79] M. Colless *et al.* (2dFGRS Team), "The 2dF Galaxy Redshift Survey: Final Data Release," arXiv:0306581 [astro-ph] .

[80] V. Springel, C. S. Frenk, and S. D. M. White, "The large-scale structure of the Universe," Nature **440**, 1137–44 (2006).

[81] S. D. M. White, C. S. Frenk, and M. Davis, "Clustering in a neutrino-dominated universe," Astrophys. J. **274**, L1 (1983).

[82] J. R. Bond, G. Efstathiou, and J. Silk, "Massive Neutrinos and the Large-Scale Structure of the Universe," Phys. Rev. Lett. **45**, 1980–1984 (1980).

[83] P. A. Oesch *et al.*, "A Remarkably Luminous Galaxy At z = 11.1 Measured With Hubble Space Telescope Grism Spectroscopy," Astrophys. J. **819**, 129 (2016).

[84] J. Lesgourgues and S. Pastor, "Massive neutrinos and cosmology," Phys. Rep. **429**, 307–379 (2006).

[85] D. J. Eisenstein *et al.* (SDSS Collaboration), "Detection of the Baryon Acoustic Peak in the Large-Scale Correlation Function of SDSS Luminous Red Galaxies," Astrophys. J. **633**, 560–574 (2005).

[86] S. Cole *et al.* (2dFGRS Team), "The 2dF Galaxy Redshift Survey: power-spectrum analysis of the final data set and cosmological implications," Mon. Not. R. Astron. Soc. **362**, 505–534 (2005).

[87] A. Veropalumbo, F. Marulli, L. Moscardini, M. Moresco, and A. Cimatti, "Measuring the distanceredshift relation with the baryon acoustic oscillations of galaxy clusters," Mon. Not. R. Astron. Soc. **458**, 1909–1920 (2016).

[88] D. J. Eisenstein and W. Hu, "Baryonic Features in the Matter Transfer Function," Astrophys. J. **496**, 605–614 (1998).

[89] M. Taoso, G. Bertone, and A. Masiero, "Dark matter candidates: a ten-point test," J. Cosmol. Astropart. Phys. 2008 (2008) 022.

[90] L. Roszkowski, "Particle dark matter — A theorist's perspective," Pramana **62**, 389–401 (2004).

[91] J. L. Feng, "Dark Matter Candidates from Particle Physics and Methods of Detection," Annu. Rev. Astron. Astrophys. **48**, 495–545 (2010).

[92] H. Nilles, "Supersymmetry, supergravity and particle physics," Phys. Rep. **110**, 1–162 (1984).

[93] D. I. Kazakov, "Beyond the Standard Model (In Search of Supersymmetry)," arXiv:0012288 [hep-ph] .

[94] J. Ellis and K. Olive, "Supersymmetric dark matter candidates," in *Part. Dark Matter Obs. Model. Searches*, edited by G. Bertone (Cambridge University Press, New York, 2010) Chap. 8, pp. 142–163.

[95] G. Jungman, M. Kamionkowski, and K. Griest, "Supersymmetric dark matter," Phys. Rep. **267**, 195–373 (1996).

[96] J. Ellis, J. Hagelin, D. Nanopoulos, K. Olive, and M. Srednicki, "Supersymmetric relics from the big bang," Nucl. Phys. B **238**, 453–476 (1984).

[97] D. Abercrombie *et al.*, "Dark Matter Benchmark Models for Early LHC Run-2 Searches: Report of the ATLAS/CMS Dark Matter Forum," arXiv:1507.00966 .

[98] M. Maniatis, "The Next-To-Minimal Supersymmetric Extension Of The Standard Model Reviewed," Int. J. Mod. Phys. A **25**, 3505–3602 (2010).

[99] K. J. de Vries *et al.*, "The pMSSM10 after LHC run 1." Eur. Phys. journal. C, Part. fields **75**, 422 (2015).

[100] O. Buchmueller, R. Cavanaugh, A. D. Roeck, M. J. Dolan, J. R. Ellis, H. Flächer, S. Heinemeyer, G. Isidori, J. Marrouche, D. M. Santos, K. A. Olive, S. Rogerson, F. J. Ronga, K. J. de Vries, and G. Weiglein, "The CMSSM and NUHM1 after LHC Run 1." Eur. Phys. journal. C, Part. fields **74**, 2922 (2014).

[101] T. Kaluza, "Zum Unitätsproblem in der Physik," Sitzungsberichte Preuss. Akad. der Wissenschaften **69**, 966–972 (1921).

[102] O. Klein, "Quantentheorie und fünfdimensionale Relativitätstheorie," Zeitschrift für Phys. **37**, 895–906 (1926).

[103] K. R. Dienes, E. Dudas, and T. Gherghetta, "Extra spacetime dimensions and unification," Phys. Lett. B **436**, 55–65 (1998).

[104] N. ArkaniHamed, S. Dimopoulos, and G. Dvali, "The hierarchy problem and new dimensions at a millimeter," Phys. Lett. B **429**, 263–272 (1998); N. Arkani-Hamed, S. Dimopoulos, and G. Dvali, "Phenomenology, astrophysics, and cosmology of theories with submillimeter dimensions and TeV scale quantum gravity," Phys. Rev. D **59**, 086004 (1999).

[105] T. Appelquist, H.-C. Cheng, and B. A. Dobrescu, "Bounds on universal extra dimensions," Phys. Rev. D **64**, 035002 (2001).

[106] G. Servant and T. M. Tait, "Is the lightest Kaluza-Klein particle a viable dark matter candidate?" Nucl. Phys. B **650**, 391–419 (2003).

[107] A. Belyaev, M. Brown, J. M. Moreno, and C. Papineau, "Discovering Minimal Universal Extra Dimensions (MUED) at the LHC," J. High Energy Phys. 2013 (2013) 80.

[108] D. Hooper, N. Weiner, and W. Xue, "Dark forces and light dark matter," Phys. Rev. D **86**, 056009 (2012).

[109] R. Foot, "Hidden sector dark matter explains the DAMA, CoGeNT, CRESST-II and CDMS/Si experiments," Phys. Rev. D **88**, 025032 (2013).

[110] M. Pospelov, A. Ritz, and M. Voloshin, "Secluded WIMP dark matter," Phys. Lett. B **662**, 53–61 (2008).

[111] J. L. Feng and J. Kumar, "Dark-matter particles without weak-scale masses or weak interactions." Phys. Rev. Lett. **101**, 231301 (2008).

[112] J. Kumar, J. L. Feng, G. Alverson, P. Nath, and B. Nelson, "WIMPless Dark Matter," in *SUSY09 7th Int. Conf. Supersymmetry Unification ofFundamental Interact.*, Vol. 1200 (AIP Publishing, 2010) pp. 1059–1062.

[113] D. Kaplan, "Single explanation for both baryon and dark matter densities." Phys. Rev. Lett. **68**, 741–743 (1992).

[114] K. Petraki and R. R. Volkas, "Review Of Asymmetric Dark Matter," Int. J. Mod. Phys. A **28**, 1330028 (2013).

[115] K. M. Zurek, "Asymmetric Dark Matter: Theories, signatures, and constraints," Phys. Rep. **537**, 91–121 (2014).

[116] T. Cohen, D. J. Phalen, A. Pierce, and K. M. Zurek, "Asymmetric dark matter from a GeV hidden sector," Phys. Rev. D **82**, 056001 (2010).

[117] D. E. Kaplan, M. A. Luty, and K. M. Zurek, "Asymmetric dark matter," Phys. Rev. D **79**, 115016 (2009).

[118] R. Foot and R. R. Volkas, "Was ordinary matter synthesized from mirror matter? An attempt to explain why $\Omega_B \approx 0.2\Omega_{dark}$," Phys. Rev. D **68**, 021304 (2003); R. Foot, "Mirror dark matter and the new DAMA/LIBRA results: A simple explanation for a beautiful experiment," Phys. Rev. D **78**, 043529 (2008); R. Foot, "Mirror dark matter interpretations of the DAMA, CoGeNT, and CRESST-II data," Phys. Rev. D **86**, 023524 (2012).

[119] H.-C. Cheng and I. Low, "TeV symmetry and the little hierarchy problem," J. High Energy Phys. 2003 (2003) 051–051.

[120] D. E. Kaplan and M. Schmaltz, "The little Higgs from a simple group," J. High Energy Phys. 2003 (2003) 039–039.

[121] M. Schmaltz and D. Tucker-Smith, "Little Higgs Theories," Annu. Rev. Nucl. Part. Sci. **55**, 229–270 (2005).

[122] M. Schmaltz, D. Stolarski, and J. Thaler, "The bestest little Higgs," J. High Energy Phys. 2010 (2010) 18.

[123] H.-C. Cheng and I. Low, "Little Hierarchy, Little Higgses, and a Little Symmetry," J. High Energy Phys. 2004 (2004) 061–061.

[124] J. L. Feng, A. Rajaraman, and F. Takayama, "Superweakly interacting massive particle dark matter signals from the early Universe," Phys. Rev. D **68**, 063504 (2003).

[125] J. L. Feng, A. Rajaraman, and F. Takayama, "Superweakly interacting massive particles." Phys. Rev. Lett. **91**, 011302 (2003).

[126] J. Ellis, K. A. Olive, Y. Santoso, and V. C. Spanos, "Gravitino dark matter in the CMSSM," Phys. Lett. B **588**, 7–16 (2004).

[127] J. L. Feng, S. Su, and F. Takayama, "SuperWIMP gravitino dark matter from slepton and sneutrino decays," Phys. Rev. D **70**, 063514 (2004).

[128] J. L. Feng, A. Rajaraman, and F. Takayama, "Graviton cosmology in universal extra dimensions," Phys. Rev. D **68**, 085018 (2003).

[129] M. Pospelov, A. Ritz, and M. Voloshin, "Bosonic super-WIMPs as keV-scale dark matter," Phys. Rev. D **78**, 115012 (2008).

[130] Y. Bai, P. J. Fox, and R. Harnik, "The Tevatron at the frontier of dark matter direct detection," J. High Energy Phys. 2010 (2010) 48.

[131] V. Khachatryan *et al.* (CMS Collaboration), "Search for dark matter, extra dimensions, and unparticles in monojet events in proton-proton collisions at $\sqrt{s} = 8$ TeV," Eur. Phys. journal. C, Part. fields **75**, 235 (2015).

[132] G. Aad *et al.* (ATLAS Collaboration), "Search for new phenomena in final states with an energetic jet and large missing transverse momentum in pp collisions at

$\sqrt{s} = 8$ TeV with the ATLAS detector." Eur. Phys. journal. C, Part. fields **75**, 299 (2015).

[133] W. B. Atwood *et al.* (Fermi LAT Collaboration), "The Large Area Telescope On The Fermi Gamma-Ray Space Telescope Mission," Astrophys. J. **697**, 1071–1102 (2009).

[134] S. Funk, "Indirect detection of dark matter with γ rays." Proc. Natl. Acad. Sci. U. S. A. **112**, 12264–71 (2015).

[135] D. Hooper and L. Goodenough, "Dark matter annihilation in the Galactic Center as seen by the Fermi Gamma Ray Space Telescope," Phys. Lett. B **697**, 412–428 (2011).

[136] T. Daylan, D. P. Finkbeiner, D. Hooper, T. Linden, S. K. Portillo, N. L. Rodd, and T. R. Slatyer, "The characterization of the gamma-ray signal from the central Milky Way: A case for annihilating dark matter," Phys. Dark Universe **12**, 1–23 (2016).

[137] D. Hooper and T. R. Slatyer, "Two emission mechanisms in the Fermi Bubbles: A possible signal of annihilating dark matter," Phys. Dark Universe **2**, 118–138 (2013).

[138] C. Weniger, "A tentative gamma-ray line from Dark Matter annihilation at the Fermi Large Area Telescope," J. Cosmol. Astropart. Phys. 2012 (2012) 007–007.

[139] E. Tempel, A. Hektor, and M. Raidal, "Fermi 130 GeV gamma-ray excess and dark matter annihilation in sub-haloes and in the Galactic centre," J. Cosmol. Astropart. Phys. 2012 (2012) 032–032.

[140] C. Weniger, "Gamma-ray lines in the Fermi-LAT data?" arXiv:1303.1798 .

[141] M. Ackermann *et al.* (Fermi-LAT Collaboration), "Search for gamma-ray spectral lines with the Fermi Large Area Telescope and dark matter implications," Phys. Rev. D **88**, 082002 (2013).

[142] F. Halzen and D. Hooper, "High-energy Neutrinos from WIMP Annihilations in the Sun," in *Part. Dark Matter Obs. Model. Searches*, edited by G. Bertone (Cambridge University Press, New York, 2010) Chap. 25, pp. 507–520.

[143] M. G. Aartsen *et al.* (IceCube Collaboration), "Search for dark matter annihilations in the sun with the 79-string IceCube detector." Phys. Rev. Lett. **110**, 131302 (2013).

[144] K. Choi *et al.*, "Search for neutrinos from annihilation of captured low-mass dark matter particles in the sun by super-kamiokande." Phys. Rev. Lett. **114**, 141301 (2015).

[145] J. J. Beatty, A. Bhattacharyya, C. Bower, S. Coutu, M. A. Duvernois, S. McKee, S. A. Minnick, D. Müller, J. Musser, S. Nutter, A. W. Labrador, M. Schubnell, S. Swordy, G. Tarlé, and A. Tomasch, "New measurement of the cosmic-ray positron fraction from 5 to 15 GeV." Phys. Rev. Lett. **93**, 241102 (2004).

[146] O. Adriani *et al.*, "Cosmic-ray positron energy spectrum measured by PAMELA." Phys. Rev. Lett. **111**, 081102 (2013).

[147] L. Accardo *et al.*, "High statistics measurement of the positron fraction in primary cosmic rays of 0.5–500 GeV with the alpha magnetic spectrometer on the international space station." Phys. Rev. Lett. **113**, 121101 (2014).

[148] M. Boudaud, S. Aupetit, S. Caroff, A. Putze, G. Belanger, Y. Genolini, C. Goy, V. Poireau, V. Poulin, S. Rosier, P. Salati, L. Tao, and M. Vecchi, "A new look at the cosmic ray positron fraction," Astron. Astrophys. **575**, A67 (2015).

[149] A. López, C. Savage, D. Spolyar, and D. Q. Adams, "Fermi/LAT observations of dwarf galaxies highly constrain a dark matter interpretation of excess positrons seen in AMS-02, HEAT, and PAMELA," J. Cosmol. Astropart. Phys. 2016 (2016) 033–033.

[150] M. H. Chan, "Indirect constraints on the dark matter interpretation of excess positrons seen by AMS-02," Phys. Rev. D **92**, 083504 (2015).

[151] D. Hooper, P. Blasi, and P. D. Serpico, "Pulsars as the sources of high energy cosmic ray positrons," J. Cosmol. Astropart. Phys. 2009 (2009) 025–025.

[152] M. D. Mauro, F. Donato, N. Fornengo, R. Lineros, and A. Vittino, "Interpretation of AMS-02 electrons and positrons data," J. Cosmol. Astropart. Phys. 2014 (2014) 006–006.

[153] M. Milgrom, "A modification of the Newtonian dynamics as a possible alternative to the hidden mass hypothesis," Astrophys. J. **270**, 365 (1983).

[154] R. H. Sanders and E. Noordermeer, "Confrontation of MOdified Newtonian Dynamics with the rotation curves of early-type disc galaxies," Mon. Not. R. Astron. Soc. **379**, 702–710 (2007).

[155] J. D. Bekenstein, "Relativistic gravitation theory for the modified Newtonian dynamics paradigm," Phys. Rev. D **70**, 083509 (2004).

[156] J. Bekenstein and M. Milgrom, "Does the missing mass problem signal the breakdown of Newtonian gravity?" Astrophys. J. **286**, 7 (1984).

[157] G. W. Angus, B. Famaey, and D. A. Buote, "X-ray group and cluster mass profiles in MOND: unexplained mass on the group scale," Mon. Not. R. Astron. Soc. **387**, 1470–1480 (2008).

[158] G. W. Angus, B. Famaey, and H. S. Zhao, "Can MOND take a bullet? Analytical comparisons of three versions of MOND beyond spherical symmetry," Mon. Not. R. Astron. Soc. **371**, 138–146 (2006).

[159] M. Feix, C. Fedeli, and M. Bartelmann, "Asymmetric gravitational lenses in TeVeS and application to the bullet cluster," Astron. Astrophys. **480**, 313–325 (2008).

[160] K. Griest, "Galactic microlensing as a method of detecting massive compact halo objects," Astrophys. J. **366**, 412 (1991).

[161] B. Paczynski, "Gravitational microlensing by the galactic halo," Astrophys. J. **304**, 1 (1986).

[162] C. Alcock *et al.* (MACHO Collaboration), "The MACHO Project: Microlensing Results from 5.7 Years of Large Magellanic Cloud Observations," Astrophys. J. **542**, 281–307 (2000).

[163] P. Tisserand *et al.* (EROS-2 Collaboration), "Limits on the Macho content of the Galactic Halo from the EROS-2 Survey of the Magellanic Clouds," Astron. Astrophys. **469**, 387–404 (2007).

[164] C.-H. Lee, A. Riffeser, S. Seitz, R. Bender, and J. Koppenhoefer, "Microlensing Events From The 11 Year Observations Of The Wendelstein Calar Alto Pixellensing Project," Astrophys. J. **806**, 161 (2015).

[165] D. G. Koch *et al.*, "Kepler Mission Design, Realized Photometric Performance, And Early Science," Astrophys. J. **713**, L79–L86 (2010).

[166] K. Griest, A. M. Cieplak, and M. J. Lehner, "New limits on primordial black hole dark matter from an analysis of Kepler source microlensing data." Phys. Rev. Lett. **111**, 181302 (2013).

[167] K. N. Abazajian *et al.*, "Light Sterile Neutrinos: A White Paper," arXiv:1204.5379 .

[168] S. Dodelson and L. Widrow, "Sterile neutrinos as dark matter." Phys. Rev. Lett. **72**, 17–20 (1994).

[169] T. Asaka, S. Blanchet, and M. Shaposhnikov, "The νMSM, dark matter and neutrino masses," Phys. Lett. B **631**, 151–156 (2005).

[170] A. Boyarsky, O. Ruchayskiy, and M. Shaposhnikov, "The Role of Sterile Neutrinos in Cosmology and Astrophysics," Annu. Rev. Nucl. Part. Sci. **59**, 191–214 (2009).

[171] A. Dolgov, "Massive sterile neutrinos as warm dark matter," Astropart. Phys. **16**, 339–344 (2002).

[172] K. C. Ng, S. Horiuchi, J. M. Gaskins, M. Smith, and R. Preece, "Improved limits on sterile neutrino dark matter using full-sky Fermi Gamma-ray Burst Monitor data," Phys. Rev. D **92**, 043503 (2015).

[173] C. A. Baker, D. D. Doyle, P. Geltenbort, K. Green, M. G. D. van der Grinten, P. G. Harris, P. Iaydjiev, S. N. Ivanov, D. J. R. May, J. M. Pendlebury, J. D. Richardson, D. Shiers, and K. F. Smith, "Improved experimental limit on the electric dipole moment of the neutron." Phys. Rev. Lett. **97**, 131801 (2006).

[174] R. D. Peccei and H. R. Quinn, "Constraints imposed by CP conservation in the presence of pseudoparticles," Phys. Rev. D **16**, 1791–1797 (1977).

[175] R. D. Peccei and H. R. Quinn, "CP Conservation in the Presence of Pseudoparticles," Phys. Rev. Lett. **38**, 1440–1443 (1977).

[176] S. Weinberg, "A New Light Boson?" Phys. Rev. Lett. **40**, 223–226 (1978).

[177] F. Wilczek, "Problem of Strong P and T Invariance in the Presence of Instantons," Phys. Rev. Lett. **40**, 279–282 (1978).

[178] P. Sikivie, "Axions," in *Part. Dark Matter Obs. Model. Searches*, edited by G. Bertone (Cambridge University Press, New York, 2010) Chap. 11, pp. 204–227.

[179] G. Raffelt, "Stellar-evolution limits on axion properties," Nucl. Phys. B - Proc. Suppl. **72**, 43–53 (1999).

[180] P. Sikivie, "Axion Cosmology," in *Axions Theory, Cosmol. Exp. Searches*, Lecture Notes in Physics, Vol. 741, edited by M. Kuster, G. Raffelt, and B. Beltrán (Springer Berlin Heidelberg, Berlin, Heidelberg, 2008) Chap. 2, pp. 19–50.

[181] E. Aprile *et al.* (XENON100 Collaboration), "First axion results from the XENON100 experiment," Phys. Rev. D **90**, 062009 (2014).

[182] M. Archidiacono, T. Basse, J. Hamann, S. Hannestad, G. Raffelt, and Y. Y. Wong, "Future cosmological sensitivity for hot dark matter axions," J. Cosmol. Astropart. Phys. 2015 (2015) 050–050.

[183] P. Gondolo and G. Gelmini, "Compatibility of DAMA dark matter detection with other searches," Phys. Rev. D **71**, 123520 (2005).

[184] J. Lewin and P. Smith, "Review of mathematics, numerical factors, and corrections for dark matter experiments based on elastic nuclear recoil," Astropart. Phys. **6**, 87–112 (1996).

[185] F. Donato, N. Fornengo, and S. Scopel, "Effects of galactic dark halo rotation on WIMP direct detection," Astropart. Phys. **9**, 247–260 (1998).

[186] A. Kurylov and M. Kamionkowski, "Generalized analysis of the direct weakly interacting massive particle searches," Phys. Rev. D **69**, 063503 (2004).

[187] K. Schneck *et al.* (SuperCDMS Collaboration), "Dark matter effective field theory scattering in direct detection experiments," Phys. Rev. D **91**, 092004 (2015).

[188] R. Catena and P. Gondolo, "Global fits of the dark matter-nucleon effective interactions," J. Cosmol. Astropart. Phys. 2014 (2014) 045–045.

[189] N. Anand, A. L. Fitzpatrick, and W. C. Haxton, "Weakly interacting massive particle-nucleus elastic scattering response," Phys. Rev. C **89**, 065501 (2014).

[190] A. L. Fitzpatrick, W. Haxton, E. Katz, N. Lubbers, and Y. Xu, "The effective field theory of dark matter direct detection," J. Cosmol. Astropart. Phys. 2013 (2013) 004–004.

[191] D. G. Cerdeño and A. M. Green, "Direct Detection of WIMPs," in *Part. Dark Matter Obs. Model. Searches*, edited by G. Bertone (Cambridge University Press, New York, 2010) Chap. 17, pp. 347–569.

[192] G. Bertone, D. Hooper, and J. Silk, "Particle dark matter: evidence, candidates and constraints," Phys. Rep. **405**, 279–390 (2005).

[193] V. Barger, W.-Y. Keung, and G. Shaughnessy, "Spin dependence of dark matter scattering," Phys. Rev. D **78**, 056007 (2008).

[194] G. Duda, A. Kemper, and P. Gondolo, "Model-independent form factors for spin-independent neutralino-nucleon scattering from elastic electron scattering data," J. Cosmol. Astropart. Phys. 2007 (2007) 012–012.

[195] R. H. Helm, "Inelastic and Elastic Scattering of 187-Mev Electrons from Selected Even-Even Nuclei," Phys. Rev. **104**, 1466–1475 (1956).

[196] J. Engel, "Nuclear form factors for the scattering of weakly interacting massive particles," Phys. Lett. B **264**, 114–119 (1991).

[197] J. Engel, S. Pittel, and P. Vogel, "Nuclear Physics Of Dark Matter Detection," Int. J. Mod. Phys. E **01**, 1–37 (1992).

[198] P. Klos, J. Menéndez, D. Gazit, and A. Schwenk, "Large-scale nuclear structure calculations for spin-dependent WIMP scattering with chiral effective field theory currents," Phys. Rev. D **88**, 083516 (2013).

[199] D. S. Akerib *et al.* (CDMS Collaboration), "Limits on spin-dependent WIMP-nucleon interactions from the Cryogenic Dark Matter Search," Phys. Rev. D **73**, 011102 (2006).

[200] V. I. Dimitrov, J. Engel, and S. Pittel, "Scattering of weakly interacting massive particles from ^{73}Ge," Phys. Rev. D **51**, R291–R295 (1995).

[201] M. Ressell and D. Dean, "Spin-dependent neutralino-nucleus scattering for A¿127 nuclei," Phys. Rev. C **56**, 535–546 (1997).

[202] M. T. Ressell, M. B. Aufderheide, S. D. Bloom, K. Griest, G. J. Mathews, and D. A. Resler, "Nuclear shell model calculations of neutralino-nucleus cross sections for ^{29}Si and ^{73}Ge," Phys. Rev. D **48**, 5519–5535 (1993).

[203] J. Filippini, *A Search for WIMP Dark Matter Using the First Five-Tower Run of the Cryogenic Dark Matter Search*, Ph.D. thesis, Univeristy of California, Berkeley (2008).

[204] J. Binney and S. Tremaine, *Galactic Dynamics*, 2nd ed. (Princeton University Press, Princeton, 2008).

[205] S. Arrenberg, *Searching for Dark Matter with the Cryogenic Dark Matter Search Experiment*, Ph.D. thesis, Universititat Zurich (2011).

[206] C. Savage, K. Freese, and P. Gondolo, "Annual modulation of dark matter in the presence of streams," Phys. Rev. D **74**, 043531 (2006).

[207] A. M. Green, "Astrophysical Uncertainties On Direct Detection Experiments," Mod. Phys. Lett. A **27**, 1230004 (2012).

[208] C. McCabe, "Astrophysical uncertainties of dark matter direct detection experiments," Phys. Rev. D **82**, 023530 (2010).

[209] D.-M. Mei and A. Hime, "Muon-induced background study for underground laboratories," Phys. Rev. D **73**, 053004 (2006).

[210] D. N. Spergel, "Motion of the Earth and the detection of weakly interacting massive particles," Phys. Rev. D **37**, 1353–1355 (1988).

[211] C. J. Copi and L. M. Krauss, "Angular signatures for galactic halo weakly interacting massive particle scattering in direct detectors: Prospects and challenges," Phys. Rev. D **63**, 043507 (2001).

[212] T. Saab, "An Introduction to Dark Matter Direct Detection Searches & Techniques," arXiv:1203.2566 .

[213] P. Cushman, "WIMP Direct Detection Searches," in *Slac Summer Inst. 2014 Shining Light Dark Matter* (2014).

[214] R. J. Gaitskell, P. D. Barnes, A. DaSilva, B. Sadoulet, and T. Shutt, "The statistics of background rejection in direct detection experiments for dark matter," Nucl. Phys. B - Proc. Suppl. **51**, 279–283 (1996).

[215] P. Cushman *et al.*, "Snowmass CF1 Summary: WIMP Dark Matter Direct Detection," arXiv:1310.8327 .

[216] D. S. Akerib *et al.* (LUX Collaboration), "First Results from the LUX Dark Matter Experiment at the Sanford Underground Research Facility," Phys. Rev. Lett. **112**, 091303 (2014).

[217] D. S. Akerib *et al.* (LUX Collaboration), "Results on the Spin-Dependent Scattering of Weakly Interacting Massive Particles on Nucleons from the Run 3 Data of the LUX Experiment," Phys. Rev. Lett. **116**, 161302 (2016).

[218] E. Aprile *et al.* (XENON100 Collaboration), "Dark Matter Results from 225 Live Days of XENON100 Data," Phys. Rev. Lett. **109**, 181301 (2012).

[219] X. Xiao *et al.* (PandaX Collaboration), "Low-mass dark matter search results from full exposure of the PandaX-I experiment," Phys. Rev. D **92**, 052004 (2015).

[220] D. Akimov *et al.*, "WIMP-nucleon cross-section results from the second science run of ZEPLIN-III," (2012).

[221] P. Agnes *et al.* (DarkSide Collaboration), "Results from the first use of low radioactivity argon in a dark matter search," Phys. Rev. D **93**, 081101 (2016).

[222] P. Agnes *et al.* (DarkSide Collaboration), "First results from the DarkSide-50 dark matter experiment at Laboratori Nazionali del Gran Sasso," Phys. Lett. B **743**, 456–466 (2015).

[223] Z. Ahmed *et al.* (CDMS Collaboration), "Dark matter search results from the CDMS II experiment," Science **327**, 1619–21 (2010).

[224] R. Agnese *et al.* (SuperCDMS Collabration), "Improved WIMP-search reach of the CDMS II germanium data," Phys. Rev. D **92**, 072003 (2015).

[225] P. Loaiza, "Latest Results of the Edelweiss-II Dark Matter Search Experiment," in *AIP Conf. Proc.* (2011) pp. 126–129.

[226] E. Behnke *et al.* (COUPP Collaboration), "First dark matter search results from a 4-kg CF$_3$I bubble chamber operated in a deep underground site," Phys. Rev. D **86**, 052001 (2012).

[227] S. Archambault *et al.* (PICASSO Collaboration), "Constraints on low-mass WIMP interactions on ^{19}F from PICASSO," Phys. Lett. B **711**, 153–161 (2012).

[228] C. Amole *et al.* (PICO Collaboration), "Dark Matter Search Results from the PICO-2L C$_3$F$_8$ Bubble Chamber," Phys. Rev. Lett. **114**, 231302 (2015).

[229] C. Amole *et al.* (PICO Collaboration), "Improved dark matter search results from PICO-2L Run 2," Phys. Rev. D **93**, 061101 (2016).

[230] C. Amole *et al.* (PICO Collaboration), "Dark matter search results from the PICO-60 CF$_3$I bubble chamber," Phys. Rev. D **93**, 052014 (2016).

[231] M. Felizardo *et al.* (SIMPLE Collaboration), "Final Analysis and Results of the Phase II SIMPLE Dark Matter Search," Phys. Rev. Lett. **108**, 201302 (2012).

[232] G. Angloher *et al.* (CRESST Collaboration), "Results from 730 kg days of the CRESST-II Dark Matter search," Eur. Phys. J. C **72**, 1971 (2012).

[233] R. Agnese *et al.* (CDMS Collaboration), "Silicon Detector Dark Matter Results from the Final Exposure of CDMS II," Phys. Rev. Lett. **111**, 251301 (2013).

[234] C. E. Aalseth, P. S. Barbeau, J. Colaresi, J. I. Collar, J. Diaz Leon, J. E. Fast, N. E. Fields, T. W. Hossbach, A. Knecht, M. S. Kos, M. G. Marino, H. S. Miley, M. L. Miller, J. L. Orrell, and K. M. Yocum (CoGeNT Collaboration), "CoGeNT: A search for low-mass dark matter using p -type point contact germanium detectors," Phys. Rev. D **88**, 012002 (2013).

[235] C. Savage, G. Gelmini, P. Gondolo, and K. Freese, "Compatibility of DAMA/LIBRA dark matter detection with other searches," J. Cosmol. Astropart. Phys. 2009 (2009) 010–010.

[236] R. Bernabei *et al.* (DAMA/LIBRA Collaboration), "New results from DAMA/LIBRA," Eur. Phys. J. C **67**, 39–49 (2010).

[237] E. Aprile *et al.* (XENON100 Collaboration), "Search for Event Rate Modulation in XENON100 Electronic Recoil Data." Phys. Rev. Lett. **115**, 091302 (2015).

[238] E. Barbosa de Souza *et al.* (DM-Ice Collaboration), "First Search for a Dark Matter Annual Modulation Signal with NaI(Tl) in the Southern Hemisphere by DM-Ice17," arXiv:1602.05939 .

[239] H. S. Lee *et al.* (KIMS Collaboration), "Search for low-mass dark matter with CsI(Tl) crystal detectors," Phys. Rev. D **90**, 052006 (2014).

[240] C. Savage, P. Gondolo, and K. Freese, "Can WIMP spin dependent couplings explain DAMA data, in light of null results from other experiments?" Phys. Rev. D **70**, 123513 (2004).

[241] J. Klinger and V. Kudryavtsev, "Muon-Induced Neutrons Do Not Explain the DAMA Data," Phys. Rev. Lett. **114**, 151301 (2015).

[242] R. Bernabei *et al.* (DAMA/LIBRA Collaboration), "Final model independent result of DAMA/LIBRA-phase1," Eur. Phys. J. C **73**, 2648 (2013).

[243] D. S. Akerib *et al.* (CDMS Collaboration), "Low-threshold analysis of CDMS shallow-site data," Phys. Rev. D **82**, 122004 (2010).

[244] Z. Ahmed *et al.* (CDMS Collaboration), "Results from a Low-Energy Analysis of the CDMS II Germanium Data," Phys. Rev. Lett. **106**, 131302 (2011).

[245] R. Agnese *et al.* (SuperCDMS Collaboration), "Search for Low-Mass Weakly Interacting Massive Particles with SuperCDMS," Phys. Rev. Lett. **112**, 241302 (2014).

[246] R. Agnese *et al.* (SuperCDMS Collaboration), "Maximum likelihood analysis of low energy CDMS II germanium data," Phys. Rev. D **91**, 052021 (2015).

[247] E. Armengaud *et al.* (EDELWEISS Collaboration), "Search for low-mass WIMPs with EDELWEISS-II heat-and-ionization detectors," Phys. Rev. D **86**, 051701 (2012).

[248] E. Armengaud *et al.* (EDELWEISS Collabaration), "Constraints on low-mass WIMPs from the EDELWEISS-III dark matter search," J. Cosmol. Astropart. Phys. 2016 (2016) 019–019.

[249] J. Angle *et al.* (XENON10 Collaboration), "Search for Light Dark Matter in XENON10 Data," Phys. Rev. Lett. **107**, 051301 (2011).

[250] J. Angle (XENON10 Collaboration), "Erratum: Search for Light Dark Matter in XENON10 Data [Phys. Rev. Lett. 107 , 051301 (2011)]," Phys. Rev. Lett. **110**, 249901 (2013).

[251] E. Aprile *et al.* (XENON100 Collaboration), "A low-mass dark matter search using ionization signals in XENON100," arXiv:1605.06262 .

[252] K. Abe *et al.* (XMass Collaboration), "Light WIMP search in XMASS," Phys. Lett. B **719**, 78–82 (2013).

[253] K. Kobayashi, X. Collaboration, B. R. et Al, S. Y, A. K. et Al, A. K. et Al, A. K. et Al, U. H. et Al, A. K. et Al, and A. K. et Al (XMASS Collaboration), "Direct dark matter search with XMASS: modulation analysis," J. Phys. Conf. Ser. **718**, 042032 (2016).

[254] W. Zhao *et al.* (CDEX Collaboration), "First results on low-mass WIMPs from the CDEX-1 experiment at the China Jinping underground laboratory," Phys. Rev. D **88**, 052004 (2013).

[255] Q. Yue *et al.* (CDEX Collaboration), "Limits on light weakly interacting massive particles from the CDEX-1 experiment with a p-type point-contact germanium detector at the China Jinping Underground Laboratory," Phys. Rev. D **90**, 091701 (2014).

[256] H. B. Li *et al.* (TEXONO Collaboration), "Limits on Spin-Independent Couplings of WIMP Dark Matter with a p -Type Point-Contact Germanium Detector," Phys. Rev. Lett. **110**, 261301 (2013).

[257] J. Barreto, H. Cease, H. Diehl, J. Estrada, B. Flaugher, N. Harrison, J. Jones, B. Kilminster, J. Molina, J. Smith, T. Schwarz, and A. Sonnenschein (DAMIC Collaboration), "Direct search for low mass dark matter particles with CCDs," Phys. Lett. B **711**, 264–269 (2012).

[258] G. Angloher *et al.* (CRESST Collaboration), "Results on light dark matter particles with a low-threshold CRESST-II detector," Eur. Phys. J. C **76**, 25 (2016).

[259] G. Angloher *et al.* (CRESST Collaboration), "Results on low mass WIMPs using an upgraded CRESST-II detector," Eur. Phys. J. C **74**, 3184 (2014).

[260] R. Agnese *et al.* (SuperCDMS Collaboration), "Search for Low-Mass Weakly Interacting Massive Particles Using Voltage-Assisted Calorimetric Ionization Detection in the SuperCDMS Experiment," Phys. Rev. Lett. **112**, 041302 (2014).

[261] C. Kittel, *Solid State Phys.*, 8th ed. (John Wiley & Sons, Inc., 2005) p. 703.

[262] F. E. Emery and T. A. Rabson, "Average Energy Expended Per Ionized Electron-Hole Pair in Silicon and Germanium as a Function of Temperature," Phys. Rev. **140**, A2089–A2093 (1965).

[263] R. Pehl, F. Goulding, D. Landis, and M. Lenzlinger, "Accurate determination of the ionization energy in semiconductor detectors," Nucl. Instruments Methods **59**, 45–55 (1968).

[264] K. M. Sundqvist, *Carrier Transport and Related Effects in Detectors of the Cryogenic Dark Matter Search*, Ph.D. thesis, University of California, Berkeley (2012).

[265] B. Cabrera, M. Pyle, R. Moffatt, K. Sundqvist, and B. Sadoulet, "Oblique propagation of electrons in crystals of germanium and silicon at sub-Kelvin temperature in low electric fields," arXiv:1004.1233 .

[266] Z. He, "Review of the Shockley-Ramo theorem and its application in semiconductor gamma-ray detectors," Nucl. Instruments Methods Phys. Res. Sect. A **463**, 250–267 (2001).

[267] D. Abrams *et al.* (CDMS Collaboration), "Exclusion limits on the WIMP-nucleon cross section from the Cryogenic Dark Matter Search," Phys. Rev. D **66**, 122003 (2002).

[268] A. Phipps, *Ionization Collection in Detectors of the Cryogenic Dark Matter Search*, Ph.D. thesis, University of California, Berkeley (2016).

[269] R. M. Clarke, *An Athermal-Phonon-Mediated Dark Matter Detector with Surface Discrimination*, Ph.D. thesis, Stanford University (1999).

[270] V. Mandic, *First Results from the Cryogenic Dark Matter Search Experiment at the Deep Site*, Ph.D. thesis, University of California, Berkeley (2004).

[271] B. Neganov and V. Trofimov, "Calorimetric method measuring ionizing radiation," Otkrytia i Izobret. **146**, 215 (1985).

[272] P. N. Luke, "Voltage-assisted calorimetric ionization detector," J. Appl. Phys. **64**, 6858 (1988).

[273] G. Wang, "Phonon emission in germanium and silicon by electrons and holes in applied electric field at low temperature," J. Appl. Phys. **107**, 094504 (2010).

[274] S. W. Leman, "Invited review article: physics and Monte Carlo techniques as relevant to cryogenic, phonon, and ionization readout of Cryogenic Dark Matter Search radiation detectors." Rev. Sci. Instrum. **83**, 091101 (2012).

[275] R. Basu Thakur, *The Cryogenic Dark Matter Search Low Ionization-Threshold Experiment*, Ph.D. thesis, University of Illinois, Urbana-Champaign (2015).

[276] N. E. Booth, "Quasiparticle trapping and the quasiparticle multiplier," Appl. Phys. Lett. **50**, 293 (1987).

[277] S. A. Hertel, *Advancing the Search for Dark Matter: from CDMS II to SuperCDMS*, Ph.D. thesis, Massachusetts Institute of Technology (2012).

[278] D. S. Akerib *et al.*, "Design and performance of a modular low-radioactivity readout system for cryogenic detectors in the CDMS experiment," Nucl. Instruments Methods Phys. Res. Sect. A **591**, 476–489 (2008).

[279] R. Agnese *et al.* (SuperCDMS Collaboration), "Demonstration of surface electron rejection with interleaved germanium detectors for dark matter searches," Appl. Phys. Lett. **103**, 164105 (2013).

[280] D. S. Akerib *et al.* (CDMS Collaboration), "Exclusion limits on the WIMP-nucleon cross section from the first run of the Cryogenic Dark Matter Search in the Soudan Underground Laboratory," Phys. Rev. D **72**, 052009 (2005).

[281] T. Hofer, *Development of CDMS-II Surface Event Rejection Techniques and Their Extensions to Lower Energy Thresholds*, Ph.D. thesis, University of Minnesota, Twin Cities (2014).

[282] U. Schötzig, K. Debertin, and K. Walz, "Standardization and decay data of 133Ba," Int. J. Appl. Radiat. Isot. **28**, 503–507 (1977).

[283] M. Divadeenam and J. Stehn, "A least-squares fit of thermal data for fissile nuclei," Ann. Nucl. Energy **11**, 375–404 (1984).

[284] D. Bauer *et al.*, "The CDMS II Data Acquisition System," Nucl. Instruments Methods Phys. Res. Sect. A **638**, 127–133 (2011).

[285] Z. Ahmed, *A Dark-Matter Search Using The Final CDMS II Dataset And A Novel Detector Of Surface Radiocontamination*, Ph.D. thesis, California Institude of Technology (2012).

[286] A. Kennedy, "K100 Run 54 Relative Calibration: Long Time Frame," UMN Intern. Detect. Test. Facil. Data Anal. Eb., 18 (2015).

[287] R. Agnese *et al.* (CDMS Collaboration), "Silicon detector results from the first five-tower run of CDMS II," Phys. Rev. D **88**, 031104 (2013).

[288] G. Heusser, "Low-Radioactivity Background Techniques," Annu. Rev. Nucl. Part. Sci. **45**, 543–590 (1995).

[289] S. B. Samat, S. Green, and A. H. Beddoe, "The activity of one gram of potassium," Phys. Med. Biol. **42**, 407–413 (1997).

[290] J. A. Formaggio and C. Martoff, "Backgrounds To Sensitive Experiments Underground," Annu. Rev. Nucl. Part. Sci. **54**, 361–412 (2004).

[291] R. Bonetti, C. Chiesa, A. Guglielmetti, R. Matheoud, G. Poli, V. L. Mikheev, and S. P. Tretyakova, "First observation of spontaneous fission and search for cluster decay of ^{232}Th," Phys. Rev. C **51**, 2530–2533 (1995).

[292] A. Sonzogni, "Nudat 2," (2016).

[293] G. Audi, M. Wang, A. Wapstra, F. Kondev, M. MacCormick, X. Xu, and B. Pfeiffer, "The Ame2012 atomic mass evaluation (1)," Chinese Phys. C **36**, 1287–1602 (2012); M. Wang, G. Audi, A. Wapstra, F. Kondev, M. MacCormick, X. Xu, and B. Pfeiffer, "The Ame2012 atomic mass evaluation (II)," Chinese Phys. C **36**, 1603–2014 (2012); B. Pritychenko and A. Sonzongni, "Q-value Calculator (QCalc)," (2012).

[294] W. B. Wilson, R. T. Perry, E. F. Shores, W. S. Charlton, T. A. Parish, G. P. Estes, T. H. Brown, E. D. Arthur, M. Bozoian, T. R. England, D. G. Madland,

and J. E. Stewart, *SOURCES 4C : a code for calculating (α,n), spontaneous fission, and delayed neutron sources and spectra.*, Tech. Rep. (Los Alamos National Laboratory, Los Alamos, NM, 2002); W. B. Wilson, R. T. Perry, W. S. Charlton, T. A. Parish, and E. F. Shores, "SOURCES: a code for calculating (α,n), spontaneous fission, and delayed neutron sources and spectra," Radiat. Prot. Dosimetry **115**, 117–121 (2005).

[295] S. Scorza, "SOURCES4 radiogenic neutron calculations - UPDATE," CDMS Intern. Backgrounds Eb., 219 (2013); S. Scorza, "sources4report," CDMS Intern. Backgrounds Eb., 202–a (2011).

[296] S. Agostinelli *et al.*, "Geant4a simulation toolkit," Nucl. Instruments Methods Phys. Res. Sect. A **506**, 250–303 (2003).

[297] J. Allison *et al.*, "Geant4 developments and applications," IEEE Trans. Nucl. Sci. **53**, 270 (2006).

[298] P. Bossew, "A very long-term HPGe-background gamma spectrum," Appl. Radiat. Isot. **62**, 635–644 (2005).

[299] J. Zhang, *A Dark Matter Search Using the Final CDMS-II Data and 100 mm SuperCDMS Germanium Detector Ionization Test*, Ph.D. thesis, University of Minnesota, Twin Cities (2014).

[300] J. Kiveni, *A Search for WIMP Dark Matter using an Optimized Chi-square Technique on the Final Data from the Cryogenic Dark Matter Search Experiment (CDMS II)*, Ph.D. thesis, Syracuse University (2012).

[301] M. Fritts, *Background Characterization and Discrimination in the Final Analysis of the CDMS II Phase of the Cryogenic Dark Matter Search*, Ph.D. thesis, University of Minnesota, Twin Cities (2011).

[302] D. Moore, "Low Threshold Analysis Cuts and Efficiencies," CDMS Intern. Run 123 Anal. Eb. (2009).

[303] M. Johnson, "Qinner analysis with new percentage cut," UMN Intern. Misc. Eb. (2010).

[304] T. Bruch, "Comparison of Run 123 gamma spectra with MC simulation," CDMS Intern. Backgrounds Eb., 171 (2008).

[305] S. M. Fallows, *Measurement of Nuclear Recoils in the CDMS II Dark Matter Search*, Ph.D. thesis, University of Minnesota, Twin Cities (2014).

[306] Canberra Industries Inc., "Extended Range Coaxial Ge Detectors (XtRa)," (2013).

[307] R. W. Schnee, M. A. Bowles, R. Bunker, K. McCabe, J. White, P. Cushman, M. Pepin, and V. E. Guiseppe, "Removal of long-lived ^{222}Rn daughters by electropolishing thin layers of stainless steel," (2013) pp. 128–131.

[308] G. J. Feldman and R. D. Cousins, "Unified approach to the classical statistical analysis of small signals," Phys. Rev. D **57**, 3873–3889 (1998).

[309] W. A. Rolke, A. M. López, and J. Conrad, "Limits and confidence intervals in the presence of nuisance parameters," Nucl. Instruments Methods Phys. Res. Sect. A **551**, 493–503 (2005).

[310] B. Hamermesh, G. R. Ringo, and S. Wexler, "The Thermal Neutron Capture Cross Section of Hydrogen," Phys. Rev. **90**, 603–606 (1953).

[311] M. Delfini, J. Kopecky, R. Chrien, H. Liou, and P. Endt, "Study of the 65Cu(n, γ)66Cu reaction," Nucl. Phys. A **404**, 250–268 (1983).

[312] M. Delfini, J. Kopecky, J. De Haas, H. Liou, R. Chrien, and P. Endt, "Study of the 63Cu(n, γ)64Cu reaction," Nucl. Phys. A **404**, 225–249 (1983).

[313] P. Luke, J. Beeman, F. Goulding, S. Labov, and E. Silver, "Calorimetric ionization detector," Nucl. Instruments Methods Phys. Res. Sect. A **289**, 406–409 (1990).

[314] D. Akerib, M. Dragowsky, D. Driscoll, S. Kamat, T. Perera, R. Schnee, G. Wang, R. Gaitskell, L. Bogdanova, and V. Trofimov, "Demonstration of feasibility of operating a silicon ZIP detector with 20 eV threshold," Nucl. Instruments Methods Phys. Res. Sect. A **520**, 163–166 (2004).

[315] J. Hall, "CDMSlite: First Results," CDMS Intern. Run 125-128 Anal. Eb., 10 (2008).

[316] R. Basu Thakur, "First note on feasibility of CDMSlite with iZIPs: Runs from UCB TF," CDMS Intern. Run 130 Anal. Eb. (2011).

[317] R. Basu Thakur, "CDMSlite STUDY: T3Z2 (G25) Detector with 40 Volts bias," CDMS Intern. Run 130 Anal. Eb. (2011).

[318] R. Bernabei, P. Belli, F. Cappella, R. Cerulli, C. J. Dai, A. D'Angelo, H. L. He, A. Incicchitti, H. H. Kuang, J. M. Ma, F. Montecchia, F. Nozzoli, D. Prosperi, X. D. Sheng, and Z. P. Ye (DAMA/LIBRA Collaboration), "First results from DAMA/LIBRA and the combined results with DAMA/NaI," Eur. Phys. J. C **56**, 333–355 (2008).

[319] R. Basu Thakur, "Transducer work," CDMS Oper. E-LOG, 683 (2013).

[320] A. Phipps, "Spare Digitizer Channel to Batviewer Mapping and Input Impedances," CDMS Oper. E-LOG, 738 (2014).

[321] A. Phipps, "New Vibration Transducer Settings/General CDMS Acoustic Receiver Notes," CDMS Oper. E-LOG, 742 (2014).

[322] D. Bauer and A. Phipps, "Activities for Jan 31," CDMS Oper. E-LOG, 744 (2014).

[323] JANIS Company, "Differences between pulse tube and Gifford-McMahon cryocoolers," (2015).

[324] R. Basu Thakur, *Transducer box # 2, circuit diagram*, Tech. Rep. (FNAL, Batavia, IL, 2014).

[325] M. Huber and Y. Chen, "Activities Jun 28-29," CDMS Oper. E-LOG, 830 (2014).

[326] W. Hampel and L. P. Remsberg, "Half-life of ^{71}Ge," Phys. Rev. C **31**, 666–667 (1985).

[327] A. Phipps, B. Sadoulet, and K. M. Sundqvist, "Observation of Impact Ionization of Shallow States in sub-Kelvin, High Purity Germanium," in *LTD-16 Proc.* (Journal of Low Temperature Physics, 2015).

[328] R. Basu Thakur and Y. Ricci, "CDMSlite - Run 1 revision," CDMS Intern. Run 133-135 Anal. Eb., 10–lite2 (2014).

[329] W. Rau, "Optimizing Energy Resolution for CDMSlite Run 2," CDMS Intern. Run 133-135 Anal. Eb., 48–lite2 (2015).

[330] A. J. Anderson, *A Search for Light Weakly-Interacting Massive Particles with SuperCDMS and Applications to Neutrino Physics by*, Ph.D. thesis, Massachusetts Institute of Technology (2015).

[331] D. Michael *et al.* (MINOS Collaboration), "The magnetized steel and scintillator calorimeters of the MINOS experiment," Nucl. Instruments Methods Phys. Res. Sect. A **596**, 190–228 (2008).

[332] J. Morales, "NuMI Cut R134," CDMS Intern. Run 133-135 Anal. Eb., 278 (2015).

[333] D. Barker, "CDMSlite R2 NuMI Cut," CDMS Intern. Run 133-135 Anal. Eb., 43–lite2 (2015).

[334] R. Bunker, "Initial Study of R133 Glitch Events," CDMS Intern. Run 133-135 Anal. Eb., 61 (2012).

[335] B. Welliver, "R133 Charge OF0 Noiseblobs," CDMS Intern. Run 133-135 Anal. Eb., 169 (2013).

[336] R. Basu Thakur, "Cryo-cooler Noise Monitors III: Integrating the Setra in data stream and first reports," CDMS Intern. Run 133-135 Anal. Eb., 227 (2014).

[337] R. Basu Thakur and M. Pepin, "CDMSlite Run 2 Low Frequency Noise v2 / Noise Monitor VI.I," CDMS Intern. Run 133-135 Anal. Eb., 18–lite2 (2014).

[338] R. Basu Thakur, "Cryo-cooler Noise Monitors IV: Detailed analysis of phonon noise using Setra metrics," CDMS Intern. Run 133-135 Anal. Eb., 241 (2014).

[339] Z. I. Botev, J. F. Grotowski, and D. P. Kroese, "Kernel density estimation via diffusion," Ann. Stat. **38**, 2916–2957 (2010).

[340] B. C. Welliver, *Dedicated Searches For Low And High Mass WIMPs With The SuperCDMS Soudan IZIP Detectors*, Ph.D. thesis, Universiy of Florida (2016).

[341] J. Hall, "CDMSlite: Low Energy Backgrounds in T2Z6," CDMS Intern. Run 125-128 Anal. Eb., 40 (2009).

[342] W. Rau, "New Position Estimators based on 2-template quantities," CDMS Intern. Run 133-135 Anal. Eb., 60–lite2 (2015).

[343] G. Cowan, *Statistical Data Analysis* (Oxford University Press Inc., New York, 1998).

[344] K. Page, "Estimating distribution of Ge-71 decays in energy and radius for fiducial volume study: Changes in implementation," CDMS Intern. Run 133-135 Anal. Eb., 63–lite2 (2015).

[345] K. Page and R. Underwood, "Calculating 10 keV line efficiency and the energy-independant part of efficiency of the radial cut in CDMSlite," CDMS Intern. Run 133-135 Anal. Eb., 68–lite2 (2015).

[346] R. Underwood, W. Rau, E. Fascione, and A. Warchuk, "Analysis of Pulse Simulation Data for Fiducial Efficiency Calculation," CDMS Intern. Run 133-135 Anal. Eb., 70–lite2 (2015).

[347] R. Underwood, "Period Alignment for Fiducial Volume cut," CDMS Intern. Run 133-135 Anal. Eb., 67–lite2 (2015).

[348] W. Rau, R. Underwood, E. Fascione, and A. Warchuk, "Analysis of Energy Resolution," CDMS Intern. Run 133-135 Anal. Eb., 72–lite2 (2015).

[349] U. Fano, "Ionization yield of radiations. II. the fluctuations of the number of ions," Phys. Rev. **72**, 26–29 (1947).

[350] R. C. Alig, S. Bloom, and C. W. Struck, "Scattering by ionization and phonon emission in semiconductors," Phys. Rev. B **22**, 5565–5582 (1980).

[351] K. W. Jones and H. W. Kraner, "Stopping of 1- to 1.8-keV 73Ge Atoms in Germanium," Phys. Rev. C **4**, 125–129 (1971).

[352] K. W. Jones and H. W. Kraner, "Energy lost to ionization by 254-eV 73Ge atoms stopping in Ge," Phys. Rev. A **11**, 1347–1353 (1975).

[353] P. S. Barbeau, J. I. Collar, and O. Tench, "Large-mass ultralow noise germanium detectors: performance and applications in neutrino and astroparticle physics," J. Cosmol. Astropart. Phys. 2007 (2007) 009–009.

[354] P. S. Barbeau, *Neutrino and astroparticle physics with P-type point contact high purity germanium detectors*, Ph.D. thesis, Univeristy of Chicago (2009).

[355] X. Ruan, "Nuclear recoil quenching factor measurement for HPGe detector," (Beijing, 2011).

[356] Y. Messous *et al.*, "Calibration of a Ge crystal with nuclear recoils for the development of a dark matter detector," Astropart. Phys. **3**, 361–366 (1995).

[357] C. Chasman, K. W. Jones, H. W. Kraner, and W. Brandt, "Band-Gap Effects in the Stopping of ^{72*}Ge Atoms in Germanium," Phys. Rev. Lett. **21**, 1430–1433 (1968).

[358] T. Shutt *et al.*, "Measurement of ionization and phonon production by nuclear recoils in a 60 g crystal of germanium at 25 mK." Phys. Rev. Lett. **69**, 3425–3427 (1992).

[359] A. R. Sattler, F. L. Vook, and J. M. Palms, "Ionization Produced by Energetic Germanium Atoms within a Germanium Lattice," Phys. Rev. **143**, 588–594 (1966).

[360] L. Baudis, J. Hellmig, H. Klapdor-Kleingrothaus, Y. Ramachers, J. Hammer, and A. Mayer, "High-purity germanium detector ionization pulse shapes of nuclear recoils, γ-interactions and microphonism," Nucl. Instruments Methods Phys. Res. Sect. A **418**, 348–354 (1998).

[361] E. Simon, L. Bergé, A. Broniatowski, R. Bouvier, B. Chambon, M. De Jésus, D. Drain, L. Dumoulin, J. Gascon, J.-P. Hadjout, A. Juillard, O. Martineau, C. Pastor, M. Stern, and L. Vagneron, "SICANE: a detector array for the measurement of nuclear recoil quenching factors using a monoenergetic neutron beam," Nucl. Instruments Methods Phys. Res. Sect. A **507**, 643–656 (2003).

[362] A. Benoit *et al.* (EDELWEISS Collaboration), "Measurement of the response of heat-and-ionization germanium detectors to nuclear recoils," Nucl. Instruments Methods Phys. Res. Sect. A **577**, 558–568 (2007).

[363] D. Barker and D.-M. Mei, "Germanium detector response to nuclear recoils in searching for dark matter," Astropart. Phys. **38**, 1–6 (2012).

[364] J. Lindhard, V. Nielsen, M. Scharff, and P. V. Thomsen, "Integral Equations Governing Radiation Effects (Notes On Atomic Collisions III)," Mat. Fys. Medd. Dan. Vid. Selsk. **33** (1963); J. Lindhard, M. Scharff, and H. Schiott, "Range Concepts And Heavy Ion Ranges (Notes On Atomic Collisions II)," Mat. Fys. Medd. Dan. Vid. Selsk. **33** (1963); J. Lindhard, V. Nielsen, and M. Scharff, "Approximation Method In Classical Scattering By Screened Coulomb Fields (Notes on Atomic Collisions, I)," Mat. Fys. Medd. Dan. Vid. Selsk. **36** (1968).

[365] D. D. Wackerly, W. Mendenhall, and R. L. Scheaffer, *Mathematical Statistics with Applications*, 7th ed. (Thomson Brooks/Cole, Belmont, CA, 2008).

[366] H. Jeffreys, "An Invariant Form for the Prior Probability in Estimation Problems," Proc. R. Soc. A Math. Phys. Eng. Sci. **186**, 453–461 (1946).

[367] S. Yellin, "Finding an upper limit in the presence of an unknown background," Phys. Rev. D **66**, 032005 (2002).

[368] S. Yellin, "Extending the optimum interval method," arXiv:0709.2701 .

[369] R. Agnese *et al.* (SuperCDMS Collaboration), "New Results from the Search for Low-Mass Weakly Interacting Massive Particles with the CDMS Low Ionization Threshold Experiment," Phys. Rev. Lett. **116**, 071301 (2016).

[370] F. J. Kerr and D. Lynden-Bell, "Review of galactic constants," Mon. Not. R. Astron. Soc. **221**, 1023–1038 (1986).

[371] R. Schönrich, J. Binney, and W. Dehnen, "Local kinematics and the local standard of rest," Mon. Not. R. Astron. Soc. **403**, 1829–1833 (2010).

[372] M. C. Smith *et al.*, "The RAVE survey: constraining the local Galactic escape speed," Mon. Not. R. Astron. Soc. **379**, 755–772 (2007).

[373] P. Salucci, F. Nesti, G. Gentile, and C. Frigerio Martins, "The dark matter density at the Sun's location," Astron. Astrophys. **523**, A83 (2010).

[374] J. I. Read, "The local dark matter density," J. Phys. G Nucl. Part. Phys. **41**, 063101 (2014).

[375] F. V. Hessman, "The difficulty of measuring the local dark matter density," Astron. Astrophys. **579**, A123 (2015).

[376] L. M. Widrow, B. Pym, and J. Dubinski, "Dynamical Blueprints for Galaxies," Astrophys. J. **679**, 1239–1259 (2008).

[377] M. Weber and W. de Boer, "Determination of the local dark matter density in our Galaxy," Astron. Astrophys. **509**, A25 (2010).

[378] R. Catena and P. Ullio, "A novel determination of the local dark matter density," J. Cosmol. Astropart. Phys. 2010 (2010) 004–004.

[379] S. Garbari, J. I. Read, and G. Lake, "Limits on the local dark matter density," Mon. Not. R. Astron. Soc. **416**, 2318–2340 (2011).

[380] S. Garbari, C. Liu, J. I. Read, and G. Lake, "A new determination of the local dark matter density from the kinematics of K dwarfs," Mon. Not. R. Astron. Soc. **425**, 1445–1458 (2012).

[381] F. Nesti and P. Salucci, "The Dark Matter halo of the Milky Way, AD 2013," J. Cosmol. Astropart. Phys. 2013 (2013) 016–016.

[382] O. Bienaymé *et al.*, "Weighing the local dark matter with RAVE red clump stars," Astron. Astrophys. **571**, A92 (2014).

[383] J. Lavalle and S. Magni, "Making sense of the local Galactic escape speed estimates in direct dark matter searches," Phys. Rev. D **91**, 023510 (2015).

[384] T. Piffl *et al.*, "The RAVE survey: the Galactic escape speed and the mass of the Milky Way," Astron. Astrophys. **562**, A91 (2014).

[385] W. Dehnen and J. J. Binney, "Local stellar kinematics from Hipparcos data," Mon. Not. R. Astron. Soc. **298**, 387–394 (1998).

[386] M. J. Reid *et al.*, "Trigonometric Parallaxes Of High Mass Star Forming Regions: The Structure And Kinematics Of The Milky Way," Astrophys. J. **783**, 130 (2014).

[387] P. J. McMillan and J. J. Binney, "The uncertainty in Galactic parameters," Mon. Not. R. Astron. Soc. **402**, 934–940 (2010).

[388] M. J. Reid, K. M. Menten, X. W. Zheng, A. Brunthaler, L. Moscadelli, Y. Xu, B. Zhang, M. Sato, M. Honma, T. Hirota, K. Hachisuka, Y. K. Choi, G. A. Moellenbrock, and A. Bartkiewicz, "Trigonometric Parallaxes Of Massive Star-Forming Regions. VI. Galactic Structure, Fundamental Parameters, And Noncircular Motions," Astrophys. J. **700**, 137–148 (2009).

[389] J. Bovy, D. W. Hogg, and H.-W. Rix, "Galactic Masers And The Milky Way Circular Velocity," Astrophys. J. **704**, 1704–1709 (2009).

[390] S. E. Koposov, H.-W. Rix, and D. W. Hogg, "Constraining The Milky Way Potential With A Six-Dimensional Phase-Space Map Of The GD-1 Stellar Stream," Astrophys. J. **712**, 260–273 (2010).

[391] V. V. Bobylev and A. T. Bajkova, "Galactic parameters from masers with trigonometric parallaxes," Mon. Not. R. Astron. Soc. **408**, 1788–1795 (2010).

[392] P. J. McMillan, "Mass models of the Milky Way," Mon. Not. R. Astron. Soc. **414**, 2446–2457 (2011).

[393] J. Bovy *et al.*, "The Milkey Way's Circular-Velocity Curve Between 4 And 14 kpc From APOGEE Data," Astrophys. J. **759**, 131 (2012).

[394] J. L. Carlin, S. R. Majewski, D. I. Casetti-Dinescu, D. R. Law, T. M. Girard, and R. J. Patterson, "Kinematics And Chemistry Of Stars Along The Sagittarius Trailing Tidal Tail And Constraints On The Milky Way Mass Distribution," Astrophys. J. **744**, 25 (2012).

[395] M. Honma *et al.*, "Fundamental Parameters of the Milky Way Galaxy Based on VLBI Astrometry," Publ. Astron. Soc. Japan **64**, 136 (2012).

[396] V. V. Bobylev and A. T. Bajkova, "Kinematic analysis of solar-neighborhood stars based on RAVE4 data," Astron. Lett. **42**, 90–99 (2016).

[397] Y.-Y. Mao, L. E. Strigari, R. H. Wechsler, H.-Y. Wu, and O. Hahn, "Halo-To-Halo Similarity And Scatter In The Velocity Distribution Of Dark Matter," Astrophys. J. **764**, 35 (2013); Y.-Y. Mao, L. E. Strigari, and R. H. Wechsler, "Connecting direct dark matter detection experiments to cosmologically motivated halo models," Phys. Rev. D **89**, 063513 (2014).

[398] A. Pillepich, M. Kuhlen, J. Guedes, and P. Madau, "The Distribution Of Dark Matter In The Milky Way's Disk," Astrophys. J. **784**, 161 (2014).

[399] K. Freese, P. Gondolo, and H. J. Newberg, "Detectability of weakly interacting massive particles in the Sagittarius dwarf tidal stream," Phys. Rev. D **71**, 043516 (2005).

[400] J. F. Navarro, C. S. Frenk, and S. D. M. White, "A Universal Density Profile from Hierarchical Clustering," Astrophys. J. **490**, 493–508 (1997).

[401] C. A. J. O'Hare, "Dark matter astrophysical uncertainties and the neutrino floor," Phys. Rev. D **94**, 20 (2016).

[402] K. E. Schneck, *Search For Low-Mass Dark Matter With SuperCDMS Soudan And Study Of Shorted Electric Field Configurations In CDMS Detectors*, Ph.D. thesis, Stanford University (2015).

[403] E. Aprile *et al.* (XENON100 Collaboration), "Limits on spin-dependent WIMP-nucleon cross sections from 225 live days of XENON100 data." Phys. Rev. Lett. **111**, 021301 (2013).

[404] M. Barnabé-Heider *et al.* (PICASSO Collaboration), "Improved spin-dependent limits from the PICASSO dark matter search experiment," Phys. Lett. B **624**, 186–194 (2005).

[405] S. K. Liu *et al.* (CDEX Collaboration), "Limits on light WIMPs with a germanium detector at 177 eVee threshold at the China Jinping Underground Laboratory," Phys. Rev. D **90**, 032003 (2014).

[406] W. Zhao *et al.* (CDEX Collaboration), "Search of low-mass WIMPs with a p-type

point contact germanium detector in the CDEX-1 experiment," Phys. Rev. D **93**, 092003 (2016).

[407] D. Tovey, R. Gaitskell, P. Gondolo, Y. Ramachers, and L. Roszkowski, "A new model-independent method for extracting spin-dependent cross section limits from dark matter searches," Phys. Lett. B **488**, 17–26 (2000).

[408] W. Page, "CDMSlite R3 Trigger Efficiency," CDMS Intern. Run 133-135 Anal. Eb., 11–lite3 (2016).

[409] D. Barker, "Low Energy Background Spectrum in CDMSlite," arXiv:1611.05792 .

[410] W. Page, "CDMSlite R3 Limit Projection," CDMS Intern. Run 133-135 Anal. Eb., 12–lite3 (2016).

[411] R. Agnese *et al.*, "Projected Sensitivity of the SuperCDMS SNOLAB experiment," arXiv:1610.00006 .

[412] D. S. Akerib *et al.*, "LUX-ZEPLIN (LZ) Conceptual Design Report," arXiv:1509.02910 .

[413] L. J. Rosenberg, "Dark-matter QCD-axion searches." Proc. Natl. Acad. Sci. U. S. A. **112**, 12278–81 (2015).

[414] A. J. Anderson, J. M. Conrad, E. Figueroa-Feliciano, K. Scholberg, and J. Spitz, "Coherent neutrino scattering in dark matter detectors," Phys. Rev. D **84**, 013008 (2011).

[415] S. R. Golwala, *Exclusion Limits on the WIMP-Nucleon Elastic-Scattering Cross Section from the Cryogenic Dark Matter Search*, Ph.D. thesis, University of California, Berkeley (2000).

[416] J.-C. Lanfranchi, *Development of a New Composite Cryogenic Detection Concept for a Radiochemical Solar Neutrino Experiment*, Ph.D. thesis, Technischen Universitat Munchen (2005).

[417] D. R. Morrison, "Updated Review Of Solar Models And Solar Neutrino Experiments," Int. J. Mod. Phys. D **01**, 281–302 (1992).

[418] W. Bambynek, H. Behrens, M. H. Chen, B. Crasemann, M. L. Fitzpatrick, K. W. D. Ledingham, H. Genz, M. Mutterer, and R. L. Intemann, "Orbital electron capture by the nucleus," Rev. Mod. Phys. **49**, 77–221 (1977).

[419] E. Schönfeld, "Calculation of fractional electron capture probabilities," Appl. Radiat. Isot. **49**, 1353–1357 (1998).

[420] B. Crasemann, "Some aspects of atomic effects in nuclear transitions," Nucl. Instruments Methods **112**, 33–39 (1973).

[421] A. Thompson and D. Vaughn, "X-Ray Data Booklet," Lawrence Berkeley Natl. Lab. (2001).

[422] D. Coster and R. D. L. Kronig, "New type of auger effect and its influence on the x-ray spectrum," Physica **2**, 13–24 (1935).

[423] M. O. Krause and J. H. Oliver, "Natural widths of atomic K and L levels, K_α X-ray lines and several KLL Auger lines," J. Phys. Chem. Ref. Data **8**, 329 (1979).

[424] E. Schönfeld and H. Janßen, "Calculation of emission probabilities of X-rays and Auger electrons emitted in radioactive disintegration processes," Appl. Radiat. Isot. **52**, 595–600 (2000).

[425] E. Schönfeld and H. Janßen, "Evaluation of atomic shell data," Nucl. Instruments Methods Phys. Res. Sect. A **369**, 527–533 (1996).

[426] J. H. Scofield, "Exchange corrections of K x-ray emission rates," Phys. Rev. A **9**, 1041–1049 (1974).

[427] S. Puri, D. Mehta, B. Chand, N. Singh, J. Hubbell, and P. Trehan, "Production of L_i subshell and M shell vacancies following inner-shell vacancy production," Nucl. Instruments Methods Phys. Res. Sect. B **83**, 21–30 (1993).

[428] S. Puri, D. Mehta, B. Chand, N. Singh, and P. N. Trehan, "L shell fluorescence yields and coster-kronig transition probabilities for the elements with $25 < Z < 96$," X-Ray Spectrom. **22**, 358–361 (1993).

[429] J. Campbell and J.-X. Wang, "Interpolated Dirac-Fock values of L-subshell x-ray emission rates including overlap and exchange effects," At. Data Nucl. Data Tables **43**, 281–291 (1989).

[430] J. H. Hubbell, P. N. Trehan, N. Singh, B. Chand, D. Mehta, M. L. Garg, R. R. Garg, S. Singh, and S. Puri, "A Review, Bibliography, and Tabulation of K, L, and Higher Atomic Shell X-Ray Fluorescence Yields," J. Phys. Chem. Ref. Data **23**, 339 (1994).

[431] R. Basu Thakur, "Cryocooler Noise monitor II," CDMS Intern. Run 133-135 Anal. Eb., 135 (2013).

[432] R. Basu Thakur, "Cryocooler Noise monitors I," CDMS Intern. Run 133-135 Anal. Eb., 134 (2013).

Appendix A

Optimal Filter Theory

In an optimal filter (OF) fit, the amplitude of a signal with known profile is estimated by maximizing the signal-to-noise. This is done by minimizing a χ^2 parameter in frequency space, which necessitates performing Fourier transformations on the signal traces. The OF fit is superior to a simple time-domain χ^2 minimization as non-white noise can cause correlations in the time domain fit, while being uncorrelated between frequency bins in the OF fit. The theory of OF fitting has been derived in several CDMS theses — notably Golwala [415], Filippini [203], and Basuthakur [275] — and only the simplest case is reviewed here in detail, with more complex results quoted from those sources.

A.1   1 × 1 OF

The simplest scenario is that of fitting a single template to a single signal pulse, known as the 1×1 OF. In this case, it is assumed that the signal $S(t)$ is a sum of a known template shape $A(t)$ and Gaussian noise $n(t)$ as[1]

$$S(t) = aA(t) + n(t), \tag{A.1}$$

where the template is scaled by some amplitude a, whose optimal value $\hat{a}$ is desired. In order to obtain $\hat{a}$, the signal and template traces are transformed to frequency ν space

---

[1] The optimal filter is in fact only "optimal" if this assumption is strictly true.

via Fourier transformations as

$$\psi(t) = \int_{-\infty}^{+\infty} \tilde{\psi}(\nu) e^{-i2\pi\nu t} \, d\nu \tag{A.2}$$

$$\tilde{\psi}(\nu) = \int_{-\infty}^{+\infty} \psi(t) e^{i2\pi\nu t} \, dt \tag{A.3}$$

to give $\tilde{A}(\nu)$ and $\tilde{S}(\nu)$. For the noise, an autocorrelation function from many noise traces $\xi(t)$ is defined, along with its Fourier transformation, the power-spectral-density (PSD) $\tilde{J}(\nu)$, as

$$\xi(t) = \lim_{T\to\infty} \frac{1}{T} \int_{-T/2}^{T/2} n(\tau) n(t+\tau) \, d\tau \tag{A.4}$$

$$\tilde{J}(\nu) = \lim_{T\to\infty} \int_{-T/2}^{+T/2} \xi(t) e^{-i2\pi\nu t} \, dt. \tag{A.5}$$

For Gaussian noise with variance σ^2, the PSD evaluates to that σ^2. Note that the PSD can also be computed directly from the Fourier transformation of the noise traces themselves as [415]

$$\tilde{J}(\nu) = \lim_{T\to\infty} \frac{1}{T} |\tilde{n}(\nu)|^2. \tag{A.6}$$

The χ^2 parameter in frequency space is then given by

$$\chi^2 = \int_{-\infty}^{+\infty} \frac{\left| \tilde{S}(\nu) - a\tilde{A}(\nu) \right|^2}{\tilde{J}(\nu)} \, d\nu \tag{A.7}$$

which is minimized by $\partial\chi^2/\partial a \big|_{a=\hat{a}} = 0$ giving

$$\hat{a} = \frac{\int_{-\infty}^{+\infty} \frac{\tilde{A}^*(\nu)\tilde{S}(\nu)}{\tilde{J}(\nu)} \, d\nu}{\int_{-\infty}^{+\infty} \frac{|\tilde{A}(\nu)|^2}{\tilde{J}(\nu)}} \, d\nu \tag{A.8}$$

with variance

$$\sigma_{\hat{a}}^2 = \left[\int_{-\infty}^{+\infty} \frac{\left| \tilde{S}(\nu) \right|^2}{\tilde{J}(\nu)} \, d\nu \right]^{-1}. \tag{A.9}$$

There are two immediate factors which make the above derivation too ideal for

CDMS uses: the start time of any given pulse may not match the start time of the template and CDMS pulses are digitized by an ADC, making them discrete vectors instead of continuous functions.

The first factor is addressed by writing the signal pulse as having some delay t_0 from the template pulse as

$$S(t) = aA(t - t_0) + n(t). \tag{A.10}$$

This delay modifies Eqs. A.7 and A.8 by taking $\tilde{A}(\nu) \to e^{-i2\pi\nu t_0}\tilde{A}(\nu)$.[2] In addition to optimizing the amplitude, the delay t_0 must also be computed. Doing so analytically is intensive, but it can be shown that $\partial\chi^2/\partial t_0 \propto \partial\hat{a}/\partial t_0$ with second derivatives such that the delay which maximizes the amplitude is the best-fit delay $\hat{t}_0$. The variance of $\hat{t}_0$ is

$$\sigma_{\hat{t}_0}^2 = \left[\hat{a}^2 \int_{-\infty}^{+\infty} (2\pi\nu)^2 \frac{\left|\tilde{A}(\nu)\right|^2}{J(\nu)} \, \mathrm{d}\nu\right]^{-1}, \tag{A.11}$$

and decreases with increasing pulse-height.

The second complication is handled by converting continuous functions of time to discrete vectors of k bins of size Δt, $g(t) \leftrightarrow g_k$. These are transformed by applying discrete Fourier Transforms (DFTs) to make frequency-space vectors of n bins of size $\Delta\nu$, $\tilde{s}(\nu) \leftrightarrow s_n/\Delta\nu$. Integrals must also be converted to summations as $\int_{-\infty}^{+\infty} \mathrm{d}t \leftrightarrow \sum_{k=-N/2}^{N/2-1} \Delta t$ or $\int_{-\infty}^{+\infty} \mathrm{d}\nu \leftrightarrow \sum_{n=-N/2}^{N/2-1} \Delta\nu$.

A.2 OF Extensions

The theory can be expanded to include M templates being simultaneously fit to N traces [275], which is termed the $N \times M$ OF. For CDMS uses, the 1×2 and 2×2 manifestations are needed in the 2T-fit and OFX algorithms respectively. These two problems are formatted using matrices as

$$S = \begin{bmatrix} A_1 & A_2 \end{bmatrix} \begin{bmatrix} a_1 \\ a_2 \end{bmatrix} + n, \tag{A.12}$$

---

[2] The complex conjugation in Eq. A.8 also applies to the t_0 prefactor.

for the 1×2 case and

$$\begin{bmatrix} S_1 \\ S_2 \end{bmatrix} = \begin{bmatrix} A_1 & A_{2X} \\ A_{1X} & A_2 \end{bmatrix} \begin{bmatrix} a_1 \\ a_2 \end{bmatrix} + \begin{bmatrix} n_1 \\ n_2 \end{bmatrix}, \tag{A.13}$$

for the 2×2 case, where the explicit time dependence has been omitted for simplicity. The general solution lies in writing the χ^2 as

$$\chi^2 = \sum_\nu \left[\tilde{S}^{*\alpha} - e^{+i2\pi\nu t_0} a^j \tilde{A}_j^{*\alpha} \right] \left\{ \tilde{V}_{\alpha\beta}^{-1} \right\} \left[\tilde{S}^\beta - e^{-i2\pi\nu t_0} a^k \tilde{A}_k^\beta \right], \tag{A.14}$$

where the explicit dependence on ν of tilde quantities is suppressed, Greek indicies are over the N traces, Latin indices are over the M templates, Einstein summation notation is used with both, and $\tilde{V}_{\alpha\beta} = \tilde{\sigma}_\alpha \tilde{\rho}_{\alpha\beta} \tilde{\sigma}_\beta$ is the covariance matrix between the different traces' noise which have correlation $\tilde{\rho}_{\alpha\beta}$ and individual variances $\tilde{\sigma}_\alpha^2$. In the usual case of the noise being uncorrelated, $\tilde{V}$ is a diagonal matrix with the $\tilde{J}_\alpha$ along the diagonal. The χ^2 is minimized by solving the N equations

$$\hat{a} = P^{-1} \cdot q(t_0), \tag{A.15}$$

where the matrices are defined via

$$P_{jk} = \sum_\nu \tilde{A}_j^{*\alpha} \left\{ \tilde{V}_{\alpha\beta}^{-1} \right\} \tilde{A}_k^\beta \tag{A.16}$$

$$q_j = \sum_\nu \tilde{A}_j^{*\alpha} \left\{ \tilde{V}_{\alpha\beta}^{-1} \right\} \tilde{S}^\beta e^{+i2\pi\nu t_0}. \tag{A.17}$$

Several computation tricks are used to write the χ^2 only in terms of t_0 [275], allowing for a simple scan of possible t_0's with the optimal solution being that t_0 with the minimum χ^2.

The final OF-algorithm used by CDMS is for when the trace profile shape varies. The above derivations assume that the signal profile is identical to that of the template profile. The presence of non-stationary noise breaks this assumption and must be addressed. Non-stationary noise is that for which the noise distribution shape has

time dependence.[3] This is relevant if one portion of a signal trace matches the template while another part does not, meaning the noise profile changes, i.e. has time-dependence, during the portion which does not match the template.

Non-stationary noise is accounted for by using a non-stationary OF (NSOF), which, mathematically, is very similar to the general $N \times M$ OF. For this case, there is only one template and trace (1×1 scheme), but there are correlations between different frequencies in the noise. The χ^2 is written as

$$\chi^2 = \sum_{\nu\nu'} \left[\tilde{S}^*(\nu)e^{+i2\pi\nu t_0} - a\tilde{A}^*(\nu) \right] \left\{ \tilde{V}(\nu,\nu')^{-1} \right\} \left[\tilde{S}(\nu')\,e^{-i2\pi\nu' t_0} - a\tilde{A}(\nu') \right], \quad \text{(A.18)}$$

where $\tilde{V}(\nu,\nu')$ is the auto-covariance, which is non-diagonal. The auto-covariance is computed by considering, in frequency space, the residual differences between many signal traces and the template. If there is a strong correlation between two frequencies ν_1, ν_2, then $\tilde{V}(\nu_1, \nu_2)$ is large and its inverse is small. The result is that the frequencies which have strong correlations are de-weighted in the χ^2 computation. The optimal amplitude, as a function of t_0 is

$$\hat{a}(t_0) = \frac{\sum_{\nu\nu'} \tilde{S}^*(\nu)e^{+i2\pi\nu t_0} \left\{ \tilde{V}(\nu,\nu')^{-1} \right\} \tilde{A}(\nu')}{\sum_{\nu\nu'} \tilde{A}^*(\nu) \left\{ \tilde{V}(\nu,\nu')^{-1} \right\} \tilde{A}(\nu')}. \quad \text{(A.19)}$$

Numerically, Eq. A.19 is substituted into Eq. A.18 to have $\chi^2(t_0)$. A scan is performed over t_0 to find the minimum value of χ^2. This gives $\hat{t}_0$ and, by Eq. A.19, $\hat{a}$.

---

[3] The noise $n(t)$ discussed previous does have time dependence, but the overall shape, usually assumed to be Gaussian, does not change. It is therefore stationary noise.

Appendix B

Electron Capture on ^{71}Ge and the Resulting De-excitation

The energy spectrum resulting from the decay of ^{71}Ge via electron capture is crucial for calibrating the energy scale of CDMSlite. ^{71}Ge is created by neutron capture on the natural ^{70}Ge found in the iZIP detectors, with the neutrons originating from the ^{252}Cf calibration source utilized by SuperCDMS. This entire processes is

$$^{70}\text{Ge} + n \longrightarrow {}^{71}\text{Ge}$$
$$^{71}\text{Ge} + e \longrightarrow {}^{71}\text{Ga} + \nu_e$$
$$^{71}\text{Ga} \longrightarrow {}^{71}\text{Ga} + \gamma\text{'s}, e\text{'s}.$$
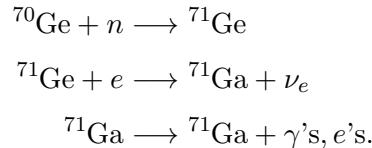
where the last line depicts atomic relaxation and the unstable ^{71}Ge has a half-life of 11.43 days [326]. The purpose of this appendix is to explore the details of the last two steps in this process with the goal of characterizing, in better detail than other sources [416, 417], the ratios of the final decay product γ's and e's.

B.1   The ^{71}Ge Electron Capture Process

An extensive review of electron-capture physics is given by Bambynek *et al.* in [418], where the underlying particle physics is espoused and many properties of the decay tabulated. At the particle level, the electron capture process is the same process as the

Shell	K	L_1	L_2	L_3	M_1	M_2	M_3	M_4	M_5	N_1	N_2
Number	2	2	4	2	2	4	2	8	2	2	2
Orbital	$1s$	$2s$	$2p_{1/2}$	$2p_{3/2}$	$3s$	$3p_{1/2}$	$3p_{3/2}$	$3d_{3/2}$	$3d_{5/2}$	$4s$	$4p_{1/2}$

Table B.1: Number of electrons in each shell for free germanium.

β^+ decay of a proton to neutron, where instead the β is brought to the left side of the reaction giving

$$p + e \longrightarrow n + \nu_e.$$

This process occurs within a parent atom of atomic mass and number (A, Z) leading to a daughter atom of $(A, Z - 1)$. For the particular decay of interest for CDMSlite, the parent is ^{71}Ge and the daughter ^{71}Ga. For many nuclei, the daughter nucleus is initially in an excited state and promptly decays to its ground state while emitting $\mathcal{O}(\text{MeV})$ γ rays. This processes, however, does not occur for ^{71}Ga and is not further discussed.

The first step in understanding the process for the ^{71}Ge decay is considering which electron is captured by the germanium nucleus. In principal, the captured electron can originate from any electron shell, as long as conservation rules are observed. For unbound germanium, there are 32 electrons in the $1s^2 2s^2 2p^6 3s^2 3p^6 4s^2 3d^{10} 4p^2$ orbitals, which completely fill the K, L, and M shells and partially fill the N shell as is shown in Table B.1. A method for computing the fractional electron-capture probabilities for each shell is given in [419] and is used for the following discussion.

The starting point for the calculation is with the obvious fact that the fractional capture probability from each shell must sum to unity

$$P_K + P_L + P_M + P_N = 1, \tag{B.1}$$

where P_i is the total probability of capture for the entire i^{th} shell. For the L and higher shells, the capture probability is dominated by the first sub-shell with small contributions from the second sub-shell. Higher sub-shells can, and will, be neglected in this discussion, though it should be explicitly stated that capture from the L_3 sub-shell is a forbidden transition and has an effective probability of zero. If the ratios of the probabilities between different shells are known, P_K can be calculated by rewriting

Eq. B.1 as

$$P_K = \left\{ 1 + \frac{P_L}{P_K} \left[1 + \frac{P_M}{P_L} \left(1 + \frac{P_N}{P_M} \right) \right] \right\}^{-1}. \tag{B.2}$$

P_L, P_M, and P_N are then calculated using the known ratios and this value of P_K.

These ratios are "known" by computation, and are products of energetic and geometrical factors as

$$\frac{P_L}{P_K} = k_{LK} \left(\frac{Q - E_{L_1}}{Q - E_K} \right)^2 \tag{B.3}$$

$$\frac{P_M}{P_L} = k_{ML} \left(\frac{Q - E_{M_1}}{Q - E_{L_1}} \right)^2 \tag{B.4}$$

$$\frac{P_N}{P_M} = k_{NM} \left(\frac{Q - E_{N_1}}{Q - E_{M_1}} \right)^2, \tag{B.5}$$

where $Q = 232.5$ keV is the energy available for the electron-capture process, E_i is the electron binding energy of the ith shell of the daughter nucleus (see Sec. B.2), and k_{jk} is the geometrical factor between the jth and k^{th} shells of the parent atom. The geometry of import in k_{jk} is that of the electron orbitals as the probability for capture increases if the given electron cloud is denser in the region of the nucleus. Subtleties involving the overlap and uncertainty on the electron waveforms in atomic configuration, as well as the relation between different sub-shells also contribute. The k_{jk} were tabulated by Schönfeld [419] and the values for germanium are $k_{LK} = 0.1110(16)$, $k_{LM} = 0.167(4)$, and $k_{NM} = 0.078(7)$.

The last component to consider for this initial process is what portion of the captures occur in the second sub-shells compared to the first. These values for a selection of atoms were collected in [418] and extrapolation to germanium gives the ratios $P_{L_2}/P_{L_1} = 0.0093$, $P_{M_2}/P_{M_1} = 0.0094$, and $P_{N_2}/P_{N_1} = 0.0046$. This last value is almost certainly not correct for crystalline germanium since the N_2 electrons are conduction band electrons and participate in chemical bonds, which affects the electron-capture process [420]. These effects are ignored here since the capture probability for that shell is very small, and, since the energy released is so low, any difference is not observable in an iZIP detector. The final fractional electron-capture probabilities for ^{71}Ge are given in Table B.2.

Shell	Probability [%]	Sub-shell	Probability [%]
K	87.57		
L	10.53	L_1	10.43
		L_2	0.10
M	1.78	M_1	1.76
		M_2	0.02
N	0.12	N_1	0.12
		N_2	< 0.01

Table B.2: Fractional electron capture probabilities by shell and sub-shell for ^{71}Ge. Sub-shells not listed have negligible capture probability. The value listed for capture from the N_2 shell is for a free atom and is most certainly not correct for a crystal and can be ignored.

B.2 The ^{71}Ga De-excitation Process

Once an electron is captured, the resulting ^{71}Ga atom has a vacancy in an electron shell due to the missing (captured) electron. This excited atom quickly de-excites through atomic processes and fills the vacant shell either by x-ray or Auger-electron (Auger-e) emission. This is a multi-step process which shifts the vacant spot to the outer shells until a stable electron configuration is reached. For an atom in a crystal, such as an iZIP detector, stability is reached when the vacancy reaches the band-gap. The energy available for release during the de-excitation process corresponds to the electron binding energy, of the daughter atom, from the shell where the vacancy starts, i.e. the shell from which the initial electron was captured. For the specific case studied here, the daughter atom is ^{71}Ga and the electron binding energies, defined to be positive for use here, for gallium are given in Table B.3.

The vacancy is filled in one of two ways: x-ray emission or Auger-e emission. For an x ray, an electron from a higher shell with binding energy E_2 falls into the vacancy at binding energy E_1 and a γ is emitted with energy equal to the difference in shell binding energies $E_\gamma = E_1 - E_2$ (note that the final and initial designations on the energies correspond to the position of the shell vacancy). Auger-e emission is similar in that a higher shell electron falls to the lower shell, but, instead of emitting an x ray, an

Shell	Energy [eV]	Shell	Energy [eV]
K	10367.0	M_2	103.5
L_1	1299.0	M_3	100.0
L_2	1143.2	M_4	18.7
L_3	1116.4	M_5	18.7
M_1	159.5	N_1	1.5

Table B.3: Electron binding energies for ^{71}Ga for the K through N_1 shells. Values from [421].

electron from a different higher shell is ejected. If the binding energy of the shell from which this electron is ejected is E_3, then the kinetic energy of the ejected Auger-e is $E_A = E_1 - E_2 - E_3$. The probability for undergoing x-ray or Auger-e emission depends on which shell contains the vacancy.

In these processes, the vacancy shifts from a lower shell to a higher shell. For instance, if the vacancy starts in the K shell and is filled by an L-shell electron, there would now be a vacancy in the L shell which would need to be filled. If the vacancy is filled by an Auger-e process, there would potentially be two vacancies. A cascade of x rays and Auger electrons occurs until the vacancy reaches the outermost shell and the ^{71}Ga becomes stable. This cascade contains nearly all of the energy of the original vacancy binding energy. The reason for this is that, in a semiconducting germanium crystal, the valance electrons in the last full electron shell, M_5, are just below the band-gap of $E_g = 0.74$ eV (at $\sim$50 mK [261]) which is below the resolution of current detectors. The cascade eventually ends with valence electrons being ejected, which reduces the kinetic energy by this negligible amount. As an example, consider an initial vacancy in the K shell which is filled by an L-shell electron and emits an x ray (process 1). The vacancy in the L shell is then filled by an Auger-e process which takes an electron from the M shell and ejects a valance electron (process 2). The M-shell gap then is both filled by and ejects a valence electron in another Auger-e process (process

3). The total energy E_t released to the crystal for this cascade is

$$E_t = \overbrace{(E_K - E_L)}^{\text{process 1}} + \overbrace{(E_L - E_M - E_g)}^{\text{process 2}} + \overbrace{(E_M - E_g - E_g)}^{\text{process 3}} \qquad \text{(B.6)}$$

$$E_t = E_K - 3E_g. \qquad \text{(B.7)}$$

At this point there are three holes in the valence band of this atom. However, when the ejected electrons relax back to the Fermi sea, two of them are filled (gallium requires one less electron than germanium to be neutral) releasing the $2E_g$ of energy to the crystal. This gives the total energy released

$$E_t = E_K - E_g \qquad \text{(B.8)}$$

$$E_t \approx E_K. \qquad \text{(B.9)}$$

This very simple[1] argument demonstrates that it is reasonable to associate the full orbital binding energy of ^{71}Ga with the features observed in the energy spectrum following an electron-capture.[2]

One final comment should be made about a particular type of Auger-electron process. This sub-process, called a Coster-Kronig transition [422], is the process whereby the initial vacancy and the filling electron come from different sub-shells of the same shell, i.e. an inter shell transition which ejects on outer electron. This process is prominent in gallium for filling vacancies in the L shell and is treated along with the other Auger-e processes in the following discussion.

The lifetime $\tau(i)$ for filling a vacancy in the ith shell and the total natural width $\Gamma(i)$ of the associated feature are related by the uncertainty principle as

$$\Gamma(i)\tau(i) \sim \hbar. \qquad \text{(B.10)}$$

The lifetime can be calculated using the width, which is the sum of the x-ray (radiative) width $\Gamma_R(i)$ and the Auger-e width $\Gamma_A(i)$ (where $\Gamma_A(i)$ includes any Coster-Kronig

---

[1] Likely oversimplified if all lattice physics were to be considered.

[2] The band gap energy becomes significant if the initial vacancy is created in the outer M or N shells, but the probability for such captures is minimal and the features which would be created by them are below current detector thresholds. This subtlety will be ignored for now, though it may become important for future detectors with better resolution and thresholds.

effects). These natural widths have been measured for gallium [423], are of $\mathcal{O}\,(\text{eV})$, and give lifetimes of $\mathcal{O}\left(10^{-16}\text{ s}\right)$. For all practical purposes, the de-excitation of ^{71}Ga can be treated as instantaneous.

Characterizing the de-excitation of ^{71}Ga requires a large and complete set of parameters which have been theoretically predicted and/or measured over many years. A guide for what is required can be found in [424], from which the following discussion is based. The first parameter is the fluorescence yield $\omega_i = \Gamma_R(i)/\Gamma(i)$ which characterizes, for the ith shell, what percentage of vacancies lead to an x-ray emission. The Auger yield, the percentage of vacancies which lead to an Auger-e process, is $\Gamma_A(i)/\Gamma(i) = (1 - \omega_i) \equiv P(e_i)$. The other parameters indicate what type of x-ray or Auger-electron process occurs.

The nomenclature to describe these different processes is as follows. For x rays, a convention has been established to name specific transitions as shown in Fig. B.1. For an x ray which does not have a specific name, the two shell levels associated with the transition are given, i.e. $\Gamma(L_2 \to L_1)$ is the width of the x-ray resulting from an L_2 electron filling a vacancy in the L_1 shell. The naming convention for Auger-electron processes uses three letters which denote, in this order: the shell of the initial vacancy, the shell of the filling electron, and the shell of the ejected electron. If the shell is denoted as X or Y, it means an M- or N-shell electron, i.e. $P(KLX) = \Gamma\,(KLX)\,/\Gamma(K)$ is the probability of the process where a K-shell vacancy is filled by an L-shell electron and ejects a M- or N-shell electron.

B.2.1 K-Shell Vacancies

Five measurable ratios are used to characterize the K-shell vacancy-filling process

$$x \equiv P(K_\beta)/P(K_\alpha) \tag{B.11}$$

$$y \equiv P(K_{\alpha_2})/(K_{\alpha_1}) \tag{B.12}$$

$$r \equiv P\left(K'_{\beta_2}\right)/P\left(K'_{\beta_1}\right) \tag{B.13}$$

$$u \equiv P(KLX)/P(KLL) \tag{B.14}$$

$$v \equiv P(KXY)/P(KLL), \tag{B.15}$$
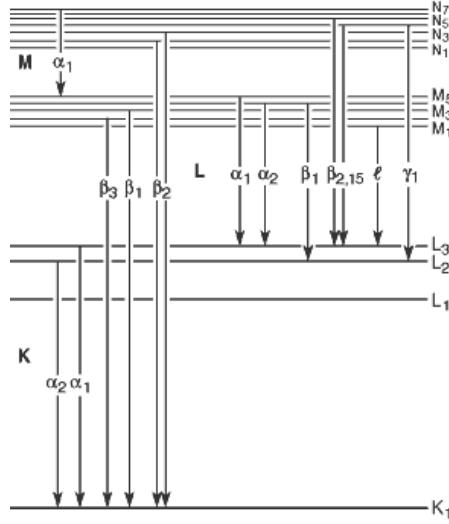
Figure B.1: Schematic of x-ray transitions along with the naming conventions used for each line. Figure from [421].

where $P(K_\alpha) = \sum_i P(K_{\alpha_i})$, $P(K_\beta) = \sum_i P(K_{\beta_i})$, $P\left(K'_{\beta_1}\right) = \sum_i P(M_i \to K)$, and $P\left(K'_{\beta_2}\right) = \sum_i P(N_i \to K)$. The values for ω_K, x, y, u, and v are found in [425], and the value for r is extrapolated from [426]. The resulting probabilities for different K-shell filling processes, along with their computation from these ratios and ω_K, are given in Table B.4.

Knowing where the new vacancies in the L, M, and N shells occur for the Auger-e processes is difficult, but can be characterized by a vacancy transfer function η_{ij}, where η_{ij} is the number of a vacancies created in the jth shell for every vacancy in the ith shell. As an example, consider η_{KL_2}, the number of vacancies created in the L_2 sub-shell by a vacancy in the K-shell, as

$$\eta_{KL_2} = \frac{\Gamma_R(L_2 \to K)}{\Gamma(K)} + \frac{2\Gamma_A(KL_2L_2) + \Gamma_A(KL_1L_2) + \Gamma_A(KL_2L_3) + \Gamma_A(KL_2X)}{\Gamma(K)}$$

(B.16)

$$\eta_{KL_2} = P(K_{\alpha_2}) + \eta^e_{KL_2},$$

(B.17)

where $\eta^e_{KL_2}$ is the number of vacancies created only by Auger-e processes. This gives

Process	Derivation	Energy [eV]	Probability [%]	New Vacancy
ω_K			51.70	
$P(K_\alpha)$	$\omega_K/(1+x)$		45.13	L
$P(K_{\alpha_1})$	$\omega_K/(1+y)$	9250.6	29.80	L_3
$P(K_{\alpha_2})$	$yP(K_{\alpha_1})$	9223.8	15.33	L_2
$P(K_\beta)$	$xP(K_\alpha)$		6.58	M or N
$P\left(K'_{\beta_1}\right)$	$P(K_\beta)/(1+r)$	10267.0/10263.5	6.54	M
$P\left(K'_{\beta_2}\right)$	$rP\left(K'_{\beta_1}\right)$	10365.5	0.03	N
$P(e_K)$	$(1-\omega_K)$		48.30	
$P(KLL)$	$P(e_K)/(1+u+v)$	155.8	36.81	$L_1,\ L_2$
$P(KLX)$	$uP(KLL)$	$\leq$9249.1	10.71	$L,\ M$ or N
$P(KXY)$	$vP(KLL)$	$\leq$10367.0	0.89	$2\times(M$ or $N)$

Table B.4: De-excitation probabilities and energies for a vacancy in the K shell of ^{71}Ga.

the number of vacancies created in the L_2 shell from Auger-e processes only as

$$\eta^e_{KL_2} = \eta_{KL_2} - P(K_{\alpha_2}).\tag{B.18}$$

Such Computations are also performed for vacancies created in the L_1, L_3, and M shells. Values for η_{Ki} are found in [427] and they, along with the computed values for η^e_{Ki}, are given in Table B.5.

Coefficient	Value	Coefficient	Value
η_{KL_1}	0.177	$\eta^e_{KL_1}$	0.177
η_{KL_2}	0.468	$\eta^e_{KL_2}$	0.315
η_{KL_3}	0.647	$\eta^e_{KL_3}$	0.349
η_{KM}	0.303	η^e_{KM}	0.237

Table B.5: Vacancy transfer coefficients, both total (left) and from only Auger-e processes (right), for a vacancy in the K shell. Values for the total coefficients are from [427].

Process	Derivation	Energy [eV]	Probability [%]	New Vacancy
ω_1			0.089	
$P(L_{\beta_3})$	$\omega_1 \cdot P(M_2)_1$	1195.5	0.031	M_2
$P(L_{\beta_4})$	$\omega_1 \cdot P(M_3)_1$	1199.0	0.057	M_3
$P(L_3 \rightarrow L_1)$	$\omega_1 \cdot P(L_3)_1$	182.6	0.001	L_3
$P(e_{L_1})$	$(1 - \omega_1)$		99.911	
$P(L_1 L_2 X)$	f_{12}	$\leq$155.8	20.500	L_2, M or N
$P(L_1 L_3 X)$	f_{13}	$\leq$182.6	72.600	L_3, M or N
$P(L_1 XY)$	$(P(e_{L_1}) - f_{12} - f_{13})$	$\leq$1299.0	6.811	$2\times(M$ or $N)$

Table B.6: De-excitation probabilities and energies for a vacancy in the L_1 shell of ^{71}Ga.

B.2.2 L- and Higher-Shell Vacancies

If a vacancy is present in one of the L sub-shells, calculations similar to that of the K shell can be performed. This is complicated, however, by the L shell having three sub-shells which must all be treated separately. There are three fluorescence yields ω_1, ω_2, and ω_3 for the L_1, L_2, and L_3 sub-shells respectively. There are also three Coster-Kronig probabilities f_{12}, f_{13}, and f_{23}, where f_{ij} indicates an Auger-e transfer from the L_i to the L_j sub-shell. Many x-ray transitions going to the L sub-shells are possible as indicated by Fig. B.1, all of which must be considered. Understanding how to fill one of the L-shell vacancies is complicated, but crucial since, in addition to the 10.5% of electrons which capture from the L-shell, many of the K-shell filling processes create an L-shell vacancy.

Values for the fluorescence yields and Coster-Kronig probabilities can be found in [428] and values for the x-ray widths can be found in [429]. The widths are used, with the fluorescence yields, to derive the probability for a given x-ray, i.e. $P(L_{\alpha_1}) = \omega_3 \cdot \Gamma(M_5 \rightarrow L_3)/\sum_i \Gamma(X_i \rightarrow L_3) \equiv \omega_3 \cdot P(M_5)_3$. The probabilities for filling L-shell vacancies are given in Tables B.6–B.8 for the L_1–L_3 sub-shells respectively. In the tables, a $\leq$ sign indicates that the exact energy of the process cannot be given, due to the participation of X and Y electrons, and the listed amount is available.

The vacancy transfer coefficients $\eta_{L_i M}$ for transferring a vacancy from an L_i shell

Process	Derivation	Energy [eV]	Probability [%]	New Vacancy
ω_2			1.220	
$P(L_\eta)$	$\omega_2 \cdot P(M_1)_2$	983.7	0.064	M_1
$P(L_{\beta_1})$	$\omega_2 \cdot P(M_4)_2$	1124.5	1.152	M_4
$P(L_{\gamma_5})$	$\omega_2 \cdot P(N_1)_2$	1141.7	0.005	N_1
$P(e_{L_2})$	$(1 - \omega_2)$		98.780	
$P(L_2 L_3 X)$	f_{23}	≤ 26.8	2.600	L_3, M or N
$P(L_2 XY)$	$(P(e_{L_2}) - f_{23})$	≤ 1143.2	96.180	$2\times(M$ or $N)$

Table B.7: De-excitation probabilities and energies for a vacancy in the L_2 shell of ^{71}Ga.

Process	Derivation	Energy [eV]	Probability [%]	New Vacancy
ω_3			1.180	
$P(L_\ell)$	$\omega_3 \cdot P(M_1)_3$	959.9	0.055	M_1
$P(L_{\alpha_2})$	$\omega_3 \cdot P(M_4)_3$	1097.7	0.115	M_4
$P(L_{\alpha_1})$	$\omega_3 \cdot P(M_5)_3$	1097.7	1.006	N_1
$P(L_{\beta_6})$	$\omega_3 \cdot P(N_1)_3$	1114.9	0.009	N_1
$P(e_{L_3})$	$(1 - \omega_3)$		98.820	
$P(L_3 XY)$	$P(e_{L_3})$	≤ 1116.4	98.820	$2\times(M$ or $N)$

Table B.8: De-excitation probabilities and energies for a vacancy in the L_3 shell of ^{71}Ga.

Coefficient	Value	Coefficient	Value
$\eta_{L_1 M}$	1.030	$\eta^e_{L_1 M}$	1.029
$\eta_{L_2 M}$	1.944	$\eta^e_{L_2 M}$	1.932
$\eta_{L_3 M}$	1.984	$\eta^e_{L_3 M}$	1.973

Table B.9: Vacancy transfer coefficients, both total (left) and from only Auger-e processes (right), for a vacancy in the L shell. Values for the total coefficients are from [427].

to the M shell can also be considered. These, along with the $\eta^e_{L_i M}$ transfer coefficients from only Auger-e processes are defined in the same manner as Eq. B.18. These values are given in Table B.9.

After the K- and L-shell de-excitations, vacancies are left in the M or N shells, where the data and theory are scarce for such a low atomic number. For the M shell, the average (between all sub-shells) fluorescence yield $\omega_M = 1.35 \times 10^{-4}$ has at least been measured and fit in [430]. This means that an M-shell vacancy will be filled by an Auger-e >98% of the time and, for the purposes here, 100% is assumed.

For the energy levels of the M and N shells, what type of radiation is generated in the de-excitation is effectively non-consequential. The reason for this is that the path-length for both x rays and electrons at these energies is so small ($\mathcal{O}\left(10 \text{ nm}\right)$ for $\sim$100 eV photons [421]) that neither will escape the detector and any energy deposition will appear the same. Considering that the cascades given in Tables B.4 and B.6–B.8 mostly end with these low energy interactions, and that the time-scale for the de-excitation is nearly-instantaneous, the low-energy part of the cascade will appear the same in a SuperCDMS detector, regardless of whether it is an x ray or an Auger-e.

A general summarization table, which combines the information in Table B.2 with that of Tables B.4–B.8, is given in Table B.10. In the summary table, the word "cascade" is used to indicate where the vacancy has shifted to and information on the new vacancy's de-excitation needs to be considered. Typically more information should be sought in the detailed de-excitation and vacancy transfer coefficient tables to completely understand what occurs during such a cascade. Also, for uncommon processes which have more than one sub-processes, i.e. K_β, the sub-process which gives the most energy to the first x ray/Auger-e is given. It is not possible to indicate the exact energy for each entry

in the table, due to summarizing multiple processes or Auger-e possibilities, and such instances are indicated with a $\leq$ sign in the table meaning that this amount of energy is available for the resulting processes.

Capture Shell	Capture Probability [%]	Decay Product	Decay Probability [%]	Decay Energy [keV]
K	87.57	Auger-e + $2 \times L$-cascade	32.23	$\leq$10.367
		K_{α_1} x ray + L_3-cascade	26.10	$9.250 + 1.116$
		K_{α_2} x ray + L_2-cascade	13.42	$9.224 + 1.143$
		Auger-e + $(L- + X-)$cascade	9.38	$\leq$9.249
		K_β x ray + X-cascade	5.76	$10.267 + 0.100$
L_1	10.43	Auger-e + L_3-cascade	7.57	$0.183 + 1.119$
		Auger-e + L_2-cascade	2.14	$0.156 + 1.143$
		Auger-e + $2 \times X$-cascade	0.71	$\leq$1.299
		L_β x ray + X-cascade	0.01	$1.199 + 0.100$
L_2	0.10	$2 \times X$-cascade	0.10	$\leq$1.143
M	1.78	Auger-e-cascade	1.78	0.160
N	0.14	Auger-e-cascade	0.14	0.002

Table B.10: Summary of the decay products for a single electron capture of ^{71}Ge including the resulting ^{71}Ga de-excitation. Capture probabilities are taken from Table B.2. Decay (de-excitation) products, energy, and probabilities are summarized from Table B.4 and Tables B.6–B.7. A "cascade" indicates where the vacancy has shifted to and information for the new vacancy's de-excitation should be sought in the detailed tables already listed as well as Tables B.5 and B.9. An "X-cascade" means the vacancy shifted to the M or N shells, which decay almost exclusively by Auger-e emission. A $\leq$ sign in the energy column indicates multiple energy configurations, all of which add up to the given available energy, depending upon which Auger-e process occurs, again see the detailed tables for these possibilities.

Appendix C

Correlated Noise Score Development

In order to assist in the understanding and removal of low-frequency noise (LF-noise) in the CDMSlite Run 2 analysis, vibrational noise monitors were installed in Soudan (Sec. 9.3). The output from those monitors is utilized in the analysis through a correlated noise score (Sec. 11.3.2). The purpose of this appendix is to detail the theoretical development of this score, and demonstrate its uses in removing LF-noise. The development proceeded in two major steps, starting with a one-dimensional score which was subsequently generalized to two-dimensions as described below. The one-dimensional score was initially developed by R. Basu Thakur [336–338, 431, 432], who was also instrumental to the creation of the SuperCDMS noise-monitoring program.

C.1   One-Dimensional Score

In this appendix, the score is developed based on a set of fake data which demonstrates the primary characteristics which the score should identify. This fake data is shown in Fig. C.1. Some variable, call it E, is measured as a function of a time. Different behavior in E is seen at different times. There is a baseline width in E with both short- and long-term fluctuations. The desired property of the final score is to identify correlated, in time, fluctuations in E. Thus the shorter bursts early and later in time should score similar to the baseline (low), while the extended burst in the middle of the data should
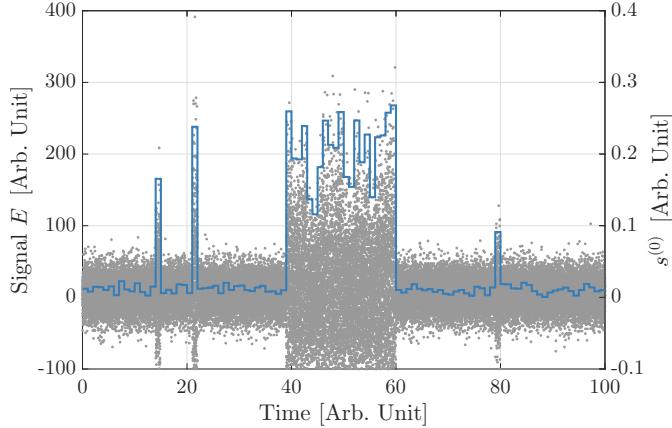
Figure C.1: Fake data, with signal E, (grey points on left vertical axis) generated to test and develop a correlated noise score. The first iteration of this score $s^{(0)}$ (blue line on right vertical axis) considers, in each time bin, what percentage of the E distribution is above the baseline distribution.

score poorly (high).

An initial score $s^{(0)}$ is developed which measures how high above baseline each portion of time is. The baseline is defined by taking an identified "good" period in time and determining the $\mu + n\sigma$ point of the corresponding PDF in E. In practice, μ and σ are found through an iterative procedure which removes outliers of the distribution. For this test data, the full time range is split into bins and the baseline E_b is computed as the $\mu + 2\sigma$ point of the data within the first five time bins. For the kth bin, $s_k^{(0)}$ is then defined as

$$s_k^{(0)} = \int_{E_b}^{\infty} \text{PDF}_k(E) = 1 - \text{CDF}_k(E_b), \tag{C.1}$$

where $\text{PDF}_k(E)$ and $\text{CDF}_k(E)$ are PDF and CDF in E of that bin. Note that although the test data has similar μ_k for each bin, thus giving higher scores to those bins with broader σ_k, the score will also give poor values for a distribution with an elevated μ_k. This initial score is, for each bin, given in Fig. C.1 as the blue line. The score tracks the behavior of the population in a linear fashion.

In addition to identifying fluctuations in E, it is desired that the score differentiate between uncorrelated and correlated fluctuations; something not accomplished by $s^{(0)}$ alone. To achieve this, corrections are made to $s^{(0)}$ based upon the score values in neighboring bins.

The first step in the correction process is to define a new score $s^{(1)}$, which is a

geometric mean of the N previous bins, as

$$s_k^{(1)} = \left(\prod_{d=0}^{N-1} s_{k-d}^{(0)} \right)^{1/N} .$$

(C.2)

Assuming that the cause of the correlated noise has a finite injection window, the $k-1$ bin should exert a stronger influence on the kth bin than the $k-3$ or earlier bins. Conversely, in the $s^{(1)}$ metric, every bin has the same effect. This is adjusted by defining a distance-dependent weight $0 \leq w_d \leq 1$ for each bin. The weight is higher for greater d, i.e. since $s_{k-d}^{(0)} \leq 1$, correcting it upwards, closer to unity, decreases its effect on the kth bin. This weighted score $s^{(2)}$ is then defined as

$$s_k^{(2)} = \left(\prod_{d=0}^{N-1} \left(s_{k-d}^{(0)} \right)^{w_d} \right)^{1/\sum_{d=0}^{N-1} w_d} .$$

(C.3)

An expression for the weight w_d can be gleaned by noticing that $\ln s^{(n)}$ resembles a digital low-pass filter. Such a filter is described by the recurrence relation

$$y_i = \alpha x_i + (1 - \alpha) y_{i-1},$$

(C.4)

where x_i/y_i are the ith input/output respectively. The weight parameter is related to the configuration of the filter as $\alpha = 1/(1 + RCf_s)$ where R, C, and f_s are the resistance, capacitance, and sampling frequency of the filter circuit respectively. Comparing this to

$$\ln \left(s_k^{(2)} \right) \propto w_0 \ln \left(s_k^{(2)} \right) + \sum_{d=1}^{N} w_d \ln \left(s_{k-d}^{(2)} \right),$$

(C.5)

leads to the inspiration for $s^{(2)}$ of $w_d = (1 - \alpha)^d$, where $0 \leq \alpha \leq 1$ is now a free parameter and d accounts for the fact that multiple bins are weighted over. As $\alpha \to 0$, $s^{(2)} \to s^{(1)}$ while as $\alpha \to 1$, $s^{(2)} \to s^{(0)}$. The analogy is not perfect, as $w_0 = 1$ instead of α, but the desired effect is the true goal, which is accomplished.

The initial and first two orders of corrections to the score are shown in Fig. C.2, where $s^{(2)}$ is given for $\alpha = 0.5$. Each score is corrected over the previous $N = 3$ bins. In considering the $s^{(2)}$ curve, the second-order score is shifted with respect to the actual
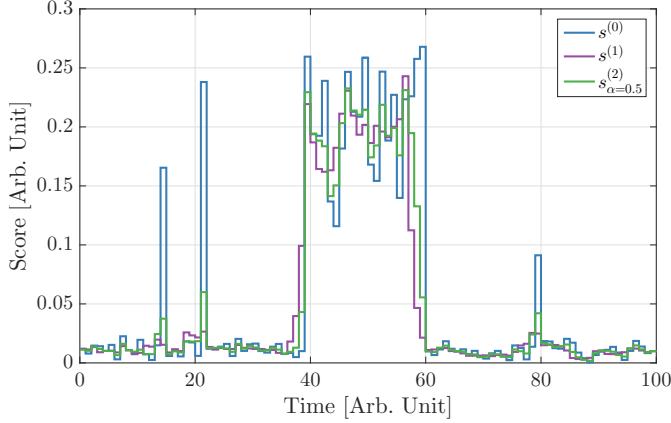
Figure C.2: Uncorrected score $s^{(0)}$ (blue) and the first two iterations of corrections $s^{(1)}$ (purple), $s^{(2)}$ (green). For the second-order score, the shaping parameter is set as $\alpha = 0.5$. Note that as $\alpha \to 0$, $s^{(2)} \to s^{(1)}$ and as $\alpha \to 1$, $s^{(2)} \to s^{(0)}$.

fluctuations, as given by the uncorrected score. This is because the correction only considers one temporal direction, i.e. the past. Whether the fluctuation continues into the future should also be considered to accurately score the fluctuations.

To account for the future duration of a fluctuation, the score is a-causally extended, i.e. correcting for neighboring bins on either side, as

$$s_k^{(3)} = \left[\left(\prod_{d=-N}^{-1} \left(s_{k-d}^{(0)} \right)^{w_d} \right) \left(s_k^{(0)} \right) \left(\prod_{d=1}^{N} \left(s_{k+d}^{(0)} \right)^{w_d} \right) \right]^{1/\sum_{d=-N}^{N} w_d}. \tag{C.6}$$

This final, third-order, corrected score is shown in Fig. C.3 for a collection of α values. The zeroth-order score is still recovered for $\alpha \to 1$ while for $\alpha \to 0$, an a-causally extended version of $s^{(1)}$ is found. From the scan of α presented here, a reasonable value of $\alpha = 0.2$ is chosen such that the correlated burst is scored high while the uncorrelated fluctuations are scored low. Given that varying α adjusts how rounded the score is for a burst, α is also referred to as the shaping parameter.

The number of bins over which to correlate has, to this point, been taken as $N = 3$ somewhat arbitrarily. A scan over $N \in \{0, 1, 2, 3, 4, 5\}$ is shown in Fig. C.4. From this scan, $N = 3$ still appears reasonable and is carried forward as the correlation size.

With the satisfactory correlated-noise score $s^{(3)}(E, t; N = 3, \alpha = 0.2)$ developed on test data, its behavior on real data is next considered. For SuperCDMS, and CDMSlite Run 2 in particular, this score is used to identified LF-noise associated with the cryocooler. The timing quantity is $\hat{t}_-$, which is the time during the cryocooler's $t_c = 0.83$ s
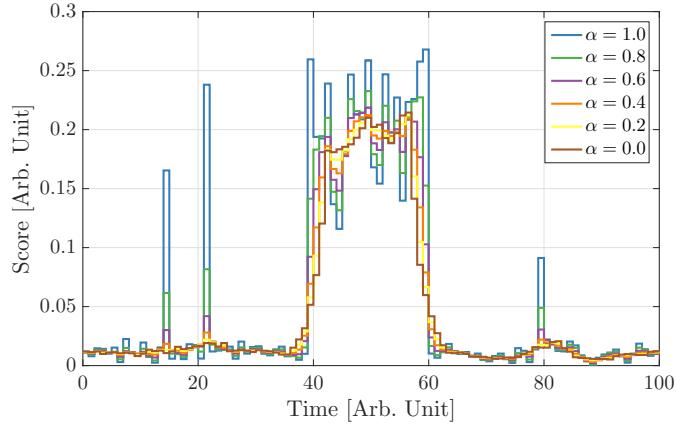
Figure C.3: A-causal correlated score $s^{(3)}$ for various shaping parameters α compared to the initial score (blue line). $\alpha = 0.2$ is chosen as a reasonable parameter value which identifies correlated noise while ignoring fluctuations.
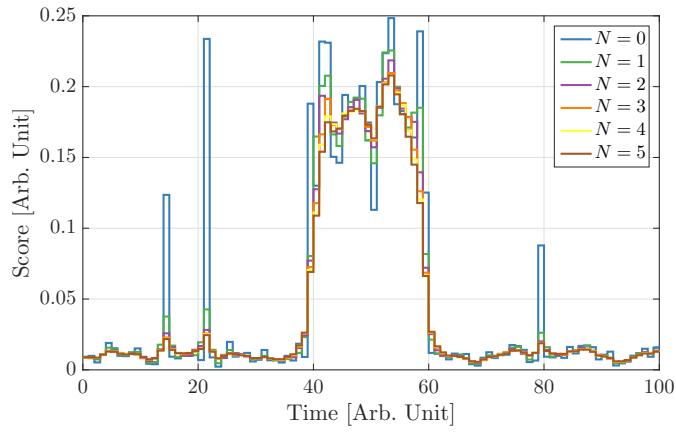

Figure C.4: A-causal correlated score $s^{(3)}$ correlated over various number of bins N compared to the initial score (blue line). $N = 3$ is chosen as a reasonable parameter value which identifies correlated noise while ignoring fluctuations.
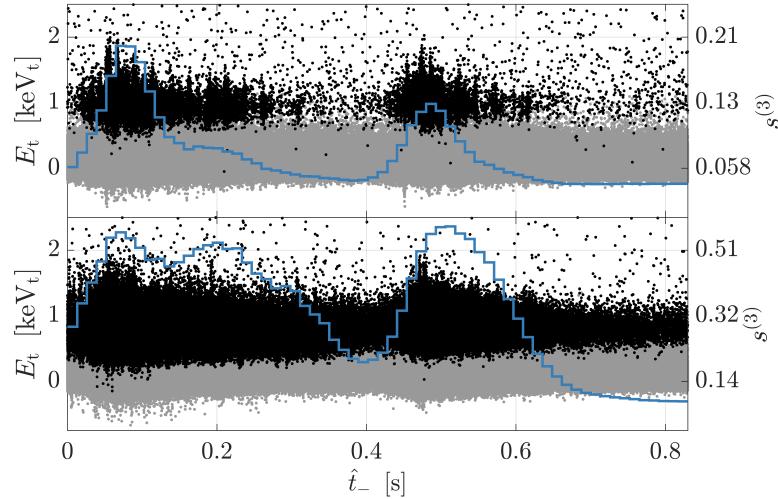
Figure C.5: Time since the start of the cryocooler cycle $\hat{t}_-$ compared to total phonon energy for the early (top) and late (bottom) parts of Run 2a (gray points, left vertical axis) and the correlated noise score $s^{(3)}$ (blue line, right axis). Triggering events are highlighted in black. Two high scoring noise fluctuations are seen due to the LF-noise (populations at $\sim$1 keV$_t$) in the early portion of the run. The later portion has induced LF-noise throughout the cryocooler cycle. Note also the difference in magnitude of $s^{(3)}$ between the periods.

cycle at which a given event triggered in the detector. The E variable is the total phonon energy, using the OF algorithm. The data for the early months of CDMSlite Run 2a, along with the $s^{(3)}$ score, are given in the top panel of Fig. C.5. The baseline is identified as the quiet periods of $\hat{t}_- \in [0.25, 0.45] \vee [0.65, 0.83]$ s. The two high-scoring regions are termed the "chirp" ($\sim$0.15 s) and the "thump" ($\sim$0.55 s).

The cryocooler degraded during Run 2a, resulting in increased LF-noise triggers. This is evident in examining the noise score as well. The data and score for the latter portion of Run 2a are given in the bottom panel of Fig. C.5. LF-noise is more prominent, occurring throughout more of the cryocooler's cycle. The baseline period used for this score is $\hat{t}_- \in [0.65, 0.83]$ s. The initial goal of such a score was to define a cut threshold η such that portions of the cryocooler cycle where $s^{(3)} > \eta$ would be removed as a live-time cut. However, given the change in cryocooler behavior during the run, defining a single score and η is no longer feasible.
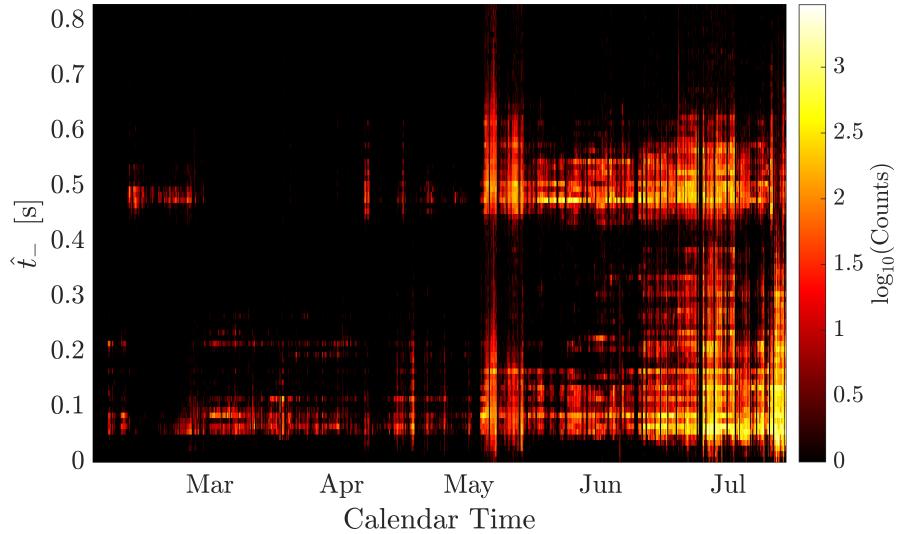
Figure C.6: Number of triggered events, near the noise, for Run 2a in the two-dimensional plane of cryocooler time, $\hat{t}_-$, and calendar time. The color scale is logarithmic with empty bins mapped to the lowest color. The thump and chirp identified in the one-dimensional plane can be seen as horizontal bands near $\hat{t}_- \sim 0.15, 0.55$ s.

C.2   Two-Dimensional Score

A new score is developed which naturally accounts for variation during the run by correlating in two dimensions: cryocooler time and calendar time. This two-dimensional plane can be seen in Fig. C.6, where the color scale gives the number of triggered events, near the noise, in each bin. The chirp and thump are identifiable as horizontal bands in cryocooler time. Importantly, notice that the rate of LF-noise injection during this cryocooler's period is not constant throughout the run. Noticeably, the thump fades in and out with calendar time and the overall deterioration is evident in late May and June.

The new score is defined directly in this plane. Since the primary quantity used in identifying noise is now a counting variable, using a Poisson distribution to define the zeroth-order score, as below, is reasonable

$$s^{(0)} = \mathrm{CDF}_{\mathrm{Poiss}}(n; \xi), \tag{C.7}$$

where n is the number of counts in each time bin and ξ is a filter parameter to be tuned.
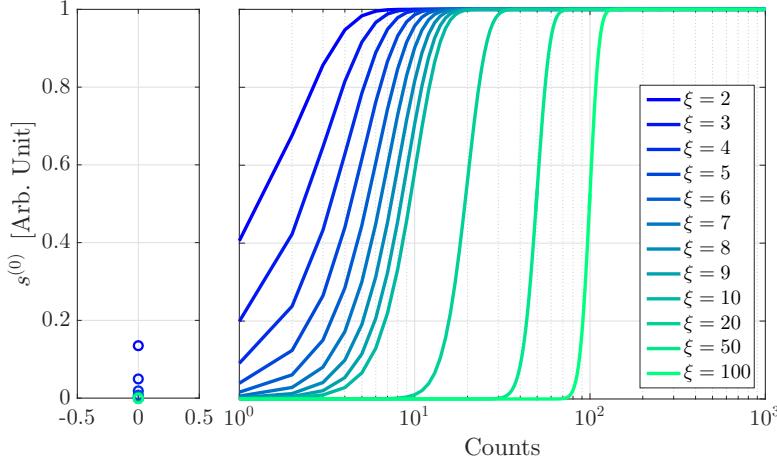
Figure C.7: Initial two-dimensional noise score for various values of counts n and filter parameters ξ. The right panel has a logarithmic horizontal score while the left panel shows the value at zero counts. Each score saturations to unity above some value of n.

The value of this score over a range of n and ξ values is given in Fig. C.7. These curves are just Poisson CDFs of mean ξ. Each score saturates to unity above some value of n. For high enough ξ, the score also tends to zero for low enough n.

Care is required when defining a quantity directly on the number of counts since fluctuations of the true background can occur and should not be treated as LF-noise. To verify that the features in the 2D plane are not true background fluctuations, the expected rate per bin is computed. The triggered event rate between the L- and K-shell activation peaks (1.4–10 keV$_{\text{ee}}$), after applying all cuts defined prior to the LF-noise cut, is $\langle \mathrm{d}R/\mathrm{d}E_{\text{ee}} \rangle = 4.57 \pm 0.09$ kg^{-1} day^{-1} keV$_{\text{ee}}^{-1}$. The expected number of counts per bin in Fig. 11.11 is

$$\langle n \rangle = \left\langle \frac{\mathrm{d}R}{\mathrm{d}E_{\text{ee}}} \right\rangle m \Delta T \Delta E \frac{\Delta t}{t_c} \tag{C.8}$$
$$= (4.66 \pm 0.01) \times 10^{-3},$$

where $m = 0.6065$ kg is the mass of the detector, ΔT is the calendar-time bin size, ΔE is the energy range of interest, and Δt is the $\hat{t}_-$ bin size. For a Poisson process with a mean of $\langle n \rangle$, the probability of having 2 counts is at the 6σ level: bins with $> \mathcal{O}(10\text{–}100)$ counts are not caused by background fluctuations. Distinguishing between the highest count bins is less important than distinguishing between the lower counts bins which motivates using lower values of ξ.

Choosing $\xi = 3$ by eye from Fig. C.7, using the above logic, and applying this metric
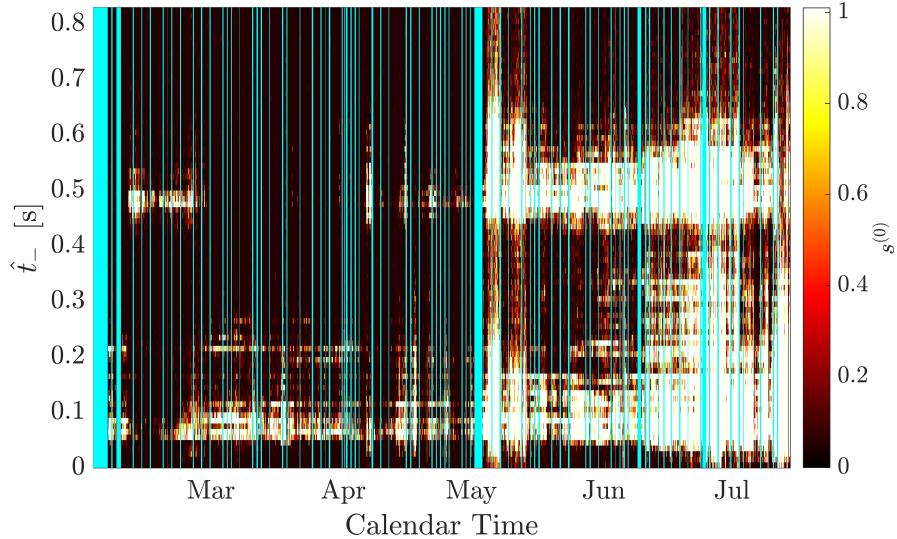
Figure C.8: Zeroth-order two-dimensional noise score $s^{(0)}$ with filter parameter $\xi = 3$ for Run 2a (color scale). Bins in calendar time are 1.2 hr while bins in cryocooler time $\hat{t}_-$ are 0.01 s. Periods of dead time are highlighted in cyan.

to the full two-dimensional plane, gives Fig. C.8. True fluctuations are seen in addition to the extremely noisy periods which saturate the score. Periods when the experiment was not taking data (dead time) are shown in cyan. These periods were for taking calibration data.

The correlation method in the two-dimensional plane is a natural extension of the one-dimensional score following Eq. C.6 which, for the i, j bin, is

$$s_{ij}^{(3)} = \left(\prod_{m=i-N}^{i+N} \prod_{n=j-N}^{j+N} \left(s_{ij}^{(0)} \right)^{w_d(i,j;m,n)} \right)^{1/\sum_{m,n} w_d}, \tag{C.9}$$

where N, α, and $w_d = (1 - \alpha)^d$ are again the number of bins to correlate over, the shaping parameter, and the weight at distance d, where that distance is now defined as $d = \sqrt{(i-m)^2 + (j-n)^2}$. There are several variables used by the score which need to be selected and optimized, if possible. $N = 3$ and $\alpha = 0.2$ are kept from the one-dimensional scans done in Figs. C.4 and C.3. Dead time should not be used in the score correlation, as it would artificially lower the scores around it, so the calendar time bins are taken as 1.2 hr so as to be able to identify single calibration series (typically

of length 3 hr). The binning in cryocooler time is essentially arbitrary as long as the thump and chirp are resolved and not influencing each other. Here it is taken as 0.01 s. A value of ξ is found by scanning various values as in Fig. C.9. $\xi = 3$ is kept as a reasonable filter parameter.

The two-dimensional correlated score in the full time-time plane, using the above parameter values, is shown in Fig. C.10. The thump and chirp are still identifiable and the extremely-high trigger periods at the end of the run are seen as well.

Defining a cut threshold η on the noise score is difficult. Four methods were investigated to simultaneously optimize η and ξ. Note that a full optimization would also include α, N, and possibly the size of time bins. However, given the soon-to-be-apparent difficulty in the simpler optimization, such a full optimization was not attempted. The four methods used were:

By Eye: This uses the already described method of scanning the parameter space and picking a "reasonable" choice.

Noise Distribution Ratio: This method attempts to minimize the number of events in the LF-noise distribution above a certain threshold while maximizing the live time kept by the cut. This (rather ad hoc) ratio is

$$R = \frac{\frac{\text{sum}(1.5 < E_\text{t} < 2)}{\text{sum}(-0.5 < E_\text{t} < 2)}}{\epsilon}, \tag{C.10}$$

where energies are in keV_t, E_t is found via the OF fit, and ϵ is the percentage of live time remaining after the cut.

Poisson Sensitivity: The most physically motivated optimization is on WIMP sensitivity. The Poisson sensitivity is considered using four WIMP masses $m_\text{WIMP} \in \{5, 7, 10, 15\}$ GeV/c^2. The optimized score and cut for the ith mass is that which minimizing the cross section

$$\sigma_i = \frac{\left\{\mu : \int_0^\mu \frac{t^n}{n!} \, \text{d}t = 0.9\right\}}{\mathcal{M}\mathcal{T}\epsilon \left(\int \frac{\text{d}R}{\text{d}t}(m_i, \sigma_0) \, \text{d}E\right)/\sigma_0}, \tag{C.11}$$

where $\mathcal{M}$ is the detector mass, $\mathcal{T}$ is the total live time, ϵ is again the fraction of remaining live time after the cut, and the term in parenthesis in the denominator
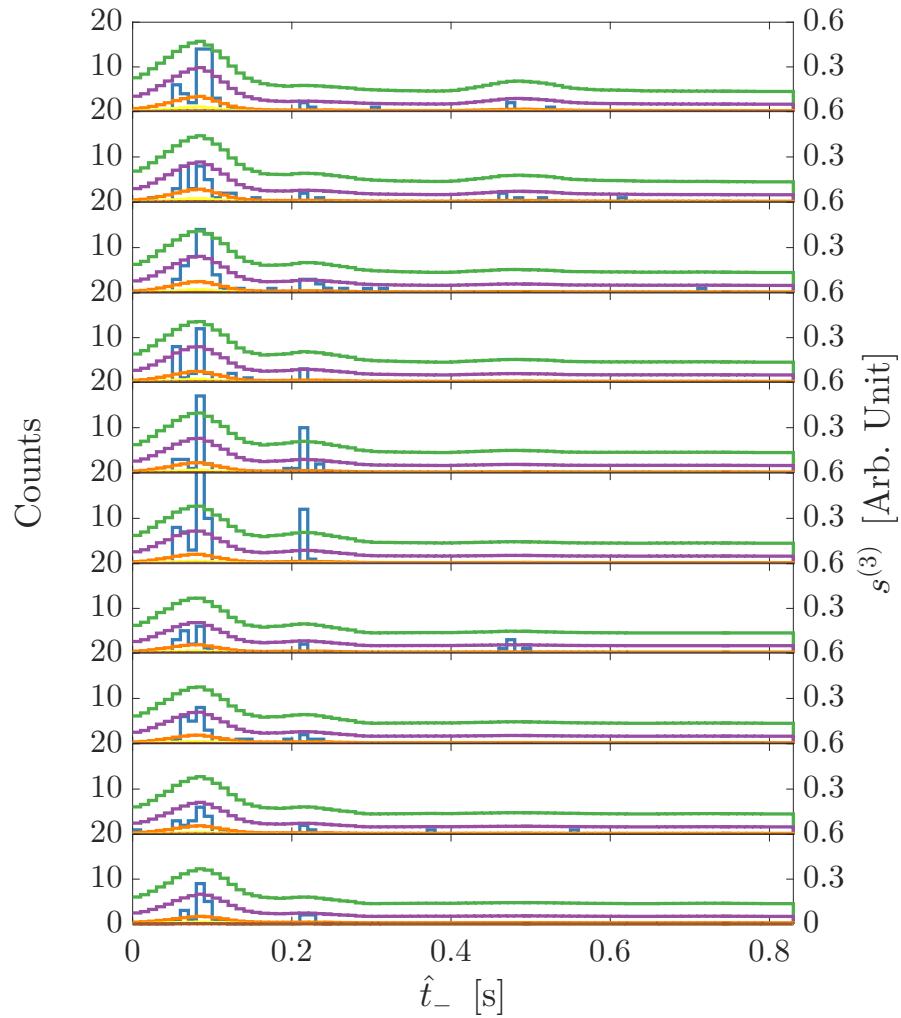
Figure C.9: Triggered events (blue, left vertical axis) and two-dimensional correlated score (right vertical axis) as a function of cryocooler time $\hat{t}_-$ for various values of the filter parameter ξ ($\xi = 2, 3, 4, 5$ as green, purple, orange, yellow, brown respectively) for ten consecutive calendar time bins. The score correlates in cryocooler time (left-right within a row) and calendar time (up-down between rows). A value of $\xi = 3$ is seen as reasonable.
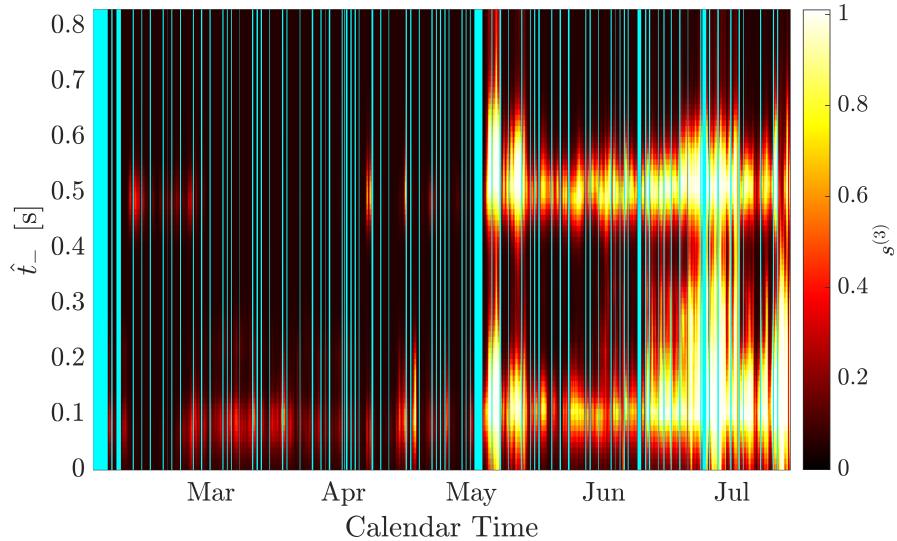
Figure C.10: Final a-causal correlated two-dimensional noise score $s^{(3)}$ with filter parameter $\xi = 3$ and shaping parameter $\alpha = 0.2$ for Run 2a. Scores are correlated over $N = 3$ bins in each direction. Bins in calendar time are 1.2 hr while bins in cryocooler time $\hat{t}_-$ are 0.01 s. Periods of dead time are highlighted in cyan.

is the integrated WIMP rate for the giving mass m_i and dummy cross section σ_0 (which is then divided out).

$\Delta\chi^2_{\text{LF}}$ **Hybrid:** This method attempts to minimize the number of events identified as LF-noise in the $\Delta\chi^2_{\text{LF}}$ plane (see Sec. 11.3.2) and above some threshold in addition to maximizing live time. The (ad hoc) function to be minimized is

$$\delta = \text{sum}\big(E_{\text{t}} > 1.5 \wedge \Delta\chi^2_{\text{LF}} > -25\big) + 1/\epsilon, \tag{C.12}$$

where E_{t} and ϵ are defined above.

The optimization results for each method are given in Table C.1. Each method gives a value of $\xi = 2\text{–}3$ with an apparent anti-correlation with the cut value η. The by-eye method is inherently biased and rejected. The noise distribution ratio is too ad hoc and not to be trusted. The sensitivity method, which has the best physical motivation, provides a biased result as it selects only live time with no events present (a full optimal interval calculation could perhaps alleviate this) and is rejected. The hybrid method is promising, but would require complicated live time-efficiency calculations to use.

Method	ξ	η	Optimization Value	Comments
By Eye	3	0.054	N/A	Inherentley biased
Noise Distribution Ratio	2.4	0.098	$R = 3.3 \times 10^{-6}$	Ad hoc, unjustified
Poisson Sensitivity	2.5	0.085	$\sigma_5 = 7.1 \times 10^{-50}$ cm^2	Biased in picking event free times.
$\Delta\chi^2_{\mathrm{LF}}$ Hybrid	2	0.14	$\delta = 2.4$	Ad hock, complicated efficiency calculation.

Table C.1: Summary of two-dimensional correlated noise score optimization methods and results. All methods yield $\xi = 2$–3 with an apparent anti-correlation with the cut position η.

None of the attempted optimization methods were promising and this led to the abandonment of a pure score-based cut. Instead, the development shifted to the determination of time blocks based on the score (Sec. 11.3.2) and a pulse-shape-based cut (Sec. 11.3.2).